Mixed Formulations to Alleviate Locking in Finite Element Analysis and Isogeometric Analysis

A thesis
submitted in partial fulfillment of the requirements
for the degree of
Doctor of Philosophy
by

Dhiraj Sanghavijay Bombarde
(Reg. no.: 176103023)

Supervisors:

Dr. Arup Nandy
and
Dr. Sachin Singh Gautam

Department of Mechanical Engineering
Indian Institute of Technology Guwahati
Assam 781039, India
June 10, 2024

Dedicated to my late father, Sanghavijay T. Bombarde, whose unwavering
support and affection during his lifetime continue to inspire me, and
to my ever-loving mother and wife, Babita and Pooja, for being my stars in every dusk and shine.


भारतीय प्रौद्योगिकी संस्थान गुवाहाटी
Indian Institute of Technology Guwahati

Declaration

I hereby declare that the information presented in the thesis titled **"Mixed Formulations to Alleviate Locking in Finite Element Analysis and Isogeometric Analysis"** is entirely my account of the research performed under the guidance of **Dr. Arup Nandy** and **Dr. Sachin S. Gautam**. I affirm that none of the information within this thesis has been previously submitted for the purpose of obtaining any academic degree, diploma, associateship, fellowship, or any equivalent recognition from any other university or institution. Furthermore, I have complied with all copyright and plagiarism regulations, and all text and figures included in this work are my original contributions. In line with the general practice of reporting scientific observations, appropriate acknowledgments or citations have been included wherever the work described is based on the discoveries of fellow researchers.

Date:

Dhiraj S. Bombarde
Department of Mechanical Engineering,
Indian Institute of Technology Guwahati, India.
✉ dhira176103023@iitg.ac.in
🌐 Google Scholar || ResearchGate || LinkedIn

Certificate

This is to certify that the work contained in thesis titled **"Mixed Formulations to Alleviate Locking in Finite Element Analysis and Isogeometric Analysis"**, submitted by **Dhiraj S. Bombarde** to the Indian Institute of Technology Guwahati, for the award of the Doctor of Philosophy degree in Mechanical Engineering, has been conducted under my direct supervision. The findings and results presented in this thesis have not been, either in whole or in part, presented to or considered for the conferral of any other academic degree or certification from any other university or institution.

Date:

Dr. Arup Nandy
Department of Mechanical Engineering,
Indian Institute of Technology Guwahati,
Guwahati 781039, Assam, India.
✉ arupn@iitg.ac.in
🌐 `https://www.iitg.ac.in/arupn/`

Dr. Sachin S. Gautam
Department of Mechanical Engineering,
Indian Institute of Technology Guwahati,
Guwahati 781039, Assam, India.
✉ ssg@iitg.ac.in
🌐 `https://www.iitg.ac.in/ssg/`

Acknowledgment

I extend my heartfelt gratitude to everyone who, in various ways, supported me through this exhilarating, challenging, and uniquely transformative journey of pursuing a Ph.D.

First and foremost, I extend my deepest gratitude to my supervisors, Dr. Arup Nandy and Dr. Sachin Singh Gautam. Throughout this journey, they have consistently supported me by demonstrating patience during challenging times, actively engaging in frequent discussions, providing invaluable suggestions, introducing new pathways for progress, and instilling faith and motivation in me. I sincerely appreciate their unparalleled commitment to their roles. I feel fortunate to have their guidance and am deeply honored to be their student.

I would also like to express my sincere gratitude to Dr. Manish Agrawal from IIT Ropar, India. While we connected later in the journey, he became an unofficial supervisor to me. His insights have undoubtedly enhanced the current work and facilitated my learning and growth throughout the process. There has never been a dull moment when working with him. He consistently encouraged and motivated me to reach new heights.

Furthermore, I extend my gratitude to my doctoral committee members, Dr. Debabrata Chakraborty, Dr. Atanu Banerjee, and Dr. Mahima Aarrawatia, for their valuable suggestions and insightful perspectives throughout the entire journey. Their constructive inputs have greatly benefited the enrichment of the research work.

I am grateful for the financial assistance provided through the MHRD fellowship during my tenure as a Ph.D. scholar. Further, I appreciate the support from SERB, DST under the projects IMP/2019/000276 and CRG/2022/002218.

I also want to thank all my friends, colleagues, and the connections I made during my Ph.D. Each one has played a special part in this journey in their own unique way. I extend my heartfelt gratitude to my lifelong friends, who have walked beside me throughout the years. In the life's bustling pace, our exchanges may be scarce. However, I place my trust in each of them, knowing they will stand by me whenever I call upon them.

Lastly, but most importantly, I owe my deepest gratitude to my late father, who may no longer be with us, yet whose memories continue to inspire me. To my mother, for her unwavering love and support throughout life's journey. To my sister, who has been there and taken on responsibilities in my absence. To my beloved wife, for standing by me through every rise and fall, and for her ever-motivating words, 'When will you finish your Ph.D.?' Lastly, to the newest addition, my little daughter. Though her first complete word was 'apple' instead of 'papa' or 'mama', I am certain her love for me exceeds than that of an apple.

Date:

Dhiraj S. Bombarde
Department of Mechanical Engineering,
Indian Institute of Technology Guwahati, India.
✉ dhira176103023@iitg.ac.in
🌐 Google Scholar || ResearchGate || LinkedIn

Abstract

The present work addresses locking in conventional finite element analysis (FEA) and isogeometric analysis (IGA) by proposing novel strategies to mitigate the issue. It begins with a comparative evaluation of various locking alleviation techniques, focusing on parameters such as accuracy, robustness, and efficiency. The work provides an elaborate understanding of the relative accuracies of individual methods, the shortcomings of the available strategies, and the key parameters influencing the selection of a particular method. The study then proposes several novel enhanced assumed strain (EAS) elements, effectively alleviating locking in FEA and thereby significantly improving the applicability of EAS elements in the FEA community. The work further explores the issue of locking in IGA, proposing effective alleviation strategies that demonstrate superior accuracy on coarse meshes, eliminate stress oscillations, and ensure overall stability throughout the analysis. Notably, the work proposes a family of stress-based solid hybrid elements to alleviate locking in non-uniform rational B-spline (NURBS)-based IGA marking a progressive development in enhancing the utility of IGA. Lastly, the present work develops strain-based solid EAS elements tailored for NURBS-based IGA, expanding their potential within the computational mechanics community.

Contents

List of Figures

List of Tables

Nomenclature

Acronyms/Abbreviations

2D	Two-dimensional
3D	Three-dimensional
ANS	Assumed natural strain
BEM	Boundary element method
CAD	Computer-aided design
CAE	Computer-aided engineering
DOFs	Degrees of freedom
EAS	Enhanced assumed strain
FEA	Finite element analysis
HR	Hellinger–Reissner
IGA	Isogeometric analysis
MITC	Mixed interpolation of tensorial components
NURBS	Non-uniform rational B-splines
PDEs	Partial differential equations
RI	Reduced integration
SRI	Selective reduced integration
VHW	Veubeke–Hu–Washizu

Element abbreviation and its descriptions

α-FE-b27	Proposed 27-node brick EAS element in FEA
α-FE-b8	8-node brick EAS element in FEA
α-FE-q4	4-node quadrilateral EAS element in FEA
α-FE-q9	9-node quadrilateral EAS element in FEA
α-FE-w18	Proposed 18-node wedge EAS element in FEA
α-FE-w6	Proposed 6-node wedge EAS element in FEA
α-IgA$^{\text{2D}}_{\text{Cub}}$	Proposed strain-based EAS element with 3rd degree NURBS interpolations in ξ and η directions with C^2 continuous displacements across element boundary in IGA
α-IgA$^{\text{3D}}_{\text{Cub}}$	Proposed strain-based EAS element with 3rd degree NURBS interpolations in ξ, η, and ζ directions with C^2 continuous displacements across element boundary in IGA

α-$\mathrm{IgA}^{\mathrm{2D}}_{\mathrm{Quad}}$	Proposed strain-based EAS element with 2^{nd} degree NURBS interpolations in ξ and η directions with C^1 continuous displacements across element boundary in IGA
α-$\mathrm{IgA}^{\mathrm{3D}}_{\mathrm{Quad}}$	Proposed strain-based EAS element with 2^{nd} degree NURBS interpolations in ξ, η, and ζ directions with C^1 continuous displacements across element boundary in IGA
α4-$\mathrm{IgA}^{\mathrm{2D}}_{\mathrm{Quad}}$	Existing EAS 2D quadratic element for NURBS-based IGA with four enhanced strain parameters
α6S-$\mathrm{IgA}^{\mathrm{2D}}_{\mathrm{Quad}}$	Existing EAS 2D quadratic element for NURBS-based IGA with six enhanced strain parameters paired with stabilization technique
up-FE-b8	Displacement-Pressure formulation based 8-node brick element with 1 pressure node
ANS*-b27	27-node brick element utilizing generalized ANS approach in FEA
ANS*-b8	8-node brick element utilizing generalized ANS approach in FEA
ANS-b8	8-node brick element utilizing ANS in FEA
ANS-q4	4-node quadrilateral element utilizing ANS in FEA
ANS-q9	9-node quadrilateral element utilizing ANS in FEA
FE-b27	Conventional 27-node brick element in FEA
FE-b8	Conventional 8-node brick element in FEA
FE-q4	Conventional 4-node quadrilateral element in FEA
FE-q9	Conventional 9-node quadrilateral element in FEA
h-FE-b27	Stress-based hybrid 27-node brick element in FEA
h-FE-b8	Stress-based hybrid 8-node brick element in FEA
h-FE-q4	Stress-based hybrid 4-node quadrilateral element in FEA
h-FE-q9	Stress-based hybrid 9-node quadrilateral element in FEA
h-$\mathrm{IgA}^{\mathrm{2D}}_{\mathrm{Cub}}$	Proposed stress-based hybrid element with 3^{rd} degree NURBS interpolations in ξ and η directions with C^2 continuous displacements across element boundary in IGA
h-$\mathrm{IgA}^{\mathrm{3D}}_{\mathrm{Cub}}$	Proposed stress-based hybrid element with 3^{rd} degree NURBS interpolations in ξ, η, and ζ directions with C^2 continuous displacements across element boundary in IGA
h-$\mathrm{IgA}^{\mathrm{2D}}_{\mathrm{Lin}}$	Stress-based hybrid element with linear NURBS interpolations in ξ and η directions with C^0 continuous displacements across element boundary in IGA
h-$\mathrm{IgA}^{\mathrm{2D}}_{\mathrm{Quad}}$	Proposed stress-based hybrid element with 2^{nd} degree NURBS interpolations in ξ and η directions with C^1 continuous displacements across element boundary in IGA
h-$\mathrm{IgA}^{\mathrm{3D}}_{\mathrm{Quad}}$	Proposed stress-based hybrid element with 2^{nd} degree NURBS interpolations in ξ, η, and ζ directions with C^1 continuous displacements across element boundary in IGA

h-$\text{IgA}^{\text{Axisym}}_{\text{Quad}}$	Proposed hybrid axisymmetric 2D NURBS-based IGA quadratic element with 2^{nd} degree NURBS interpolations in ξ and η directions with C^1 continuous displacements across element boundary in IGA
$\text{IgA}^{\text{2D}}_{\text{Cub}}$	Element with 3^{rd} degree NURBS interpolations in ξ and η directions with C^2 continuity across element boundary in IGA
$\text{IgA}^{\text{3D}}_{\text{Cub}}$	Element with 3^{rd} degree NURBS interpolations in ξ, η, and ζ directions with C^2 continuity across element boundary in IGA
$\text{IgA}^{\text{2D}}_{\text{Lin}}$	Element with linear NURBS interpolations in ξ and η directions with C^0 continuity across element boundary in IGA
$\text{IgA}^{\text{2D}}_{\text{Quad}}$	Element with 2^{nd} degree NURBS interpolations in ξ and η directions with C^1 continuity across element boundary in IGA
$\text{IgA}^{\text{3D}}_{\text{Quad}}$	Element with 2^{nd} degree NURBS interpolations in ξ, η, and ζ directions with C^1 continuity across element boundary in IGA
$\text{IgA}^{\text{Axisym}}_{\text{Quad}}$	Axisymmetric 2D NURBS-based IGA quadratic element with 2^{nd} degree NURBS interpolations in ξ and η directions with C^1 continuous displacements across element boundary in IGA
MITC3+	3-node MITC shell element
MITC4+	4-node MITC shell element
MITC9	9-node MITC shell element
SRI-b27	27-node brick element utilizing SRI approach in FEA
SRI-b8	8-node brick element utilizing SRI approach in FEA
SRI-q4	4-node quadrilateral element utilizing SRI approach in FEA
SRI-q9	9-node quadrilateral element utilizing SRI approach in FEA

Greek Symbols

$\bar{\boldsymbol{A}}$	Matrix of the coefficients of a_k
$\bar{\boldsymbol{B}}$	Strain-displacement matrix in covariant frame
$\bar{\boldsymbol{B}}^{\text{ANS}}$	Strain-displacement matrix in ANS method
$\bar{\boldsymbol{\varepsilon}}^u$	Vector representations of $\boldsymbol{\varepsilon}^u$
$\bar{\boldsymbol{\sigma}}$	Vector representations of $\boldsymbol{\sigma}$
$\bar{\boldsymbol{\sigma}}^u$	Vector form of stress tensor derived from displacements
$\bar{\boldsymbol{\sigma}}^\alpha$	Vector form of stress tensor corresponding to enhanced strain
$\boldsymbol{B}$	Strain-displacement matrix
$\boldsymbol{C}$	Material constitutive tensor of the second order
$\boldsymbol{C}_\lambda$	Volumetric part of the material tensor
$\boldsymbol{C}_\mu$	Deviatoric part of the material tensor
$\hat{\boldsymbol{\beta}}$	Vector of stress parameters
$\boldsymbol{G}$	Enhanced strain interpolation matrix in physical space
$\boldsymbol{J}$	Jacobian that relates the physical and natural coordinate system
$\boldsymbol{J}_0$	Jacobian evaluated at the element center

$\boldsymbol{K}$	Stiffness matrix
$\boldsymbol{K}^e_\lambda$	Elemental stiffness matrix constituting volumetric part of the material tensor in SRI
$\boldsymbol{K}^e_\mu$	Elemental stiffness matrix constituting deviatoric part of the material tensor in SRI
$\boldsymbol{K}^{\text{eas}}$	Global stiffness matrix for EAS method
$\boldsymbol{K}^{\text{eas}}_e$	Elemental stiffness matrix for EAS method
$\mathbf{0}_{i^*}$	Null vector of prescribed size $(i = a,\ b,\ c)$
$\mathbf{0}_i$	Null vector of prescribed size $(i = a,\ b,\ c)$
$\mathbf{0}_{m\times n}$	Null matrix of size $m \times n$
$\mathbf{0}_m$	Null vector of size $1 \times m$
$\bar{\boldsymbol{\varepsilon}}^\alpha$	Vector representations of $\boldsymbol{\varepsilon}^\alpha$
$\boldsymbol{\mathcal{H}}$	Knot vector along η direction
$\boldsymbol{\mathcal{X}}_{i,j,k}$	Control point coordinates for $(i, j, k)^{th}$ control point.
$\boldsymbol{\mathcal{X}}_{i,j}$	Control point coordinates for $(i, j)^{th}$ control point.
$\boldsymbol{\mathcal{X}}_i$	Control point coordinates for $(i)^{th}$ control point.
$\boldsymbol{\mathcal{Z}}$	Knot vector along ζ direction
$\boldsymbol{\varepsilon}$	Compatible strain tensor
$\boldsymbol{\varepsilon}^\alpha$	Enhanced strain field
$\boldsymbol{\varepsilon}^s$	Strain tensor obtained from stress-strain relations
$\boldsymbol{\varepsilon}^u$	Strain tensor derived from the displacements
$\boldsymbol{\varepsilon}_d$	Deviatoric strain tensor
$\boldsymbol{\varepsilon}_v$	Volumetric strain tensor
$\boldsymbol{\Xi}$	Knot vector along ξ direction
$\boldsymbol{b}$	Vector representing body force per unit volume
$\boldsymbol{P}$	Stress interpolation matrix in physical space
$\boldsymbol{\sigma}$	Cauchy stress tensor
$\boldsymbol{\sigma}^u$	Stress tensor derived from displacements
$\boldsymbol{\sigma}^\alpha$	Stress tensor corresponding to enhanced strain
$\boldsymbol{\sigma}^\varepsilon$	Stress tensor obtained by applying the stress-strain relation
$\boldsymbol{T}$	Transformation matrix
$\boldsymbol{T}^{\text{h}}_{\text{ref}}$	Transformation matrix responsible for h-refinement in IGA
$\boldsymbol{T}_0$	Transformation matrix evaluated at element center
$\boldsymbol{u}$	Displacement field
$\delta\bar{\boldsymbol{\sigma}}$	Vector representations of variation of $\boldsymbol{\sigma}$
$\delta\bar{\boldsymbol{\varepsilon}}^u$	Vector representations of variations of $\boldsymbol{\varepsilon}^u$
$\delta\bar{\boldsymbol{\varepsilon}}^\alpha$	Vector representations of variation of $\boldsymbol{\varepsilon}^\alpha$
$\delta\boldsymbol{\varepsilon}$	Variation of strain field
$\delta\boldsymbol{\sigma}$	Variation of stress field
$\delta\boldsymbol{u}$	Variation of displacement field

$\hat{\boldsymbol{\alpha}}$	Vector of enhanced strain parameters
$\hat{\boldsymbol{f}}$	Load vector
$\hat{\boldsymbol{u}}$	Displacement vector
$\hat{\delta\boldsymbol{u}}$	Vector of displacement variation
$\hat{\Omega}$	Parametric space
$\mathbb{C}$	Material constitutive tensor of the fourth order
$\tilde{\mathcal{R}}$	Domain in natural coordinate system
$\mathcal{H}^1$	Sobolev space
$\mathcal{K}$	Bulk modulus
$\mathcal{L}^2(\mathcal{R})$	Space of square-integrable functions
$\mathcal{R}$	Open domain
$\mathcal{U}_{\mathrm{d}}^{\mathrm{e}}$	Elemental internal energy due to deviatoric part
$\mathcal{U}_{\mathrm{tot}}^{\mathrm{e}}$	Total internal energy of an element
$\mathcal{U}_{\mathrm{v}}^{\mathrm{e}}$	Elemental internal energy due to volumetric part
$\mathcal{V}_{\boldsymbol{\varepsilon}}$	Space associated with strain field
$\mathcal{V}_{\boldsymbol{\sigma}^u}$	Space associated with stresses derived from displacements
$\mathcal{V}_{\boldsymbol{\sigma}^\alpha}$	Space associated with stresses derived from enhanced strain
$\mathcal{V}_{\boldsymbol{\sigma}}$	Space associated with stress field
$\mathcal{V}_{\boldsymbol{u}}$	Space associated with admissible displacements
$\mathcal{V}_{\tilde{\phi}}$	Complete polynomial space in the master coordinate system for the given element
ν	Poisson's ratio
Ω	Physical space
$\partial\mathcal{R}$	Boundary of the open domain $\mathcal{R}$
$\partial\mathcal{R}_t$	Traction boundary
$\partial\mathcal{R}_u$	Displacement boundary
σ_r	Stress along radial direction
σ_θ	Stress along theta direction
$\bar{\boldsymbol{t}}$	External traction on the boundary $\partial\mathcal{R}_t$
$\tilde{\boldsymbol{P}}_H$	Higher-order stress interpolation matrix in natural coordinate system
$\tilde{\boldsymbol{P}}_L$	Lower-order stress interpolation matrix in natural coordinate system
$\tilde{\boldsymbol{P}}$	Stress interpolation matrix in natural space
$\tilde{\boldsymbol{\sigma}}_H^e$	Higher-order stress field
$\tilde{\boldsymbol{\sigma}}_L^e$	Lower-order stress field
$\tilde{\boldsymbol{G}}$	Enhanced strain interpolation matrix in natural coordinate system
$\tilde{\Omega}$	Master space
$\tilde{\varepsilon}_{ij}$	Strains in covariants frame
$\varepsilon^{\mathrm{ANS}}$	Assumed strain field in ANS method
ε_v	Volumetric strain
$\varnothing$	Null

E	Young's modulus
$L_{k,q}(\zeta)$	k^{th} B-spline basis function in ζ direction of degree r
$M_{j,q}(\eta)$	j^{th} B-spline basis function in η direction of degree q
$N(\boldsymbol{G}_e)$	Null space of $\boldsymbol{G}_e$
n_d	Degrees of freedom for each node
n_e	Count of nodes in each element
$n_{\hat{\beta}}$	Number of enhanced strain parameters per element
n_{cp}^e	Total number of control points per element
N_{dof}^u	Number of free/active degrees of freedom
$N_{i,j,k}^{p,q,r}(\xi,\eta,\zeta)$	trivariate B-spline basis function (Product of i^{th} B-spline basis function in ξ direction of degree p, j^{th} B-spline basis function in η direction of degree q and k^{th} B-spline basis function in ζ direction of degree r
$N_{i,j}^{p,q}(\xi,\eta)$	Bivariate B-spline basis function (Product of i^{th} B-spline basis function in ξ direction of degree p and j^{th} B-spline basis function in η direction of degree q)
$N_{i,p}(\xi)$	i^{th} B-spline basis function in ξ direction of degree p
$R_{i,j,k}^{p,q,r}(\xi,\eta,\zeta)$	trivariate NURBS basis function (Product of i^{th} NURBS basis function in ξ direction of degree p, j^{th} NURBS basis function in η direction of degree q and k^{th} NURBS basis function in ζ direction of degree r
$R_{i,j}^{p,q}(\xi,\eta)$	Bivariate NURBS basis function (Product of i^{th} NURBS basis function in ξ direction of degree p and j^{th} NURBS basis function in η direction of degree q)
$R_{i,p}(\xi)$	i^{th} NURBS basis function in ξ direction of degree p
$R_{j,q}(\eta)$	j^{th} NURBS basis function in η direction of degree q
$R_{k,q}(\zeta)$	k^{th} NURBS basis function in ζ direction of degree r
u_i^{ref}	Reference/benchmark value for i^{th} component of displacement at prescribed location
u_r	Radial displacement
u_θ	Displacement along θ

Chapter 1

Introduction

The chapter gives a brief overview of finite element analysis and isogeometric analysis. It discusses a common limitation in both methods and explores current state-of-the-art approaches to mitigate the limitation. Furthermore, the section identifies the research gaps and outlines the objectives of the current work, with the aim of making a novel contribution to the scientific discourse.

1.1 Finite element analysis

Finite element analysis (FEA) is a widely practiced numerical procedure to solve a mathematical model driven by differential equations that govern most of the physical problems in real life. Over a period of time, FEA has found numerous applications in a diverse set of engineering fields such as solid mechanics, fluid mechanics, biomechanics, electromagnetics, and many more [1]. It has brought a fundamental transformation in the approach to scientific modeling and engineering design, impacting a wide range of applications across various fields of study.

1.1.1 Foundations and milestones: The history of FEA

The FEA has a rich and evolving history that spans several decades, marked by significant developments in numerical methods, computing technology, and diverse applications across engineering disciplines. The origins of FEA can be traced back to the 1940s, marked by the pioneering efforts of engineers and mathematicians. Their work in this era laid the foundational groundwork for numerical methods, providing the initial impetus for the development of FEA [2–5].

Building upon the initial developments, the 1960s witnessed the emergence of FEA as a powerful tool for structural analysis [6, 7]. Engineers began applying FEA to solve complex problems in civil and aerospace engineering, leveraging its capabilities to provide solutions to complex structural challenges. During this period, the fundamental concept of dividing structures into smaller, more manageable elements connected at nodes became foundational to the FEA approach. This innovative approach laid the groundwork for more accurate and efficient simulations, transforming FEA into a mainstream methodology for structural analysis.

During the 1970s and 1980s, significant advancements were made in computational methods and algorithms dedicated to solving partial differential equations, with a particular focus on the FEA. This era witnessed the introduction of commercial FEA software by NASTRAN and ANSYS, making FEA more accessible to engineers and researchers. The availability of such sophisticated software provided a pivotal shift, enabling a broader engineering community to utilize FEA for diverse applications. This increased accessibility played a crucial role in the widespread adoption and integration of FEA into various engineering disciplines, including mechanical, aerospace, automotive, and civil engineering. Increasing computing power and improved algorithms allowed for more complex simulations, enabling engineers to analyze a broad range of problems.

In the 21st century, FEA expanded into multidisciplinary applications, encompassing thermal analysis, fluid dynamics, electromagnetics, and coupled-field problems. The integration of FEA with other simulation techniques led to a more comprehensive understanding of complex engineering systems. Ongoing advancements in computing technology and parallel processing in the 2000s have enabled engineers to perform simulations of unprecedented complexity and scale. The development of open-source FEA software, alongside improvements in commercial packages, has democratized access to simulation tools.

Throughout its history, FEA has evolved from a specialized tool for structural analysis to a versatile and indispensable tool in engineering design and analysis. Ongoing research continues to refine algorithms, improve accuracy, and extend the applicability of FEA to new and challenging domains. For reader's interest, detailed historical insights into the origin and successful development of FEA can be found in a recently published article by Liu et al. [1].

1.1.2 Fundamental insights into FEA

The fundamental steps associated with the FEA process are shown in Fig. 1.1, which offers a comprehensive overview of the different methodological stages in FEA [8]. The physical problem at hand usually entails a real-world structure or its components experiencing specific loads. To translate this physical problem into a mathematical model, certain assumptions are made, which ultimately leads to the formulation of differential equations that govern the behavior of the physical problem. FEA plays a critical role in solving these intricate mathematical models.

Conventionally, FEA employs classical variational methods to solve these differential equations governing physical systems. The fundamental approach involves transforming the governing equations into an equivalent weighted-integral form. Followed by approximating the solution across the domain using a linear combination of suitably

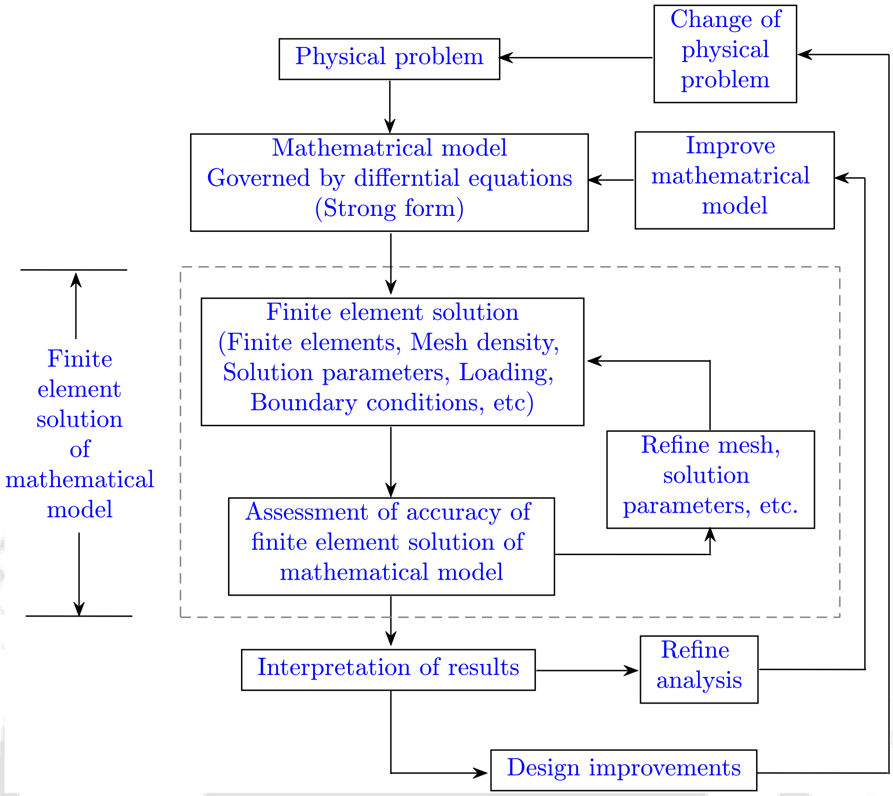

Figure 1.1: The process of finite element analysis.

chosen approximation functions (ϕ_j) and unknown coefficients (c_j). The determination of these coefficients (c_j) is carried out to ensure the satisfaction of an integral statement equivalent to the original differential equation. Various variational methods, such as Ritz-Galerkin, collocation, and least squares methods, distinguish themselves by their unique choices in integral form, weighted functions, and/or approximation functions. Each method offers a distinct perspective on how to effectively formulate and solve the mathematical model, providing flexibility in adapting to the characteristics of specific engineering problems [9].

After selecting the suitable variational method, the domain is segmented into subdomains/elements. Within each subdomain/element, traditional variation methods approximate the governing differential equation. This approach leverages the simplicity of representing complex functions as collections of simple polynomials, streamlining the computational process in FEA. Finally, the assembled system of equations is solved to evaluate the solution parameters. As FEA is a numerical procedure, it is imperative to assess solution accuracy. If the predefined accuracy criteria are not met, the numerical solution has to be repeated with refined parameters until a satisfactory level of accuracy is attained. For a comprehensive exploration of this topic, one can refer to standard FEA books such as those by Bathe [8] and Reddy [9].

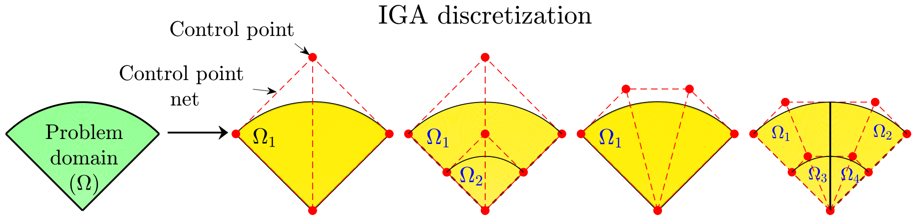

(a) (b) (c) (d) (e)

Figure 1.2: Discretization of physical geometry (a) into different NURBS-based elements ((b)-(e)), where Ω_e denotes the element domain.

1.2 Isogeometric analysis

Another recent numerical method which has been developed is isogeometric analysis (IGA), which provides an efficient integration of computer-aided design (CAD) and FEA [10, 11]. The ability to provide exact geometry in the analysis framework, convenience in achieving higher inter-element continuity, and appreciably lower reliance on CAD for refinement contribute to its effective utilization across diverse engineering fields. A typical example of IGA discretization is shown in Fig. 1.2, where irrespective of the number or type of elements, the exact geometry of the physical domain is maintained.

1.2.1 A historical background

The concept of IGA was introduced by Hughes et al. in 2005 [10], wherein CAD was seamlessly integrated with FEA through the utilization of Non-Uniform Rational B-Splines (NURBS) interpolation functions. NURBS are extensively employed in engineering design, offering advantages in modeling free-form surfaces and accurately representing conic sections like circles, spheres, and cylinders. They also feature numerous effective and numerically stable algorithms. Along with these, they retain essential mathematical properties such as non-negativity of basis functions, linear independence, partition of unity, and variation diminishing property [12, 13]. Recognizing these merits over other geometric techniques, NURBS serve as a foundational concept in IGA.

However, the NURBS-based IGA is not the only method to integrate CAD with the FEA framework. Previous attempts existed with similar capabilities, utilizing computational geometric techniques for FE analysis, although with certain downsides. CAD technology can be categorized into five main stages, with the first three named after their authors: Coons, Gordon, and Bezier. The fourth is B-splines, and the last is the NURBS representation of geometries [14]. With each developmental stage in CAD, efforts were made to utilize these developments within the FE analysis framework.

The initial steps in integrating CAD with FEA were taken at the Mathematical Department of General Motors, Detroit, USA, with significant contributions from William Gordon. He introduced a mesh generation technique in FEA that utilized bivariate and trivariate ‘blending-function’ interpolations. These functions were originally developed for defining the geometric characteristics of problems in CAD [15]. This framework enabled the incorporation of the same interpolation functions in FEA. The term ‘transfinite’ was introduced to characterize the general class of interpolation schemes, ensuring the matching of primitive functions at a nondenumerable number of points. This facilitated the mapping of the domain of interest to a standard unit square. Collaborating with associates Cavendish and Hall, efforts extended towards the development of blending functions and their implementation in the Ritz–Galerkin method [16].

The next stage in CAD technology is attributed to the work of Bezier. Notably, the non-rational Bezier interpolation functions are equivalent to those produced by Lagrange polynomials, offering the added advantage of control points. Provatidis extended this concept [17], introducing Bezier-type elements for both static and dynamic analysis within the FEA framework. The theory was applied to study several examples, concluding that Lagrangian and Bezierian-type finite elements are equivalent. Despite the conventional Lagrangian elements relying on nodal coordinates and Bezierian elements on control points, the results obtained were identical.

A subsequent evolution in CAD technology involves the development of spline interpolation, particularly B-splines. Hollig played a pioneering role by publishing the work on B-spline-based FEA [18], recognizing the potential of B-splines in approximations and geometric modeling in CAD. For an extended period of time, B-splines were considered as standard for free-form designs and geometry processing. As CAD/CAE integration was not a new concept by then, it became apparent to direct efforts towards utilizing B-splines as basis functions in FEA.

In his work, Hollig introduced three types of basis functions for FEA: (i) weighted B-splines, (ii) web-splines, and (iii) hierarchical B-splines. This diversity aimed to model boundary conditions accurately and provide uniform stability for a restricted B-spline basis. The efficiency of the B-spline-based formulation was demonstrated across various problem classes, including Poisson’s equation with inhomogeneous Dirichlet and Neumann boundary conditions, incompressible flow, the biharmonic equation for plate problems, and the Lame–Navier system in linear elasticity. Hollig’s work was further advanced as he explored the possibilities of combining the advantages offered by B-splines in FEA. These advancements ultimately overcome the demanding and often time-consuming preprocessing step in FEA by eliminating the need for mesh generation for successive refinements.

The subsequent significant milestone in CAD technology involves the collective efforts of many researchers focusing on NURBS [19]. Recognizing the advantages of NURBS over other geometric techniques, researchers proposed integrating NURBS into FEA [20] and the boundary element method (BEM) [21]. However, these efforts remained in the shadows as most of the attention was directed towards advancements in FEA.

Years later, Hughes and co-workers presented a systematic approach to integrate NURBS into the FEA framework [10, 11]. This integration, known as IGA, aimed to maintain exact geometry during discretization, irrespective of mesh coarseness. Another objective was to simplify mesh refinement, removing the dependency on CAD once the initial mesh was created. The authors successfully applied the concept of IGA to various problem domains that included solids, fluids, and fluid-structure interaction. Their work aroused significant interest within the scientific community, leading to widespread collaboration and ongoing successful research in the field of IGA.

The aforementioned milestones represent significant progress in the integration of CAD with CAE. For further insights and detailed developments in FEA alongside expansions in geometric technologies, interested readers are referred to [14, 19] and the references therein.

1.2.2 Applications of IGA in various fields

Since its introduction in 2005, IGA has proved to be a powerful numerical method in computational mechanics. Notably, in contact formulations, IGA offers higher and desired inter-element continuity and smooth representation of contact surfaces which effectively contributes to minimize jumps and artificial oscillations in solutions [22–24].

In the field of structural shape optimization, IGA excels by facilitating a tight coupling between CAD geometries and FEA models. This leads to smooth and realistic optimal designs, in contrast to the less favorable outcomes often obtained in FEA-based optimization [25, 26].

In the field of fluid and fluid-structure analysis, numerical strategies often involve the need to solve higher order partial differential spatial operators. Due to this reason, it requires the use of basis functions that are piecewise smooth and possess higher global continuity. To this extent, there are limited numbers of FE elements which possess C^1 continuity and can represent the complex geometries as well. Whereas in IGA, higher continuity of the elements can be achieved with ease and hence, promote its successful implementation in this domain [27, 28].

In the field of structural vibration problem, while handling higher frequencies in the spectra, large errors and oscillations add discontinuities in wave propagation problems. Once again, IGA has shown promising results with only a finite number of frequencies constituting the stated discontinuities even with linear parameterization. Extending the same with non-linear parameterization by incorporating higher-order NURBS basis functions retains the same convergence rates. Still, overall accuracy of the spectrum in the case of IGA based elements is much greater than that of its FEA counterpart [29, 30].

Another field where IGA has shown significant benefits is shell and plate problems. Literature exposed the fact that analysis of thin structures are highly sensitive towards geometric imperfections. This motivated the successful implementation of IGA into dedicated plate and shell theories as it retains the exact geometry at all points. Furthermore, Kirchhoff-Love shell theory, one of the various plate and shell theories, often demands higher-order continuity for the description of elements. This requirement can be effortlessly achieved using NURBS-based IGA [31, 32], thereby making it a promising platform.

The effective implementation also influenced researchers to make an effort to integrate IGA in existing commercial software. As an effect, LS-DYNA and Abaqus introduced NURBS based isogeometric elements into its analysis framework [33–35]. Other than available commercial software, several efforts are made to develop a dedicated tool for isogeometric analysis of PDEs, e.g., GeoPDEs, PetIGA, and Πgasus [36–38].

1.3 Locking phenomena: A hurdle in structural mechanics

The aforementioned methods have successfully demonstrated their efficacy across a diverse set of engineering fields, however, they are not without limitations. One notable limitation prevalent in both of these numerical methods is locking which has detrimental effects on the accuracy of results when analyzing thin structural geometries or modeling incompressible/near-incompressible material behaviors.

The mathematical interpretation of the term ‘locking’ implies the ill-conditioning of the system of equations obtained through FEA/IGA for a prescribed set of governing partial differential equations. However, in the engineering literature, ‘locking’ is often used to describe a wide range of numerical phenomena that lead to poor approximations of solutions [39–47]. Some of the common signs of locking include suboptimal convergence rates, non-robustness with respect to the variations of participating parameters, stiffer behavior of an element, and wildly oscillating resultant stresses.

The conventional formulations entail parameter dependence, and for the special cases of these parameter descriptions, the mathematical formulation associated with them leads to locking. More frequently, the locking is categorized into shear, membrane, curvature thickness or trapezoidal, and volumetric locking based on the involvement of specific parameters or the special constraints responsible for the formulation’s failure.

1.3.1 Locking in thin structures

Locking associated with the thin structural geometries is often referred to as shear [43, 47] and membrane [42] locking, where the high aspect ratio (ratio of the longest dimension to the shortest dimension of an object/geometric shape) of the domain promotes stiffer behavior of elements along with high oscillations of the resulting shear stresses. A typical example is the bending of a thin beam where the parasitic shear stresses cause the element to behave significantly stiffer than it actually is. This results in a high underestimation of the bending displacements. This effect gets more prominent

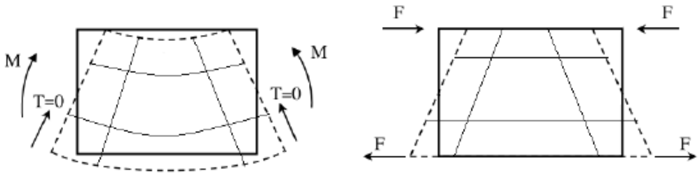

(a) Exact **(b)** FEA approximation

Figure 1.3: Behavior of an element in pure bending problem.

as the structure gets thinner and even minor discretization flaws in shear terms result in unacceptable errors [43].

To have an elaborate understanding of the topic, consider a trilinear displacement field used for a standard eight-node hexahedral element in the natural coordinate system (ξ, η, ζ) as:

$$u = a_0 + a_1\xi + a_2\eta + a_3\zeta + a_4\xi\eta + a_5\eta\zeta + a_6\xi\zeta + a_7\xi\eta\zeta, \tag{1.1a}$$

$$v = b_0 + b_1\xi + b_2\eta + b_3\zeta + b_4\xi\eta + b_5\eta\zeta + b_6\xi\zeta + b_7\xi\eta\zeta, \tag{1.1b}$$

$$w = c_0 + c_1\xi + c_2\eta + c_3\zeta + c_4\xi\eta + c_5\eta\zeta + c_6\xi\zeta + c_7\xi\eta\zeta, \tag{1.1c}$$

where a_i, b_i, and c_i $(i = 0 \text{ to } 7)$ are constant coefficients. Now, consider a pure bending situation, as shown in Fig. 1.3a, while assuming that the natural coordinate system coincides with the physical coordinate system. In this context, if a uniform bending is applied along the η direction, the shear strain $\gamma_{\xi\eta}$ or $2\varepsilon_{\xi\eta}$ should ideally be zero. However, the present choice of interpolation functions (Eq. 1.1) leads to the following expression of shear strain:

$$\gamma_{\xi\eta} = 2\varepsilon_{\xi\eta} = \frac{\partial u}{\partial \eta} + \frac{\partial v}{\partial \xi} = (a_2 + b_1) + a_4\xi + b_4\eta + (a_5 + b_6)\zeta + a_7\xi\zeta + b_7\eta\zeta. \tag{1.2}$$

The above expression leads to zero shear strain only if $a_2 + b_1 = 0$, $a_4 = 0$, $b_4 = 0$, $a_5 + b_6 = 0$, $a_7 = 0$, and $b_7 = 0$. However, these conditions are not satisfied. The coefficients a_4, b_4, a_7, and b_7 are non-zero that come directly from the displacement interpolation. This gives rise to strains and corresponding stresses that should not be present in the given problem but emerge in the formulation due to the considered approximations. These strains and stresses are commonly referred to as parasitic strains and stresses and responsible for the shear locking in the domain. A similar argument is true for other shear strain components. Hence, shear locking is often defined as the inability of an element to undergo specific deformations without introducing the parasitic strain or stresses into the system [43]. Further in the literature, a similar phenomenon has been explained using the beam elements [48]. It has been shown that certain conditions, i.e., shear forces in bending, cannot be ideally zero for the admissible deformation for high slenderness ratios. The detailed discussion can be found in [43].

Analogous behavior is observed in membrane locking when analyzing thin curved element geometries. It causes an overestimation of the bending stiffness and gets more apparent as the thickness reaches zero. Similar to shear locking, here the solution is plagued with parasitic membrane stresses, which are supposed to be zero, in case of pure bending condition. This phenomenon is often defined as the inability of an element to bend without stretching, promoting significantly higher bending stiffness [42]. Another type of locking that relates to the geometric parameter of structure is the curvature thickness or trapezoidal locking. Like membrane locking, curvature locking appears in thin curved structural geometries where the mesh often contains elements with tapered shapes to closely approximate the geometry. The parasitic normal strains are responsible for this locking [49–51].

1.3.2 Locking influenced by the material parameters

Locking associated with the incompressibility or nearly incompressibility of the material is called volumetric locking (also known as Poisson's or dilatation locking), where a low convergence rate for a practical range of discretization or unrealistic solutions often dominates the quality of results [44, 52–54]. Often the incompressible constraint in the problem description is not satisfied by interpolations involved in the normal strains of displacement-based elements. Volumetric locking is the result of over-stiffening of the element due to the failure to obtain the zero volumetric strain in an incompressible range (Poisson's ratio ≈ 0.5).

For a comprehensive understanding of volumetric locking, let us examine the same trilinear displacement field defined in Eq. 1.1. Assuming the natural coordinate system aligns with the physical coordinate system, the compatible normal strains in natural space can be evaluated as:

$$\varepsilon_{\xi\xi} = \frac{\partial u}{\partial \xi} = a_1 + a_4\eta + a_6\zeta + a_7\eta\zeta, \tag{1.3a}$$

$$\varepsilon_{\eta\eta} = \frac{\partial v}{\partial \eta} = b_2 + b_4\xi + b_5\zeta + b_7\xi\zeta, \tag{1.3b}$$

$$\varepsilon_{\zeta\zeta} = \frac{\partial w}{\partial \zeta} = c_3 + c_5\eta + c_6\xi + c_7\xi\eta. \tag{1.3c}$$

If the material is incompressible or nearly incompressible, then the volumetric strain, i.e., ε_v should be ideally zero. However, with the present selection of displacement approximation (Eq. 1.1), the volumetric strain is calculated as

$$\begin{aligned}\varepsilon_v &= \varepsilon_{\xi\xi} + \varepsilon_{\eta\eta} + \varepsilon_{\zeta\zeta},\\ &= (a_1 + b_2 + c_3) + (b_4 + c_6)\xi + (a_4 + c_5)\eta + (a_6 + b_5)\zeta + (a_7\eta\zeta + b_7\xi\zeta + c_7\xi\eta),\\ &\neq 0.\end{aligned}$$

Above expression of ε_v leads to zero volumetric strain only if $a_1+b_2+c_3=0$, $b_4+c_6=0$, $a_4+c_5=0$, $a_6+b_5=0$, $a_7=0$, $b_7=0$, and $c_7=0$. These conditions are not satisfied with the conventional choice of interpolation functions. In particular, the coefficients a_7, b_7, and c_7 are different from zero if we choose the conventional interpolations to approximate the field variable. They are included to achieve the completeness of the interpolation functions, see Eq. 1.1. Forcefully implementing incompressibility condition makes these coefficients zero and excessive stiffness is generated which leads to volumetric locking.

It can be further explained using the total internal energy of an element. Let $\mathcal{U}^e_{\text{tot}}$ be the total internal energy of an element which can be defined as the contributions of internal energy due to deviatoric and volumetric part as follows:

$$\mathcal{U}^e_{\text{tot}} = \mathcal{U}^e_{\text{d}} + \mathcal{U}^e_{\text{v}} = 2G \int_{\Omega_e} \boldsymbol{\varepsilon}_d : \boldsymbol{\varepsilon}_d \, d\Omega + \mathcal{K} \int_{\Omega_e} \text{tr}(\boldsymbol{\varepsilon})^2 \, d\Omega, \tag{1.4}$$

where $\mathcal{U}^e_{\text{d}}$ and $\mathcal{U}^e_{\text{v}}$ are the elemental internal energy due to deviatoric and volumetric part, respectively. Here, $\mathcal{K}$ is the bulk modulus while $\boldsymbol{\varepsilon}_d$ and $\boldsymbol{\varepsilon}_v$ are the deviatoric and volumetric strains such that

$$\begin{aligned}
\mathcal{K} &= \frac{2}{3}\left(\frac{1+\nu}{1-2\nu}\right) G, \\
\boldsymbol{\varepsilon}_v &= \frac{1}{3}\varepsilon_{ii}\boldsymbol{I} = \frac{1}{3}\text{tr}(\boldsymbol{\varepsilon})\boldsymbol{I}, \\
\boldsymbol{\varepsilon}_d &= \boldsymbol{\varepsilon} - \boldsymbol{\varepsilon}_v.
\end{aligned}$$

For ν in the incompressible limit, i.e., as $\nu \to 0.5$, $\mathcal{K}$ tends to infinity. Hence, if $\text{tr}(\boldsymbol{\varepsilon}) = 0$ is not satisfied at any element, it will lead to high stiffness due to the contribution of $\mathcal{U}^e_{\text{v}}$. This configuration frequently induces volumetric locking, leading to suboptimal convergence rates and yielding impractical solutions within a practical range of discretization.

1.4 Existing strategies to alleviate locking in FEA

Over time, numerous strategies have been developed to address the issue of locking. Among these, prominent solutions involve the utilization of specialized shell elements based on well-established shell theories, such as the Reissner–Mindlin shell theory [55–62] and Kirchhoff–Love shell theory [63–69]. These elements play a pivotal role in the analysis of thin structures, effectively addressing challenges posed due to shear or membrane locking. A comprehensive review of some key milestones in shell finite elements can be found in [70, 71].

Another popular category of shell elements relies on the method of mixed interpolation of tensorial components (MITC)[72, 73]. In the literature, improved versions of these elements, such as MITC4+ [74, 75] and MITC3+ [76, 77], have been proposed. Additionally, higher-order MITC shell elements like MITC9 and MITC16 [78] have been introduced for effectively analyzing thin structural geometries.

Another approach to analyzing the behavior of thin structures is by using degenerated shell approach. It is a simpler version of shell theories where three-dimensional (3D) formulation can be reduced (degenerated) into two-dimensional (2D) shell formulation with only mid-surface nodal variables [79–82]. These elements discretized the fundamental 3D governing equations onto the mid-surface using the physical assumptions of shell theories while retaining the shear deformations across the thickness in the formulation.

Next, the techniques like reduced (RI) and selective reduced integrations (SRI) have been found remarkably accurate in handling several locking situations [40, 60, 83–94]. In the RI approach, the integrands involved in elemental stiffness evaluations are solved using lower order Gauss quadrature rule rather than using the full integration scheme. A sophisticated version of the RI approach is SRI, where the part of the material tensor responsible for producing high stiffness leading to locking is separated. It is then integrated with lower-order Gauss quadrature while the other part is integrated with full Gauss quadrature to reduce the excessive overall stiffness.

Another effective method to alleviate the shear locking is the assumed natural strain (ANS) method. The early development of ANS approach was in context of various shell models [58, 72]. Following its success, the method has been further extended to develop the so-called ‘solid-shell’ elements [78, 95–106]. In ANS formulation, different entities of strains are treated independently. This often includes choosing a certain class of interpolations for the transverse shear strains that are responsible for shear locking. Literature covers its application on the locking situations in thin structural geometries to handle shear, membrane or curvature thickness locking. However, the method is not suitable for alleviating the volumetric locking on its own. Nevertheless, ANS can be coupled with other methods to develop a locking-free element [48, 96, 99].

Further, strain projection techniques such as $\bar{\mathrm{B}}$ [52, 107–110] and $\bar{\mathrm{F}}$ [110–113] methods are found to be effective in analyzing the problem in incompressibility limit. The $\bar{\mathrm{B}}$ method is a sophisticated generalization of SRI. Explicit separation of factors driving the volumetrically stiff behavior from the remaining contributions is not always apparent in SRI, especially for anisotropic or nonlinear problems. The $\bar{\mathrm{B}}$ approach, which provides adaptability for a wide variety of problem descriptions, can be used to circumvent this limitation. The $\bar{\mathrm{F}}$ method follows some of the conceptual similarities as the $\bar{\mathrm{B}}$ method. The approach splits the deformation gradient into multiplicative deviatoric and volumetric parts, after which the compatible deformation gradient field is replaced with an assumed modified counterpart. Both of these approaches retain the displacement-based structure of FEA and are applicable to arbitrary material models.

Apart from the stated methods, various efforts have been made to address the issue of locking by developing several multi-field variation formulations. Early mixed formulations can be traced back to the 1960’s [114, 115]. These methods consist of formulations based on different combinations of two or more field variables (stress, strain, and displacement) into the variational principle. The often practiced methods are the displacement-pressure (u-p) formulations [116–120], enhanced assumed strains (EAS) [54, 121–135], and mixed/hybrid formulations [32, 126, 136–146] that satisfactorily handle the situations where the standard FE locks severely.

Among these methods, variations often exists in the selection of interpolation functions to approximate the additional independent field. The choice of interpolations for the additional field is a crucial determinant of the effectiveness of elements that are derived based on multi-field formulations. For stress-based hybrid elements, the current work mainly focuses on the elements proposed by the Jog [141, 142], where special treatment is adopted to develop the locking-free hybrid stress elements. The method's efficacy and robustness have been demonstrated by its successful implementation in a variety of application fields, including structural acoustics [147], contact mechanics [148], coupled fluid-structure problem [149], analysis of electromechanical systems [150], electromagnetic analysis [151], and linear elasticity problems using NURBS-based hybrid isogeometric analysis [143, 152–154].

1.5 Existing strategies to alleviate locking in IGA

To overcome locking in IGA, the explored contributions are limited. Existing contributions are often the adaptations of locking alleviation techniques originally developed in FEA, subsequently modified to align with the unique characteristics of NURBS-based IGA. One such strategy involves the use of classical shell theories, commonly employed in the analysis of thin structures to mitigate shear and membrane locking. These theories have been adapted and modified to work with the framework of IGA.

Popular choices include the Reissner–Mindlin shell theory that has been implemented into the NURBS-based IGA to analyze the plate and shell structures [61, 155]. Further advancement has been carried out in developing the rotation-free isogeometric shell elements with C^k continuous NURBS interpolations based on the Reissner–Mindlin shell theory [156]. The Kirchhoff–Love theory demands higher order continuity for a description of elements which can be achieved promisingly with the use of NURBS-based interpolation functions. This leads to a successful development of NURBS-based Kirchhoff-Love elements from the well-established Kirchhoff–Love shell theory [65]. Further advancements like blended shell theory for plate and shell problems which comprises of combined assumptions in classical Reissner–Mindlin and Kirchhoff–Love shell theory have also been successfully modified to develop blended isogeometric shell elements [31]. Furthermore, the application of IGA has been extended to the degenerated shell approach or solid-like shell formulation [61, 157], as well as NURBS-based solid shell elements [158].

Another popular and widely employed strategy to address various types of locking is the RI and SRI techniques, which were originally explored in the context of FEA. These strategies utilize fewer number of Gauss points than are required to solve the integrand exactly. The application of these techniques has been extended to IGA with promising results [60, 159]. However, it is crucial to note that while these techniques offer practical benefits, they come with their own limitations. They often compensate one error over another without a comprehensive mathematical explanation.

Furthermore, methods like $\bar{B}$ and $\bar{F}$ strain projection techniques have also investigated in the context of NURBS-based IGA. The higher continuity of NURBS basis functions tends to produce robust and accurate results. These projection methods effectively handles volumetric locking in case of incompressible or nearly incompressible problem domain [110, 160].

Another method is the ANS approach, where different components of strains are treated independently. Initially proposed for Lagrangian basis functions, this method has been successfully extended to NURBS-based IGA. The technique improves the performance of the element by alleviating shear and membrane locking [101, 102]. The ANS approach is computationally efficient but it is often coupled with other techniques to address other types of lockings. This integration takes away the advantage of computational efficiency.

Multi-field variational techniques are found to be effective in alleviating different types of locking in IGA. Popular methods include displacements-pressure formulation [161] and enhanced assumed strains (EAS) [135, 162], which satisfactorily handle situations where the standard IGA is prone to locking. Further, stress-based improvements in the context of IGA-based shell formulations have been explored by Echter et al. [32, 146] to address the membrane locking in various shell models. Furthermore, in [144, 145] the application of the Hellinger-Reissner principle in shell elements is presented. However, the stated shell formulations utilize the kinematic assumptions, restricting their applicability to relatively thin geometries.

To provide a concise overview of techniques for addressing locking in conventional Lagrangian-based FEA and their adaptations for NURBS-based IGA, including their advantages and disadvantages, refer to Table 1.1.

1.6 Limitations of the existing strategies

The shell theories necessitate the complex mathematical formulation involving the additional rotational degrees of freedom. Furthermore, these theories are restricted to the analysis of relatively thin structures due to the involvement of kinematic assumptions [163]. Further, it takes additional effort to couple the shell elements with the solid geometry. This limits the practicality while handling the problems consisting of integrated thin and thick structural geometries.

In the RI approach, using a lower-order Gauss quadrature rule for evaluating elemental stiffness integrands, instead of the full integration scheme, can lead to instabilities

Table 1.1: Existing techniques to alleviate locking.

Method	FEA	IGA	Advantages	Disadvantages
Shell theories	✓	✓	• Computationally effective. • Alleviates shear or membrane locking.	• Restricted to thin structures due to kinematic assumptions. • Complexity due to rotational DOFs. • Complexity in coupling shell elements with the solid geometry. • Special treatment to address volumetric locking.
Degenerated or solid shell elements	✓	✓	• Simpler compared to shell theories. • Alleviates shear or membrane locking.	• Additional integration over the thickness. • Special treatment to address volumetric locking.
RI and SRI strategies	✓	✓	• Locking-free response in special cases • Computationally effective	• Lacks mathematical explanation • Not reliable or robust • Often requires additional stabilization techniques
$\bar{B}$ and $\bar{F}$ techniques	✓	✓	• Addresses volumetric locking.	• Not applicable for thin structures.
ANS	✓	✓	• Alleviates shear and membrane locking. • Computationally effective.	• Special treatment required for volumetric locking, hence adding computational cost.
EAS	✓	✓	• Contains only displacement DOFs. • Simplified formulation for ease of application. • Effective for shear, membrane and volumetric locking.	• Computational cost is relatively higher than ANS. • Some variations of the methods are coupled with stabilization strategies.
Stress-based hybrid solid elements	✓	-	• Contains only displacement DOFs. • Simplified formulation for ease of application. • Addresses all types of locking. • Robust and easier to couple different problem domains.	• Computationally expensive at coarser meshes.

like ‘spurious singular modes’ or ‘hourglass modes’ in the formulation. To circumvent these instabilities, RI approach often requires a suitable stabilization technique [92, 93]. Meanwhile, in the SRI method, explicit separation of factors driving the volumetrically stiff behavior from the remaining contributions is not always apparent. Hence, it becomes a devious process to separate out the locking affected part of the material tensor with the rest of the formulation, especially while dealing with arbitrary non-linear material models.

The ANS method improves the performance of the element but is limited to situations affected by shear and membrane locking. It fails to address problems influenced by volumetric locking [105, 164]. While it is possible to couple ANS with other techniques to address various types of lockings, this integration reduces the computational efficiency of the method.

The $\bar{B}$ and $\bar{F}$ strain projection techniques, along with the displacement-pressure formulation [161], are limited to addressing incompressibility and are ineffective for shear and membrane locking problems. On the other hand, EAS elements are effective in alleviating various locking types. However, certain variations of the method require stabilization methods to prevent instabilities, such as hourglass modes.

1.7 Motivation

Despite the extensive literature on locking alleviation in FEA and IGA, the efforts persist in developing generalized elements that can perform well in any scenario, whether the problem involves thin or thick structures or requires handling incompressibility or near-incompressibility of materials, without compromising their performance in any aspect.

Towards this goal, multi-field variation formulations have provided viable options. These formulations assume additional independent fields, such as stress or strain fields, alongside the displacement field. The commonly employed strain-based formulations are based on the Veubeke–Hu–Washizu (VHW) variational principle [54, 121–134, 165–167], whereas the stress-based elements are derived from the Hellinger–Reissner (HR) variational principle [32, 126, 136, 137, 139–143, 145, 146]. Both of these formulations are widely recognized for their ability to effectively address the locking issue and have the capacity to solve thick and thin geometries without introducing additional complexity. Furthermore, the additional degrees of freedom associated with the strain or stress field are eliminated at the element level. As a result, there is no increase in the size of the global stiffness matrix in comparison to the conventional displacement-based elements.

The present work is dedicated to the development of elements capable of excelling in diverse scenarios without compromising their performance. It introduces novel strategies for alleviating locking in both FEA and IGA, with the goal of providing superior performance across various situations involving thin structures and material incompressibility or near-incompressibility. The specific emphasis lies in the development of multi-field variational formulations, particularly strain-based formulations based on VHW variational principle and stress-based elements derived from the HR variational principle. The research scope in this domain is outlined as follows.

1.7.1 Performance assessment of locking alleviation strategies

The comparative assessment of different methods to address locking has received limited attention. There are currently no studies that focus on the relative accuracies of individual methods, the shortcomings of the available strategies, and the parameters deciding the selection of a particular method. Hence, it is imperative to evaluate the performance of frequently utilized locking alleviation strategies. The idea is to test these methods for several parameters, such as best-suited environment, robustness, and efficiency, through the investigation of numerous benchmark problems.

1.7.2 Alleviating locking in FEA through novel EAS elements

To develop versatile elements for diverse scenarios, especially in locking-dominated problems, multi-field variational formulations provide promising alternatives. Among these, the EAS [124] approach stands out as a viable option. However, existing 3D EAS elements are solely developed for linear eight-node elements. The potential advantages offered by higher-order elements have not been exploited to their fullest by the EAS community. Therefore, the present work proposes an EAS formulation for several novel 3D EAS elements, namely twenty-seven hexahedral, six-node wedge, and eighteen-node wedge EAS elements.

1.7.3 Alleviating locking in IGA with novel hybrid elements

Addressing locking in IGA has received limited attention, particularly in the context of stress-based approaches, despite their promising performance in conventional FEA. Currently, there is no stress-based solid element formulation available for IGA. Hence, there is a need for the development of a robust class of stress-based solid hybrid elements in IGA to provide a locking-free response during the analysis of thin structural geometries or problems involving almost incompressible materials.

1.7.4 Alleviating locking in IGA through novel EAS elements

The strain-based approach, particularly the EAS method, has received limited attention in the context of IGA. The existing literature in IGA on the EAS method focuses on 2D problems and is primarily concerned with alleviating volumetric locking [135]. Moreover, it requires an additional stabilization strategy to function effectively in non-locking scenarios. Therefore, there is a scope to develop a robust class of strain-based solid EAS elements that are tailored for NURBS-based IGA to provide a locking-free response during the analysis of thin structural geometries or problems involving near-incompressible materials.

1.8 Objectives of the present work

Based on the scope of research identified in the previous section, the objectives of the present work are as follows:

1. To carry out a comprehensive performance evaluation of various numerical strategies that are known for their ability to alleviate shear, membrane, and volumetric locking.
2. To develop a novel family of EAS elements by investigating the interrelation between the two-field HR and three-field VHW variational formulations to alleviate locking in FEA.
3. To develop HR principle-based stress-displacement formulation to alleviate locking in NURBS-based IGA.
4. To develop a robust family of strain-based EAS elements to alleviate locking in NURBS-based IGA.

1.9 Organization of the thesis

The thesis is organized into eight chapters, which are followed by the appendices and references:

In **Chapter 1**, a foundational introduction to FEA and IGA is presented. It discusses a common limitation in both methods and explores current state-of-the-art approaches to overcome this challenge. Additionally, the chapter identifies unexplored research gaps within the existing literature and outlines the objectives of the current work, with the explicit aim of introducing a novel contribution to the scientific discourse.

In **Chapter 2**, essential details on the governing equation for a classical linear elasticity problem, weak form, and the participating variational statement for the conventional single-field FE formulation are outlined. The focus then transitions to multi-field formulations, specifically the VHW principle-based EAS formulation and HR-based stress-based formulation. The chapter outlines the fundamental concepts in both formulations, encompassing additional constraints, modified weak forms, associated variational statements, and existing choices for stress and enhanced strain interpolation functions. Additionally, it discusses fundamental concepts of SRI, ANS, and generalized ANS formulations, and highlights their distinctions from conventional FE formulations.

In **Chapter 3**, a comprehensive performance evaluation of existing locking alleviation strategies is conducted through numerous numerical examples encompassing a diverse range of 2D and 3D problems. The methods are evaluated under increasing shear and coupled shear-membrane locking influences, followed by assessments in scenarios involving severe volumetric locking. The relative efficacy is determined for SRI, ANS, EAS, and a hybrid formulation class, alongside the conventional FE formulation.

In **Chapter 4**, three novel strain-based EAS elements, namely twenty-seven node hexahedral, six-node wedge, and eighteen-node wedge EAS elements are proposed to alleviate the locking effects in conventional FEA. Furthermore, it outlines the systematic procedure for deriving the aforementioned elements, emphasizing the investigation of the interrelation between the two-field HR and three-field VHW variational formulations. Finally, the robustness and performance of the proposed EAS elements is demonstrated through numerous examples.

In **Chapter 5**, a brief overview of IGA is presented. This is followed by the mathematical preliminaries crucial for understanding fundamental concepts in geometric description using B-spline and NURBS interpolation functions. The chapter also provides insights into refinement strategies used to discretize geometry in the context of IGA, along with details on the mapping of spaces involved in IGA.

In **Chapter 6**, the stress-based locking alleviation strategy in the context of IGA is examined. The chapter proposes quadratic and cubic NURBS-based hybrid IGA elements in both 2D and 3D settings, formulated under the two-field stress-based HR variational principle. The chapter details the systematic development of admissible stress interpolation functions tailored for NURBS-based IGA elements. The performance of the proposed elements is thoroughly evaluated across diverse scenarios, including severely locking-dominated problems with different types of locking, as well as non-locking scenarios, providing a comprehensive assessment.

In **Chapter 7**, the strain-based locking alleviation strategy within the framework of IGA is presented. The chapter introduces proposed quadratic and cubic NURBS-based EAS elements in both 2D and 3D settings, formulated under the VHW variational principle-based EAS method. It elaborates on the crucial aspects of the development of enhanced strain interpolation functions for NURBS-based IGA. Finally, the chapter provides a comprehensive assessment of the proposed elements using numerous benchmark numerical examples.

Finally, **Chapter 8** summarizes the present work and its novel contributions to the existing literature. The conclusions drawn from the results presented in various chapters are then outlined, offering insights into the implications of the findings. Further, it presents the potential avenues for future research, identifying areas where further exploration and advancements can be made. Finally, the chapter provides a list of publications derived from the research.

Chapter 2

Formulations

This chapter presents an overview of the classical linear elasticity problem, encompassing details on the governing equation, weak form, and variational statement within the conventional single-field FE formulation. Further, it explores multi-field formulations, focusing on the Veubeke–Hu–Washizu (VHW) principle-based EAS formulation and stress-based Hellinger–Reissner (HR) formulation. Fundamental concepts in both formulations are discussed, incorporating additional constraints, modified weak forms, stress/enhanced strain interpolation functions, and step-wise implementation procedures. Furthermore, the chapter discusses critical aspects of SRI, ANS, and generalized ANS formulations.

2.1 A classical linear elasticity problem

Let $\mathcal{R}$ be the open domain with boundary $\partial\mathcal{R}$, such that $\partial\mathcal{R} = \partial\mathcal{R}_u \cup \partial\mathcal{R}_t$, where $\partial\mathcal{R}_u$ and $\partial\mathcal{R}_t$ represents the displacement and traction boundaries, respectively. The equations that govern the static linear elasticity problem are as follows [143]:

$$\boldsymbol{\nabla} \cdot \boldsymbol{\sigma} + \boldsymbol{b} = \boldsymbol{0} \quad \text{on } \mathcal{R}, \tag{2.1a}$$

$$\boldsymbol{\sigma}\boldsymbol{n} = \boldsymbol{t} \quad \text{on } \partial\mathcal{R}, \tag{2.1b}$$

$$\boldsymbol{u} = \bar{\boldsymbol{u}} \quad \text{on } \partial\mathcal{R}_u, \tag{2.1c}$$

$$\boldsymbol{t} = \bar{\boldsymbol{t}} \quad \text{on } \partial\mathcal{R}_t, \tag{2.1d}$$

where $\boldsymbol{\sigma}$ denotes the Cauchy stress tensor, $\boldsymbol{n}$ represents the unit outward normal to the boundary $\partial\mathcal{R}$, $\bar{\boldsymbol{t}}$ is the defined traction on the boundary $\partial\mathcal{R}_t$, and $\boldsymbol{b}$ is the vector representing body force per unit volume. The strain tensor $\boldsymbol{\varepsilon}$ is the symmetric part of the displacement gradient $\boldsymbol{\nabla u}$, which is expressed as follows:

$$\boldsymbol{\varepsilon}(\boldsymbol{u}) = \mathrm{Sym}\,(\boldsymbol{\nabla u}) = \frac{1}{2}\Big[(\boldsymbol{\nabla u}) + (\boldsymbol{\nabla u})^T\Big], \tag{2.2}$$

The relationship between stress and strain is expressed as $\boldsymbol{\sigma} = \mathbb{C}\boldsymbol{\varepsilon}$, where $\mathbb{C}$ is the fourth order material constitutive tensor.

2.2 Conventional single-field FE formulation

The variational formulation is obtained by employing the method of weighted residuals. Let $\delta\boldsymbol{u}$ represent the variation of the displacement field $(\boldsymbol{u})$ in such a way that

$$\mathcal{V}_{\boldsymbol{u}} = \Big\{\delta\boldsymbol{u} \in \mathcal{H}^1(\mathcal{R}) : \delta\boldsymbol{u} = \boldsymbol{0} \text{ on } \partial\mathcal{R}_u\Big\}, \tag{2.3}$$

where $\mathcal{V}_{\boldsymbol{u}}$ is the space associated with the admissible variations $\delta\boldsymbol{u}$. Then, the single-field variational statement is obtained by weakly enforcing Eq. 2.1a and Eq. 2.1d. If the necessary boundary condition expressed in Eq. 2.1c and stress-strain relation hold strongly, then the imposition of the prescribed conditions for the specified linear elasticity problem results in

$$\int_{\mathcal{R}} \underbrace{\delta\boldsymbol{u}\cdot(\boldsymbol{\nabla}\cdot\boldsymbol{\sigma} + \boldsymbol{b})}_{\substack{\text{weak imposition}\\ \text{of Eq. 2.1a}}}\,\mathrm{d}\mathcal{R} + \int_{\partial\mathcal{R}_t} \underbrace{\delta\boldsymbol{u}\cdot(\bar{\boldsymbol{t}} - \boldsymbol{t})}_{\substack{\text{weak imposition}\\ \text{of Eq. 2.1d}}}\,\mathrm{d}A = 0. \tag{2.4}$$

By using the identity $\boldsymbol{\nabla}\cdot(\boldsymbol{\sigma}^T\delta\boldsymbol{u}) = \delta\boldsymbol{u}\cdot(\boldsymbol{\nabla}\cdot\boldsymbol{\sigma}) + \boldsymbol{\nabla}\delta\boldsymbol{u} : \boldsymbol{\sigma}$ and the symmetry of stress tensor followed by the Gauss divergence theorem, the above expression reduces to

$$-\int_{\mathcal{R}} \boldsymbol{\sigma} : (\boldsymbol{\nabla}\delta\boldsymbol{u})\,\mathrm{d}\mathcal{R} + \int_{\partial\mathcal{R}} \delta\boldsymbol{u}\cdot\boldsymbol{t}\,\mathrm{d}A + \int_{\mathcal{R}} \delta\boldsymbol{u}\cdot\boldsymbol{b}\,\mathrm{d}\mathcal{R} + \int_{\partial\mathcal{R}_t} \delta\boldsymbol{u}\cdot\bar{\boldsymbol{t}}\,\mathrm{d}A - \int_{\partial\mathcal{R}_t} \delta\boldsymbol{u}\cdot\boldsymbol{t}\,\mathrm{d}A = 0 \tag{2.5}$$

As boundary $\partial\mathcal{R}$ is composed of two disjoint regions such that $\partial\mathcal{R} = \partial\mathcal{R}_u \cup \partial\mathcal{R}_t$ and the displacement on $\partial\mathcal{R}_u$ is prescribed, the integral $\int_{\partial\mathcal{R}} \delta\boldsymbol{u}\cdot\boldsymbol{t}\,\mathrm{d}A$ can be written as follows:

$$\int_{\partial\mathcal{R}} \delta\boldsymbol{u}\cdot\boldsymbol{t}\,\mathrm{d}A = \int_{\partial\mathcal{R}_u} \delta\boldsymbol{u}\cdot\boldsymbol{t}\,\mathrm{d}A + \int_{\partial\mathcal{R}_t} \delta\boldsymbol{u}\cdot\boldsymbol{t}\,\mathrm{d}A = \int_{\partial\mathcal{R}_t} \delta\boldsymbol{u}\cdot\boldsymbol{t}\,\mathrm{d}A. \tag{2.6}$$

After substituting Eq. 2.6 into Eq. 2.5 and introducing the Voigt notations for stress and strain tensor as $\bar{\boldsymbol{\sigma}}$ and $\bar{\boldsymbol{\varepsilon}}^u$ in such a way that $\boldsymbol{\sigma} : (\boldsymbol{\nabla}\delta\boldsymbol{u}) = \boldsymbol{\sigma} : \boldsymbol{\varepsilon}(\delta\boldsymbol{u}) = (\delta\bar{\boldsymbol{\varepsilon}}^{\boldsymbol{u}})^T\bar{\boldsymbol{\sigma}}$ then, the Eq. 2.5 simplifies to following single-field variational statement:

$$\int_{\mathcal{R}} (\delta\bar{\boldsymbol{\varepsilon}}^u)^T\bar{\boldsymbol{\sigma}}\,\mathrm{d}\mathcal{R} = \int_{\mathcal{R}} \delta\boldsymbol{u}^T\boldsymbol{b}\,\mathrm{d}\mathcal{R} + \int_{\partial\mathcal{R}_t} \delta\boldsymbol{u}^T\bar{\boldsymbol{t}}\,\mathrm{d}A \qquad \forall\, \delta\boldsymbol{u} \in \mathcal{V}_{\boldsymbol{u}}. \tag{2.7}$$

The independent displacement field and its variation is interpolated using the following expressions:

$$\boldsymbol{u} = \boldsymbol{N}\hat{\boldsymbol{u}}, \text{ and } \delta\boldsymbol{u} = \boldsymbol{N}\delta\hat{\boldsymbol{u}}, \tag{2.8}$$

where $\boldsymbol{N}$ is the Lagrange shape function matrix, $\hat{\boldsymbol{u}}$ is the nodal displacement vector. The vector $\bar{\boldsymbol{\varepsilon}}^u$ can be expressed as:

$$\bar{\boldsymbol{\varepsilon}}^u = \begin{bmatrix} \varepsilon_{xx} \\ \varepsilon_{yy} \\ \varepsilon_{zz} \\ \varepsilon_{xy} \\ \varepsilon_{yz} \\ \varepsilon_{xz} \end{bmatrix} = \begin{bmatrix} u_{x,x} \\ u_{y,y} \\ u_{z,z} \\ \frac{1}{2}\left(u_{x,y} + u_{y,x}\right) \\ \frac{1}{2}\left(u_{y,z} + u_{z,y}\right) \\ \frac{1}{2}\left(u_{x,z} + u_{z,x}\right) \end{bmatrix} = \boldsymbol{B}\hat{\boldsymbol{u}}, \tag{2.9}$$

where u_x, u_y, and u_z are the components of displacement vector $\boldsymbol{u}$, $u_{i,j}$ represent the partial derivation of i^{th} component of $\boldsymbol{u}$ with respect to j^{th} coordinate variable (x, y, or z), and $\boldsymbol{B}$ is the strain-displacement matrix. Substituting Eqs. 2.8 and 2.9 in Eq. 2.7 followed by utilizing the arbitrariness of $\delta\hat{\boldsymbol{u}}$, we get

$$\left[\int_{\mathcal{R}} \boldsymbol{B}^T \boldsymbol{C} \boldsymbol{B} \, \mathrm{d}\mathcal{R}\right] \hat{\boldsymbol{u}} - \left[\int_{\mathcal{R}} \boldsymbol{N}^T \boldsymbol{b} \, \mathrm{d}\mathcal{R} + \int_{\partial\mathcal{R}_t} \boldsymbol{N}^T \bar{\boldsymbol{t}} \, \mathrm{d}A\right] = \boldsymbol{0}. \tag{2.10}$$

This can be further written as

$$\begin{gathered} \boldsymbol{K}\hat{\boldsymbol{u}} = \hat{\boldsymbol{f}}, \text{ where} \\ \boldsymbol{K} = \int_{\mathcal{R}} \boldsymbol{B}^T \boldsymbol{C} \boldsymbol{B} \, \mathrm{d}\mathcal{R}, \ \hat{\boldsymbol{f}} = \int_{\mathcal{R}} \boldsymbol{N}^T \boldsymbol{b} \, \mathrm{d}\mathcal{R} + \int_{\partial\mathcal{R}_t} \boldsymbol{N}^T \bar{\boldsymbol{t}} \, \mathrm{d}A. \end{gathered} \tag{2.11}$$

Here, $\boldsymbol{K}$ represents the stiffness matrix and $\hat{\boldsymbol{f}}$ denotes the load vector. After establishing above relations, stiffness matrices and load vectors are calculated for individual elements and assembled into a global stiffness matrix and global load vector, respectively. Finally, after imposing the essential boundary conditions, the system of equations can then solved to determine displacements.

2.3 VHW variational principle for EAS method

The VHW variational principle consists of three primary field variables: displacement ($\boldsymbol{u}$), stress ($\boldsymbol{\sigma}$), and strain ($\boldsymbol{\varepsilon}$). The admissible variations of these variables are represented by $\delta\boldsymbol{u}$, $\delta\boldsymbol{\sigma}$, and $\delta\boldsymbol{\varepsilon}$, respectively. Let $\mathcal{V}_{\boldsymbol{u}}$, $\mathcal{V}_{\boldsymbol{\sigma}}$, and $\mathcal{V}_{\boldsymbol{\varepsilon}}$ be the spaces associated with $\delta\boldsymbol{u}$, $\delta\boldsymbol{\sigma}$ and $\delta\boldsymbol{\varepsilon}$, respectively, which can be expressed as follows:

$$\mathcal{V}_{\boldsymbol{u}} = \left\{\delta\boldsymbol{u} \in \mathcal{H}^1(\mathcal{R}) : \delta\boldsymbol{u} = \boldsymbol{0} \text{ on } \partial\mathcal{R}_u\right\}, \tag{2.12}$$

$$\mathcal{V}_{\boldsymbol{\sigma}} = \left\{\delta\boldsymbol{\sigma} \in \mathcal{L}^2(\mathcal{R}) : \delta\boldsymbol{\sigma} = \delta\boldsymbol{\sigma}^T\right\}, \tag{2.13}$$

$$\mathcal{V}_{\boldsymbol{\varepsilon}} = \left\{\delta\boldsymbol{\varepsilon} \in \mathcal{L}^2(\mathcal{R}) : \delta\boldsymbol{\varepsilon} = \delta\boldsymbol{\varepsilon}^T\right\}. \tag{2.14}$$

Let $\boldsymbol{\sigma}^{\varepsilon}$ denote the stress tensor obtained by applying the stress-strain relation ($\boldsymbol{\sigma} = \mathbb{C}\boldsymbol{\varepsilon}$), and $\boldsymbol{\varepsilon}^{u}$ represent the strain tensor derived from the displacements using Eq. 2.2. Then, the three-field VHW variational principle is obtained by weakly enforcing Eq. 2.1a, Eq. 2.1d, equality of the strain tensors ($\boldsymbol{\varepsilon}^{u} = \boldsymbol{\varepsilon}$), and equality of the stress tensors ($\boldsymbol{\sigma}^{\varepsilon} = \boldsymbol{\sigma}$). However, the necessary boundary condition (Eq. 2.1c) and stress-strain relation are strongly satisfied, leading to the following form of VHW variational principle:

$$\begin{split}\int_{\mathcal{R}} \underbrace{\delta\boldsymbol{u}\cdot(\boldsymbol{\nabla}\cdot\boldsymbol{\sigma}+\boldsymbol{b})}_{\substack{\text{weak imposition}\\ \text{of Eq. 2.1a}}}\,\mathrm{d}\mathcal{R} + \int_{\partial\mathcal{R}_t} \underbrace{\delta\boldsymbol{u}\cdot(\bar{\boldsymbol{t}}-\boldsymbol{t})}_{\substack{\text{weak imposition}\\ \text{of Eq. 2.1d}}}\,\mathrm{d}A + \int_{\mathcal{R}} \underbrace{\delta\boldsymbol{\sigma} : (\boldsymbol{\varepsilon}^{u}-\boldsymbol{\varepsilon})}_{\substack{\text{weak imposition}\\ \text{of } \boldsymbol{\varepsilon}^{u}=\boldsymbol{\varepsilon}}}\,\mathrm{d}\mathcal{R} \\ + \int_{\mathcal{R}} \underbrace{\delta\boldsymbol{\varepsilon} : (\boldsymbol{\sigma}^{\varepsilon}-\boldsymbol{\sigma})}_{\substack{\text{weak imposition}\\ \text{of } \boldsymbol{\sigma}^{\varepsilon}=\boldsymbol{\sigma}}}\,\mathrm{d}\mathcal{R} = 0.\end{split} \tag{2.15}$$

The foundation of the EAS method is based on the above VHW principle. In EAS method, the strain $\boldsymbol{\varepsilon}$ is divided into two parts as follows:

$$\boldsymbol{\varepsilon} = \boldsymbol{\varepsilon}^{u} + \boldsymbol{\varepsilon}^{\alpha}, \tag{2.16}$$

where $\boldsymbol{\varepsilon}^{u}$ is the compatible strain field defined by Eq. 2.2 and $\boldsymbol{\varepsilon}^{\alpha}$ is the independent enhanced strain field introduced to alleviate the locking. Substituting Eq. 2.16 in Eq. 2.15 leads to

$$\begin{split}\int_{\mathcal{R}} (\delta\boldsymbol{\varepsilon}^{u} : \boldsymbol{\sigma}^{\varepsilon})\,\mathrm{d}\mathcal{R} - \int_{\mathcal{R}} (\delta\boldsymbol{\sigma} : \boldsymbol{\varepsilon}^{\alpha})\,\mathrm{d}\mathcal{R} + \int_{\mathcal{R}} [\delta\boldsymbol{\varepsilon}^{\alpha} : (\boldsymbol{\sigma}^{\varepsilon}-\boldsymbol{\sigma})]\,\mathrm{d}\mathcal{R} \\ = \int_{\mathcal{R}} \delta\boldsymbol{u}^{T}\boldsymbol{b}\,\mathrm{d}\mathcal{R} + \int_{\partial\mathcal{R}_t} \delta\boldsymbol{u}^{T}\bar{\boldsymbol{t}}\,\mathrm{d}A.\end{split} \tag{2.17}$$

In order to avoid the dependency on $\boldsymbol{\sigma}$ in VHW variational principle, an orthogonality condition is introduced between $\boldsymbol{\sigma}$ and $\boldsymbol{\varepsilon}^{\alpha}$ such that

$$\int_{\mathcal{R}} \delta\boldsymbol{\sigma} : \boldsymbol{\varepsilon}^{\alpha}\,\mathrm{d}\mathcal{R} = 0 \quad \text{or} \quad \int_{\mathcal{R}} \delta\bar{\boldsymbol{\sigma}}^{T}\bar{\boldsymbol{\varepsilon}}^{\alpha}\,\mathrm{d}\mathcal{R} = 0, \tag{2.18}$$

where $\delta\bar{\boldsymbol{\sigma}}$ and $\bar{\boldsymbol{\varepsilon}}^{\alpha}$ are the vector form of $\delta\boldsymbol{\sigma}$ and $\boldsymbol{\varepsilon}^{\alpha}$, respectively. Finally, the variational statement involved in EAS is derived by consecutively choosing zero variations of displacements and assumed strains separately, i.e., $(\delta\boldsymbol{u}, \delta\boldsymbol{\varepsilon}^{\alpha}) = (\delta\boldsymbol{u}, \boldsymbol{0})$ and $(\delta\boldsymbol{u}, \delta\boldsymbol{\varepsilon}^{\alpha}) = (\boldsymbol{0}, \delta\boldsymbol{\varepsilon}^{\alpha})$. Assuming the orthogonality as per Eq. 2.18, the EAS approach can be formulated through the following variational statement:

$$\int_{\mathcal{R}} (\delta\bar{\boldsymbol{\varepsilon}}^{u})^{T}\bar{\boldsymbol{\sigma}}^{\varepsilon}\,\mathrm{d}\mathcal{R} = \int_{\mathcal{R}} \delta\boldsymbol{u}^{T}\boldsymbol{b}\,\mathrm{d}\mathcal{R} + \int_{\partial\mathcal{R}_t} \delta\boldsymbol{u}^{T}\bar{\boldsymbol{t}}\,\mathrm{d}A \qquad \forall\ \delta\boldsymbol{u} \in \mathcal{V}_{\boldsymbol{u}}, \tag{2.19}$$

$$\int_{\mathcal{R}} (\delta\bar{\boldsymbol{\varepsilon}}^{\alpha})^{T}(\bar{\boldsymbol{\sigma}}^{\varepsilon} - \bar{\boldsymbol{\sigma}})\,\mathrm{d}\mathcal{R} = 0, \tag{2.20}$$

where $\bar{\boldsymbol{\varepsilon}}^u$, $\bar{\boldsymbol{\varepsilon}}^\alpha$, and $\bar{\boldsymbol{\sigma}}$ are the vector representations of $\boldsymbol{\varepsilon}^u$, $\boldsymbol{\varepsilon}^\alpha$, and $\boldsymbol{\sigma}$, respectively. The above EAS variational statements only contain $\boldsymbol{u}$ and $\boldsymbol{\varepsilon}^\alpha$ as the participating independent field variables.

2.3.1 Approximation of field variables

The VHW-based EAS variational principles necessitate the use of independent interpolation techniques for approximating the independent field variables. These field variables are defined using the following expressions:

$$\boldsymbol{u} = \boldsymbol{N}\hat{\boldsymbol{u}}, \quad \delta\boldsymbol{u} = \boldsymbol{N}\delta\hat{\boldsymbol{u}}; \quad \forall\, \hat{\boldsymbol{u}}, \delta\hat{\boldsymbol{u}} \in \mathbb{R}^{n_d \times n_e}, \tag{2.21}$$

$$\bar{\boldsymbol{\varepsilon}}^\alpha = \boldsymbol{G}\hat{\boldsymbol{\alpha}}, \quad \delta\bar{\boldsymbol{\varepsilon}}^\alpha = \boldsymbol{G}\delta\hat{\boldsymbol{\alpha}}; \quad \forall\, \hat{\boldsymbol{\alpha}}, \delta\hat{\boldsymbol{\alpha}} \in \mathbb{R}^{n_{\hat{\alpha}}}. \tag{2.22}$$

Here, n_e represents the number of nodes in each element, n_d denotes the degrees of freedom for each node, and $n_{\hat{\beta}}$ is the number of enhanced strain parameters per element. The matrix $\boldsymbol{N}$ and $\boldsymbol{G}$ are the displacement and strain interpolation matrices. Conventionally, $\boldsymbol{N}$ is composed of the Lagrange interpolation functions, whereas special schemes must be developed to choose appropriate $\boldsymbol{G}$ interpolation matrices.

The matrix $\boldsymbol{G}$ in physical coordinate systems relates with the strain interpolation matrix in natural coordinate system using the following relation:

$$\boldsymbol{G} = \frac{\mid \boldsymbol{J}_0 \mid}{\mid \boldsymbol{J} \mid} \boldsymbol{T}_0^{-T} \tilde{\boldsymbol{G}}, \tag{2.23}$$

where $\tilde{\boldsymbol{G}}$ are the strain interpolation matrix defined in the natural coordinate system, the Jacobian $\boldsymbol{J}$ relates the physical and natural coordinate system, whereas $\boldsymbol{J}_0$ is the Jacobian evaluated at the element center. The transformation matrix, $\boldsymbol{T}_0$, connects the $\tilde{\boldsymbol{G}}$ in the natural space to their corresponding counterparts in the physical space. The matrix $\boldsymbol{T}_0$ is evaluated at the element center in order to pass the requirement of the patch test. The expression for $\boldsymbol{T}$ is given as follows:

$$\boldsymbol{T} = \begin{bmatrix} J_{11}^2 & J_{21}^2 & J_{31}^2 & 2J_{11}J_{21} & 2J_{21}J_{31} & 2J_{11}J_{31} \\ J_{12}^2 & J_{22}^2 & J_{32}^2 & 2J_{12}J_{22} & 2J_{22}J_{32} & 2J_{12}J_{32} \\ J_{13}^2 & J_{23}^2 & J_{33}^2 & 2J_{13}J_{23} & 2J_{23}J_{33} & 2J_{13}J_{33} \\ J_{11}J_{12} & J_{21}J_{22} & J_{31}J_{32} & (J_{11}J_{22} + J_{21}J_{12}) & (J_{21}J_{32} + J_{31}J_{22}) & (J_{11}J_{32} + J_{31}J_{12}) \\ J_{12}J_{13} & J_{22}J_{23} & J_{32}J_{33} & (J_{12}J_{23} + J_{13}J_{22}) & (J_{22}J_{33} + J_{32}J_{23}) & (J_{12}J_{33} + J_{32}J_{13}) \\ J_{11}J_{13} & J_{21}J_{23} & J_{31}J_{33} & (J_{11}J_{23} + J_{21}J_{13}) & (J_{21}J_{33} + J_{31}J_{23}) & (J_{11}J_{33} + J_{31}J_{13}) \end{bmatrix}, \tag{2.24}$$

The matrix $\boldsymbol{T}$ for 2D problems is reduces to the following form:

$$\boldsymbol{T} = \begin{bmatrix} J_{11}^2 & J_{21}^2 & 2J_{11}J_{21} \\ J_{12}^2 & J_{22}^2 & 2J_{12}J_{22} \\ J_{11}J_{12} & J_{21}J_{22} & (J_{11}J_{22} + J_{12}J_{21}) \end{bmatrix}, \tag{2.25}$$

Table 2.1: Possible choices of $\tilde{\boldsymbol{G}}$ matrix for four-node quadrilateral element

n_α[1]	Columns[2]	Capability
2	1-2	Alleviate only volumetric locking.
4	1-4	Alleviate volumetric and shear locking.
7	1-7	Better performance under distorted mesh.

[1] n_α represents number of enhanced strain parameters.
[2] Columns states the participating columns of $\tilde{\boldsymbol{G}}$ shown in Eq. 2.26.

where J_{ij} are the components of the $\boldsymbol{J}$.

2.3.2 Existing choices of strain interpolation matrix

Multiple options for the $\tilde{\boldsymbol{G}}$ matrix are available to address specific requirements. The selection of the $\tilde{\boldsymbol{G}}$ matrix varies for different elements. The specific choices are outlined as follows:

2.3.2.1 Four-node quadrilateral element

There are several choices available for the $\tilde{\boldsymbol{G}}$ matrix for four-node quadrilateral element. However, the current work mainly focuses on the most robust option [125], which is given as follows:

$$\tilde{\boldsymbol{G}}(\xi,\eta) = \begin{bmatrix} \xi & 0 & 0 & 0 & \xi\eta & 0 & 0 \\ 0 & \eta & 0 & 0 & 0 & \xi\eta & 0 \\ 0 & 0 & \xi & \eta & 0 & 0 & \xi\eta \end{bmatrix} \tag{2.26}$$

It is possible to utilize the subset of the above $\tilde{\boldsymbol{G}}$ matrix, to specifically address certain types of locking. While this reduces computational costs, it also limits the applicability of an element to specific problem descriptions. Table 2.1 enlists the possible subsets of $\tilde{\boldsymbol{G}}$ and its best-fit applicability.

2.3.2.2 Nine-node quadrilateral element

For a nine-node quadrilateral element, $\bar{\varepsilon}^\alpha$ is interpolated using the following $\tilde{\boldsymbol{G}}$ matrix [168]:

$$\tilde{\boldsymbol{G}}(\xi,\eta) = \begin{bmatrix} \tilde{\boldsymbol{G}}_1 & \mathbf{0}_a & \mathbf{0}_b \\ \mathbf{0}_a & \tilde{\boldsymbol{G}}_2 & \mathbf{0}_b \\ \mathbf{0}_a & \mathbf{0}_a & \tilde{\boldsymbol{G}}_3 \end{bmatrix}, \tag{2.27}$$

where $\mathbf{0}_a$ and $\mathbf{0}_b$ are null matrices of dimensions 1×3 and 1×5, respectively. The vectors $\tilde{\boldsymbol{G}}_1$, $\tilde{\boldsymbol{G}}_2$ and $\tilde{\boldsymbol{G}}_3$ are given as follows:

$$\tilde{\boldsymbol{G}}_1 = \begin{bmatrix} f(\xi) & \eta f(\xi) & f(\xi)f(\eta) \end{bmatrix}, \quad \tilde{\boldsymbol{G}}_2 = \begin{bmatrix} f(\eta) & \xi f(\eta) & f(\xi)f(\eta) \end{bmatrix},$$
$$\tilde{\boldsymbol{G}}_3 = \begin{bmatrix} f(\xi) & \eta f(\xi) & f(\eta) & \xi f(\eta) & f(\xi)f(\eta) \end{bmatrix},$$

where $f(\xi) = 3\xi^2 - 1,\ f(\eta) = 3\eta^2 - 1$.

2.3.2.3 Eight-node brick element

A robust strain interpolation matrix used to approximate the enhanced strains of a eight-node brick element is given as follows:

$$\tilde{\boldsymbol{G}}(\xi,\eta,\zeta) = \begin{bmatrix} \tilde{\boldsymbol{G}}_1 \\ \tilde{\boldsymbol{G}}_2 \\ \tilde{\boldsymbol{G}}_3 \\ \tilde{\boldsymbol{G}}_4 \\ \tilde{\boldsymbol{G}}_5 \\ \tilde{\boldsymbol{G}}_6 \end{bmatrix}, \tag{2.28}$$

where
$$\begin{aligned}
\tilde{\boldsymbol{G}}_1 &= \begin{bmatrix} \xi & \mathbf{0}_{1\times 14} & \xi\eta & \xi\zeta & \mathbf{0}_{1\times 7} & \xi\eta\zeta & \mathbf{0}_{1\times 5} \end{bmatrix}, \\
\tilde{\boldsymbol{G}}_2 &= \begin{bmatrix} \mathbf{0}_{1\times 1} & \eta & \mathbf{0}_{1\times 15} & \xi\eta & \eta\zeta & \mathbf{0}_{1\times 6} & \xi\eta\zeta & \mathbf{0}_{1\times 4} \end{bmatrix}, \\
\tilde{\boldsymbol{G}}_3 &= \begin{bmatrix} \mathbf{0}_{1\times 2} & \zeta & \mathbf{0}_{1\times 16} & \xi\zeta & \eta\zeta & \mathbf{0}_{1\times 5} & \xi\eta\zeta & \mathbf{0}_{1\times 3} \end{bmatrix}, \\
\tilde{\boldsymbol{G}}_4 &= \begin{bmatrix} \mathbf{0}_{1\times 3} & \xi & \eta & \mathbf{0}_{1\times 4} & \xi\zeta & \eta\zeta & \mathbf{0}_{1\times 10} & \xi\eta & \mathbf{0}_{1\times 5} & \xi\eta\zeta & \mathbf{0}_{1\times 2} \end{bmatrix}, \\
\tilde{\boldsymbol{G}}_5 &= \begin{bmatrix} \mathbf{0}_{1\times 5} & \eta & \zeta & \mathbf{0}_{1\times 4} & \xi\eta & \xi\zeta & \mathbf{0}_{1\times 9} & \eta\zeta & \mathbf{0}_{1\times 5} & \xi\eta\zeta & \mathbf{0}_{1\times 1} \end{bmatrix}, \\
\tilde{\boldsymbol{G}}_6 &= \begin{bmatrix} \mathbf{0}_{1\times 7} & \xi & \zeta & \mathbf{0}_{1\times 4} & \xi\eta & \eta\zeta & \mathbf{0}_{1\times 8} & \xi\zeta & \mathbf{0}_{1\times 5} & \xi\eta\zeta \end{bmatrix},
\end{aligned}$$

where $\mathbf{0}_{m\times n}$ is the zero vector consisting m rows and n columns. Similar to four-node quadrilateral element, it is possible to use subset of Eq. 2.28 to reduce the computational efforts. The choice of the subset is governed by the problem description and the type of locking. Table 2.2 enlists the possible subsets of $\tilde{\boldsymbol{G}}$ and its best-fit applicability.

Table 2.2: Possible choices of $\tilde{\boldsymbol{G}}$ matrix for eight-node brick element

n_α[1]	Columns[2]	Capability
3	1-3	Alleviate only volumetric locking
6	4-9	Alleviate only shear locking
9	1-9	Alleviate shear and volumetric locking
12	1-9, 16, 19, 20	Better performance in incompressible problem domain than EAS9
15	1-15	Better bending behavior than EAS9
21	1-21	Free of volumetric locking and partial shear locking may be present for badly shaped meshes
24	1-24	Free of shear and volumetric locking
30	1-30	Free of shear and volumetric locking and performs better in distorted meshes

[1] n_α represents number of enhanced strain parameters.

[2] Columns states the participating columns of $\tilde{\boldsymbol{G}}$ shown in Eq. 2.28.

2.3.3 Elemental equations for EAS method

To complete the discussion on EAS formulation, the current section briefly summarizes the expression of the stiffness matrix involved in the EAS formulation. Recalling the expressions of $\boldsymbol{u}$, $\bar{\boldsymbol{\sigma}}$, and $\bar{\varepsilon}^{\alpha}$ and its respective variations $\delta\boldsymbol{u}$, $\delta\bar{\boldsymbol{\sigma}}$, and $\delta\bar{\varepsilon}^{\alpha}$ (Eqs. 2.21 and 2.22) and substituting into Eqs. 2.19 and 2.20, followed by utilizing the arbitrariness of $\delta\hat{\boldsymbol{u}}$ and $\delta\hat{\boldsymbol{\alpha}}$, results in the following expressions:

$$\left[\int_{\mathcal{R}} \boldsymbol{B}^T\boldsymbol{C}\boldsymbol{B}\,\mathrm{d}\mathcal{R}\right]\hat{\boldsymbol{u}} + \left[\int_{\mathcal{R}} \boldsymbol{B}^T\boldsymbol{C}\boldsymbol{G}\,\mathrm{d}\mathcal{R}\right]\hat{\boldsymbol{\alpha}} - \left[\int_{\mathcal{R}} \boldsymbol{N}^T\boldsymbol{b}\,\mathrm{d}\mathcal{R} + \int_{\partial\mathcal{R}_t} \boldsymbol{N}^T\bar{\boldsymbol{t}}\,\mathrm{d}A\right] = \boldsymbol{0}, \tag{2.29}$$

$$\left[\int_{\mathcal{R}} \boldsymbol{G}^T\boldsymbol{C}\boldsymbol{B}\,\mathrm{d}\mathcal{R}\right]\hat{\boldsymbol{u}} + \left[\int_{\mathcal{R}} \boldsymbol{G}^T\boldsymbol{C}\boldsymbol{G}\,\mathrm{d}\mathcal{R}\right]\hat{\boldsymbol{\alpha}} = \boldsymbol{0}. \tag{2.30}$$

Let $\boldsymbol{K}^c$, $\boldsymbol{M}$, $\boldsymbol{H}$, and $\hat{\boldsymbol{f}}$ be defined by the following expressions:

$$\boldsymbol{K}^c = \int_{\mathcal{R}} \boldsymbol{B}^T\boldsymbol{C}\boldsymbol{B}\,\mathrm{d}\mathcal{R}, \quad \boldsymbol{M} = \int_{\mathcal{R}} \boldsymbol{G}^T\boldsymbol{C}\boldsymbol{B}\,\mathrm{d}\mathcal{R}, \quad \boldsymbol{H} = \int_{\mathcal{R}} \boldsymbol{G}^T\boldsymbol{C}\boldsymbol{G}\,\mathrm{d}\mathcal{R},$$
$$\hat{\boldsymbol{f}} = \int_{\mathcal{R}} \boldsymbol{N}^T\boldsymbol{b}\,\mathrm{d}\mathcal{R} + \int_{\partial\mathcal{R}_t} \boldsymbol{N}^T\bar{\boldsymbol{t}}\,\mathrm{d}A.$$

Then, it is possible to express Eqs. 2.53 and 2.54 as follows:

$$\begin{bmatrix} \boldsymbol{K}^c & \boldsymbol{M}^T \\ \boldsymbol{M} & \boldsymbol{H} \end{bmatrix} \begin{Bmatrix} \hat{\boldsymbol{u}} \\ \hat{\boldsymbol{\alpha}} \end{Bmatrix} = \begin{Bmatrix} \hat{\boldsymbol{f}} \\ \boldsymbol{0} \end{Bmatrix}. \tag{2.31}$$

By calculating the expression for $\hat{\boldsymbol{\alpha}}$ from Eq. 2.55, the above expression reduces to the following relations:

$$\hat{\boldsymbol{\alpha}} = -\boldsymbol{H}^{-1}\boldsymbol{M}\hat{\boldsymbol{u}}, \tag{2.32}$$

$$\underbrace{\left[\boldsymbol{K}^c - \boldsymbol{M}^T\boldsymbol{H}^{-1}\boldsymbol{M}\right]}_{\boldsymbol{K}^{\mathrm{eas}}}\hat{\boldsymbol{u}} = \hat{\boldsymbol{f}} \rightarrow \boldsymbol{K}^{\mathrm{eas}}\hat{\boldsymbol{u}} = \hat{\boldsymbol{f}}, \tag{2.33}$$

where the stiffness matrix for EAS element is $\boldsymbol{K}^{\mathrm{eas}} = \boldsymbol{K}^c - \boldsymbol{M}^T\boldsymbol{H}^{-1}\boldsymbol{M}$. The inverse of $\boldsymbol{H}$ can be computed at the element level as the strain interpolations are discontinuous between the elements. Hence, $\boldsymbol{K}^{\mathrm{eas}}$ of an element can be expressed as follows:

$$\boldsymbol{K}_e^{\mathrm{eas}} = \left[\boldsymbol{K}_e^c - \boldsymbol{M}_e^T\boldsymbol{H}_e^{-1}\boldsymbol{M}_e\right],$$
$$\text{where } \boldsymbol{K}_e^c = \int_{\mathcal{R}_e} \boldsymbol{B}_e^T\boldsymbol{C}\boldsymbol{B}_e\,\mathrm{d}\mathcal{R}_e,\ \boldsymbol{M}_e = \int_{\mathcal{R}_e} \boldsymbol{G}_e^T\boldsymbol{C}\boldsymbol{B}_e\,\mathrm{d}\mathcal{R}_e, \text{ and } \boldsymbol{H}_e = \int_{\mathcal{R}_e} \boldsymbol{G}_e^T\boldsymbol{C}\boldsymbol{G}_e\,\mathrm{d}\mathcal{R}_e.$$

The above expressions demonstrate that the additional degrees of freedom are condensed out at the elemental level. Therefore, the EAS formulation is ultimately composed solely of displacement degrees of freedom. The methodical algorithmic procedure for step-by-step implementation of VHW variational principle-based EAS method in FEA is given in Algorithm 1.

2.4 Stress-based HR variational principle

The HR variational principle comprises of two independent field variables, i.e., displacement and stress. Let $\boldsymbol{u}$ and $\boldsymbol{\sigma}$ be the independent displacement and stress field, respectively, while $\delta\boldsymbol{u}$ and $\delta\boldsymbol{\sigma}$ represent their respective variations in such a way that

$$\mathcal{V}_{\boldsymbol{u}} = \Big\{ \delta\boldsymbol{u} \in \mathcal{H}^1(\mathcal{R}) : \delta\boldsymbol{u} = \boldsymbol{0} \text{ on } \partial\mathcal{R}_u \Big\}, \tag{2.34}$$

$$\mathcal{V}_{\boldsymbol{\sigma}} = \Big\{ \delta\boldsymbol{\sigma} \in \mathcal{L}^2(\mathcal{R}) : \delta\boldsymbol{\sigma} = \delta\boldsymbol{\sigma}^T \Big\}, \tag{2.35}$$

where $\mathcal{V}_{\boldsymbol{u}}$ and $\mathcal{V}_{\boldsymbol{\sigma}}$ are the spaces associated with the admissible variations $\delta\boldsymbol{u}$ and $\delta\boldsymbol{\sigma}$, respectively. Let the strain tensors obtained from $\boldsymbol{\sigma} = \mathbb{C}\boldsymbol{\varepsilon}$ and Eq. 2.2 be represented as $\boldsymbol{\varepsilon}^s$ and $\boldsymbol{\varepsilon}^u$, respectively. Then, the two-field HR variational statement is obtained by weakly enforcing Eq. 2.1a, Eq. 2.1d, and the equality of the strain tensors ($\boldsymbol{\varepsilon}^s = \boldsymbol{\varepsilon}^u$). If the necessary boundary condition expressed in Eq. 2.1c and stress-strain relation hold strongly, and $(\delta\boldsymbol{u}, \delta\boldsymbol{\sigma}) \in (\mathcal{V}_{\boldsymbol{u}} \times \mathcal{V}_{\boldsymbol{\sigma}})$, then the imposition of the prescribed conditions in the specified linear elasticity problem results in

$$\int_{\mathcal{R}} \underbrace{\delta\boldsymbol{u} \cdot (\boldsymbol{\nabla} \cdot \boldsymbol{\sigma} + \boldsymbol{b})}_{\substack{\text{weak imposition} \\ \text{of Eq. 2.1a}}} \, \mathrm{d}\mathcal{R} + \int_{\partial\mathcal{R}_t} \underbrace{\delta\boldsymbol{u} \cdot (\bar{\boldsymbol{t}} - \boldsymbol{t})}_{\substack{\text{weak imposition} \\ \text{of Eq. 2.1d}}} \, \mathrm{d}A + \int_{\mathcal{R}} \underbrace{\delta\boldsymbol{\sigma} : (\boldsymbol{\varepsilon}^u - \boldsymbol{\varepsilon}^s)}_{\substack{\text{weak imposition} \\ \text{of } \boldsymbol{\varepsilon}^u = \boldsymbol{\varepsilon}^s}} \, \mathrm{d}\mathcal{R} = 0. \tag{2.36}$$

The two-field variational statement can be derived by consecutively choosing $(\delta\boldsymbol{u}, \delta\boldsymbol{\sigma}) = (\delta\boldsymbol{u}, \boldsymbol{0})$ and $(\delta\boldsymbol{u}, \delta\boldsymbol{\sigma}) = (\boldsymbol{0}, \delta\boldsymbol{\sigma})$ independently. For $(\delta\boldsymbol{u}, \delta\boldsymbol{\sigma}) = (\delta\boldsymbol{u}, \boldsymbol{0})$, the Eq. 2.36 leads to the following expression:

$$\int_{\mathcal{R}} \delta\boldsymbol{u} \cdot (\boldsymbol{\nabla} \cdot \boldsymbol{\sigma} + \boldsymbol{b}) \, \mathrm{d}\mathcal{R} + \int_{\partial\mathcal{R}_t} \delta\boldsymbol{u} \cdot (\bar{\boldsymbol{t}} - \boldsymbol{t}) \, \mathrm{d}A. \tag{2.37}$$

The above expression is identical to Eq. 2.4 discussed in Section 2.2 in the case of conventional FEA formulation. Pursuing analogous procedures, it can be further expressed as follows:

$$\int_{\mathcal{R}} (\delta\bar{\varepsilon}^{\boldsymbol{u}})^T \bar{\boldsymbol{\sigma}} \, \mathrm{d}\mathcal{R} = \int_{\mathcal{R}} \delta\boldsymbol{u}^T \boldsymbol{b} \, \mathrm{d}\mathcal{R} + \int_{\partial\mathcal{R}_t} \delta\boldsymbol{u}^T \bar{\boldsymbol{t}} \, \mathrm{d}A \quad \forall \, \delta\boldsymbol{u} \in \mathcal{V}_{\boldsymbol{u}}.$$

After enforcing the second condition, i.e., $(\delta\boldsymbol{u}, \delta\boldsymbol{\sigma}) = (\boldsymbol{0}, \delta\boldsymbol{\sigma})$, Eq. 2.36 simplifies to the following expression:

$$\int_{\mathcal{R}} \delta\boldsymbol{\sigma} : (\boldsymbol{\varepsilon}^u - \boldsymbol{\varepsilon}^s) \, \mathrm{d}\mathcal{R} = 0. \tag{2.38}$$

The above expression can be further simplified by applying the following relations:

$$\delta\boldsymbol{\sigma} : \boldsymbol{\varepsilon}^u = (\delta\bar{\boldsymbol{\sigma}}^u)^T \bar{\boldsymbol{\varepsilon}}^u, \tag{2.39}$$

$$\delta\boldsymbol{\sigma} : \boldsymbol{\varepsilon}^s = \delta\bar{\boldsymbol{\sigma}}^T \bar{\boldsymbol{\varepsilon}}^s = \delta\bar{\boldsymbol{\sigma}}^T \boldsymbol{C}^{-1} \bar{\boldsymbol{\sigma}}. \tag{2.40}$$

Substituting the Eqs. 2.39 and 2.40 into Eq. 2.38, we get:

$$\int_{\mathcal{R}} \delta\bar{\boldsymbol{\sigma}}^T \left[\bar{\varepsilon}^u(\boldsymbol{u}) - \boldsymbol{C}^{-1}\bar{\boldsymbol{\sigma}}\right] \mathrm{d}\mathcal{R} = 0 \qquad \forall\, \delta\bar{\boldsymbol{\sigma}}, \tag{2.41}$$

where $\bar{\boldsymbol{\sigma}}$ and $\bar{\varepsilon}^u$ are the vector representations of $\boldsymbol{\sigma}$ and ε^u, respectively and $\boldsymbol{C}$ is the second order material constitutive tensor.

Summarizing, the resulting two-field HR variational statement for the linear elasticity problem can be expressed as follows:

$$\int_{\mathcal{R}} (\delta\bar{\varepsilon}^u)^T \bar{\boldsymbol{\sigma}} d\mathcal{R} = \int_{\mathcal{R}} \delta\boldsymbol{u}^T \mathbf{b} d\mathcal{R} + \int_{\partial\mathcal{R}_t} \delta\boldsymbol{u}^T \bar{\mathbf{t}} dA \qquad \forall\, \delta\boldsymbol{u} \in \mathcal{V}_{\boldsymbol{u}}, \tag{2.42}$$

$$\int_{\mathcal{R}} \delta\bar{\boldsymbol{\sigma}}^T \left[\bar{\varepsilon}^u(\boldsymbol{u}) - \boldsymbol{C}^{-1}\bar{\boldsymbol{\sigma}}\right] d\mathcal{R} = 0 \qquad \forall\, \delta\bar{\boldsymbol{\sigma}}. \tag{2.43}$$

2.4.1 Approximation of field variables

The two-field HR variational principle necessitate the use of independent interpolation techniques for approximating the independent $\boldsymbol{u}$ and $\bar{\boldsymbol{\sigma}}$. These primary field variables and their involved function spaces are defined as follows:

$$\mathcal{V}_{\boldsymbol{u}} = \left\{\boldsymbol{u}, \delta\boldsymbol{u} : \boldsymbol{u} = \boldsymbol{N}\hat{\boldsymbol{u}},\ \delta\boldsymbol{u} = \boldsymbol{N}\delta\hat{\boldsymbol{u}};\ \hat{\boldsymbol{u}}, \delta\hat{\boldsymbol{u}} \in \mathbb{R}^{n_d \times n_e}\right\}, \tag{2.44}$$

$$\mathcal{V}_{\boldsymbol{\sigma}} = \left\{\bar{\boldsymbol{\sigma}}, \delta\bar{\boldsymbol{\sigma}} : \bar{\boldsymbol{\sigma}} = \boldsymbol{P}\hat{\boldsymbol{\beta}},\ \delta\bar{\boldsymbol{\sigma}} = \boldsymbol{P}\delta\hat{\boldsymbol{\beta}};\ \hat{\boldsymbol{\beta}}, \delta\hat{\boldsymbol{\beta}} \in \mathbb{R}^{n_{\hat{\beta}}}\right\}. \tag{2.45}$$

Here, $\mathcal{V}_{\boldsymbol{u}}$ and $\mathcal{V}_{\boldsymbol{\sigma}}$ are the function spaces for $\boldsymbol{u}$ and $\boldsymbol{\sigma}$, respectively. Similar to previous section, n_e represents the number of nodes in each element, while n_d denotes the degrees of freedom for each node. The number of stress parameters per element is represented by $n_{\hat{\beta}}$. The matrix $\boldsymbol{N}$ and $\boldsymbol{P}$ are the displacement and stress interpolation matrices. Conventionally, $\boldsymbol{N}$ comprises of Lagrange interpolation functions. However, for HR-based elements, the effectiveness greatly depends on the careful selection of stress interpolation functions that are utilized to define $\boldsymbol{P}$.

The matrix $\boldsymbol{P}$ in physical coordinate systems relates with the stress interpolation matrix in natural coordinate system using the following relation:

$$\boldsymbol{P} = \boldsymbol{T}\tilde{\boldsymbol{P}}, \tag{2.46}$$

where $\tilde{\boldsymbol{P}}$ are the stress interpolation matrix defined in the natural coordinate system. The transformation matrix, $\boldsymbol{T}$, connects the $\tilde{\boldsymbol{P}}$ in the natural space to their corresponding counterparts in the physical space. The expression for $\boldsymbol{T}$ is defined in Eq. 2.24.

2.4.2 Existing choices of stress interpolation matrix

Accuracy of stress-based elements is highly sensitive towards the choice of stress interpolation functions. The present work focuses on a particular type of hybrid elements

[141, 142]. The efficacy, robustness and the consistently improved coarse mesh accuracy of these elements have been shown in several application domains such as structural acoustics [147], contact mechanics [148], coupled fluid-structure problem [149], analysis of electromechanical systems [150], and electromagnetic analysis [151], and many more. In the stated work, a systematic methodological procedure is developed to determine robust and efficient choices of approximating functions for the independent stress field. The derived stress interpolation functions, expressed in the natural coordinate system for various elements, are provided as follows:

2.4.2.1 Four-node quadrilateral element

The stress interpolation matrix for a 2D four-node quadrilateral element is given as follows:

$$\tilde{\boldsymbol{P}}(\xi,\eta) = \begin{bmatrix} 1 & \eta & 0 & 0 & 0 \\ 0 & 0 & 1 & \xi & 0 \\ 0 & 0 & 0 & 0 & 1 \end{bmatrix}. \tag{2.47}$$

Note: The above choice of stress interpolation is identical to the one presented by Pian and Sumihara [136].

2.4.2.2 Nine-node quadrilateral element

The stress interpolation matrix for higher-order 2D nine-node quadrilateral element is given as follows:

$$\tilde{\boldsymbol{P}}(\xi,\eta) = \begin{bmatrix} 1 & \xi & \eta & \xi\eta & \eta^2 & \eta^2\xi & 0 & 0 & 0 & 0 & 0 & 0 & 0 & 0 & 0 & 0 \\ 0 & 0 & 0 & 0 & 0 & 0 & 1 & \xi & \eta & \xi\eta & \xi^2 & \eta\xi^2 & 0 & 0 & 0 & 0 \\ 0 & 0 & 0 & 0 & 0 & 0 & 0 & 0 & 0 & 0 & 0 & 0 & 1 & \xi & \eta & \xi\eta \end{bmatrix}. \tag{2.48}$$

2.4.2.3 Eight-node brick element

The stress interpolation matrix for 3D eight-node brick element is given as follows:

$$\tilde{\boldsymbol{P}}(\xi,\eta,\zeta) = \begin{bmatrix} \tilde{\boldsymbol{P}}_1 & \boldsymbol{0}_a & \boldsymbol{0}_a & \boldsymbol{0}_b & \boldsymbol{0}_b & \boldsymbol{0}_b \\ \boldsymbol{0}_a & \tilde{\boldsymbol{P}}_2 & \boldsymbol{0}_a & \boldsymbol{0}_b & \boldsymbol{0}_b & \boldsymbol{0}_b \\ \boldsymbol{0}_a & \boldsymbol{0}_a & \tilde{\boldsymbol{P}}_3 & \boldsymbol{0}_b & \boldsymbol{0}_b & \boldsymbol{0}_b \\ \boldsymbol{0}_a & \boldsymbol{0}_a & \boldsymbol{0}_a & \tilde{\boldsymbol{P}}_4 & \boldsymbol{0}_b & \boldsymbol{0}_b \\ \boldsymbol{0}_a & \boldsymbol{0}_a & \boldsymbol{0}_a & \boldsymbol{0}_b & \tilde{\boldsymbol{P}}_5 & \boldsymbol{0}_b \\ \boldsymbol{0}_a & \boldsymbol{0}_a & \boldsymbol{0}_a & \boldsymbol{0}_b & \boldsymbol{0}_b & \tilde{\boldsymbol{P}}_6 \end{bmatrix},$$

where $\boldsymbol{0}_a$ and $\boldsymbol{0}_b$ are the null or zero vectors of the size 1×4 and 1×2, respectively. The vectors $\tilde{\boldsymbol{P}}_i$ are given as follows:

$$\tilde{\boldsymbol{P}}_1 = \begin{bmatrix} 1 & \zeta & \eta & \zeta\eta \end{bmatrix}, \tilde{\boldsymbol{P}}_2 = \begin{bmatrix} 1 & \zeta & \xi & \zeta\xi \end{bmatrix}, \tilde{\boldsymbol{P}}_3 = \begin{bmatrix} 1 & \eta & \xi & \eta\xi \end{bmatrix},$$

$$\tilde{\boldsymbol{P}}_4 = \begin{bmatrix} 1 & \zeta \end{bmatrix}, \; \tilde{\boldsymbol{P}}_5 = \begin{bmatrix} 1 & \xi \end{bmatrix}, \; \tilde{\boldsymbol{P}}_6 = \begin{bmatrix} 1 & \eta \end{bmatrix}.$$

2.4.2.4 Twenty-seven node brick element

The stress interpolation matrix for higher-order 3D twenty-seven node brick element is given as follows:

$$\tilde{\boldsymbol{P}}(\xi,\eta,\zeta) = \begin{bmatrix} \tilde{\boldsymbol{P}}_1 & \mathbf{0}_a & \mathbf{0}_a & \mathbf{0}_b & \mathbf{0}_b & \mathbf{0}_b \\ \mathbf{0}_a & \tilde{\boldsymbol{P}}_2 & \mathbf{0}_a & \mathbf{0}_b & \mathbf{0}_b & \mathbf{0}_b \\ \mathbf{0}_a & \mathbf{0}_a & \tilde{\boldsymbol{P}}_3 & \mathbf{0}_b & \mathbf{0}_b & \mathbf{0}_b \\ \mathbf{0}_a & \mathbf{0}_a & \mathbf{0}_a & \tilde{\boldsymbol{P}}_4 & \mathbf{0}_b & \mathbf{0}_b \\ \mathbf{0}_a & \mathbf{0}_a & \mathbf{0}_a & \mathbf{0}_b & \tilde{\boldsymbol{P}}_5 & \mathbf{0}_b \\ \mathbf{0}_a & \mathbf{0}_a & \mathbf{0}_a & \mathbf{0}_b & \mathbf{0}_b & \tilde{\boldsymbol{P}}_6 \end{bmatrix}, \tag{2.49}$$

where $\mathbf{0}_a$ and $\mathbf{0}_b$ are the null or zero vectors of the size 1×18 and 1×12, respectively. The vectors $\tilde{\boldsymbol{P}}_1, \tilde{\boldsymbol{P}}_2, \ldots, \tilde{\boldsymbol{P}}_6$ are given as

$$\begin{aligned}
\tilde{\boldsymbol{P}}_1 &= \begin{bmatrix} 1 & \zeta & \zeta^2 & \eta & \zeta\eta & \zeta^2\eta & \eta^2 & \zeta\eta^2 & \zeta^2\eta^2 & \xi & \zeta\xi & \zeta^2\xi & \eta\xi & \zeta\eta\xi & \zeta^2\eta\xi & \eta^2\xi & \zeta\eta^2\xi & \zeta^2\eta^2\xi \end{bmatrix}, \\
\tilde{\boldsymbol{P}}_2 &= \begin{bmatrix} 1 & \zeta & \zeta^2 & \eta & \zeta\eta & \zeta^2\eta & \xi & \zeta\xi & \zeta^2\xi & \eta\xi & \zeta\eta\xi & \zeta^2\eta\xi & \xi^2 & \zeta\xi^2 & \zeta^2\xi^2 & \eta\xi^2 & \zeta\eta\xi^2 & \zeta^2\eta\xi^2 \end{bmatrix}, \\
\tilde{\boldsymbol{P}}_3 &= \begin{bmatrix} 1 & \zeta & \eta & \zeta\eta & \eta^2 & \zeta\eta^2 & \xi & \zeta\xi & \eta\xi & \zeta\eta\xi & \eta^2\xi & \zeta\eta^2\xi & \xi^2 & \zeta\xi^2 & \eta\xi^2 & \zeta\eta\xi^2 & \eta^2\xi^2 & \zeta\eta^2\xi^2 \end{bmatrix}, \\
\tilde{\boldsymbol{P}}_4 &= \begin{bmatrix} 1 & \eta & \zeta & \xi & \xi\eta & \xi\zeta & \zeta^2 & \eta\zeta & \xi\eta\zeta & \zeta^2\eta & \zeta^2\xi & \xi\eta\zeta^2 \end{bmatrix}, \\
\tilde{\boldsymbol{P}}_5 &= \begin{bmatrix} 1 & \xi & \zeta & \eta & \xi^2 & \xi\eta & \eta\zeta & \xi\zeta & \xi^2\zeta & \xi\eta\zeta & \xi^2\eta & \xi^2\eta\zeta \end{bmatrix}, \\
\tilde{\boldsymbol{P}}_6 &= \begin{bmatrix} 1 & \eta & \zeta & \xi & \xi\eta & \xi\zeta & \eta^2 & \eta\zeta & \xi\eta\zeta & \eta^2\zeta & \eta^2\xi & \xi\eta^2\zeta \end{bmatrix}.
\end{aligned}$$

2.4.2.5 Wedge element

The wedge elements often serve as transition elements or, in some cases, can be used to mesh the whole domain. Two commonly used types of wedge elements are the six-node and eighteen-node wedge elements. Hybrid counterparts have been developed for these elements to enhance their performance. The stress interpolation matrix for these elements is provided below.

1. Six-node wedge element:

$$\tilde{\boldsymbol{P}}(\xi,\eta,\zeta) = \begin{bmatrix} 1 & \zeta & 0 & 0 & 0 & 0 & 0 & 0 & 0 & 0 & 0 & 0 & 0 & 0 & 0 \\ 0 & 0 & 1 & \zeta & 0 & 0 & 0 & 0 & 0 & 0 & 0 & 0 & 0 & 0 & 0 \\ 0 & 0 & 0 & 0 & 1 & \xi & \eta & 0 & 0 & 0 & 0 & 0 & 0 & 0 & 0 \\ 0 & 0 & 0 & 0 & 0 & 0 & 0 & 1 & \zeta & 0 & 0 & 0 & 0 & 0 & 0 \\ 0 & 0 & 0 & 0 & 0 & 0 & 0 & 0 & 0 & 1 & \xi & \eta & 0 & 0 & 0 \\ 0 & 0 & 0 & 0 & 0 & 0 & 0 & 0 & 0 & 0 & 0 & 0 & 1 & \xi & \eta \end{bmatrix}. \tag{2.50}$$

2. Eighteen-node wedge element:

$$\tilde{\boldsymbol{P}}(\xi,\eta,\zeta) = \begin{bmatrix} \tilde{\boldsymbol{P}}_1 & \mathbf{0}_a & \mathbf{0}_b & \mathbf{0}_a & \mathbf{0}_c & \mathbf{0}_c \\ \mathbf{0}_a & \tilde{\boldsymbol{P}}_2 & \mathbf{0}_b & \mathbf{0}_a & \mathbf{0}_c & \mathbf{0}_c \\ \mathbf{0}_a & \mathbf{0}_a & \tilde{\boldsymbol{P}}_3 & \mathbf{0}_a & \mathbf{0}_c & \mathbf{0}_c \\ \mathbf{0}_a & \mathbf{0}_a & \mathbf{0}_b & \tilde{\boldsymbol{P}}_4 & \mathbf{0}_c & \mathbf{0}_c \\ \mathbf{0}_a & \mathbf{0}_a & \mathbf{0}_b & \mathbf{0}_a & \tilde{\boldsymbol{P}}_5 & \mathbf{0}_c \\ \mathbf{0}_a & \mathbf{0}_a & \mathbf{0}_b & \mathbf{0}_a & \mathbf{0}_c & \tilde{\boldsymbol{P}}_6 \end{bmatrix} \tag{2.51}$$

where $\mathbf{0}_a$, $\mathbf{0}_b$, $\mathbf{0}_b$ are the null or zero vectors of the size 1×9, 1×12, and 1×6, respectively. The vectors $\tilde{\boldsymbol{P}}_1, \tilde{\boldsymbol{P}}_2, \ldots, \tilde{\boldsymbol{P}}_6$ are given as

$$\begin{aligned} \tilde{\boldsymbol{P}}_1 = \tilde{\boldsymbol{P}}_2 = \tilde{\boldsymbol{P}}_4 &= \begin{bmatrix} 1 & \xi & \eta & \zeta & \xi\zeta & \eta\zeta & \zeta^2 & \xi\zeta^2 & \eta\zeta^2 \end{bmatrix}, \\ \tilde{\boldsymbol{P}}_3 &= \begin{bmatrix} 1 & \xi & \eta & \zeta & \xi\zeta & \eta\zeta & \xi^2 & \xi\eta & \eta^2 & \xi^2\zeta & \eta^2\zeta & \xi\eta\zeta \end{bmatrix}, \\ \tilde{\boldsymbol{P}}_5 = \tilde{\boldsymbol{P}}_6 &= \begin{bmatrix} 1 & \xi & \eta & \zeta & \xi\zeta & \eta\zeta \end{bmatrix}, \end{aligned}$$

2.4.2.6 Axisymmetric hybrid elements

Axisymmetric elements in FEA are specialized elements designed to model structures with rotational symmetry around an axis. These elements are particularly useful for problems involving cylindrical or rotationally symmetric geometries. Such problems can be treated as 2D problems since there is no dependence of any of the variables on θ. Because of the symmetry about the z-axis, the involved stresses are σ_{rr}, σ_{zz}, σ_{rz}, and $\sigma_{\theta\theta}$. If the Jacobian matrix that relates the r-z space to the natural space is defined as follows:

$$\boldsymbol{J} = \begin{bmatrix} \dfrac{\partial r}{\partial \xi} & \dfrac{\partial z}{\partial \xi} \\ \dfrac{\partial r}{\partial \eta} & \dfrac{\partial z}{\partial \eta} \end{bmatrix} = \begin{bmatrix} J_{11} & J_{12} \\ J_{21} & J_{22} \end{bmatrix}. \tag{2.52}$$

Then, the stresses in four-node and nine-node axisymmetric elements are interpolated as follows:

1. Four-node axisymmetric element:

$$\begin{bmatrix} \sigma_{rr} \\ \sigma_{zz} \\ \sigma_{rz} \end{bmatrix} = \underbrace{\begin{bmatrix} J_{11}^2 & J_{21}^2 & 2J_{11}J_{21} \\ J_{12}^2 & J_{22}^2 & 2J_{12}J_{22} \\ J_{11}J_{12} & J_{21}J_{22} & (J_{21}J_{12} + J_{11}J_{22}) \end{bmatrix}}_{\text{transformation matrix}} \underbrace{\begin{bmatrix} 1 & \eta & 0 & 0 & 0 \\ 0 & 0 & 1 & \xi & 0 \\ 0 & 0 & 0 & 0 & 1 \end{bmatrix}}_{\tilde{\boldsymbol{P}}(\xi,\eta)} \begin{bmatrix} \hat{\beta}_1 \\ \hat{\beta}_2 \\ \vdots \\ \hat{\beta}_5 \end{bmatrix}$$

$$\sigma_{\theta\theta} = \hat{\beta}_6 + \hat{\beta}_7(J_{12}\xi + J_{22}\eta)$$

2. Nine-node axisymmetric element:

$$\begin{bmatrix}\sigma_{rr}\\ \sigma_{zz}\\ \sigma_{rz}\end{bmatrix} = \underbrace{\begin{bmatrix} J_{11}^2 & J_{21}^2 & 2J_{11}J_{21}\\ J_{12}^2 & J_{22}^2 & 2J_{12}J_{22}\\ J_{11}J_{12} & J_{21}J_{22} & (J_{21}J_{12}+J_{11}J_{22})\end{bmatrix}}_{\text{transformation matrix}} \tilde{\boldsymbol{P}}(\xi,\eta)\begin{bmatrix}\hat{\beta}_1\\ \hat{\beta}_2\\ \vdots\\ \hat{\beta}_{16}\end{bmatrix},$$

where

$$\tilde{\boldsymbol{P}}(\xi,\eta) = \begin{bmatrix} 1 & \xi & \eta & \xi\eta & \eta^2 & \eta^2\xi & 0 & 0 & 0 & 0 & 0 & 0 & 0 & 0 & 0 & 0\\ 0 & 0 & 0 & 0 & 0 & 0 & 1 & \xi & \eta & \xi\eta & \xi^2 & \eta\xi^2 & 0 & 0 & 0 & 0\\ 0 & 0 & 0 & 0 & 0 & 0 & 0 & 0 & 0 & 0 & 0 & 0 & 1 & \xi & \eta & \xi\eta\end{bmatrix}, \text{ and}$$

$$\sigma_{\theta\theta} = \hat{\beta}_{17} + \hat{\beta}_{18}\xi + \hat{\beta}_{19}\eta + \beta_{20}\xi\eta + \beta_{21}\xi^2 + \beta_{22}\eta^2 + \beta_{23}(J_{12}\xi^2\eta + J_{22}\xi\eta^2)$$

where J_{ij} is the component of $\boldsymbol{J}$ defined in Eq. 2.52.

2.4.3 Elemental equations for stress-based HR formulation

To complete the discussion on stress-based HR formulation, the current section briefly summarizes the expression of the stiffness matrix involved in the HR formulation. Recalling the expressions of $\boldsymbol{u}$ nad $\bar{\boldsymbol{\sigma}}$ and its respective variations $\delta\boldsymbol{u}$ and $\delta\bar{\boldsymbol{\sigma}}$ (Eqs. 2.44 and 2.45) and substituting into Eqs. 2.42 and 2.43, followed by utilizing the arbitrariness of $\delta\hat{\boldsymbol{u}}$ and $\delta\hat{\boldsymbol{\beta}}$, results in the following expressions:

$$\left[\int_{\mathcal{R}} \boldsymbol{B}^T\boldsymbol{P}\,\mathrm{d}\mathcal{R}\right]\hat{\boldsymbol{\beta}} - \left[\int_{\mathcal{R}} \boldsymbol{N}^T\boldsymbol{b}\,\mathrm{d}\mathcal{R} + \int_{\partial\mathcal{R}_t} \boldsymbol{N}^T\bar{\boldsymbol{t}}\,\mathrm{d}A\right] = \boldsymbol{0}, \tag{2.53}$$

$$\left[\int_{\mathcal{R}} \boldsymbol{P}^T\boldsymbol{B}\,\mathrm{d}\mathcal{R}\right]\hat{\boldsymbol{u}} - \left[\int_{\mathcal{R}} \boldsymbol{P}^T\boldsymbol{S}\boldsymbol{P}\,\mathrm{d}\mathcal{R}\right]\hat{\boldsymbol{\beta}} = \boldsymbol{0}, \tag{2.54}$$

where $\boldsymbol{S}$ is the compliance matrix given by $\boldsymbol{S} = \boldsymbol{C}^{-1}$. Let the entities $\boldsymbol{G}$, $\boldsymbol{H}$, $\hat{\boldsymbol{g}}$, and $\hat{\boldsymbol{f}}$ be defined as follows:

$$\boldsymbol{G} = \int_{\mathcal{R}} \boldsymbol{P}^T\boldsymbol{B}\,\mathrm{d}\mathcal{R},\ \boldsymbol{H} = \int_{\mathcal{R}} \boldsymbol{P}^T\boldsymbol{S}\boldsymbol{P}\,\mathrm{d}\mathcal{R},\ \hat{\boldsymbol{g}} = \boldsymbol{0},\ \text{and}\ \hat{\boldsymbol{f}} = \int_{\mathcal{R}} \boldsymbol{N}^T\boldsymbol{b}\,\mathrm{d}\mathcal{R} + \int_{\partial\mathcal{R}_t} \boldsymbol{N}^T\bar{\boldsymbol{t}}\,\mathrm{d}A.$$

Then, the Eqs. 2.53 and 2.54 can be written as

$$\begin{bmatrix} -\boldsymbol{H} & \boldsymbol{G}\\ \boldsymbol{G}^T & \boldsymbol{0}\end{bmatrix}\begin{Bmatrix}\hat{\boldsymbol{\beta}}\\ \hat{\boldsymbol{u}}\end{Bmatrix} = \begin{Bmatrix}\hat{\boldsymbol{g}}\\ \hat{\boldsymbol{f}}\end{Bmatrix}. \tag{2.55}$$

Evaluating the expression for $\hat{\boldsymbol{\beta}}$ from Eq. 2.55 results in following expressions:

$$\hat{\boldsymbol{\beta}} = \boldsymbol{H}^{-1}\boldsymbol{G}\hat{\boldsymbol{u}}, \tag{2.56}$$

$$\underbrace{\boldsymbol{G}^T\boldsymbol{H}^{-1}\boldsymbol{G}}_{\boldsymbol{K}}\,\hat{\boldsymbol{u}} = \hat{\boldsymbol{f}} \rightarrow \boldsymbol{K}\hat{\boldsymbol{u}} = \hat{\boldsymbol{f}}, \tag{2.57}$$

where $\boldsymbol{K} = \boldsymbol{G}^T\boldsymbol{H}^{-1}\boldsymbol{G}$ is the stiffness matrix for the two-field stress-based HR formulation. The matrix $\boldsymbol{H}^{-1}$ can be evaluated at the element level since the stress interpolations are chosen such that they are not continuous across element boundaries. Thus, the elemental stiffness matrix is given as

$$\boldsymbol{K}^e = \boldsymbol{G}_e^T\boldsymbol{H}_e^{-1}\boldsymbol{G}_e, \text{ where } \boldsymbol{G}_e = \int_{\mathcal{R}_e} \boldsymbol{P}_e^T\boldsymbol{B}_e\,\mathrm{d}\mathcal{R}_e, \text{ and } \boldsymbol{H}_e = \int_{\mathcal{R}_e} \boldsymbol{P}_e^T\boldsymbol{S}\boldsymbol{P}_e\,\mathrm{d}\mathcal{R}.$$

Finally, the algorithm for step-by-step implementation of HR variational principle-based hybrid elements in FEA is given in Algorithm 2.

2.5 Selective reduced integration

The selective reduced integration (SRI) is an advancement of the reduced integration approach to alleviate locking in locking-dominated problems [60, 83–86]. The principal notion followed in SRI is to split the material elasticity tensor into two parts. The part of the stiffness matrix that is responsible for locking is then evaluated using the reduced Gaussian quadrature integration scheme, whereas the full-integration scheme is applied for the other part. SRI has shown to be effective in several applications. However, the method is often considered as a trick that compensates for one error by introducing another one. Moreover, in the case of arbitrary non-linear material models, it is not very obvious to condense out the part that is responsible for locking.

There are several possible ways to split the material tensor. The key criterion that governs the splitting of a material tensor is the problem domain and the type of locking. The problems considered in the present work mainly focus on linear elasticity regime where the SRI is used to alleviate the volumetric locking in problems dominated with incompressibility constraint. The material constitutive tensor for a generalized 3D linear elasticity problem that is affected by volumetric locking is split as follows:

$$\boldsymbol{C} = \boldsymbol{C}_\mu + \boldsymbol{C}_\lambda, \text{ where } \boldsymbol{C}_\mu = \mu\begin{bmatrix} 2&0&0&0&0&0\\ 0&2&0&0&0&0\\ 0&0&2&0&0&0\\ 0&0&0&1&0&0\\ 0&0&0&0&1&0\\ 0&0&0&0&0&1 \end{bmatrix}, \boldsymbol{C}_\lambda = \lambda\begin{bmatrix} 1&1&1&0&0&0\\ 1&1&1&0&0&0\\ 1&1&1&0&0&0\\ 0&0&0&0&0&0\\ 0&0&0&0&0&0\\ 0&0&0&0&0&0 \end{bmatrix}. \tag{2.58}$$

The variables μ and λ are Lame's constants and are defined as follows:

$$\mu = \frac{E}{2(1+\nu)}, \quad \lambda = \frac{E\nu}{(1+\nu)(1-2\nu)},$$

where E and ν are Young's modulus and Poisson's ratio, respectively. Here, $\boldsymbol{C}_\mu$ and $\boldsymbol{C}_\lambda$ are associated with the deviatoric part and volumetric part of the material tensor, respectively.

For the plane-strain problem descriptions that are dominated by volumetric locking in near-incompressible or incompressible range, the material tensor $\boldsymbol{C}$ is divided as

$$\boldsymbol{C} = \boldsymbol{C}_\mu + \boldsymbol{C}_\lambda, \text{ where } \boldsymbol{C}_\mu = \mu \begin{bmatrix} 2 & 0 & 0 \\ 0 & 2 & 0 \\ 0 & 0 & 1 \end{bmatrix}, \text{ and } \boldsymbol{C}_\lambda = \lambda \begin{bmatrix} 1 & 1 & 0 \\ 1 & 1 & 0 \\ 0 & 0 & 0 \end{bmatrix}. \tag{2.59}$$

Substituting Eqs. 2.58 or 2.59 into the conventional stiffness matrix expression (Eq. 2.11) leads to the modified expression for element stiffness matrix $\boldsymbol{K}_e$ as

$$\boldsymbol{K}_e = \int_{\mathcal{R}_e} \boldsymbol{B}^T \boldsymbol{C}_\mu \boldsymbol{B} \, \mathrm{d}\mathcal{R}_e + \int_{\mathcal{R}_e} \boldsymbol{B}^T \boldsymbol{C}_\lambda \boldsymbol{B} \, \mathrm{d}\mathcal{R}_e = \boldsymbol{K}^e_\mu + \boldsymbol{K}^e_\lambda. \tag{2.60}$$

For $\nu = 0.5$ or $\nu \approx 0.5$, $\boldsymbol{K}^e_\lambda \rightarrow \infty$ due to the presence of λ in material tensor $\boldsymbol{C}_\lambda$ and hence excessive stiffness is introduced. To alleviate this effect, the volumetric part $(\boldsymbol{K}^e_\lambda)$ from Eq. 2.60 that is responsible for locking is evaluated with one order less Gaussian quadrature integration while $\boldsymbol{K}^e_\mu$ is calculated with full-integration.

2.6 Assumed natural strain

The ANS is a numerical procedure to alleviate the adverse effect of shear locking in thin structural domains. Initially the method was developed for different shell models [58, 72] which was later extended to develop the locking-free solid-shell elements [78, 95–106]. It has been found significantly effective under severely distorted meshes [101, 102, 105, 106]. The key idea is to introduce certain interpolating functions along with a set of tying points that will replace standard integration points to evaluate strains that are otherwise responsible for shear locking. The formulation proceeds with defining the strains in covariants frame as follows:

$$\tilde{\varepsilon}_{ij}(\xi, \eta, \zeta) = \frac{1}{2} \left(\frac{\partial \boldsymbol{u}}{\partial \xi_i} \boldsymbol{g}_j + \frac{\partial \boldsymbol{u}}{\partial \xi_j} \boldsymbol{g}_i \right), \tag{2.61}$$

where $\boldsymbol{g}_i = \dfrac{\partial \boldsymbol{x}}{\partial \xi_i}$ are the covariant base vectors. Alternatively, the $\boldsymbol{g}_i$ vectors are the specific rows of the Jacobian relating the corresponding spaces which is defined as

$$\boldsymbol{J} = \begin{bmatrix} \dfrac{\partial x}{\partial \xi} & \dfrac{\partial y}{\partial \xi} & \dfrac{\partial z}{\partial \xi} \\ \dfrac{\partial x}{\partial \eta} & \dfrac{\partial y}{\partial \eta} & \dfrac{\partial z}{\partial \eta} \\ \dfrac{\partial x}{\partial \zeta} & \dfrac{\partial y}{\partial \zeta} & \dfrac{\partial z}{\partial \zeta} \end{bmatrix} \tag{2.62}$$

Strain-displacement matrix in covariant frame is given as

$$\bar{\boldsymbol{B}} = \begin{bmatrix} \bar{\boldsymbol{B}}_1 & \bar{\boldsymbol{B}}_2 & \bar{\boldsymbol{B}}_3 & \cdots & \bar{\boldsymbol{B}}_{n_e} \end{bmatrix}, \tag{2.63}$$

where $\bar{\boldsymbol{B}}_i$ is defined as

$$\text{For 3D: } \bar{\boldsymbol{B}}_i = \begin{bmatrix} \frac{\partial N_i}{\partial \xi}\boldsymbol{J}_1 \\ \frac{\partial N_i}{\partial \eta}\boldsymbol{J}_2 \\ \frac{\partial N_i}{\partial \zeta}\boldsymbol{J}_3 \\ \frac{\partial N_i}{\partial \eta}\boldsymbol{J}_1 + \frac{\partial N_i}{\partial \xi}\boldsymbol{J}_2 \\ \frac{\partial N_i}{\partial \zeta}\boldsymbol{J}_2 + \frac{\partial N_i}{\partial \eta}\boldsymbol{J}_3 \\ \frac{\partial N_i}{\partial \zeta}\boldsymbol{J}_1 + \frac{\partial N_i}{\partial \xi}\boldsymbol{J}_3 \end{bmatrix}, \text{ For 2D: } \bar{\boldsymbol{B}}_i = \begin{bmatrix} \frac{\partial N_i}{\partial \xi}\boldsymbol{J}_1 \\ \frac{\partial N_i}{\partial \eta}\boldsymbol{J}_2 \\ \frac{\partial N_i}{\partial \eta}\boldsymbol{J}_1 + \frac{\partial N_i}{\partial \xi}\boldsymbol{J}_2 \end{bmatrix}. \tag{2.64}$$

Here, $\boldsymbol{J}_i$ is the i^{th} row of Jacobian matrix from Eq. 2.62. Furthermore, the strain-displacement matrix in covariant frame is related to the physical space with the following relation:

$$\boldsymbol{B} = \boldsymbol{T}^{-T}\bar{\boldsymbol{B}}, \tag{2.65}$$

where $\boldsymbol{T}$ is transformation matrix defined in Eq. 2.24.

By defining a set of tying points and the corresponding interpolations among these set, the updated strain-displacement matrix is evaluated and replaced with the conventional $\bar{\boldsymbol{B}}$ matrix. The choice of tying points is closely related to the order of integration. For calculation of shear stress in four-node quadrilateral elements, tying points will be located at integration points with one order lower integration. For instance, the tying points for the four-node quadrilateral elements are the 1 × 1 Gauss integration points, i.e., an order less than the Gauss points in full integration that is performed to evaluate the elemental stiffness. Hence, the shear stress is evaluated at element center rather than the conventional integration point. Hence, the $\bar{\boldsymbol{B}}^{\text{ANS}}$ for 2D four-node quadrilateral element is evaluated by modifying the shear strain ($\varepsilon_{\xi\eta}$) such that

$$\underbrace{\begin{bmatrix} \frac{\partial N_i}{\partial \xi}\boldsymbol{J}_1 \\ \frac{\partial N_i}{\partial \eta}\boldsymbol{J}_2 \\ \frac{\partial N_i}{\partial \eta}\boldsymbol{J}_1 + \frac{\partial N_i}{\partial \xi}\boldsymbol{J}_2 \end{bmatrix}}_{\bar{\boldsymbol{B}}_i(\xi,\eta)} \to \underbrace{\begin{bmatrix} \frac{\partial N_i}{\partial \xi}\boldsymbol{J}_1 \\ \frac{\partial N_i}{\partial \eta}\boldsymbol{J}_2 \\ \left(\frac{\partial N_i}{\partial \eta}\boldsymbol{J}_1 + \frac{\partial N_i}{\partial \xi}\boldsymbol{J}_2\right)_{(o)} \end{bmatrix}}_{\bar{\boldsymbol{B}}_i{}^{\text{ANS}}(\xi,\eta)},$$

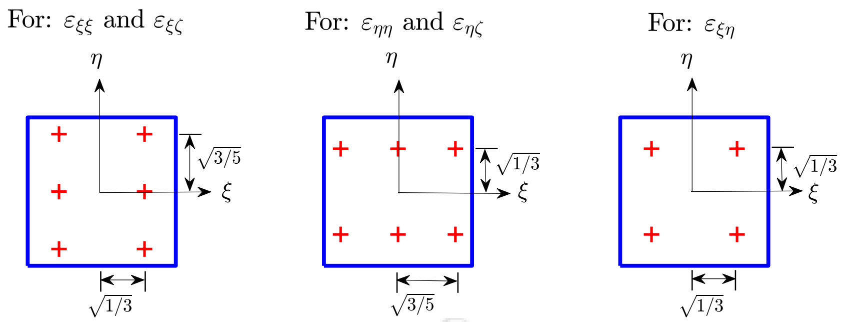

Figure 2.1: Tying point representation for the integration of different strain components for twenty seven node brick element.

where (o) is the tying point with natural coordinates as $\xi = \eta = 0$. Further, in the classical ANS approach, the $\bar{\boldsymbol{B}}_i^{\text{ANS}}(\xi, \eta, \zeta)$ for 3D eight-node brick element is given as

$$\bar{\boldsymbol{B}}_i^{\text{ANS}} = \begin{bmatrix} \dfrac{\partial N_i}{\partial \xi}\boldsymbol{J}_1 \\ \dfrac{\partial N_i}{\partial \eta}\boldsymbol{J}_2 \\ \dfrac{\partial N_i}{\partial \zeta}\boldsymbol{J}_3 \\ \dfrac{\partial N_i}{\partial \eta}\boldsymbol{J}_1 + \dfrac{\partial N_i}{\partial \xi}\boldsymbol{J}_2 \\ (\boldsymbol{B}^*)_i^{\eta\zeta} \\ (\boldsymbol{B}^*)_i^{\xi\zeta} \end{bmatrix},$$

where

$$(\boldsymbol{B}^*)_i^{\eta\zeta} = \frac{1}{2}(1-\xi)\left(\frac{\partial N_i}{\partial \zeta}\boldsymbol{J}_2 + \frac{\partial N_i}{\partial \eta}\boldsymbol{J}_3\right)_{(T1)} + \frac{1}{2}(1+\xi)\left(\frac{\partial N_i}{\partial \zeta}\boldsymbol{J}_2 + \frac{\partial N_i}{\partial \eta}\boldsymbol{J}_3\right)_{(T2)},$$
$$(\boldsymbol{B}^*)_i^{\xi\zeta} = \frac{1}{2}(1-\eta)\left(\frac{\partial N_i}{\partial \zeta}\boldsymbol{J}_1 + \frac{\partial N_i}{\partial \xi}\boldsymbol{J}_3\right)_{(T3)} + \frac{1}{2}(1+\eta)\left(\frac{\partial N_i}{\partial \zeta}\boldsymbol{J}_1 + \frac{\partial N_i}{\partial \xi}\boldsymbol{J}_3\right)_{(T4)},$$

Here, $(T1)$, $(T2)$, $(T3)$, and $(T4)$ are the set of tying points with the (ξ, η) coordinate as (-1,0), (1,0), (0,-1), and (0,1), respectively.

Higher-order elements follow a similar structure. However, these elements are not as popular as linear elements and they lack the straightforward implementation that linear elements have. Nevertheless, there exist a generalized structure for ANS, which can be used irrespective of the type of element [78, 101]. To better understand the method, let us consider a twenty-seven node brick element. A 3 × 3 × 3 Gauss quadrature rule is applied to perform the full integration of the integrals associated with the element stiffness matrix. The tying points are chosen such that the $\varepsilon_{\xi\xi}$ and $\varepsilon_{\xi\zeta}$ are employed with one order lower quadrature rule in ξ direction and full integration is employed in η direction. Similar arguments holds for $\varepsilon_{\eta\eta}$ and $\varepsilon_{\eta\zeta}$, whereas for $\varepsilon_{\xi\eta}$ one order lower Gauss-quadrature in applied in both ξ and η direction, see Fig. 2.1.

Once the tying points are recognized, evaluate the local Lagrangian polynomial such that they are interpolatory at the prescribed tying points and form an vector consisting of the tensor product of evaluated polynomials. Let $\Phi_i(\xi)$ and $\Psi_j(\eta)$ be the Lagrange polynomial interpolating at the tying points then the components of the vector representing the tensor product will be $\Phi_i(\xi)\Psi_j(\eta)$ where i and j will vary from 1 to number of tying points in ξ and η direction, respectively. Let $\bar{\boldsymbol{N}}$ be the vector of tensor product then, the assumed strain field is derived as

$$\varepsilon^{\text{ANS}} = \bar{\boldsymbol{N}}^T(\xi,\eta)\bar{\boldsymbol{\varepsilon}}_c(\hat{\xi},\hat{\eta},\zeta), \tag{2.66}$$

where $\bar{\boldsymbol{\varepsilon}}_c(\hat{\xi},\hat{\eta},\zeta)$ is the vector of corresponding strain component evaluated at chosen tying points. Here, $(\hat{\xi},\hat{\eta})$ is the tying point coordinate, whereas ζ is evaluated at Gauss point. For example, let us evaluate the modified $\varepsilon_{\xi\zeta}$ component. The tying points associated with the said components are shown in left sub-figure in Fig. 2.1. Let $\Phi_1(\xi)$, $\Phi_2(\xi)$, and $\Phi_3(\xi)$ are the Lagrange polynomials interpolatory at tying points along ξ direction and $\Psi_1(\eta)$ and $\Psi_2(\eta)$ are the polynomials along η direction. Hence, the $\bar{\boldsymbol{N}}$ matrix can be defined as

$$\bar{\boldsymbol{N}} = \begin{bmatrix} \Phi_1(\xi)\Psi_1(\eta) & \Phi_2(\xi)\Psi_1(\eta) & \Phi_3(\xi)\Psi_1(\eta) & \Phi_1(\xi)\Psi_2(\eta) & \Phi_2(\xi)\Psi_2(\eta) & \Phi_3(\xi)\Psi_2(\eta) \end{bmatrix}^T,$$

and the vector $\bar{\boldsymbol{\varepsilon}}_c(\hat{\xi},\hat{\eta},\zeta)$ will consist the $\varepsilon_{\xi\zeta}$ evaluated at each tying points such that

$$\bar{\boldsymbol{\varepsilon}}_c(\hat{\xi},\hat{\eta},\zeta) = \begin{bmatrix} \varepsilon^1_{\xi\zeta} & \varepsilon^2_{\xi\zeta} & \varepsilon^3_{\xi\zeta} & \varepsilon^4_{\xi\zeta} & \varepsilon^5_{\xi\zeta} & \varepsilon^6_{\xi\zeta} \end{bmatrix}^T,$$

where superscript represent the specific tying point identifier. This will lead to the following expression for the modified $\varepsilon_{\xi\zeta}$:

$$\begin{aligned} \varepsilon^{\text{ANS}}_{\xi\zeta} =& \Phi_1(\xi)\Psi_1(\eta)\varepsilon^1_{\xi\zeta} + \Phi_2(\xi)\Psi_1(\eta)\varepsilon^2_{\xi\zeta} + \Phi_3(\xi)\Psi_1(\eta)\varepsilon^3_{\xi\zeta} + \Phi_1(\xi)\Psi_2(\eta)\varepsilon^4_{\xi\zeta} \\ &+ \Phi_2(\xi)\Psi_2(\eta)\varepsilon^5_{\xi\zeta} + \Phi_3(\xi)\Psi_2(\eta)\varepsilon^6_{\xi\zeta}. \end{aligned} \tag{2.67}$$

The above relation results in the following expression for modified strain–displacement matrix:

$$\begin{aligned} [(\boldsymbol{B}^*)^{\xi\zeta}_i]^{\text{ANS}} = & \Phi_1(\xi)\Psi_1(\eta)[\bar{\boldsymbol{B}}^{\xi\zeta}_i]^1 + \Phi_2(\xi)\Psi_1(\eta)[\bar{\boldsymbol{B}}^{\xi\zeta}_i]^2 + \Phi_2(\xi)\Psi_1(\eta)[\bar{\boldsymbol{B}}^{\xi\zeta}_i]^3 \\ &+ \Phi_1(\xi)\Psi_2(\eta)[\bar{\boldsymbol{B}}^{\xi\zeta}_i]^4 + \Phi_2(\xi)\Psi_2(\eta)[\bar{\boldsymbol{B}}^{\xi\zeta}_i]^5 + \Phi_3(\xi)\Psi_2(\eta)[\bar{\boldsymbol{B}}^{\xi\zeta}_i]^6, \end{aligned},$$

where $[\bar{\boldsymbol{B}}^{\xi\zeta}_i]^k$ is the part of conventional strain–displacement matrix defined in Eq. 2.64 evaluated at k^{th} tying point and $[(\boldsymbol{B}^*)^{\xi\zeta}_i]^{\text{ANS}}$ is the modified part of strain–displacement matrix which will replace the original matrix.

Following a similar approach, one can derive the remaining modified strain components and replace them with the conventional strain field. For the reader's interest, the literature that has been followed to present the procedure involves an additional projection matrix [101]. However, as the chosen Lagrange polynomial are interpolatory at the Gauss points, the resultant projection matrix will result in an identity matrix. Hence, the authors present a simplified version of the same procedure without the involvement of a projection matrix. Lastly, the methodical algorithmic procedure for step-by-step implementation of ANS method is given in Algorithm 3.

Chapter 3

Performance Evaluation of FE Strategies for Alleviating Locking[*]

In this chapter, we present a performance comparison of different locking alleviation FE strategies discussed in Chapter 2. The strategies under evaluation include VHW principle-based EAS (Section 2.3), a specific class of stress-based HR principle-based hybrid formulation (Section 2.4), SRI (Section 2.5), ANS (Section 2.6), and the conventional FE formulation (Section 2.2). Various parameters, such as the method's applicability, robustness, and efficiency, are scrutinized to provide a comprehensive understanding of the optimal approach for locking-dominated problems.

3.1 Performance evaluation parameters

The parameters used for quantifying the performance of various locking alleviation strategies are defined as follows:

1. Normalized displacement at a specific location in the domain: It is defined as the ratio of numerical value of displacement (u_i) obtained using FEA and the analytical/benchmark solution (u_i^{ref}) of the displacements at the specified location, and given as follows:

$$\text{Normalized displacment} = \frac{u_i}{u_i^{\text{ref}}} \tag{3.1}$$

---

[*] D. S. Bombarde, S. L. Narayan, S. S. Gautam, A. Nandy, "A comprehensive comparative review of various advanced finite elements to alleviate shear, membrane and volumetric locking", *Archives of Computational Methods in Engineering* **(In press)**

2. L_2 error norm of displacement:

$$L_2^u = \frac{\left\|\boldsymbol{u} - \boldsymbol{u}^{\text{ref}}\right\|}{\left\|\boldsymbol{u}^{\text{ref}}\right\|} = \left[\frac{\sum_{i=1}^{n}\sum_{j=1}^{m}(u_{i,j} - u_{i,j}^{\text{ref}})^2}{\sum_{i=1}^{n}\sum_{j=1}^{m}(u_{i,j}^{\text{ref}})^2}\right]^{\frac{1}{2}}, \tag{3.2}$$

   where n and m are the total number of nodes and number of components of $\boldsymbol{u}$, respectively.

3. L_2 error norm of stress:

$$L_2^\sigma = \frac{\left\|\boldsymbol{\sigma} - \boldsymbol{\sigma}^{\text{ref}}\right\|}{\left\|\boldsymbol{\sigma}^{\text{ref}}\right\|} = \left[\frac{\sum_{i=1}^{n}\sum_{j=1}^{l}(\sigma_{i,j} - \sigma_{i,j}^{\text{ref}})^2}{\sum_{i=1}^{n}\sum_{j=1}^{l}(\sigma_{i,j}^{\text{ref}})^2}\right]^{\frac{1}{2}}, \tag{3.3}$$

   where $\boldsymbol{\sigma}$ and $\boldsymbol{\sigma}^{\text{ref}}$ are the stress values obtained at the point of interest in the domain using FEA and reference solution, respectively. l denotes the number of components of stress and n is the total number of nodes.

3.2 Abbreviations for elements

Notations used in the subsequent numerical examples are as follows: The notation **q4** and **q9** represents the 2D four-node and nine-node quadrilateral elements, respectively. The suffix **b8** and **b27** signifies the use of 3D eight-node and twenty-seven node brick element, respectively. **FE** denotes the conventional single-field FEA formulation, whereas **SRI**, **$\boldsymbol{\alpha}$-FE**, and **ANS** imply the use of SRI, EAS, and classical ANS approaches, respectively. The **ANS*** and **h-FE** represents the generalized ANS approach and two-field hybrid stress formulation, respectively.

3.3 Numerical examples

The study includes the analysis of numerous numerical benchmark examples, spanning a wide range of 2D and 3D problems. It begins with 2D problems, where the first two problems assess the methods for shear locking effect. These problems include both straight and curved cantilever beam problems with end loads, covering a range of slenderness ratios. Following this, we evaluate the standard Cook's membrane problem to assess the methods in relation to volumetric locking. Additionally, a plate with a hole problem is studied, both with and without the influence of volumetric locking.

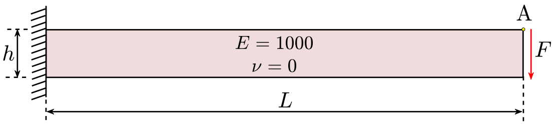

Figure 3.1: Problem set-up and corresponding boundary conditions for straight cantilever beam problem.

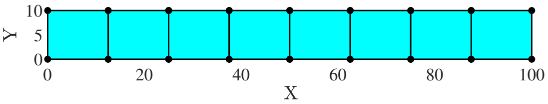

Figure 3.2: The mesh of 8 × 1 q4 elements for a straight cantilever beam with $L/h = 10$.

Table 3.1: The mesh size and respective N^u_{dof} for a straight cantilever beam problem.

Meshes	N^u_{dof}	
$n^L_{\text{ele}} \times n^h_{\text{ele}}$	q4	q9
1×1	4	12
2×1	8	24
4×1	16	48
8×1	32	96
16×1	64	192
32×1	128	384
64×1	256	768
128×1	512	1536
256×1	1024	3072
512×1	2048	6144

The study is extended to some 3D problems starting with a 3D version of the straight and curved cantilever beam problems. Through these problems, various methods are tested for combined shear and membrane locking. Each problem is solved for three different slenderness ratios so as to gradually introduce the locking effect. The next example included is the well-known Scordelis–Lo roof problem, which is affected by both the shear and the membrane locking. Finally, a 3D incompressible cube subjected to distributed loading is studied with different strategies to study their performance for volumetric locking.

It is essential to note that all parameters used in numerical simulations adhere to a consistent system of units that aligns with the governing equations. Users have the flexibility to choose a consistent system of units, whether it be SI, FPS, or any unit system of choice, for forces, displacements, stresses, and material properties in all the examples. As a standard practice, we implicitly assume the use of a consistent unit system for the data provided in numerical examples.

3.3.1 Straight cantilever beam

The first numerical example investigates the linear-elastic deformation of a straight cantilever beam of length (L) and three different thickness values (h). The slenderness ratio (L/h) is gradually increased to introduce the shear locking effect into the problem

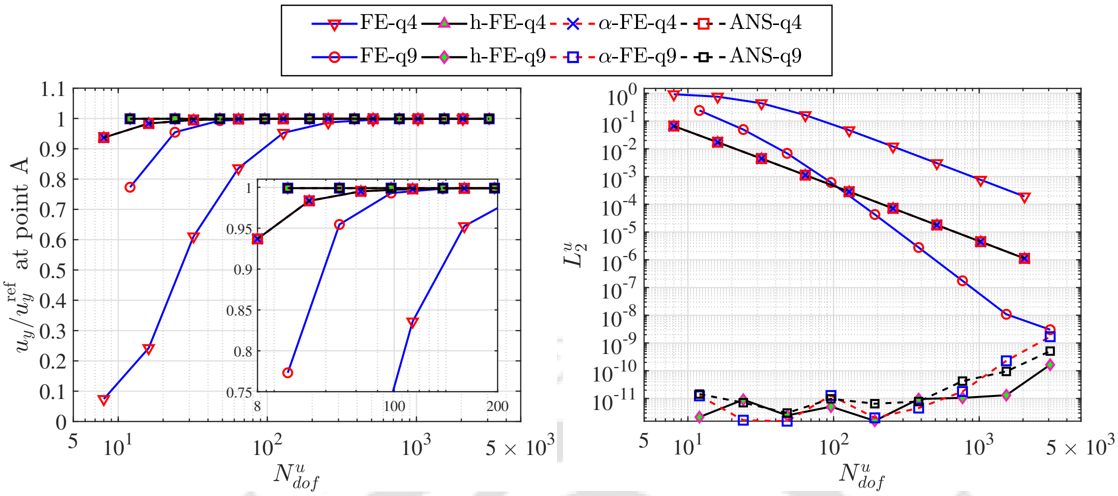

(a) u_y/u_y^{ref} $(L/h = 10)$

(b) L^u_2 $(L/h = 10)$

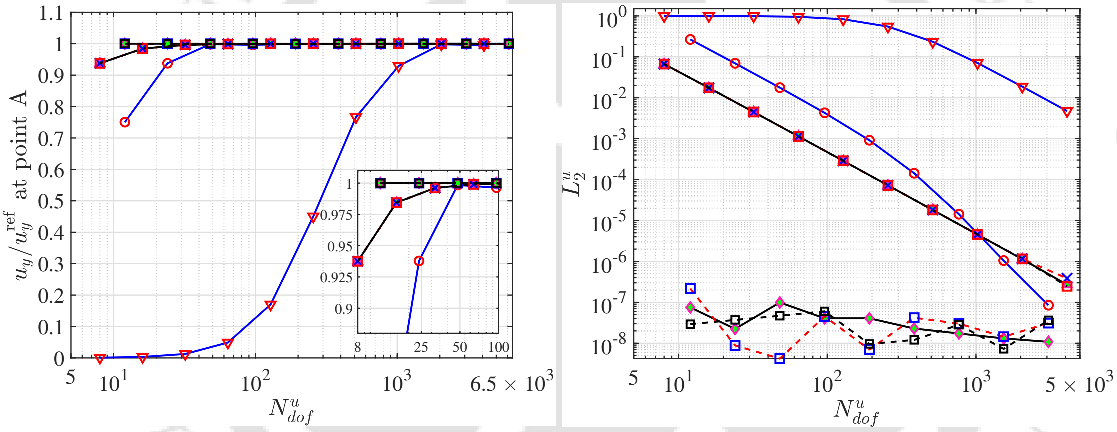

(c) u_y/u_y^{ref} $(L/h = 100)$

(d) L^u_2 $(L/h = 100)$

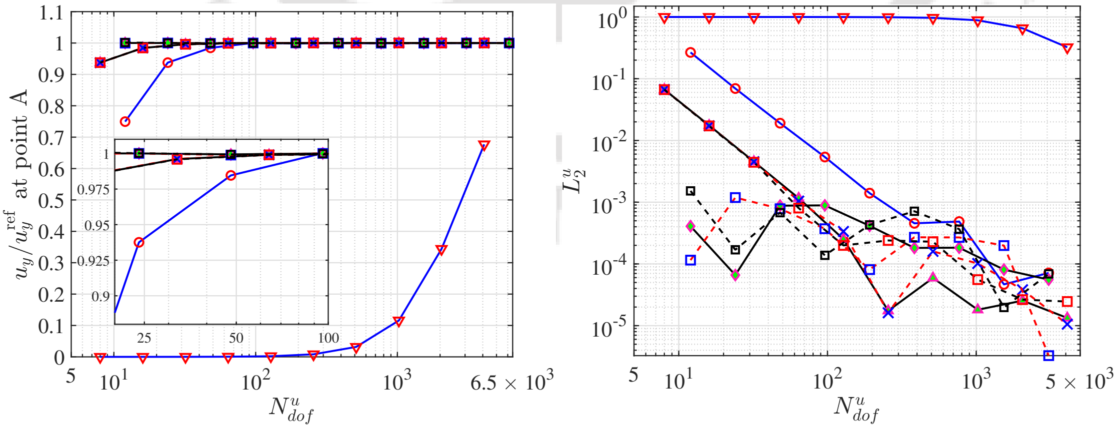

(e) u_y/u_y^{ref} $(L/h = 1000)$

(f) L^u_2 $(L/h = 1000)$

Figure 3.3: Normalized tip displacement and L_2 error norm of displacement for a straight cantilever beam with different slenderness ratios.

domain [152, 153]. The problem description and the corresponding boundary conditions are shown in Fig. 3.1.

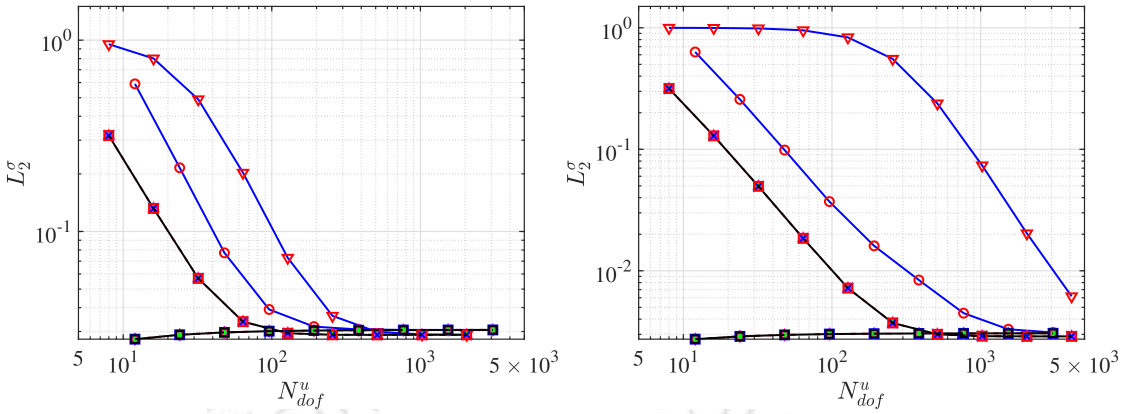

(a) L_2^σ $(L/h = 10)$ **(b)** L_2^σ $(L/h = 100)$

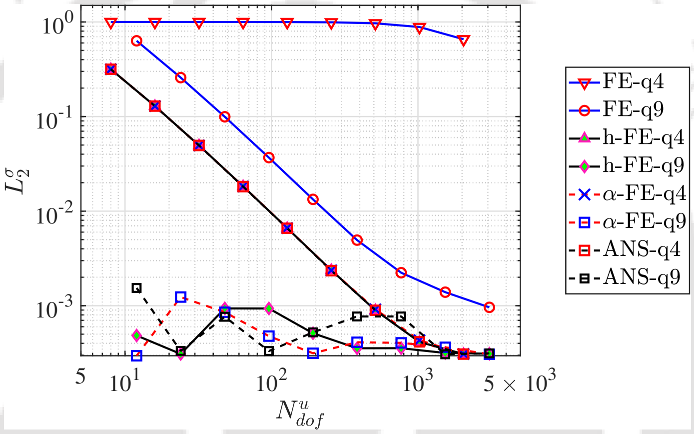

(c) L_2^σ $(L/h = 1000)$

Figure 3.4: L_2 error norm of stress for a straight cantilever beam with different slenderness ratios.

The specific parameters that define the problem for the three cases are as follows:

1. $L = 100,\ h = 10,\ L/h = 10,\ F = 4.97018 \times 10^{-3}$,
2. $L = 100,\ h = 1,\ L/h = 100,\ F = 4.9997 \times 10^{-6}$,
3. $L = 100,\ h = 0.1,\ L/h = 1000,\ F = 4.9999 \times 10^{-9}$.

The analytical solution for the vertical displacement (u_y^{ref}) at point 'A' is evaluated using the Euler beam theory [169] as 0.02 for all three cases.

The problem is solved using the conventional FEA alongside the existing locking alleviation FE strategies for all three cases with different mesh sizes. One such mesh of eight q4 elements for $L/h = 10$ is shown in Fig. 3.2. The h-refinement is carried out by increasing the number of elements in L direction. The mesh description and the corresponding number of free degrees of freedom (N^u_{dof}) are shown in Table 3.1, where n^L_{ele} and n^h_{ele} are the number of elements in L and h direction, respectively.

The problem is solved for all three cases, and respective results for the defined parameters (see Section 3.1) against N^u_{dof} are shown in Figs. 3.3 and 3.4. The substantially low effect of locking has been observed for the lower L/h ratio. For such a case, even the

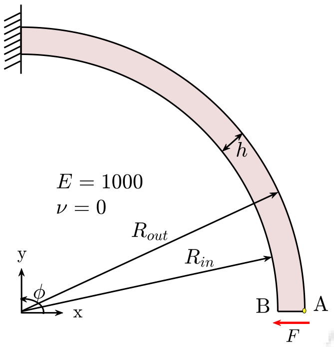

Figure 3.5: Problem set-up and corresponding boundary conditions for the curved cantilever beam problem.

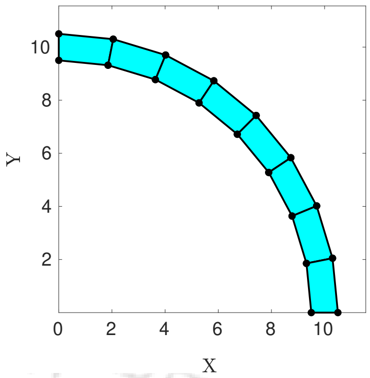

Figure 3.6: The mesh of 8×1 q4 elements for a curved cantilever beam ($R_{\mathrm{m}}/h = 10$).

conventional FEA converges to the solution with acceptable coarse mesh accuracy. However, the advanced FE strategies provide a marginal improvement over the conventional FEA.

The effect of shear locking is significantly prominent with higher L/h ratios, see Figs. 3.3 and 3.4. The performance of FE-q4 formulation consistently deteriorates with the increasing L/h ratio. In extreme cases where the $L/h = 1000$, the FE-q4 fails to converge even after significant refinement. On the contrary, the advanced FE strategies perform consistently irrespective of the L/h ratio. Similar observations are made for the numerical stresses in the domain. The conventional FE formulation, either with q4 or q9 elements, converges at a slower rate. On the other hand, the convergence of L_2^{σ} with all the advanced FE strategies is significantly better than that of the conventional formulation. Regardless of the element type, these techniques provide higher accuracy of stresses with significantly coarse mesh description in each case. For all three advanced FE strategies, higher-order elements have better coarse mesh accuracy. Performance of all three strategies are almost comparable for this example.

3.3.2 Curved cantilever beam

In the present numerical example, the linear-elastic behavior of a curved cantilever beam is investigated. The problem is of particular interest as it allows to assess the performance of different FE strategies under the influence of shear locking using distorted mesh discretization. The problem is composed of curved beam of mean radius (R_{m}) and thickness (h), fixed on one end and subjected to horizontal load on the opposite end, see Fig. 3.5 [101]. The slenderness ratio (R_{m}/h) is gradually increased to introduce the shear locking effect into the problem domain. The problem parameters for the three different cases are given as follows:

1. $R_{\mathrm{in}} = 9.5$, $R_{\mathrm{out}} = 10.5$, $R_{\mathrm{m}}/h = 10$, $F = 0.1$,
2. $R_{\mathrm{in}} = 9.95$, $R_{\mathrm{out}} = 10.05$, $R_{\mathrm{m}}/h = 100$, $F = 1 \times 10^{-3}$,

Table 3.2: The mesh size and respective N^u_{dof} for a curved cantilever beam problem.

Meshes	N^u_{dof}	
$n^{\phi}_{\text{ele}} \times n^{R}_{\text{ele}}$	q4	q9
1×1	4	12
2×1	8	24
4×1	16	48
8×1	32	96
16×1	64	192
32×1	128	384
64×1	256	768
128×1	512	1536
256×1	1024	3072
512×1	2048	6144

3. $R_{\text{in}} = 9.995$, $R_{\text{out}} = 10.005$, $R_{\text{m}}/h = 1000$, $F = 1 \times 10^{-5}$.

The analytical solution for the radial displacement at point 'A', i.e., u^{ref}_x is 0.943 for the three cases [101, 152]. Further, the analytical expression for radial and angular displacement at any point $\bar{\boldsymbol{x}}(r, \theta)$ in the problem domain is given as [169]

$$\begin{aligned}
u_r &= \frac{1}{E}\left\{-2D\theta\cos\theta + \sin\theta\left[D(1-\nu)\log r + A(1-3\nu)r^2 + \frac{B}{r^2}(1+\nu)\right]\right\} \\
&\quad + K\sin\theta + L\cos\theta \\
u_\theta &= \frac{1}{E}\left\{2D\theta\sin\theta - \cos\theta\left[A(5+\nu)r^2 + \frac{B}{r^2}(1+\nu) - D[(1-\nu)\log r + 1 + \nu]\right]\right\} \\
&\quad + K\cos\theta - L\sin\theta
\end{aligned}$$

and the stresses in the domain are given as

$$\begin{aligned}
\sigma_r &= \left\{2Ar - \frac{2B}{r^3} + \frac{D}{r}\right\}\sin\theta, \\
\sigma_\theta &= \left\{6Ar + \frac{2B}{r^3} + \frac{D}{r}\right\}\sin\theta, \\
\sigma_{r\theta} &= -\left\{2Ar - \frac{2B}{r^3} + \frac{D}{r}\right\}\cos\theta,
\end{aligned}$$

where

$$\begin{aligned}
N &= R^2_{\text{in}} - R^2_{\text{out}} + (R^2_{\text{in}} + R^2_{\text{out}})\log\frac{R_{\text{out}}}{R_{\text{in}}}, \\
K &= \frac{1}{E}\left[D(1-\nu)\log r + A(1-3\nu)r^2 + \frac{B}{r^2}(1+\nu)\right], \\
A &= \frac{f}{2N}, \quad B = -\frac{fR^2_{\text{in}}R^2_{\text{out}}}{2N}, \quad L = \frac{D\pi}{E}, \quad D = -\frac{f(R^2_{\text{in}} + R^2_{\text{out}})}{N}.
\end{aligned}$$

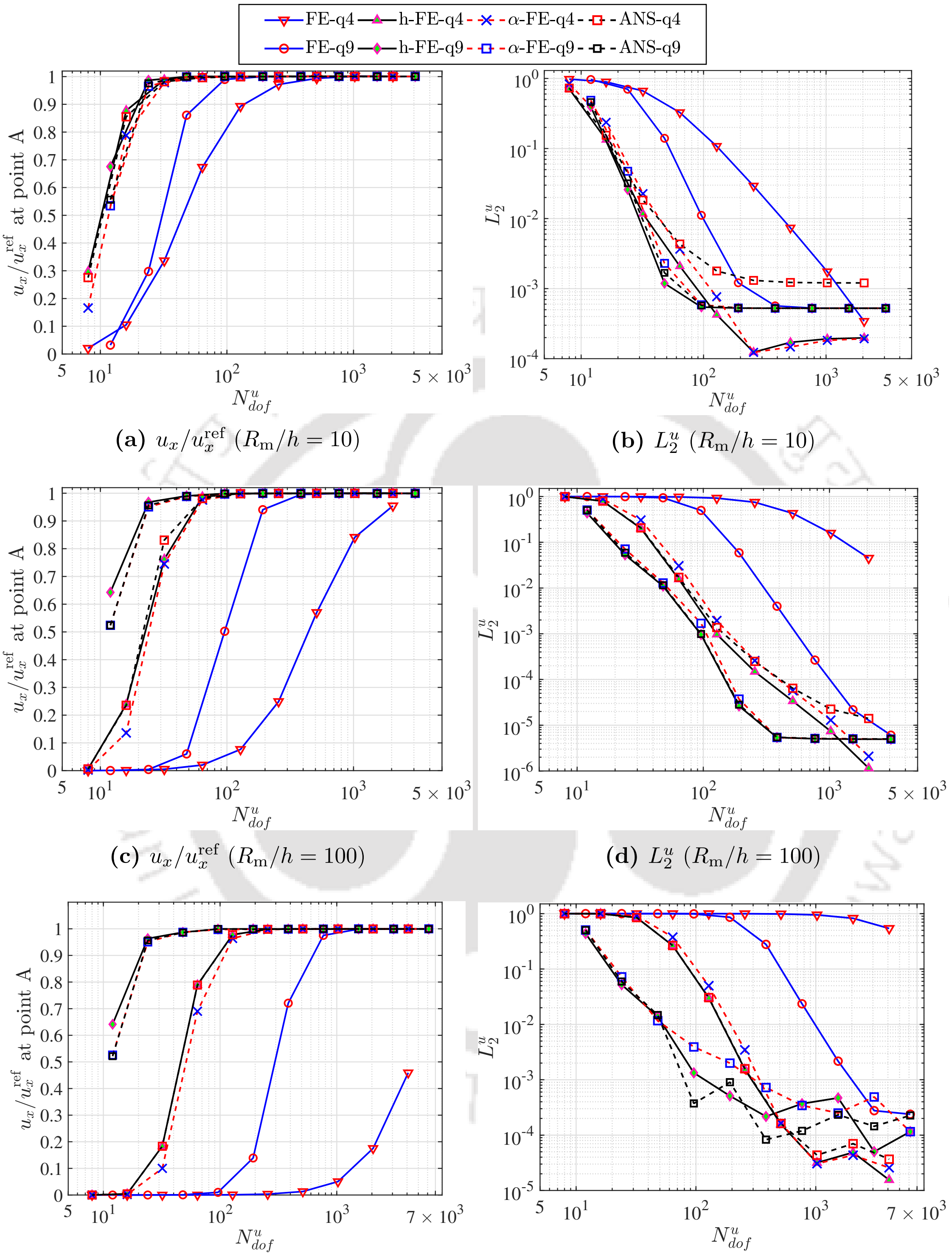

(a) u_x/u_x^{ref} $(R_{\text{m}}/h = 10)$ **(b)** L^u_2 $(R_{\text{m}}/h = 10)$

(c) u_x/u_x^{ref} $(R_{\text{m}}/h = 100)$ **(d)** L^u_2 $(R_{\text{m}}/h = 100)$

(e) u_x/u_x^{ref} $(R_{\text{m}}/h = 1000)$ **(f)** L^u_2 $(R_{\text{m}}/h = 1000)$

Figure 3.7: Normalized tip displacement and L_2 error norm of displacement for a curved cantilever beam with different slenderness ratios.

The preceding analytical expressions are resolved into the Cartesian coordinate system for evaluating the L^u_2 and L^σ_2 values for the stated three cases.

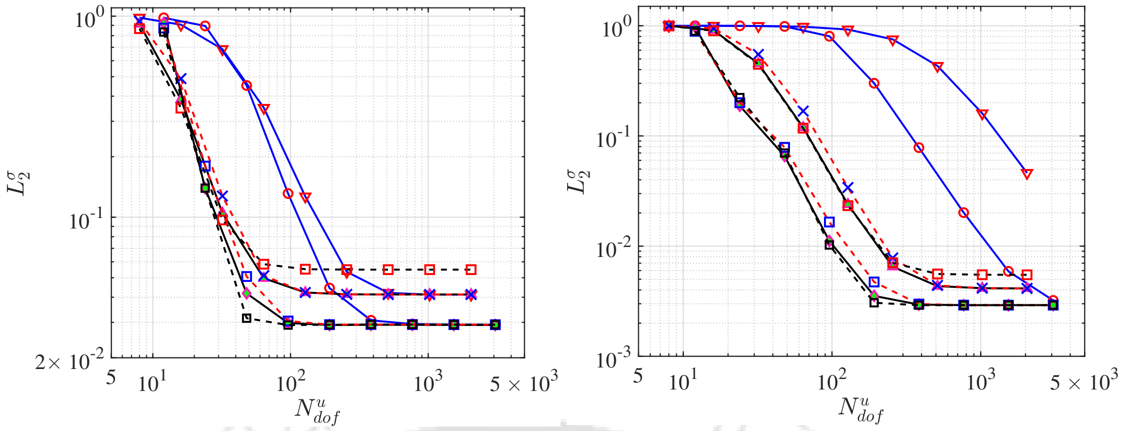

(a) L_2^σ $(R_\text{m}/h = 10)$ **(b)** L_2^σ $(R_\text{m}/h = 100)$

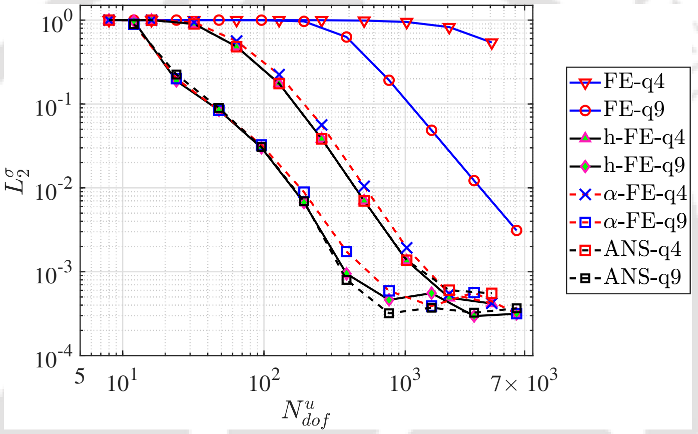

(c) L_2^σ $(R_\text{m}/h = 1000)$

Figure 3.8: L_2 error norm of stress for a curved cantilever beam with different slenderness ratios.

The problem is solved using different locking alleviation FE strategies alongside the conventional FE formulation for the three cases with different mesh discretization. One such mesh of eight q4 elements for $R_\text{m}/h = 10$ is illustrated in Fig. 3.6. h-refinement is carried out by increasing the number of elements in ϕ direction while keeping a single element along the thickness direction. The mesh description and the corresponding number of free degrees of freedom (N_{dof}^u) are shown in Table 3.2, where n_ele^ϕ and n_ele^R are the number of elements in ϕ and R direction, respectively.

The problem is solved for three cases and the normalized displacement of a point of interest, L_2^u, and L_2^σ error norms are evaluated against N_{dof}^u as shown in Figs. 3.7 and 3.8. The effect of distorted mesh coupled with the shear locking can be observed distinctively in all three cases. For lower R_m/h ratio, the conventional q4 and q9 elements converged to the solution with considerably low refinement as compared to higher slenderness ratios. However, the h-FE, α-FE and ANS elements have shown comparatively better coarse mesh accuracy than the conventional elements, see Figs. 3.7a, 3.7b, and 3.8a. The locking effect gets more prominent as R_m/h ratio increases, see Figs. 3.7c-3.7f,

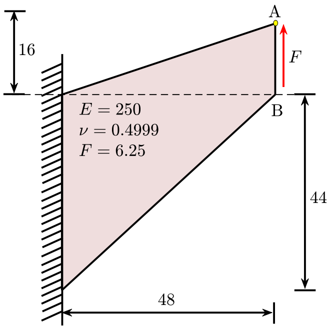

Figure 3.9: Problem set-up and corresponding boundary conditions for the Cook's membrane problem.

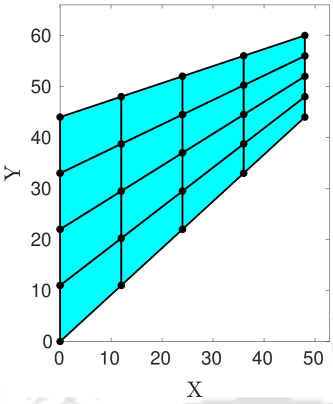

Figure 3.10: The mesh of 4×4 q4 elements for a Cook's membrane problem.

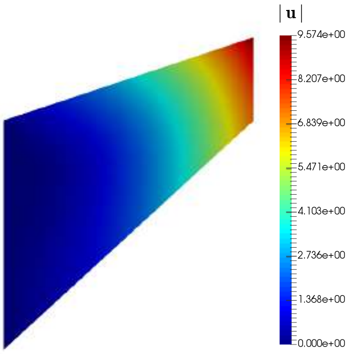

Figure 3.11: The contour plot of displacement evaluated using a mesh of 64×64 h-FE-q9 elements for a Cook's membrane problem.

3.8b, and 3.8c. The effect of shear locking is significant when $R_{\mathrm{m}}/h = 1000$, which makes the problem ideal to assess the performance of different FE strategies. It can be observed that while dealing with high slenderness ratios, the FE-q4 elements fails to converge and FE-q9 elements needs significant refinement to reach to the solution. On the other hand, h-FE-q4, α-FE-q4, and ANS-q4 converged to the solution with fairly low number of elements, whereas h-FE-q9, ANS-q9, and α-FE-q9 elements have shown highest convergence rate among all.

The lower R_{m}/h ratio of the problem domain is less affected by locking. The conventional formulation with acceptable refinement successfully converges to the solution. However, with respect to coarse mesh accuracy, EAS, ANS, and hybrid formulations provide superior result quality. In all three cases, α-FE and h-FE elements have the fastest convergence rate regardless of the type of element. Furthermore, the performance of ANS-q9 is comparable with α-FE and h-FE elements. However, the convergence rate for ANS-q4 for $R_{\mathrm{m}}/h = 10$ and 100 is inferior to the α-FE and h-FE elements.

3.3.3 Cook's membrane

The Cook's membrane problem is considered across various literatures [107, 170–172] to assess the performance of the formulation under the influence of volumetric locking. The problem is composed of a tapered plate subjected to vertical shear load on one end and fixed on the other end. The problem set-up is shown in Fig. 3.9, where E, ν and F are the Young's modulus, Poisson's ratio and load per unit length, respectively. The problem is solved for the plane-strain condition for nearly-incompressible problem domain. The plane-strain condition along with $\nu = 0.4999$, makes the problem a typical case of volumetric locking.

Table 3.3: The mesh size and respective N^u_{dof} for Cook's membrane problem.

Meshes	N^u_{dof}	
$n^x_{\text{ele}} \times n^y_{\text{ele}}$	q4	q9
1×1	4	12
2×2	12	40
4×4	40	144
8×8	144	544
16×16	544	2112
32×32	2112	8320
64×64	8320	-

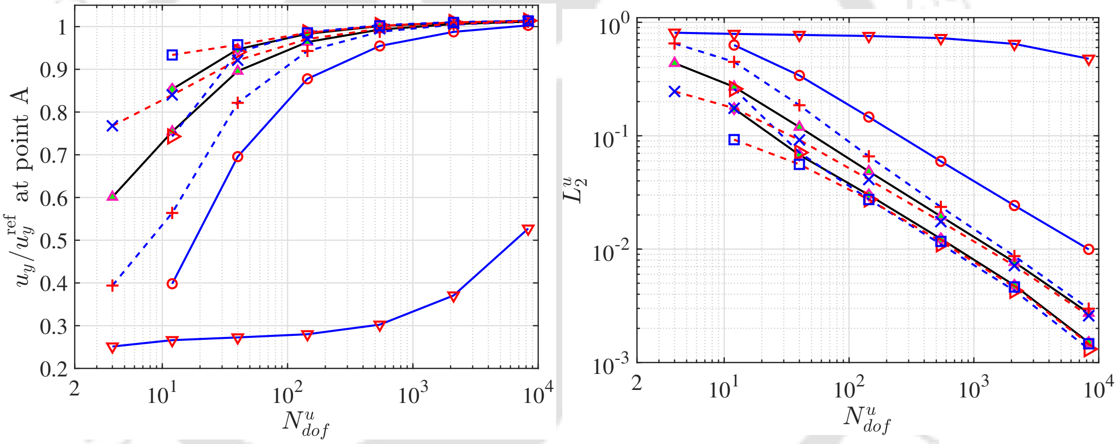

(a) u_y/u_y^{ref} at point A (b) L^u_2

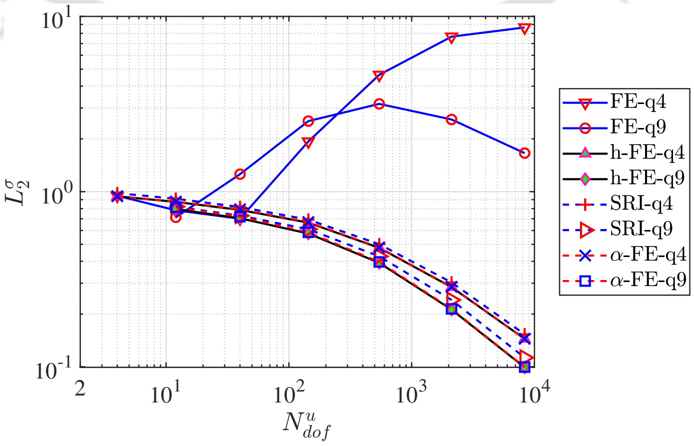

(c) L^σ_2

Figure 3.12: Normalized tip displacement and L_2 error norm of displacement and stresses for a for a Cook's membrane problem.

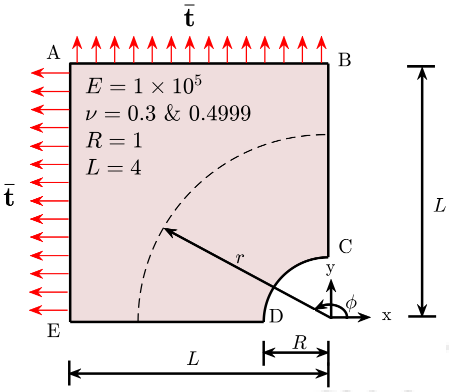

Figure 3.13: Problem set-up and corresponding boundary conditions for plate with a hole problem.

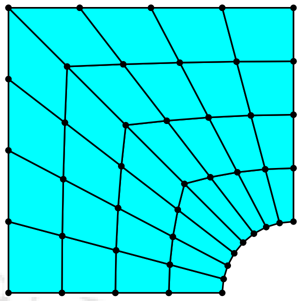

Figure 3.14: The mesh of 4 × 8 q4 elements for plate with a hole problem.

The problem is solved using SRI, EAS, ANS, and hybrid formulation alongside the conventional FE formulation. The refinement is carried out using h and p-refinement strategies. A typical mesh description where the domain is discretized using sixteen q4 elements is shown in Fig. 3.10. For every discretization, the number of elements in both the directions is kept same. The mesh description and the corresponding N^u_{dof} are shown in Table 3.3, where n^x_{ele} and n^y_{ele} are the number of elements in x and y direction, respectively.

As the analytical expressions describing the displacements or stresses at any prescribed point in the domain are not available in the literature, results of a well-refined mesh of 64 × 64 h-FE-q9 elements have been taken as reference for evaluating L_2 norm. The contour plots showing the magnitude of displacement ($|\boldsymbol{u}|$) for the stated reference mesh is shown in Fig. 3.11. The normalized vertical displacement of point ‘A’ against the reference value of 7.6437 is shown in Fig. 3.12a. Furthermore, the L_2 error norm of displacement and stresses is evaluated, see Figs. 3.12b and 3.12c. The selected FE strategies effectively alleviate the locking regardless of the type of the element. However, the FE-q4 fails to converge to the solution even after a significant refinement. Order elevation in conventional FE formulation provides acceptable accuracy in case of displacements. However, the diverging results of stresses are noticed for both FE-q4 and FE-q9. On the contrary, SRI, EAS, and hybrid formulation provides excellent coarse mesh accuracy. The fastest convergence can be obtained using α-FE or h-FE formulation either with q4 or q9 elements. It is important to note that there exists a singularity in stresses at the top-left corner. As a result, the L_2 norm of stresses may not attain a very low value, as the variation at that location can dominate the overall results.

3.3.4 Plate with a hole

The next example is the 2D infinite plate with a circular hole loaded under the constant uniaxial in-plane tension. Due to the symmetry of the problem, only a quarter portion

Table 3.4: The mesh size and respective N^u_{dof} for plate with a hole problem.

Meshes $n^r_{\text{ele}} \times n^\phi_{\text{ele}}$	N^u_{dof} q4	 q9
1×2	8	24
2×4	24	80
3×6	48	168
4×8	80	288
5×10	120	440
6×12	168	624
7×14	224	840
8×16	288	1088
9×18	360	1368
10×20	440	1680
11×22	528	2024
13×26	728	2808
16×32	1088	4224
21×42	1848	-
29×58	3480	-
31×62	3968	-

of the plate is considered for the analysis. The schematic of the problem is shown in Fig. 3.13. The problem set-up consists of a finite square plate of the dimension $L \times L$ with a circular hole of radius R and symmetric boundary condition on edge ED and BC. The stress field on the edge AB and AE is given as follows [110, 173, 174]:

$$\begin{aligned}
\sigma_{xx} &= 1 - \frac{R^2}{r^2}\left(\frac{3}{2}\cos 2\phi + \cos 4\phi\right) + \frac{3R^4}{2r^4}\cos 4\phi,\\
\sigma_{yy} &= -\frac{R^2}{r^2}\left(\frac{1}{2}\cos 2\phi - \cos 4\phi\right) - \frac{3R^4}{2r^4}\cos 4\phi,\\
\tau_{xy} &= -\frac{R^2}{r^2}\left(\frac{1}{2}\sin 2\phi + \sin 4\phi\right) + \frac{3R^4}{2r^4}\sin 4\phi,
\end{aligned}$$

where $r = \sqrt{x^2+y^2}$ and $\phi = \tan^{-1}(y/x)$.

The analytical expression for the displacement field is given as [169]

$$\begin{aligned}
u_x(r,\phi) &= \frac{R}{8\mu}\left[\frac{r}{R}(k+1)\cos\phi\frac{2R}{r}((1+k)\cos\phi + \cos 3\phi) - \frac{2R^3}{r^3}\cos 3\phi\right],\\
u_y(r,\phi) &= \frac{R}{8\mu}\left[\frac{r}{R}(k-3)\sin\phi + \frac{2R}{r}((1-k)\sin\phi + \sin 3\phi) - \frac{2R^3}{r^3}\sin 3\phi\right],
\end{aligned}$$

where $\mu = \dfrac{E}{2(1+\nu)}$ and $k = 3 - 4\nu$ (for plane-strain condition).

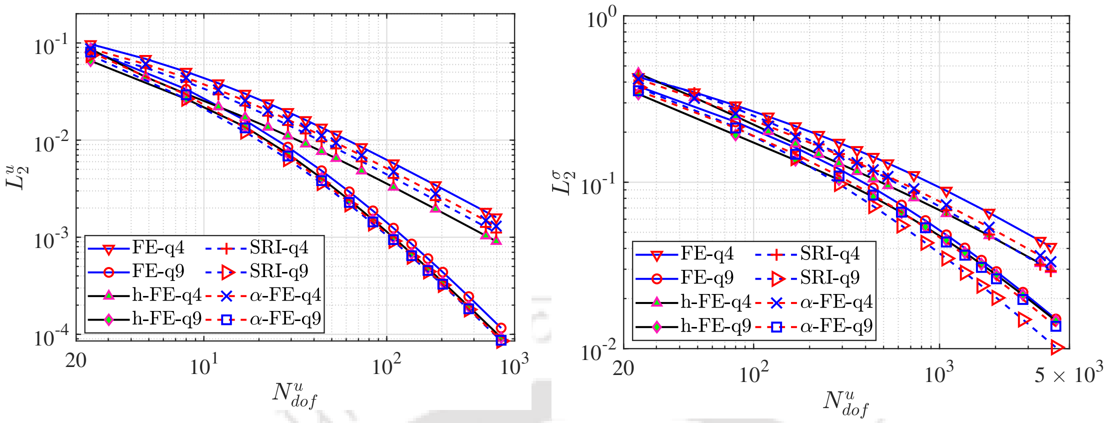

(a) L_2^u (b) L_2^σ

Figure 3.15: L_2 error norm of displacement and stresses for plate with a hole problem with $\nu = 0.3$

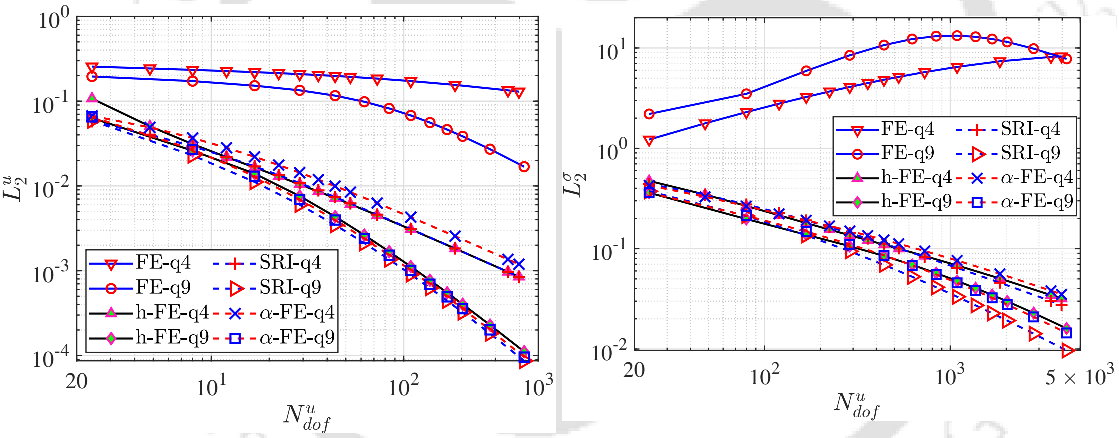

(a) L_2^u (b) L_2^σ

Figure 3.16: L_2 error norm of displacement and stresses for plate with a hole problem with $\nu = 0.4999$

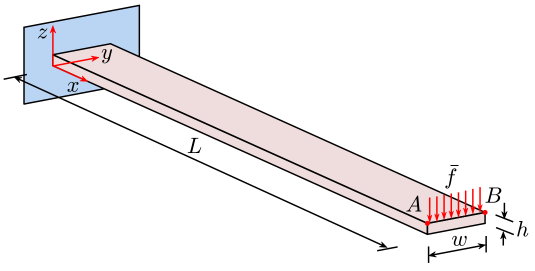

Figure 3.17: Problem set-up and corresponding boundary conditions for 3D straight cantilever beam problem.

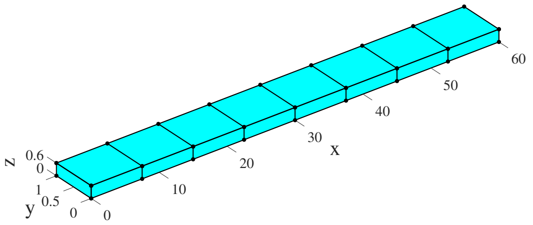

Figure 3.18: The mesh of $8 \times 1 \times 1$ b8 elements for 3D straight cantilever beam problem with $L/h = 100$.

Table 3.5: The mesh size and respective N^u_{dof} for a 3D straight cantilever beam problem.

Meshes $n^L_{\text{ele}} \times n^w_{\text{ele}} \times n^h_{\text{ele}}$	N^u_{dof} b8	 b27
1×1×1	12	54
2×1×1	24	108
4×1×1	48	216
8×1×1	96	432
16×1×1	192	864
32×1×1	384	1728
64×1×1	768	3456
128×1×1	1536	6912
256×1×1	3072	13824
512×1×1	6144	-
1024×1×1	12288	-

The problem is solved for two different values of Poisson's ratio (ν): 0.3 and 0.4999. As ν approaches 0.5, the adverse effects of volumetric locking are introduced into the domain. The refinement is carried out using h and p-refinement strategies. A typical mesh description, where the domain is discretized using thirty-two q4 elements, is shown in Fig. 3.14. The mesh description and the corresponding N^u_{dof} are shown in Table 3.4, where n^r_{ele} and n^ϕ_{ele} are the number of elements in r and ϕ direction, respectively.

The problem is solved using different FE strategies alongside the conventional formulation, see Figs. 3.15 and 3.16. For $\nu = 0.3$, irrespective of the formulation that has been used, the improvements with advanced FE elements are marginal for both q4 and q9 elements against the conventional elements. However, the results of conventional FE elements are largely affected when ν is considered as 0.4999. Regardless of the element type, the conventional elements lock severely with non-convergent results for displacements and diverging results for stresses, see Fig. 3.16. On the contrary, the advanced FE strategies perform consistently irrespective of the element type. The q9 elements, when coupled with the advanced FE formulations, show overall better accuracy. Out of them, the SRI shows the highest rate of convergence. α-FE and h-FE elements also provide comparable coarse mesh accuracies for displacements and stresses for both the cases.

3.3.5 Three-dimensional straight cantilever beam

The present problem is an extension of the 2D straight cantilever beam problem discussed in Section 3.3.1. The problem is considered to evaluate the performance of various 3D FE elements under the influence of shear locking. The problem comprises of a straight beam of length L, width w, and thickness h, clamped on one end and subjected to vertical load $\bar{f}$ along the top edge of the other end [169], see Fig. 3.17. The material parameters, i.e., Young's modulus (E) and Poisson's ratio (ν) are taken as 1500 and 0, respectively. The slenderness ratio L/h is varied from 10 to 1000 with the intention of progressively introducing the adverse effect of shear locking into the problem domain and studying the response of different FE elements.

The problem parameters for the three different cases are given as follows:

1. $L = 60$, $h = 6$, $w = 1$, $L/h = 10$, $\bar{f} = 2.73375$,
2. $L = 60$, $h = 0.6$, $w = 1$, $L/h = 100$, $\bar{f} = 2.73375 \times 10^{-3}$,
3. $L = 60$, $h = 0.06$, $w = 1$, $L/h = 1000$, $\bar{f} = 2.73375 \times 10^{-6}$.

The analytical solution for the vertical displacement (u_z^{ref}) at point 'A' is evaluated using the Euler beam theory [169]. The u_z^{ref} of point 'A' is estimated as 7.29 for all the three cases.

Similar to previous examples, the problem is solved using different elements for all three cases with different mesh discretization. One such mesh of eight b8 elements for $L/h = 100$ is shown in Fig. 3.18. The h-refinement is carried out by increasing the number of elements in L direction while keeping a single element in h and w directions, respectively. The mesh description and the corresponding number of free degrees of freedom (N_{dof}^u) are shown in Table 3.5, where n_{ele}^L, n_{ele}^w, and n_{ele}^h are the number of elements in L, w, and h direction, respectively.

The problem is solved for the normalized displacement of the point 'A' and L_2^u error in the domain against N_{dof}^u. The corresponding results are noted in Fig. 3.19. The locking effect for the lower L/h ratios is comparatively low, see Figs. 3.19a and 3.19b. For such cases, even the conventional elements converge to the solution with acceptable refinement. The advanced FE strategies provide superior coarse mesh accuracy for b8 elements. However, the generalized ANS*-b8 elements show no improvement when compared to the conventional FE-b8 elements. A marginal improvement over FE-b27 for ANS*-b27 elements is observed.

The effect of locking is significantly more for higher L/h ratios, specifically in linear b8 elements. The performance of FE-b8 elements deteriorates consistently with the increasing L/h ratio. In extreme cases, i.e., $L/h = 1000$, the FE-b8 fails to converge even after significantly high refinement. On the contrary, the advanced FE techniques perform consistently irrespective of the L/h ratio, with an exception for ANS*-b8 elements. The ANS*-b8 elements perform similar to the conventional elements irrespective of L/h ratio. These elements fail to alleviate locking for the defined problem parameters. Similar observations can be seen for the overall L_2^u error in the domain. The conventional FE formulation, in particular b8 elements, converges at a slower rate for a lower L/h ratio and fails to provide acceptable accuracy for higher L/h ratios. On the other hand, the convergence of L_2^u with other advanced FE techniques is significantly better than that of the conventional formulation with an exception of ANS*-b8 elements. At higher L/h

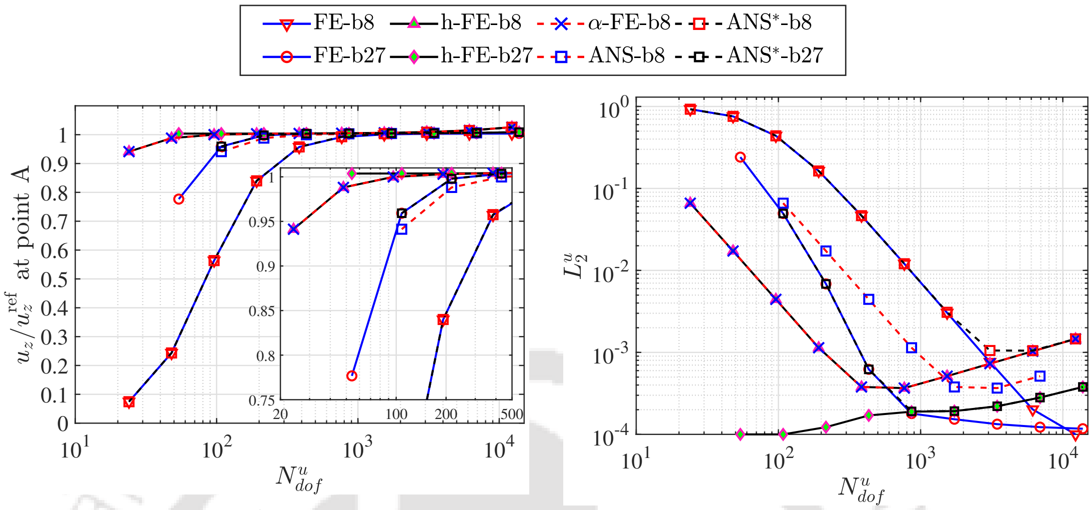

(a) u_z/u_z^{ref} $(L/h = 10)$

(b) L_2^u $(L/h = 10)$

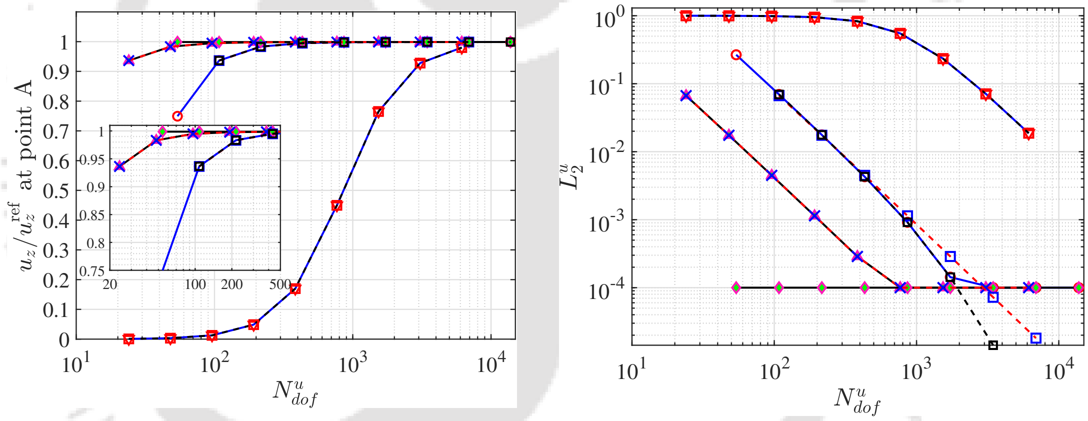

(c) u_z/u_z^{ref} $(L/h = 100)$

(d) L_2^u $(L/h = 100)$

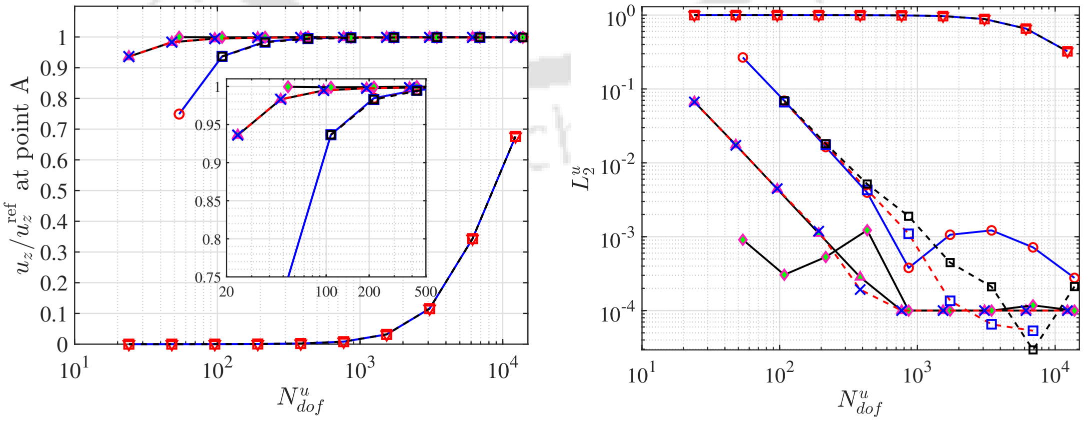

(e) u_z/u_z^{ref} $(L/h = 1000)$

(f) L_2^u $(L/h = 1000)$

Figure 3.19: Normalized tip displacement and L_2 norm of displacement for a 3D straight cantilever beam with different slenderness ratios.

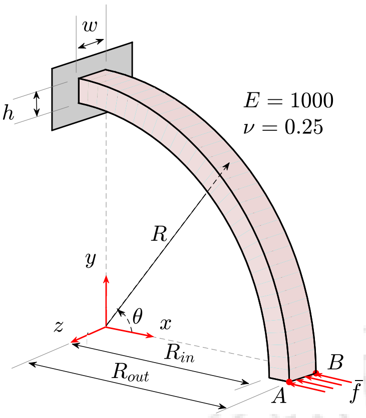

Figure 3.20: Problem set-up and corresponding boundary conditions for 3D curved cantilever beam problem.

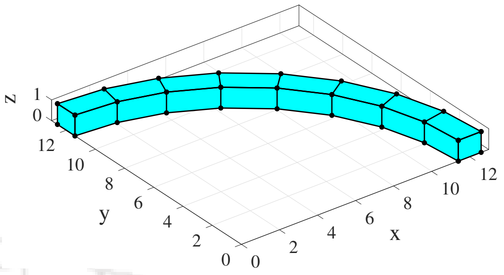

Figure 3.21: The mesh of 8 × 1 × 1 b8 elements for 3D curved cantilever beam problem with $R/h = 10$.

Table 3.6: The mesh size and respective N^u_{dof} for a 3D curved cantilever beam problem.

Meshes	N^u_{dof}	
$n^\theta_{\text{ele}} \times n^R_{\text{ele}} \times n^w_{\text{ele}}$	b8	b27
1×1×1	12	54
2×1×1	24	108
4×1×1	48	216
8×1×1	96	432
16×1×1	192	864
32×1×1	384	1728
64×1×1	768	3456
128×1×1	1536	6912
256×1×1	3072	13824
512×1×1	6144	-
1024×1×1	12288	-

ratios, h-FE-b8 and α-FE-b8 show almost similar and satisfactory coarse mesh accuracy, whereas h-FE-b27 has a marginal improvement over h-FE-b8.

3.3.6 Three-dimensional curved cantilever beam

The next problem is a 3D extension of the curved cantilever problem. The problem serves as an excellent case to assess the performance of several 3D FE elements under coupled shear and membrane locking effect. The problem comprises of a curved beam of mean radius R, width w, and thickness h, clamped at one end, and subjected to horizontal load $\bar{f} = 0.1h^3$ along the top edge of the other end [101, 143], see Fig. 3.20. The material parameters E and ν are taken as 1000 and 0.25, respectively. The slenderness ratio R/h is varied from 10 to 1000 in order to gradually introduce the negative effects of shear and membrane locking into the problem domain and investigate the response of various FE elements.

The problem parameters for the three different cases are given as follows:

1. $R_{\text{in}} = 11.4$, $R_{\text{out}} = 12.6$, $R/h = 10$, $\bar{f} = 1.728 \times 10^{-1}$,
2. $R_{\text{in}} = 11.94$, $R_{\text{out}} = 12.06$, $R/h = 100$, $\bar{f} = 1.728 \times 10^{-4}$,
3. $R_{\text{in}} = 11.994$, $R_{\text{out}} = 12.006$, $R/h = 1000$, $\bar{f} = 1.728 \times 10^{-7}$.

The reference horizontal displacement (u_x^{ref}) of point 'A' is 1.6338, 1.6236, and 1.5852 for $R/h = 10$, 100, and 1000, respectively [143].

The problem is solved using different elements for the stated three cases with different mesh descriptions. One such mesh of eight b8 elements for $R/h = 10$ is shown in Fig. 3.21. The h-refinement is carried out by increasing the number of elements in the θ direction while keeping a single element along the h and w directions, respectively. The mesh description and the corresponding N^u_{dof} are shown in Table 3.6, where n^{θ}_{ele}, n^{R}_{ele}, and n^{w}_{ele} are the number of elements in θ, R, and w direction, respectively. By taking into account the reference solution of a highly refined mesh of h-FE-b27 elements, the relative L^u_2 error norm has been assessed.

The effect of shear and membrane locking can be observed distinctively in all three cases. Even with a lower R/h ratio, the FE-b8 elements converge at a slightly lower value than that of the reference solution, see Fig. 3.22a. This promoted comparatively higher values of overall L^u_2 error in the domain, see Fig. 3.22b. Additionally, the classical (ANS-b8) and generalized (ANS*-b8) ANS approach performed similar to the conventional formulation for $R/h = 10$. Both of these methods failed to alleviate the locking that plagued the results of FE-b8 elements. On the contrary, the h-FE-b8 and α-FE-b8 converged to the reference solution with a fairly low number of elements. The higher-order conventional elements (FE-b27) are less affected by locking. The supposedly superior alternatives, i.e., ANS*-b27 elements, show no improvement when compared to FE-b27 elements.

The effect of locking is more pronounced in higher R/h ratios, see Figs. 3.22c, 3.22d, 3.22e, and 3.22f. The performance of FE-b8 and ANS*-b8 consistently degrades with the increase in R/h ratio. The classical ANS-b8 elements comparatively perform better than the conventional elements, yet the results are widely plagued with locking. The higher-order conventional FE elements converge to the solution with considerable refinement irrespective of the R/h ratio. Similar to the lower R/h ratio problem description, the performance of ANS*-b27 shows no visible improvement over conventional elements. On the contrary, h-FE-b8, h-FE-b27, and α-FE-b8 performed consistently superior in terms of coarse mesh accuracy and lower overall L^u_2 error in the domain. Among them, h-FE-b27 has shown the best performance, especially at higher R/h ratios.

The results presented are based on the meshing strategy outlined in this section. However, further improvements can be achieved by increasing the number of elements

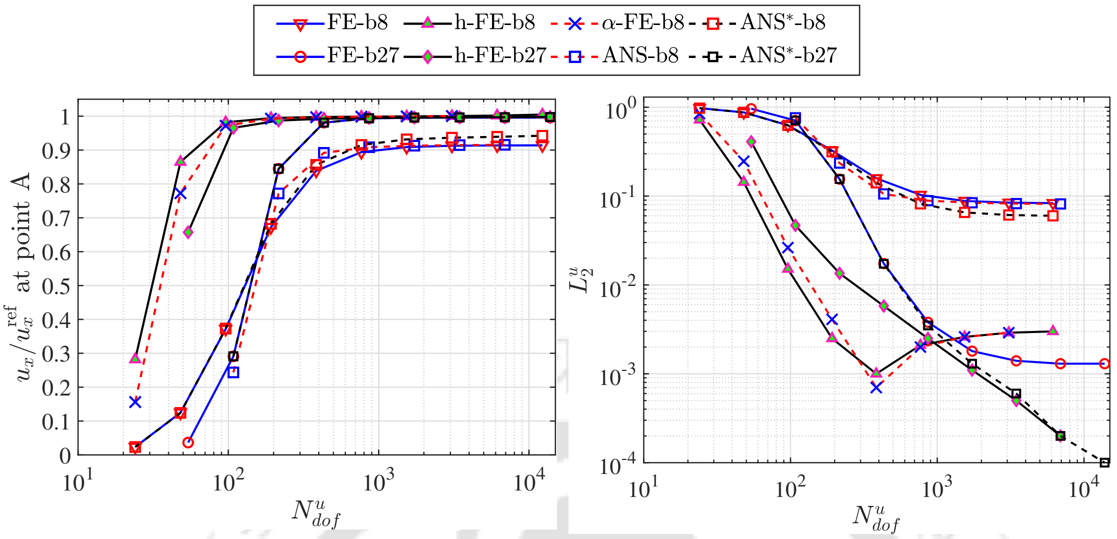

(a) u_x/u_x^{ref} $(R/h = 10)$ **(b)** L_2^u $(R/h = 10)$

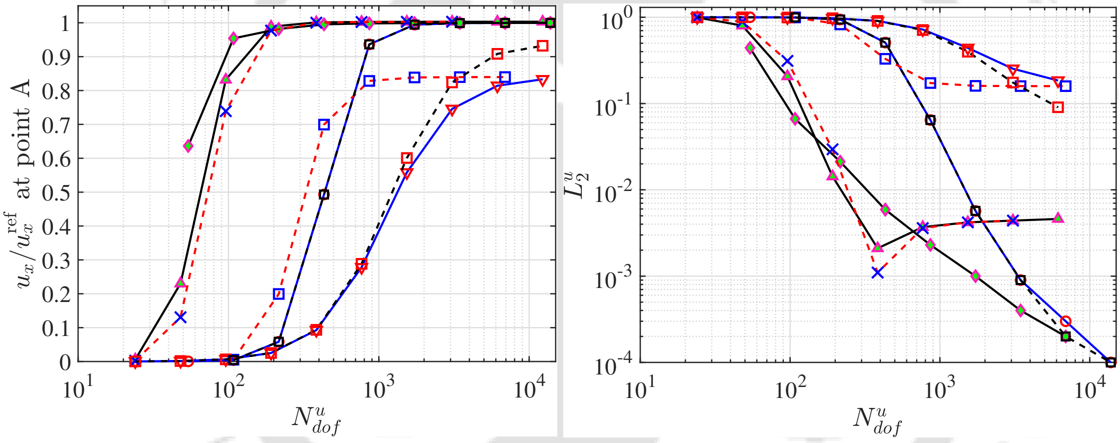

(c) u_x/u_x^{ref} $(R/h = 100)$ **(d)** L_2^u $(R/h = 100)$

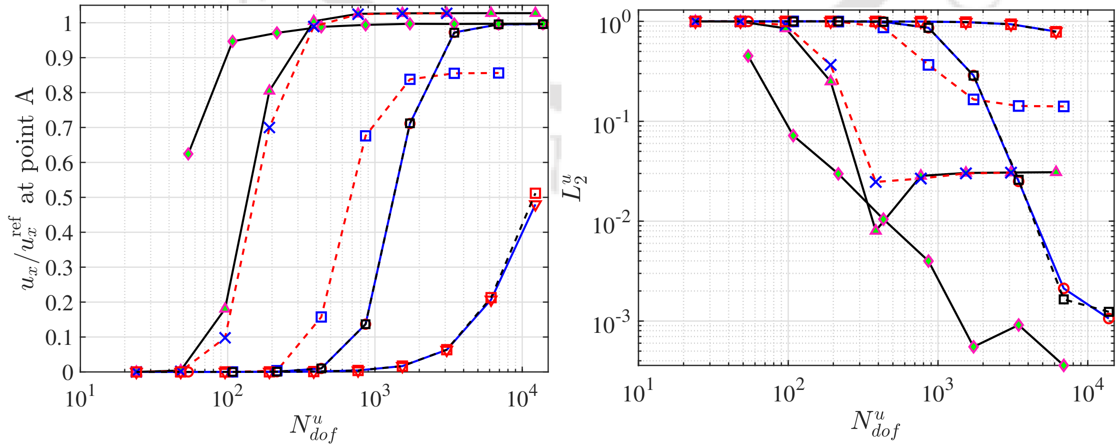

(e) u_x/u_x^{ref} $(R/h = 1000)$ **(f)** L_2^u $(R/h = 1000)$

Figure 3.22: Normalized tip displacement and L_2 norm of displacement for a 3D curved cantilever beam with different slenderness ratios.

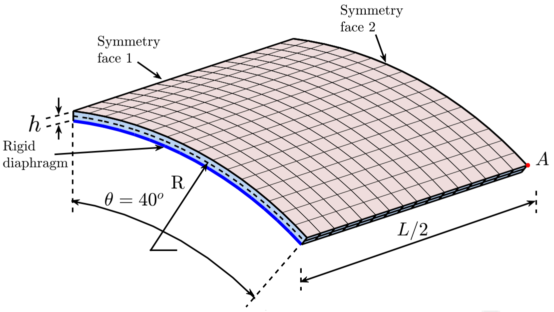

Figure 3.23: Problem set-up and corresponding boundary conditions for a quarter domain of the Scordelis–Lo roof problem.

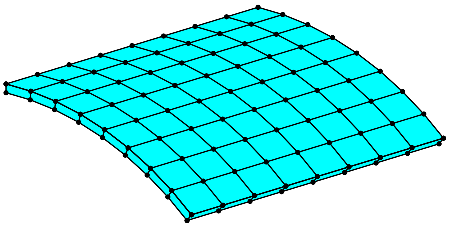

Figure 3.24: The mesh of 1 × 8 × 8 b8 elements for a Scordelis–Lo roof problem.

Table 3.7: The mesh size and respective N^u_{dof} for a Scordelis–Lo roof problem.

Meshes $n^R_{\text{ele}} \times n^\theta_{\text{ele}} \times n^L_{\text{ele}}$	N^u_{dof} b8	 b27
1×2×2	43	202
1×4×4	121	658
1×8×8	457	2530
1×16×16	1633	9538
1×32×32	6433	37473
1×64×64	24970	-

in the w and h directions for $R/h = 10$ and adding more elements in the w direction for R/h ratios of 100 and 1000.

3.3.7 Scordelis–Lo roof problem

The Scordelis–Lo roof problem is one of the shell obstacle course problems and has been treated as a standard test problem to assess the performance of a FE formulation under the influence of locking [175]. The problem is composed of an 80° section of the circular cylinder having thickness h, length L, and mean radius R. The circular section is constrained at both ends with the rigid diaphragm while the remaining two sides are free. The effect of body force per unit volume (ρg) on the defined problem set-up is investigated. Only one-fourth of the cylindrical segment is examined due to the symmetry of the problem. The problem set-up and corresponding boundary conditions are shown in Fig. 3.23, where $L = 50$, $h = 0.25$, and $R = 25$. The material parameters E and ν are taken as 4.32×10^8 and 0, respectively. The body force per unit volume is considered as $\rho g = 360$, where ρ denotes the specific mass of the body and g is the acceleration due to gravity. The reference vertical displacement (u_z^{ref}) of point 'A' is 0.3024 [175].

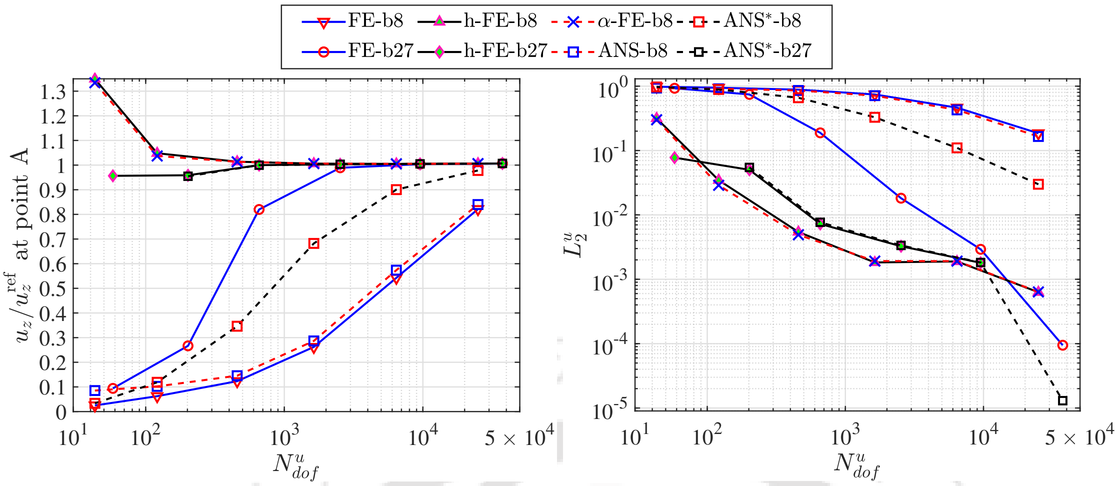

(a) u_z/u_z^{ref} (b) L_2^u

Figure 3.25: Normalized tip displacement and L_2 norm of displacement for a Scordelis–Lo roof problem.

The problem is solved using different elements for the different mesh descriptions. One such mesh of sixty-four b8 elements is shown in Fig. 3.24. The h-refinement is carried out by increasing the number of elements in θ and L direction while keeping a single element along the thickness. The mesh description and the corresponding N^u_{dof} are shown in Table 3.7, where n^R_{ele}, n^θ_{ele}, and n^L_{ele} are the number of elements in R, θ, and L direction, respectively. By taking into account the reference solution of a highly refined mesh of h-FE-b27 elements ($1 \times 32 \times 32$), the relative L^u_2 error norm has been assessed.

The vertical displacement (u_z) of point 'A' is evaluated for different elements and normalized against the reference solution, see Fig. 3.25a. The problem is further investigated by calculating the overall L_2 error norm of the displacement against N^u_{dof} and the results are shown in Fig. 3.25b. It can be seen that the conventional FE-b8 and the classical ANS-b8 elements lock severely and fail to converge to the reference value even after significant refinement. The results for generalized ANS*-b8 are better yet not of acceptable accuracy. On the contrary, the b8 elements developed using hybrid and EAS formulation successfully alleviates locking and show very good coarse mesh accuracy. The FE-b27 elements converge to the solution with refinement; however, the h-FE-b27 and ANS*-b27 show superior results than that of the conventional formulation.

3.3.8 Incompressible cube with pressurized section

The last example is a well-known problem to determine the performance of various 3D elements under the influence of volumetric locking arising due to near-incompressibility constraint [54, 143, 176]. The problem is composed of a rectangular block of length $2L$, width $2L$, and height L with a pressurized section at the center of the block. Let P is the pressure load applied at the mid cross-section area of dimension $L \times L$. Owing to the

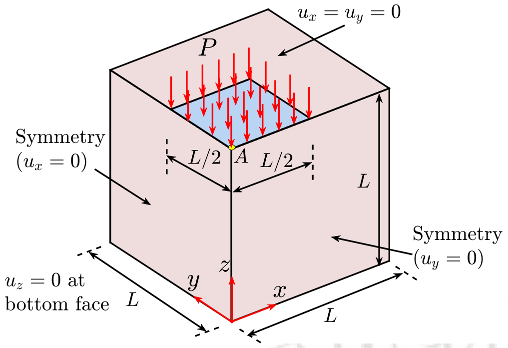

Figure 3.26: Problem set-up and corresponding boundary conditions for a quarter domain of a 3D incompressible block problem.

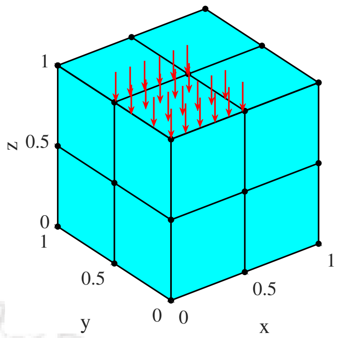

Figure 3.27: The mesh of 2 × 2 × 2 b8 elements for 3D incompressible block problem.

Table 3.8: The mesh size and respective N^u_{dof} for a 3D incompressible block problem.

Meshes	N^u_{dof}	
$n^x_{\text{ele}} \times n^y_{\text{ele}} \times n^z_{\text{ele}}$	b8	b27
2×2×2	42	260
4×4×4	260	1800
8×8×8	1800	13328
16×16×16	13328	102432
32×32×32	102432	-

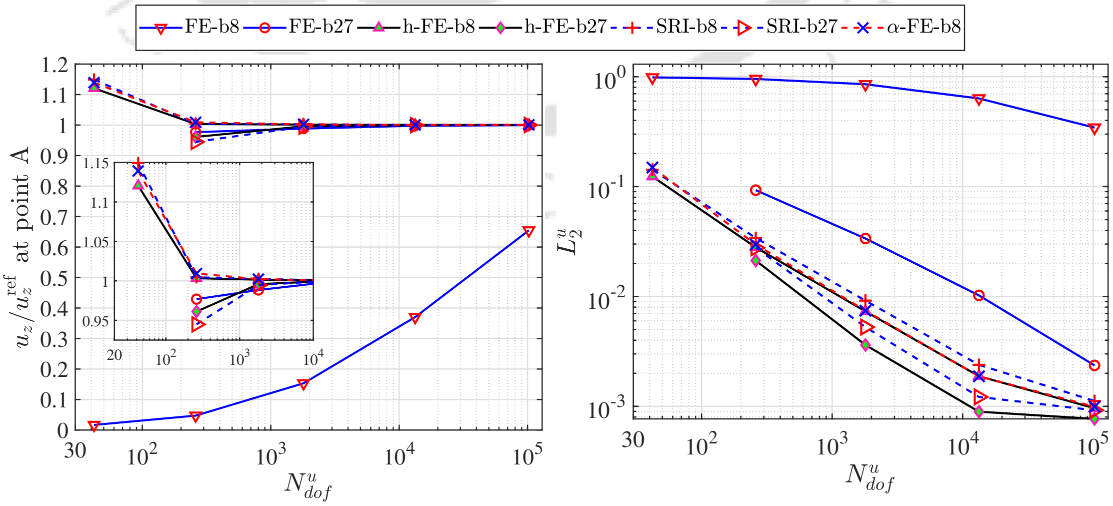

(a) u_z/u_z^{ref}

(b) L^u_2

Figure 3.28: Normalized tip displacement and L_2 norm of displacement for a 3D incompressible block problem

Table 3.9: Mesh description and number of N^u_{dof} for achieving 95% accuracy in displacements. (SB-10, SB-100, and SB-1000 represent the straight cantilever beam problem for slenderness ratios 10, 100, and 1000, respectively. Similarly, CB-10, CB-100, and CB-1000 denote the curved cantilever beam problem for slenderness ratios 10, 100, and 1000, respectively. CM indicates Cook's membrane problem, whereas PH represents the plate with a hole problem. N.C. represents 'Not Converging', N.A. describes 'Not Applicable' and the number of N^u_{dof} is stated inside () besides the mesh sizes.)

Problem	Type of element and paired FE technique				
	FE-q4	SRI-q4	α-FE-q4	ANS-q4	h-FE-q4
SB-10	32×1 (128)	N.A.	3×1 (12)	3×1 (12)	3×1 (12)
SB-100	334×1 (1336)	N.A.	3×1 (12)	3×1 (12)	3×1 (12)
SB-1000	N.C.	N.A.	3×1 (12)	3×1 (12)	3×1 (12)
CB-10	56×1 (224)	N.A.	8×1 (32)	7×1 (28)	7×1 (28)
CB-100	502×1 (2008)	N.A.	16×1 (64)	15×1 (60)	15×1 (60)
CB-1000	N.C.	N.A.	32×1 (128)	30×1 (120)	30×1 (120)
CM	N.C.	11×11 (264)	7×7 (112)	N.A.	8×8 (144)
PH	N.C.	3×6 (48)	3×6 (48)	N.A.	3×6 (48)

Problem	Type of element and paired FE technique				
	FE-q9	SRI-q9	α-FE-q9	ANS-q9	h-FE-q9
SB-10	2×1 (24)	N.A.	1×1 (12)	1×1 (12)	1×1 (12)
SB-100	3×1 (36)	N.A.	1×1 (12)	1×1 (12)	1×1 (12)
SB-1000	3×1 (36)	N.A.	1×1 (12)	1×1 (12)	1×1 (12)
CB-10	7×1 (84)	N.A.	2×1 (24)	2×1 (24)	2×1 (24)
CB-100	19×1 (228)	N.A.	3×1 (36)	3×1 (36)	2×1 (24)
CB-1000	61×1 (732)	N.A.	3×1 (36)	3×1 (36)	2×1 (24)
CM	8×8 (544)	3×3 (84)	3×3 (84)	N.A.	3×3 (84)
PH	10×20 (1680)	2×4 (80)	2×4 (80)	N.A.	2×4 (80)

symmetry of the problem, only one-fourth of the problem domain is investigated. The problem set-up and involved boundary conditions are described in detail in Fig. 3.26, where $L = 1$ and $P = 80$. The material parameters E and ν are taken as 240.56839 and 0.4999, respectively. The Poisson's ratio is kept close to 0.5 to simulate the near-incompressibility constraint in the defined problem.

The problem is solved using different elements that are known to alleviate the volumetric locking alongside the conventional formulation. A typical FE mesh of eight b8 elements is shown in Fig. 3.27. The h-refinement is carried out by uniformly increasing the number of elements in x, y, and z directions. The mesh description and the corresponding N^u_{dof} are shown in Table 3.8, where n^x_{ele}, n^y_{ele}, and n^z_{ele} are the number of elements in x, y, and z direction, respectively. The reference vertical displacement (u_z^{ref}) at point 'A' is 0.2165 [143]. Further, the relative L^u_2 error norm has been assessed by taking into account the reference solution of a highly refined mesh of h-FE-b27 elements ($32 \times 32 \times 32$ elements).

Table 3.10: Mesh description and number of N^u_{dof} for achieving 90% accuracy in stresses. (SB-10, SB-100, and SB-1000 represent the straight cantilever beam problem for slenderness ratios 10, 100, and 1000, respectively. Similarly, CB-10, CB-100, and CB-1000 denote the curved cantilever beam problem for slenderness ratios 10, 100, and 1000, respectively. CM indicates Cook's membrane problem, whereas PH represents the plate with a hole problem. N.C. represents 'Not Converging', N.A. describes 'Not Applicable' and the number of N^u_{dof} is stated inside () besides the mesh sizes.)

Problem	Type of element and paired FE technique				
	FE-q4	SRI-q4	α-FE-q4	ANS-q4	h-FE-q4
SB-10	29×1 (116)	N.A.	6×1 (24)	6×1 (24)	6×1 (24)
SB-100	236×1 (944)	N.A.	6×1 (24)	6×1 (24)	6×1 (24)
SB-1000	N.C.	N.A.	6×1 (24)	6×1 (24)	6×1 (24)
CB-10	44×1 (176)	N.A.	11×1 (44)	8×1 (32)	8×1 (32)
CB-100	392×1 (1568)	N.A.	25×1 (100)	19×1 (76)	20×1 (80)
CB-1000	N.C.	N.A.	56×1 (224)	50×1 (200)	50×1 (200)
CM	N.C.	64×64 (8320)	62×62 (7812)	N.A.	62×62 (7812)
PH	N.C.	11×22 (528)	12×24 (624)	N.A.	10×20 (440)

Problem	Type of element and paired FE technique				
	FE-q9	SRI-q9	α-FE-q9	ANS-q9	h-FE-q9
SB-10	4×1 (48)	N.A.	1×1 (12)	1×1 (12)	1×1 (12)
SB-100	4×1 (48)	N.A.	1×1 (12)	1×1 (12)	1×1 (12)
SB-1000	4×1 (48)	N.A.	1×1 (12)	1×1 (12)	1×1 (12)
CB-10	11×1 (132)	N.A.	3×1 (36)	3×1 (36)	3×1 (36)
CB-100	31×1 (372)	N.A.	3×1 (36)	3×1 (36)	3×1 (36)
CB-1000	105×1 (1260)	N.A.	3×1 (36)	3×1 (36)	3×1 (36)
CM	N.C.	28×28 (6384)	25×25 (5100)	N.A.	25×25 (5100)
PH	N.C.	4×8 (288)	5×10 (440)	N.A.	4×8 (288)

The problem is solved for the vertical displacement at point 'A' and the results are normalized against the reference solution, see Fig. 3.28a. Further, the overall L_2 error norm of the displacement against N^u_{dof} is evaluated and the results are shown in Fig. 3.28b. The adverse effects of volumetric locking plagued the results of conventional FE-b8 elements. Even after significantly high refinement, FE-b8 elements fail to converge to the reference solution. The advanced FE techniques, irrespective of the element type, successfully alleviate volumetric locking. The high coarse mesh accuracy is observed for h-FE, α-FE, and SRI elements. The results obtained with these techniques only marginally vary from each other.

3.4 Key findings

This work presents a comprehensive study of VHW principle-based EAS, a specific class of stress-based HR principle-based hybrid formulation, SRI, ANS approach alongside the

Table 3.11: Mesh description and number of N^u_{dof} for achieving more than 95% accuracy in displacements in 3D problem domains. (SB*-10, SB*-100, and SB*-1000 represent the 3D straight cantilever beam problem for slenderness ratios 10, 100, and 1000, respectively. Similarly, CB*-10, CB*-100, and CB*-1000 denote the 3D curved cantilever beam problem for slenderness ratios 10, 100, and 1000, respectively. SDL and IB indicates the Scordelis–Lo roof and incompressible block problem, respectively. N.C. represents 'Not Converging', N.A. describes 'Not Applicable' and the number of N^u_{dof} is stated inside () besides the mesh sizes.)

Problem	Type of element and paired FE technique				
	FE-b8	SRI-b8	α-FE-b8	ANS-b8	h-FE-b8
SB*-10	32×1×1 (384)	N.A.	3×1×1 (36)	3×1×1 (36)	3×1×1 (36)
SB*-100	512×1×1 (6144)	N.A.	3×1×1 (36)	3×1×1 (36)	3×1×1 (36)
SB*-1000	N.C.	N.A.	3×1×1 (36)	3×1×1 (36)	3×1×1 (36)
CB*-10	N.C.	N.A.	6×1×1 (72)	N.C.	5×1×1 (60)
CB*-100	N.C.	N.A.	15×1×1 (180)	N.C.	14×1×1 (168)
CB*-1000	N.C.	N.A.	32×1×1 (384)	N.C.	30×1×1 (360)
SDL	N.C.	N.A.	1×4×4 (121)	N.C.	1×4×4 (121)
IB	N.C.	4×4×4 (260)	4×4×4 (260)	N.A.	4×4×4 (260)

Problem	Type of element and paired FE technique				
	ANS*-b8	FE-b27	SRI-b27	ANS*-b27	h-FE-b27
SB*-10	32×1×1 (384)	2×1×1 (108)	N.A.	2×1×1 (108)	1×1×1 (54)
SB*-100	512×1×1 (6144)	3×1×1 (162)	N.A.	3×1×1 (162)	1×1×1 (54)
SB*-1000	N.C.	3×1×1 (162)	N.A.	3×1×1 (162)	1×1×1 (54)
CB*-10	N.C.	5×1×1 (270)	N.A.	5×1×1 (270)	2×1×1 (108)
CB*-100	N.C.	21×1×1 (1134)	N.A.	21×1×1 (1134)	3×1×1 (162)
CB*-1000	N.C.	64×1×1 (3456)	N.A.	64×1×1 (3456)	8×1×1 (432)
SDL	1×64×64 (24970)	1×8×8 (2530)	N.A.	1×8×8 (2530)	1×4×4 (658)
IB	N.A.	4×4×4 (1800)	2×2×2 (260)	N.A.	2×2×2 (260)

conventional FE formulation. The performance of the these FE alleviation strategies is assessed by the evaluation of normalized displacement of a specific location against the reference solution and the relative L_2 error norms of displacement and stress on numerous benchmark examples. The adverse effect of locking is prominently observed in low-order conventional elements. Higher-order elements are less prone to locking, even with the conventional FE formulation. However, the SRI, α-FE, and h-FE elements effectively alleviate the locking and provide superior coarse mesh accuracy irrespective of the element type. The classical ANS elements in 2D regime have shown improved performance against the conventional element. However, its extension to 3D problems has shown no notable gain in the solution quality while dealing with locking.

To summarize the findings, the ability of a method to achieve an accuracy of 95% in displacement and 90% in stress against the minimum number of N^u_{dof} required is evaluated, see Tables 3.9, 3.10, and 3.11. The results obtained for each numerical example and the comparative performance of individual method leads to the following conclusions:

1. The SRI approach provides high convergence rates in the problems affected by volumetric locking. However, the method is restricted to alleviate volumetric locking in conventional solid elements. The method's effectiveness lies in how efficiently we can isolate the part that is responsible for locking. This separation is not possible for other types of locking in solid elements. Hence, the method is less robust and applicability is restricted to compatible problem domains.
2. The classical ANS method effectively alleviates the shear locking in 2D thin structural geometries such as straight and curved cantilever beam problems with a high slenderness ratio. Furthermore, the method provides better computational efficiency over other methods. However, the method is restricted to problems affected by shear locking. The extension of the method to the 3D problems is not a viable option as the elements developed show no considerable improvement over conventional elements.
3. The EAS method based on VHW and hybrid formulation based on the HR principle performs effectively and consistently irrespective of the type of locking. The presented hybrid elements show a marginal improvement in coarse mesh accuracy over EAS while handling the curved cantilever beam under the influence of shear locking and alleviating the volumetric locking in plate with a hole problem.

The above findings state that the presented class of hybrid formulation provides a robust, reliable, and efficient numerical approach to alleviate different types of locking. The immediate alternative to hybrid elements is the EAS method which provides equivalent accuracy in many cases but is marginally inferior to hybrid elements in certain situations. However, EAS elements exhibit greater stability in severely distorted meshes compared to the presented class of hybrid elements.

Chapter 4

Development of Quadratic EAS Elements[†]

The EAS elements are widely used in the literature to address the issue of locking associated with conventional elements. However, existing literature in the context of three-dimensional (3D) elasticity problems is predominantly restricted to the eight-node linear EAS (Section 2.3.2.3) elements. Thus, existing 3D EAS elements do not exploit the superior performance offered by quadratic elements over linear elements.

In this chapter, we propose a novel twenty-seven node quadratic EAS element, which is the first such attempt in the literature. Additionally, the chapter also presents a six-node wedge and an eighteen-node wedge EAS element. Furthermore, it outlines the systematic procedure for deriving the aforementioned elements, emphasizing the investigation of the interrelation between the two-field HR (Section 2.4) and three-field VHW (Section 2.3) variational formulations. Finally, the robustness and performance of the proposed EAS elements is demonstrated through numerous examples.

4.1 Introduction

Locking poses a challenge in FEA, and in response, numerous techniques have been proposed in the literature to address the issue of locking, see Section 1.4. However, these techniques are limited in their applicability and are most suited to a specific set of problems, lacking generality across a wide range of problems. For instance, shell theories are limited to analyze thin structures due to kinematic assumptions and require complex mathematical formulation. Further, reducing the Gaussian quadrature rule order in RI can cause instabilities like “hourglass modes”, while separating the locking-affected part of the material tensor in SRI is not always possible. ANS method is suited only

---

[†] D. S. Bombarde, M. Agrawal, S. S. Gautam, A. Nandy, “Development of quadratic enhanced assumed strain elements for three-dimensional linear elasticity”, *Computers & Structures* 291 (2024) 107217. `https://doi.org/10.1016/j.compstruc.2023.107217`

for alleviating shear locking, whereas the strain projection techniques are restricted to problems involving incompressibility.

Extensive efforts have been made in the literature to develop generalized elements that can perform well in any scenario, whether the problem involves thin or thick structures or requires handling incompressibility or near-incompressibility of materials, without compromising their performance in any aspect. Towards this goal, multi-field variation formulations have provided viable options. These formulations assume additional independent fields, such as stress or strain fields, alongside the displacement. The commonly employed strain-based formulations are based on the VHW variational principle [54, 121–134, 165–167], whereas the stress-based elements are derived from the HR variational principle [32, 126, 136, 137, 139–143, 145, 146]. Both of these formulations are widely recognized for their ability to effectively address the locking issue and have the capacity to solve thick and thin geometries without introducing additional complexity. Furthermore, the additional degrees of freedom associated with the strain or stress field are eliminated at the element level. As a result, there is no alteration in the size of the global stiffness matrix in comparison to conventional displacement-based elements.

The strain-based formulation, particularly the EAS method, has become the most extensively used technique due to its ease of implementation. The EAS method has been applied to a range of problems, demonstrating good bending behavior, locking-free response in incompressible materials and thin structural geometries, and good accuracy with relatively coarse mesh [54, 121–134, 165–167]. However, existing 3D EAS elements are solely developed on linear eight-node elements, despite literature indicating that conventional quadratic elements demonstrate a higher convergence rate compared to linear elements [8]. Hence, the potential advantages offered by higher-order elements, such as twenty-seven node elements, have not been exploited to their fullest by the EAS community. In this chapter, we propose an EAS formulation for the 3D quadratic hexahedral element. The proposed element offers the combined advantages of the EAS formulation and quadratic elements. Apart from this, the current work also presents the novel six-node and eighteen-node wedge EAS elements derived under the same framework. These new EAS elements will significantly enhance the applicability of EAS elements in the FEM community.

A crucial aspect in the development of the proposed EAS elements is the careful selection of a feasible set of interpolation functions to approximate the enhanced strain field. To accomplish this, the equivalence between the stress-based HR and the VHW-based EAS formulation is utilized. Achieving equivalence requires ensuring orthogonality between the independent stress field in the HR-based formulation and the enhanced strain field in the VHW-based EAS formulations, along with satisfying certain conditions on their respective spaces [125, 126, 177, 178]. The present work employs the independent stress field proposed in [141, 142], which provides efficient and robust hybrid elements. These elements employ a distinct approach to obtain a unique set of stress interpolation functions that have proven effective in diverse applications [143, 147–151], demonstrating the versatility of the method in practical settings. The current study utilizes these stress interpolations and explores the orthogonality condition to derive an efficient choice for the enhanced strain field in both quadratic hexahedral and wedge EAS elements. Although the primary attention was on the aforementioned proposed elements, the methodology outlined in this work can be employed to generate a variety of EAS elements from their corresponding stress-based elements in a systematic framework.

The proposed EAS elements are extensively tested with several benchmark numerical examples, which demonstrate their capability to alleviate locking and provide higher accuracy with coarser mesh compared to conventional elements. The efficiency, reliability, and robustness of the proposed elements make them a viable option for solving a diverse range of problem domains, especially in cases where volumetric, transverse shear, and membrane locking are dominant factors. Moreover, the twenty-seven node brick EAS element provides either superior or similar performance as the existing eight-node brick EAS elements. As a result, it presents an attractive alternative to the available EAS elements. Further, the current work also presents a set of wedge EAS elements. These wedge EAS elements have been shown to reduce the stress oscillations that plagued the results of a volumetric locking-dominated domain, leading to improved result quality.

The rest of the chapter is organized as follows: In **Section 4.2**, the fundamental concepts in the two-field stress-based HR variational principle and VHW variational principle for the EAS method are recollected from the preceding chapters. It further discusses the equivalence between both approaches and the conditions that lead to their equivalence. **Section 4.3** primarily focuses on evaluating the strain interpolation functions employed in the proposed EAS elements. In **Section 4.4**, the proposed EAS elements are assessed by analyzing their performance in multiple benchmark numerical examples. Finally, **Section 4.5** summarizes the work and additional supporting information is provided in the **Appendix**.

4.2 Introduction to VHW-based EAS method, stress-based HR variational principle, and their equivalence

The present section briefly recollect the preliminary concepts involved in the VHW variational principle for EAS method and the two-field stress-based HR variational principle. Further, the section explores the interrelation between these two approaches, emphasizing their equivalence and the necessary conditions for establishing equivalence. These concepts are crucial for comprehending the development of the proposed EAS element, as they contribute to the overall completeness of the chapter.

4.2.1 VHW variational principle for EAS method

The VHW variational principle consists of three primary field variables: displacement ($\boldsymbol{u}$), stress ($\boldsymbol{\sigma}$), and strain ($\boldsymbol{\varepsilon}$). The admissible variations of these variables are represented by $\delta\boldsymbol{u}$, $\delta\boldsymbol{\sigma}$, and $\delta\boldsymbol{\varepsilon}$, respectively. Let $\mathcal{V}_{\boldsymbol{u}}$, $\mathcal{V}_{\boldsymbol{\sigma}}$, and $\mathcal{V}_{\boldsymbol{\varepsilon}}$ be the spaces associated with $\delta\boldsymbol{u}$, $\delta\boldsymbol{\sigma}$ and $\delta\boldsymbol{\varepsilon}$, respectively, which can be expressed as follows:

$$\mathcal{V}_{\boldsymbol{u}} = \Big\{\delta\boldsymbol{u} \in \mathcal{H}^1(\mathcal{R}) : \delta\boldsymbol{u} = \boldsymbol{0} \text{ on } \partial\mathcal{R}_u\Big\}, \tag{4.1}$$

$$\mathcal{V}_{\boldsymbol{\sigma}} = \Big\{\delta\boldsymbol{\sigma} \in \mathcal{L}^2(\mathcal{R}) : \delta\boldsymbol{\sigma} = \delta\boldsymbol{\sigma}^T\Big\}, \tag{4.2}$$

$$\mathcal{V}_{\boldsymbol{\varepsilon}} = \Big\{\delta\boldsymbol{\varepsilon} \in \mathcal{L}^2(\mathcal{R}) : \delta\boldsymbol{\varepsilon} = \delta\boldsymbol{\varepsilon}^T\Big\}. \tag{4.3}$$

The foundation of the EAS method is based on the above VHW principle. In EAS method, the $\boldsymbol{\varepsilon}$ is divided into two parts as follows:

$$\boldsymbol{\varepsilon} = \boldsymbol{\varepsilon}^u + \boldsymbol{\varepsilon}^\alpha, \tag{4.4}$$

where $\boldsymbol{\varepsilon}^u$ is the compatible strain field defined by Eq. 2.2 and $\boldsymbol{\varepsilon}^\alpha$ is the independent enhanced strain field introduced to alleviate the locking. In order to avoid the dependency on $\boldsymbol{\sigma}$ in VHW variational principle, an orthogonality condition is introduced between $\boldsymbol{\sigma}$ and $\boldsymbol{\varepsilon}^\alpha$ such that

$$\int_{\mathcal{R}} \delta\boldsymbol{\sigma} : \boldsymbol{\varepsilon}^\alpha \, \mathrm{d}\mathcal{R} = 0 \quad \text{or} \quad \int_{\mathcal{R}} \delta\bar{\boldsymbol{\sigma}}^T \bar{\boldsymbol{\varepsilon}}^\alpha \, \mathrm{d}\mathcal{R} = 0, \tag{4.5}$$

where $\delta\bar{\boldsymbol{\sigma}}$ and $\bar{\boldsymbol{\varepsilon}}^\alpha$ are the vector form of $\delta\boldsymbol{\sigma}$ and $\boldsymbol{\varepsilon}^\alpha$, respectively. Finally, the variational statement involved in EAS is derived by consecutively choosing zero variations of displacements and assumed strains separately, i.e., $(\delta\boldsymbol{u}, \delta\boldsymbol{\varepsilon}^\alpha) = (\delta\boldsymbol{u}, \boldsymbol{0})$ and $(\delta\boldsymbol{u}, \delta\boldsymbol{\varepsilon}^\alpha) = (\boldsymbol{0}, \delta\boldsymbol{\varepsilon}^\alpha)$. Assuming the orthogonality as per Eq. 4.5, the EAS approach for the given classical linear elasticity problem (Section 2.1) can be formulated through the following variational statement:

$$\int_{\mathcal{R}} (\delta\bar{\boldsymbol{\varepsilon}}^u)^T \bar{\boldsymbol{\sigma}}^\varepsilon \, \mathrm{d}\mathcal{R} = \int_{\mathcal{R}} \delta\boldsymbol{u}^T \boldsymbol{b} \, \mathrm{d}\mathcal{R} + \int_{\partial\mathcal{R}_t} \delta\boldsymbol{u}^T \bar{\boldsymbol{t}} \, \mathrm{d}A \qquad \forall\, \delta\boldsymbol{u} \in \mathcal{V}_{\boldsymbol{u}}, \tag{4.6}$$

$$\int_{\mathcal{R}} (\delta\bar{\boldsymbol{\varepsilon}}^\alpha)^T (\bar{\boldsymbol{\sigma}}^\varepsilon - \bar{\boldsymbol{\sigma}}) \, \mathrm{d}\mathcal{R} = 0, \tag{4.7}$$

where $\bar{\boldsymbol{\varepsilon}}^u$, $\bar{\boldsymbol{\varepsilon}}^\alpha$, and $\bar{\boldsymbol{\sigma}}$ are the vector representations of $\boldsymbol{\varepsilon}^u$, $\boldsymbol{\varepsilon}^\alpha$, and $\boldsymbol{\sigma}$, respectively. The detailed derivation of the participating variational statement is discussed in Section 2.3.

4.2.2 Stress-based HR variational principle

The HR variational principle comprises of two independent field variables, i.e., displacement and stress. Let $\boldsymbol{u}$ and $\boldsymbol{\sigma}$ be the independent displacement and stress field, respectively, while $\delta\boldsymbol{u}$ and $\delta\boldsymbol{\sigma}$ represent their respective variations in such a way that

$$\mathcal{V}_{\boldsymbol{u}} = \left\{\delta\boldsymbol{u} \in \mathcal{H}^1(\mathcal{R}) : \delta\boldsymbol{u} = \boldsymbol{0} \text{ on } \partial\mathcal{R}_u\right\}, \tag{4.8}$$

$$\mathcal{V}_{\boldsymbol{\sigma}} = \left\{\delta\boldsymbol{\sigma} \in \mathcal{L}^2(\mathcal{R}) : \delta\boldsymbol{\sigma} = \delta\boldsymbol{\sigma}^T\right\}, \tag{4.9}$$

where $\mathcal{V}_{\boldsymbol{u}}$ and $\mathcal{V}_{\boldsymbol{\sigma}}$ are the spaces associated with the admissible variations $\delta\boldsymbol{u}$ and $\delta\boldsymbol{\sigma}$, respectively. For the linear elasticity problem defined in Section 2.1, the resulting variational statement can be expressed as follows:

$$\int_{\mathcal{R}} (\delta\bar{\boldsymbol{\varepsilon}}^u)^T \bar{\boldsymbol{\sigma}} \, \mathrm{d}\mathcal{R} = \int_{\mathcal{R}} \delta\boldsymbol{u}^T \boldsymbol{b} \, \mathrm{d}\mathcal{R} + \int_{\partial\mathcal{R}_t} \delta\boldsymbol{u}^T \bar{\boldsymbol{t}} \, \mathrm{d}A \qquad \forall\, \delta\boldsymbol{u} \in \mathcal{V}_{\boldsymbol{u}}, \tag{4.10}$$

$$\int_{\mathcal{R}} \delta\bar{\boldsymbol{\sigma}}^T \left[\bar{\boldsymbol{\varepsilon}}^u(\boldsymbol{u}) - \boldsymbol{C}^{-1}\bar{\boldsymbol{\sigma}}\right] \mathrm{d}\mathcal{R} = 0 \qquad \forall\, \delta\bar{\boldsymbol{\sigma}}, \tag{4.11}$$

where $\bar{\boldsymbol{\sigma}}$ and $\bar{\boldsymbol{\varepsilon}}^u$ are the vector representations of $\boldsymbol{\sigma}$ and $\boldsymbol{\varepsilon}^u$, respectively and $\boldsymbol{C}$ is the material constitutive tensor. A more comprehensive exploration of the topic is presented in Section 2.4.

4.2.3 Approximation of field variables and involved function spaces

The HR and VHW-based EAS variational principles necessitate the use of independent interpolation techniques for approximating the independent $\boldsymbol{u}$, $\bar{\boldsymbol{\sigma}}$, and $\bar{\boldsymbol{\varepsilon}}^\alpha$. These primary field variables and their involved function spaces are defined as follows:

$$\mathcal{V}_{\boldsymbol{u}} = \left\{\boldsymbol{u}, \delta\boldsymbol{u} : \boldsymbol{u} = \boldsymbol{N}\hat{\boldsymbol{u}},\ \delta\boldsymbol{u} = \boldsymbol{N}\delta\hat{\boldsymbol{u}};\ \hat{\boldsymbol{u}}, \delta\hat{\boldsymbol{u}} \in \mathbb{R}^{n_d \times n_e}\right\}, \tag{4.12}$$

$$\mathcal{V}_{\boldsymbol{\sigma}} = \left\{\bar{\boldsymbol{\sigma}}, \delta\bar{\boldsymbol{\sigma}} : \bar{\boldsymbol{\sigma}} = \boldsymbol{P}\hat{\boldsymbol{\beta}},\ \delta\bar{\boldsymbol{\sigma}} = \boldsymbol{P}\delta\hat{\boldsymbol{\beta}};\ \hat{\boldsymbol{\beta}}, \delta\hat{\boldsymbol{\beta}} \in \mathbb{R}^{n_{\hat{\beta}}}\right\}, \tag{4.13}$$

$$\mathcal{V}_{\boldsymbol{\varepsilon}^\alpha} = \left\{\bar{\boldsymbol{\varepsilon}}^\alpha, \delta\bar{\boldsymbol{\varepsilon}}^\alpha : \bar{\boldsymbol{\varepsilon}}^\alpha = \boldsymbol{G}\hat{\boldsymbol{\alpha}},\ \delta\bar{\boldsymbol{\varepsilon}}^\alpha = \boldsymbol{G}\delta\hat{\boldsymbol{\alpha}};\ \hat{\boldsymbol{\alpha}}, \delta\hat{\boldsymbol{\alpha}} \in \mathbb{R}^{n_{\hat{\alpha}}}\right\}. \tag{4.14}$$

Here, $\mathcal{V}_{\boldsymbol{u}}$, $\mathcal{V}_{\boldsymbol{\sigma}}$, and $\mathcal{V}_{\boldsymbol{\varepsilon}^\alpha}$ are the function spaces for $\boldsymbol{u}$, $\boldsymbol{\sigma}$, and $\boldsymbol{\varepsilon}^\alpha$, respectively. n_e represents the count of nodes in each element, while n_d denotes the degrees of freedom for each node. The number of stress and strain parameters per element is represented by $n_{\hat{\beta}}$ and $n_{\hat{\alpha}}$, respectively. The matrix $\boldsymbol{N}$, $\boldsymbol{P}$, and $\boldsymbol{G}$ are the displacement, stress, and strain interpolation matrices. Conventionally, the $\boldsymbol{N}$ is composed of the Lagrange interpolation functions, whereas special schemes must be developed to choose appropriate $\boldsymbol{P}$ and $\boldsymbol{G}$ interpolation matrices. In addition to the above spaces, the spaces for dependent variables are defined as

$$\mathcal{V}_{\boldsymbol{\sigma}^u} = \left\{\bar{\boldsymbol{\sigma}}^u : \bar{\boldsymbol{\sigma}}^u = \boldsymbol{C}\bar{\boldsymbol{\varepsilon}}^u = \boldsymbol{C}\boldsymbol{B}\hat{\boldsymbol{u}}\ \forall\ \boldsymbol{u} \in \mathcal{V}_{\boldsymbol{u}}\right\}, \tag{4.15}$$

$$\mathcal{V}_{\boldsymbol{\sigma}^\alpha} = \left\{\bar{\boldsymbol{\sigma}}^\alpha : \bar{\boldsymbol{\sigma}}^\alpha = \boldsymbol{C}\bar{\boldsymbol{\varepsilon}}^\alpha\ \forall\ \bar{\boldsymbol{\varepsilon}}^\alpha \in \mathcal{V}_{\boldsymbol{\varepsilon}^\alpha}\right\}, \tag{4.16}$$

where $\mathcal{V}_{\boldsymbol{\sigma}^u}$ and $\mathcal{V}_{\boldsymbol{\sigma}^\alpha}$ is the function space of $\boldsymbol{\sigma}^u$ and $\boldsymbol{\sigma}^\alpha$, respectively and $\boldsymbol{B}$ is the strain-displacement matrix.

4.2.4 Conditions for equivalence between HR-based hybrid and VHW-based EAS elements

The section briefly outlines the key conditions and requirements that result in exact equivalence between HR principle-based hybrid elements and VHW principle-based EAS elements. The two methods lead to identical elements and exhibit exact equivalence if the resulting displacement from both hybrid and EAS elements is identical and if the stress evaluated in the hybrid elements ($\boldsymbol{\sigma}$) is equal to the stresses obtained in EAS elements ($\boldsymbol{\sigma}^{\text{eas}} = \boldsymbol{\sigma}^u + \boldsymbol{\sigma}^\alpha$), at every point in the element domain [125, 126, 178]. Here, $\boldsymbol{\sigma}^u$ and $\boldsymbol{\sigma}^\alpha$ are the stresses evaluated using $\boldsymbol{u}$ and ε^α, respectively. The conditions that guarantee the exact equivalence are given as follows:

(a) *Orthogonality condition:* An orthogonality condition is introduced between $\boldsymbol{\sigma}$ and ε^α that implies

$$\int_{\mathcal{R}} \delta\boldsymbol{\sigma} : \varepsilon^\alpha \; \mathrm{d}\mathcal{R} = 0 \quad \text{or} \quad \int_{\mathcal{R}} \delta\bar{\boldsymbol{\sigma}}^T \bar{\varepsilon}^\alpha \; \mathrm{d}\mathcal{R} = 0. \tag{4.17}$$

The above criterion also entails that the $\mathcal{V}_{\boldsymbol{\sigma}}$ and $\mathcal{V}_{\varepsilon^\alpha}$ do not share the function space, i.e., $\mathcal{V}_{\boldsymbol{\sigma}} \cap \mathcal{V}_{\varepsilon^\alpha} = \varnothing$. Let $\bar{\boldsymbol{\sigma}}$ and $\bar{\varepsilon}^\alpha$ be approximated as per Eqs. 4.13 and 4.14, then the transformations that relate the natural coordinate system to physical space are given as

$$\bar{\boldsymbol{\sigma}} = \boldsymbol{P}\hat{\boldsymbol{\beta}} = \boldsymbol{T}_0\tilde{\boldsymbol{P}}\hat{\boldsymbol{\beta}}, \tag{4.18}$$

$$\bar{\varepsilon}^\alpha = \boldsymbol{G}\hat{\boldsymbol{\alpha}} = \frac{|\,\boldsymbol{J}_0\,|}{|\,\boldsymbol{J}\,|}\boldsymbol{T}_0^{-T}\tilde{\boldsymbol{G}}\hat{\boldsymbol{\alpha}}, \tag{4.19}$$

where $\tilde{\boldsymbol{P}}$ and $\tilde{\boldsymbol{G}}$ are the stress and strain interpolation matrix defined in the natural coordinate system, the Jacobian $\boldsymbol{J}$ relates the physical and natural coordinate system, whereas $\boldsymbol{J}_0$ is the Jacobian evaluated at the element center. The transformation matrix, $\boldsymbol{T}_0$, connects the matrices $\tilde{\boldsymbol{P}}$ and $\tilde{\boldsymbol{G}}$ in the natural space to their corresponding counterparts in the physical space. The matrix $\boldsymbol{T}_0$ is evaluated at the element center in order to pass the requirement of the patch test. The expression for $\boldsymbol{T}_0$ can be found in Eq. 2.24. Finally, by substituting Eq. 4.18 and 4.19 in Eq. 4.17, a following relation for the interpolation matrices can be derived:

$$\int_{\tilde{\mathcal{R}}} \tilde{\boldsymbol{P}}^T\tilde{\boldsymbol{G}} \; \mathrm{d}\tilde{\mathcal{R}} = 0, \tag{4.20}$$

where $\tilde{R}$ represent the domain in natural coordinates.

(b) *Condition on the direct sum of functional spaces:* The condition on the functional spaces of stresses requires that the direct sum of $\mathcal{V}_{\boldsymbol{\sigma}}$ and $\mathcal{V}_{\boldsymbol{\sigma}^\alpha}$ should include $\mathcal{V}_{\boldsymbol{\sigma}^u}$, i.e.,

$$\mathcal{V}_{\boldsymbol{\sigma}^u} \subseteq \mathcal{V}_{\boldsymbol{\sigma}} \oplus \mathcal{V}_{\boldsymbol{\sigma}^\alpha} \tag{4.21}$$

Since $\boldsymbol{C}$ is a positive definite matrix, Eq. 4.21 can be further expressed as

$$\mathcal{V}_{\boldsymbol{\sigma}^u} \subseteq \mathcal{V}_{\boldsymbol{\sigma}} \oplus \mathcal{V}_{\boldsymbol{\varepsilon}^\alpha} \tag{4.22}$$

The above equation, along with the orthogonality condition, implies that for every $\boldsymbol{\sigma}^u \in \mathcal{V}_{\boldsymbol{\sigma}^u}$ there exists a unique $\boldsymbol{\sigma} \in \mathcal{V}_{\boldsymbol{\sigma}}$ and $\boldsymbol{\varepsilon}^\alpha \in \mathcal{V}_{\boldsymbol{\varepsilon}^\alpha}$ such that $\boldsymbol{\sigma}^u = \boldsymbol{\sigma} - \boldsymbol{C}\boldsymbol{\varepsilon}^\alpha$.

4.3 Exploring orthogonality to derive a stable and robust function space for EAS

In this section, a systematic approach is introduced to determine the space of interpolation functions for approximating $\bar{\boldsymbol{\varepsilon}}^\alpha$ for deriving a locking-free and stable EAS element. The methodology is based on the orthogonality of $\bar{\boldsymbol{\sigma}}$ and $\bar{\boldsymbol{\varepsilon}}^\alpha$ as stated in Eq. 4.17 which must hold for any pair of $(\bar{\boldsymbol{\sigma}}, \bar{\boldsymbol{\varepsilon}}^\alpha) \in (\mathcal{V}_{\boldsymbol{\sigma}} \times \mathcal{V}_{\boldsymbol{\varepsilon}^\alpha})$. To ensure this, let's revisit the Eq. 4.17 and express it in the following manner:

$$\int_{\mathcal{R}} \bar{\boldsymbol{\sigma}}^T \bar{\boldsymbol{\varepsilon}}^\alpha \; \mathrm{d}\mathcal{R} = 0 \rightarrow \int_{\mathcal{R}} \boldsymbol{P}^T \bar{\boldsymbol{\varepsilon}}^\alpha \; \mathrm{d}\mathcal{R} = 0, \tag{4.23}$$

where $\boldsymbol{P}$ denotes the interpolation matrix of the stress field $\bar{\boldsymbol{\sigma}}$ in stress-based hybrid elements. The choice of $\boldsymbol{P}$ is taken from the stress-based hybrid elements introduced in [141, 142] due to their proven efficiency, robustness, and extensive testing in a wide range of applications. Note that the present work utilized matrix $\boldsymbol{T}_0$ while in [141, 142] the transformation matrix has been calculated at each Gauss point. In these elements, the interpolation of each component of the stress is independent of each other, thus giving rise to the following block structure of $\boldsymbol{P}$:

$$\boldsymbol{P} = \boldsymbol{T}_0 \tilde{\boldsymbol{P}} = \boldsymbol{T}_0 \begin{bmatrix} \tilde{\boldsymbol{P}}_L & \tilde{\boldsymbol{P}}_H \end{bmatrix} = \boldsymbol{T}_0 \begin{bmatrix} \tilde{\boldsymbol{P}}_1 & \mathbf{0}_b & \mathbf{0}_c & \mathbf{0}_d & \mathbf{0}_e & \mathbf{0}_f \\ \mathbf{0}_a & \tilde{\boldsymbol{P}}_2 & \mathbf{0}_c & \mathbf{0}_d & \mathbf{0}_e & \mathbf{0}_f \\ \mathbf{0}_a & \mathbf{0}_b & \tilde{\boldsymbol{P}}_3 & \mathbf{0}_d & \mathbf{0}_e & \mathbf{0}_f \\ \mathbf{0}_a & \mathbf{0}_b & \mathbf{0}_c & \tilde{\boldsymbol{P}}_4 & \mathbf{0}_e & \mathbf{0}_f \\ \mathbf{0}_a & \mathbf{0}_b & \mathbf{0}_c & \mathbf{0}_d & \tilde{\boldsymbol{P}}_5 & \mathbf{0}_f \\ \mathbf{0}_a & \mathbf{0}_b & \mathbf{0}_c & \mathbf{0}_d & \mathbf{0}_e & \tilde{\boldsymbol{P}}_6 \end{bmatrix}, \tag{4.24}$$

where $\tilde{\boldsymbol{P}}_L$ and $\tilde{\boldsymbol{P}}_H$ denote the lower and higher-order stress interpolation matrices, respectively. The vector $\tilde{\boldsymbol{P}}_i$ represents the set of stress interpolation functions, which includes a total of n_i functions. Additionally, the vectors $\mathbf{0}_a$, $\mathbf{0}_b$, …, $\mathbf{0}_f$ are zero vectors of size n_1, n_2, …, n_6, respectively. The block nature of the $\tilde{\boldsymbol{P}}$ matrix implies that the orthogonality condition can be restated as follow:

$$\int_{\mathcal{R}} \boldsymbol{P}_i^T \bar{\varepsilon}_i^\alpha \; \mathrm{d}\mathcal{R} = \mathbf{0} \qquad \left(i = 1\ ,\ 2, \ldots, 6.\ \text{no summation over `}i\text{'} \right), \tag{4.25}$$

where $\boldsymbol{P}_i = \boldsymbol{T}_0\tilde{\boldsymbol{P}}_i$. Here, $\tilde{\boldsymbol{P}}_i$ refers to the vectors $\tilde{\boldsymbol{P}}_1$, $\tilde{\boldsymbol{P}}_2$, …, $\tilde{\boldsymbol{P}}_6$ and the corresponding $\bar{\varepsilon}_i^\alpha$ is the i^{th} component of a vector $\bar{\boldsymbol{\varepsilon}}^\alpha$, where $\bar{\boldsymbol{\varepsilon}}^\alpha$ can be expressed as $\bar{\boldsymbol{\varepsilon}}^\alpha = \begin{bmatrix}\bar{\varepsilon}_1^\alpha = \bar{\varepsilon}_{xx}^\alpha & \bar{\varepsilon}_2^\alpha = \bar{\varepsilon}_{yy}^\alpha & \bar{\varepsilon}_3^\alpha = \bar{\varepsilon}_{zz}^\alpha & \bar{\varepsilon}_4^\alpha = \bar{\varepsilon}_{xy}^\alpha & \bar{\varepsilon}_5^\alpha = \bar{\varepsilon}_{yz}^\alpha & \bar{\varepsilon}_6^\alpha = \bar{\varepsilon}_{xz}^\alpha\end{bmatrix}^T$. For interpolation of $\bar{\boldsymbol{\varepsilon}}^\alpha$, we similarly assume that all the enhanced strain components are independently interpolated from each other. To put it another way, there are no shared strain parameters between the enhanced strain components. Thus, the strain interpolation matrix also has the block form and is given by the following expression:

$$\bar{\boldsymbol{\varepsilon}}^\alpha = \frac{|\boldsymbol{J}_0|}{|\boldsymbol{J}|}\boldsymbol{T}_0^{-T}\tilde{\boldsymbol{G}}\hat{\boldsymbol{\alpha}}, \text{ such that } \tilde{\boldsymbol{G}} = \begin{bmatrix} \tilde{\boldsymbol{G}}_1 & \mathbf{0}_{b*} & \mathbf{0}_{c*} & \mathbf{0}_{d*} & \mathbf{0}_{e*} & \mathbf{0}_{f*} \\ \mathbf{0}_{a*} & \tilde{\boldsymbol{G}}_2 & \mathbf{0}_{c*} & \mathbf{0}_{d*} & \mathbf{0}_{e*} & \mathbf{0}_{f*} \\ \mathbf{0}_{a*} & \mathbf{0}_{b*} & \tilde{\boldsymbol{G}}_3 & \mathbf{0}_{d*} & \mathbf{0}_{e*} & \mathbf{0}_{f*} \\ \mathbf{0}_{a*} & \mathbf{0}_{b*} & \mathbf{0}_{c*} & \tilde{\boldsymbol{G}}_4 & \mathbf{0}_{e*} & \mathbf{0}_{f*} \\ \mathbf{0}_{a*} & \mathbf{0}_{b*} & \mathbf{0}_{c*} & \mathbf{0}_{d*} & \tilde{\boldsymbol{G}}_5 & \mathbf{0}_{f*} \\ \mathbf{0}_{a*} & \mathbf{0}_{b*} & \mathbf{0}_{c*} & \mathbf{0}_{d*} & \mathbf{0}_{e*} & \tilde{\boldsymbol{G}}_6 \end{bmatrix} \text{ and } \hat{\boldsymbol{\alpha}} = \begin{Bmatrix} \hat{\boldsymbol{\alpha}}^1 \\ \hat{\boldsymbol{\alpha}}^2 \\ \hat{\boldsymbol{\alpha}}^3 \\ \hat{\boldsymbol{\alpha}}^4 \\ \hat{\boldsymbol{\alpha}}^5 \\ \hat{\boldsymbol{\alpha}}^6 \end{Bmatrix},$$

where $\tilde{\boldsymbol{G}}_i$ is the set of m_i strain interpolation functions in natural coordinates. The vectors $\mathbf{0}_{a*}$, $\mathbf{0}_{b*}$, …, $\mathbf{0}_{f*}$ are zero vectors of size m_1, m_2, …, m_6, respectively.

Furthermore, it is assumed that the function space of components of the $\tilde{\boldsymbol{G}}$, i.e., $\mathcal{V}_{\tilde{\boldsymbol{G}}_i}$, is defined in the following manner:

$$\mathcal{V}_{\tilde{\boldsymbol{G}}_i} = \left\{ \tilde{\boldsymbol{\phi}} \cdot \boldsymbol{a} \;:\; \int_{\tilde{\mathcal{R}}} \tilde{\boldsymbol{P}}_i^T \tilde{\boldsymbol{\phi}} \cdot \boldsymbol{a} \; \mathrm{d}\tilde{\mathcal{R}} = \mathbf{0} \right\}. \tag{4.26}$$

Here, $\tilde{\boldsymbol{\phi}}$ represents a set of functions in the natural coordinate system, and $\boldsymbol{a}$ corresponds to a vector of constants. The constraint on $\tilde{\boldsymbol{\phi}} \cdot \boldsymbol{a}$ arises from the orthogonality condition stated in Eq. 4.25. The functions in $\tilde{\boldsymbol{\phi}}$ are chosen in such a way that the second condition of the equivalence, as described in Eq. 4.22, can be met, particularly in the case of constant Jacobian. The most straightforward way to do so is to take all the interpolation functions that are part of displacement interpolation. For instance, in an eight-node brick element, $\tilde{\boldsymbol{\phi}}$ consists of all the trilinear polynomial functions in ξ, η, and ζ. After determining the suitable $\tilde{\boldsymbol{\phi}}$, Eq. 4.26 leads to the following system of linear equations:

$$\int_{\tilde{\mathcal{R}}} \tilde{\boldsymbol{P}}_i^T \left[\sum_{k=1}^{r} a_k \phi_k(\xi, \eta, \zeta) \right] \mathrm{d}\tilde{\mathcal{R}} = \mathbf{0}. \tag{4.27}$$

The above equation indicates that the assumed $\tilde{\boldsymbol{\phi}} \cdot \boldsymbol{a}$ should be orthogonal to every component of $\tilde{\boldsymbol{P}}_i$, and each equation in the system of linear equation represents the fulfillment of this condition. The above expression can be written in a concise form and subsequently solved for the vector $\boldsymbol{a}$ as follows:

$$\bar{\boldsymbol{A}}\boldsymbol{a} = \mathbf{0}, \tag{4.28}$$

where $\bar{\boldsymbol{A}}$ is the matrix of the coefficients of a_k after performing the integration over the domain $\tilde{\mathcal{R}}$. Every feasible vector in the null space of $\bar{\boldsymbol{A}}$ is an acceptable solution for $\boldsymbol{a}$. Let $\boldsymbol{a}^j$ be the basis of the null space of $\bar{\boldsymbol{A}}$ and the dimension of the null space is n_A. Then, the expression for $\tilde{\boldsymbol{G}}_i$, which serves as an approximation of the enhanced strain field, can be written in the following form:

$$\tilde{\boldsymbol{G}}_i = \begin{bmatrix} \boldsymbol{a}^1 \cdot \tilde{\boldsymbol{\phi}} & \boldsymbol{a}^2 \cdot \tilde{\boldsymbol{\phi}} & \ldots & \boldsymbol{a}^{n_A} \cdot \tilde{\boldsymbol{\phi}} \end{bmatrix} \tag{4.29}$$

By following the above-mentioned methodology, enhanced strain interpolation functions can be obtained for any arbitrary element. Furthermore, this methodology can be extended to derive a range of EAS elements, such as the proposed twenty-seven node brick, six-node wedge, and eighteen-node wedge EAS elements, in addition to the existing EAS elements. Several benchmark problems are solved in Section 4.4 to showcase the efficacy and robustness of the proposed EAS elements, confirming their superior coarse mesh accuracy over conventional elements.

4.3.1 Evaluation of strain interpolation matrix for a twenty-seven node quadratic element

In the present section, a systematic derivation of the admissible space for the strain interpolation functions for a three-dimensional twenty-seven node quadratic element is presented to better comprehend the evaluation of the $\tilde{\boldsymbol{G}}$ matrix in the proposed EAS elements. To the best of the author's knowledge, this is the first attempt in the literature to obtain enhanced strain modes for 3D quadratic elements. To obtain the strain interpolation functions for defining $\bar{\boldsymbol{\varepsilon}}^{\alpha}$, the process initiates by stating the $\tilde{\boldsymbol{P}}(\xi, \eta, \zeta)$ matrix. The expression of $\tilde{\boldsymbol{P}}(\xi, \eta, \zeta)$, as given in [142], for a twenty-seven node element can be written as follows:

$$\begin{Bmatrix} \sigma_{\xi\xi} \\ \sigma_{\eta\eta} \\ \sigma_{\zeta\zeta} \\ \sigma_{\xi\eta} \\ \sigma_{\eta\zeta} \\ \sigma_{\xi\zeta} \end{Bmatrix} = \begin{bmatrix} \tilde{\boldsymbol{P}}_1 & \mathbf{0}_a & \mathbf{0}_a & \mathbf{0}_b & \mathbf{0}_b & \mathbf{0}_b \\ \mathbf{0}_a & \tilde{\boldsymbol{P}}_2 & \mathbf{0}_a & \mathbf{0}_b & \mathbf{0}_b & \mathbf{0}_b \\ \mathbf{0}_a & \mathbf{0}_a & \tilde{\boldsymbol{P}}_3 & \mathbf{0}_b & \mathbf{0}_b & \mathbf{0}_b \\ \mathbf{0}_a & \mathbf{0}_a & \mathbf{0}_a & \tilde{\boldsymbol{P}}_4 & \mathbf{0}_b & \mathbf{0}_b \\ \mathbf{0}_a & \mathbf{0}_a & \mathbf{0}_a & \mathbf{0}_b & \tilde{\boldsymbol{P}}_5 & \mathbf{0}_b \\ \mathbf{0}_a & \mathbf{0}_a & \mathbf{0}_a & \mathbf{0}_b & \mathbf{0}_b & \tilde{\boldsymbol{P}}_6 \end{bmatrix} \begin{Bmatrix} \hat{\beta}_1 \\ \hat{\beta}_2 \\ \hat{\beta}_3 \\ \hat{\beta}_4 \\ \vdots \\ \hat{\beta}_{90} \end{Bmatrix} = \tilde{\boldsymbol{P}}(\xi, \eta, \zeta)\hat{\boldsymbol{\beta}}, \tag{4.30}$$

where $\hat{\boldsymbol{\beta}}$ is the vector of stress parameters and $\mathbf{0}_a$ and $\mathbf{0}_b$ denotes the zero vectors with dimensions 1 × 18 and 1 × 12, respectively. The vectors $\tilde{\boldsymbol{P}}_1, \tilde{\boldsymbol{P}}_2, \ldots, \tilde{\boldsymbol{P}}_6$ are expressed as:

$$\tilde{\boldsymbol{P}}_1 = \begin{bmatrix} 1 & \zeta & \zeta^2 & \eta & \zeta\eta & \zeta^2\eta & \eta^2 & \zeta\eta^2 & \zeta^2\eta^2 & \xi & \zeta\xi & \zeta^2\xi & \eta\xi & \zeta\eta\xi & \zeta^2\eta\xi & \eta^2\xi & \zeta\eta^2\xi & \zeta^2\eta^2\xi \end{bmatrix},$$
$$\tilde{\boldsymbol{P}}_2 = \begin{bmatrix} 1 & \zeta & \zeta^2 & \eta & \zeta\eta & \zeta^2\eta & \xi & \zeta\xi & \zeta^2\xi & \eta\xi & \zeta\eta\xi & \zeta^2\eta\xi & \xi^2 & \zeta\xi^2 & \zeta^2\xi^2 & \eta\xi^2 & \zeta\eta\xi^2 & \zeta^2\eta\xi^2 \end{bmatrix},$$

$$\begin{aligned}
\tilde{\boldsymbol{P}}_3 &= \begin{bmatrix}1 & \zeta & \eta & \zeta\eta & \eta^2 & \zeta\eta^2 & \xi & \zeta\xi & \eta\xi & \zeta\eta\xi & \eta^2\xi & \zeta\eta^2\xi & \xi^2 & \zeta\xi^2 & \eta\xi^2 & \zeta\eta\xi^2 & \eta^2\xi^2 & \zeta\eta^2\xi^2\end{bmatrix},\\
\tilde{\boldsymbol{P}}_4 &= \begin{bmatrix}1 & \eta & \zeta & \xi & \xi\eta & \xi\zeta & \zeta^2 & \eta\zeta & \xi\eta\zeta & \zeta^2\eta & \zeta^2\xi & \xi\eta\zeta^2\end{bmatrix},\\
\tilde{\boldsymbol{P}}_5 &= \begin{bmatrix}1 & \xi & \zeta & \eta & \xi^2 & \xi\eta & \eta\zeta & \xi\zeta & \xi^2\zeta & \xi\eta\zeta & \xi^2\eta & \xi^2\eta\zeta\end{bmatrix},\\
\tilde{\boldsymbol{P}}_6 &= \begin{bmatrix}1 & \eta & \zeta & \xi & \xi\eta & \xi\zeta & \eta^2 & \eta\zeta & \xi\eta\zeta & \eta^2\zeta & \eta^2\xi & \xi\eta^2\zeta\end{bmatrix}.
\end{aligned}$$

Assuming that the required $\tilde{\boldsymbol{G}}$ is in the form of Eq. 4.3, the next step is to evaluate the unknown sets of strain interpolation functions, i.e., $\tilde{\boldsymbol{G}}_i$. This is achieved by selecting the appropriate $\tilde{\boldsymbol{\phi}}$ that defines the components of the enhanced strain field in the natural coordinate system. The optimal choice of $\tilde{\boldsymbol{\phi}}$ is a set of functions that contains all the modes in $\boldsymbol{u}$ in order to satisfy the second condition for equivalence stated in Eq. 4.22. This results in the collection of functions that define a full quadratic polynomial in ξ, η and ζ such that

$$\begin{aligned}
\tilde{\boldsymbol{\phi}} = \Big[\, & 1 \;\; \zeta \;\; \zeta^2 \;\; \eta \;\; \eta\zeta \;\; \eta\zeta^2 \;\; \eta^2 \;\; \eta^2\zeta \;\; \eta^2\zeta^2 \;\; \xi \;\; \xi\zeta \;\; \xi\zeta^2 \;\; \xi\eta \;\; \xi\eta\zeta \;\; \xi\eta\zeta^2 \;\; \xi\eta^2 \\
& \xi\eta^2\zeta \;\; \xi\eta^2\zeta^2 \;\; \xi^2 \;\; \xi^2\zeta \;\; \xi^2\zeta^2 \;\; \xi^2\eta \;\; \xi^2\eta\zeta \;\; \xi^2\eta\zeta^2 \;\; \xi^2\eta^2 \;\; \xi^2\eta^2\zeta \;\; \xi^2\eta^2\zeta^2 \,\Big].
\end{aligned} \tag{4.31}$$

After selecting the suitable $\tilde{\boldsymbol{\phi}}$ and substituting it into Eq. 4.27, a system of linear equations can be formed for each individual enhanced strain component. To illustrate the procedure, the evaluation of the strain interpolation function for $\bar{\varepsilon}^{\alpha}_{\xi\xi}$ is explained in detail. Following the relation expressed in Eq. 4.27, let us assume that the $\mathcal{V}_{\tilde{\boldsymbol{G}}_1}$ is the function space of $\tilde{\boldsymbol{G}}_1$ such that $\int_{\tilde{\mathcal{R}}} \tilde{\boldsymbol{P}}_1^T \tilde{\boldsymbol{\phi}} \cdot \boldsymbol{a} \; \mathrm{d}\tilde{\mathcal{R}} = \boldsymbol{0}$. This orthogonality condition leads to the following linear system:

$$\bar{\boldsymbol{A}}\boldsymbol{a} = \boldsymbol{0}. \tag{4.32}$$

The above set of linear equations is solved for $\boldsymbol{a}$, where the feasible solutions for $\boldsymbol{a}$ are vectors that lie in the null space of $\bar{\boldsymbol{A}}$. The null space dimension n_A for Eq. 4.32 is nine, and the basis vectors $\boldsymbol{a}^j$ for the null space are evaluated as follows:

$$\begin{aligned}
\boldsymbol{a}^1 &= \begin{bmatrix}0 & 0 & 0 & 0 & 0 & 0 & 0 & 0 & -\tfrac{1}{3} & 0 & 0 & 0 & 0 & 0 & 0 & 0 & 0 & 0 & 0 & 0 & 0 & 0 & 0 & 0 & 0 & 0 & 1\end{bmatrix}^T,\\
\boldsymbol{a}^2 &= \begin{bmatrix}0 & 0 & 0 & 0 & 0 & 0 & 0 & -\tfrac{1}{3} & 0 & 0 & 0 & 0 & 0 & 0 & 0 & 0 & 0 & 0 & 0 & 0 & 0 & 0 & 0 & 0 & 0 & 1 & 0\end{bmatrix}^T,\\
\boldsymbol{a}^3 &= \begin{bmatrix}0 & 0 & 0 & 0 & 0 & 0 & -\tfrac{1}{3} & 0 & 0 & 0 & 0 & 0 & 0 & 0 & 0 & 0 & 0 & 0 & 0 & 0 & 0 & 0 & 0 & 0 & 1 & 0 & 0\end{bmatrix}^T,\\
\boldsymbol{a}^4 &= \begin{bmatrix}0 & 0 & 0 & 0 & 0 & -\tfrac{1}{3} & 0 & 0 & 0 & 0 & 0 & 0 & 0 & 0 & 0 & 0 & 0 & 0 & 0 & 0 & 0 & 0 & 0 & 1 & 0 & 0 & 0\end{bmatrix}^T,\\
\boldsymbol{a}^5 &= \begin{bmatrix}0 & 0 & 0 & 0 & -\tfrac{1}{3} & 0 & 0 & 0 & 0 & 0 & 0 & 0 & 0 & 0 & 0 & 0 & 0 & 0 & 0 & 0 & 0 & 0 & 1 & 0 & 0 & 0 & 0\end{bmatrix}^T,\\
\boldsymbol{a}^6 &= \begin{bmatrix}0 & 0 & 0 & -\tfrac{1}{3} & 0 & 0 & 0 & 0 & 0 & 0 & 0 & 0 & 0 & 0 & 0 & 0 & 0 & 0 & 0 & 0 & 0 & 1 & 0 & 0 & 0 & 0 & 0\end{bmatrix}^T,\\
\boldsymbol{a}^7 &= \begin{bmatrix}0 & 0 & -\tfrac{1}{3} & 0 & 0 & 0 & 0 & 0 & 0 & 0 & 0 & 0 & 0 & 0 & 0 & 0 & 0 & 0 & 0 & 0 & 1 & 0 & 0 & 0 & 0 & 0 & 0\end{bmatrix}^T,
\end{aligned}$$

$$
\begin{aligned}
\boldsymbol{a}^8 &= \begin{bmatrix}0 & -\frac{1}{3} & 0 & 0 & 0 & 0 & 0 & 0 & 0 & 0 & 0 & 0 & 0 & 0 & 0 & 0 & 0 & 0 & 0 & 1 & 0 & 0 & 0 & 0 & 0 & 0 & 0\end{bmatrix}^T, \\
\boldsymbol{a}^9 &= \begin{bmatrix}-\frac{1}{3} & 0 & 0 & 0 & 0 & 0 & 0 & 0 & 0 & 0 & 0 & 0 & 0 & 0 & 0 & 0 & 0 & 0 & 1 & 0 & 0 & 0 & 0 & 0 & 0 & 0 & 0\end{bmatrix}^T.
\end{aligned}
$$

Substituting the above null space vectors in the Eq. 4.29 the strain component $\bar{\varepsilon}^{\alpha}_{\xi\xi}$ is given by the following expression:

$$
\bar{\varepsilon}^{\alpha}_{\xi\xi} = \tilde{\boldsymbol{G}}_1 \hat{\boldsymbol{\alpha}}_1,
$$

where

$$
\tilde{\boldsymbol{G}}_1 = \Big[\ \Phi(\xi)\ \ \zeta\Phi(\xi)\ \ \zeta^2\Phi(\xi)\ \ \eta\Phi(\xi)\ \ \zeta\eta\Phi(\xi)\ \ \zeta^2\eta\Phi(\xi)\ \ \eta^2\Phi(\xi)\ \ \zeta\eta^2\Phi(\xi)\ \ \zeta^2\eta^2\Phi(\xi)\ \Big],
$$
$$
\hat{\boldsymbol{\alpha}}_1 = \begin{bmatrix}\hat{\alpha}_1 & \hat{\alpha}_2 & \dots & \hat{\alpha}_9\end{bmatrix}^T, \text{ and } \Phi(\xi) = (1 - 3\xi^2).
$$

A similar approach is adopted to evaluate the participating function space of the rest of $\tilde{\boldsymbol{G}}_i$ vectors. This results in the following $\tilde{\boldsymbol{G}}$ matrix for a three-dimensional twenty-seven node quadratic element:

$$
\begin{Bmatrix}
\bar{\varepsilon}^{\alpha}_{\xi\xi} \\ \bar{\varepsilon}^{\alpha}_{\eta\eta} \\ \bar{\varepsilon}^{\alpha}_{\zeta\zeta} \\ \bar{\varepsilon}^{\alpha}_{\xi\eta} \\ \bar{\varepsilon}^{\alpha}_{\eta\zeta} \\ \bar{\varepsilon}^{\alpha}_{\xi\zeta}
\end{Bmatrix}
= \tilde{\boldsymbol{G}}\hat{\boldsymbol{\alpha}} = \tilde{\boldsymbol{G}}
\begin{Bmatrix}
\hat{\boldsymbol{\alpha}}_1 \\ \hat{\boldsymbol{\alpha}}_2 \\ \hat{\boldsymbol{\alpha}}_3 \\ \hat{\boldsymbol{\alpha}}_4 \\ \hat{\boldsymbol{\alpha}}_5 \\ \hat{\boldsymbol{\alpha}}_6
\end{Bmatrix}
=
\begin{bmatrix}
\tilde{\boldsymbol{G}}_1 & \mathbf{0}_{a^*} & \mathbf{0}_{a^*} & \mathbf{0}_{b^*} & \mathbf{0}_{b^*} & \mathbf{0}_{b^*} \\
\mathbf{0}_{a^*} & \tilde{\boldsymbol{G}}_2 & \mathbf{0}_{a^*} & \mathbf{0}_{b^*} & \mathbf{0}_{b^*} & \mathbf{0}_{b^*} \\
\mathbf{0}_{a^*} & \mathbf{0}_{a^*} & \tilde{\boldsymbol{G}}_3 & \mathbf{0}_{b^*} & \mathbf{0}_{b^*} & \mathbf{0}_{b^*} \\
\mathbf{0}_{a^*} & \mathbf{0}_{a^*} & \mathbf{0}_{a^*} & \tilde{\boldsymbol{G}}_4 & \mathbf{0}_{b^*} & \mathbf{0}_{b^*} \\
\mathbf{0}_{a^*} & \mathbf{0}_{a^*} & \mathbf{0}_{a^*} & \mathbf{0}_{b^*} & \tilde{\boldsymbol{G}}_5 & \mathbf{0}_{b^*} \\
\mathbf{0}_{a^*} & \mathbf{0}_{a^*} & \mathbf{0}_{a^*} & \mathbf{0}_{b^*} & \mathbf{0}_{b^*} & \tilde{\boldsymbol{G}}_6
\end{bmatrix}
\begin{Bmatrix}
\hat{\alpha}_1 \\ \hat{\alpha}_2 \\ \hat{\alpha}_3 \\ \hat{\alpha}_4 \\ \vdots \\ \hat{\alpha}_{72}
\end{Bmatrix}, \tag{4.33}
$$

where $\mathbf{0}_{a^*}$ and $\mathbf{0}_{b^*}$ denotes the zero vectors with dimensions 1×9 and 1×15, respectively. The vectors $\hat{\boldsymbol{\alpha}}_i$ are of size 9×1 for $i = 1$ to 3 and 15×1 for $i = 4$ to 6. The vectors $\tilde{\boldsymbol{G}}_1, \tilde{\boldsymbol{G}}_2, \dots, \tilde{\boldsymbol{G}}_6$ are derived as:

$$
\begin{aligned}
\tilde{\boldsymbol{G}}_1 &= \Big[\ \Phi(\xi)\ \ \zeta\Phi(\xi)\ \ \zeta^2\Phi(\xi)\ \ \eta\Phi(\xi)\ \ \zeta\eta\Phi(\xi)\ \ \zeta^2\eta\Phi(\xi)\ \ \eta^2\Phi(\xi)\ \ \zeta\eta^2\Phi(\xi)\ \ \zeta^2\eta^2\Phi(\xi)\ \Big], \\
\tilde{\boldsymbol{G}}_2 &= \Big[\ \Phi(\eta)\ \ \zeta\Phi(\eta)\ \ \zeta^2\Phi(\eta)\ \ \Phi(\eta)\xi\ \ \zeta\Phi(\eta)\xi\ \ \zeta^2\Phi(\eta)\xi\ \ \Phi(\eta)\xi^2\ \ \zeta\Phi(\eta)\xi^2\ \ \zeta^2\Phi(\eta)\xi^2\ \Big], \\
\tilde{\boldsymbol{G}}_3 &= \Big[\ \Phi(\zeta)\ \ \Phi(\zeta)\eta\ \ \Phi(\zeta)\eta^2\ \ \Phi(\zeta)\xi\ \ \Phi(\zeta)\eta\xi\ \ \Phi(\zeta)\eta^2\xi\ \ \Phi(\zeta)\xi^2\ \ \Phi(\zeta)\eta\xi^2\ \ \Phi(\zeta)\eta^2\xi^2\ \Big], \\
\tilde{\boldsymbol{G}}_4 &= \Big[\ \Phi(\eta)\ \ \zeta\Phi(\eta)\ \ \zeta^2\Phi(\eta)\ \ \Phi(\eta)\xi\ \ \zeta\Phi(\eta)\xi\ \ \zeta^2\Phi(\eta)\xi\ \ \Phi(\xi)\ \ \zeta\Phi(\xi)\ \ \zeta^2\Phi(\xi)\ \ \eta\Phi(\xi) \\
&\qquad \zeta\eta\Phi(\xi)\ \ \zeta^2\eta\Phi(\xi)\ \ \Psi(\xi,\eta)\ \ \zeta\Psi(\xi,\eta)\ \ \zeta^2\Psi(\xi,\eta)\ \Big], \\
\tilde{\boldsymbol{G}}_5 &= \Big[\ \Phi(\zeta)\ \ \Phi(\zeta)\eta\ \ \Phi(\eta)\ \ \zeta\Phi(\eta)\ \ \Psi(\eta,\zeta)\ \ \Phi(\zeta)\xi\ \ \Phi(\zeta)\eta\xi\ \ \Phi(\eta)\xi\ \ \zeta\Phi(\eta)\xi\ \ \Psi(\eta,\zeta)\xi \\
&\qquad \Phi(\zeta)\xi^2\ \ \Phi(\zeta)\eta\xi^2\ \ \Phi(\eta)\xi^2\ \ \zeta\Phi(\eta)\xi^2\ \ \Psi(\eta,\zeta)\xi^2\ \Big], \\
\tilde{\boldsymbol{G}}_6 &= \Big[\ \Phi(\zeta)\ \ \Phi(\zeta)\eta\ \ \Phi(\zeta)\eta^2\ \ \Phi(\zeta)\xi\ \ \Phi(\zeta)\eta\xi\ \ \Phi(\zeta)\eta^2\xi\ \ \Phi(\xi)\ \ \zeta\Phi(\xi)\ \ \Psi(\xi,\zeta)\ \ \eta\Phi(\xi) \\
&\qquad \zeta\eta\Phi(\xi)\ \ \eta\Psi(\xi,\zeta)\ \ \eta^2\Phi(\xi)\ \ \zeta\eta^2\Phi(\xi)\ \ \eta^2\Psi(\xi,\zeta)\ \Big],
\end{aligned}
$$

where $\Phi(x)$ and $\Psi(x, y)$ are given as $\Phi(x) = (1 - 3x^2)$ and $\Psi(x, y) = (9x^2y^2 - 1)$, respectively. As can be seen through this example, the presented methodology is simple and can be readily used to obtain the enhanced strain modes for any arbitrary element.

In addition, the proposed twenty-seven node EAS element satisfies the conditions required to achieve exact equivalence with HR-based elements in the case of a constant Jacobian. To verify this assertion, let us consider a space $\mathcal{V}_{\tilde{\phi}}$, which corresponds to a complete tri-quadratic space in the master coordinate system for the given element. In accordance to the orthogonality condition and under constant Jacobian, the following condition can be formulated:

$$\mathcal{V}_{\boldsymbol{\sigma}} \oplus \mathcal{V}_{\boldsymbol{\varepsilon}^{\alpha}} = \mathcal{V}_{\tilde{\phi}}. \tag{4.34}$$

Furthermore, since $\mathcal{V}_{\tilde{\phi}}$ is chosen as specified in Eq. 4.31 along with $\mathcal{V}_{\tilde{\phi}} \supseteq \mathcal{V}_{\boldsymbol{u}}$, it can be inferred that

$$\mathcal{V}_{\tilde{\phi}} \supseteq \mathcal{V}_{\boldsymbol{\sigma}^{u}}, \tag{4.35}$$

which implies the following relation:

$$\mathcal{V}_{\boldsymbol{\sigma}} \oplus \mathcal{V}_{\boldsymbol{\varepsilon}^{\alpha}} \supseteq \mathcal{V}_{\boldsymbol{\sigma}^{u}}. \tag{4.36}$$

Hence, satisfying the condition on the spaces mentioned in Eq. 4.22. By combining this assertion with the previously established orthogonality of the proposed elements, it is confirmed that exact equivalence with HR-based elements is achieved for a constant Jacobian. This demonstrates that the EAS method performs at par with the thoroughly tested hybrid element and the approach can generate a set of robust and effective EAS elements that will greatly improve the usability of EAS elements in the FEM field.

4.3.2 Strain interpolation matrix for wedge elements

The wedge elements often serve as transition elements or, in some cases, can be used to mesh the whole domain. However, wedge elements that are tailored for the EAS approach has not been proposed in the literature. The present section provides $\tilde{\boldsymbol{G}}$ matrices for six-node and eighteen-node wedge EAS elements, which are developed using the methodology presented in the current manuscript. The $\tilde{\boldsymbol{G}}$ matrix for the six-node wedge element is derived as

$$\begin{Bmatrix} \bar{\varepsilon}^{\alpha}_{\xi\xi} \\ \bar{\varepsilon}^{\alpha}_{\eta\eta} \\ \bar{\varepsilon}^{\alpha}_{\zeta\zeta} \\ \bar{\varepsilon}^{\alpha}_{\xi\eta} \\ \bar{\varepsilon}^{\alpha}_{\eta\zeta} \\ \bar{\varepsilon}^{\alpha}_{\xi\zeta} \end{Bmatrix} = \tilde{\boldsymbol{G}}\hat{\boldsymbol{\alpha}} = \tilde{\boldsymbol{G}} \begin{Bmatrix} \hat{\boldsymbol{\alpha}}_1 \\ \hat{\boldsymbol{\alpha}}_2 \\ \hat{\boldsymbol{\alpha}}_3 \\ \hat{\boldsymbol{\alpha}}_4 \\ \hat{\boldsymbol{\alpha}}_5 \\ \hat{\boldsymbol{\alpha}}_6 \end{Bmatrix} = \begin{bmatrix} \tilde{\boldsymbol{G}}_1 & \boldsymbol{0}_{a^*} & \boldsymbol{0}_{b^*} & \boldsymbol{0}_{a^*} & \boldsymbol{0}_{b^*} & \boldsymbol{0}_{b^*} \\ \boldsymbol{0}_{a^*} & \tilde{\boldsymbol{G}}_2 & \boldsymbol{0}_{b^*} & \boldsymbol{0}_{a^*} & \boldsymbol{0}_{b^*} & \boldsymbol{0}_{b^*} \\ \boldsymbol{0}_{a^*} & \boldsymbol{0}_{a^*} & \tilde{\boldsymbol{G}}_3 & \boldsymbol{0}_{a^*} & \boldsymbol{0}_{b^*} & \boldsymbol{0}_{b^*} \\ \boldsymbol{0}_{a^*} & \boldsymbol{0}_{a^*} & \boldsymbol{0}_{b^*} & \tilde{\boldsymbol{G}}_4 & \boldsymbol{0}_{b^*} & \boldsymbol{0}_{b^*} \\ \boldsymbol{0}_{a^*} & \boldsymbol{0}_{a^*} & \boldsymbol{0}_{b^*} & \boldsymbol{0}_{a^*} & \tilde{\boldsymbol{G}}_5 & \boldsymbol{0}_{b^*} \\ \boldsymbol{0}_{a^*} & \boldsymbol{0}_{a^*} & \boldsymbol{0}_{b^*} & \boldsymbol{0}_{a^*} & \boldsymbol{0}_{b^*} & \tilde{\boldsymbol{G}}_6 \end{bmatrix} \begin{Bmatrix} \hat{\alpha}_1 \\ \hat{\alpha}_2 \\ \hat{\alpha}_3 \\ \hat{\alpha}_4 \\ \vdots \\ \hat{\alpha}_{21} \end{Bmatrix}, \tag{4.37}$$

where $\mathbf{0}_{a^*}$ and $\mathbf{0}_{b^*}$ denotes the zero vectors with dimensions 1×4 and 1×3, respectively. For $i = 1$, 2, and 4, the vectors $\hat{\boldsymbol{\alpha}}_i$ are of size 4×1, while for $i = 3$, 5, and 6, the vectors are of size 3×1. The vectors $\tilde{\boldsymbol{G}}_1, \tilde{\boldsymbol{G}}_2, \ldots, \tilde{\boldsymbol{G}}_6$ are expressed as:

$$\tilde{\boldsymbol{G}}_1 = \tilde{\boldsymbol{G}}_2 = \tilde{\boldsymbol{G}}_4 = \Big[\, (\zeta - 3\xi\zeta) \;\; (\zeta - 3\eta\zeta) \;\; (1 - 3\eta) \;\; (1 - 3\xi) \,\Big],$$
$$\tilde{\boldsymbol{G}}_3 = \tilde{\boldsymbol{G}}_5 = \tilde{\boldsymbol{G}}_6 = \Big[\, \xi\zeta \;\; \eta\zeta \;\; \zeta \,\Big].$$

Similarly, the $\tilde{\boldsymbol{G}}$ for eighteen-node wedge element is derived as

$$\begin{Bmatrix} \bar{\varepsilon}^{\alpha}_{\xi\xi} \\ \bar{\varepsilon}^{\alpha}_{\eta\eta} \\ \bar{\varepsilon}^{\alpha}_{\zeta\zeta} \\ \bar{\varepsilon}^{\alpha}_{\xi\eta} \\ \bar{\varepsilon}^{\alpha}_{\eta\zeta} \\ \bar{\varepsilon}^{\alpha}_{\xi\zeta} \end{Bmatrix} = \tilde{\boldsymbol{G}}\hat{\boldsymbol{\alpha}} = \tilde{\boldsymbol{G}} \begin{Bmatrix} \hat{\boldsymbol{\alpha}}_1 \\ \hat{\boldsymbol{\alpha}}_2 \\ \hat{\boldsymbol{\alpha}}_3 \\ \hat{\boldsymbol{\alpha}}_4 \\ \hat{\boldsymbol{\alpha}}_5 \\ \hat{\boldsymbol{\alpha}}_6 \end{Bmatrix} = \begin{bmatrix} \tilde{\boldsymbol{G}}_1 & \mathbf{0}_{a^*} & \mathbf{0}_{b^*} & \mathbf{0}_{a^*} & \mathbf{0}_{c^*} & \mathbf{0}_{c^*} \\ \mathbf{0}_{a^*} & \tilde{\boldsymbol{G}}_2 & \mathbf{0}_{b^*} & \mathbf{0}_{a^*} & \mathbf{0}_{c^*} & \mathbf{0}_{c^*} \\ \mathbf{0}_{a^*} & \mathbf{0}_{a^*} & \tilde{\boldsymbol{G}}_3 & \mathbf{0}_{a^*} & \mathbf{0}_{c^*} & \mathbf{0}_{c^*} \\ \mathbf{0}_{a^*} & \mathbf{0}_{a^*} & \mathbf{0}_{b^*} & \tilde{\boldsymbol{G}}_4 & \mathbf{0}_{c^*} & \mathbf{0}_{c^*} \\ \mathbf{0}_{a^*} & \mathbf{0}_{a^*} & \mathbf{0}_{b^*} & \mathbf{0}_{a^*} & \tilde{\boldsymbol{G}}_5 & \mathbf{0}_{c^*} \\ \mathbf{0}_{a^*} & \mathbf{0}_{a^*} & \mathbf{0}_{b^*} & \mathbf{0}_{a^*} & \mathbf{0}_{c^*} & \tilde{\boldsymbol{G}}_6 \end{bmatrix} \begin{Bmatrix} \hat{\alpha}_1 \\ \hat{\alpha}_2 \\ \hat{\alpha}_3 \\ \hat{\alpha}_4 \\ \vdots \\ \hat{\alpha}_{57} \end{Bmatrix}, \tag{4.38}$$

where $\mathbf{0}_{a^*}$, $\mathbf{0}_{b^*}$ and $\mathbf{0}_{c^*}$ denotes the zero vectors with dimensions 1×9, 1×6 and 1×12, respectively. For $i = 1$, 2, and 4, the vectors $\hat{\boldsymbol{\alpha}}_i$ are of size 9×1. The dimensions of $\hat{\boldsymbol{\alpha}}_3$ are 6×1, while for $i = 5$ and 6, the vectors are of size 12×1. The vectors $\tilde{\boldsymbol{G}}_1, \tilde{\boldsymbol{G}}_2, \ldots, \tilde{\boldsymbol{G}}_6$ are expressed as:

$$\begin{aligned} \tilde{\boldsymbol{G}}_1 = \tilde{\boldsymbol{G}}_2 = \tilde{\boldsymbol{G}}_4 = \Big[\, & (\zeta - 8\xi\zeta + 10\xi^2\zeta) \;\; (\zeta^2 - 8\xi\zeta^2 + 10\xi^2\zeta^2) \;\; (10\xi^2 + 8\eta - 40\xi\eta - 1) \\ & (5\xi^2\zeta - 2\xi\zeta + 2\eta\zeta - 10\xi\eta\zeta) \;\; (5\xi^2\zeta^2 - 2\xi\zeta^2 + 2\eta\zeta^2 - 10\xi\eta\zeta^2) \;\; (\xi^2 - 4\xi\eta + \eta^2) \\ & (\xi^2\zeta - 4\xi\eta\zeta + \eta^2\zeta) \;\; (\xi^2\zeta^2 - 4\xi\eta\zeta^2 + \eta^2\zeta^2) \;\; (-1 + 8\xi - 10\xi^2) \,\Big], \\ \tilde{\boldsymbol{G}}_3 = \Big[\, & (3\zeta^2 - 1) \;\; (\eta - 3\eta\zeta^2) \;\; (\eta^2 - 3\eta^2\zeta^2) \;\; (\xi - 3\xi\zeta^2) \;\; (\xi\eta - 3\xi\eta\zeta^2) \;\; (\xi^2 - 3\xi^2\zeta^2) \,\Big], \\ \tilde{\boldsymbol{G}}_5 = \tilde{\boldsymbol{G}}_6 = \Big[\, & (\zeta - 8\xi\zeta + 10\xi^2\zeta) \;\; (-1 + 24\xi\zeta^2 - 30\xi^2\zeta^2) \;\; (\xi\eta - 3\xi\eta\zeta^2) \;\; (\xi^2 - 3\xi^2\zeta^2) \\ & (-1 + 3\zeta^2) \;\; (-1 + 8\eta + 30\xi^2\zeta^2 - 120\xi\eta\zeta^2) \;\; (-2\xi\zeta + 5\xi^2\zeta + 2\eta\zeta - 10\xi\eta\zeta) \\ & (-1 + 30\xi^2\zeta^2 + 24\eta\zeta^2 - 120\xi\eta\zeta^2) \;\; (\eta^2 + 3\xi^2\zeta^2 - 12\xi\eta\zeta^2) \;\; (\xi^2\zeta - 4\xi\eta\zeta + \eta^2\zeta) \\ & (\xi^2\zeta^2 - 4\xi\eta\zeta^2 + \eta^2\zeta^2) \;\; (-1 + 8\xi - 30\xi^2\zeta^2) \,\Big]. \end{aligned}$$

By construction, the proposed six-node and eighteen-node wedge EAS elements satisfy the orthogonality of $\bar{\boldsymbol{\sigma}}$ and $\bar{\boldsymbol{\varepsilon}}^{\alpha}$ as described in Eq. 4.17. and follows similar relationships of their respective spaces as mentioned in Eqs. 4.34-4.36. As a result, the wedge EAS elements too attain exact equivalence with HR-based elements. In addition to the above elements, various other EAS elements can be derived utilizing a similar methodology. For completeness, the derived $\tilde{\boldsymbol{G}}$ matrix for some of the popular elements is presented in subsequent section. However, the resulting $\tilde{\boldsymbol{G}}$ matrix for these elements comes out to be identical to the ones that already exist in the literature (Section 2.3.2) and are well-tested on numerous benchmark problems.

4.3.3 Strain interpolation functions for existing EAS elements in the same framework

The systematic approach presented in the study can also be adapted to derive $\tilde{\boldsymbol{G}}$ matrix for some of the popular elements. It is noteworthy to observe that the process leads to an identical $\tilde{\boldsymbol{G}}$ matrix, which has been explored in a number of previous studies [125, 134, 167, 168]. For instance, the strain $\tilde{\boldsymbol{G}}$ for the two-dimensional four-node linear element is derived as

$$\tilde{\boldsymbol{G}}(\xi,\eta) = \begin{bmatrix} \xi & 0 & 0 & 0 & \xi\eta & 0 & 0 \\ 0 & \eta & 0 & 0 & 0 & \xi\eta & 0 \\ 0 & 0 & \xi & \eta & 0 & 0 & \xi\eta \end{bmatrix}. \tag{4.39}$$

There are different options for selecting the $\tilde{\boldsymbol{G}}$ matrix for a four-node quadrilateral element. Among them, the most effective $\tilde{\boldsymbol{G}}$ is the one presented in Eq. 4.39 [125]. It is possible to use only a subset of the $\tilde{\boldsymbol{G}}$ matrix shown in Eq. 4.39 to alleviate a specific type of locking. Although it reduces the computational cost, it makes an element significantly restricted to the particular problem description.

For a two-dimensional nine-node quadrilateral element, the interpolation matrix for $\bar{\varepsilon}^{\alpha}$ [168] is derived as

$$\tilde{\boldsymbol{G}} = \begin{bmatrix} f(\xi) & \eta f(\xi) & f(\xi)f(\eta) & 0 & 0 & 0 & 0 & 0 & 0 & 0 & 0 \\ 0 & 0 & 0 & f(\eta) & \xi f(\eta) & f(\xi)f(\eta) & 0 & 0 & 0 & 0 & 0 \\ 0 & 0 & 0 & 0 & 0 & 0 & f(\xi) & \eta f(\xi) & f(\eta) & \xi f(\eta) & f(\xi)f(\eta) \end{bmatrix}, \tag{4.40}$$

where $f(\xi) = 3\xi^2 - 1,\ f(\eta) = 3\eta^2 - 1$. Finally, for a 3D eight-node brick element, the admissible $\tilde{\boldsymbol{G}}$ [167] matrix is derived as

$$\tilde{\boldsymbol{G}} = \begin{bmatrix} \tilde{\boldsymbol{G}}_1 & \mathbf{0}_{a^*} & \mathbf{0}_{a^*} & \mathbf{0}_{b^*} & \mathbf{0}_{b^*} & \mathbf{0}_{b^*} \\ \mathbf{0}_{a^*} & \tilde{\boldsymbol{G}}_2 & \mathbf{0}_{a^*} & \mathbf{0}_{b^*} & \mathbf{0}_{b^*} & \mathbf{0}_{b^*} \\ \mathbf{0}_{a^*} & \mathbf{0}_{a^*} & \tilde{\boldsymbol{G}}_3 & \mathbf{0}_{b^*} & \mathbf{0}_{b^*} & \mathbf{0}_{b^*} \\ \mathbf{0}_{a^*} & \mathbf{0}_{a^*} & \mathbf{0}_{a^*} & \tilde{\boldsymbol{G}}_4 & \mathbf{0}_{b^*} & \mathbf{0}_{b^*} \\ \mathbf{0}_{a^*} & \mathbf{0}_{a^*} & \mathbf{0}_{a^*} & \mathbf{0}_{b^*} & \tilde{\boldsymbol{G}}_5 & \mathbf{0}_{b^*} \\ \mathbf{0}_{a^*} & \mathbf{0}_{a^*} & \mathbf{0}_{a^*} & \mathbf{0}_{b^*} & \mathbf{0}_{b^*} & \tilde{\boldsymbol{G}}_6 \end{bmatrix}, \tag{4.41}$$

where $\mathbf{0}_{a^*}$ and $\mathbf{0}_{b^*}$ denotes the zero vectors with dimensions 1×4 and 1×6, respectively. The vectors $\tilde{\boldsymbol{G}}_1, \tilde{\boldsymbol{G}}_2, \ldots, \tilde{\boldsymbol{G}}_6$ are expressed as

$$\tilde{\boldsymbol{G}}_1 = \begin{bmatrix} \xi & \xi\eta & \xi\zeta & \xi\eta\zeta \end{bmatrix}, \quad \tilde{\boldsymbol{G}}_2 = \begin{bmatrix} \eta & \xi\eta & \eta\zeta & \xi\eta\zeta \end{bmatrix}, \quad \tilde{\boldsymbol{G}}_3 = \begin{bmatrix} \zeta & \xi\zeta & \eta\zeta & \xi\eta\zeta \end{bmatrix},$$
$$\tilde{\boldsymbol{G}}_4 = \begin{bmatrix} \xi & \eta & \xi\zeta & \eta\zeta & \xi\eta & \xi\eta\zeta \end{bmatrix}, \quad \tilde{\boldsymbol{G}}_5 = \begin{bmatrix} \eta & \zeta & \xi\eta & \xi\zeta & \eta\zeta & \xi\eta\zeta \end{bmatrix},$$

$$\tilde{\boldsymbol{G}}_6 = \left[\xi \;\; \zeta \;\; \xi\eta \;\; \eta\zeta \;\; \xi\zeta \;\; \xi\eta\zeta \right].$$

Similar to the four-node quadrilateral element, it is possible to use a subset of Eq. 4.41 to reduce the computational efforts. The choice of the subset is governed by the problem description and the type of locking. However, the presented approach leads to the full $\tilde{\boldsymbol{G}}$ matrix rather than a subset, which has been found to be the most robust of them all.

4.3.4 Elemental equations for EAS method

In the preceding section, strain interpolation functions required for approximating $\bar{\boldsymbol{\varepsilon}}^{\alpha}$ for different elements have been derived. To complete the discussion on EAS formulation, the current section briefly summarizes the expression of the stiffness matrix involved in the EAS formulation.

The final variational statement can be express as follows:

$$\begin{bmatrix} \boldsymbol{K}^c & \boldsymbol{M}^T \\ \boldsymbol{M} & \boldsymbol{H} \end{bmatrix} \begin{Bmatrix} \hat{\boldsymbol{u}} \\ \hat{\boldsymbol{\alpha}} \end{Bmatrix} = \begin{Bmatrix} \hat{\boldsymbol{f}} \\ \boldsymbol{0} \end{Bmatrix}, \tag{4.42}$$

where

$$\boldsymbol{K}^c = \int_{\mathcal{R}} \boldsymbol{B}^T \boldsymbol{C} \boldsymbol{B} \, \mathrm{d}\mathcal{R}, \quad \boldsymbol{M} = \int_{\mathcal{R}} \boldsymbol{G}^T \boldsymbol{C} \boldsymbol{B} \, \mathrm{d}\mathcal{R}, \quad \boldsymbol{H} = \int_{\mathcal{R}} \boldsymbol{G}^T \boldsymbol{C} \boldsymbol{G} \, \mathrm{d}\mathcal{R},$$
$$\hat{\boldsymbol{f}} = \int_{\mathcal{R}} \boldsymbol{N}^T \boldsymbol{b} \, \mathrm{d}\mathcal{R} + \int_{\partial\mathcal{R}_t} \boldsymbol{N}^T \bar{\boldsymbol{t}} \, \mathrm{d}A.$$

By calculating the expression for $\hat{\boldsymbol{\alpha}}$ from Eq. 4.42, the above expression reduces to the following relations:

$$\hat{\boldsymbol{\alpha}} = -\boldsymbol{H}^{-1} \boldsymbol{M} \hat{\boldsymbol{u}}, \tag{4.43}$$

$$\underbrace{\left[\boldsymbol{K}^c - \boldsymbol{M}^T \boldsymbol{H}^{-1} \boldsymbol{M} \right]}_{\boldsymbol{K}^{\mathrm{eas}}} \hat{\boldsymbol{u}} = \hat{\boldsymbol{f}} \rightarrow \boldsymbol{K}^{\mathrm{eas}} \hat{\boldsymbol{u}} = \hat{\boldsymbol{f}}, \tag{4.44}$$

where the stiffness matrix for the EAS element can be represented as $\boldsymbol{K}^{\mathrm{eas}} = \left[\boldsymbol{K}^c - \boldsymbol{M}^T \boldsymbol{H}^{-1} \boldsymbol{M} \right]$. The inverse of $\boldsymbol{H}$ can be computed at the element level as the strain interpolations are discontinuous between the elements. Hence, the stiffness matrix of an element can be expressed as follows:

$$\boldsymbol{K}_e^{\mathrm{eas}} = \left[\boldsymbol{K}_e^c - \boldsymbol{M}_e^T \boldsymbol{H}_e^{-1} \boldsymbol{M}_e \right],$$
$$\text{where } \boldsymbol{K}_e^c = \int_{\mathcal{R}_e} \boldsymbol{B}_e^T \boldsymbol{C} \boldsymbol{B}_e \, \mathrm{d}\mathcal{R}_e, \; \boldsymbol{M}_e = \int_{\mathcal{R}_e} \boldsymbol{G}_e^T \boldsymbol{C} \boldsymbol{B}_e \, \mathrm{d}\mathcal{R}_e, \; \boldsymbol{H}_e = \int_{\mathcal{R}_e} \boldsymbol{G}_e^T \boldsymbol{C} \boldsymbol{G}_e \, \mathrm{d}\mathcal{R}_e.$$

The above expressions demonstrate that the additional degrees of freedom are condensed out at the elemental level. Therefore, the EAS formulation is ultimately composed solely of displacement degrees of freedom. After deriving the relevant expressions for the EAS formulation, the next step involves evaluating the performance of the proposed EAS elements. This is achieved through several numerical benchmark examples, which will be presented in the following section.

4.4 Numerical examples

The present section demonstrates the effectiveness of the proposed EAS elements against conventional and existing EAS elements. Several numerical benchmark examples are used to show the coarse mesh accuracy, efficiency, and robustness of the proposed elements. First, it has been shown that the proposed elements successfully pass basic tests, which include the patch test, zero energy mode test, and isotropic element test. In the next two examples, the domain is affected by coupled shear-membrane locking, while in the fourth example, it is significantly influenced by volumetric locking. In the next three examples, the widely studied shell obstacle course problems are presented to demonstrate the robustness of the EAS elements. The computational efficiency of the proposed elements is studied for a clamped square plate, incompressible block, and pinched cylinder problems. The computational time reported in the manuscript is obtained using a serial implementation of the proposed formulation in MATLAB®, employing the vectorized approach [179]. The consistent system of units (SI/FPS) is assumed for all parameters used in numerical simulations. The term ‘reference solution’ refers to either the benchmark values documented in the literature or a result of a highly refined mesh that converged to a known solution at a specific location, available in the literature, using established and previously validated elements. Abbreviations that frequently appear in the subsequent problems are defined in Table 4.1.

4.4.1 Numerical tests

In this section, a comprehensive assessment of the proposed elements is conducted through the patch test, zero energy mode test, and isotropic element test. The performance of these tests affirms that the proposed elements successfully meet the criteria to pass each of these mentioned tests.

4.4.1.1 Patch test

A typical patch test consists of a square block where minimal constraints are imposed to prevent rigid body motions and is subjected to distinct sets of loading at its boundaries to generate a constant state of stress throughout the block [181], see Fig. 4.1. In this test, the elements should be able to predict the constant state of stress with machine precision even after experiencing significant distortion. The square block is meshed using seven α-FE-b27 elements, as shown in Fig. 4.2. The results of the two load cases (Fig. 4.1)

Table 4.1: List of elements abbreviation used in the present study.

Element abbreviation	Description
FE-b8	Conventional 8-node brick element
FE-b27	Conventional 27-node brick element
FE-w6	Conventional 6-node wedge element
FE-w18	Conventional 18-node wedge element
h-FE-b8	8-node hybrid brick element [180]
h-FE-w6	6-node hybrid wedge element [141, 142]
MITC3+	3-node MITC shell element [76, 77]
MITC9	9-node MITC shell element [78]
α-FE-b8	8-node brick EAS element [167]
α-FE-b27	Proposed 27-node brick EAS element
α-FE-w6	Proposed 6-node wedge EAS element
α-FE-w18	Proposed 18-node wedge EAS element
h-FE-b27	27-node hybrid brick element [142]
h-FE-w18	18-node hybrid wedge element [142]
MITC4+	4-node MITC shell element [74, 77]
up-FE-b8	8-node *up* brick element with 1 pressure node [120]

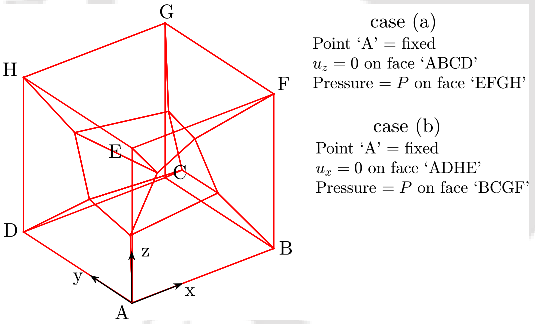

Figure 4.1: A problem definition for a patch test (A cube of unit length, Young's modulus (E) = 2.1×10^6, Poisson's ratio (ν) = 0.3, $P = 2$).

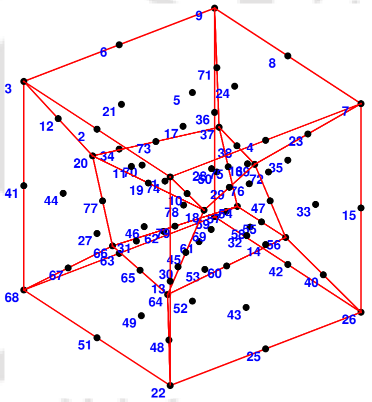

Figure 4.2: A patch of seven α-FE-b27 elements.

are presented in Fig. 4.3. In both cases, the relevant normal stress remains constant throughout the block, while the other stresses are equal to zero with machine precision. This demonstrates that the proposed α-FE-b27 element is successfully passing the patch test. Similar results are observed for wedge elements, affirming that these elements also successfully pass the patch test.

4.4.1.2 Zero energy mode test

The test is carried out by confirming that the single unsupported element should consist of six zero eigenvalues, which corresponds to the six rigid body modes [73]. To demon-

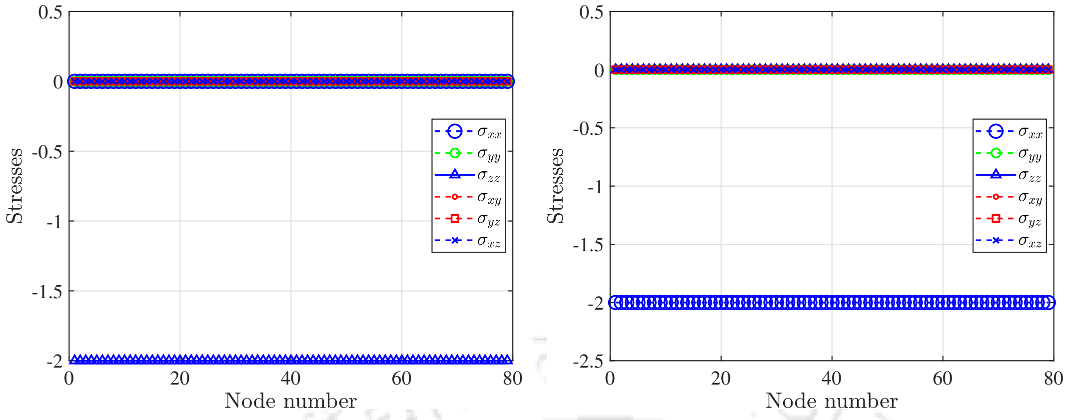

(a) Case (a)

(b) Case (b)

Figure 4.3: Stresses at each node for two different load cases of the patch test.

strate that the proposed elements satisfy this criterion, let's consider a single element such that its physical coordinate system coincides with the natural coordinate system. In this setting, the general representation of the rigid body modes for the three-dimensional space can be expressed as follows:

$$u = \gamma_1;\ v = 0;\ w = 0, \qquad (4.45a) \qquad u = \gamma_4\eta;\ v = -\gamma_4\xi;\ w = 0, \qquad (4.45d)$$

$$u = 0;\ v = \gamma_2;\ w = 0, \qquad (4.45b) \qquad u = 0;\ v = \gamma_5\zeta;\ w = -\gamma_5\eta, \qquad (4.45e)$$

$$u = 0;\ v = 0;\ w = \gamma_3, \qquad (4.45c) \qquad u = \gamma_6\zeta;\ v = 0;\ w = -\gamma_6\xi, \qquad (4.45f)$$

where the values of γ_i are constant. Next, the null space dimension of the stiffness matrix $\boldsymbol{K}^{\text{eas}}$, see Eq. 4.44, is determined for a single unsupported α-FE-b27, α-FE-w6, and α-FE-w18 element. For all three elements, the null space dimension is equal to six. Additionally, the basis for the null space of the stiffness matrices for the proposed elements is evaluated, which results in six independent vectors that define the space for zero-energy modes. Substituting these basis vectors into Eq. 4.12 and performing symbolic calculations yields the following expression for displacement:

$$u = c_1 + c_4\eta + c_6\zeta, \quad v = c_2 - c_4\xi + c_5\zeta, \quad w = c_3 - c_5\eta - c_6\xi, \qquad (4.46)$$

where values of c_i are constant. The above expressions of $\boldsymbol{u}$ represent a linear combination of the general rigid body modes as defined in Eq. 4.45. This confirms that the proposed elements are free from the spurious energy modes.

4.4.1.3 Isotropic element test:

The proposed α-FE-b27 element trivially satisfied the isotropic test since both the element formulation and geometry are perfectly symmetric with respect to the parametric coordinates. However, satisfying the isotropy in the case of the proposed α-FE-w6 and α-FE-w18 wedge element is more complex. Hence, to show compliance with the test, we

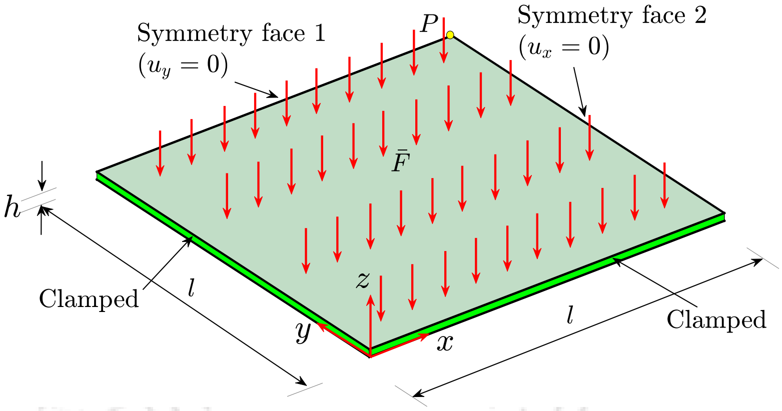

Figure 4.4: Problem geometry and corresponding boundary conditions of a quarter domain of the square plate problem.

have considered a single distorted α-FE-w6 and α-FE-w18 wedge elements, subjecting each of them to a three-dimensional loading condition. We have considered all six possible node numbering sequences while keeping the connectivity constant and have verified that identical results are achieved in each case. Thus, all three proposed elements successfully satisfy the isotropic element test.

4.4.2 Clamped square plate

The present example investigates the response of a three-dimensional solid square plate with a length of $2l$ and thickness h under the influence of locking. The square plate is fixed at its edges and loaded with a uniformly distributed load $\bar{F}$ on its top surface. Due to the symmetrical nature of the problem, only one-quarter of the square plate is analyzed, see Fig. 4.4. To evaluate the effectiveness of the proposed EAS elements, the problem is solved for different slenderness ratios (l/h) that involve situations where locking is a concern. The problem comprises of two l/h ratios, i.e, 100 and 1000, achieved by decreasing h to 0.1 and 0.01, respectively, while keeping the length constant at $2l = 20$. The top surface of the plate is subjected to a load of $\bar{F} = 0.5$ per unit area. The value of Young's modulus E is set as 10^7 and 10^{10} for $l/h = 100$ and $l/h = 1000$, respectively. The Poisson's ratio ν is kept constant at 0.3. The benchmark value of vertical displacement at the center of the plate (u_z^{ref}) is 0.1101 for both $l/h = 100$ and $l/h = 1000$ [64]. The mesh, used to discretize the domain, is defined as $n_{\text{ele}}^x \times n_{\text{ele}}^y \times n_{\text{ele}}^z$, where n_{ele}^x, n_{ele}^y, and n_{ele}^z are the number of elements in x, y, and z direction, respectively. The domain is uniformly meshed in the x-y plane, with $n_{\text{ele}}^x = n_{\text{ele}}^y = 2$, 4, 8, 16, and 32, whereas a single element is considered in the thickness direction.

The plots of vertical displacement of point 'P', normalized against the reference solution for both cases, are shown in Figs. 4.5a and 4.5b. Severe locking is observed in the FE-b8 elements for both cases, and this issue becomes more prominent as l/h ratio increases. The FE-b27 elements converge to the solution with a similar rate of convergence for both $l/h = 100$ and $l/h = 1000$ but with significant refinement. On the

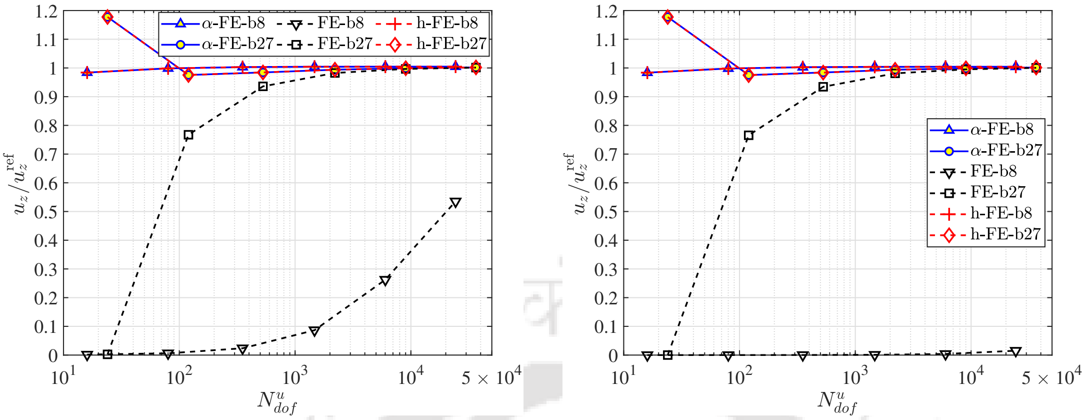

(a) u_z/u_z^{ref} $(l/h = 100)$ **(b)** u_z/u_z^{ref} $(l/h = 1000)$

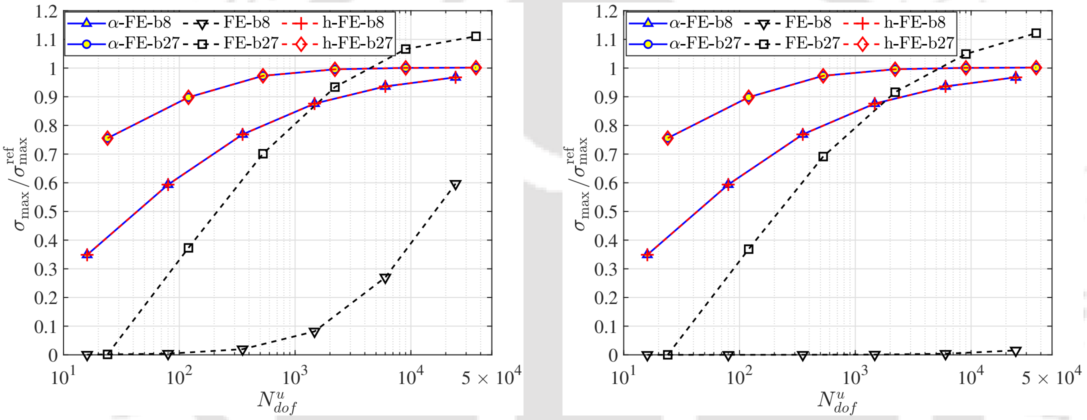

(c) $\sigma_{\max}/\sigma_{\max}^{\text{ref}}$ $(l/h = 100)$ **(d)** $\sigma_{\max}/\sigma_{\max}^{\text{ref}}$ $(l/h = 1000)$

Figure 4.5: Investigation of normalized displacement at the point 'P' and normalized stress at the center of clamped boundary for a clamped square plate problem for different l/h ratios.

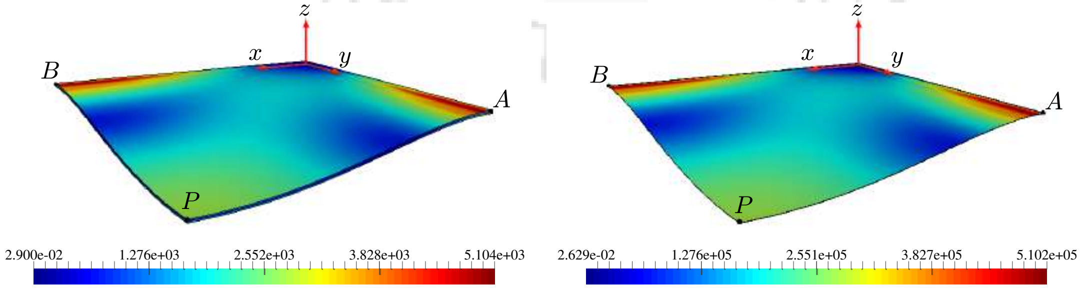

(a) $l/h = 100$, Mesh: $16 \times 16 \times 1$ elements **(b)** $l/h = 1000$, Mesh: $16 \times 16 \times 1$ elements

Figure 4.6: The von Mises stress distribution in the quarter domain of the clamped square plate problem using α-FE-b27 elements for different l/h ratios. (Deformed geometry is scaled with a factor of 15 for better visualization.)

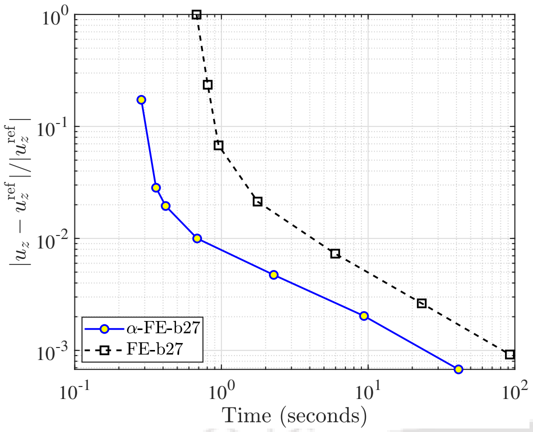

Figure 4.7: Computational efficiency of the proposed α-FE-b27 elements against the conventional FE-b27 elements for a clamped square plate problem with $l/h = 100$.

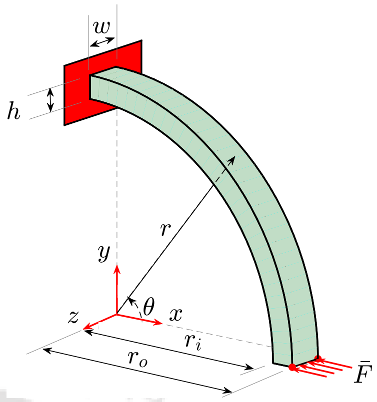

Figure 4.8: Problem geometry and corresponding boundary conditions of a curved cantilever beam.

other hand, the α-FE-b8 and α-FE-b27 elements exhibit favorable convergence rates, regardless of the l/h ratio.

The given problem set-up exhibits the maximum stress at the center of the clamped boundary (Point 'A' or 'B'), denoted by $\sigma_{\text{max}}^{\text{ref}}$. The benchmark values for $\sigma_{\text{max}}^{\text{ref}}$ are 6.1560×10^3 and 6.1560×10^5 for $l/h = 100$ and 1000, respectively. The plots of stress at the center of the clamped boundary, normalized with respect to the reference solution for both cases, are shown in Figs. 4.5c and 4.5d. The FE-b8 elements fail to converge to the solution even with significant refinement and the locking effect becomes prominently higher with higher l/h ratios. The FE-27 elements are also subject to locking, which causes them to overestimate stresses with increasing refinement and prevents them from converging to a particular value. In contrast, the α-FE-b27 elements accurately predict and converge to the stress values. Additionally, upon comparing the performance of α-FE-b27 with that of the existing α-FE-b8 elements, it becomes apparent that the latter often requires a higher number of N_{dof}^{u} to converge to the reference solution. Thus, α-FE-b27 elements exhibit higher coarse mesh accuracy compared to the α-FE-b8 elements, regardless of the l/h ratios. Further, the distribution of σ_{vm} across the domain for both l/h ratios is presented in Fig. 4.6, revealing the absence of any spurious stress values in the domain.

Lastly, an assessment of computational efficiency for the case with $l/h = 100$ has been conducted. The relative error $\left(\frac{|u_z - u_z^{\text{ref}}|}{|u_z^{\text{ref}}|}\right)$ against time is presented in Fig. 4.7 for both proposed α-FE-b27 and conventional FE-b27 elements. The results show that achieving a comparable accuracy with FE-b27 elements necessitates significantly more computing time as compared to α-FE-b27. For example, achieving a relative error of 10^{-2} for the maximum vertical displacement requires approximately 0.7 seconds with

α-FE-b27, while conventional elements require approximately 4 seconds for the same accuracy.

4.4.3 Curved Cantilever beam

The present example investigates the response of a 3D curved cantilever beam that experiences the effects of combined shear and membrane locking. The problem consists of a curved beam of thickness h, mean radius r, and width w. The beam is fixed at one end while the edge at the opposite extremity is subjected to a horizontal load $\bar{F}$, see Fig. 4.8 [101]. Here, r_i and r_o are the inner and outer radii.

In order to assess the performance of the proposed EAS elements, the problem is solved for various slenderness ratios (r/h), encompassing situations where locking is a dominant issue. The problem consists of three r/h ratios, i.e, 10, 100, and 1000, which were attained by gradually decreasing h to 1.2, 0.12, and 0.012, respectively, while keeping $r = 12$ and $w = 1$. The edge is subjected to a load of $\bar{F} = 0.1h^3$ per unit length, and the material parameters, Young's modulus E and Poisson's ratio ν, are set to 1000 and 0.25, respectively. The benchmark radial displacements (u_x^{ref}) at the tip are 1.6338, 1.6236, and 1.5852 for $r/h = 10$, 100, and 1000, respectively [143]. The mesh used for solving the problem is defined by the number of elements in the radial (n^r_{ele}), circumferential (n^θ_{ele}), and transverse (n^z_{ele}) directions, and denoted as $n^r_{\text{ele}} \times n^\theta_{\text{ele}} \times n^z_{\text{ele}}$. The refinement of the mesh is performed along the circumferential direction, with n^θ_{ele} ranging from 2 to 128 ($n^\theta_{\text{ele}} = 2, 4, 8, 16, \ldots, 128$), while keeping $n^r_{\text{ele}} = n^z_{\text{ele}} = 1, 1, 1, 1, 2, 4, 8$ for $r/h = 10$. However, for $r/h = 100$ and 1000, the stress convergence is achieved after refining the mesh in the transverse direction while keeping a single element along the thickness. As a result, the mesh for $r/h = 100$ and 1000 is obtained by setting $n^\theta_{\text{ele}} = 2, 4, 8, 16, \ldots, 256$, $n^z_{\text{ele}} = 1, 1, 1, 1, 2, 2, 4, 8$, and $n^r_{\text{ele}} = 1$.

The radial displacement at the loaded edge has been evaluated and normalized against the reference solution, see Figs. 4.9a, 4.9c, and 4.9e. Further, Figs. 4.9b, 4.9d, and 4.9f show the relative L_2 error norm of displacement against the total number of active degrees of freedom (N^u_{dof}). To gain better insights into the performance of the proposed elements with change in the slenderness ratio, Fig. 4.10 shows the normalized tip displacement for various r/h ratios using two fixed mesh descriptions. The results show that as the r/h ratio increases, FE-b8 and FE-b27 elements experience significant locking, whereas α-FE-b8 and α-FE-b27 perform consistently throughout. Furthermore, the results show close similarity between the displacement fields obtained from h-FE and α-FE elements. It is important to note that the h-FE elements are derived from the formulation outlined in [142], where the transformation matrix is computed at each Gauss point. The small disparity between h-FE and α-FE elements can be entirely eliminated by adopting the same strategy for computing the transformation matrix.

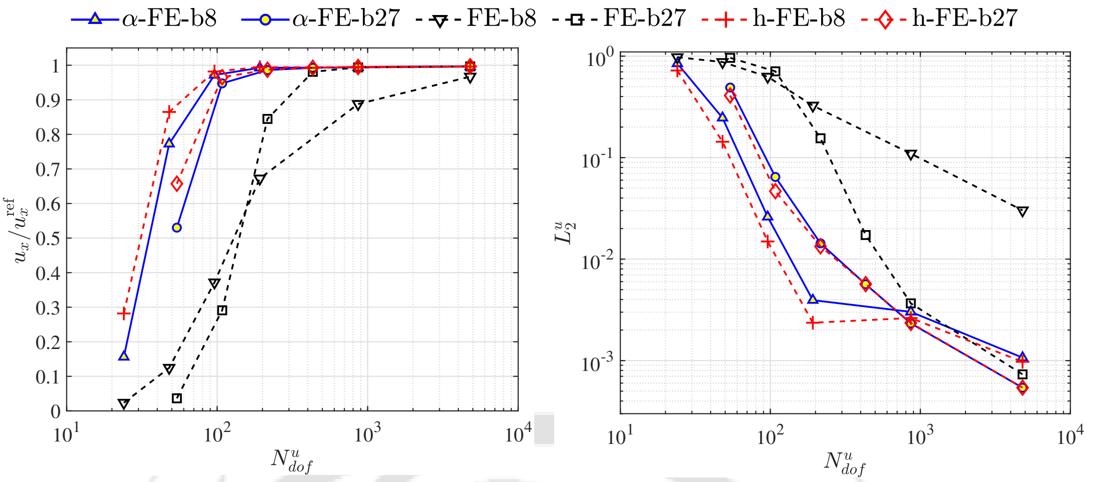

(a) u_x/u_x^{ref} for $r/h = 10$ **(b)** L_2^u for $r/h = 10$

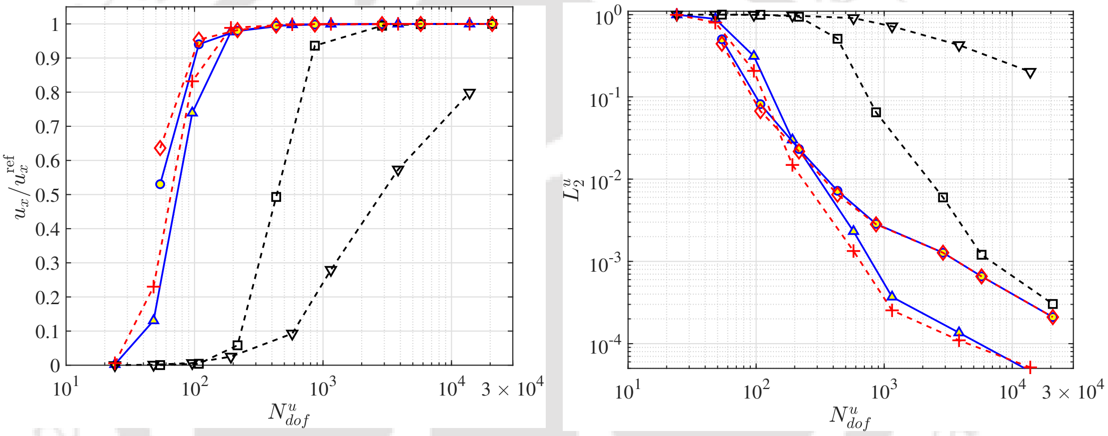

(c) u_x/u_x^{ref} for $r/h = 100$ **(d)** L_2^u for $r/h = 100$

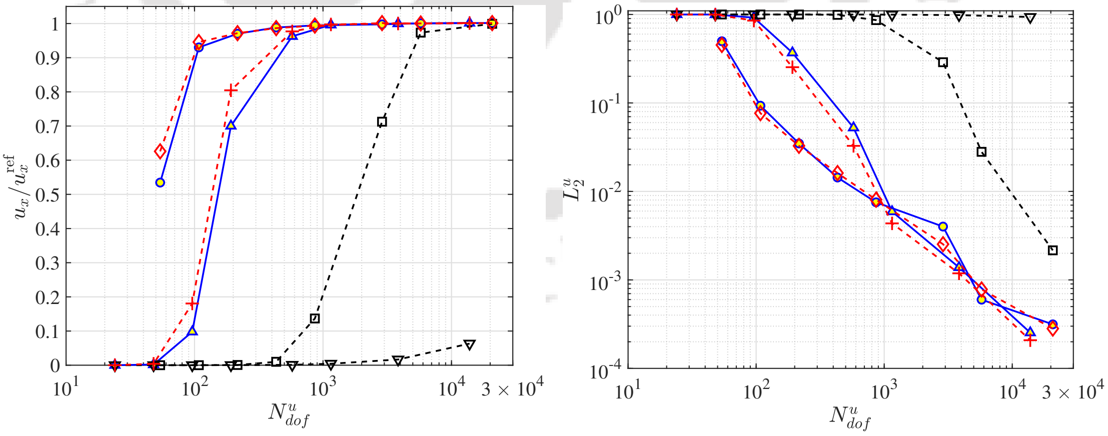

(e) u_x/u_x^{ref} for $r/h = 1000$ **(f)** L_2^u for $r/h = 1000$

Figure 4.9: Investigation of normalized displacement at the loaded edge and L_2^u error norm for a curved cantilever beam problem with varying r/h ratios.

The locking is relatively less for the lower values of r/h, see Figs. 4.9a and 4.9b. In such cases, conventional elements can adequately converge to the analytical solution with relatively few active degrees of freedom. However, the EAS elements provide more

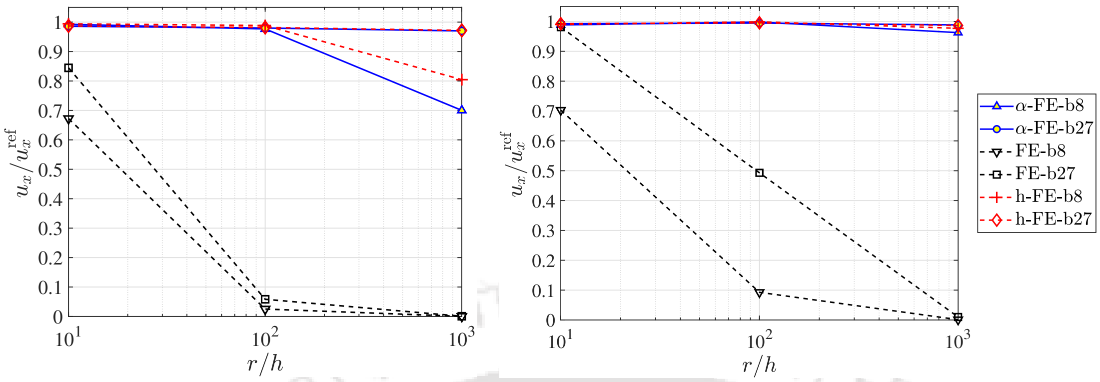

(a) $N^u_{dof} \approx 200$ **(b)** $N^u_{dof} \approx 500$

Figure 4.10: Normalized displacement at the loaded edge for curved cantilever beam problem with varying r/h ratios and different mesh descriptions.

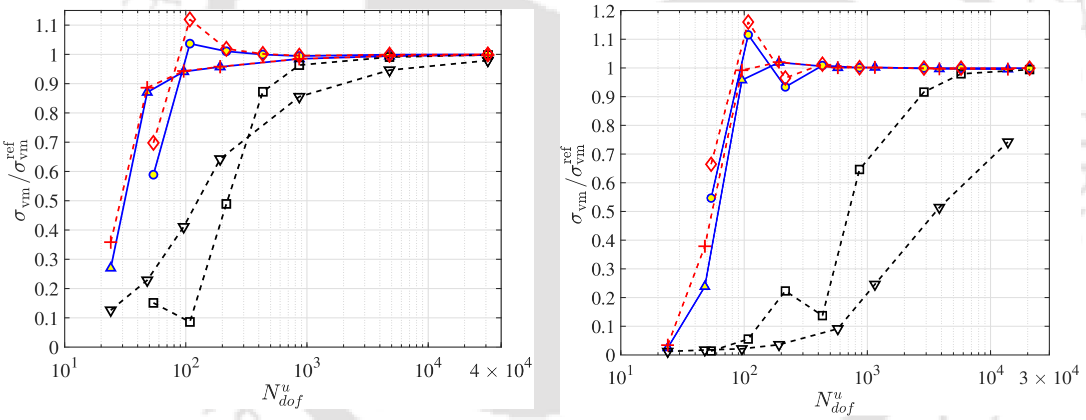

(a) $\sigma_{\text{vm}}/\sigma_{\text{vm}}^{\text{ref}}$ for $r/h = 10$ **(b)** $\sigma_{\text{vm}}/\sigma_{\text{vm}}^{\text{ref}}$ for $r/h = 100$

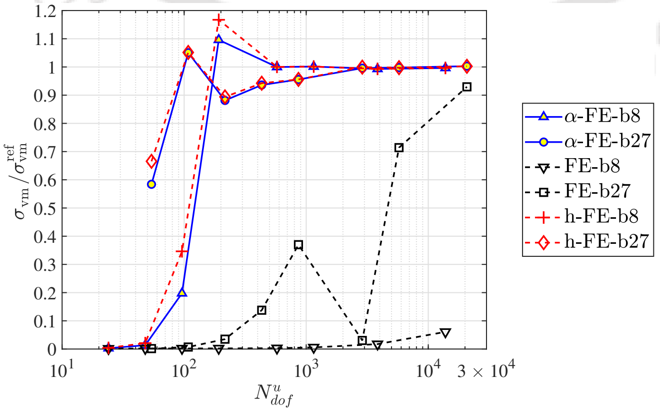

(c) $\sigma_{\text{vm}}/\sigma_{\text{vm}}^{\text{ref}}$ for $r/h = 1000$

Figure 4.11: Normalized von Mises stress at $r = r_i$, $\theta = 45°$, $z = 0$ for three different r/h ratios of a curved cantilever beam problem.

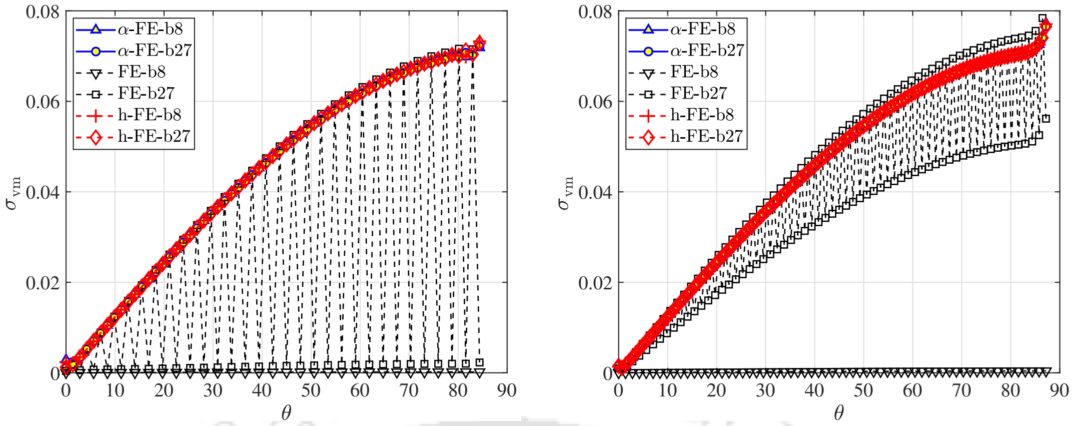

(a) Mesh of 1 × 32 × 2 elements **(b)** Mesh of 1 × 64 × 2 elements

Figure 4.12: Variation of von Mises stress along θ and at $r = r_i$ and $z = 0$ for $r/h = 1000$ in a curved beam problem with different mesh descriptions.

accurate results for coarse meshes. For instance, a mesh with 1 × 8 × 1 α-FE-b27 elements results in 0.5652 % of L_2^u error, whereas conventional FE-b27 elements for the same mesh result in 1.7280 % L_2^u error. It takes twice as many elements as the α-FE-b27 formulation to attain a similar accuracy with conventional FE-b27 elements.

At higher values of the r/h ratio, i.e., 100 and 1000, the quality of the solution for conventional elements is considerably degraded by locking. For instance, FE-b27 suffers from locking at higher r/h ratios and achieving convergence demands substantial refinement, see Figs. 4.9c, 4.9d, 4.9e, and 4.9f. Conversely, α-FE elements consistently outperform conventional elements regardless of the r/h ratio. For example, a mesh of 1 × 16 × 1 ($N_{dof}^u = 864$) α-FE-b27 elements is able to provide a solution that closely matches the reference value for r/h ratios of 100 and 1000, with L_2 errors of 0.2857% and 0.7532%, respectively. However, to attain comparable accuracy with FE-b27 elements, it is necessary to use four times the number of elements for $r/h = 100$ (mesh: $1 \times 32 \times 2$, $N_{dof}^u = 2880$, $L_2 = 0.5993\%$) and eight times the number of elements for $r/h = 1000$ (mesh: $1 \times 64 \times 2$, $N_{dof}^u = 5760$, $L_2 = 2.8027\%$).

For each of the three r/h ratios, the von Mises stress (σ_{vm}) is calculated at $r = r_i$, $\theta = 45°$, and $z = 0$. The benchmark values ($\sigma_{\text{vm}}^{\text{ref}}$) of 6.4025, 0.5963, and 0.0505 [143] corresponding to r/h ratios of 10, 100, and 1000, respectively, have been utilized to normalize the obtained results. The convergence behavior is shown in Figs. 4.11a, 4.11b, and 4.11c. Furthermore, the σ_{vm} is assessed along θ with $r = r_i$ and $z = 0$ for two mesh configurations, as illustrated in Figs. 4.12a and 4.12b. Large stress oscillations can be seen in the case of FE-b27 elements, whereas α-FE-b27 elements consistently outperform the FE-b27 elements. Finally, the distribution of σ_{vm} over the domain for different r/h ratios is shown in Figs. 4.13a, 4.13b, and 4.13c. The results demonstrate that there are no anomalous stress values throughout the domain.

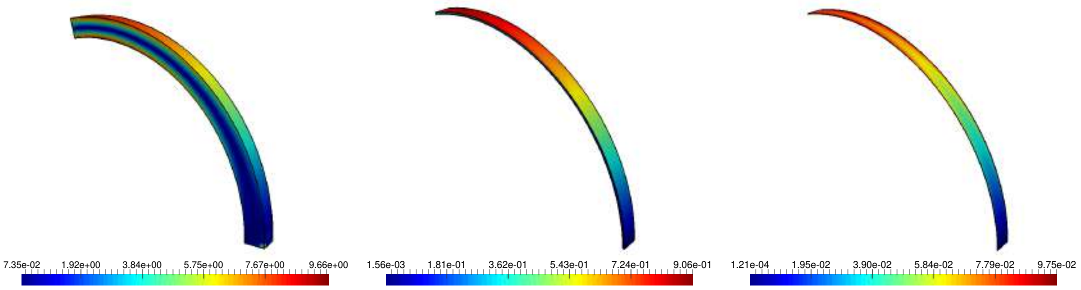

(a) $r/h = 10$, Mesh: $2 \times 32 \times 2$ elements **(b)** $r/h = 100$, Mesh: $1 \times 64 \times 2$ elements **(c)** $r/h = 1000$, Mesh: $1 \times 64 \times 2$ elements

Figure 4.13: The von Mises stress distribution for the curved cantilever beam with different r/h ratios using α-FE-b27 elements.

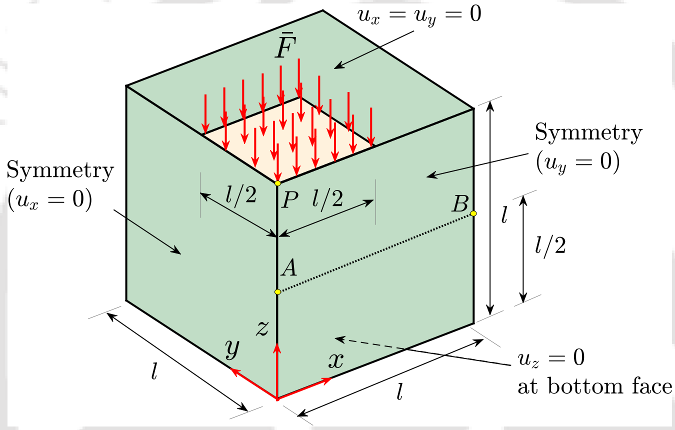

Figure 4.14: Problem geometry and corresponding boundary conditions of a quarter domain of the incompressible block problem.

4.4.4 Incompressible block

The next example serves as a standard test to assess the performance of the proposed elements while analyzing the domain under volumetric locking due to the material's incompressibility [54, 143]. The problem comprises a rectangular block with dimensions of $2l \times 2l \times l$, where a central region of the upper face of the block with a cross-sectional area of $l \times l$ is subjected to a pressure load of $\bar{F}$. The length l is considered as unity. The magnitude of $\bar{F}$ is 80, and the material parameters, Young's modulus E and Poisson's ratio ν, are set to 250.5684 and 0.4999, respectively. The problem's symmetry allows to do the analysis with only a quarter of the domain. The problem definition and associated boundary conditions are shown in Fig. 4.14. The problem is uniformly meshed, with $n^x_{\text{ele}} = n^y_{\text{ele}} = n^z_{\text{ele}} = 2$, 4, 8, 16, and 32, where n^x_{ele}, n^y_{ele}, and n^z_{ele} are the number of brick elements in x, y, and z direction, respectively.

The vertical displacement at point 'P' has been evaluated and results are normalized using $u^{\text{ref}}_z = 0.2165$ [143], see Fig. 4.15a. In addition, the von Mises stress (σ_{vm}) is computed at the location which corresponds to point 'A' with coordinates [0, 0, 0.5]. The results are normalized using $\sigma^{\text{ref}}_{\text{vm}} = 62.7484$ [143] and presented in Fig. 4.15b. FE-b8 el-

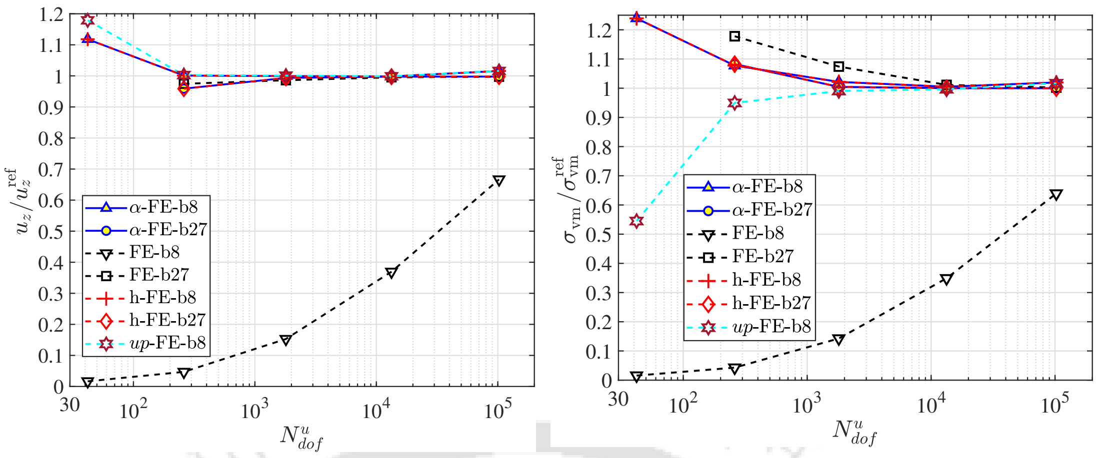

(a) u_z/u_z^{ref} **(b)** $\sigma_{\mathrm{vm}}/\sigma_{\mathrm{vm}}^{\mathrm{ref}}$

Figure 4.15: Investigation of normalized displacement at a point 'P' and von Mises stress at point 'A' corresponding to $x = 0$, $y = 0$, $z = 0.5$ for incompressible block problem using brick elements.

ements exhibit the severe effects of locking, while both α-FE and h-FE elements, regardless of their specific type, converge to the solution by alleviating the locking phenomenon. Although the higher-order FE-b27 elements seem to exhibit similar performance to the EAS elements, this observation does not provide a comprehensive representation of the situation. Upon further examination of the stress distribution on the 'y' plane, it becomes apparent that the higher-order conventional FE-b27 elements are not immune to locking. In fact, the results obtained from these elements are significantly plagued with the adverse effect of volumetric locking.

To investigate these effects, results for stresses along a line AB on the y plane, where x values range from 0 to 1, $y = 0$, and $z = 0.5$, have been analyzed. When evaluating stresses along the line AB, substantial oscillation can be observed in normal stresses obtained using FE-b27 elements. Even after considerable refinement, these oscillations persist, as demonstrated in Fig. 4.16. Moreover, since the boundary conditions are symmetric at this location, the shear stresses σ_{xy} and σ_{zy} should be zero. However, conventional FE elements fail to predict accurate solutions for this condition, see Fig. 4.17. In contrast, the proposed EAS elements do not exhibit any oscillations in normal stresses. Further, the shear stress condition is better satisfied with α-FE-b27 elements compared to the conventional and existing α-FE-b8 or *up*-FE-b8 elements, with the magnitude of σ_{xy} and σ_{zy} being very close to zero. Next, the computational efficiency of the problem is assessed by evaluating the time against the L_2 error norm of displacement and stresses, see Figs. 4.19a and 4.19b. The results show a notable difference in computational time for achieving a comparable level of accuracy in displacement and stress field between FE-b27 and α-FE-b27. For example, to attain an L_2 error of displacement of order 10^{-3} with conventional elements requires approximately 2×10^3 seconds, whereas EAS elements achieve the same accuracy in only about 3 sec-

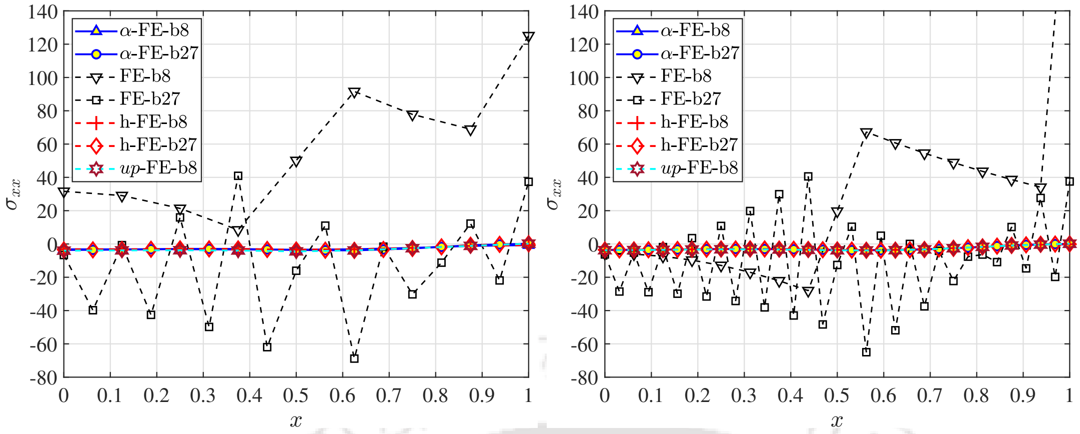

(a) σ_{xx}, Mesh: $8 \times 8 \times 8$ elements **(b)** σ_{xx}, Mesh: $16 \times 16 \times 16$ elements

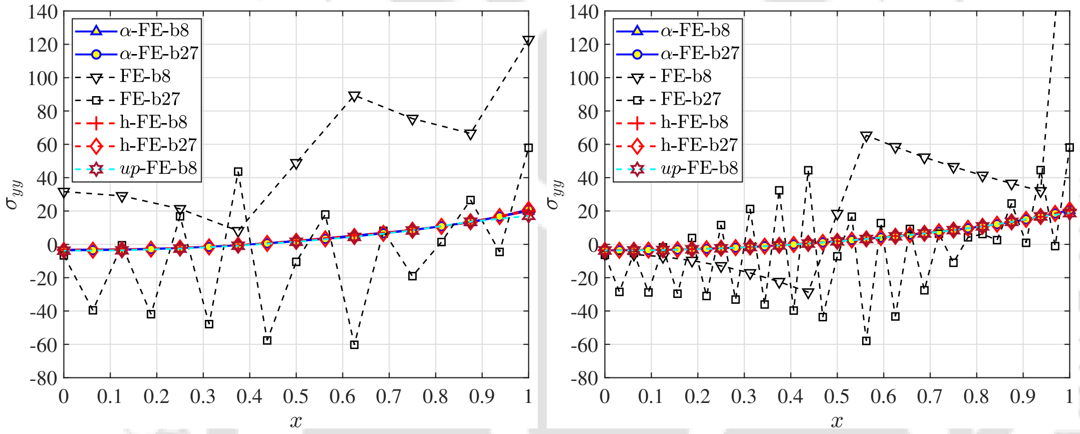

(c) σ_{yy}, Mesh: $8 \times 8 \times 8$ elements **(d)** σ_{yy}, Mesh: $16 \times 16 \times 16$ elements

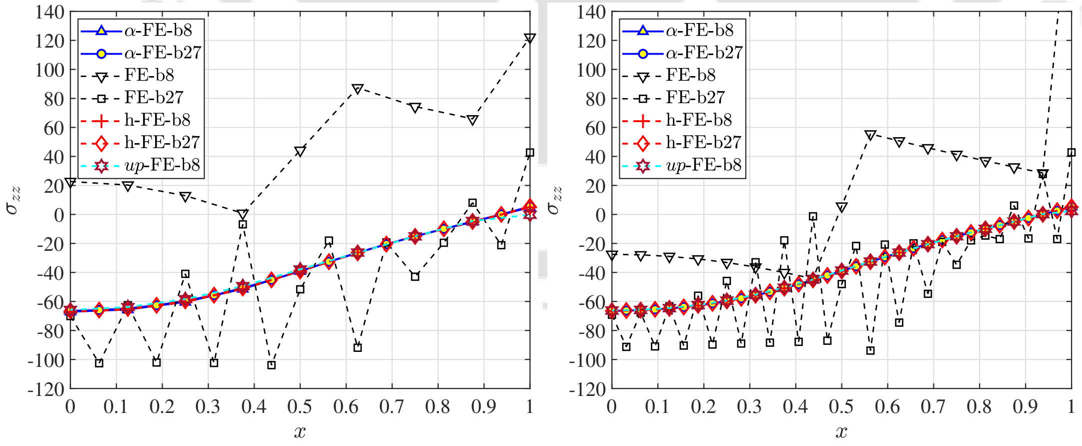

(e) σ_{zz}, Mesh: $8 \times 8 \times 8$ elements **(f)** σ_{zz}, Mesh: $16 \times 16 \times 16$ elements

Figure 4.16: Assessment of normal stresses along line AB in an incompressible block problem with two different mesh descriptions.

onds. Regarding the stress field, the convergence of conventional elements is notably slower, and it would require a significantly higher amount of time to attain the same level of accuracy as EAS elements. Lastly, in order to provide a comprehensive analysis,

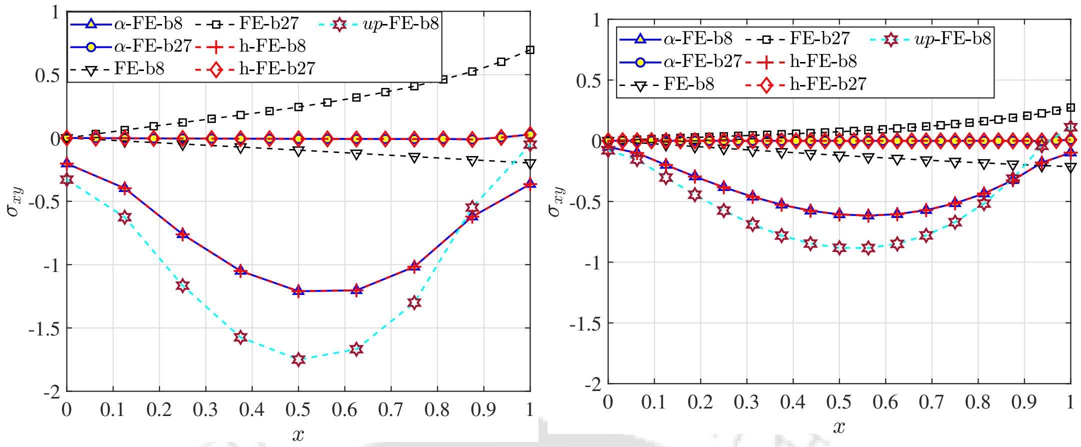

(a) σ_{xy}, Mesh: $8 \times 8 \times 8$ elements **(b)** σ_{xy}, Mesh: $16 \times 16 \times 16$ elements

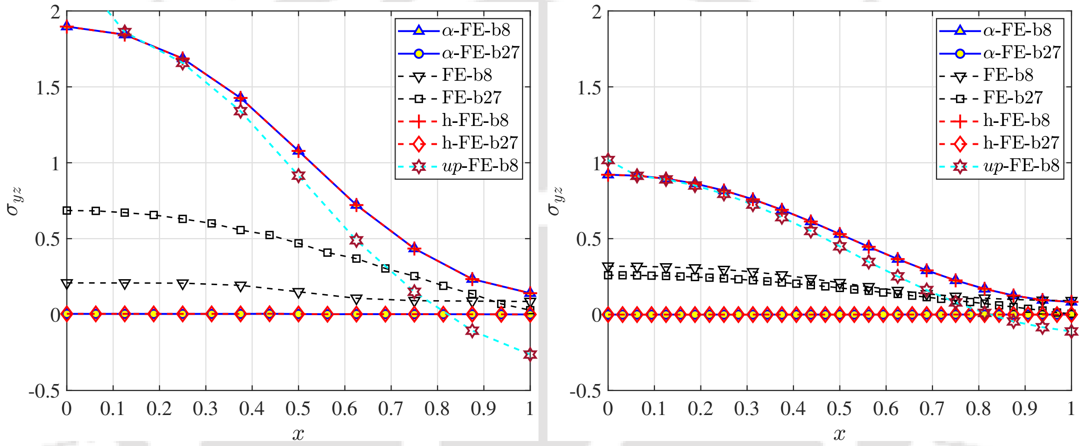

(c) σ_{yz}, Mesh: $8 \times 8 \times 8$ elements **(d)** σ_{yz}, Mesh: $16 \times 16 \times 16$ elements

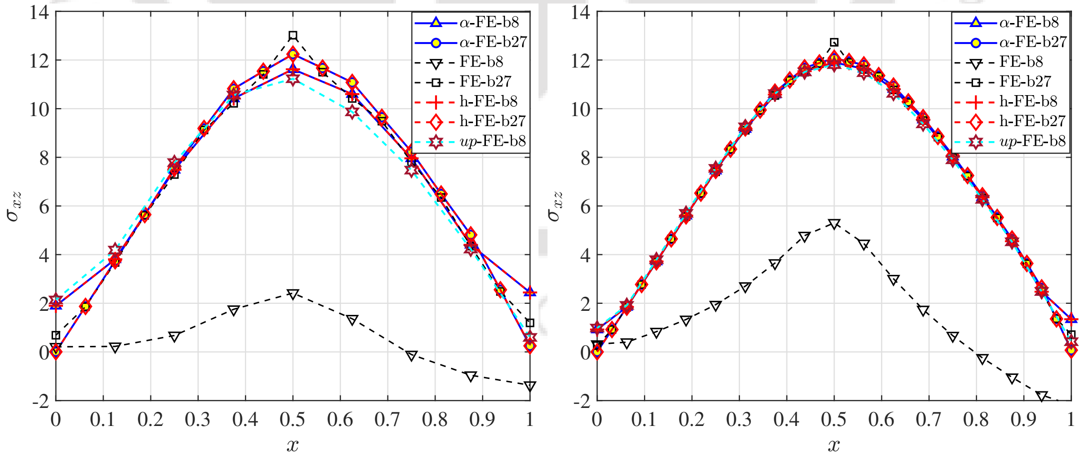

(e) σ_{xz}, Mesh: $8 \times 8 \times 8$ elements **(f)** σ_{xz}, Mesh: $16 \times 16 \times 16$ elements

Figure 4.17: Assessment of shear stresses along line AB in an incompressible block problem with two different mesh descriptions.

Fig. 4.18 shows the von Mises stress along line AB, and Fig. 4.20 presents a contour plot of the distribution of σ_{vm} over the domain.

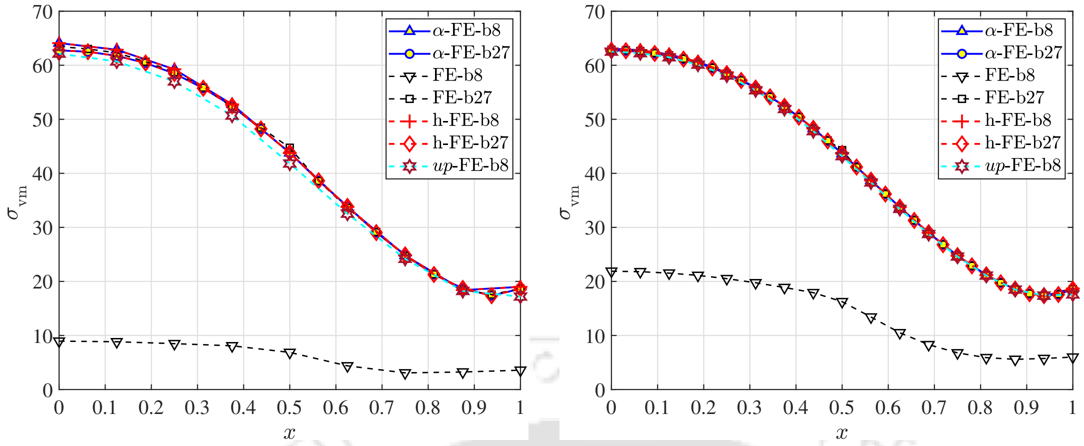

(a) Mesh: 8 × 8 × 8 **(b)** Mesh: 16 × 16 × 16

Figure 4.18: The von Mises stresses along line AB on the y-plane for incompressible block problem using different mesh configurations.

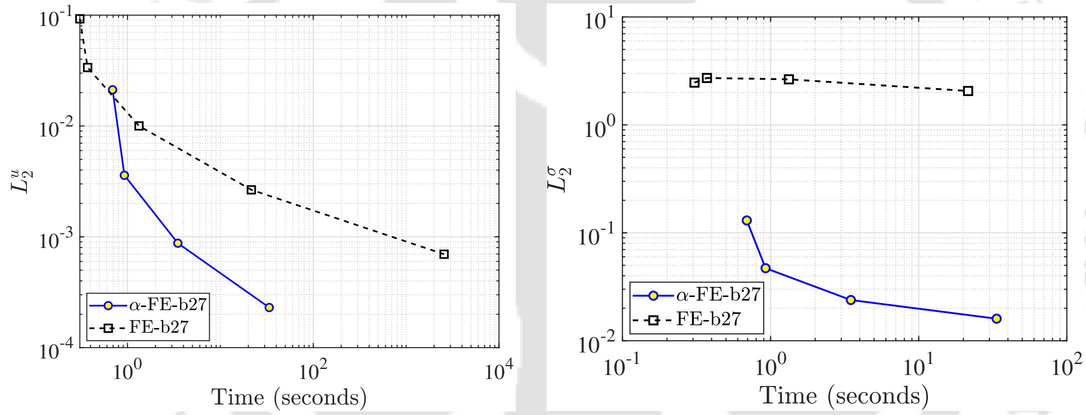

(a) L_2^u **(b)** L_2^σ

Figure 4.19: Computational efficiency of the proposed α-FE-b27 elements against the conventional FE-b27 elements for a incompressible block problem.

Further, the performance of wedge elements is assessed by examining the same problem in a scenario where the domain is exclusively meshed using wedge elements. The discretization of the domain follows a similar meshing approach as mentioned before. However, in this case, each brick element is divided into two wedge elements, where a triangular face of each wedge element is oriented parallel to the x-y plane. A sample mesh for this configuration is shown in Fig. 4.21. Similar to the previous case, the problem is solved for the vertical displacement and von Mises stress at the same respective points of interest and results are normalized against the reference solution, see Figs. 4.22a and 4.22b. The results show that the conventional FE-w6 elements suffer significantly from locking, while α-FE-w6 alleviates the effects of locking to a greater extent. Similar to the previous case, the performance of the FE-w18 and α-FE-w18 elements appear comparable, but this observation does not fully represent the situation. Further investigation of individual stress components reveals significant oscillation when

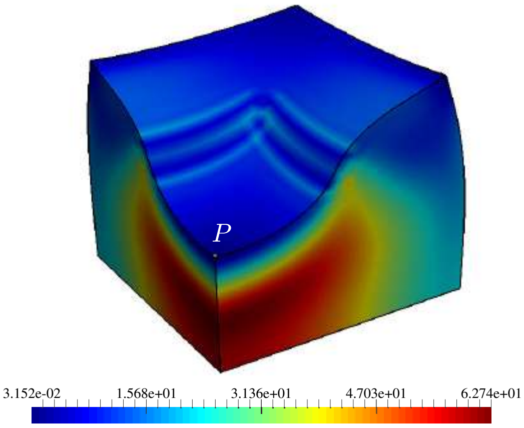

Figure 4.20: The von Mises stress distribution for incompressible block problem using a mesh of 16 × 16 × 16 α-FE-b27 elements. (Deformed geometry is scaled 2.5 times for better visualization.)

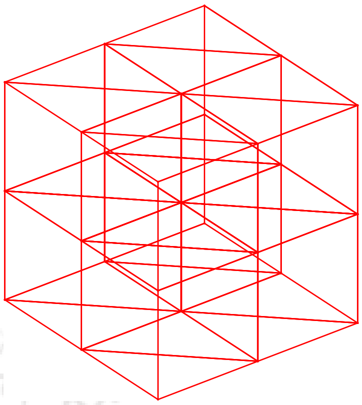

Figure 4.21: A sample mesh for an incompressible block problem utilizing only wedge elements.

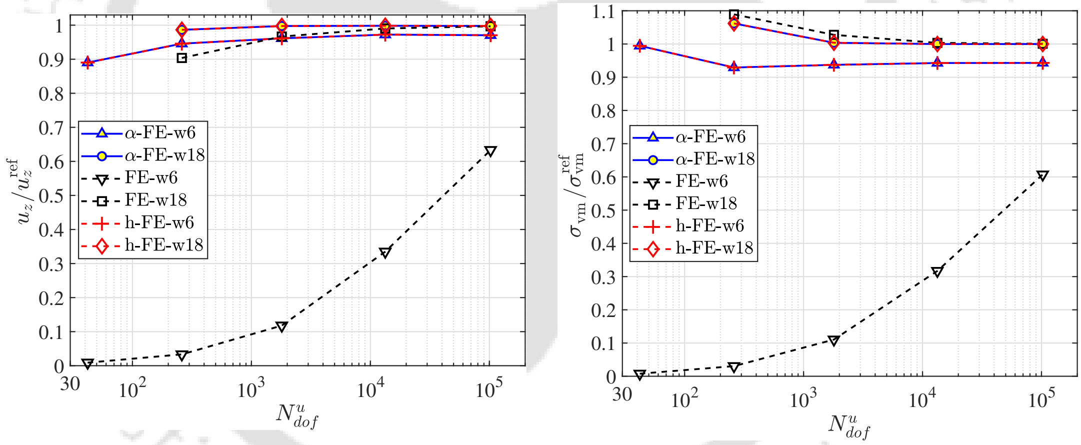

(a) u_z/u_z^{ref} **(b)** $\sigma_{\text{vm}}/\sigma_{\text{vm}}^{\text{ref}}$

Figure 4.22: Investigation of normalized displacement at a point 'P' and von Mises stress at point 'A' corresponding to $x = 0$, $y = 0$, $z = 0.5$ for incompressible block problem using only wedge elements.

using conventional FE-w6 or FE-w18 elements, see Fig. 4.23. In contrast, the proposed α-FE-w6 and α-FE-w18 are not plagued with spurious stress oscillations.

Remark: When examining the normalized displacements (Figs. 4.15a and 4.22a), normalized von Mises stress (Figs. 4.15b and 4.22b) or von Mises stress along a line on the y plane (Fig. 4.18), the conventional higher order elements such as FE-b27 and FE-w18 elements appear to be a viable option for simulation. However, the situation becomes severely unfavorable for FE-b27 or FE-w18 elements when examining individual stress components.

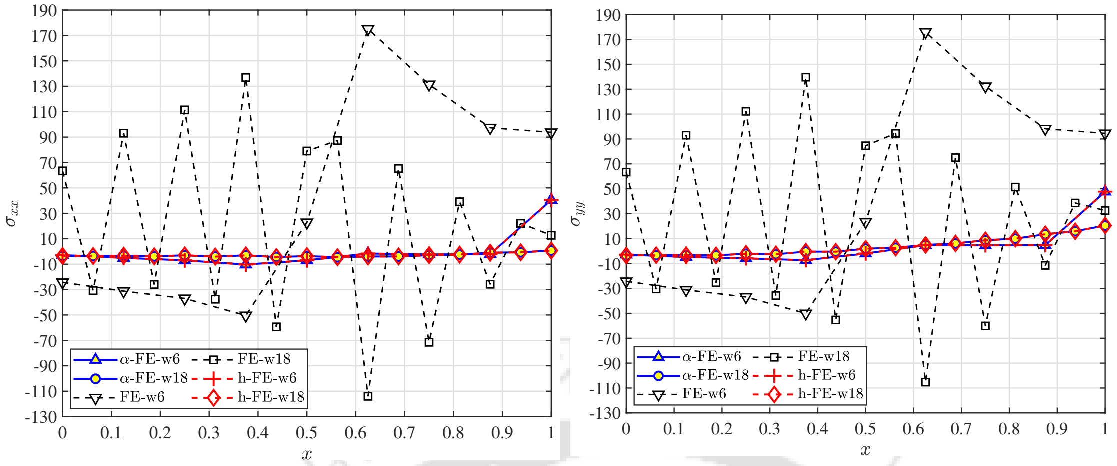

(a) σ_{xx} **(b)** σ_{yy}

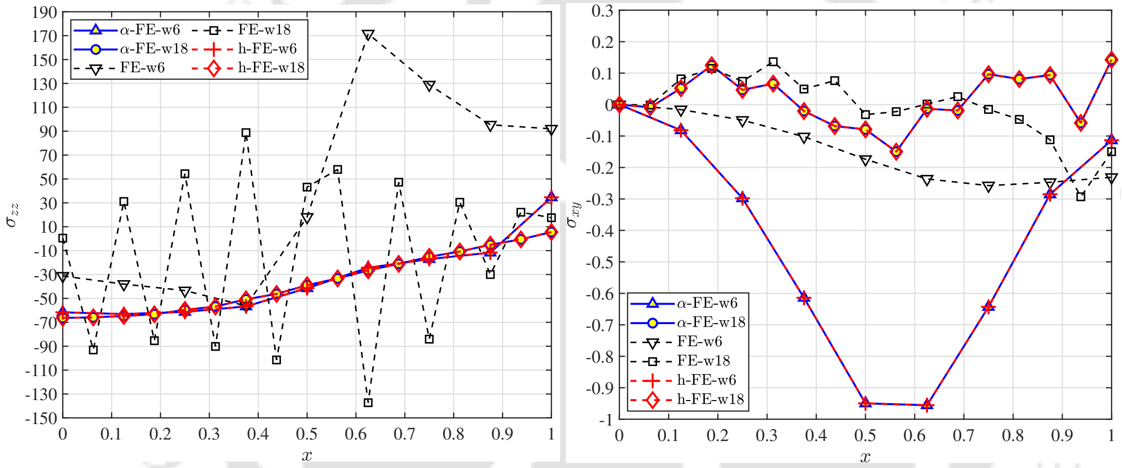

(c) σ_{zz} **(d)** σ_{xy}

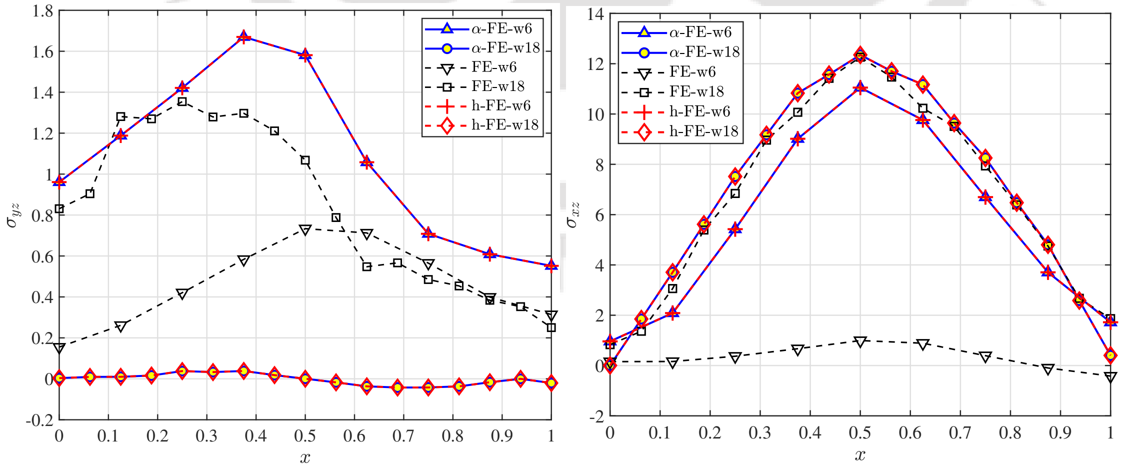

(e) σ_{yz} **(f)** σ_{xz}

Figure 4.23: Assessment of different stresses in an incompressible block problem using 1024 wedge elements. (A mesh of 8 × 8 × 8 brick elements is converted to a mesh of wedge elements by dividing each brick element into two wedge elements.)

4.4.5 Pinched cylinder

One of the shell obstacle course problems [101] concerns a pinched cylinder of mean radius r, thickness h, and axial length l with the rigid diaphragm at both of its ends and is prone to both shear and membrane locking. The ends of the cylinder are fixed with rigid diaphragms and the mid-section is subjected to a pair of equal and opposite concentrated loads $\bar{F}$. Since the problem exhibits symmetry, only one-eighth of the cylinder is analyzed, see Fig. 4.24. The geometric parameters of the problem include $r = 300$, $l = 600$, and $h = 3$, while the material parameters are taken as $E = 3 \times 10^6$ and $\nu = 0.3$. The load applied is $\bar{F} = 1$. The problem is solved using meshes defined by $n^r_{\text{ele}} \times n^\theta_{\text{ele}} \times n^l_{\text{ele}}$, where n^r_{ele}, n^θ_{ele}, and n^l_{ele} denote the number of elements in the radial, circumferential, and axial directions, respectively. The meshes are refined along the θ and l directions, with values of n^θ_{ele} and n^l_{ele} set to 2, 4, 8, 16, and 32, while n^r_{ele} is kept constant at 1.

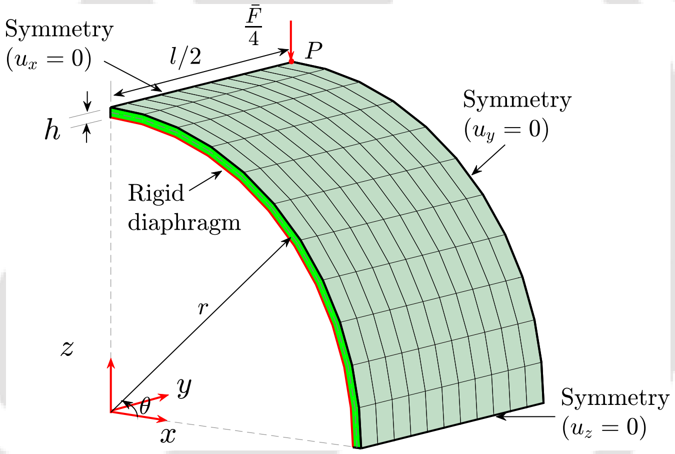

Figure 4.24: Problem geometry and corresponding boundary conditions of one-eighth domain of the pinched cylinder problem.

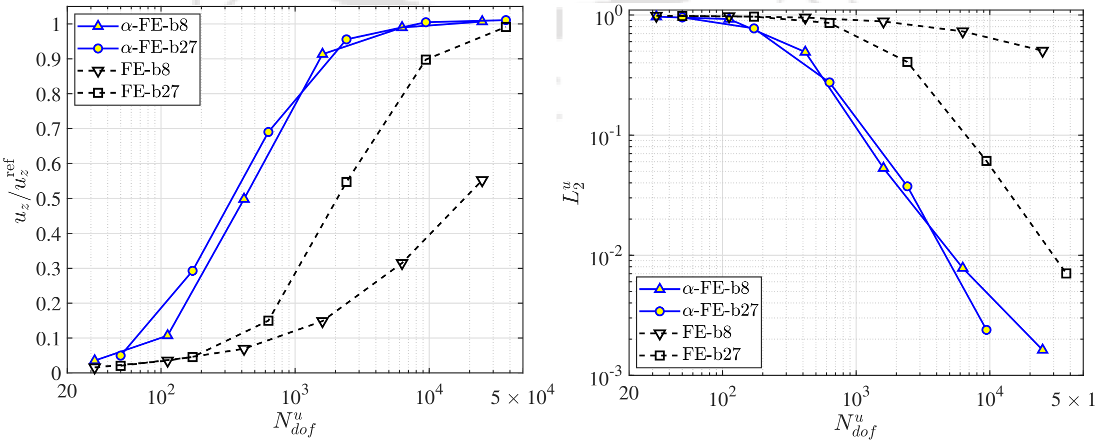

(a) u_z/u_z^{ref} **(b)** $L_2^{\boldsymbol{u}}$

Figure 4.25: Investigation of normalized displacement at the point of application of load and L_2^u error norm of displacement for a pinched cylinder problem.

The displacement in the radial direction at the point where the load is applied has been evaluated. Fig. 4.25a shows the obtained vertical displacement at the point of interest normalized by the benchmark solution ($u_z^{\text{ref}} = 1.8248 \times 10^{-5}$ [101]). Fig. 4.25b shows the relative L_2^u error norm of displacement with respect to the total number of active degrees of freedom. To evaluate the L_2^u norm, a reference solution is established using a significantly fine mesh of $1 \times 64 \times 64$ h-FE-b27 elements. The results demonstrate that the conventional FE-b8 elements experience severe locking, and even with significant refinement, they fail to converge to the solution. The higher-order FE-b27 elements require considerable refinement to converge to the solution. In contrast, both α-FE-b8 and α-FE-b27 elements show relatively better convergence with fewer elements. Moreover, α-FE-b27 elements exhibit significantly higher coarse mesh accuracy compared to FE-b27 elements.

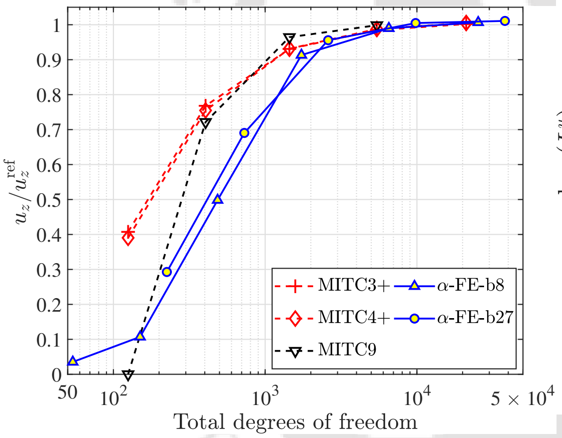

Figure 4.26: Performance evaluation of proposed EAS elements and MITC elements for the pinched cylinder problem.

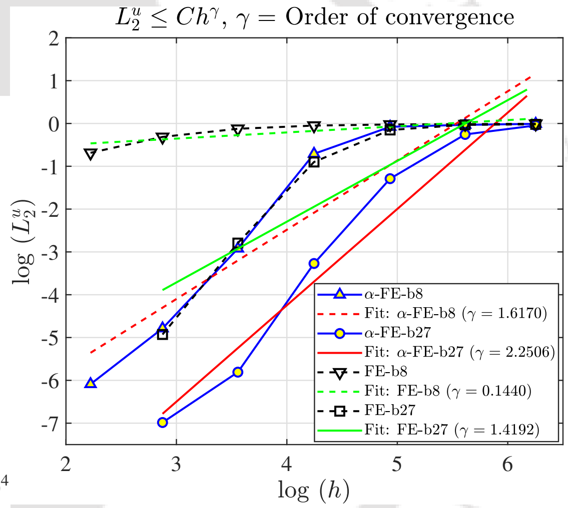

Figure 4.27: Convergence rates for analyzing the pinched cylinder problem using various elements. ('Fit: element type' represents a linear fit for the respective element type, and h is the smallest diagonal length of an element in the selected mesh.)

Next, the performance of the proposed element is compared with the MITC shell elements in Fig. 4.26. The results show that the α-FE-b27 elements exhibit comparable performance to the MITC elements. However, the MITC shell elements exhibit a slight advantage over the proposed elements. It is crucial to emphasize that the α-FE-b27 elements show good performance without making any kinematic assumptions in their formulation. Further, the convergence rates of the proposed elements in comparison to conventional elements are investigated in Fig. 4.27. Notably, the order of convergence for α-FE-b27 element is significantly higher compared to both conventional elements and the existing EAS elements.

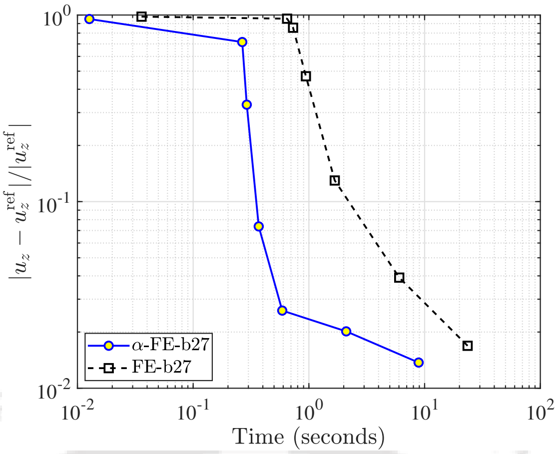

Figure 4.28: Computational efficiency of the proposed α-FE-b27 elements against the conventional FE-b27 elements for a pinched cylinder problem.

Finally, the study of computational efficiency is conducted and the results are presented in Fig. 4.28. It shows the relative error with respect to time for both the proposed α-FE-b27 and the conventional FE-b27 elements. The results indicate that attaining a similar level of accuracy with FE-b27 elements requires considerably more computational time when compared to α-FE-b27. For example, to obtain the relative error of 0.1 for the maximum vertical displacement, the conventional elements require approximately 2 sec, while the proposed α-FE-b27 elements achieve the same accuracy in only 0.35 seconds.

4.4.6 Pinched hemisphere

The present numerical example involves a hemispherical shell with and without a hole, both having thickness h and a mean radius r [141]. The shell is subjected to a pair of concentrated loads of equal magnitude and opposite direction, applied at the equator plane and in a diametrically opposite direction. Similar to the previous problem, only one-quarter of the domain is considered due to the problem's symmetry. The problem configuration, along with its boundary conditions, is presented in Figs. 4.29a and 4.29b. The boundary at $z = 0$ in the peripheral region of the shell is unconstrained, while a point at the top is fixed to avoid rigid body motions. The problem geometry is characterized by $r = 10$ and $h = 0.04$, while the material properties are taken as $E = 6.825 \times 10^7$ and $\nu = 0.3$. The applied load is $\bar{F} = 1$. The problem is discretized using a mesh composed of elements in three directions: r, θ, and ϕ. The mesh is defined as $n^r_{\mathrm{ele}} \times n^\theta_{\mathrm{ele}} \times n^\phi_{\mathrm{ele}}$, where n^r_{ele}, n^θ_{ele}, and n^ϕ_{ele} represent the number of elements in each direction. The angles θ and ϕ correspond to the azimuthal and polar angles, respectively, with θ being the angle in the xy-plane. The mesh is refined in the θ and ϕ directions using $n^\theta_{\mathrm{ele}} = n^\phi_{\mathrm{ele}} = 2, 4, 8, 16, 32$, while the number of elements in the r direction is kept constant at $n^r_{\mathrm{ele}} = 1$.

The full hemispherical shell is discretized using a combination of wedge and brick elements, with wedge elements utilized at the center of the hemispherical shell, while

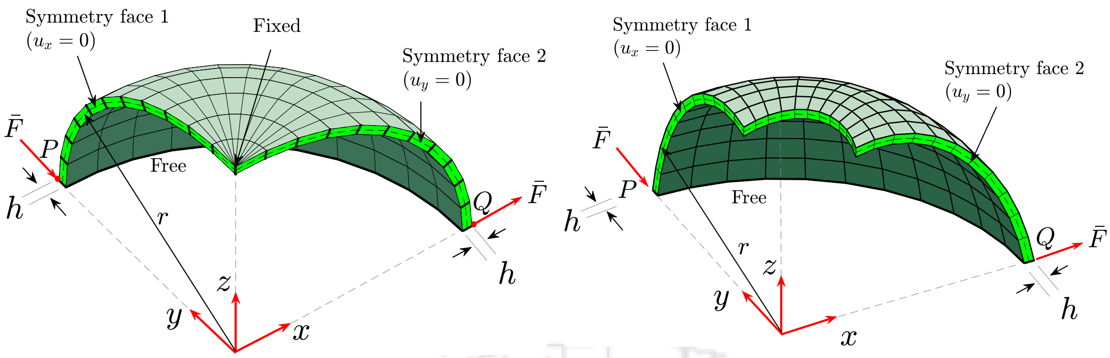

(a) Problem set-up and corresponding boundary conditions for a full hemispherical shell.

(b) Problem set-up and corresponding boundary conditions for a hemisphere with an 18° hole at the top.

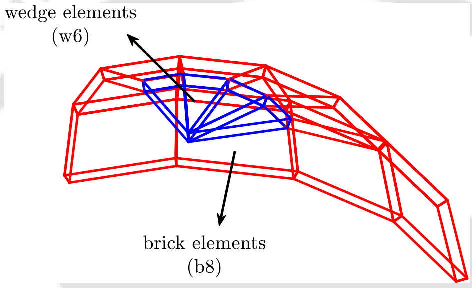

(c) Discretized problem domain using a mesh of 1×4×4 elements consisting of w6b8 combination.

Figure 4.29: A pinched hemisphere problem definition and discretized domain using a sample mesh for the quarter domain.

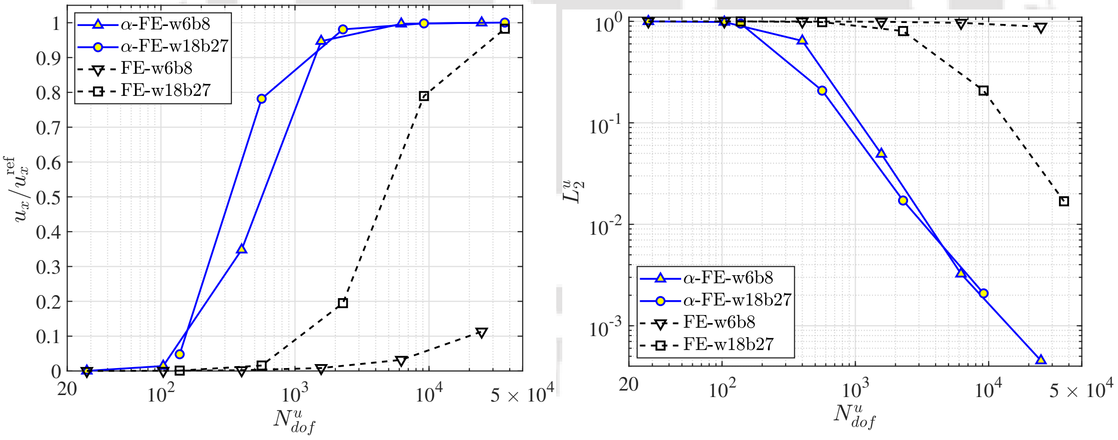

(a) u_x/u_x^{ref} **(b)** $L_2^{\boldsymbol{u}}$

Figure 4.30: Investigation of normalized displacement at the point of application of load (point 'Q') and L_2^u error norm of displacement for the pinched hemisphere problem with full hemispherical shell.

brick elements are used for the remaining domain. The notation "w6b8" refers to a combination of six-node wedge and eight-node brick elements, while "w18b27" refers to a combination of eighteen-node wedge and twenty-seven node brick elements. A sample mesh comprising the "w6b8" element combination and consisting of 1 × 4 × 4 elements

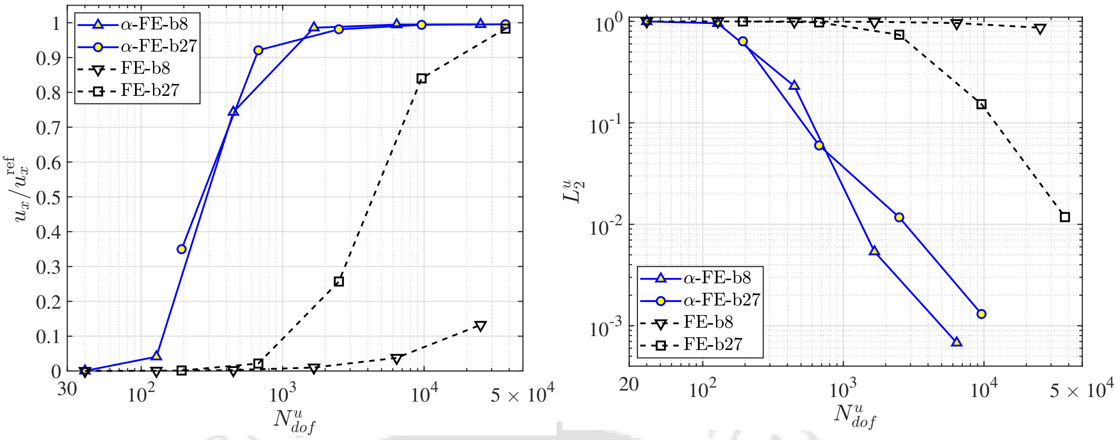

(a) u_x/u_x^{ref} **(b)** $L_2^{\boldsymbol{u}}$

Figure 4.31: Investigation of normalized displacement at the point of application of load (point 'Q') and L_2^u error norm of displacement for the pinched hemisphere with an 18° hole.

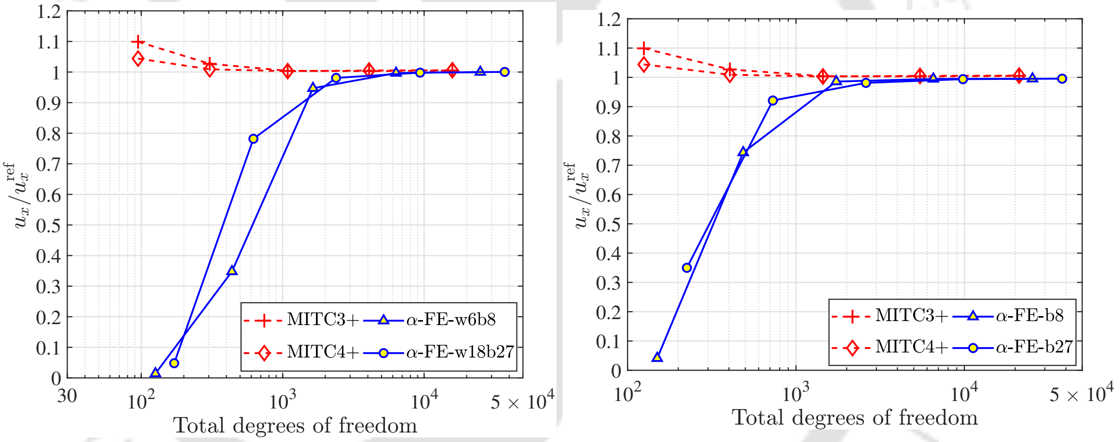

(a) Full hemisphere **(b)** Hemisphere with hole

Figure 4.32: Performance evaluation of proposed EAS elements and MITC elements for the pinched hemisphere problem.

is shown in Fig. 4.29c. The hemisphere with an 18° hole is meshed using the brick elements.

The problem is solved to determine the displacement at point 'Q' in the direction of the applied load. The x-displacement at point 'Q' is computed and normalized to the benchmark solution $u_x^{\text{ref}} = 0.0924$ (for full hemispherical shell) and $u_x^{\text{ref}} = 0.09355$ (for hemisphere with hole) [141], see Figs. 4.30a and 4.31a. The results show that the conventional FE-w6b8 or FE-b8 elements are prone to severe locking, and despite substantial refinement, they are unable to attain the solution. The higher-order FE-w18b27 or FE-b27 elements also demand a considerable degree of refinement to converge to the solution. It can be seen that α-FE-w18b27 elements offer better accuracy with coarse meshes compared to conventional and α-FE-w6b8 elements in full hemispherical shell case. Results demonstrating this observation for a few coarse meshes are presented

Table 4.2: Normalized displacement at point 'Q' for the pinched hemisphere problem consisting of the full hemispherical shell.

Nodes/side	Conventional elements		EAS elements	
	FE-w6b8	FE-w18b27	α-FE-w6b8	α-FE-w18b27
5	0.000530	0.001090	0.014236	0.0480535
9	0.002181	0.015659	0.347956	0.781711
17	0.008469	0.194777	0.947051	0.980879

in Table 4.2, highlighting the clear advantage of α-FE-w18b27 elements over others with the same number of nodes per side. Similarly, in the case of a hemisphere with an 18° hole, the proposed α-FE-b27 elements show favorable convergence by alleviating locking.

In addition, the relative L_2^u error norm of displacement against N_{dof}^u is presented in Figs. 4.30b and 4.31b. The L_2^u norm is computed using a reference solution obtained from a finely refined mesh composed of $1 \times 64 \times 64$ hybrid elements. Considerable enhancements in the accuracy for the α-FE elements are noted. For instance, in the case of a full hemispherical shell, a mesh of $1 \times 16 \times 16$ ($N_{dof}^u = 9168$) of α-FE-w18b27 elements is capable of providing an accurate approximation to the reference solution with an L_2^u error of 0.2084%. In contrast, the conventional FE-w18b27, despite four times as many elements ($1 \times 32 \times 32$, $N_{dof}^u = 36768$), offers lower accuracy with an L_2^u error of 1.6861% compared to the α-FE-w18b27 elements. In the case of the hemisphere with a hole, a mesh of $1 \times 8 \times 8$ ($N_{dof}^u = 2497$) of α-FE-b27 elements provides a close approximation to the reference solution with an L_2^u error of 1.1704%. In contrast, the conventional FE-b27 requires sixteen times as many elements ($1 \times 32 \times 32$, $N_{dof}^u = 37633$) to reach an L_2^u error of 1.1782%. This indicates the considerably higher coarse mesh accuracy of the proposed elements. Finally, the performance of the proposed element is assessed against the MITC elements in Fig. 4.32. In this problem, MITC elements exhibit higher accuracy on coarser meshes. However, the proposed elements offer an advantage by not being constrained by geometric limitations, i.e., they can be used for both thin and thick geometries. In contrast, MITC elements are limited to relatively thin geometries due to its inherent kinematic assumptions.

4.4.7 Scordelis–Lo roof

The Scordelis–Lo roof problem [175] is the last shell obstacle course problem that is being examined using the proposed elements. It involves an 80° portion of a cylinder with mean radius r, length l, and thickness h. The cylinder has rigid diaphragms at opposite ends, while the remaining two sides are unconstrained. As the problem exhibits symmetry, only one-quarter of the cylindrical section is analyzed, see Fig. 4.33. The problem is subjected to a body force per unit volume ρg, where ρ and g are the

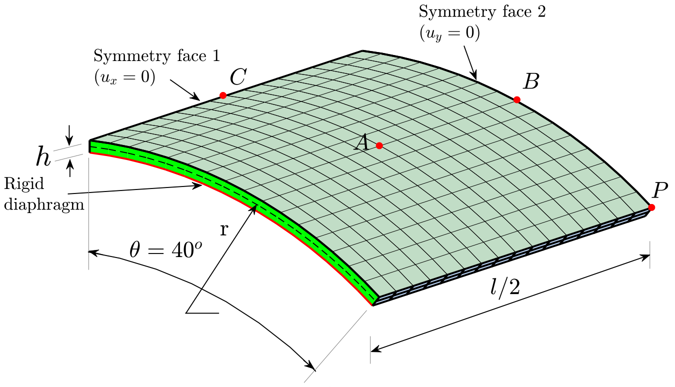

Figure 4.33: Problem geometry and corresponding boundary conditions of a quarter domain of the Scordelis–Lo roof problem.

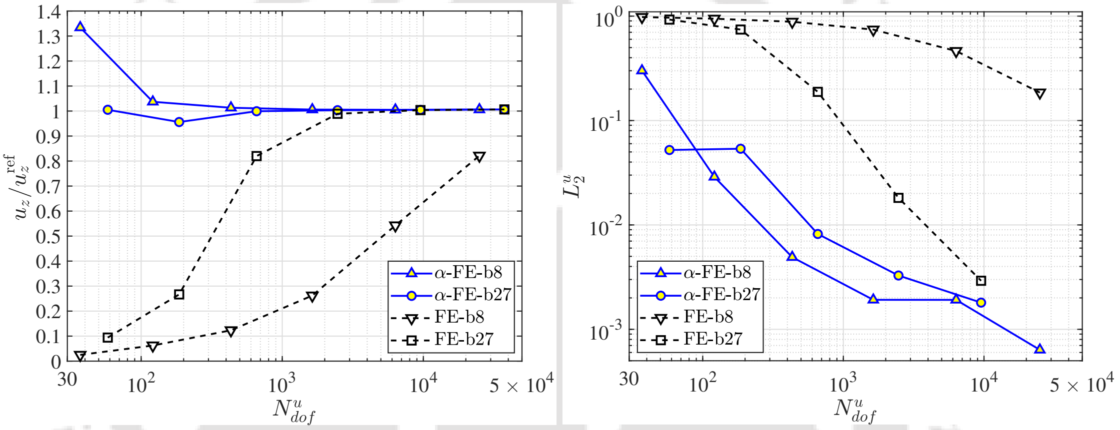

(a) u_z/u_z^{ref} **(b)** $L_2^{\boldsymbol{u}}$

Figure 4.34: Investigation of normalized displacement at the point 'P' and L_2^u error norm of displacement for a Scordelis–Lo roof problem.

specific mass of the body and acceleration due to gravity, respectively. The dimensions of the problem domain are defined by $r = 25$, $l = 50$, and $h = 0.25$, and its material properties are given as $E = 4.32 \times 10^8$ and $\nu = 0$. The body force per unit volume is $\rho g = 360$. The meshes used to solve the problem are defined as $n^r_{\mathrm{ele}} \times n^\theta_{\mathrm{ele}} \times n^l_{\mathrm{ele}}$, where n^r_{ele}, n^θ_{ele}, and n^l_{ele} are the number of elements in the radial, circumferential, and axial direction, respectively. The mesh is refined in the θ and l directions with values of $n^\theta_{\mathrm{ele}} = n^l_{\mathrm{ele}} = 2, 4, 8, 16, 32$, while n^r_{ele} is kept constant at 1.

The displacement at the center of the free side of a cylindrical shell (point 'P') has been evaluated. The results shown in Fig. 4.34a have been normalized by the benchmark solution $u_z^{\mathrm{ref}} = 0.3024$ [175]. Additionally, Fig. 4.34b shows the relative L_2^u error norm of displacement with respect to the total number of active degrees of freedom. The L_2^u norm is calculated using a reference solution obtained from a refined mesh comprising of $1 \times 64 \times 64$ h-FE-b27 elements. Both α-FE-b8 and α-FE-b27 have effectively alleviate locking issues that afflict the conventional elements. The problem is further examined by analyzing the stresses at three different points within the domain. The convergence of

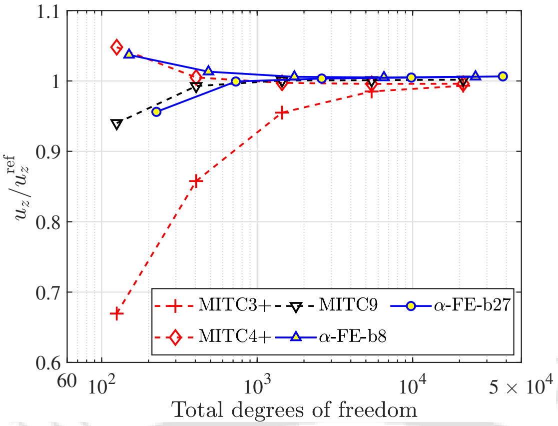

Figure 4.35: Performance evaluation of proposed EAS elements and MITC elements for a Scordelis–Lo roof problem.

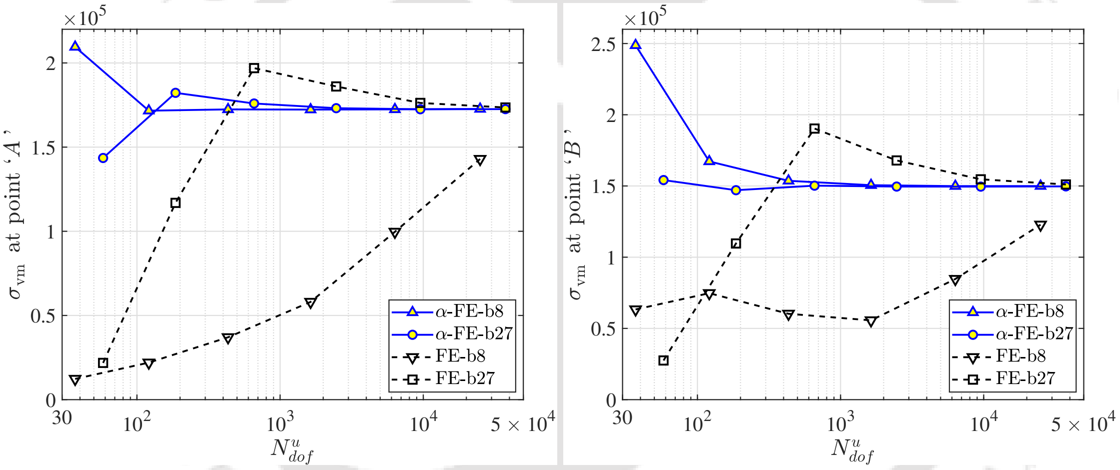

(a) σ_{vm} at point A **(b)** σ_{vm} at point B

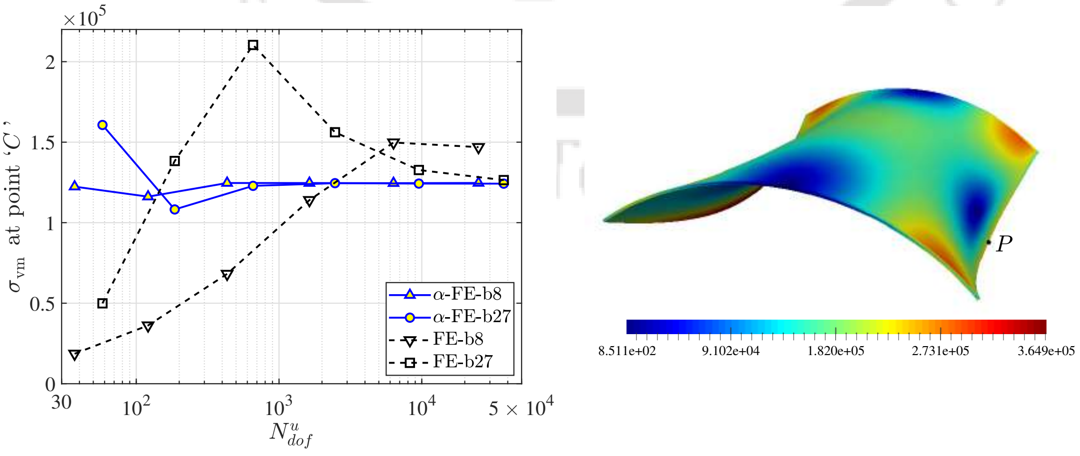

(c) σ_{vm} at point C **(d)** σ_{vm} distribution over the domain

Figure 4.36: Investigation of von Mises stress at different points in the domain and contour plot of σ_{vm} distribution for a Scordelis–Lo roof problem. (Deformed geometry is scaled for visualization.)

von Mises stresses at points A, B, and C is shown in Fig. 4.36, along with the distribution of σ_{vm} over the entire domain. The α-FE-b27 elements yield desirable stress values at all three points. Lastly, the performance is compared with the MITC elements in Fig. 4.35, showcasing a close approximation between the performance of the proposed and MITC elements.

4.5 Summary

The present work proposes three strain-based EAS elements, namely twenty-seven node hexahedral, six-node wedge, and eighteen-node wedge EAS elements aimed at alleviating the locking effects in conventional FEA. These elements have been obtained by investigating the equivalence between the two-field stress-based HR and VHW-based EAS formulations. The performance of the proposed elements is demonstrated through several numerical benchmark examples. The primary emphasis is on the proposed twenty-seven node hexahedral EAS elements, which offer the combined benefits of the EAS formulation and quadratic elements. The proposed twenty-seven node EAS element demonstrates higher accuracy on coarse meshes, yields result without any stress oscillations, and devoid of any unstable behavior. Further, when compared to existing eight-node brick EAS elements, the proposed elements deliver improved or similar performance, making it a compelling alternative to existing options. In addition, this study proposes novel six-node and eighteen-node wedge EAS elements that are shown to effectively mitigate the stress oscillations in locking-dominated domains. Although the emphasis of the current work is on the aforementioned EAS elements, the methodology outlined is generic and can be employed to generate a variety of EAS elements from their corresponding stress-based elements in a systematic manner.

Chapter 5

Overview of Isogeometric Analysis

The chapter presents a brief introduction of IGA. It begins with an overview of IGA, followed by a discussion on the essential mathematical preliminaries crucial for understanding fundamental concepts in geometric description using B-spline and NURBS interpolation functions. Topics covered include knot vectors, B-spline functions, the construction of B-spline geometries, and their extension to NURBS functions and geometries. Additionally, the chapter provides insights into refinement strategies used to discretize geometry in the context of IGA, along with details on the mapping of spaces involved in IGA.

5.1 Isogeometric analysis

Hughes et al. introduced the concept of IGA in 2005 to provide an efficient integration between CAD and FEA [10]. IGA discretization keeps the physical geometry intact regardless of the type or number of elements. Furthermore, once the initial coarse mesh is created, IGA simplifies the mesh refinement by removing the further dependency on CAD. This is well illustrated in Fig. 1.2, where a physical domain is discretized using different NURBS based elements. In all the cases, irrespective of the number or type of elements, the exact geometry representing the physical domain is maintained.

The fundamental idea behind the framework of IGA is to replace conventional Lagrangian interpolation functions with NURBS basis functions to approximate both geometry and field variables. The major differentiating features of IGA from a conventional FE analysis are tabulated in Table 5.1. The motivation behind utilizing this particular class of basis functions was derived from the fact that the NURBS are extensively utilized in engineering design with the advantage of modeling free form surfaces, accurately representing conic sections like circle, sphere, cylinder, etc., and the existence of numerous effective and numerically stable algorithms. Along with these, they also

Table 5.1: Differentiating features between IGA and FEA

Isogeometric analysis	**Finite element analysis**
Maintain the exact geometry.	Geometry is approximated.
Field variables are assigned at control points which may or may not lie on the geometry.	Field variables are assigned at nodes always lie on geometry.
Uses NURBS basis functions with the following properties: • Basis functions do not interpolates at control points • Non-negative for all parametric values • Partition of unity • Linear independence • Variation diminishing property	Uses Lagrangian basis function having the following properties: • Basis functions interpolates at nodes • Not restricted • Partition of unity • Linear independence

retain the essential mathematical properties like non-negativity of basis functions, linear independence, partition of unity, and variation diminishing property [12]. Due to the above merits, NURBS became a foundation for isogeometric analysis.

5.2 Mathematical preliminaries

This section focuses on a brief introduction to the fundamental concepts of geometric description using B-spline and NURBS interpolations. To comprehend the extended explanation on the topic, one can refer to Piegl and Tiller [12] or Rogers [182]. This section outlines the vital mathematical expressions for deriving the required basis interpolations in IGA formulation.

5.2.1 Knot vector

A set of non-decreasing parametric values over a specific direction is defined as a knot vector. A typical knot vector is represented as $\Xi = \{\xi_1, \xi_2, \ldots, \xi_{n+p+1}\}$ where $\xi_i \in \mathbb{R}$ (one dimensional space) with i is the knot index which varies from 1 to $n+p+1$, where p and n are degree of polynomial function and number of basis functions respectively. The knot vector decides the division of the parametric space into finite intervals which are known as knot spans. Knot vectors are categorized into two types: *uniform* and *non-uniform*. If the knots are equally spaced in the parametric space then the knot vector is said to be *uniform* otherwise it is called as *non-uniform* knot vector. Successive knots in a knot vector can have identical values which allow having multiple knot entries at the same coordinate in the parametric space. A number of repeating knots is referred as the multiplicity of a knot. If the first and last knots have $p+1$ multiplicity (i.e., repeating

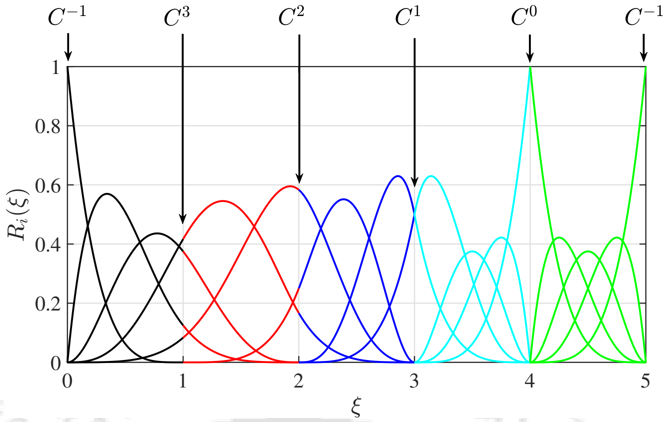

Figure 5.1: B-spline basis functions of degree four ($p = 4$) for an open, non-uniform knot vector $\boldsymbol{\Xi} = \{0, 0, 0, 0, 0, 1, 2, 2, 3, 3, 3, 4, 4, 4, 4, 5, 5, 5, 5, 5\}$ and its continuity across each knot.

$p+1$ times) then the knot vector is termed as an *open knot vector*. Multiplicity of knot also defines the continuity at that knot which is given as C^{p-k} where k is the number of repeated occurrence of a knot in a knot vector. For instance, an open knot vector in which the first and last knots are repeated $p+1$ times shows C^{-1} continuity at the extremities.

A typical example of an open knot is shown in Fig. 5.1 which shows the continuity of basis functions at each knot with respect to its multiplicity. Open knot vectors are the standards in CAD technologies. One of the important property of these knot vector is that they are interpolatory at the extremities of the parameter space, $[\xi_1, \xi_{n+p+1}]$ (first and last entry in a knot vector), and at the edges of patches in multi-dimensional model. However, they may or may not be interpolatory at internal knots. This is a distinguishing feature of the knots from the so called 'nodes' in conventional FEA.

5.2.2 B-spline basis functions

A basis function can be defined as a single curve element or piecewise polynomial which is used as a basis of linear combination to describe a specific curve. For a given knot vector $\boldsymbol{\Xi} = \{\xi_1, \xi_2, \ldots, \xi_{n+p+1}\}$, the i^{th} B-spline basis functions are defined in a recursive form as follows:

$$\text{for } p = 0, N_{i,p}(\xi) = \begin{cases} 1 & \text{if } \xi_i \leq \xi < \xi_{i+1} \\ 0 & \text{Otherwise} \end{cases}, \tag{5.1}$$

$$\text{for } p \geq 1, N_{i,p}(\xi) = \frac{\xi - \xi_i}{\xi_{i+p} - \xi_i} N_{i,p-1} + \frac{\xi_{i+p+1} - \xi}{\xi_{i+p+1} - \xi_{i+1}} N_{i+1,p-1}. \tag{5.2}$$

This is referred to as the Cox-de Boor recursion formula [12]. During the evaluation of these functions, the ratios of the form $\frac{0}{0}$ or $\frac{1}{0}$ are considered to be equal to 0. The B-spline basis functions for polynomial degree 0 and 1 will result in standard piecewise

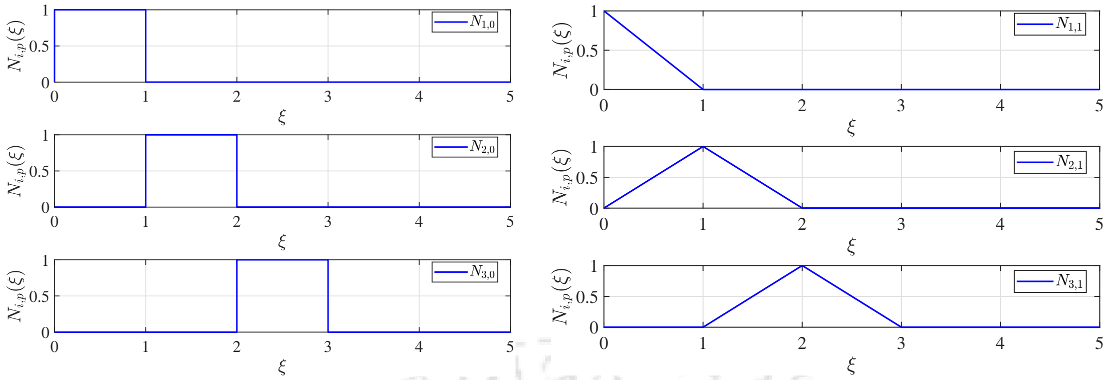

(a) $\Xi = \{0, 1, 2, 3, 4, 5\}$, $p = 0$ **(b)** $\Xi = \{0, 0, 1, 2, 3, 4, 5, 5\}$, $p = 1$

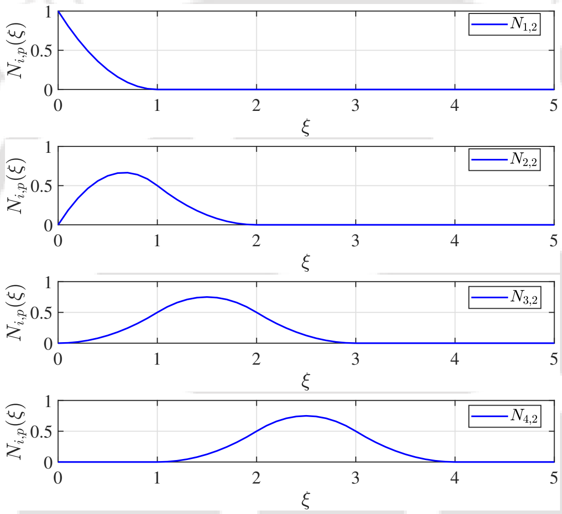

(c) $\Xi = \{0, 0, 0, 1, 2, 3, 4, 5, 5, 5\}$, $p = 2$

Figure 5.2: Selected B-spline basis functions of degree 0, 1, and 2.

constant and Lagrangian interpolation functions, respectively. However, higher-degree basis functions ($p \geqslant 2$) differ from their FEA counterparts, see Fig. 5.2. B-splines basis functions also exhibit important mathematical properties like non-negativity of basis functions, linear independence, partition of unity, and variation diminishing property [12].

Multivariate B-spline basis function are used to obtain B-spline surfaces or solids. These functions are the tensor product of univariate basis functions. A bivariate B-spline basis function can be defined as follows:

$$N_{i,j}^{p,q}(\xi, \eta) = N_{i,p}(\xi) M_{j,q}(\eta), \tag{5.3}$$

whereas a trivariate function is given as

$$N_{i,j,k}^{p,q,r}(\xi, \eta, \zeta) = N_{i,p}(\xi) M_{j,q}(\eta) L_{k,r}(\zeta), \tag{5.4}$$

where N, M and L are p, q and r^{th} degree basis function in ξ, η and ζ direction, respectively.

The derivatives of these basis functions can be derived while considering the recursive nature of the basis. For a given knot vector $\boldsymbol{\Xi}$ and polynomial order p, the k^{th} derivative of a basis function [12] is given as,

$$\frac{d^k}{d\xi^k} N_{i,p}(\xi) = \frac{p!}{(p-k)!} \sum_{j=0}^{k} \alpha_{k,j} N_{i+j,p-k}(\xi), \tag{5.5}$$

where

$$\alpha_{0,0} = 1,\ \alpha_{k,0} = \frac{\alpha_{k-1,0}}{\xi_{i+p-k+1} - \xi_i},\ \alpha_{k,j} = \frac{\alpha_{k-1,j} - \alpha_{k-1,j-1}}{\xi_{i+p+j-k+1} - \xi_{i+j}},\ \alpha_{k,k} = \frac{-\alpha_{k-1,k-1}}{\xi_{i+p+1} - \xi_{i+k}}.$$

5.2.3 B-spline curves, surfaces, and solids

A p^{th} degree B-spline curve for a given knot vector and a set of control points is defined as

$$\boldsymbol{C}(\xi) = \sum_{i=1}^{n} N_{i,p}(\xi) \boldsymbol{\mathcal{X}}_i, \tag{5.6}$$

whereas the B-spline surfaces are constructed by considering a bidirectional net of control points, two knot vectors and the tensor product of two univariate B-spline basis functions and given as

$$\boldsymbol{S}(\xi, \eta) = \sum_{i=1}^{n} \sum_{j=1}^{m} N_{i,j}^{p,q}(\xi, \eta) \boldsymbol{\mathcal{X}}_{i,j} = \sum_{i=1}^{n} \sum_{j=1}^{m} N_{i,p}(\xi) M_{j,q}(\eta)(\xi, \eta) \boldsymbol{\mathcal{X}}_{i,j}. \tag{5.7}$$

Similarly, the B-spline volumes are defined as

$$\begin{aligned} \boldsymbol{V}(\xi, \eta, \zeta) &= \sum_{i=1}^{n} \sum_{j=1}^{m} \sum_{k=1}^{l} N_{i,j,k}^{p,q,r}(\xi, \eta, \zeta) \boldsymbol{\mathcal{X}}_{i,j,k} \\ &= \sum_{i=1}^{n} \sum_{j=1}^{m} \sum_{k=1}^{l} N_{i,p}(\xi) M_{j,q}(\eta) L_{k,r}(\zeta) \boldsymbol{\mathcal{X}}_{i,j,k}, \end{aligned} \tag{5.8}$$

where n, m and l are number of basis functions in ξ, η and ζ direction, respectively. $\boldsymbol{\mathcal{X}}_i$, $\boldsymbol{\mathcal{X}}_{i,j}$, and $\boldsymbol{\mathcal{X}}_{i,j,k}$ are control point coordinates ($[x\ y\ z]^T$) for $(i)^{th}$, $(i,j)^{th}$, and $(i,j,k)^{th}$ control point.

5.2.4 NURBS basis functions

The evolution of B-spline interpolations to NURBS provides an advantage of representing a wide range of objects including conic sections like circle, sphere, cylinder, etc. NURBS are the generalization of B-splines basis functions where 'Non-Uniform' refers to a non-uniform knot vector, whereas 'Rational B-splines' describe the rationalization of B-spline basis functions. It inherits all the mathematical properties of B-splines with the added advantage of weights which allows them to offer great flexibility and accuracy in generation of CAD geometries. A univariate NURBS basis function is defined as

$$R_{i,p}(\xi) = \frac{w_i N_{i,p}(\xi)}{W(\xi)}, \tag{5.9}$$

where $W(\xi) = \sum\limits_{i=1}^{n_{cp}} w_i N_{i,p}(\xi)$ and $N_{i,p}(\xi)$ is a standard B-spline basis function, w_i is strictly positive ($w_i > 0$) set of weights associated with control points, and n_{cp} denotes the total number of control points.

A bivariate NURBS basis function can be defined as

$$\begin{aligned} R_{i,j}^{p,q}(\xi,\eta) &= R_{i,p}(\xi) R_{j,q}(\eta) \\ &= \frac{N_{i,p}(\xi) M_{j,q}(\eta) w_{i,j}}{\sum_{i=1}^{n} \sum_{j=1}^{m} N_{i,p}(\xi) M_{j,q}(\eta) w_{i,j}}, \end{aligned} \tag{5.10}$$

whereas a trivariate function is given as

$$\begin{aligned} R_{i,j,k}^{p,q,r}(\xi,\eta,\zeta) &= R_{i,p}(\xi) R_{j,q}(\eta) R_{k,r}(\zeta) \\ &= \frac{N_{i,p}(\xi) M_{j,q}(\eta) L_{k,r}(\zeta) w_{i,j,k}}{\sum_{i=1}^{n} \sum_{j=1}^{m} \sum_{k=1}^{l} N_{i,p}(\xi) M_{j,q}(\eta) L_{k,r}(\zeta) w_{i,j,k}}, \end{aligned} \tag{5.11}$$

where N, M and L are p, q and r^{th} degree B-spline basis function in ξ, η and ζ direction respectively with $w_{i,j}$ and $w_{i,j,k}$ being the weights associated with control points.

Derivative of these basis functions can be derived by simply applying quotient rule to above formulas which will eventually results in

$$\frac{d^k}{d\xi^k} R_{i,p}(\xi) = \frac{A_i^{(k)} - \sum_{j=1}^{k} \begin{pmatrix} k \\ j \end{pmatrix} W^{(j)}(\xi) \frac{d^{(k-j)}}{d\xi^{(k-j)}} R_{i,p}(\xi)}{W(\xi)} \tag{5.12}$$

where

$$\begin{pmatrix} k \\ j \end{pmatrix} = \frac{k!}{j!(k-j)!}, \; W^{(k)}(\xi) = \frac{d^k}{d\xi^k} W(\xi), \text{ and } A_i^{(k)} = w_i \frac{d^k}{d\xi^k} N_{i,p}(\xi).$$

5.2.5 NURBS curves, surfaces, and solids

A p^{th} degree NURBS curve for a given knot vector and a set of control points is defined as

$$\boldsymbol{C}(\xi) = \sum_{i=1}^{n} R_{i,p}(\xi) \boldsymbol{\mathcal{X}}_i = \sum_{i=1}^{n} \frac{w_i N_{i,p}(\xi)}{\sum_{\alpha=1}^{n} w_\alpha N_{\alpha,p}(\xi)} \boldsymbol{\mathcal{X}}_i. \tag{5.13}$$

The NURBS surfaces are constructed by considering a bidirectional net of control points, two knot vectors and the tensor product of two univariate NURBS basis functions and given as

$$\begin{aligned}\boldsymbol{S}(\xi,\eta) &= \sum_{i=1}^{n}\sum_{j=1}^{m} R_{i,j}^{p,q}(\xi,\eta)\boldsymbol{\mathcal{X}}_{i,j}\\ &= \sum_{i=1}^{n}\sum_{j=1}^{m} R_{i,p}(\xi)R_{j,q}(\eta)\boldsymbol{\mathcal{X}}_{i,j},\\ &= \sum_{i=1}^{n}\sum_{j=1}^{m} \frac{N_{i,p}(\xi)M_{j,q}(\eta)w_{i,j}}{\sum_{\alpha=1}^{n}\sum_{\beta=1}^{m} N_{\alpha,p}(\xi)M_{\beta,q}(\eta)w_{\alpha,\beta}}\boldsymbol{\mathcal{X}}_{i,j},\end{aligned} \tag{5.14}$$

and the NURBS volumes are defined as

$$\begin{aligned}\boldsymbol{V}(\xi,\eta,\zeta) &= \sum_{i=1}^{n}\sum_{j=1}^{m}\sum_{k=1}^{l} R_{i,j,k}^{p,q,r}(\xi,\eta,\zeta)\boldsymbol{\mathcal{X}}_{i,j,k}\\ &= \sum_{i=1}^{n}\sum_{j=1}^{m}\sum_{k=1}^{l} R_{i,p}(\xi)R_{j,q}(\eta)R_{k,r}(\zeta)\boldsymbol{\mathcal{X}}_{i,j,k},\\ &= \sum_{i=1}^{n}\sum_{j=1}^{m}\sum_{k=1}^{l} \frac{N_{i,p}(\xi)M_{j,q}(\eta)L_{k,r}(\zeta)w_{i,j,k}\boldsymbol{\mathcal{X}}_{i,j,k}}{\sum\limits_{\alpha=1}^{n}\sum\limits_{\beta=1}^{m}\sum\limits_{\gamma=1}^{l} N_{\alpha,p}(\xi)M_{\beta,q}(\eta)L_{\gamma,r}(\zeta)w_{\alpha,\beta,\gamma}},\end{aligned} \tag{5.15}$$

where $R_{i,p}(\xi)$, $R_{i,j}^{p,q}(\xi,\eta)$, and $R_{i,j,k}^{p,q,r}(\xi,\eta,\zeta)$ are the univariate, bivariate and trivariate NURBS basis functions, $N_{i,p}(\xi)$, $M_{j,q}(\eta)$ and $L_{k,r}(\zeta)$ are the B-spline interpolation functions of degree p, q, and r in ξ, η, and ζ directions, respectively, w_α, $w_{\alpha,\beta}$, and $w_{\alpha,\beta,\gamma}$ are strictly positive weights associated with the respective control points. The fundamental properties of the NURBS basis functions are outlined as follows:

1. The NURBS basis functions follows the partition of unity property: $\sum_{i=1}^{p+1} R_{i,p}(\xi) = 1$
2. The continuity and support are similar to B-spline basis functions, i.e., in absence of repeated knots continuity of $p-1$ order is maintained, whereas with repetition of knot by k times, its continuity decrease by k.
3. The NURBS basis functions are positive over the complete parametric domain similar to B-splines (one can see in Fig. 5.1): $R_{i,p}(\xi) \geq 0$
4. If the weights associated with each control point are kept equal, the expressions of NURBS basis functions will reduce to standard B-spline interpolation functions.
5. NURBS exhibit affine covariance property which assures that any transformation on a NURBS curve is evaluated by applying the transformation directly to the control points.
6. NURBS surfaces and solids are the projective transformations of tensor product, piecewise polynomial entities.

5.3 Refinement strategies

An inherent advantage of incorporating CAD polynomials within the framework of IGA lies in the ease of refinement of the constructed geometries. The two fundamental methods employed for geometry refinement are *knot insertion*, wherein additional knots or elements are introduced into a designated knot vector, and *order elevation*, a process that elevates the interpolation order of the basis functions. A specific refinement strategy, denoted as *k-refinement*, involves the application of knot insertion followed by order elevation. These methodologies provide a desired control over parameters such as knot span or mesh size, inter-element continuity, and interpolation order of the underlying basis functions. Importantly, these controls are exerted while preserving the exact geometry and its parameterization. Another big advantage is that, once the geometry is constructed, all the above refinements can be done without further interaction with the CAD software.

5.3.1 Knot insertion or h-refinement

The knot insertion or h-refinement strategy is the process that introduces a new knot into an existing knot vector. The results is similar to the h-refinement strategy in FEA where the number of elements are increased without increasing the order of elements. Analogous refinement is done in IGA but with the help of knot vectors. Adding a unique knot into the knot vector will increase the number of knot span which are responsible for discretization of domain. In simpler words, more the knot spans more the number of elements. Employing the knot insertion strategy preserves the geometry and parametrization of the curve, however it introduces an extra basis function and, consequently, an additional control point. Moreover, the expressions of the basis functions undergoes modification, although the order of the basis functions remains unchanged. A typical example of h-refinement is shown in Fig. 5.3. Here, a curve initially composed of two elements undergoes further meshing, resulting in four elements of the same degree. This refinement is achieved by the introduction of knots, i.e., 0.25 and 0.75, into the existing knot vector.

To understand the underlying concept, consider a knot vector $\Xi = \{\xi_1, \xi_2, \ldots, \xi_{n+p+1}\}$ to model the initial geometry. Let $\bar{\Xi} = \{\bar{\xi_1}, \bar{\xi_2}, \ldots\}$ be the new knots to be inserted in order to discretized the geometry into more number of elements without affecting the geometry. This is achieved by a transformation given as follows:

$$\bar{\mathcal{P}} = \boldsymbol{T}^{\mathrm{h}}_{\mathrm{ref}} \mathcal{P}, \tag{5.16}$$

where $\mathcal{P}$ and $\bar{\mathcal{P}}$ are the existing and new control points vector, respectively and $\boldsymbol{T}^{\mathrm{h}}_{\mathrm{ref}}$ is the transformation matrix responsible to determine new set of control points. The

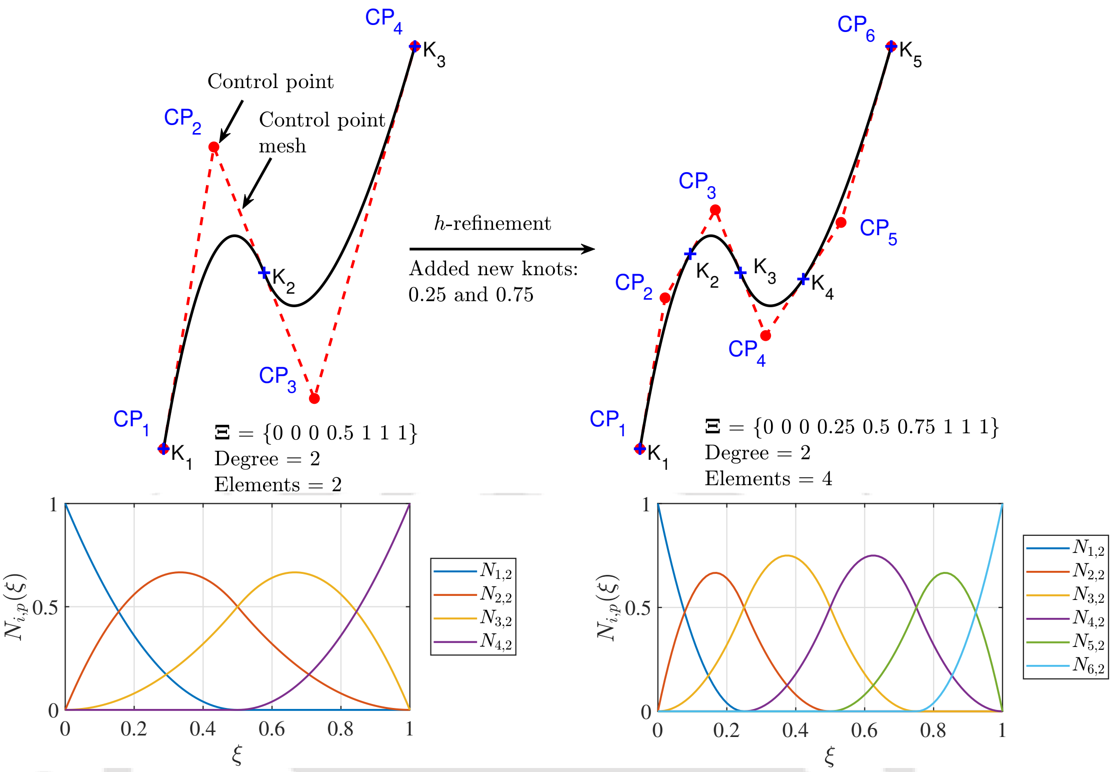

Figure 5.3: Knot insertion or *h*-refinement procedure: Visualizing transformations in the initial curve, basis functions, and control points before and after refinement. (Weights assigned to each control point are unity; hence, NURBS and B-spline basis functions are identical.)

evaluation of $\boldsymbol{T}^{\mathrm{h}}_{\mathrm{ref}}$ is carried out with another recursive formula defined as follows:

$$(T^{\mathrm{h}}_{\mathrm{ref}})^{0}_{ij} = \begin{cases} 1 & \text{if } \bar{\xi}_i \in [\xi_j, \xi_{j+1}) \\ 0 & \text{Otherwise} \end{cases}, \tag{5.17}$$

$$(T^{\mathrm{h}}_{\mathrm{ref}})^{k+1}_{ij} = \frac{\bar{\xi}_{i+k} - \xi_j}{\xi_{j+k} - \xi_j}(T^{\mathrm{h}}_{\mathrm{ref}})^{k}_{ij} + \frac{\xi_{j+k+1} - \bar{\xi}_{i+k}}{\xi_{j+k+1} - \xi_{j+1}}(T^{\mathrm{h}}_{\mathrm{ref}})^{k}_{ij+1}, \tag{5.18}$$

where $k = 0,\ 1,\ 2,\ \ldots,\ p-1$ and p is the degree of basis function. There exist numerous efficient algorithm to incorporate the stated conditions which is quite convenient and effective than meshing efforts required in conventional FEA.

5.3.2 Order elevation or *p*-refinement

The second method for enhancing basis functions is the order elevation or *p*-refinement strategy. This strategy, as the name suggests, increases the interpolation order of the underlying basis functions utilized to represent the geometry and solution field rather than the number of elements. One way to elevate the order of NURBS basis functions with an extra knot at the extremities of knot vector. It differs from *h*-refinement in the sense that the knots are added in such a way that they will not create an additional knot

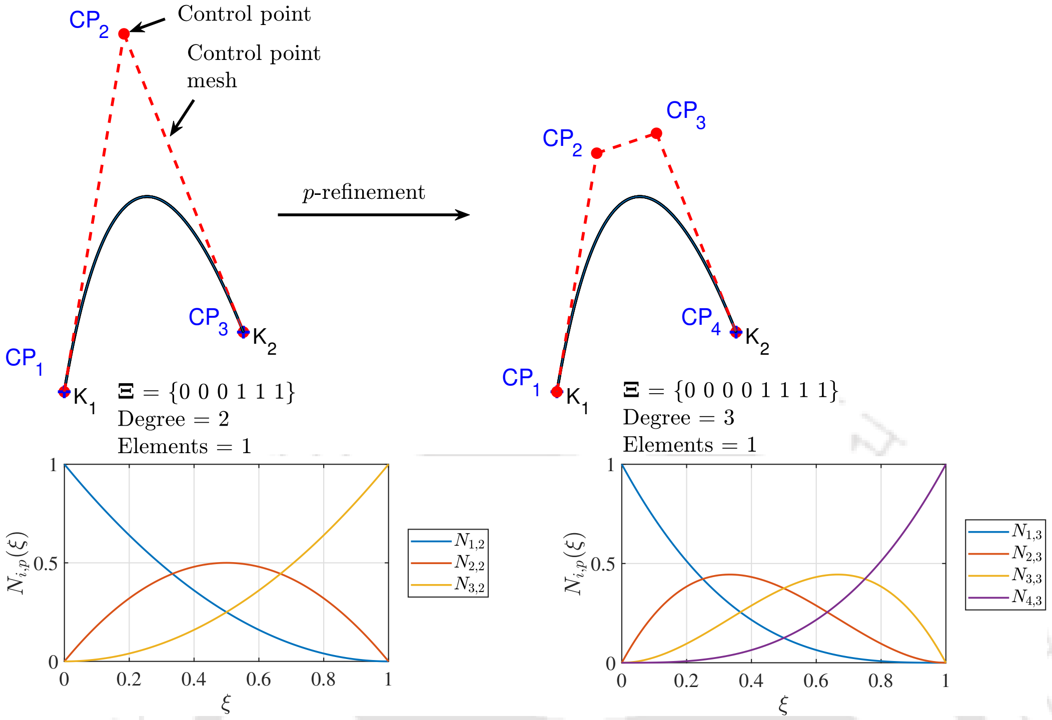

(a) Case 1: Degree and continuity is elevated

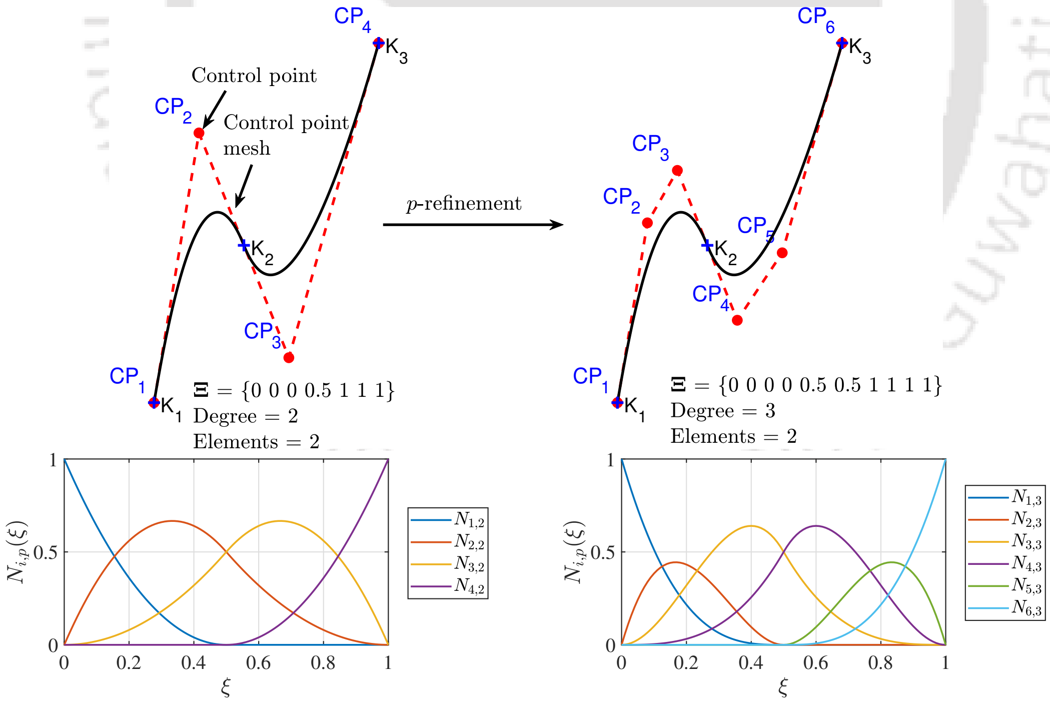

(b) Case 2: Original continuity is maintained at intermittent knots

Figure 5.4: Order elevation or p-refinement procedure: Visualizing transformations in the initial curve, basis functions, and control points before and after refinement. (Weights assigned to each control point are unity; hence, NURBS and B-spline basis functions are identical.)

span but adding knots at the extremities to maintain the multiplicity with the order of the NURBS. A typical example of p-refinement is illustrated in Fig. 5.4a, where C^1 continuous second degree curve is refined into a C^2 continuous third degree curve.

It is also possible to elevate the degree without affecting the continuity of the knots which can be achieved by adding a knot at extremities as well increasing the multiplicity (k) of each knot in-between, see Fig. 5.4b. For example p^{th} order basis function for a particular knot vector with continuity C^{p-k-1}. For no multiplicity, the continuity will be C^{p-1}. Assume adding as extra knot which will increase the order of basis function to q, so the continuity will now be C^{q-k-1}. But once the multiplicity of each knot increased to $k = q - p$, knots will maintain the initial C^{p-1} continuity. The above refinement is conveniently achieved once the initial low order coarse mesh model is created and so eliminating the need to go too and fro with the CAD description.

5.3.3 k-refinement

The k-refinement strategy has found predominant use in diverse applications of IGA in comparison to order elevation. This prevalence is attributed to its advantageous characteristic, which concurrently increases both inter-element continuity and the interpolation degree of the basis functions. No similar strategies exists in conventional FEA. As discussed in Section 5.2.1, the maximum level of continuity achievable at a unique knot value for a p^{th} degree basis function is $C^{(p-1)}$. In the execution of k-refinement, the initial interpolation order of the original p-degree functions, possessing $C^{(p-1)}$ continuity, is increased to the desired value. Each step of order elevation results in increase in the continuity of the basis functions, considering the coarsest conceivable form of the knot vector for a given geometry. Subsequently, the specified knot values are introduced, thereby generating new elements in the process. In summary, it performs the degree elevation of the coarsest possible geometry followed by knot insertion, which leads to the basis functions of desired degree with better continuity with same number of elements.

A typical example of k-refinement is shown in Fig. 5.5. In the first case, the original curve is refined by initially performing knot insertion or h-refinement followed by p-refinement, as illustrated in Fig. 5.5a. This results in a mesh of two elements of cubic degree; however, the inter-element continuity at knot 0.5 is restricted to C^1. On the contrary, in the second case, both the degree and continuity of the curve are increased at the end of the refinement process. Furthermore, the number of control points in the case of k-refinement is fewer than that in the first case, even though both scenarios result in an identical number of elements. Another example of k-refinement is presented in Fig. 5.6, demonstrating a distinct advantage in terms of elevated continuity and higher-degree basis functions, achieved with a reduced number of control points, while maintaining an equivalent number of elements.

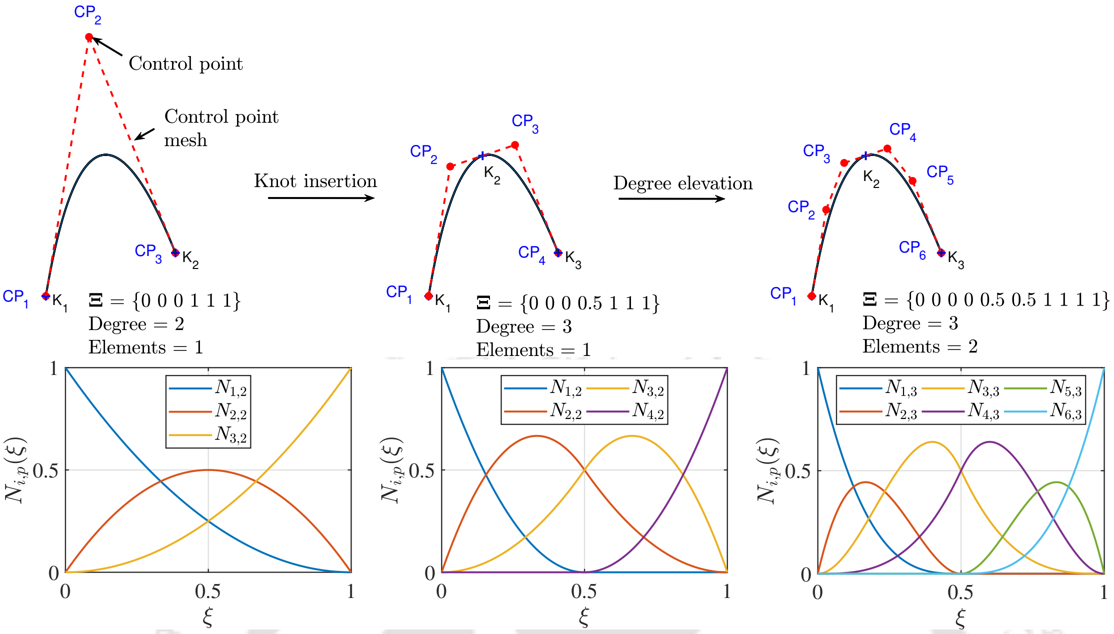

(a) Case 1: Knot insertion followed by degree elevation

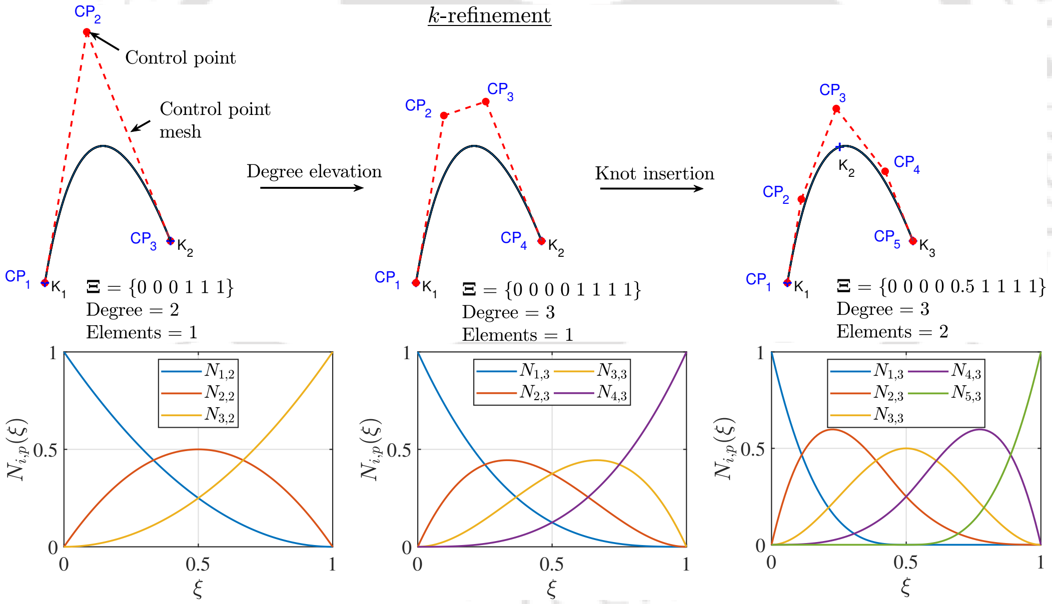

(b) Case 2: k-refinement (Degree elevation followed by knot insertion)

Figure 5.5: k-refinement procedure: Visualizing transformations in the initial curve, basis functions, and control points before and after refinement. (Weights assigned to each control point are unity; hence, NURBS and B-spline basis functions are identical.)

5.4 Mappings involved while handling NURBS basis function

To compute the integrals associated with element stiffness matrix and element force vector, Gauss–Legendre quadrature rule is applied. The process is similar to FE but the

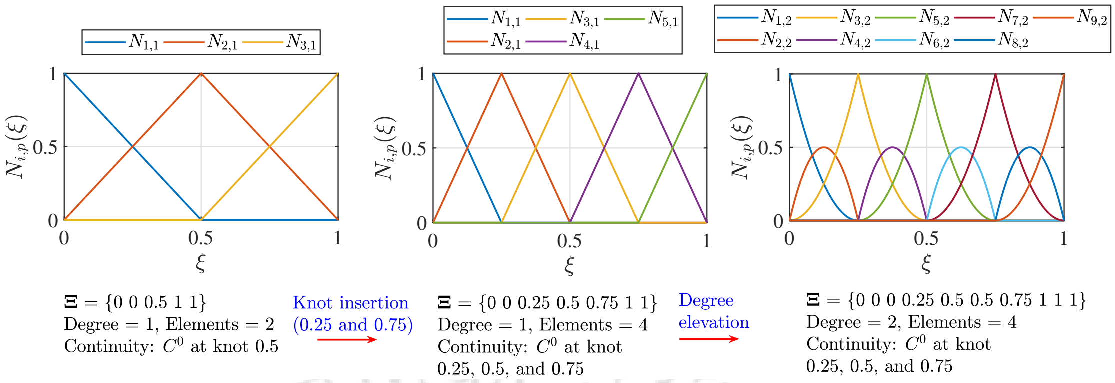

(a) Case 1: Knot insertion followed by degree elevation.

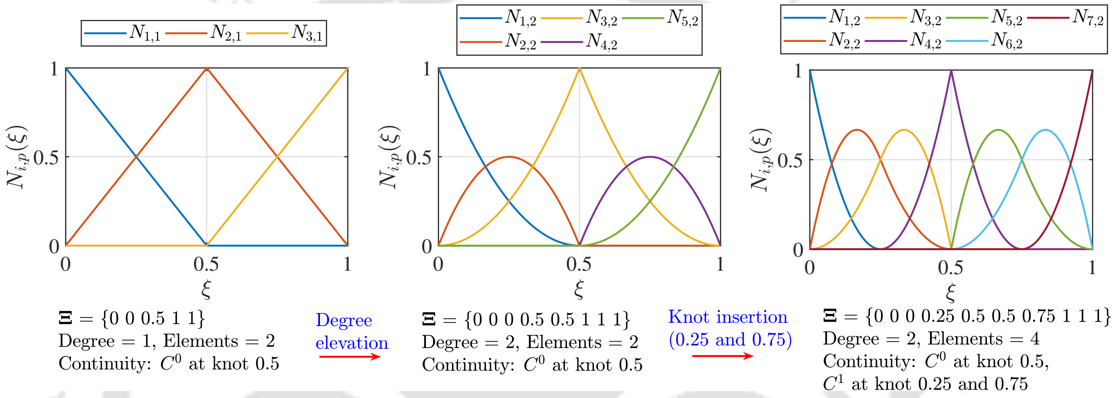

(b) Case 2: Degree elevation followed by knot insertion. (k-refinement)

Figure 5.6: Alteration in continuity of NURBS basis functions during k-refinement. (Weights assigned to each control point are unity; hence, NURBS and B-spline basis functions are identical.)

major difference in IGA is the involvement of two different mapping spaces to get the prescribed format of Gauss-Legendre quadrature rule. In convectional FEA, elements are represented in the parent domain and in the physical space. When it comes to IGA, elements have three spaces. One in physical space (Ω), another in parametric space ($\hat{\Omega}$) and last one in parent or master space ($\tilde{\Omega}$) as shown in Fig. 5.7. Apart from above mentioned spaces, there is one other important notion which is the index space of a patch which identifies each knot separately irrespective of its multiplicity and discretizes the space accordingly. Also, a NURBS based geometry will have two notions of mesh. One is control mesh which is defined by control points and other one is physical mesh which divides the complete domain into number of sub-domains. These sub-domains are often called as micro-elements or patches.

5.4.1 Mapping of the physical space (Ω) to parametric space ($\hat{\Omega}$)

Let us consider an equation for element stiffness matrix, i.e., $\boldsymbol{K}_e = \int_{\Omega^e} \boldsymbol{B}^T \boldsymbol{C} \boldsymbol{B} \, \mathrm{d}\Omega$. First mapping, from physical space to parametric space (Ω to $\hat{\Omega}$), can be derived with the

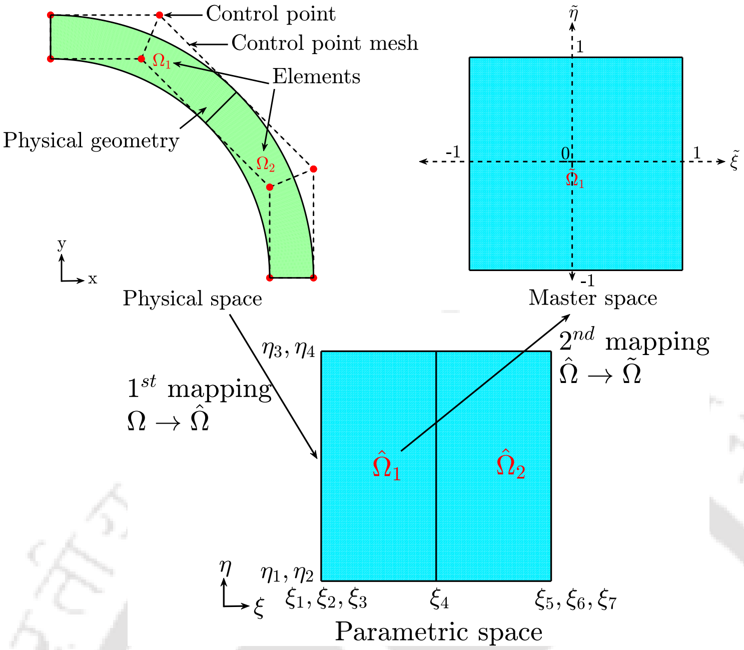

Figure 5.7: Mapping and different spaces involved in IGA framework

help of formula for NURBS surface which relates the physical space with parametric space and given as follows:

$$\boldsymbol{S}(\xi,\eta) = \begin{Bmatrix} x \\ y \\ z \end{Bmatrix} = \sum_{i=1}^{n}\sum_{j=1}^{m} R_{i,j}^{p,q}(\xi,\eta) \begin{Bmatrix} \mathcal{X}_{i,j}^{x} \\ \mathcal{X}_{i,j}^{y} \\ \mathcal{X}_{i,j}^{z} \end{Bmatrix} \tag{5.19}$$

For the 2D problems, the choice of control points ($\boldsymbol{\mathcal{X}}_{i,j}$) will be in such a way that z will always be equal to 0 which leads to following expressions:

$$x = \sum_{i=1}^{n}\sum_{j=1}^{m} R_{i,j}^{p,q}(\xi,\eta)\mathcal{X}_{i,j}^{x}, \text{ and } y = \sum_{i=1}^{n}\sum_{j=1}^{m} R_{i,j}^{p,q}(\xi,\eta)\mathcal{X}_{i,j}^{y}. \tag{5.20}$$

Hence, the Jacobian ($\boldsymbol{J}_1$) that relates Ω and $\hat{\Omega}$ can be written as:

$$\boldsymbol{J}_1 = \begin{bmatrix} \dfrac{\partial x}{\partial \xi} & \dfrac{\partial x}{\partial \eta} \\ \dfrac{\partial y}{\partial \xi} & \dfrac{\partial y}{\partial \eta} \end{bmatrix}, \tag{5.21}$$

where

$$\frac{\partial x}{\partial \xi} = \sum_{k=1}^{n_{cp}^{e}} \frac{\partial R_k}{\partial \xi}\mathcal{X}_k^{x}, \quad \frac{\partial x}{\partial \eta} = \sum_{k=1}^{n_{cp}^{e}} \frac{\partial R_k}{\partial \eta}\mathcal{X}_k^{x}, \quad \frac{\partial y}{\partial \xi} = \sum_{k=1}^{n_{cp}^{e}} \frac{\partial R_k}{\partial \xi}\mathcal{X}_k^{y}, \quad \frac{\partial y}{\partial \eta} = \sum_{k=1}^{n_{cp}^{e}} \frac{\partial R_k}{\partial \eta}\mathcal{X}_k^{y}.$$

Here, n_{cp}^{e} is the total number of control points per element and k denotes the global numbering assigned to the control points/basis function for a specific combination of i and j. Using the above relations, the first mapping of stiffness matrix can be given as

$$\Omega \rightarrow \hat{\Omega} : \quad \int_x \int_y \boldsymbol{B}^T \boldsymbol{C} \boldsymbol{B} \, \mathrm{d}x \, \mathrm{d}y \rightarrow \int_{\xi_{ui}}^{\xi_{ui+1}} \int_{\eta_{uj}}^{\eta_{uj+1}} \boldsymbol{B}^T \boldsymbol{C} \boldsymbol{B} \, |\boldsymbol{J}_1| \, \mathrm{d}\xi \, \mathrm{d}\eta, \tag{5.22}$$

where ξ varies from ξ_{ui} to ξ_{ui+1} and η varies from η_{uj} to η_{uj+1}. The index ui and uj represents the unique knot entires in corresponding knot vectors.

5.4.2 Mapping of the parametric space ($\hat{\Omega}$) to the master space ($\tilde{\Omega}$)

Second mapping is linear or affine mapping which relates the parametric space to the master space and relation is given as follows:

$$\xi(\tilde{\xi}, \tilde{\eta}) = \frac{1}{2}[(\xi_{i+1} - \xi_i)\tilde{\xi} + (\xi_{i+1} + \xi_i)], \tag{5.23}$$

$$\eta(\tilde{\xi}, \tilde{\eta}) = \frac{1}{2}[(\eta_{j+1} - \eta_j)\tilde{\eta} + (\eta_{j+1} + \eta_j)]. \tag{5.24}$$

Hence, the Jacobian ($\boldsymbol{J}_2$) that relates $\hat{\Omega}$ and $\tilde{\Omega}$ can be written as:

$$\boldsymbol{J}_2 = \begin{bmatrix} \dfrac{\partial \xi}{\partial \tilde{\xi}} & \dfrac{\partial \xi}{\partial \tilde{\eta}} \\ \dfrac{\partial \eta}{\partial \tilde{\xi}} & \dfrac{\partial \eta}{\partial \tilde{\eta}} \end{bmatrix} = \begin{bmatrix} \dfrac{\partial \xi}{\partial \tilde{\xi}} & 0 \\ 0 & \dfrac{\partial \eta}{\partial \tilde{\eta}} \end{bmatrix}, \tag{5.25}$$

where $\dfrac{\partial \xi}{\partial \tilde{\xi}} = \dfrac{1}{2}(\xi_{i+1} - \xi_i)$ and $\dfrac{\partial \eta}{\partial \tilde{\eta}} = \dfrac{1}{2}(\eta_{j+1} - \eta_j)$. Using the above relations, the second mapping of stiffness matrix can be given as

$$\hat{\Omega} \rightarrow \tilde{\Omega} : \quad \int_\xi \int_\eta \boldsymbol{B}^T \boldsymbol{C} \boldsymbol{B} \, |\boldsymbol{J}_1| \, \mathrm{d}\xi \, \mathrm{d}\eta \rightarrow \int_{-1}^{1} \int_{-1}^{1} \boldsymbol{B}^T \boldsymbol{C} \boldsymbol{B} \, |\boldsymbol{J}_1| \, |\boldsymbol{J}_2| \, \mathrm{d}\tilde{\xi} \, \mathrm{d}\tilde{\eta}, \tag{5.26}$$

where $\tilde{\xi}$ and $\tilde{\eta}$ varries from -1 to 1 which is a standard form for applying Gauss-Legendre quadrature rule.

5.5 Imposition of boundary conditions

Different types of boundary conditions encountered during the solution procedure are Dirichlet boundary conditions, Neumann boundary conditions, and Robin boundary conditions. The numerical examples presented in the current work deal with the homogeneous Dirichlet boundary condition, i.e., $\boldsymbol{u} = 0$ on displacement boundary, which can be imposed by setting the corresponding control variables as zero. The process includes identifying the control points responsible for modeling the boundary of interest and restricting the degrees of freedom corresponding to identified control points. However, special treatment needs to be followed if there is a need to restrict a single point on the domain. In such a case, ensuring the control point lies on the geometry and at a point interest is mandatory. This can be achieved by reducing the continuity at that location to C^{-1} and then restricting the point of interest.

In IGA, the control point may or may not lie on the geometry. Hence, a distinctive treatment is required when imposing inhomogeneous boundary conditions. NURBS basis functions, owing to their higher C^{p-1} continuity, typically do not interpolate across all control points defining the geometry. In this context, the enforcement procedure for inhomogeneous Dirichlet boundary conditions changes in IGA. One such process to impose these conditions is the least square minimization method [13].

In summary, the chapter presents an overview of IGA and the underlying concepts that distinguish it from the conventional FEA. The concepts introduced in this chapter form the foundation for comprehending the IGA principles in Chapter 6 and 7.

Chapter 6

HR Principle-based Hybrid Elements in NURBS-based IGA[‡,§]

In the present chapter, we propose stress-based hybrid solid elements to alleviate locking in IGA. The key highlight of the present work is the evaluation of stress interpolation functions for HR principle-based hybrid elements in NURBS-based IGA. These stress interpolation functions have been derived systemically for various orders of NURBS displacement interpolation. Further, we show mathematically that the choice of the stress interpolation functions is free from spurious zero-energy modes. Additionally, the chapter demonstrates the efficacy and robustness of the proposed elements with the treatment of several 2D and 3D linear-elastic benchmark problems alongside the conventional single-field IGA, Lagrangian-based FEA, and hybrid FEA formulation.

6.1 Introduction

The IGA was conceptualized by Hughes et al. [10] to provide an efficient integration of CAD and FEA. Through this seamless integration, the IGA significantly minimizes the effort required in pre-processing to create an analysis-ready model. Moreover, the ability to provide exact geometry in the analysis framework, convenience in achieving the higher inter-element continuity, and appreciably lower reliance on CAD for successive refinement strategies [11] complements the growing interest in IGA.

Since its introduction, IGA has been widely practiced in different directions and proved to be the powerful method that out-perform FEA in most of the numerical aspects, see Section 1.2.2. However, similar to FEA, IGA suffers from locking [183] and

---

[‡] D. S. Bombarde, S. S. Gautam, A. Nandy, "A novel hybrid isogeometric element based on two-field Hellinger–Reissner principle to alleviate different types of locking", *Sadhana* (2022), 47:148. https://doi.org/10.1007/s12046-022-01867-6

[§] D. S. Bombarde, M. Agrawal, S. S. Gautam, A. Nandy, "Hellinger–Reissner principle based stress–displacement formulation for three-dimensional isogeometric analysis in linear elasticity", *Computer Methods in Applied Mechanics and Engineering* 394 (2022) 114920. https://doi.org/10.1016/j.cma.2022.114920 displays over-stiff behavior along with the high oscillations of the resulting stresses on a range of applications. Locking also contributes to low convergence rates and yields unrealistic solutions within a practical range of discretization, thereby adversely impacting solution accuracy in IGA.

In the literature, several attempts have been made to alleviate the locking in the context of IGA, see Section 1.5. However, most of the explored contributions in the development of locking-free mixed formulations in NURBS-based IGA are restricted to the strain-based approaches. The formulations derived from the stress-based approaches, which have shown great potential in conventional FEM [147–151], have been given limited attention. The stress-based formulations are known to provide a stable, robust, and efficient formulation, whereas strain-based approaches often need stabilization [135, 184]. The stress-based improvements in the context of IGA-based shell formulations have been explored in the work of Echter et al. [32, 146] to address the membrane locking in various shell models. Furthermore, in [144, 145] the application of the HR principle in shell elements is presented. However, the stated shell formulations utilize the kinematic assumptions, restricting their applicability to relatively thin geometries.

The absence of stress-based mixed formulation has inspired the present work on the development of a robust class of stress-based solid hybrid elements in the IGA framework for linear elasticity problems. The NURBS-based hybrid elements are constructed based on a two-field HR variational principle that effectively provides a locking-free response regardless of the type of locking. The formulation involves independent interpolation techniques for approximating the two field variables. Standard NURBS interpolation functions are utilized for approximating the displacement field, whereas the unique stress interpolation functions are proposed to approximate the stress field variable. Evaluation of these interpolations is inspired by the principles explored by Jog [141, 142] for Lagrangian-based FEA. However, the recursive nature and higher-continuity properties of the NURBS interpolation contribute to higher complexity in the derivation of the stress interpolation function.

The efficacy and stability of the stress-based hybrid elements are strongly dependent on the choice of interpolation functions used for the stress field. The present work proposes the systematic derivation of the stress field interpolation functions for cubic and quadratic NURBS elements. To ensure the stability of the proposed formulation, it has been shown that there is no presence of spurious zero-energy modes, and the stiffness matrix is going to be full rank after suppressing the rigid body modes. Even in conventional FEA, the literature for hybrid elements is restricted to linear and quadratic elements and has not been explored for higher degree elements. So, the derivation of the participating spurious energy modes and their treatment to provide a stable formulation for cubic elements is another unique addition of the present study. The elements derived from the stated approach provide a locking-free response during the analysis of thin structural geometries or problems involving almost incompressible materials in the setting of linear elasticity. Moreover, unlike shell formulations [32], the developed elements can be used for both ‘thin’ and ‘chunky’ [142] geometries since they do not involve any kinematic assumptions.

The rest of the chapter is organized as follows: **Section 6.2** briefly recollects the underlying concepts in the two-field stress-based HR variational principle in the IGA framework. **Section 6.3** includes a step-wise implementation strategy with the required algorithms and devotes particular focus on evaluating proposed stress interpolation functions for different NURBS-based elements. **Section 6.4** addresses the assessment of the method on several benchmark numerical examples. Finally, **Section 6.5** summarizes the work and additional supporting information is provided in the **Appendix**.

6.2 Introduction to two-field hybrid IGA formulation

The current section briefly revisits the foundational concepts of two-field stress-based HR variational principle. These concepts play a pivotal role in enhancing the overall completeness of the chapter.

6.2.1 Stress-based HR variational principle

The HR variational principle comprises of two independent field variables, i.e., displacement and stress. Let $\boldsymbol{u}$ and $\boldsymbol{\sigma}$ be the independent displacement and stress field, respectively, while $\delta\boldsymbol{u}$ and $\delta\boldsymbol{\sigma}$ represent their respective variations in such a way that

$$\mathcal{V}_{\boldsymbol{u}} = \Big\{ \delta\boldsymbol{u} \in \mathcal{H}^1(\mathcal{R}) : \delta\boldsymbol{u} = \boldsymbol{0} \text{ on } \partial\mathcal{R}_u \Big\}, \tag{6.1}$$

$$\mathcal{V}_{\boldsymbol{\sigma}} = \Big\{ \delta\boldsymbol{\sigma} \in \mathcal{L}^2(\mathcal{R}) : \delta\boldsymbol{\sigma} = \delta\boldsymbol{\sigma}^T \Big\}, \tag{6.2}$$

where $\mathcal{V}_{\boldsymbol{u}}$ and $\mathcal{V}_{\boldsymbol{\sigma}}$ are the spaces associated with the admissible variations $\delta\boldsymbol{u}$ and $\delta\boldsymbol{\sigma}$, respectively. For the linear elasticity problem defined in Section 2.1, the resulting variational statement can be expressed as follows:

$$\int_{\mathcal{R}} (\delta\bar{\varepsilon}^u)^T \bar{\boldsymbol{\sigma}} d\mathcal{R} = \int_{\mathcal{R}} \delta\boldsymbol{u}^T \boldsymbol{b} d\mathcal{R} + \int_{\partial\mathcal{R}_t} \delta\boldsymbol{u}^T \bar{\boldsymbol{t}} dA \qquad \forall\, \delta\boldsymbol{u} \in \mathcal{V}_{\boldsymbol{u}}, \tag{6.3}$$

$$\int_{\mathcal{R}} \delta\bar{\boldsymbol{\sigma}}^T \left[\bar{\varepsilon}^u(\boldsymbol{u}) - \boldsymbol{C}^{-1}\bar{\boldsymbol{\sigma}} \right] d\mathcal{R} = 0 \qquad \forall\, \delta\bar{\boldsymbol{\sigma}}, \tag{6.4}$$

where $\bar{\boldsymbol{\sigma}}$ and $\bar{\varepsilon}^u$ are the vector representations of $\boldsymbol{\sigma}$ and $\boldsymbol{\varepsilon}^u$, respectively and $\boldsymbol{C}$ is the material constitutive tensor. A more comprehensive exploration of the topic is presented in Section 2.4.

6.2.2 Approximating functions

As a standard practice in IGA, NURBS basis functions are used to interpolate the the displacement field ($\boldsymbol{u}$) rather than the conventional Lagrangian interpolation functions.

Hence, $\boldsymbol{u}$ can be interpolated as follows:

$$\boldsymbol{u} = \sum_{I=1}^{n^e_{cp}} R_I \tilde{u}_I = \boldsymbol{R}\tilde{\boldsymbol{u}}, \quad \delta\boldsymbol{u} = \sum_{I=1}^{n^e_{cp}} R_I \delta\tilde{u}_I = \boldsymbol{R}\delta\tilde{\boldsymbol{u}}, \tag{6.5}$$

where I is the global index associated with the control point net, and n^e_{cp} is the total number of control points per element. The displacement vector $\tilde{\boldsymbol{u}}$ is associated with the control points, which may or may not lie on the physical domain. The term R_I represents the trivariate $(R^{p,q,r}_{\alpha,\beta,\gamma}(\xi,\eta,\zeta))$ or bivariate $(R^{p,q}_{\alpha,\beta}(\xi,\eta))$ NURBS basis function with I as a unique global number assigned for every combination of α, β, and γ. The detailed expressions for these functions are discussed in Chapter 5. The basis function matrix ($\boldsymbol{R}$) and displacement vector ($\tilde{\boldsymbol{u}}$) can be written as

$$\tilde{\boldsymbol{u}} = \begin{bmatrix} \tilde{u}_1 & \tilde{u}_2 & \dots & \tilde{u}_{3n^e_{cp}} \end{bmatrix}^T, \ \boldsymbol{R} = \begin{bmatrix} \bar{R}_1 & \bar{R}_2 & \dots & \bar{R}_{n^e_{cp}} \end{bmatrix} \text{ where, } \bar{R}_i = \begin{bmatrix} R_i & 0 & 0 \\ 0 & R_i & 0 \\ 0 & 0 & R_i \end{bmatrix}. \tag{6.6}$$

Secondly, the vector form of stress field ($\tilde{\boldsymbol{\sigma}}$) and its variation ($\delta\tilde{\boldsymbol{\sigma}}$) in the natural coordinates are interpolated as:

$$\tilde{\boldsymbol{\sigma}} = \tilde{\boldsymbol{P}}\hat{\boldsymbol{\beta}}, \qquad \delta\tilde{\boldsymbol{\sigma}} = \tilde{\boldsymbol{P}}\delta\hat{\boldsymbol{\beta}}, \tag{6.7}$$

where $\tilde{\boldsymbol{\sigma}} = \begin{bmatrix} \sigma_{\tilde{\xi}\tilde{\xi}} & \sigma_{\tilde{\eta}\tilde{\eta}} & \sigma_{\tilde{\zeta}\tilde{\zeta}} & \sigma_{\tilde{\xi}\tilde{\eta}} & \sigma_{\tilde{\eta}\tilde{\zeta}} & \sigma_{\tilde{\xi}\tilde{\zeta}} \end{bmatrix}^T$, $\boldsymbol{P}$ is the stress interpolation matrix, $\hat{\boldsymbol{\beta}}$ and $\delta\hat{\boldsymbol{\beta}}$ are the vectors consisting of the stress parameters and stress variation parameters, respectively. The stresses $\tilde{\boldsymbol{\sigma}}(\tilde{\xi},\tilde{\eta},\tilde{\zeta})$ are related with the stresses in physical space $(\bar{\boldsymbol{\sigma}}(x,y,z))$ with the following transformation:

$$\bar{\boldsymbol{\sigma}}(x,y,z) = \boldsymbol{T}\tilde{\boldsymbol{\sigma}}(\tilde{\xi},\tilde{\eta},\tilde{\zeta}), \tag{6.8}$$

where $\boldsymbol{T}$ is the transformation matrix that relates the corresponding spaces, see Eq. 2.24. As IGA involves two mapping spaces, it is essential to note that the Jacobian used to evaluate $\boldsymbol{T}$ is defined as $\boldsymbol{J} = \boldsymbol{J}_2\boldsymbol{J}_1$, where $\boldsymbol{J}_1$ and $\boldsymbol{J}_2$ are the Jacobians for mapping parametric space to physical space and master space to parametric space, respectively. Further, the matrix $\boldsymbol{P}$ in physical space is related with the stress interpolation matrix in master space ($\tilde{\boldsymbol{P}}$) with the following transformation:

$$\boldsymbol{P} = \boldsymbol{T}\tilde{\boldsymbol{P}}, \tag{6.9}$$

The solution accuracy and stability of hybrid elements are strongly dependent on the selection of $\tilde{\boldsymbol{P}}$. The unique NURBS-compatible stress interpolations are derived in detail in the subsequent sections.

6.2.3 Elemental IGA equations for two-field variation principle

Using the displacement approximation (Eq. 6.5) and the definition of strain tensor (Eq. 2.2), the engineering form of strain and its variation can be evaluated as

$$\bar{\boldsymbol{\varepsilon}}^u = \underbrace{\begin{bmatrix} R'_1 & R'_2 & \dots & R'_{n^e_{cp}} \end{bmatrix}}_{\boldsymbol{B}} \underbrace{\begin{bmatrix} \tilde{u}_1 \\ \tilde{u}_2 \\ \vdots \\ \tilde{u}_{3n^e_{cp}} \end{bmatrix}}_{\tilde{\boldsymbol{u}}}, \quad \text{where} \quad R'_I = \begin{bmatrix} R_{1,x} & 0 & 0 \\ 0 & R_{1,y} & 0 \\ 0 & 0 & R_{1,z} \\ R_{1,y} & R_{1,x} & 0 \\ 0 & R_{1,z} & R_{1,y} \\ R_{1,z} & 0 & R_{1,z} \end{bmatrix}, \tag{6.10}$$

$$\bar{\boldsymbol{\varepsilon}}^u = \boldsymbol{B}\tilde{\boldsymbol{u}}, \tag{6.11}$$

$$\text{and,} \quad \bar{\boldsymbol{\varepsilon}}^{\delta u} = \boldsymbol{B}\boldsymbol{\delta}\tilde{\boldsymbol{u}}. \tag{6.12}$$

Substituting the Eqs. 6.5, 6.9, 6.11, and 6.12 into weak form (Eq. 6.3 and 6.4) and using the arbitrariness of $\boldsymbol{\delta u}$ and $\bar{\boldsymbol{\sigma}}$, Eq. 6.3 and 6.4 reduce to

$$\left[\int_{\mathcal{R}} \boldsymbol{B}^T \boldsymbol{P} \, \mathrm{d}\mathcal{R}\right] \hat{\boldsymbol{\beta}} - \left[\int_{\mathcal{R}} \boldsymbol{R}^T \boldsymbol{b} \, \mathrm{d}\mathcal{R} + \int_{\partial\mathcal{R}_t} \boldsymbol{R}^T \bar{\boldsymbol{t}} \, \mathrm{d}A\right] = \boldsymbol{0}, \tag{6.13}$$

$$\left[\int_{\mathcal{R}} \boldsymbol{P}^T \boldsymbol{B} \, \mathrm{d}\mathcal{R}\right] \tilde{\boldsymbol{u}} - \left[\int_{\mathcal{R}} \boldsymbol{P}^T \boldsymbol{S} \boldsymbol{P} \, \mathrm{d}\mathcal{R}\right] \hat{\boldsymbol{\beta}} = \boldsymbol{0}, \tag{6.14}$$

where $\boldsymbol{S}$ is the compliance matrix given by $\boldsymbol{S} = \boldsymbol{C}^{-1}$. Let the entities $\boldsymbol{G}$, $\boldsymbol{H}$, $\hat{\boldsymbol{g}}$, and $\hat{\boldsymbol{f}}$ be defined as follows:

$$\boldsymbol{G} = \int_{\mathcal{R}} \boldsymbol{P}^T \boldsymbol{B} \, \mathrm{d}\mathcal{R}, \ \boldsymbol{H} = \int_{\mathcal{R}} \boldsymbol{P}^T \boldsymbol{S} \boldsymbol{P} \, \mathrm{d}\mathcal{R}, \ \hat{\boldsymbol{g}} = \boldsymbol{0}, \ \text{and } \hat{\boldsymbol{f}} = \int_{\mathcal{R}} \boldsymbol{R}^T \boldsymbol{b} \, \mathrm{d}\mathcal{R} + \int_{\partial\mathcal{R}_t} \boldsymbol{R}^T \bar{\boldsymbol{t}} \, \mathrm{d}A.$$

Then the Eqs. 6.13 and 6.14 can be written as

$$\begin{bmatrix} -\boldsymbol{H} & \boldsymbol{G} \\ \boldsymbol{G}^T & \boldsymbol{0} \end{bmatrix} \begin{Bmatrix} \hat{\boldsymbol{\beta}} \\ \tilde{\boldsymbol{u}} \end{Bmatrix} = \begin{Bmatrix} \hat{\boldsymbol{g}} \\ \hat{\boldsymbol{f}} \end{Bmatrix}. \tag{6.15}$$

Evaluating the expression for $\hat{\boldsymbol{\beta}}$ from Eq. 6.15 leads to the following expressions:

$$\hat{\boldsymbol{\beta}} = \boldsymbol{H}^{-1}\boldsymbol{G}\tilde{\boldsymbol{u}}, \tag{6.16}$$

$$\underbrace{\boldsymbol{G}^T\boldsymbol{H}^{-1}\boldsymbol{G}}_{\boldsymbol{K}}\tilde{\boldsymbol{u}} = \hat{\boldsymbol{f}} \rightarrow \boldsymbol{K}\tilde{\boldsymbol{u}} = \hat{\boldsymbol{f}}, \tag{6.17}$$

where $\boldsymbol{G}^T\boldsymbol{H}^{-1}\boldsymbol{G}$ is the stiffness matrix for the two-field IGA formulation. $\boldsymbol{H}^{-1}$ can be evaluated at the element level since the stress interpolations are chosen such that they are not continuous across element boundaries. Thus, the elemental stiffness matrix is given as

$$\boldsymbol{K}^e = \boldsymbol{G}_e^T \boldsymbol{H}_e^{-1}\boldsymbol{G}_e, \text{ where } \boldsymbol{G}_e = \int_{\mathcal{R}_e} \boldsymbol{P}_e^T \boldsymbol{B}_e \,\mathrm{d}\mathcal{R}_e, \text{ and } \boldsymbol{H}_e = \int_{\mathcal{R}_e}\boldsymbol{P}_e^T \boldsymbol{S}\boldsymbol{P}_e\,\mathrm{d}\mathcal{R}.$$

6.3 Proposed stress interpolation matrix for NURBS-based elements

The performance of the stress-based elements is significantly dependent on the selected space of stress interpolation functions. We should carefully choose the interpolation functions meeting the conflicting objective of stability and coarse mesh accuracy. One of the essential considerations while deriving these functions is that the interpolation functions should not introduce any spurious zero strain energy modes into the system. To ensure the stated condition, let us consider the strain energy ($\mathcal{W}$) in an element by an admissible deformation $\boldsymbol{u}_e$, which is given as follows:

$$\mathcal{W} = \frac{1}{2}\tilde{\boldsymbol{u}}_e^T \boldsymbol{K}_e \tilde{\boldsymbol{u}}_e = \frac{1}{2} \left[\int_{\mathcal{R}_e} [\bar{\varepsilon}(\boldsymbol{u}_e)]^T \boldsymbol{P}_e\,\mathrm{d}\mathcal{R}\right] \boldsymbol{H}_e^{-1}\left[\int_{\mathcal{R}_e}\boldsymbol{P}_e^T\,[\bar{\varepsilon}(\boldsymbol{u}_e)]\,\mathrm{d}\mathcal{R}\right]. \tag{6.18}$$

Consequently, Eq. 6.18 leads to zero strain energy or a non-invertible singular stiffness matrix if

$$\int_{\mathcal{R}_e}\boldsymbol{P}_e^T\,[\bar{\varepsilon}_c(\boldsymbol{u}_e)]\,\mathrm{d}\mathcal{R} = \boldsymbol{0} \quad\rightarrow\quad \left[\int_{\mathcal{R}_e}\boldsymbol{P}_e^T\boldsymbol{B}_e\,\mathrm{d}\mathcal{R}\right]\tilde{\boldsymbol{u}}_e = \boldsymbol{0}. \tag{6.19}$$

Let $\boldsymbol{G}_e = \int_{\mathcal{R}_e}\boldsymbol{P}_e^T\boldsymbol{B}_e\,\mathrm{d}\mathcal{R}$ then, $\tilde{\boldsymbol{u}}_e \in N(\boldsymbol{G}_e)$ represents the space of zero-energy modes where $N(\boldsymbol{G}_e)$ is the null space of $\boldsymbol{G}_e$. Thus, any admissible $\boldsymbol{u}_e$ that lies in the $N(\boldsymbol{G}_e)$ is going to be responsible for the zero strain energy in the system. For the elements to be stable, it is essential that null space should comprise only the rigid body modes.

To obtain the interpolation matrix ($\tilde{\boldsymbol{P}}_e$), the participating stress field ($\tilde{\boldsymbol{\sigma}}$) is assumed to be partitioned into two parts. The first is the lower-order stress field $\tilde{\boldsymbol{\sigma}}_L^e$ that is approximated using full lower-order interpolation terms. The second is the higher-order stress field $\tilde{\boldsymbol{\sigma}}_H^e$, which is approximated with selected higher-order interpolations. Let $\boldsymbol{\sigma}_c$ for an element be defined as

$$\tilde{\boldsymbol{\sigma}}^e = \tilde{\boldsymbol{\sigma}}_L^e + \tilde{\boldsymbol{\sigma}}_H^e = \underbrace{\begin{bmatrix}\tilde{\boldsymbol{P}}_L^e & \tilde{\boldsymbol{P}}_H^e\end{bmatrix}}_{\tilde{\boldsymbol{P}}_e}\underbrace{\begin{bmatrix}\hat{\boldsymbol{\beta}}_L^e\\ \hat{\boldsymbol{\beta}}_H^e\end{bmatrix}}_{\hat{\boldsymbol{\beta}}_e}, \tag{6.20}$$

where $\tilde{\boldsymbol{P}}_L^e$, and $\tilde{\boldsymbol{P}}_H^e$ are the lower and higher-order stress interpolation matrix. The feasible space for $\tilde{\boldsymbol{P}}_L^e$ is an order less than that of the displacement interpolations.

To ensure the absence of spurious zero-energy modes and have a full rank of the stiffness matrix ($\boldsymbol{K}$), the number of stress parameters should satisfy the following necessary condition [114]

$$n_{\hat{\beta}} \geq n_d - n_r, \tag{6.21}$$

where $n_{\hat{\beta}}$, n_d, and n_r are the numbers of stress parameters involved in $\hat{\boldsymbol{\beta}}$, displacement degrees of freedom associated with each element and rigid body modes, respectively. The aforementioned requirement can not be met if $\tilde{\boldsymbol{\sigma}}^e$ is assumed to be approximated using solely the $\tilde{\boldsymbol{P}}_L^e$ interpolations, resulting in spurious zero-energy modes in the formulation. Hence, the terms of $\tilde{\boldsymbol{P}}_H^e$ are chosen particularly to suppress these zero-energy modes that lead to a stable locking-free formulation. It is worth mentioning that although the absence of the spurious modes is essential but it is not sufficient to achieve a stable element. It is also important to satisfy certain additional criteria, such as the completeness of interpolation functions, to ensure the stability of elements. Furthermore, it should be pointed out that a lower number of stress parameters leads to a smaller dimension of $\tilde{\boldsymbol{P}}$ matrix and a lower value of the stiffness matrix. Based on the relation stated in Eq. 6.21, the minimum value for $n_{\hat{\beta}}$ is equal to $(n_d - n_r)$; however, this leads to instabilities in transient problems [142]. Hence, to obtain a robust formulation, the number of stress parameters are preferably considered to be greater than the $(n_d - n_r)$.

Based on the stated implications, the systematic procedural steps to identify the feasible space for $\tilde{\boldsymbol{P}}$ can be formulated as follows [142]:

1. Identifying the feasible space for lower-order stress interpolations functions $(\tilde{\boldsymbol{P}}_L^e)$.
2. Incorporate $\tilde{\boldsymbol{P}}^e = \tilde{\boldsymbol{P}}_L^e$ and evaluate the total number of independent participating zero-energy modes along with their exact symbolic expressions.
3. Adding the additional modes to suppress the identified spurious zero-energy modes and define the feasible space for higher-order stress interpolations functions $(\tilde{\boldsymbol{P}}_H^e)$. The interpolations for approximating the normal stresses are obtained by differentiating the displacement interpolations with respect to natural coordinates. This provides an effective feasible space that suppresses the majority of identified spurious zero-energy modes. The remaining modes are suppressed using the higher-order terms in shear stress interpolations.
4. While introducing the relevant stress parameter (β), it is vital to allow stress components to vary independently. Thus, an independent β should be associated with each individual component of the stress interpolations. There should not be any sharing of β terms among the stress components.
5. Identifying the additional higher-order terms to achieve the completeness to ensure the stability of the element.
6. Verifying that the proposed stress interpolations provide a formulation that is free of spurious zero-energy mode.

To better understand the evaluation of $\tilde{\boldsymbol{P}}$ matrix in the proposed hybrid IGA elements, the subsequent section presents a systematic derivation of feasible stress interpolation spaces for NURBS-based 3D “cubic element”.

6.3.1 Stress interpolation functions for 3D cubic elements

The term "cubic element" refers to the 3D cubic interpolation functions in all three directions with the highest possible continuity. Let Ξ, $\boldsymbol{\mathcal{H}}$, and $\boldsymbol{\mathcal{Z}}$ be the knot vectors and p, q, and r be the degree of basis functions along ξ, η, and ζ direction. A single cubic element is modeled by employing Ξ, $\boldsymbol{\mathcal{H}}$, and $\boldsymbol{\mathcal{Z}} = \{0,\ 0,\ 0,\ 0,\ 1,\ 1,\ 1,\ 1\}$ and p, q, and $r = 3$. For the stated geometric description, there are four univariate basis functions ($N_{\alpha,p}(\xi)$, $M_{\beta,q}(\eta)$, and $L_{\gamma,r}(\zeta)$ for $\alpha, \beta, \gamma = 1, 2, 3, 4$) along each direction.

6.3.1.1 Choice of $\tilde{\boldsymbol{P}}_L^e$

The feasible space for $\tilde{\boldsymbol{P}}_L^e$ is an order less than that of the NURBS interpolations used for approximating the displacements. Hence, the choice of $\tilde{\boldsymbol{P}}_L^e$ for the described cubic element is the full tri-quadratic space in master coordinates given as follows:

$$\begin{aligned}\tilde{\boldsymbol{P}}_L^e = \Big[\ &\boldsymbol{I}_6\ \ \tilde{\zeta}\boldsymbol{I}_6\ \ \tilde{\zeta}^2\boldsymbol{I}_6\ \ \tilde{\eta}\boldsymbol{I}_6\ \ \tilde{\zeta}\tilde{\eta}\boldsymbol{I}_6\ \ \tilde{\zeta}^2\tilde{\eta}\boldsymbol{I}_6\ \ \tilde{\eta}^2\boldsymbol{I}_6\ \ \tilde{\zeta}\tilde{\eta}^2\boldsymbol{I}_6\ \ \tilde{\zeta}^2\tilde{\eta}^2\boldsymbol{I}_6\ \ \tilde{\xi}\boldsymbol{I}_6\ \ \tilde{\zeta}\tilde{\xi}\boldsymbol{I}_6\ \ \tilde{\zeta}^2\tilde{\xi}\boldsymbol{I}_6 \\ &\tilde{\eta}\tilde{\xi}\boldsymbol{I}_6\ \ \tilde{\zeta}\tilde{\eta}\tilde{\xi}\boldsymbol{I}_6\ \ \tilde{\zeta}^2\tilde{\eta}\tilde{\xi}\boldsymbol{I}_6\ \ \tilde{\eta}^2\tilde{\xi}\boldsymbol{I}_6\ \ \tilde{\zeta}\tilde{\eta}^2\tilde{\xi}\boldsymbol{I}_6\ \ \tilde{\zeta}^2\tilde{\eta}^2\tilde{\xi}\boldsymbol{I}_6\ \ \tilde{\xi}^2\boldsymbol{I}_6\ \ \tilde{\zeta}\tilde{\xi}^2\boldsymbol{I}_6\ \ \tilde{\zeta}^2\tilde{\xi}^2\boldsymbol{I}_6\ \ \tilde{\eta}\tilde{\xi}^2\boldsymbol{I}_6 \\ &\tilde{\zeta}\tilde{\eta}\tilde{\xi}^2\boldsymbol{I}_6\ \ \tilde{\zeta}^2\tilde{\eta}\tilde{\xi}^2\boldsymbol{I}_6\ \ \tilde{\eta}^2\tilde{\xi}^2\boldsymbol{I}_6\ \ \tilde{\zeta}\tilde{\eta}^2\tilde{\xi}^2\boldsymbol{I}_6\ \ \tilde{\zeta}^2\tilde{\eta}^2\tilde{\xi}^2\boldsymbol{I}_6\ \Big],\end{aligned} \tag{6.22}$$

where $\boldsymbol{I}_6$ is the identity matrix of dimension 6×6.

6.3.1.2 Evaluation of participating zero-energy modes

The participating spurious zero-energy modes are then evaluated assuming $\bar{\boldsymbol{\sigma}}^e$ to be approximated using solely the $\boldsymbol{P}_L^e$ interpolations. However, considering only the lower interpolations results in an unstable element due to the presence of spurious zero-energy modes. This can be demonstrated by substituting the $\boldsymbol{P}_e = \boldsymbol{P}_L^e$ in the expression of $\boldsymbol{G}_e$, which results in

$$\left[\int_{\mathcal{R}_e} (\boldsymbol{P}_L^e)^T \boldsymbol{B}_e \,\mathrm{d}\mathcal{R}\right] \tilde{\boldsymbol{u}}_e = \boldsymbol{0} \quad \rightarrow \quad \boldsymbol{G}_L^e \tilde{\boldsymbol{u}}_e = \boldsymbol{0}. \tag{6.23}$$

Hence, this signifies the presence of spurious zero-energy modes if only $\boldsymbol{P}_L^e$ is considered for stress interpolation. The total number of zero-energy modes are obtained after evaluating the dimensions of $N(\boldsymbol{G}_L^e)$. For the prescribed setting of $\boldsymbol{P}_L^e$ in combination with the NURBS interpolations for displacements, the dimension of $N(\boldsymbol{G}_L^e)$ is 45, out of which the total number of spurious zero-energy modes are 39, and rigid body modes are 6. The strategy for evaluating these modes is adopted from the work of Lee et al. [185, 186] or Sze et al. [187].

To identify the stated 39 zero-energy modes, consider a cubic element in its master space where the surfaces are given by $\tilde{\xi} = \pm 1$, $\tilde{\eta} = \pm 1$ and $\tilde{\zeta} = \pm 1$. If $\bar{\boldsymbol{\sigma}}$ is interpolated solely based on $\boldsymbol{P}_L^e$, the highest degree polynomial term in Eq. 6.23 is at most of the fifth-degree interpolation in its master coordinates. Hence, a three-point Gauss quadrature rule is sufficient to evaluate the integral exactly. The spurious zero-energy modes are then defined as the admissible deformations that produce the zero strain field that eventually lead the integral in Eq. 6.23 to zero. Thus, if an admissible $\boldsymbol{u}$ leads to a strain field that is zero at every Gauss point, this $\boldsymbol{u}$ corresponds to the spurious zero-energy mode in the system. The expressions for the linearly independent admissible deformations $\boldsymbol{u}_e$ that yield $\bar{\boldsymbol{\varepsilon}}_c(\boldsymbol{u}_e) = \boldsymbol{0}$ at the $3 \times 3 \times 3$ Gauss quadrature points $\left(\tilde{\xi} = \pm\sqrt{\frac{3}{5}}\,, 0;\ \tilde{\eta} = \pm\sqrt{\frac{3}{5}}, 0;\ \text{and}\ \tilde{\zeta} = \pm\sqrt{\frac{3}{5}}, 0\right)$ are given as follows:

$$
\begin{array}{ll}
u = \alpha_1 f(\tilde{\zeta}) f(\tilde{\eta});\quad v = 0;\ w = 0; & u = 0;\ v = \alpha_{11} f(\tilde{\zeta}) f(\tilde{\eta});\quad w = 0; \\
u = \alpha_2 f(\tilde{\zeta}) f(\tilde{\xi});\quad v = 0;\ w = 0; & u = 0;\ v = \alpha_{12} f(\tilde{\zeta}) f(\tilde{\xi});\quad w = 0; \\
u = \alpha_3 f(\tilde{\eta}) f(\tilde{\xi});\quad v = 0;\ w = 0; & u = 0;\ v = \alpha_{13} f(\tilde{\eta}) f(\tilde{\xi});\quad w = 0; \\
u = \alpha_4 \tilde{\zeta} f(\tilde{\eta}) f(\tilde{\xi});\quad v = 0;\ w = 0; & u = 0;\ v = \alpha_{14} \tilde{\zeta} f(\tilde{\eta}) f(\tilde{\xi});\quad w = 0; \\
u = \alpha_5 f(\tilde{\zeta}) \tilde{\eta} f(\tilde{\xi});\quad v = 0;\ w = 0; & u = 0;\ v = \alpha_{15} f(\tilde{\zeta}) \tilde{\eta} f(\tilde{\xi});\quad w = 0; \\
u = \alpha_6 f(\tilde{\zeta}) f(\tilde{\eta}) \tilde{\xi};\quad v = 0;\ w = 0; & u = 0;\ v = \alpha_{16} f(\tilde{\zeta}) f(\tilde{\eta}) \tilde{\xi};\quad w = 0; \\
u = \alpha_7 \tilde{\zeta}^2 f(\tilde{\eta}) f(\tilde{\xi});\ v = 0;\ w = 0; & u = 0;\ v = \alpha_{17} \tilde{\zeta}^2 f(\tilde{\eta}) f(\tilde{\xi}); w = 0; \\
u = \alpha_8 f(\tilde{\zeta}) \tilde{\eta}^2 f(\tilde{\xi});\ v = 0;\ w = 0; & u = 0;\ v = \alpha_{18} f(\tilde{\zeta}) \tilde{\eta}^2 f(\tilde{\xi}); w = 0; \\
u = \alpha_9 f(\tilde{\zeta}) f(\tilde{\eta}) \tilde{\xi}^2;\ v = 0;\ w = 0; & u = 0;\ v = \alpha_{19} f(\tilde{\zeta}) f(\tilde{\eta}) \tilde{\xi}^2; w = 0; \\
u = \alpha_{10} f(\tilde{\zeta}) f(\tilde{\eta}) \tilde{\xi}^3; v = 0;\ w = 0; & u = 0;\ v = \alpha_{20} f(\tilde{\xi}) \tilde{\eta}^3 f(\tilde{\zeta}); w = 0;
\end{array}
$$

$$
\begin{array}{ll}
u = 0;\ v = 0;\ w = \alpha_{21} f(\tilde{\zeta}) f(\tilde{\eta}); & u = 0;\ v = 0;\ w = \alpha_{26} f(\tilde{\zeta}) f(\tilde{\eta}) \tilde{\xi}; \\
u = 0;\ v = 0;\ w = \alpha_{22} f(\tilde{\zeta}) f(\tilde{\xi}); & u = 0;\ v = 0;\ w = \alpha_{27} \tilde{\zeta}^2 f(\tilde{\eta}) f(\tilde{\xi}); \\
u = 0;\ v = 0;\ w = \alpha_{23} f(\tilde{\eta}) f(\tilde{\xi}); & u = 0;\ v = 0;\ w = \alpha_{28} f(\tilde{\zeta}) \tilde{\eta}^2 f(\tilde{\xi}); \\
u = 0;\ v = 0;\ w = \alpha_{24} \tilde{\zeta} f(\tilde{\eta}) f(\tilde{\xi}); & u = 0;\ v = 0;\ w = \alpha_{29} f(\tilde{\zeta}) f(\tilde{\eta}) \tilde{\xi}^2; \\
u = 0;\ v = 0;\ w = \alpha_{25} f(\tilde{\zeta}) \tilde{\eta} f(\tilde{\xi}); & u = 0;\ v = 0;\ w = \alpha_{30} f(\tilde{\xi}) f(\tilde{\eta}) \tilde{\zeta}^3;
\end{array}
$$

$$
\begin{array}{lll}
u = \alpha_{31} g(\tilde{\xi}) f(\tilde{\eta}); & v = -\alpha_{31} f(\tilde{\xi}) g(\tilde{\eta}); & w = 0; \\
u = \alpha_{32} g(\tilde{\xi}) f(\tilde{\zeta}); & v = 0; & w = -\alpha_{32} f(\tilde{\xi}) g(\tilde{\zeta}); \\
u = 0; & v = \alpha_{33} g(\tilde{\eta}) f(\tilde{\zeta}); & w = -\alpha_{33} f(\tilde{\eta}) g(\tilde{\zeta}); \\
u = \alpha_{34} g(\tilde{\xi}) f(\tilde{\eta}) \tilde{\zeta}^2; & v = -\alpha_{34} f(\tilde{\xi}) g(\tilde{\eta}) \tilde{\zeta}^2; & w = 0; \\
u = \alpha_{35} g(\tilde{\xi}) f(\tilde{\zeta}) \tilde{\eta}^2; & v = 0; & w = -\alpha_{35} f(\tilde{\xi}) g(\tilde{\zeta}) \tilde{\eta}^2; \\
u = 0; & v = \alpha_{36} g(\tilde{\eta}) f(\tilde{\zeta}) \tilde{\xi}^2; & w = -\alpha_{36} f(\tilde{\eta}) g(\tilde{\zeta}) \tilde{\xi}^2; \\
u = \alpha_{37} g(\tilde{\xi}) f(\tilde{\eta}) \tilde{\zeta}^3; & v = -\alpha_{37} f(\tilde{\xi}) g(\tilde{\eta}) \tilde{\zeta}^3; & w = 0; \\
u = \alpha_{38} g(\tilde{\xi}) f(\tilde{\zeta}) \tilde{\eta}^3; & v = 0; & w = -\alpha_{38} f(\tilde{\xi}) g(\tilde{\zeta}) \tilde{\eta}^3; \\
u = 0; & v = \alpha_{39} g(\tilde{\eta}) f(\tilde{\zeta}) \tilde{\xi}^3; & w = -\alpha_{39} f(\tilde{\eta}) g(\tilde{\zeta}) \tilde{\xi}^3;
\end{array}
$$

where $f(x) = \left(\dfrac{3x}{5} - x^3\right)$ and $g(x) = \left(\dfrac{3}{5} - 3x^2\right)$. It can be easily verified that the aforementioned displacement field provides the strain field, which is zero at all $3 \times 3 \times 3$

Gauss points. It can be further proved that all the derived spurious zero-energy modes are linearly independent. This is achieved by performing the rank analysis of the matrix formed by coefficients of each variable in each mode. The resultant matrix leads to a full rank matrix, hence confirming the independence of the derived modes. So, in summary, the 39 spurious zero-energy modes are evaluated with the above exercise.

6.3.1.3 The feasible space for $\tilde{\boldsymbol{P}}_{H}^{e}$

After identifying the involved zero-energy modes, every 'α' in the enlisted modes is suppressed by adding the higher-order terms according to the guidelines presented at the start of the section. This leads to the following expressions for stress distribution:

$$\begin{aligned}
\sigma_{\tilde{\xi}\tilde{\xi}}^{H} = {} & \hat{\beta}_{1}^{H}\tilde{\zeta}^{3} + \hat{\beta}_{2}^{H}\tilde{\zeta}^{3}\tilde{\eta} + \hat{\beta}_{3}^{H}\tilde{\zeta}^{3}\tilde{\eta}^{2} + \hat{\beta}_{4}^{H}\tilde{\eta}^{3} + \hat{\beta}_{5}^{H}\tilde{\zeta}\tilde{\eta}^{3} + \hat{\beta}_{6}^{H}\tilde{\zeta}^{2}\tilde{\eta}^{3} + \hat{\beta}_{7}^{H}\tilde{\zeta}^{3}\tilde{\eta}^{3} \\
& + \hat{\beta}_{8}^{H}\tilde{\zeta}^{3}\tilde{\xi} + \hat{\beta}_{9}^{H}\tilde{\zeta}^{3}\tilde{\eta}\tilde{\xi} + \hat{\beta}_{10}^{H}\tilde{\zeta}^{3}\tilde{\eta}^{2}\tilde{\xi} + \hat{\beta}_{11}^{H}\tilde{\eta}^{3}\tilde{\xi} + \hat{\beta}_{12}^{H}\tilde{\zeta}\tilde{\eta}^{3}\tilde{\xi} + \hat{\beta}_{13}^{H}\tilde{\zeta}^{2}\tilde{\eta}^{3}\tilde{\xi} \\
& + \hat{\beta}_{14}^{H}\tilde{\zeta}^{3}\tilde{\eta}^{3}\tilde{\xi} + \hat{\beta}_{15}^{H}\tilde{\zeta}^{3}\tilde{\xi}^{2} + \hat{\beta}_{16}^{H}\tilde{\zeta}^{3}\tilde{\eta}\tilde{\xi}^{2} + \hat{\beta}_{17}^{H}\tilde{\zeta}^{3}\tilde{\eta}^{2}\tilde{\xi}^{2} + \hat{\beta}_{18}^{H}\tilde{\eta}^{3}\tilde{\xi}^{2} + \hat{\beta}_{19}^{H}\tilde{\zeta}\tilde{\eta}^{3}\tilde{\xi}^{2} \\
& + \hat{\beta}_{20}^{H}\tilde{\zeta}^{2}\tilde{\eta}^{3}\tilde{\xi}^{2} + \hat{\beta}_{21}^{H}\tilde{\zeta}^{3}\tilde{\eta}^{3}\tilde{\xi}^{2},
\end{aligned} \tag{6.27}$$

$$\begin{aligned}
\sigma_{\tilde{\eta}\tilde{\eta}}^{H} = {} & \hat{\beta}_{22}^{H}\tilde{\zeta}^{3} + \hat{\beta}_{23}^{H}\tilde{\zeta}^{3}\tilde{\eta} + \hat{\beta}_{24}^{H}\tilde{\zeta}^{3}\tilde{\eta}^{2} + \hat{\beta}_{25}^{H}\tilde{\zeta}^{3}\tilde{\xi} + \hat{\beta}_{26}^{H}\tilde{\zeta}^{3}\tilde{\eta}\tilde{\xi} + \hat{\beta}_{27}^{H}\tilde{\zeta}^{3}\tilde{\eta}^{2}\tilde{\xi} + \hat{\beta}_{28}^{H}\tilde{\zeta}^{3}\tilde{\xi}^{2} \\
& + \hat{\beta}_{29}^{H}\tilde{\zeta}^{3}\tilde{\eta}\tilde{\xi}^{2} + \hat{\beta}_{30}^{H}\tilde{\zeta}^{3}\tilde{\eta}^{2}\tilde{\xi}^{2} + \hat{\beta}_{31}^{H}\tilde{\xi}^{3} + \hat{\beta}_{32}^{H}\tilde{\zeta}\tilde{\xi}^{3} + \hat{\beta}_{33}^{H}\tilde{\zeta}^{2}\tilde{\xi}^{3} + \hat{\beta}_{34}^{H}\tilde{\zeta}^{3}\tilde{\xi}^{3} + \hat{\beta}_{35}^{H}\tilde{\eta}\tilde{\xi}^{3} \\
& + \hat{\beta}_{36}^{H}\tilde{\zeta}\tilde{\eta}\tilde{\xi}^{3} + \hat{\beta}_{37}^{H}\tilde{\zeta}^{2}\tilde{\eta}\tilde{\xi}^{3} + \hat{\beta}_{38}^{H}\tilde{\zeta}^{3}\tilde{\eta}\tilde{\xi}^{3} + \hat{\beta}_{39}^{H}\tilde{\eta}^{2}\tilde{\xi}^{3} + \hat{\beta}_{40}^{H}\tilde{\zeta}\tilde{\eta}^{2}\tilde{\xi}^{3} + \hat{\beta}_{41}^{H}\tilde{\zeta}^{2}\tilde{\eta}^{2}\tilde{\xi}^{3} \\
& + \hat{\beta}_{42}^{H}\tilde{\zeta}^{3}\tilde{\eta}^{2}\tilde{\xi}^{3},
\end{aligned} \tag{6.28}$$

$$\begin{aligned}
\sigma_{\tilde{\zeta}\tilde{\zeta}}^{H} = {} & \hat{\beta}_{43}^{H}\tilde{\eta}^{3} + \hat{\beta}_{44}^{H}\tilde{\zeta}\tilde{\eta}^{3} + \hat{\beta}_{45}^{H}\tilde{\zeta}^{2}\tilde{\eta}^{3} + \hat{\beta}_{46}^{H}\tilde{\eta}^{3}\tilde{\xi} + \hat{\beta}_{47}^{H}\tilde{\zeta}\tilde{\eta}^{3}\tilde{\xi} + \hat{\beta}_{48}^{H}\tilde{\zeta}^{2}\tilde{\eta}^{3}\tilde{\xi} + \hat{\beta}_{49}^{H}\tilde{\eta}^{3}\tilde{\xi}^{2} \\
& + \hat{\beta}_{50}^{H}\tilde{\zeta}\tilde{\eta}^{3}\tilde{\xi}^{2} + \hat{\beta}_{51}^{H}\tilde{\zeta}^{2}\tilde{\eta}^{3}\tilde{\xi}^{2} + \hat{\beta}_{52}^{H}\tilde{\xi}^{3} + \hat{\beta}_{53}^{H}\tilde{\zeta}\tilde{\xi}^{3} + \hat{\beta}_{54}^{H}\tilde{\zeta}^{2}\tilde{\xi}^{3} + \hat{\beta}_{55}^{H}\tilde{\eta}\tilde{\xi}^{3} + \hat{\beta}_{56}^{H}\tilde{\zeta}\tilde{\eta}\tilde{\xi}^{3} \\
& + \hat{\beta}_{57}^{H}\tilde{\zeta}^{2}\tilde{\eta}\tilde{\xi}^{3} + \hat{\beta}_{58}^{H}\tilde{\eta}^{2}\tilde{\xi}^{3} + \hat{\beta}_{59}^{H}\tilde{\zeta}\tilde{\eta}^{2}\tilde{\xi}^{3} + \hat{\beta}_{60}^{H}\tilde{\zeta}^{2}\tilde{\eta}^{2}\tilde{\xi}^{3} + \hat{\beta}_{61}^{H}\tilde{\eta}^{3}\tilde{\xi}^{3} + \hat{\beta}_{62}^{H}\tilde{\zeta}\tilde{\eta}^{3}\tilde{\xi}^{3} \\
& + \hat{\beta}_{63}^{H}\tilde{\zeta}^{2}\tilde{\eta}^{3}\tilde{\xi}^{3},
\end{aligned} \tag{6.29}$$

$$\begin{aligned}
\sigma_{\tilde{\xi}\tilde{\eta}}^{H} = {} & \hat{\beta}_{64}^{H}\tilde{\zeta}^{3} + \hat{\beta}_{65}^{H}\tilde{\zeta}^{3}\tilde{\eta} + \hat{\beta}_{66}^{H}\tilde{\zeta}^{3}\tilde{\eta}^{2} + \hat{\beta}_{67}^{H}\tilde{\zeta}^{3}\tilde{\xi} + \hat{\beta}_{68}^{H}\tilde{\zeta}^{3}\tilde{\eta}\tilde{\xi} + \hat{\beta}_{69}^{H}\tilde{\zeta}^{3}\tilde{\eta}^{2}\tilde{\xi} + \hat{\beta}_{70}^{H}\tilde{\zeta}^{3}\tilde{\xi}^{2} \\
& + \hat{\beta}_{71}^{H}\tilde{\zeta}^{3}\tilde{\eta}\tilde{\xi}^{2} + \hat{\beta}_{72}^{H}\tilde{\zeta}^{3}\tilde{\eta}^{2}\tilde{\xi}^{2},
\end{aligned} \tag{6.30}$$

$$\begin{aligned}
\sigma_{\tilde{\eta}\tilde{\zeta}}^{H} = {} & \hat{\beta}_{73}^{H}\tilde{\xi}^{3} + \hat{\beta}_{74}^{H}\tilde{\zeta}\tilde{\xi}^{3} + \hat{\beta}_{75}^{H}\tilde{\zeta}^{2}\tilde{\xi}^{3} + \hat{\beta}_{76}^{H}\tilde{\eta}\tilde{\xi}^{3} + \hat{\beta}_{77}^{H}\tilde{\zeta}\tilde{\eta}\tilde{\xi}^{3} + \hat{\beta}_{78}^{H}\tilde{\zeta}^{2}\tilde{\eta}\tilde{\xi}^{3} + \hat{\beta}_{79}^{H}\tilde{\eta}^{2}\tilde{\xi}^{3} \\
& + \hat{\beta}_{80}^{H}\tilde{\zeta}\tilde{\eta}^{2}\tilde{\xi}^{3} + \hat{\beta}_{81}^{H}\tilde{\zeta}^{2}\tilde{\eta}^{2}\tilde{\xi}^{3},
\end{aligned} \tag{6.31}$$

$$\begin{aligned}
\sigma_{\tilde{\xi}\tilde{\zeta}}^{H} = {} & \hat{\beta}_{82}^{H}\tilde{\eta}^{3} + \hat{\beta}_{83}^{H}\tilde{\zeta}\tilde{\eta}^{3} + \hat{\beta}_{84}^{H}\tilde{\zeta}^{2}\tilde{\eta}^{3} + \hat{\beta}_{85}^{H}\tilde{\eta}^{3}\tilde{\xi} + \hat{\beta}_{86}^{H}\tilde{\zeta}\tilde{\eta}^{3}\tilde{\xi} + \hat{\beta}_{87}^{H}\tilde{\zeta}^{2}\tilde{\eta}^{3}\tilde{\xi} + \hat{\beta}_{88}^{H}\tilde{\eta}^{3}\tilde{\xi}^{2} \\
& + \hat{\beta}_{89}^{H}\tilde{\zeta}\tilde{\eta}^{3}\tilde{\xi}^{2} + \hat{\beta}_{90}^{H}\tilde{\zeta}^{2}\tilde{\eta}^{3}\tilde{\xi}^{2}.
\end{aligned} \tag{6.32}$$

From the above expressions, it can be identified that the higher-order terms in $\sigma_{\tilde{\xi}\tilde{\xi}}$, $\sigma_{\tilde{\eta}\tilde{\eta}}$, and $\sigma_{\tilde{\zeta}\tilde{\zeta}}$, that are obtained by differentiating the displacement interpolations with respect to natural coordinates, suppress a total of 36 zero-energy modes. This can be validated numerically by updating the $\tilde{\boldsymbol{P}}^{e}$ to include the higher-order terms of normal stresses and evaluating the dimension of $N(\boldsymbol{G}_{L}^{e})$. The remaining three modes (α_1, α_{12}, and α_{23}) are suppressed using the higher-order terms in shear stress interpolations.

Moreover, all the terms of the corresponding order of interpolation are also incorporated in shear stresses to achieve the stability of the element. For instance, the necessary condition to suppress the remaining zero-energy modes is to have a single higher-order term $\tilde{\zeta}^3$, $\tilde{\eta}^3$, and $\tilde{\xi}^3$ while defining $\sigma_{\tilde{\xi}\tilde{\eta}}$, $\sigma_{\tilde{\xi}\tilde{\zeta}}$, and $\sigma_{\tilde{\eta}\tilde{\zeta}}$ respectively. However, the additional terms ($\tilde{\zeta}^3\tilde{\eta}$, $\tilde{\zeta}^3\tilde{\eta}^2$, $\tilde{\zeta}^3\tilde{\xi}$, $\tilde{\zeta}^3\tilde{\eta}\tilde{\xi}$, $\tilde{\zeta}^3\tilde{\eta}^2\tilde{\xi}$, $\tilde{\zeta}^3\tilde{\xi}^2$, $\tilde{\zeta}^3\tilde{\eta}\tilde{\xi}^2$, $\tilde{\zeta}^3\tilde{\eta}^2\tilde{\xi}^2$), ($\tilde{\zeta}\tilde{\eta}^3$, $\tilde{\zeta}^2\tilde{\eta}^3$, $\tilde{\eta}^3\tilde{\xi}$, $\tilde{\zeta}\tilde{\eta}^3\tilde{\xi}$, $\tilde{\zeta}^2\tilde{\eta}^3\tilde{\xi}$, $\tilde{\eta}^3\tilde{\xi}^2$, $\tilde{\zeta}\tilde{\eta}^3\tilde{\xi}^2$, $\tilde{\zeta}^2\tilde{\eta}^3\tilde{\xi}^2$), and ($\tilde{\zeta}\tilde{\xi}^3$, $\tilde{\zeta}^2\tilde{\xi}^3$, $\tilde{\eta}\tilde{\xi}^3$, $\tilde{\zeta}\tilde{\eta}\tilde{\xi}^3$, $\tilde{\zeta}^2\tilde{\eta}\tilde{\xi}^3$, $\tilde{\eta}^2\tilde{\xi}^3$, $\tilde{\zeta}\tilde{\eta}^2\tilde{\xi}^3$, $\tilde{\zeta}^2\tilde{\eta}^2\tilde{\xi}^3$) are added while defining $\sigma_{\tilde{\xi}\tilde{\eta}}$, $\sigma_{\tilde{\xi}\tilde{\zeta}}$, and $\sigma_{\tilde{\eta}\tilde{\zeta}}$ respectively. This ensures the completeness of the interpolations functions and complements the element's overall stability [142]. Finally, the proposed stress distribution for the cubic NURBS element can be written as follows:

$$\begin{Bmatrix} \sigma_{\tilde{\xi}\tilde{\xi}} \\ \sigma_{\tilde{\eta}\tilde{\eta}} \\ \sigma_{\tilde{\zeta}\tilde{\zeta}} \\ \sigma_{\tilde{\xi}\tilde{\eta}} \\ \sigma_{\tilde{\eta}\tilde{\zeta}} \\ \sigma_{\tilde{\xi}\tilde{\zeta}} \end{Bmatrix} = \begin{bmatrix} \tilde{\boldsymbol{P}}^e_L & \tilde{\boldsymbol{P}}^e_H \end{bmatrix} \begin{bmatrix} \hat{\boldsymbol{\beta}}^e_L \\ \hat{\boldsymbol{\beta}}^e_H \end{bmatrix} = \underbrace{\begin{bmatrix} \tilde{\boldsymbol{P}}_1 & \mathbf{0}_c & \mathbf{0}_c & \mathbf{0}_d & \mathbf{0}_d & \mathbf{0}_d \\ \mathbf{0}_c & \tilde{\boldsymbol{P}}_2 & \mathbf{0}_c & \mathbf{0}_d & \mathbf{0}_d & \mathbf{0}_d \\ \mathbf{0}_c & \mathbf{0}_c & \tilde{\boldsymbol{P}}_3 & \mathbf{0}_d & \mathbf{0}_d & \mathbf{0}_d \\ \mathbf{0}_c & \mathbf{0}_c & \mathbf{0}_c & \tilde{\boldsymbol{P}}_4 & \mathbf{0}_d & \mathbf{0}_d \\ \mathbf{0}_c & \mathbf{0}_c & \mathbf{0}_c & \mathbf{0}_d & \tilde{\boldsymbol{P}}_5 & \mathbf{0}_d \\ \mathbf{0}_c & \mathbf{0}_c & \mathbf{0}_c & \mathbf{0}_d & \mathbf{0}_d & \tilde{\boldsymbol{P}}_6 \end{bmatrix}}_{\tilde{\boldsymbol{P}}(\tilde{\xi},\tilde{\eta},\tilde{\zeta})} \underbrace{\begin{Bmatrix} \tilde{\beta}_1 \\ \tilde{\beta}_2 \\ \tilde{\beta}_3 \\ \tilde{\beta}_4 \\ \vdots \\ \tilde{\beta}_{252} \end{Bmatrix}}_{\hat{\boldsymbol{\beta}}}, \tag{6.33}$$

where $\mathbf{0}_c$ and $\mathbf{0}_d$ are the null or zero vectors of the size 1×48 and 1×36, respectively. The vectors $\tilde{\boldsymbol{P}}_1, \tilde{\boldsymbol{P}}_2, \ldots, \tilde{\boldsymbol{P}}_6$ can be given as $\tilde{\boldsymbol{P}}_i = \begin{bmatrix} \tilde{\boldsymbol{P}}^L & \tilde{\boldsymbol{P}}^H_i \end{bmatrix}$, where

$$\begin{aligned} \tilde{\boldsymbol{P}}^L = \Big[& 1 \;\; \tilde{\zeta} \;\; \tilde{\zeta}^2 \;\; \tilde{\eta} \;\; \tilde{\zeta}\tilde{\eta} \;\; \tilde{\zeta}^2\tilde{\eta} \;\; \tilde{\eta}^2 \;\; \tilde{\zeta}\tilde{\eta}^2 \;\; \tilde{\zeta}^2\tilde{\eta}^2 \;\; \tilde{\xi} \;\; \tilde{\zeta}\tilde{\xi} \;\; \tilde{\zeta}^2\tilde{\xi} \;\; \tilde{\eta}\tilde{\xi} \;\; \tilde{\zeta}\tilde{\eta}\tilde{\xi} \;\; \tilde{\zeta}^2\tilde{\eta}\tilde{\xi} \;\; \tilde{\eta}^2\tilde{\xi} \;\; \tilde{\zeta}\tilde{\eta}^2\tilde{\xi} \;\; \tilde{\zeta}^2\tilde{\eta}^2\tilde{\xi} \\ & \tilde{\xi}^2 \;\; \tilde{\zeta}\tilde{\xi}^2 \;\; \tilde{\zeta}^2\tilde{\xi}^2 \;\; \tilde{\eta}\tilde{\xi}^2 \;\; \tilde{\zeta}\tilde{\eta}\tilde{\xi}^2 \;\; \tilde{\zeta}^2\tilde{\eta}\tilde{\xi}^2 \;\; \tilde{\eta}^2\tilde{\xi}^2 \;\; \tilde{\zeta}\tilde{\eta}^2\tilde{\xi}^2 \;\; \tilde{\zeta}^2\tilde{\eta}^2\tilde{\xi}^2 \Big], \\ \tilde{\boldsymbol{P}}^H_1 = \Big[& \tilde{\zeta}^3 \;\; \tilde{\zeta}^3\tilde{\eta} \;\; \tilde{\zeta}^3\tilde{\eta}^2 \;\; \tilde{\eta}^3 \;\; \tilde{\zeta}\tilde{\eta}^3 \;\; \tilde{\zeta}^2\tilde{\eta}^3 \;\; \tilde{\zeta}^3\tilde{\eta}^3 \;\; \tilde{\zeta}^3\tilde{\xi} \;\; \tilde{\zeta}^3\tilde{\eta}\tilde{\xi} \;\; \tilde{\zeta}^3\tilde{\eta}^2\tilde{\xi} \;\; \tilde{\eta}^3\tilde{\xi} \;\; \tilde{\zeta}\tilde{\eta}^3\tilde{\xi} \;\; \tilde{\zeta}^2\tilde{\eta}^3\tilde{\xi} \;\; \tilde{\zeta}^3\tilde{\eta}^3\tilde{\xi} \\ & \tilde{\zeta}^3\tilde{\xi}^2 \;\; \tilde{\zeta}^3\tilde{\eta}\tilde{\xi}^2 \;\; \tilde{\zeta}^3\tilde{\eta}^2\tilde{\xi}^2 \;\; \tilde{\eta}^3\tilde{\xi}^2 \;\; \tilde{\zeta}\tilde{\eta}^3\tilde{\xi}^2 \;\; \tilde{\zeta}^2\tilde{\eta}^3\tilde{\xi}^2 \;\; \tilde{\zeta}^3\tilde{\eta}^3\tilde{\xi}^2 \Big], \\ \tilde{\boldsymbol{P}}^H_2 = \Big[& \tilde{\zeta}^3 \;\; \tilde{\zeta}^3\tilde{\eta} \;\; \tilde{\zeta}^3\tilde{\eta}^2 \;\; \tilde{\zeta}^3\tilde{\xi} \;\; \tilde{\zeta}^3\tilde{\eta}\tilde{\xi} \;\; \tilde{\zeta}^3\tilde{\eta}^2\tilde{\xi} \;\; \tilde{\zeta}^3\tilde{\xi}^2 \;\; \tilde{\zeta}^3\tilde{\eta}\tilde{\xi}^2 \;\; \tilde{\zeta}^3\tilde{\eta}^2\tilde{\xi}^2 \;\; \tilde{\xi}^3 \;\; \tilde{\zeta}\tilde{\xi}^3 \;\; \tilde{\zeta}^2\tilde{\xi}^3 \;\; \tilde{\zeta}^3\tilde{\xi}^3 \;\; \tilde{\eta}\tilde{\xi}^3 \\ & \tilde{\zeta}\tilde{\eta}\tilde{\xi}^3 \;\; \tilde{\zeta}^2\tilde{\eta}\tilde{\xi}^3 \;\; \tilde{\zeta}^3\tilde{\eta}\tilde{\xi}^3 \;\; \tilde{\eta}^2\tilde{\xi}^3 \;\; \tilde{\zeta}\tilde{\eta}^2\tilde{\xi}^3 \;\; \tilde{\zeta}^2\tilde{\eta}^2\tilde{\xi}^3 \;\; \tilde{\zeta}^3\tilde{\eta}^2\tilde{\xi}^3 \Big], \\ \tilde{\boldsymbol{P}}^H_3 = \Big[& \tilde{\eta}^3 \;\; \tilde{\zeta}\tilde{\eta}^3 \;\; \tilde{\zeta}^2\tilde{\eta}^3 \;\; \tilde{\eta}^3\tilde{\xi} \;\; \tilde{\zeta}\tilde{\eta}^3\tilde{\xi} \;\; \tilde{\zeta}^2\tilde{\eta}^3\tilde{\xi} \;\; \tilde{\eta}^3\tilde{\xi}^2 \;\; \tilde{\zeta}\tilde{\eta}^3\tilde{\xi}^2 \;\; \tilde{\zeta}^2\tilde{\eta}^3\tilde{\xi}^2 \;\; \tilde{\xi}^3 \;\; \tilde{\zeta}\tilde{\xi}^3 \;\; \tilde{\zeta}^2\tilde{\xi}^3 \;\; \tilde{\eta}\tilde{\xi}^3 \;\; \tilde{\zeta}\tilde{\eta}\tilde{\xi}^3 \\ & \tilde{\zeta}^2\tilde{\eta}\tilde{\xi}^3 \;\; \tilde{\eta}^2\tilde{\xi}^3 \;\; \tilde{\zeta}\tilde{\eta}^2\tilde{\xi}^3 \;\; \tilde{\zeta}^2\tilde{\eta}^2\tilde{\xi}^3 \;\; \tilde{\eta}^3\tilde{\xi}^3 \;\; \tilde{\zeta}\tilde{\eta}^3\tilde{\xi}^3 \;\; \tilde{\zeta}^2\tilde{\eta}^3\tilde{\xi}^3 \Big], \\ \tilde{\boldsymbol{P}}^H_4 = \Big[& \tilde{\zeta}^3 \;\; \tilde{\zeta}^3\tilde{\eta} \;\; \tilde{\zeta}^3\tilde{\eta}^2 \;\; \tilde{\zeta}^3\tilde{\xi} \;\; \tilde{\zeta}^3\tilde{\eta}\tilde{\xi} \;\; \tilde{\zeta}^3\tilde{\eta}^2\tilde{\xi} \;\; \tilde{\zeta}^3\tilde{\xi}^2 \;\; \tilde{\zeta}^3\tilde{\eta}\tilde{\xi}^2 \;\; \tilde{\zeta}^3\tilde{\eta}^2\tilde{\xi}^2 \Big], \\ \tilde{\boldsymbol{P}}^H_5 = \Big[& \tilde{\xi}^3 \;\; \tilde{\zeta}\tilde{\xi}^3 \;\; \tilde{\zeta}^2\tilde{\xi}^3 \;\; \tilde{\eta}\tilde{\xi}^3 \;\; \tilde{\zeta}\tilde{\eta}\tilde{\xi}^3 \;\; \tilde{\zeta}^2\tilde{\eta}\tilde{\xi}^3 \;\; \tilde{\eta}^2\tilde{\xi}^3 \;\; \tilde{\zeta}\tilde{\eta}^2\tilde{\xi}^3 \;\; \tilde{\zeta}^2\tilde{\eta}^2\tilde{\xi}^3 \Big], \\ \tilde{\boldsymbol{P}}^H_6 = \Big[& \tilde{\eta}^3 \;\; \tilde{\zeta}\tilde{\eta}^3 \;\; \tilde{\zeta}^2\tilde{\eta}^3 \;\; \tilde{\eta}^3\tilde{\xi} \;\; \tilde{\zeta}\tilde{\eta}^3\tilde{\xi} \;\; \tilde{\zeta}^2\tilde{\eta}^3\tilde{\xi} \;\; \tilde{\eta}^3\tilde{\xi}^2 \;\; \tilde{\zeta}\tilde{\eta}^3\tilde{\xi}^2 \;\; \tilde{\zeta}^2\tilde{\eta}^3\tilde{\xi}^2 \Big]. \end{aligned}$$

6.3.1.4 Validation of the proposed stress interpolations

It can be further proved that the newly developed $\boldsymbol{P}_e$ matrix is free of spurious zero-energy modes and the $N(\boldsymbol{G}_e)$ consists of admissible deformations $\boldsymbol{u}_e$, which represent

Table 6.1: Values of constants in Eq. 6.35 for individual $\boldsymbol{g}$ vector.

$\boldsymbol{g}_i$	γ_1	γ_2	γ_3	γ_4	γ_5	γ_6
$\boldsymbol{g}_1$	0.20917	-0.067232	-0.067232	- 0.13449	0	0
$\boldsymbol{g}_2$	0	0.16044	-0.057801	-0.0036561	-0.12732	0.037134
$\boldsymbol{g}_3$	0	-0.046043	0.14019	-0.0121401	0.04824	0.0091005
$\boldsymbol{g}_4$	0	0.082658	0.147915	0.125178	-0.147912	0.054822
$\boldsymbol{g}_5$	0	0.061718	0.031137	0.148686	0.122316	0.059307
$\boldsymbol{g}_6$	0	-0.026998	-0.088149	0.0152283	0.029613	0.173739

solely the rigid body modes in the case of unconstrained element domain. To authenticate the validity of the statement, consider the $\boldsymbol{P}_e$ matrix as given in Eq. 6.33 and evaluate the dimensions and basis for $N(\boldsymbol{G}_e)$. Let $\boldsymbol{g}_1, \boldsymbol{g}_2, \ldots \boldsymbol{g}_6$ be the resultant basis for $N(\boldsymbol{G}_e)$ and any linear combination of these vectors represents the space of admissible deformations that results in zero strain energy. In general, the rigid body modes for the three-dimensional space can be expressed as

$$u = \gamma_1;\ v = 0;\ w = 0; \qquad (6.34a) \qquad u = \gamma_4\tilde{\eta};\ v = -\gamma_4\tilde{\xi};\ w = 0; \qquad (6.34d)$$

$$u = 0;\ v = \gamma_2;\ w = 0; \qquad (6.34b) \qquad u = 0;\ v = \gamma_5\tilde{\zeta};\ w = -\gamma_5\tilde{\eta}; \qquad (6.34e)$$

$$u = 0;\ v = 0;\ w = \gamma_3; \qquad (6.34c) \qquad u = \gamma_6\tilde{\zeta};\ v = 0;\ w = -\gamma_6\tilde{\xi}; \qquad (6.34f)$$

A Mathematica code has been developed to derive the symbolic expressions of the NURBS interpolation functions. The implementation steps and key commands are presented in Algorithm 5. Using these symbolic expressions for R_I and substituting $\tilde{\boldsymbol{u}} = \boldsymbol{g}_i$, Eq. 6.5 results in

$$u = \gamma_1 + \gamma_4\tilde{\eta} + \gamma_6\tilde{\zeta}; \quad v = \gamma_2 - \gamma_4\tilde{\xi} + \gamma_5\tilde{\zeta}; \quad w = \gamma_3 - \gamma_5\tilde{\eta} - \gamma_6\tilde{\xi}; \qquad (6.35)$$

The above expressions of $\boldsymbol{u}$ are indeed a linear combination of general rigid body modes expressed in Eq. 6.34. The value of the constants γ_i for each independent $\boldsymbol{g}$ vector is shown in Table 6.1. To further visualize the obtained space of rigid body modes, consider $\tilde{\boldsymbol{u}} = \sum_{i=1}^{6} a_i \boldsymbol{g}_i$. Any linear combination of $\boldsymbol{g}_i$ results in an undeformed geometric configuration coupled with either translation or rotation or both. Few of such resultant geometric descriptions are shown in Fig. 6.1.

6.3.2 Stress interpolation functions for 3D quadratic elements

A similar approach is followed to derive the $\boldsymbol{P}_e$ for 3D quadratic elements. Let us consider a single quadratic 3D element that is modeled by employing Ξ, $\boldsymbol{\mathcal{H}}$, and $\boldsymbol{\mathcal{Z}} = \{0,\ 0,\ 0,\ 1,\ 1,\ 1\}$ and p, q, and r as 2. For the stated geometric description, there are three univariate basis functions ($N_{\alpha,p}(\xi)$, $M_{\beta,q}(\eta)$, and $L_{\gamma,r}(\zeta)$ for $\alpha, \beta, \gamma = 1, 2, 3$) along each direction and the corresponding expressions are evaluated as follows:

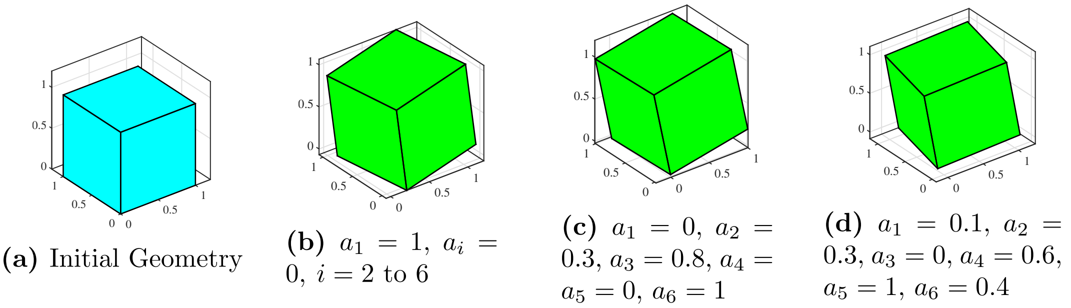
(a) Initial Geometry (b) $a_1 = 1$, $a_i = 0$, $i = 2$ to 6 (c) $a_1 = 0$, $a_2 = 0.3$, $a_3 = 0.8$, $a_4 = a_5 = 0$, $a_6 = 1$ (d) $a_1 = 0.1$, $a_2 = 0.3$, $a_3 = 0$, $a_4 = 0.6$, $a_5 = 1$, $a_6 = 0.4$

Figure 6.1: Initial and deformed geometric description for the displacement vectors in $N(\boldsymbol{G}_e)$.

$$N_{1,2} := \begin{cases} \xi^2 - 2\xi + 1 & 0 \le \xi \le 1 \\ 0 & \text{Otherwise} \end{cases}, \qquad M_{1,2} := \begin{cases} \eta^2 - 2\eta + 1 & 0 \le \eta \le 1 \\ 0 & \text{Otherwise} \end{cases},$$

$$N_{2,2} := \begin{cases} -2\left(\xi^2 - \xi\right) & 0 \le \xi \le 1 \\ 0 & \text{Otherwise} \end{cases}, \qquad M_{2,2} := \begin{cases} -2\left(\eta^2 - \eta\right) & 0 \le \eta \le 1 \\ 0 & \text{Otherwise} \end{cases},$$

$$N_{3,2} := \begin{cases} \xi^2 & 0 \le \xi \le 1 \\ 0 & \text{Otherwise} \end{cases}, \qquad M_{3,2} := \begin{cases} \eta^2 & 0 \le \eta \le 1 \\ 0 & \text{Otherwise} \end{cases},$$

$$L_{1,2} := \begin{cases} \zeta^2 - 2\zeta + 1 & 0 \le \zeta \le 1 \\ 0 & \text{Otherwise} \end{cases},$$

$$L_{2,2} := \begin{cases} -2\left(\zeta^2 - \zeta\right) & 0 \le \zeta \le 1 \\ 0 & \text{Otherwise} \end{cases},$$

$$L_{3,2} := \begin{cases} \zeta^2 & 0 \le \zeta \le 1 \\ 0 & \text{Otherwise} \end{cases}.$$

If $f_1(x) := x^2 - 2x + 1$, $f_2(x) := -2(x^2 - x)$ and $f_3(x) := x^2$, then the participating basis functions are defined as

$$\begin{aligned}
R_1 &:= f_1(\zeta)f_1(\eta)f_1(\xi), & R_{10} &:= f_2(\zeta)f_1(\eta)f_1(\xi), & R_{19} &:= f_3(\zeta)f_1(\eta)f_1(\xi),\\
R_2 &:= f_1(\zeta)f_1(\eta)f_2(\xi), & R_{11} &:= f_2(\zeta)f_1(\eta)f_2(\xi), & R_{20} &:= f_3(\zeta)f_1(\eta)f_2(\xi),\\
R_3 &:= f_1(\zeta)f_1(\eta)f_3(\xi), & R_{12} &:= f_2(\zeta)f_1(\eta)f_3(\xi), & R_{21} &:= f_3(\zeta)f_1(\eta)f_3(\xi),\\
R_4 &:= f_1(\zeta)f_2(\eta)f_1(\xi), & R_{13} &:= f_2(\zeta)f_2(\eta)f_1(\xi), & R_{22} &:= f_3(\zeta)f_2(\eta)f_1(\xi),\\
R_5 &:= f_1(\zeta)f_2(\eta)f_2(\xi), & R_{14} &:= f_2(\zeta)f_2(\eta)f_2(\xi), & R_{23} &:= f_3(\zeta)f_2(\eta)f_2(\xi),\\
R_6 &:= f_1(\zeta)f_2(\eta)f_3(\xi), & R_{15} &:= f_2(\zeta)f_2(\eta)f_3(\xi), & R_{24} &:= f_3(\zeta)f_2(\eta)f_3(\xi),\\
R_7 &:= f_1(\zeta)f_3(\eta)f_1(\xi), & R_{16} &:= f_2(\zeta)f_3(\eta)f_1(\xi), & R_{25} &:= f_3(\zeta)f_3(\eta)f_1(\xi),\\
R_8 &:= f_1(\zeta)f_3(\eta)f_2(\xi), & R_{17} &:= f_2(\zeta)f_3(\eta)f_2(\xi), & R_{26} &:= f_3(\zeta)f_3(\eta)f_2(\xi),\\
R_9 &:= f_1(\zeta)f_3(\eta)f_3(\xi), & R_{18} &:= f_2(\zeta)f_3(\eta)f_3(\xi), & R_{27} &:= f_3(\zeta)f_3(\eta)f_3(\xi).
\end{aligned}$$

Substituting the expressions of R_I $(I = 1, 2, \ldots 27)$ in Eq. 6.5, the expression of $\boldsymbol{u}$ will result in a tri-quadratic expression with the coefficients associated with each constant collected as follows:

$$\Big\{ 1,\ \zeta,\ \zeta^2,\ \eta,\ \zeta\eta,\ \zeta^2\eta,\ \eta^2,\ \zeta\eta^2,\ \zeta^2\eta^2,\ \xi,\ \zeta\xi,\ \zeta^2\xi,\ \eta\xi,\ \zeta\eta\xi,\ \zeta^2\eta\xi,\ \eta^2\xi, \\ \zeta\eta^2\xi,\ \zeta^2\eta^2\xi,\ \xi^2,\ \zeta\xi^2,\ \zeta^2\xi^2,\ \eta\xi^2,\ \zeta\eta\xi^2,\ \zeta^2\eta\xi^2,\ \eta^2\xi^2,\ \zeta\eta^2\xi^2,\ \zeta^2\eta^2\xi^2 \Big\}.$$

Let the choice of $\boldsymbol{P}_L^e$ in master space be the full tri-linear space given as follows:

$$\boldsymbol{P}_L^e = \Big[\, \boldsymbol{I}_6\ \ \tilde{\zeta}\boldsymbol{I}_6\ \ \tilde{\eta}\boldsymbol{I}_6\ \ \tilde{\zeta}\tilde{\eta}\boldsymbol{I}_6\ \ \tilde{\xi}\boldsymbol{I}_6\ \ \tilde{\zeta}\tilde{\xi}\boldsymbol{I}_6\ \ \tilde{\eta}\tilde{\xi}\boldsymbol{I}_6\ \ \tilde{\zeta}\tilde{\eta}\tilde{\xi}\boldsymbol{I}_6 \,\Big], \tag{6.36}$$

where $\boldsymbol{I}_6$ is the identity matrix of dimension 6 × 6. Substituting $\boldsymbol{P}_e = \boldsymbol{P}_L^e$ in the expression of $\boldsymbol{G}_e$ leads to

$$\left[\int_{\mathcal{R}_e} (\boldsymbol{P}_L^e)^T \boldsymbol{B}_e \,\mathrm{d}\mathcal{R}\right] \tilde{\boldsymbol{u}}_e = \boldsymbol{0} \quad \rightarrow \quad \boldsymbol{G}_L^e \tilde{\boldsymbol{u}}_e = \boldsymbol{0}. \tag{6.37}$$

Hence, it signifies the presence of zero-energy modes if only $\boldsymbol{P}_L^e$ is considered for stress interpolation. For the prescribed setting of $\boldsymbol{P}_L^e$ in combination with the NURBS interpolations for displacements, the dimension of $N(\boldsymbol{G}_L^e)$ is 33, out of which the total number of spurious-energy modes are 27, and the rigid body modes are 6.

To identify the stated 27 zero-energy modes, consider a quadratic element in its master space where the surfaces are given by $\tilde{\xi} = \pm 1$, $\tilde{\eta} = \pm 1$ and $\tilde{\zeta} = \pm 1$. If $f(x) := (1 - 3x^2)$, then the expressions for the admissible deformations $\boldsymbol{u}_e$ that yield $\bar{\boldsymbol{\varepsilon}}_c(\boldsymbol{u}_e) = \boldsymbol{0}$ at the 2 × 2 × 2 Gauss quadrature points $\left(\tilde{\xi} = \pm\sqrt{\tfrac{1}{3}};\ \tilde{\eta} = \pm\sqrt{\tfrac{1}{3}};\ \text{and}\ \tilde{\zeta} = \pm\sqrt{\tfrac{1}{3}}\right)$ are given as follows:

$$\begin{array}{llll}
u = \alpha_1 f(\tilde{\zeta}) f(\tilde{\eta}); & v = 0; w = 0; & u = 0;\ v = \alpha_8 f(\tilde{\zeta}) f(\tilde{\eta}); & w = 0; \\
u = \alpha_2 f(\tilde{\zeta}) f(\tilde{\xi}); & v = 0; w = 0; & u = 0;\ v = \alpha_9 f(\tilde{\zeta}) f(\tilde{\xi}); & w = 0; \\
u = \alpha_3 f(\tilde{\eta}) f(\tilde{\xi}); & v = 0; w = 0; & u = 0;\ v = \alpha_{10} f(\tilde{\eta}) f(\tilde{\xi}); & w = 0; \\
u = \alpha_4 \tilde{\zeta} f(\tilde{\eta}) f(\tilde{\xi}); & v = 0; w = 0; & u = 0;\ v = \alpha_{11} \tilde{\zeta} f(\tilde{\eta}) f(\tilde{\xi}); & w = 0; \\
u = \alpha_5 f(\tilde{\zeta}) \tilde{\eta} f(\tilde{\xi}); & v = 0; w = 0; & u = 0;\ v = \alpha_{12} f(\tilde{\zeta}) \tilde{\eta} f(\tilde{\xi}); & w = 0; \\
u = \alpha_6 f(\tilde{\zeta}) f(\tilde{\eta}) \tilde{\xi}; & v = 0; w = 0; & u = 0;\ v = \alpha_{13} f(\tilde{\zeta}) f(\tilde{\eta}) \tilde{\xi}; & w = 0; \\
u = \alpha_7 f(\tilde{\zeta}) f(\tilde{\eta}) f(\tilde{\xi}); & v = 0; w = 0; & u = 0;\ v = \alpha_{14} f(\tilde{\zeta}) f(\tilde{\eta}) f(\tilde{\xi}); & w = 0;
\end{array}$$

$$\begin{array}{ll}
u = 0;\ v = 0;\ w = \alpha_{15} f(\tilde{\zeta}) f(\tilde{\eta}); & u = -\alpha_{22} \tilde{\xi} f(\tilde{\eta});\ v = \alpha_{22} f(\tilde{\xi}) \tilde{\eta};\ w = 0; \\
u = 0;\ v = 0;\ w = \alpha_{16} f(\tilde{\zeta}) f(\tilde{\xi}); & u = \alpha_{23} \tilde{\xi} f(\tilde{\zeta});\ v = 0;\ w = -\alpha_{23} f(\tilde{\xi}) \tilde{\zeta}; \\
u = 0;\ v = 0;\ w = \alpha_{17} f(\tilde{\eta}) f(\tilde{\xi}); & u = 0;\ v = -\alpha_{24} \tilde{\eta} f(\tilde{\zeta});\ w = \alpha_{24} f(\tilde{\eta}) \tilde{\zeta}; \\
u = 0;\ v = 0;\ w = \alpha_{18} \tilde{\zeta} f(\tilde{\eta}) f(\tilde{\xi}); & u = -\alpha_{25} \tilde{\xi} f(\tilde{\eta}) \tilde{\zeta};\ v = \alpha_{25} f(\tilde{\xi}) \tilde{\eta} \tilde{\zeta};\ w = 0; \\
u = 0;\ v = 0;\ w = \alpha_{19} f(\tilde{\zeta}) \tilde{\eta} f(\tilde{\xi}); & u = \alpha_{26} \tilde{\xi} \tilde{\eta} f(\tilde{\zeta});\ v = 0;\ w = -\alpha_{26} \tilde{\zeta} \tilde{\eta} f(\tilde{\xi}); \\
u = 0;\ v = 0;\ w = \alpha_{20} f(\tilde{\zeta}) f(\tilde{\eta}) \tilde{\xi}; & u = 0;\ v = -\alpha_{27} \tilde{\eta} \tilde{\xi} f(\tilde{\zeta});\ w = \alpha_{27} \tilde{\zeta} \tilde{\xi} f(\tilde{\eta}). \\
u = 0;\ v = 0;\ w = \alpha_{21} f(\tilde{\zeta}) f(\tilde{\eta}) f(\tilde{\xi}); &
\end{array}$$

Finally, every 'α' in the enlisted zero-energy modes is suppressed using an individual '$\hat{\beta}$' in such a way that no '$\hat{\beta}$' term is shared. This leads to the following stress distribution in the master space

$$
\begin{aligned}
\sigma_{\tilde{\xi}\tilde{\xi}} &= \hat{\beta}_1 + \tilde{\zeta}\hat{\beta}_2 + \tilde{\zeta}^2\hat{\beta}_3 + \tilde{\eta}\hat{\beta}_4 + \tilde{\zeta}\tilde{\eta}\hat{\beta}_5 + \tilde{\zeta}^2\tilde{\eta}\hat{\beta}_6 + \tilde{\eta}^2\hat{\beta}_7 + \tilde{\zeta}\tilde{\eta}^2\hat{\beta}_8 + \tilde{\zeta}^2\tilde{\eta}^2\hat{\beta}_9 + \tilde{\xi}\hat{\beta}_{10} \\
&\quad + \tilde{\zeta}\tilde{\xi}\hat{\beta}_{11} + \tilde{\zeta}^2\tilde{\xi}\hat{\beta}_{12} + \tilde{\eta}\tilde{\xi}\hat{\beta}_{13} + \tilde{\zeta}\tilde{\eta}\tilde{\xi}\hat{\beta}_{14} + \tilde{\zeta}^2\tilde{\eta}\tilde{\xi}\hat{\beta}_{15} + \tilde{\eta}^2\tilde{\xi}\hat{\beta}_{15} + \tilde{\zeta}\tilde{\eta}^2\tilde{\xi}\hat{\beta}_{17} + \tilde{\zeta}^2\tilde{\eta}^2\tilde{\xi}\hat{\beta}_{18}, \\
\sigma_{\tilde{\eta}\tilde{\eta}} &= \hat{\beta}_{19} + \tilde{\zeta}\hat{\beta}_{20} + \tilde{\zeta}^2\hat{\beta}_{21} + \tilde{\eta}\hat{\beta}_{22} + \tilde{\zeta}\tilde{\eta}\hat{\beta}_{23} + \tilde{\zeta}^2\tilde{\eta}\hat{\beta}_{24} + \tilde{\xi}\hat{\beta}_{25} + \tilde{\zeta}\tilde{\xi}\hat{\beta}_{26} + \tilde{\zeta}^2\tilde{\xi}\hat{\beta}_{27} + \tilde{\eta}\tilde{\xi}\hat{\beta}_{28} \\
&\quad + \tilde{\zeta}\tilde{\eta}\tilde{\xi}\hat{\beta}_{29} + \tilde{\zeta}^2\tilde{\eta}\tilde{\xi}\hat{\beta}_{30} + \tilde{\xi}^2\hat{\beta}_{31} + \tilde{\zeta}\tilde{\xi}^2\hat{\beta}_{32} + \tilde{\zeta}^2\tilde{\xi}^2\hat{\beta}_{33} + \tilde{\eta}\tilde{\xi}^2\hat{\beta}_{34} + \tilde{\zeta}\tilde{\eta}\tilde{\xi}^2\hat{\beta}_{35} + \tilde{\zeta}^2\tilde{\eta}\tilde{\xi}^2\hat{\beta}_{36}, \\
\sigma_{\tilde{\zeta}\tilde{\zeta}} &= \hat{\beta}_{37} + \tilde{\zeta}\hat{\beta}_{38} + \tilde{\eta}\hat{\beta}_{39} + \tilde{\zeta}\tilde{\eta}\hat{\beta}_{40} + \tilde{\eta}^2\hat{\beta}_{41} + \tilde{\zeta}\tilde{\eta}^2\hat{\beta}_{42} + \tilde{\xi}\hat{\beta}_{43} + \tilde{\zeta}\tilde{\xi}\hat{\beta}_{44} + \tilde{\eta}\tilde{\xi}\hat{\beta}_{45} + \tilde{\zeta}\tilde{\eta}\tilde{\xi}\hat{\beta}_{46} \\
&\quad + \tilde{\eta}^2\tilde{\xi}\hat{\beta}_{47} + \tilde{\zeta}\tilde{\eta}^2\tilde{\xi}\hat{\beta}_{48} + \tilde{\xi}^2\hat{\beta}_{49} + \tilde{\zeta}\tilde{\xi}^2\hat{\beta}_{50} + \tilde{\eta}\tilde{\xi}^2\hat{\beta}_{51} + \tilde{\zeta}\tilde{\eta}\tilde{\xi}^2\hat{\beta}_{52} + \tilde{\eta}^2\tilde{\xi}^2\hat{\beta}_{53} + \tilde{\zeta}\tilde{\eta}^2\tilde{\xi}^2\hat{\beta}_{54}, \\
\sigma_{\tilde{\xi}\tilde{\eta}} &= \hat{\beta}_{55} + \tilde{\eta}\hat{\beta}_{56} + \tilde{\zeta}\hat{\beta}_{57} + \tilde{\xi}\hat{\beta}_{58} + \tilde{\xi}\tilde{\eta}\hat{\beta}_{59} + \tilde{\xi}\tilde{\zeta}\hat{\beta}_{60} + \tilde{\zeta}^2\hat{\beta}_{61} + \tilde{\eta}\tilde{\zeta}\hat{\beta}_{62} + \tilde{\xi}\tilde{\eta}\tilde{\zeta}\hat{\beta}_{63} + \tilde{\zeta}^2\tilde{\eta}\hat{\beta}_{64} \\
&\quad + \tilde{\zeta}^2\tilde{\xi}\hat{\beta}_{65} + \tilde{\xi}\tilde{\eta}\tilde{\zeta}^2\hat{\beta}_{66}, \\
\sigma_{\tilde{\eta}\tilde{\zeta}} &= \hat{\beta}_{67} + \tilde{\xi}\hat{\beta}_{68} + \tilde{\zeta}\hat{\beta}_{69} + \tilde{\eta}\hat{\beta}_{70} + \tilde{\xi}^2\hat{\beta}_{71} + \tilde{\xi}\tilde{\eta}\hat{\beta}_{72} + \tilde{\eta}\tilde{\zeta}\hat{\beta}_{73} + \tilde{\xi}\tilde{\zeta}\hat{\beta}_{74} + \tilde{\xi}^2\tilde{\zeta}\hat{\beta}_{75} + \tilde{\xi}\tilde{\eta}\tilde{\zeta}\hat{\beta}_{76} \\
&\quad + \tilde{\xi}^2\tilde{\eta}\hat{\beta}_{77} + \tilde{\xi}^2\tilde{\eta}\tilde{\zeta}\hat{\beta}_{78}, \\
\sigma_{\tilde{\xi}\tilde{\zeta}} &= \hat{\beta}_{79} + \tilde{\eta}\hat{\beta}_{80} + \tilde{\zeta}\hat{\beta}_{81} + \tilde{\xi}\hat{\beta}_{82} + \tilde{\xi}\tilde{\eta}\hat{\beta}_{83} + \tilde{\xi}\tilde{\zeta}\hat{\beta}_{84} + \tilde{\eta}^2\hat{\beta}_{85} + \tilde{\eta}\tilde{\zeta}\hat{\beta}_{86} + \tilde{\xi}\tilde{\eta}\tilde{\zeta}\hat{\beta}_{87} + \tilde{\eta}^2\tilde{\zeta}\hat{\beta}_{88} \\
&\quad + \tilde{\eta}^2\tilde{\xi}\hat{\beta}_{89} + \tilde{\xi}\tilde{\eta}^2\tilde{\zeta}\hat{\beta}_{90}.
\end{aligned}
$$

Hence, the resultant feasible interpolations in $\tilde{\boldsymbol{P}}_e$ matrix for the quadratic element are derived as follows:

$$
\begin{Bmatrix} \sigma_{\tilde{\xi}\tilde{\xi}} \\ \sigma_{\tilde{\eta}\tilde{\eta}} \\ \sigma_{\tilde{\zeta}\tilde{\zeta}} \\ \sigma_{\tilde{\xi}\tilde{\eta}} \\ \sigma_{\tilde{\eta}\tilde{\zeta}} \\ \sigma_{\tilde{\xi}\tilde{\zeta}} \end{Bmatrix} = \underbrace{\begin{bmatrix} \tilde{\boldsymbol{P}}_1 & \mathbf{0}_a & \mathbf{0}_a & \mathbf{0}_b & \mathbf{0}_b & \mathbf{0}_b \\ \mathbf{0}_a & \tilde{\boldsymbol{P}}_2 & \mathbf{0}_a & \mathbf{0}_b & \mathbf{0}_b & \mathbf{0}_b \\ \mathbf{0}_a & \mathbf{0}_a & \tilde{\boldsymbol{P}}_3 & \mathbf{0}_b & \mathbf{0}_b & \mathbf{0}_b \\ \mathbf{0}_a & \mathbf{0}_a & \mathbf{0}_a & \tilde{\boldsymbol{P}}_4 & \mathbf{0}_b & \mathbf{0}_b \\ \mathbf{0}_a & \mathbf{0}_a & \mathbf{0}_a & \mathbf{0}_b & \tilde{\boldsymbol{P}}_5 & \mathbf{0}_b \\ \mathbf{0}_a & \mathbf{0}_a & \mathbf{0}_a & \mathbf{0}_b & \mathbf{0}_b & \tilde{\boldsymbol{P}}_6 \end{bmatrix}}_{\tilde{\boldsymbol{P}}(\tilde{\xi},\tilde{\eta},\tilde{\zeta})} \underbrace{\begin{Bmatrix} \tilde{\beta}_1 \\ \tilde{\beta}_2 \\ \tilde{\beta}_3 \\ \tilde{\beta}_4 \\ \vdots \\ \tilde{\beta}_{90} \end{Bmatrix}}_{\hat{\boldsymbol{\beta}}}, \tag{6.40}
$$

where $\mathbf{0}_a$ and $\mathbf{0}_b$ are the null or zero vectors of size 1 × 18 and 1 × 12, respectively. The vectors $\tilde{\boldsymbol{P}}_1, \tilde{\boldsymbol{P}}_2, \ldots, \tilde{\boldsymbol{P}}_6$ are given as

$$
\begin{aligned}
\tilde{\boldsymbol{P}}_1 &= \begin{bmatrix} 1 & \tilde{\zeta} & \tilde{\zeta}^2 & \tilde{\eta} & \tilde{\zeta}\tilde{\eta} & \tilde{\zeta}^2\tilde{\eta} & \tilde{\eta}^2 & \tilde{\zeta}\tilde{\eta}^2 & \tilde{\zeta}^2\tilde{\eta}^2 & \tilde{\xi} & \tilde{\zeta}\tilde{\xi} & \tilde{\zeta}^2\tilde{\xi} & \tilde{\eta}\tilde{\xi} & \tilde{\zeta}\tilde{\eta}\tilde{\xi} & \tilde{\zeta}^2\tilde{\eta}\tilde{\xi} & \tilde{\eta}^2\tilde{\xi} & \tilde{\zeta}\tilde{\eta}^2\tilde{\xi} & \tilde{\zeta}^2\tilde{\eta}^2\tilde{\xi} \end{bmatrix}, \\
\tilde{\boldsymbol{P}}_2 &= \begin{bmatrix} 1 & \tilde{\zeta} & \tilde{\zeta}^2 & \tilde{\eta} & \tilde{\zeta}\tilde{\eta} & \tilde{\zeta}^2\tilde{\eta} & \tilde{\xi} & \tilde{\zeta}\tilde{\xi} & \tilde{\zeta}^2\tilde{\xi} & \tilde{\eta}\tilde{\xi} & \tilde{\zeta}\tilde{\eta}\tilde{\xi} & \tilde{\zeta}^2\tilde{\eta}\tilde{\xi} & \tilde{\xi}^2 & \tilde{\zeta}\tilde{\xi}^2 & \tilde{\zeta}^2\tilde{\xi}^2 & \tilde{\eta}\tilde{\xi}^2 & \tilde{\zeta}\tilde{\eta}\tilde{\xi}^2 & \tilde{\zeta}^2\tilde{\eta}\tilde{\xi}^2 \end{bmatrix}, \\
\tilde{\boldsymbol{P}}_3 &= \begin{bmatrix} 1 & \tilde{\zeta} & \tilde{\eta} & \tilde{\zeta}\tilde{\eta} & \tilde{\eta}^2 & \tilde{\zeta}\tilde{\eta}^2 & \tilde{\xi} & \tilde{\zeta}\tilde{\xi} & \tilde{\eta}\tilde{\xi} & \tilde{\zeta}\tilde{\eta}\tilde{\xi} & \tilde{\eta}^2\tilde{\xi} & \tilde{\zeta}\tilde{\eta}^2\tilde{\xi} & \tilde{\xi}^2 & \tilde{\zeta}\tilde{\xi}^2 & \tilde{\eta}\tilde{\xi}^2 & \tilde{\zeta}\tilde{\eta}\tilde{\xi}^2 & \tilde{\eta}^2\tilde{\xi}^2 & \tilde{\zeta}\tilde{\eta}^2\tilde{\xi}^2 \end{bmatrix}, \\
\tilde{\boldsymbol{P}}_4 &= \begin{bmatrix} 1 & \tilde{\eta} & \tilde{\zeta} & \tilde{\xi} & \tilde{\xi}\tilde{\eta} & \tilde{\xi}\tilde{\zeta} & \tilde{\zeta}^2 & \tilde{\eta}\tilde{\zeta} & \tilde{\xi}\tilde{\eta}\tilde{\zeta} & \tilde{\zeta}^2\tilde{\eta} & \tilde{\zeta}^2\tilde{\xi} & \tilde{\xi}\tilde{\eta}\tilde{\zeta}^2 \end{bmatrix}, \\
\tilde{\boldsymbol{P}}_5 &= \begin{bmatrix} 1 & \tilde{\xi} & \tilde{\zeta} & \tilde{\eta} & \tilde{\xi}^2 & \tilde{\xi}\tilde{\eta} & \tilde{\eta}\tilde{\zeta} & \tilde{\xi}\tilde{\zeta} & \tilde{\xi}^2\tilde{\zeta} & \tilde{\xi}\tilde{\eta}\tilde{\zeta} & \tilde{\xi}^2\tilde{\eta} & \tilde{\xi}^2\tilde{\eta}\tilde{\zeta} \end{bmatrix},
\end{aligned}
$$

Table 6.2: Values of constants in Eq. 6.41 for individual $\boldsymbol{g}$ vector.

$\boldsymbol{g}_i$	γ_1	γ_2	γ_3	γ_4	γ_5	γ_6
$\boldsymbol{g}_1$	-0.006514	-0.26139	0.12977	-0.19805	0.1289	0.051254
$\boldsymbol{g}_2$	0	-0.033028	-0.13633	0.039134	0.13913	-0.187364
$\boldsymbol{g}_3$	0	0.015857	0.15377	0.107586	0.137538	-0.120254
$\boldsymbol{g}_4$	0	-0.11516	0.060068	0.13794	0.138954	0.051634
$\boldsymbol{g}_5$	-0.30422	0.096905	0.088529	0.18686	-0.00276	0.18152
$\boldsymbol{g}_6$	0	0.016563	-0.14858	0.06957	-0.19212	-0.19212

$$\tilde{\boldsymbol{P}}_6 = \begin{bmatrix} 1 & \tilde{\eta} & \tilde{\zeta} & \tilde{\xi} & \tilde{\xi}\tilde{\eta} & \tilde{\xi}\tilde{\zeta} & \tilde{\eta}^2 & \tilde{\eta}\tilde{\zeta} & \tilde{\xi}\tilde{\eta}\tilde{\zeta} & \tilde{\eta}^2\tilde{\zeta} & \tilde{\eta}^2\tilde{\xi} & \tilde{\xi}\tilde{\eta}^2\tilde{\zeta} \end{bmatrix}.$$

The higher-order terms in $\sigma_{\tilde{\xi}\tilde{\xi}}$, $\sigma_{\tilde{\eta}\tilde{\eta}}$, and $\sigma_{\tilde{\zeta}\tilde{\zeta}}$ suppress a total of 24 zero-energy modes, and the remaining three modes (α_1, α_9, and α_{17}) are suppressed using the higher-order terms in shear stress interpolations. Moreover, all the terms of the corresponding order of interpolation are also incorporated in shear stresses to achieve the stability of the element. For instance, the necessary condition to suppress the zero-energy modes for $\sigma_{\tilde{\xi}\tilde{\eta}}$ is to have two higher-order terms ($\tilde{\zeta}^2\tilde{\eta}$, $\tilde{\zeta}^2\tilde{\xi}$). However, the terms ($\tilde{\zeta}^2$, $\tilde{\zeta}^2\tilde{\eta}$, $\tilde{\zeta}^2\tilde{\xi}$, $\tilde{\zeta}^2\tilde{\xi}\tilde{\eta}$) are added to achieve the completeness of the interpolations.

Furthermore, the developed $\boldsymbol{P}_e$ matrix in combination with the NURBS interpolations is free of spurious zero-energy modes and the $N(\boldsymbol{G}_e)$ consists of admissible deformations $\boldsymbol{u}_e$, which represent solely the rigid body modes in the case of unconstrained element domain. The statement is validated by evaluating the basis for $N(\boldsymbol{G}_e)$ and using these basis to symbolically evaluate Eq. 6.5, which results in the following expressions

$$u = \gamma_1 + \gamma_4\tilde{\eta} + \gamma_6\tilde{\zeta}; \quad v = \gamma_2 - \gamma_4\tilde{\xi} + \gamma_5\tilde{\zeta}; \quad w = \gamma_3 - \gamma_5\tilde{\eta} - \gamma_6\tilde{\xi}. \tag{6.41}$$

The above expressions of $\boldsymbol{u}$ are indeed a linear combination of general rigid body modes expressed in Eq. 6.34. The value of the constants γ_i for each independent $\boldsymbol{g}$ vector is evaluated as shown in Table 6.2.

6.3.3 Stress interpolation functions for 2D hybrid elements

A similar approach is employed to assess stress interpolation functions for 2D NURBS elements. Analogous to the 3D elements, the term “cubic or quadratic element” in this context denotes the utilization of cubic or quadratic interpolation functions in both directions with the highest possible continuity. The resultant feasible interpolations in $\tilde{\boldsymbol{P}}_e$ matrix for the these elements are derived as follows:

6.3.3.1 Cubic elements

The stress interpolation matrix for 2D cubic elements, featuring third-degree NURBS interpolation in both ξ and η directions with C^2 inter-element continuity, is given as follows:

$$\begin{Bmatrix} \sigma_{\tilde{\xi}\tilde{\xi}} \\ \sigma_{\tilde{\eta}\tilde{\eta}} \\ \sigma_{\tilde{\xi}\tilde{\eta}} \end{Bmatrix} = \underbrace{\begin{bmatrix} \tilde{\boldsymbol{P}}_1 & \mathbf{0}_a & \mathbf{0}_b \\ \mathbf{0}_a & \tilde{\boldsymbol{P}}_2 & \mathbf{0}_b \\ \mathbf{0}_a & \mathbf{0}_a & \tilde{\boldsymbol{P}}_3 \end{bmatrix}}_{\tilde{\boldsymbol{P}}(\tilde{\xi},\tilde{\eta})} \underbrace{\begin{Bmatrix} \tilde{\beta}_1 \\ \tilde{\beta}_2 \\ \vdots \\ \tilde{\beta}_{33} \end{Bmatrix}}_{\tilde{\boldsymbol{\beta}}}, \tag{6.42}$$

where $\mathbf{0}_a$ and $\mathbf{0}_b$ are the zero vectors of size 1×12 and 1×9, respectively. The vectors $\tilde{\boldsymbol{P}}_1$, $\tilde{\boldsymbol{P}}_2$, and $\tilde{\boldsymbol{P}}_3$ are evaluated as

$$\begin{aligned} \tilde{\boldsymbol{P}}_1 &= \begin{bmatrix} 1 & \tilde{\xi} & \tilde{\eta} & \tilde{\xi}^2 & \tilde{\eta}\tilde{\xi} & \tilde{\eta}^2 & \tilde{\eta}\tilde{\xi}^2 & \tilde{\eta}^2\tilde{\xi} & \tilde{\eta}^2\tilde{\xi}^2 & \tilde{\eta}^3\tilde{\xi}^2 & \tilde{\eta}^3\tilde{\xi} & \tilde{\eta}^3 \end{bmatrix}, \\ \tilde{\boldsymbol{P}}_2 &= \begin{bmatrix} 1 & \tilde{\xi} & \tilde{\eta} & \tilde{\xi}^2 & \tilde{\eta}\tilde{\xi} & \tilde{\eta}^2 & \tilde{\eta}\tilde{\xi}^2 & \tilde{\eta}^2\tilde{\xi} & \tilde{\eta}^2\tilde{\xi}^2 & \tilde{\eta}\tilde{\xi}^3 & \tilde{\eta}^2\tilde{\xi}^3 & \tilde{\xi}^3 \end{bmatrix}, \\ \tilde{\boldsymbol{P}}_3 &= \begin{bmatrix} 1 & \tilde{\xi} & \tilde{\eta} & \tilde{\xi}^2 & \tilde{\eta}\tilde{\xi} & \tilde{\eta}^2 & \tilde{\eta}\tilde{\xi}^2 & \tilde{\eta}^2\tilde{\xi} & \tilde{\eta}^2\tilde{\xi}^2 \end{bmatrix}. \end{aligned}$$

6.3.3.2 Quadratic elements

The stress interpolation matrix for 2D quadratic elements, having second-degree NURBS interpolation in both ξ and η directions with C^1 inter-element continuity, is given as follows:

$$\begin{Bmatrix} \sigma_{\tilde{\xi}\tilde{\xi}} \\ \sigma_{\tilde{\eta}\tilde{\eta}} \\ \sigma_{\tilde{\xi}\tilde{\eta}} \end{Bmatrix} = \underbrace{\begin{bmatrix} \tilde{\boldsymbol{P}}_1 & \mathbf{0}_a & \mathbf{0}_b \\ \mathbf{0}_a & \tilde{\boldsymbol{P}}_2 & \mathbf{0}_b \\ \mathbf{0}_a & \mathbf{0}_a & \tilde{\boldsymbol{P}}_3 \end{bmatrix}}_{\tilde{\boldsymbol{P}}(\tilde{\xi},\tilde{\eta})} \underbrace{\begin{Bmatrix} \tilde{\beta}_1 \\ \tilde{\beta}_2 \\ \vdots \\ \tilde{\beta}_{16} \end{Bmatrix}}_{\tilde{\boldsymbol{\beta}}}, \tag{6.43}$$

where $\mathbf{0}_a$ and $\mathbf{0}_b$ are the zero vectors of size 1×6 and 1×4, respectively. The vectors $\tilde{\boldsymbol{P}}_1$, $\tilde{\boldsymbol{P}}_2$, and $\tilde{\boldsymbol{P}}_3$ are given as

$$\tilde{\boldsymbol{P}}_1 = \begin{bmatrix} 1 & \tilde{\xi} & \tilde{\eta} & \tilde{\xi}\tilde{\eta} & \tilde{\eta}^2 & \tilde{\eta}^2\tilde{\xi} \end{bmatrix}, \quad \tilde{\boldsymbol{P}}_2 = \begin{bmatrix} 1 & \tilde{\xi} & \tilde{\eta} & \tilde{\xi}\tilde{\eta} & \tilde{\xi}^2 & \tilde{\eta}\tilde{\xi}^2 \end{bmatrix}, \\ \tilde{\boldsymbol{P}}_3 = \begin{bmatrix} 1 & \tilde{\xi} & \tilde{\eta} & \tilde{\xi}\tilde{\eta} \end{bmatrix}$$

6.4 Numerical examples

The present section demonstrates the performance of the proposed formulation against the standard single-field IGA, the Lagrangian FEA, and the hybrid FEA formulation. The coarse mesh accuracy, efficacy, and robustness of the method are shown using several benchmark numerical examples. The process commences by assessing the proposed 2D quadratic and cubic hybrid IGA elements, with the initial two scenarios, where the problem domain is under influence of shear locking. These problems encompass straight and curved cantilever beam configurations with end loads and varying slenderness ratios ranging from 10 to 1000. Subsequently, we analyze the standard Cook's membrane

Table 6.3: List of elements abbreviation used in the present study.

Element	Description
FE-q4	Conventional 4-node quadrilateral element
FE-q9	Conventional 9-node quadrilateral element
FE-b8	Conventional 8-node brick element
FE-b27	Conventional 27-node brick element
h-FE-q4	4-node hybrid quadrilateral element
h-FE-q9	9-node hybrid quadrilateral element
h-FE-b8	8-node hybrid brick element
h-FE-b27	27-node hybrid brick element
$\text{IgA}^{\text{2D}}_{\text{Lin}}$	Conventional 2D NURBS-based linear element
$\text{IgA}^{\text{2D}}_{\text{Quad}}$	Conventional 2D NURBS-based quadratic element
$\text{IgA}^{\text{2D}}_{\text{Cub}}$	Conventional 2D NURBS-based cubic element
$\text{h-IgA}^{\text{2D}}_{\text{Lin}}$	Stress-based hybrid 2D NURBS-based linear element
$\text{h-IgA}^{\text{2D}}_{\text{Quad}}$	Proposed stress-based hybrid 2D quadratic element for NURBS-based IGA
$\text{h-IgA}^{\text{2D}}_{\text{Cub}}$	Proposed stress-based hybrid 2D cubic element for NURBS-based IGA
$\text{IgA}^{\text{3D}}_{\text{Quad}}$	Conventional 3D NURBS-based quadratic element
$\text{IgA}^{\text{3D}}_{\text{Cub}}$	Conventional 3D NURBS-based cubic element
$\text{h-IgA}^{\text{3D}}_{\text{Quad}}$	Proposed stress-based hybrid 3D quadratic element for NURBS-based IGA
$\text{h-IgA}^{\text{3D}}_{\text{Cub}}$	Proposed stress-based hybrid 3D cubic element for NURBS-based IGA

problem, evaluating the element's performance under the volumetric locking. Furthermore, we investigate a plate with a hole problem, both in the presence and absence of volumetric locking effects.

Later in the section, we redirect our attention towards the proposed 3D quadratic and cubic hybrid IGA elements. These elements are assessed by analyzing the behavior of different types of beams under the influence of shear and coupled shear-membrane locking. These problems involves the 3D version of the straight and curved cantilever beam problems. Next, we present the well-established shell obstacle course problems to validate the superior efficacy of the proposed formulations against the conventional formulation. These problems commonly includes the pinched cylinder, pinched hemisphere and Scordelis–Lo roof problem. The computational complexity of the proposed hybrid elements against the conventional formulation is also addressed through the Scordelis–Lo roof problem. Finally, a problem dominated by volumetric locking is solved to establish the robustness of the method. The consistent system of units (SI/FPS) is assumed for all parameters used in numerical simulations. Abbreviations that frequently appear in the subsequent problems are defined in Table 6.3.

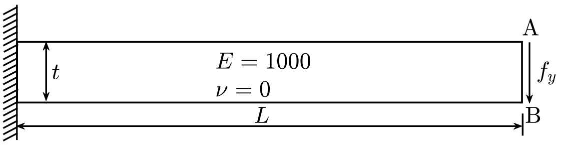

Figure 6.2: A straight cantilever beam problem, material data, and boundary conditions.

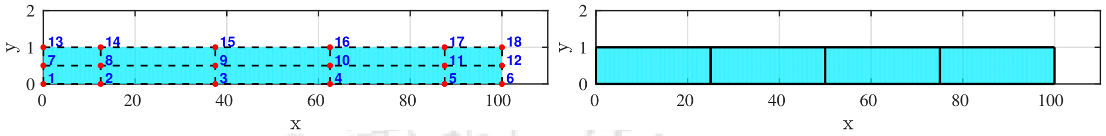

(a) Control point mesh **(b)** Discretized problem domain

Figure 6.3: Geometric description of a straight cantilever beam problem ($L/t = 100$) for four NURBS elements with quadratic basis along ξ and η direction.

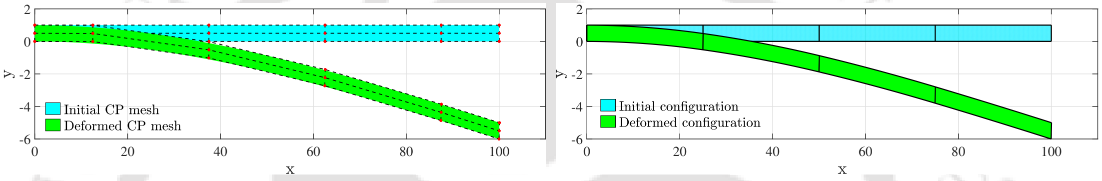

(a) Deformed control point mesh **(b)** Deformed discretized problem domain

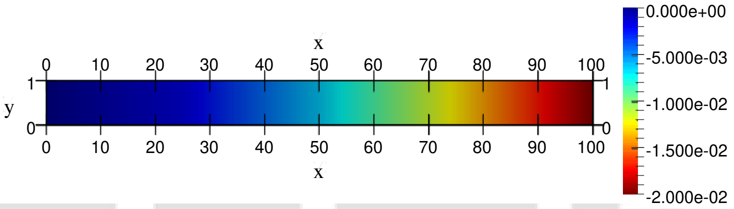

(c) u_y

Figure 6.4: Deformed geometric description (scaled for visualization, scaling factor = 300) and contour plot for vertical displacement of a straight cantilever beam problem ($L/t = 100$) using a mesh of four h-IgA$^{2D}_{Quad}$ elements.

6.4.1 Straight cantilever beam

For the first numerical example, a linear elastic behavior of a 2D cantilever beam of length L and thickness t subjected to vertical load f_y is investigated. The problem is kept simple to test the reliability of the proposed formulation under the influence of the shear locking, see Fig. 6.2 [169].

The control point and the respective weights to model the coarsest possible mesh representing the exact geometry is provided in the Appendix B (Table B.1). Once the initial mesh is generated, the sequence of meshes is constructed using the h and k-refinement. One such mesh of 4×1 IgA$^{2D}_{Quad}$ elements, for the slenderness ratio (L/t) 100, is shown in Fig. 6.3, which highlights the required number of control points, the control point mesh, and the respective discretization of a domain into IgA$^{2D}_{Quad}$ elements. In the interest of embracing the proposed formulation, the elaborated results are presented in Fig. 6.4, which gives an idea about the deformed configuration of control point mesh and the discretized domain along with the contour plot for vertical displacement for the stated mesh.

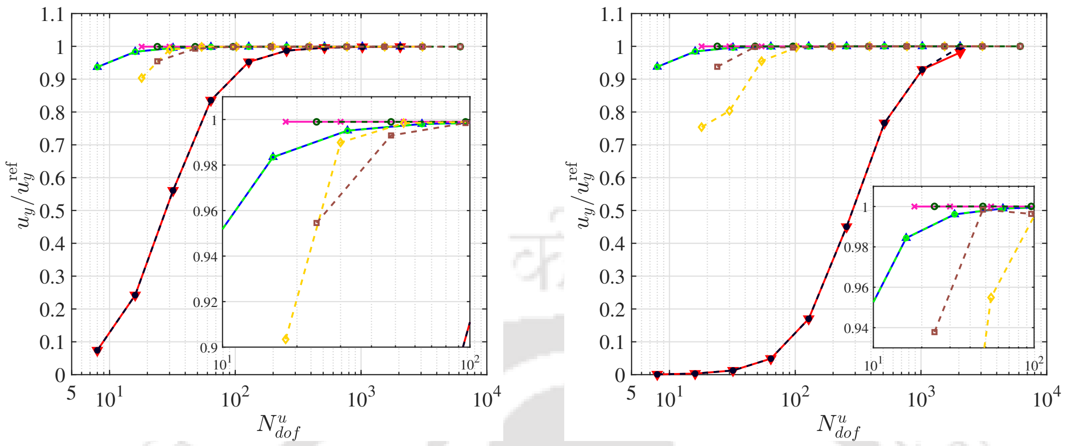

(a) $L/t = 10$ **(b)** $L/t = 100$

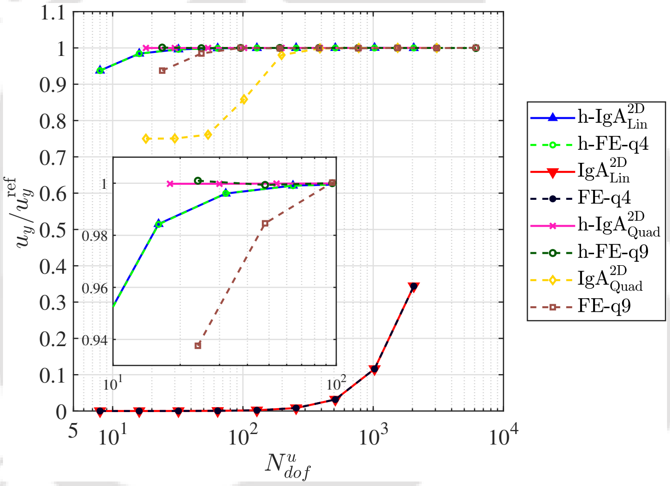

(c) $L/t = 1000$

Figure 6.5: Normalized vertical displacement at point 'A' for straight rectangular cantilever beam problem for three L/t ratios.

The problem is studied by employing the FEA and IGA formulations for three different slenderness ratios (10, 100, and 1000) in order to gradually introduce the shear locking effect into the problem domain. The problem data considered for the three cases is given as follows:

1. $L/t = 10,\ L = 100,\ t = 10,\ f_y = 4.97018 \times 10^{-3}$,
2. $L/t = 100,\ L = 100,\ t = 1,\ f_y = 4.9997 \times 10^{-6}$,
3. $L/t = 1000,\ L = 100,\ t = 0.1,\ f_y = 4.9999 \times 10^{-9}$.

For all three cases, the analytical solution for the vertical displacement (u_y) at point 'A' is 0.02.

The vertical displacement at point 'A' is numerically evaluated for all three cases against the active number of degrees of freedom (N_{dof}^u). The corresponding results are presented in Fig. 6.5. For the lower value of slenderness ratio ($L/t = 10$, Fig. 6.5a),

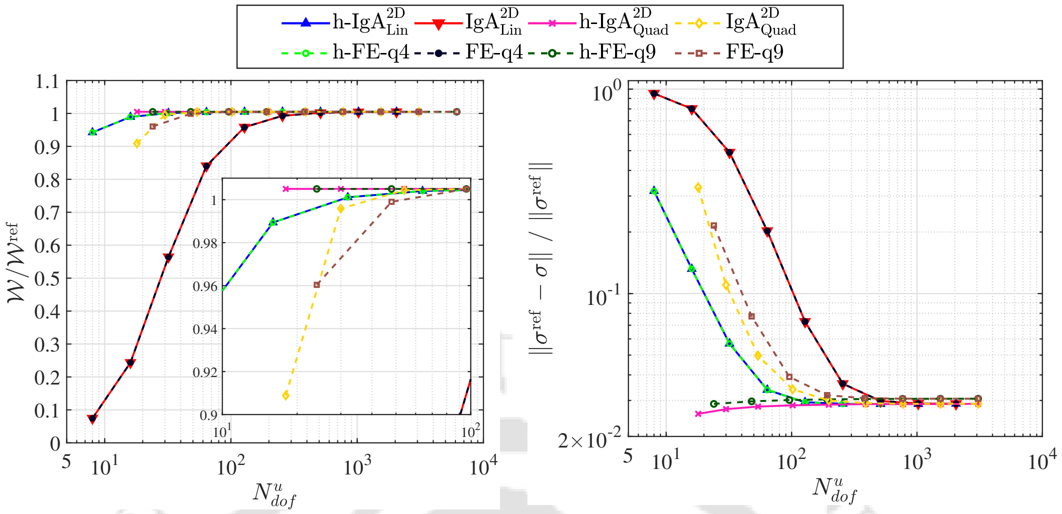

(a) $L/t = 10$ **(b)** $L/t = 10$

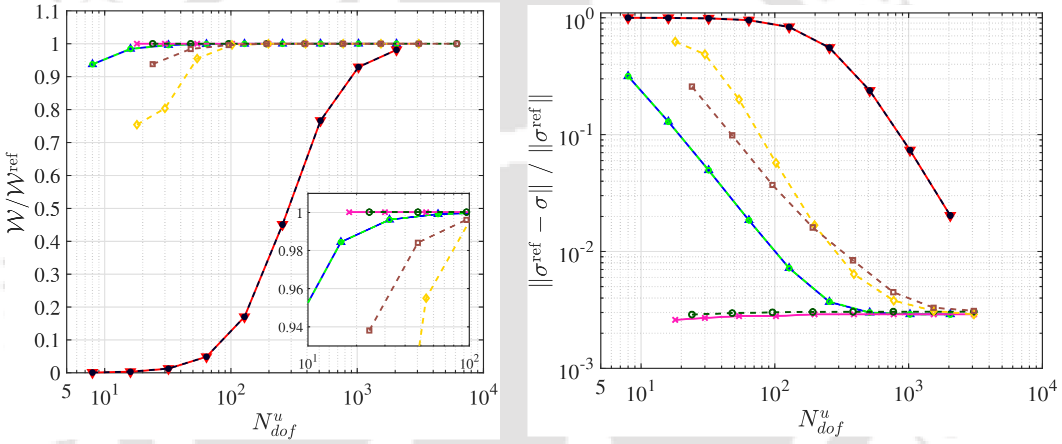

(c) $L/t = 100$ **(d)** $L/t = 100$

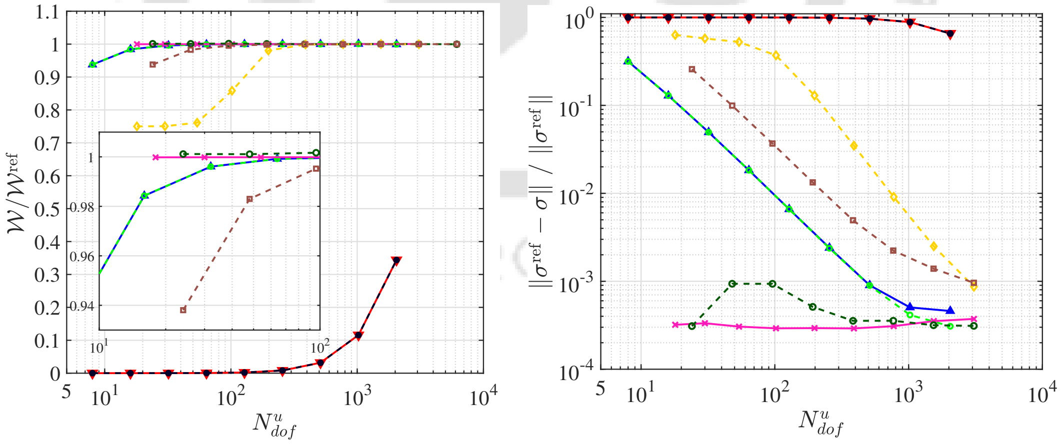

(e) $L/t = 1000$ **(f)** $L/t = 1000$

Figure 6.6: Normalized strain energy ((a), (c), and (e)) and L_2 error norm of stress ((b), (d), and (f)) for a straight cantilever beam problem for different L/t ratios.

the locking effect is significantly low whether it is IGA or FEA formulation. However, the proposed hybrid IGA out-performs the conventional formulation with coarse mesh accuracy. For instance, with only two h-IgA$^{\text{2D}}_{\text{Quad}}$ elements ($N^u_{dof} = 18$), the hybrid IGA formulation is capable of providing the results which are in close approximation with the analytical solution. Whereas, with the conventional IGA, further refinement is needed to achieve similar accuracy.

The effect of the shear locking can be distinctively observed in conventional IGA while using the lower degree basis functions with a higher slenderness ratio of the problem domain. As illustrated in Figs. 6.5b and 6.5c, IgA$^{\text{2D}}_{\text{Quad}}$ locks with a higher value of L/t and a significant refinement is needed to alleviate the anomaly. On the other hand, h-IgA$^{\text{2D}}_{\text{Quad}}$ elements performs convincingly well in all the conditions by alleviating the locking and providing superior coarse mesh accuracy. Furthermore, the use of higher degree NURBS, either with conventional or hybrid IGA, significantly reduced the locking. The results for cubic NURBS interpolations are not presented for this particular problem as the formulation, either it is conventional IGA or hybrid IGA, converges to the exact solution with a minimum number of active degrees of freedom itself. For the point of interest, the results obtained by IgA$^{\text{2D}}_{\text{Lin}}$/h-IgA$^{\text{2D}}_{\text{Lin}}$ and FE-q4/h-FE-q4 elements are identical because the NURBS basis functions of degree 1 with weights as 1 will reduce to the conventional Lagrangian basis functions used for q4 elements.

Furthermore, to have a comprehensive understanding about the performance of the proposed hybrid IGA formulation, the normalized strain energy and L_2 error of stress field has been shown in Fig. 6.6. The strain energy ($\mathcal{W}^{\text{ref}}$) for different slenderness ratios is normalized against the analytical solution obtained using the following expression [101]:

$$\mathcal{W}^{\text{ref}} = \frac{2 f_y^2 L^3}{E t^3},$$

whereas the L_2 error for stresses are calculated using the following Timoshenko stress solution [169]

$$\sigma_x = f_y (L - x)(y - t/2)\frac{12}{t^3}, \quad \sigma_y = 0,$$

$$\sigma_{xy} = \frac{-6 f_y}{t^3}\left[\frac{t^2}{4} - (y - t/2)^2\right].$$

6.4.2 Curved cantilever beam

In the present example, a linear elastic behavior of a 2D curved cantilever beam is investigated. The problem is composed of a curved beam subjected to horizontal load on one end and fixed on the other end. The problem setup and the boundary conditions are illustrated in Fig. 6.7a, where R_{in} and R_{out} are the inner and outer radii measured from the origin, R is the mean radius, and t is the thickness of the beam. f_x is the magnitude of the load at the free end such that radial displacement at the tip (Point ‘A’) is evaluated as 0.942 [101]. It is calculated as, $f_x = 0.1t^3$. ν is the Poisson’s ratio, and E is the Young’s modulus.

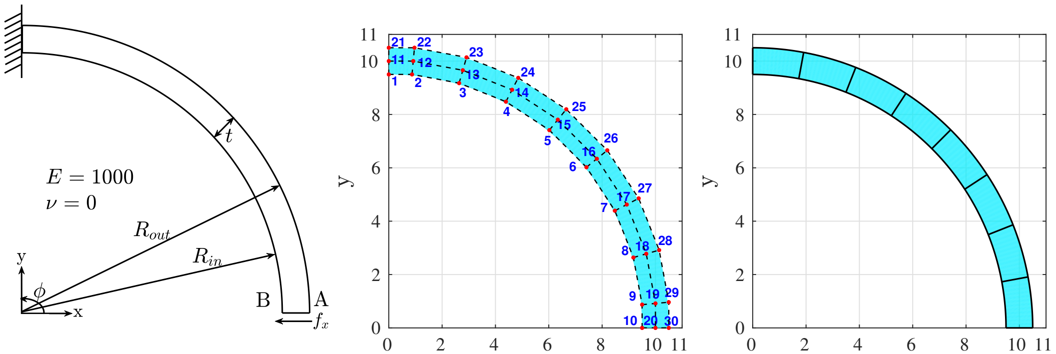

(a) A curved beam, material data, and boundary conditions **(b)** Control point mesh **(c)** Discretized domain

Figure 6.7: The problem definition and geometric description of a curved cantilever beam problem ($R/t = 10$) for 8×1 NURBS elements with quadratic basis along ξ and η direction.

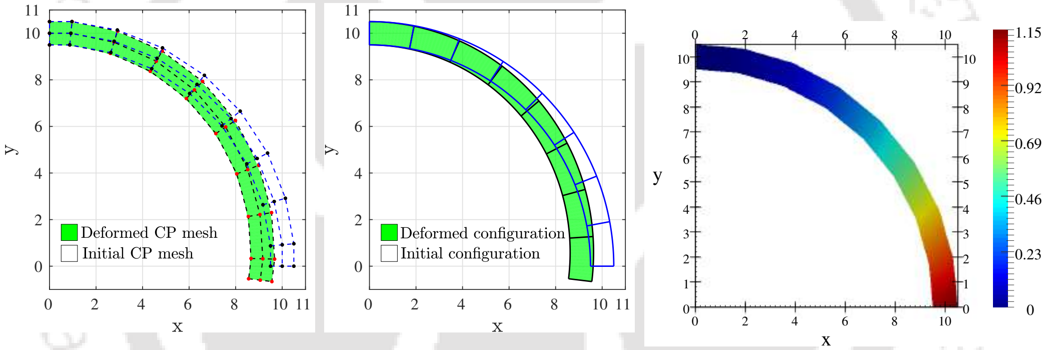

(a) Deformed control point mesh **(b)** Deformed discretized domain **(c)** u

Figure 6.8: ((a) and (b)) Deformed geometric description and (c) contour plot of the magnitude of total displacement using a mesh of 8×1 h-IgA$^{2D}_{Quad}$ elements for a curved beam problem.

To exactly represent the circular edges of the problem domain, the minimum requirement is to incorporate the quadratic NURBS basis functions along the curvature. The required control point along with the respective weights to model the coarsest possible mesh representing the exact geometry is provided in the Appendix B (Table B.2). Once the initial mesh is generated, the sequence of meshes is constructed using the h and k-refinement. One such mesh of 8×1 quadratic NURBS elements, for the slenderness ratio (R/t) 10, is shown in Figs. 6.7b and 6.7c, which focuses on the number of control points involved, the control point mesh, and the respective element discretization of a domain. To achieve the sense of completeness, the extensive result for the stated mesh is presented in Fig. 6.8 which elaborates the deformed configuration of the problem domain (Figs. 6.8a and 6.8b) along with the contour plots for displacement field (Fig. 6.8c) obtained by incorporating the hybrid IGA formulation.

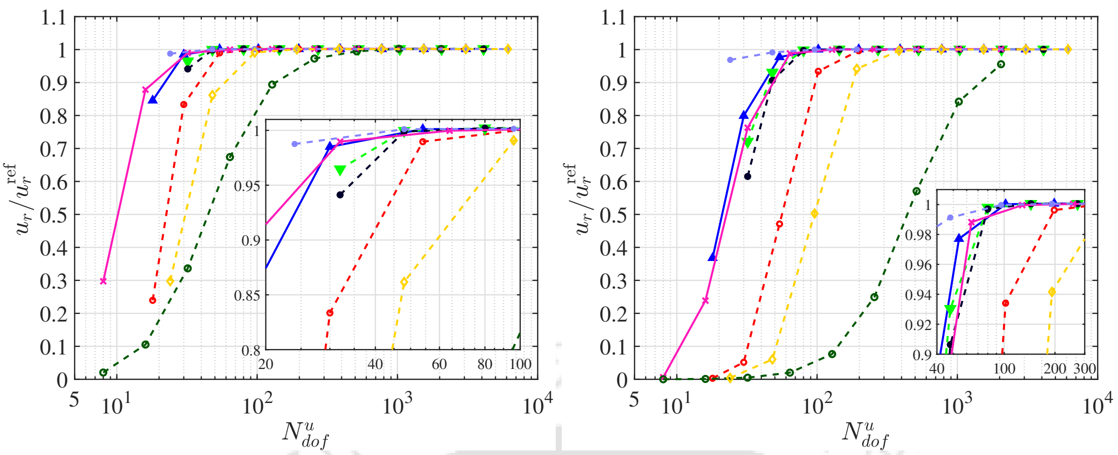

(a) $R/t = 10$ (b) $R/t = 100$

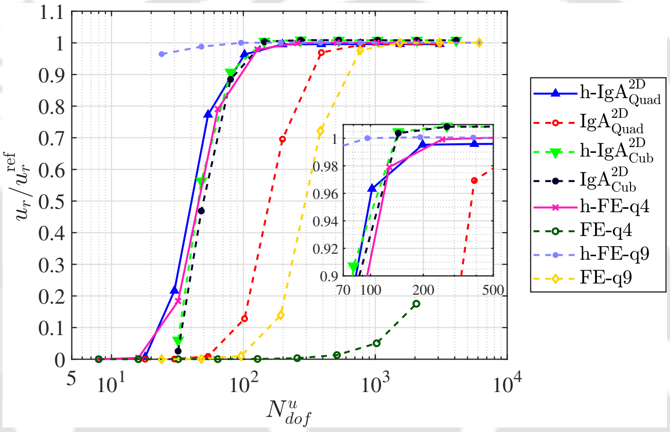

(c) $R/t = 1000$

Figure 6.9: Normalized radial displacement at point ‘A’ for a curved cantilever beam problem for three R/t ratios.

The problem is solved using the FEA and IGA formulations for three different slenderness ratios (10, 100, and 1000) in order to gradually introduce the shear locking effect into the problem domain. The problem data considered for the three cases is given as follows:

1. $R/t = 10$, $R_{in} = 9.5$, $R_{out} = 10.5$, $R = 10$, $t = 1$, $f_x = 0.1$,
2. $R/t = 100$, $R_{in} = 9.95$, $R_{out} = 10.05$, $R = 10$, $t = 0.1$, $f_x = 0.1 \times 10^{-3}$,
3. $R/t = 1000$, $R_{in} = 9.995$, $R_{out} = 10.005$, $R = 10$, $t = 0.01$, $f_x = 0.1 \times 10^{-6}$.

For all three cases, the analytical solution for the radial displacement (u_a) at point ‘A’ is 0.942.

The radial displacement at point ‘A’ is numerically evaluated by employing the different formulations and results are presented in Fig. 6.9. For the lower value of slenderness ratio ($R/t = 10$, Fig. 6.9a), it can be seen that the locking effect is substantially low whether it is IGA or FEA formulation. However, the proposed hybrid IGA outperforms conventional formulation with coarse mesh accuracy. For instance, the results using h-IgA$^{2D}_{\text{Quad}}$ elements are in close approximation with the analytical solution even with merely 30 active degrees of freedom (N^u_{dof}), whereas the results for conventional IGA even with the cubic basis are inferior for nearly the same degrees of freedom.

As the slenderness ratio increases, the influence of the shear locking in the conventional IGA formulation can be observed distinctly while using the lower degree basis functions. As illustrated in Figs. 6.9b and 6.9c, $\text{IgA}^{2\text{D}}_{\text{Quad}}$ locks severely with a higher value of R/t. On the other hand, the $\text{h-IgA}^{2\text{D}}_{\text{Quad}}$ performs convincingly well in all the conditions by alleviating the locking. Furthermore, the use of higher degree NURBS significantly reduces the locking, but hybrid results can be seen marginally better than the conventional formulation. From a comparative perspective, the IGA results, either conventional or hybrid, seem to be better than their FE counterparts.

6.4.3 Cook's membrane problem

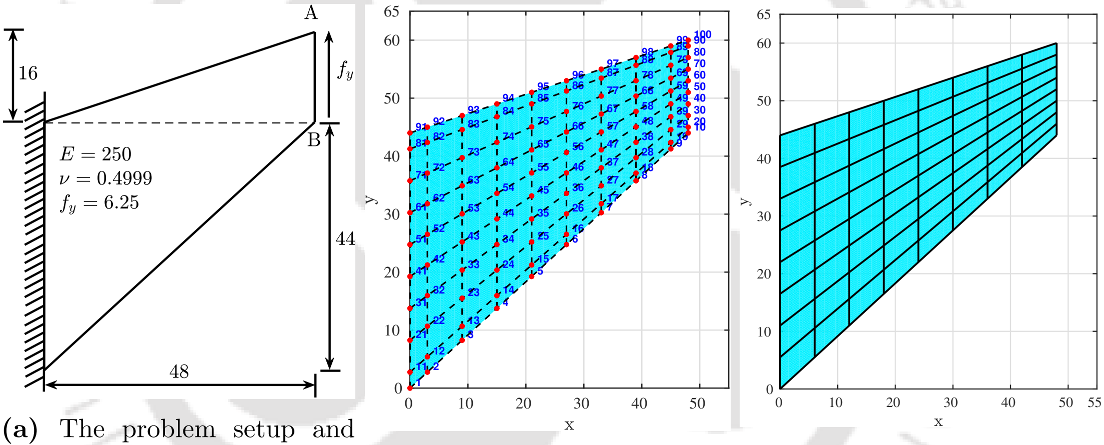

(a) The problem setup and boundary conditions **(b)** Control point mesh **(c)** Discretized domain

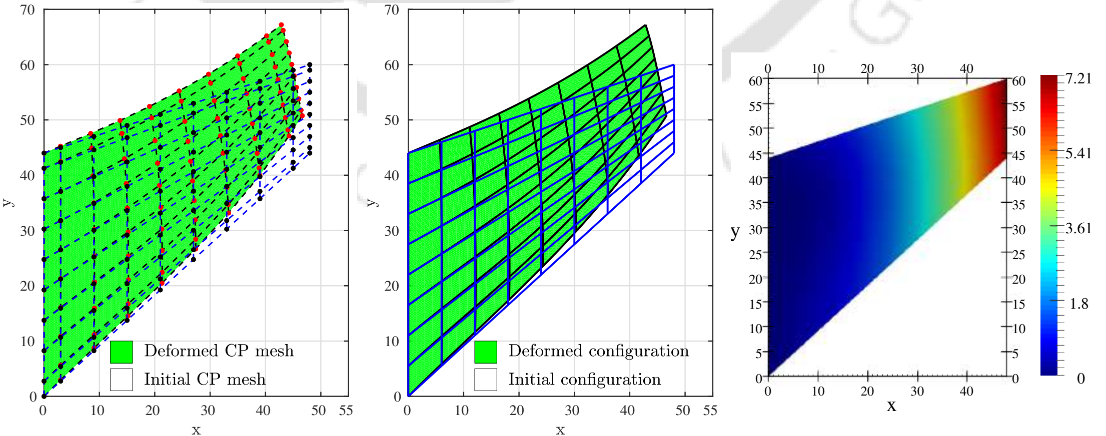

(d) Deformed control point mesh **(e)** Deformed discretized domain **(f)** u_y

Figure 6.10: (a) The problem setup and boundary conditions for a Cook's membrane problem, ((b) and (c)) geometric description consisting 8×8 quadratic NURBS elements, ((d) and (e)) respective deformed configuration, and (f) the contour plot for vertical displacement using hybrid IGA formulation.

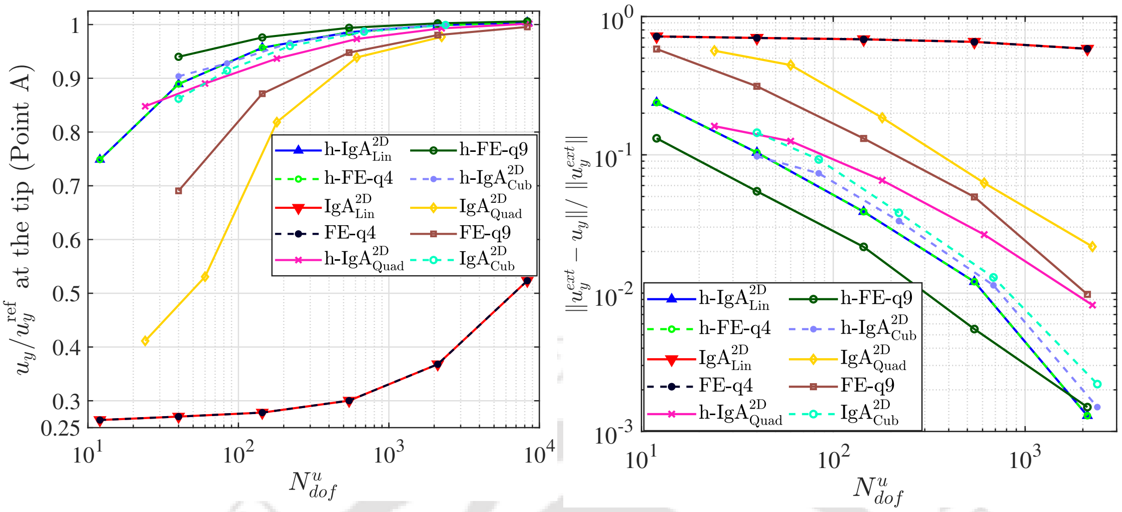

(a) u_y/u_a **(b)** L_2^u

Figure 6.11: Normalized vertical displacement at point ‘A’ and L_2 error norm for vertical displacement versus the active degrees of freedom for the Cook’s membrane problem.

Next, the Cook’s membrane problem is simulated [110]. The problem setup and the boundary conditions are illustrated in Fig. 6.10a, where f_y is the load per unit length. Setting $\nu = 0.4999$, the problem becomes a typical case of volumetric locking while investigating the nearly incompressible behavior of the domain under combined bending and shear deformation.

The geometric data to construct the coarsest possible mesh, representing the exact geometry, is provided in the Appendix B (Table B.3). Once the initial mesh is generated, the sequence of refined meshes are modeled using the refinement techniques. One such mesh of 8×8 NURBS elements, having the quadratic basis functions along the ξ and η direction, is shown in Figs. 6.10b and 6.10c. The elaborated results are presented in the Figs. 6.10d and 6.10f which focuses on the deformed configuration of control point mesh and the discretized domain along with the contour plot for vertical displacement for the stated mesh.

The normalized vertical displacement at the point ‘A’ against the reference solution of 7.7 [132] is evaluated as shown in Fig. 6.11a. Furthermore, the convergence of the relative L_2 error norm of displacement versus the number of active degrees of freedom (N^u_{dof}) is shown in Fig. 6.11b. As analytical expressions for the displacements are not well established for the stated problem, the reference to evaluate the L_2 norm is the well-converged solution of highly-refined mesh of h-IgA$^{\text{2D}}_{\text{Cub}}$ elements.

It can be observed that the FE-q4 and its equivalent IgA$^{\text{2D}}_{\text{Lin}}$ elements locks severely. Even with the significantly high refinement, the results only marginally improve. On the other hand, the hybrid formulation can successfully alleviate locking to produce superior results. Moving to higher degree basis functions, where the IGA basis functions are different from the Lagrangian basis functions, it can be seen that the IgA$^{\text{2D}}_{\text{Quad}}$ elements

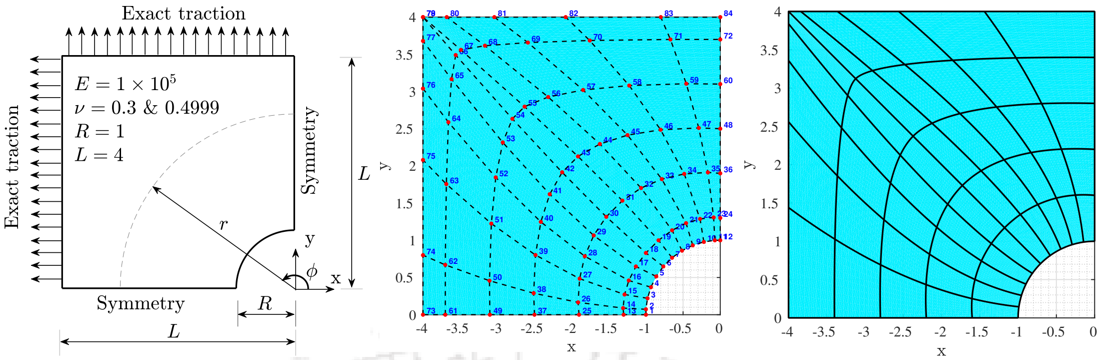

(a) Problem setup **(b)** Control point mesh **(c)** Element discretization

Figure 6.12: (a) The problem setup and boundary conditions for an infinite plate with a circular hole problem under constant in-plane tension ($T = 1$) at infinity, and ((b) and (c)) geometric description (a quarter portion) consisting 10×5 NURBS elements with quadratic basis along ξ and η direction.

lock significantly for lower mesh refinements. However, the proposed h-IgA$^{\text{2D}}_{\text{Quad}}$ elements works very well even with a very low number of N^u_{dof} and provides better coarse mesh accuracy. With further elevation in the degree of basis function, the gap between the conventional and hybrid IGA results gets insignificant, yet hybrid IGA is marginally better than the conventional IGA formulation.

6.4.4 Infinite plate with a hole problem

The problem consists of a 2D infinite plate with a circular hole under constant uni-axial in-plane tension ($T = 1$) at infinity [110], see Fig. 6.12a. Owing to the symmetry of the problem only a quarter portion of the plate is considered, as shown in Fig. 6.12a.

The problem setup and the boundary conditions are shown in Fig. 6.12a, which includes the symmetric boundary condition on edge ED and BC, and the Neumann boundary condition on edge AB and AE. The exact traction, applied on the boundary AB and AE, is evaluated using the analytical expression of stresses (Eqs. 6.44, 6.45, and 6.46) for the stated problem setup.

A plane-strain condition is assumed, and the analytical solution [110] for the stress field is given as follows:

$$\sigma_{xx} = 1 - \frac{R^2}{r^2}\left(\frac{3}{2}\cos 2\phi + \cos 4\phi\right) + \frac{3R^4}{2r^4}\cos 4\phi, \tag{6.44}$$

$$\sigma_{yy} = -\frac{R^2}{r^2}\left(\frac{1}{2}\cos 2\phi - \cos 4\phi\right) - \frac{3R^4}{2r^4}\cos 4\phi, \tag{6.45}$$

$$\tau_{xy} = -\frac{R^2}{r^2}\left(\frac{1}{2}\sin 2\phi + \sin 4\phi\right) + \frac{3R^4}{2r^4}\sin 4\phi, \tag{6.46}$$

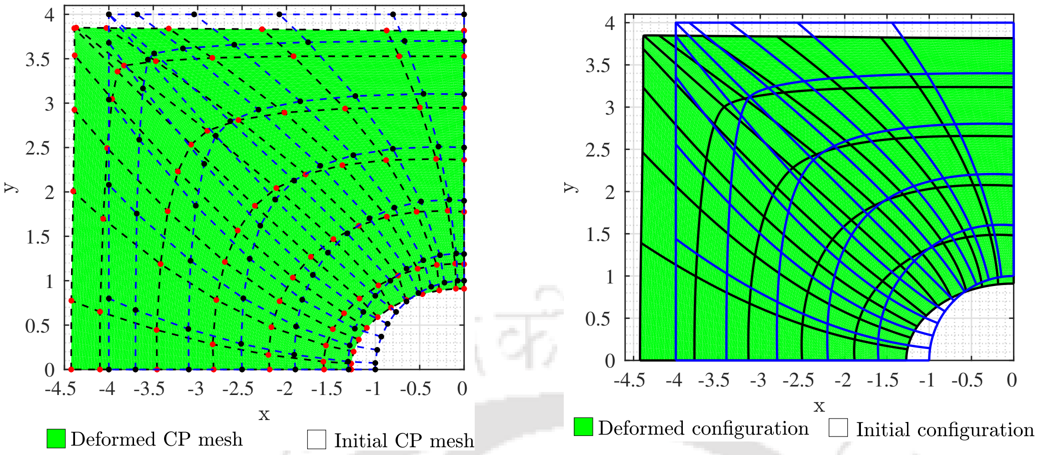

(a) Deformed control point mesh **(b)** Deformed discretized domain

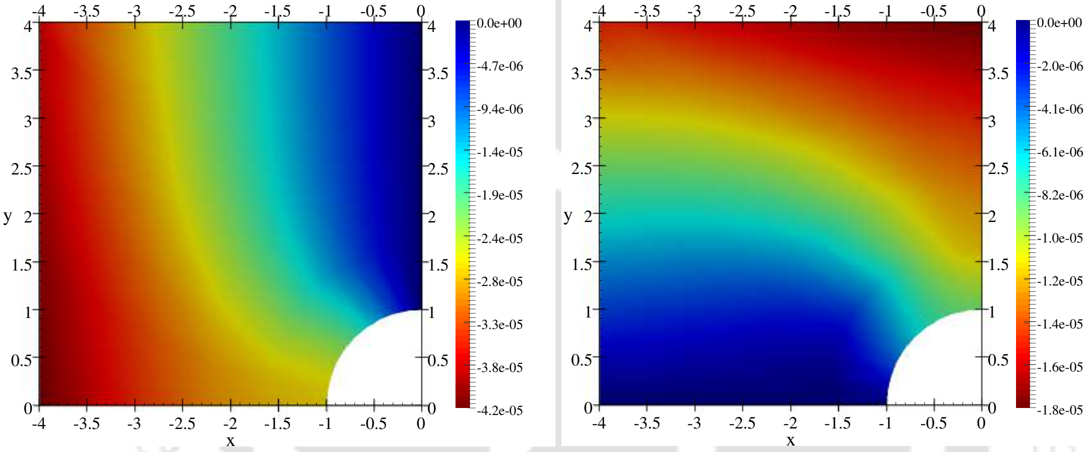

(c) $u_x^{\text{h-IgA}}$ **(d)** $u_y^{\text{h-IgA}}$

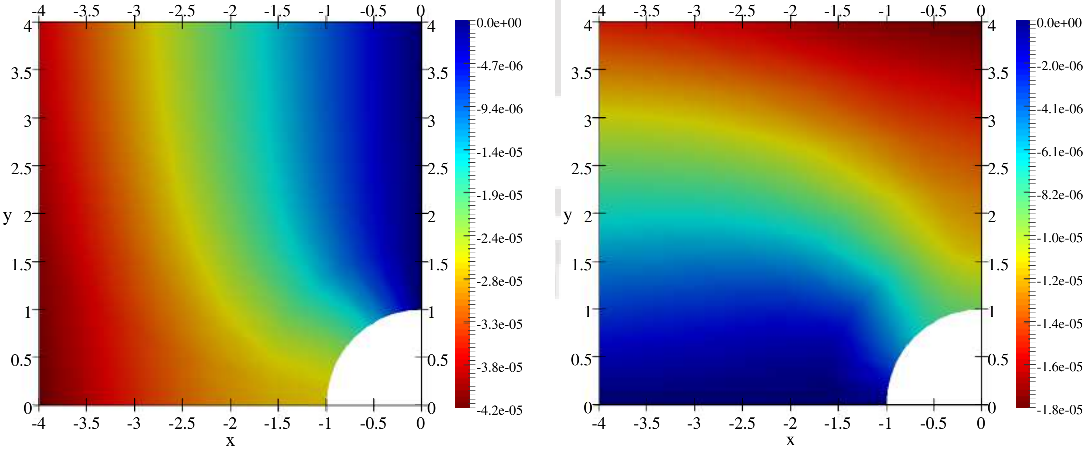

(e) u_x^{exact} **(f)** u_y^{exact}

Figure 6.13: ((a) and (b)) Deformed geometric description of an infinite plate with a hole problem (a quarter portion) for 10×5 NURBS elements with quadratic basis along ξ and η direction (magnified by the factor of 1×10^4 for better visualization), and contour plots for horizontal and vertical displacement for the mesh illustrated in Figs. 6.12b and 6.12c using hybrid IGA formulation ((c) and (d)) alongside the analytical solution ((e) and (f)) for $\nu = 0.3$.

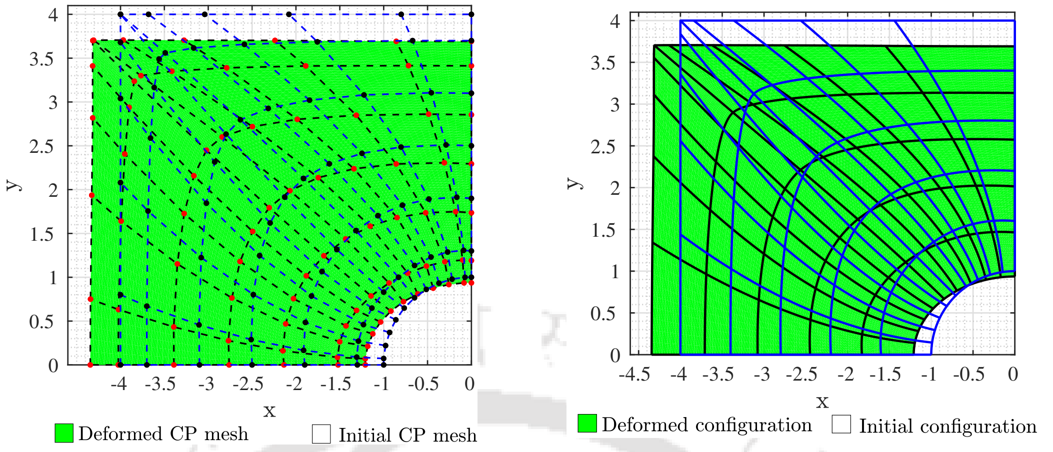

(a) Deformed control point mesh **(b)** Deformed discretized problem domain

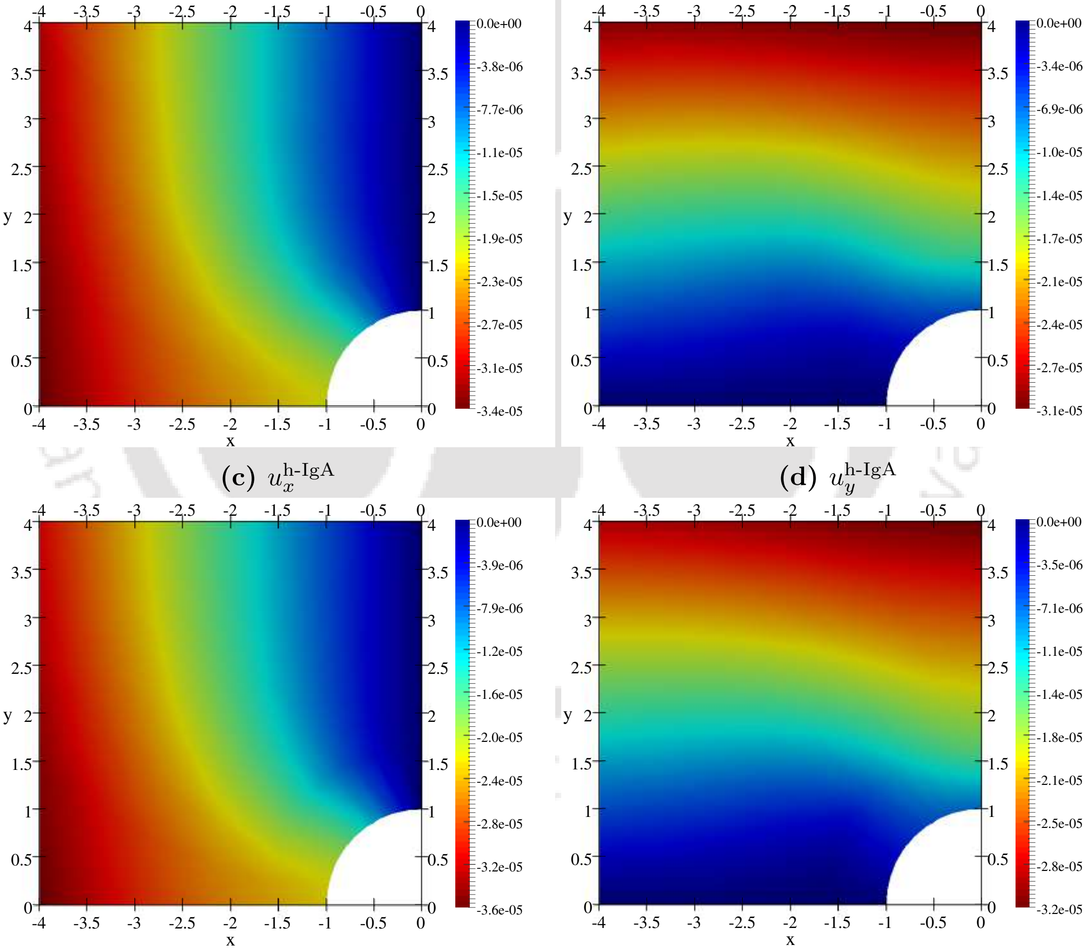

(c) $u_x^{\text{h-IgA}}$ **(d)** $u_y^{\text{h-IgA}}$

(e) u_x^{exact} **(f)** u_y^{exact}

Figure 6.14: ((a) and (b)) Deformed geometric description of an infinite plate with a hole problem (a quarter portion) for 10×5 NURBS elements with quadratic basis along ξ and η direction (magnified by the factor of 1×10^4 for better visualization), and contour plots for horizontal and vertical displacement for the mesh illustrated in Figs. 6.12b and 6.12c using hybrid IGA formulation ((c) and (d)) alongside the analytical solution ((e) and (f)) for $\nu = 0.4999$.

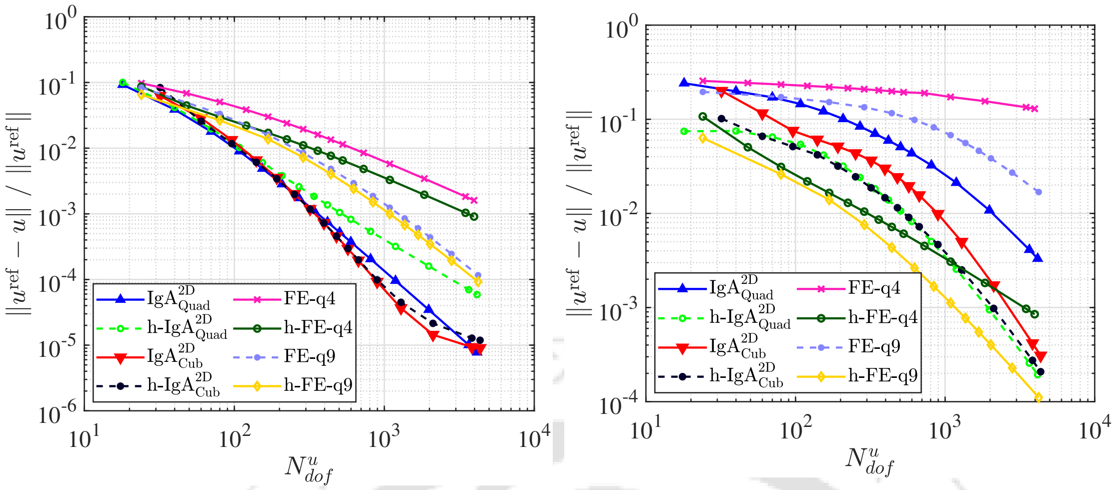

(a) $\nu = 0.3$ **(b)** $\nu = 0.4999$

Figure 6.15: Convergence study of a relative L_2 error norm of displacement versus the active degrees of freedom for a plate with hole problem.

where $r = \sqrt{x^2 + y^2}$ and $\phi = \tan^{-1}(y/x)$. The analytical expression for the displacement field is given as

$$u_x(r,\phi) = \frac{R}{8\mu}\left[\frac{r}{R}(k+1)\cos\phi + \frac{2R}{r}((1+k)\cos\phi + \cos 3\phi) - \frac{2R^3}{r^3}\cos 3\phi\right],$$
$$u_y(r,\phi) = \frac{R}{8\mu}\left[\frac{r}{R}(k-3)\sin\phi + \frac{2R}{r}((1-k)\sin\phi + \sin 3\phi) - \frac{2R^3}{r^3}\sin 3\phi\right],$$

where $\mu = \dfrac{E}{2(1+\nu)}$ and $k = 3 - 4\nu$ (for plane-strain condition).

The minimal requirement to maintain the exact geometry is to use the quadratic NURBS basis functions along the ϕ direction. Furthermore, the coarsest possible mesh to represent the exact geometry consists of two quadratic elements, one in the radial direction and two in the ϕ direction. The control point coordinates and the respective weights are given in the Appendix B (Table B.4). Once the initial mesh is generated, the sequence of meshes is constructed using the h-refinement. One such mesh of 10×5 elements is shown in Figs. 6.12b and 6.12c, which focuses on the number of control points involved, the control point mesh, and the respective element discretization of a domain. For a better understanding, the comprehensive results for the mesh described in Figs. 6.12b and 6.12c are presented in Figs. 6.13 and 6.14, which focuses on the deformed configuration of the problem domain along with the numerical displacement field in comparison with the analytical solution for different Poisson's ratios.

The problem is solved using the conventional and hybrid IGA alongside their FE counterparts. To test the efficiency and robustness of the method, the problem is studied for the two cases. For the first case, ν is considered as 0.3 so that the solution is unaffected by volumetric locking. Secondly, the ν value is considered as 0.4999 to analyze the nearly incompressible behavior which is highly influenced by locking.

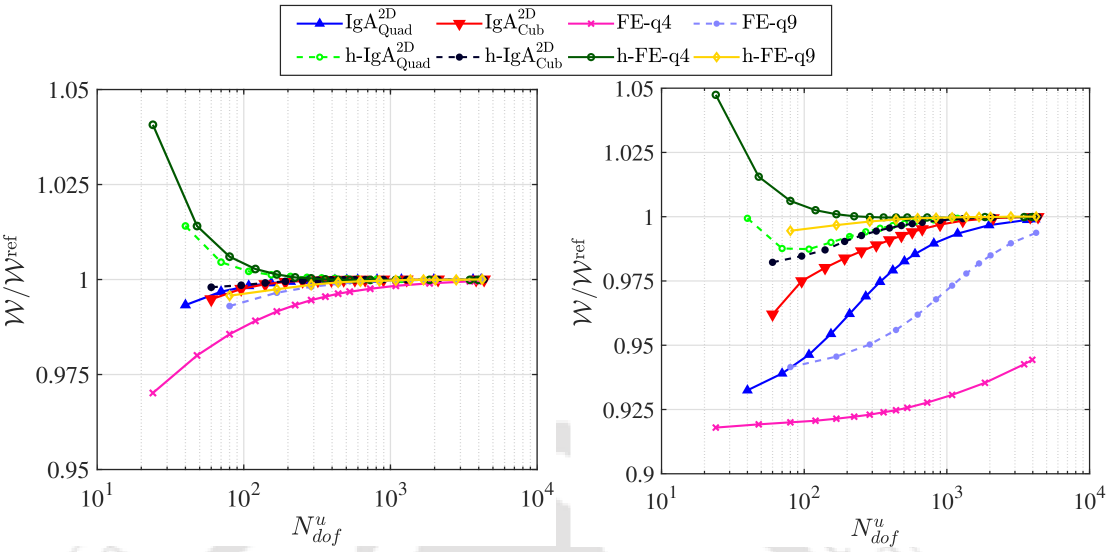

(a) $\nu = 0.3$ **(b)** $\nu = 0.4999$

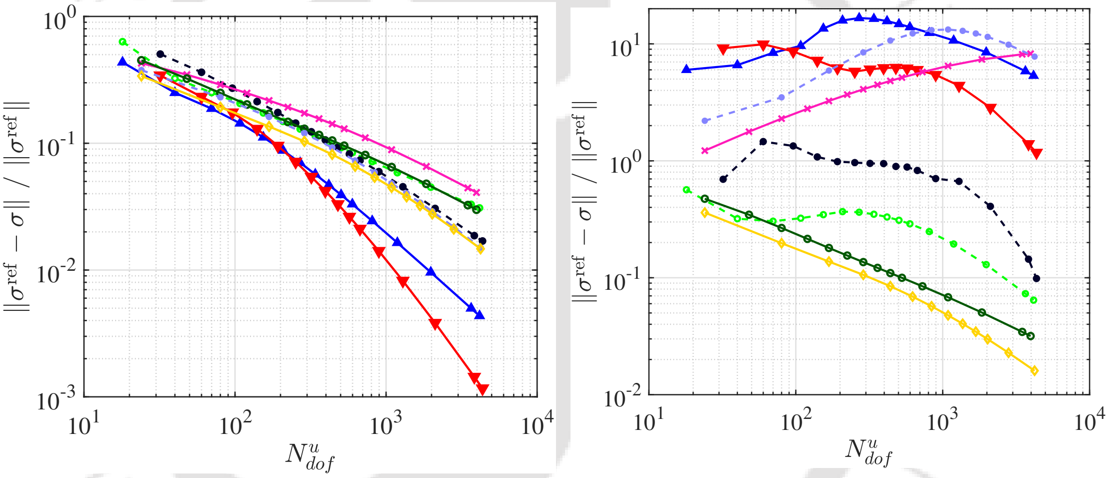

(c) $\nu = 0.3$ **(d)** $\nu = 0.4999$

Figure 6.16: Normalized strain energy and L_2 error norm of stress for a plate with hole problem for different Poisson's ratios.

For the first case, the convergence of the relative L_2 error norm of displacement versus the number of active degrees of freedom (N^u_{dof}) is evaluated as shown in Fig. 6.15a. It can be seen that the convergence rates for the conventional and hybrid IGA are closely identical, whether it is for quadratic or cubic basis functions. This authenticates the fact that the hybrid IGA formulation is not restricted to locking-dominated problem domains but can also be effectively used for problems that are not influenced by the locking.

In the second case, the nearly incompressible behavior is investigated by setting the Poisson's ratio close to the value 0.5. The convergence curves specific to $\nu = 0.4999$ are presented in Fig. 6.15b. It can be seen that the conventional IGA locks while using the quadratic basis functions. Though refinement considerably reduces the error, the proposed h-IgA$^{2D}_{Quad}$ outperforms the IgA$^{2D}_{Quad}$ elements in terms of coarse mesh accuracy.

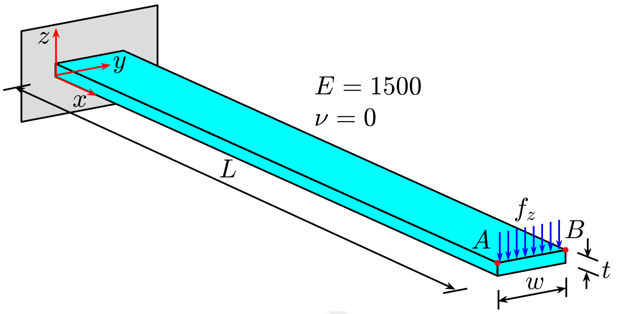

Figure 6.17: A straight cantilever beam problem, material data, and boundary conditions.

Similar results are obtained with cubic basis functions, conventional IGA is less sensitive to locking, but the h-IgA$^{2D}_{Cub}$ provides better accuracy at a relatively low number of elements.

To have thorough insights on the performance of hybrid elements, the problem is further investigated for the normalized strain energy (Figs. 6.16a and 6.16b), L_2 error of stress field (Figs. 6.16c and 6.16d). The reference strain energy ($\mathcal{W}^{\text{ref}}$) for normalizing the evaluated results is obtained using the well-converged solution of high-refined mesh. The $\mathcal{W}^{\text{ref}}$ value in case of $\nu = 0.3$ is 7.6937×10^{-5} and for $\nu = 0.4999$ is 6.3739×10^{-5}. The reference solution for evaluating the L_2 error of stress is obtained using Eqs. 6.44, 6.45, and 6.46. Furthermore, the stress concentration factor (S_f) has been evaluated using the expression $S_f = \sigma_x^{\max}/T$ which leads to $S_f = 2.9999$ for $\nu = 0.3$ and $S_f = 3.6146$ for $\nu = 0.4999$ for the converged mesh.

6.4.5 Three-dimensional straight cantilever beam

A 3D straight cantilever beam is solved to assess the performance of the proposed stress-based NURBS elements under the influence of shear locking [169]. The schematic of the problem and boundary conditions are shown in Fig. 6.17. The slenderness ratio (L/t) is varied from 10 to 1000 to analyze the effect of various aspect ratios. The problem parameters consist of three L/t ratios, i.e., 10, 100, and 1000, obtained by gradually reducing the thickness as 6, 0.6, and 0.06 for a constant length $L = 60$. The load per unit length along the edge is given by $f_z = 1.26563t^3 \times 10^{-2}$. The analytical solution (u_z^{ref}) using the Euler-Bernoulli beam theory for the vertical displacement at the tip in all three cases is 7.29. The control point coordinates and the corresponding weights to design the initial coarse mesh illustrating the exact geometry of the problem domain are presented in the Appendix B (Table B.5). After defining the coarse mesh, further refinement is carried out using h- or k-refinement techniques. The meshes used to solve the problem are defined as $n_{\text{ele}}^L \times n_{\text{ele}}^t \times n_{\text{ele}}^w$, where n_{ele}^L, n_{ele}^t, and n_{ele}^w are the number of elements in length, thickness, and width directions, respectively. The refinement has been done along the length direction in such a way that $n_{\text{ele}}^L = 2, 4, 8, 16, \ldots, 256$ while keeping $n_{\text{ele}}^t = n_{\text{ele}}^w = 1$ for all three L/t ratios.

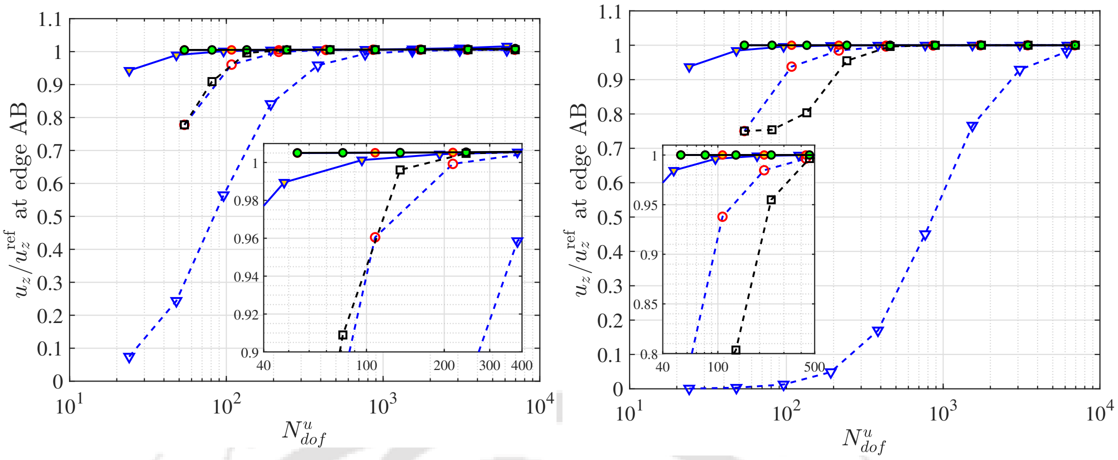

(a) u_z/u_z^{ref} for $L/t = 10$ **(b)** u_z/u_z^{ref} for $L/t = 100$

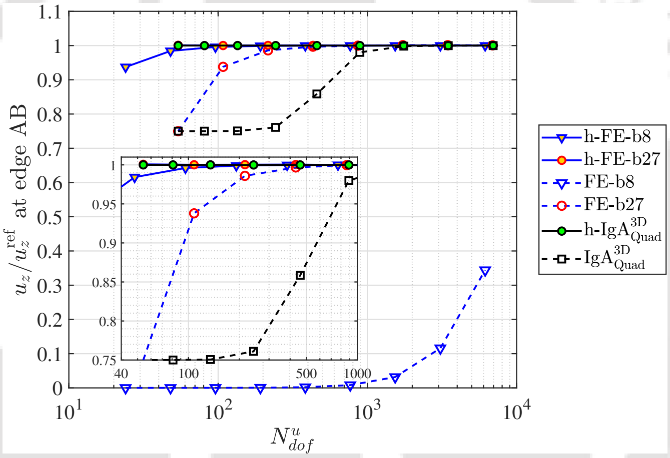

(c) u_z/u_z^{ref} for $L/t = 1000$

Figure 6.18: Normalized vertical displacement at point ‘A’ for a straight cantilever beam problem for three L/t ratios.

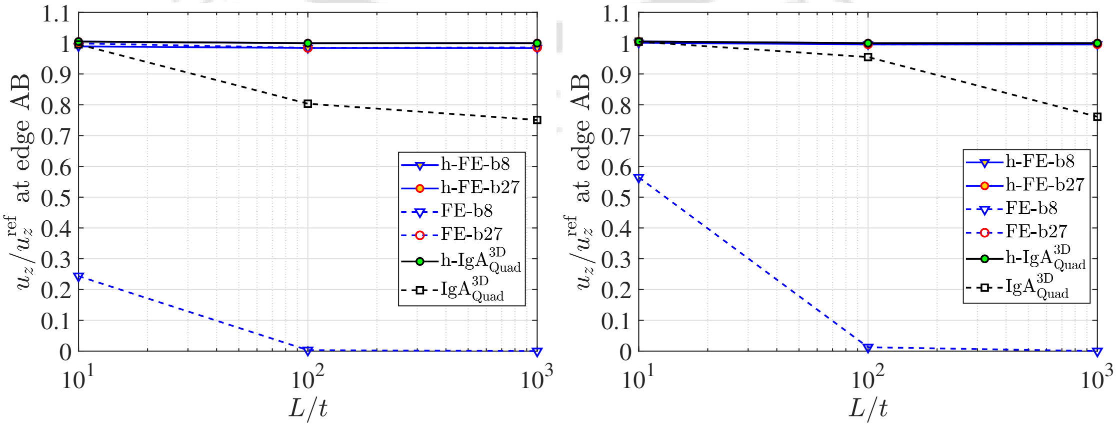

(a) Mesh: 4 × 1 × 1 **(b)** Mesh: 8 × 1 × 1

Figure 6.19: Normalized tip displacement versus L/t ratio for straight cantilever beam problem.

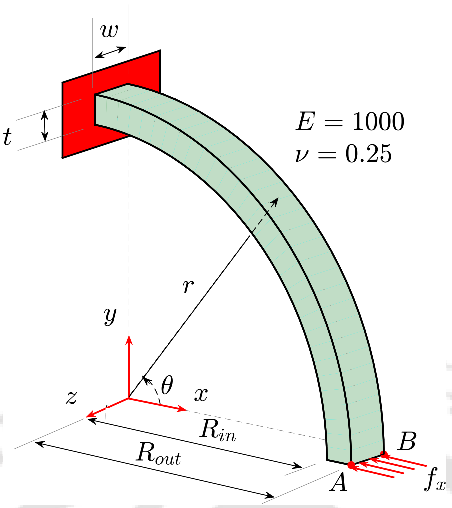

Figure 6.20: A curved cantilever beam problem, material data, and boundary conditions.

The problem is solved for the vertical displacement at the tip. The normalized results against the analytical solution versus the total number of active degrees of freedom (N^u_{dof}) are presented in Fig. 6.18. For the low value of L/t (Fig. 6.18a), the locking is insignificant. For such a case, even conventional formulations converge to the analytical solution fairly quickly. However, the proposed stress-based elements provide improved coarse mesh accuracy with even a single quadratic element discretization (h-IgA$^{\text{3D}}_{\text{Quad}}$, $N^u_{dof} = 54$) converging to the desired analytical solution. To achieve the equivalent accuracy, conventional IGA needs further refinement for the same class of NURBS-based elements.

The shear locking is more prominent in high L/t ratios. The adverse effects on the solution quality can be perceived distinctively for lower degree NURBS elements in the case of conventional formulation. For instance, IgA$^{\text{3D}}_{\text{Quad}}$ locks with higher L/t ratios, see Figs. 6.18b and 6.18c, and a considerable refinement of the domain has to be performed to alleviate the locking. In contrast, the performance of h-IgA$^{\text{3D}}_{\text{Quad}}$ formulation is consistently superior regardless of the L/t ratios. To further compare the performance of the proposed elements against the conventional formulation, the normalized tip displacement against the increasing L/t ratio for two different mesh descriptions is shown in Fig. 6.19. As the L/t increases, locking effects can be seen in IgA$^{\text{3D}}_{\text{Quad}}$ elements; however, h-IgA$^{\text{3D}}_{\text{Quad}}$ performs consistently throughout. IgA$^{\text{3D}}_{\text{Cub}}$ or h-IgA$^{\text{3D}}_{\text{Cub}}$ are less susceptible to locking in all three cases and converge to the reference solution with the minimum possible number of active degrees of freedom.

6.4.6 Three-dimensional curved cantilever beam

The present example addresses the behavior of a 3D curved cantilever beam under the influence of combined shear and membrane locking. The problem is composed of a

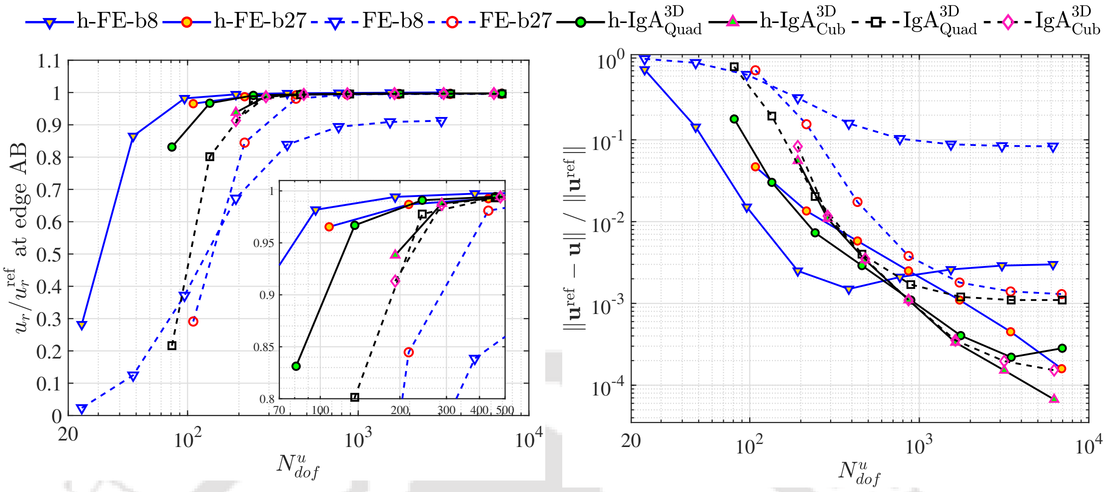

(a) u_r/u_r^{ref} for $R/t = 10$ **(b)** $L_2^{\boldsymbol{u}}$ for $R/t = 10$

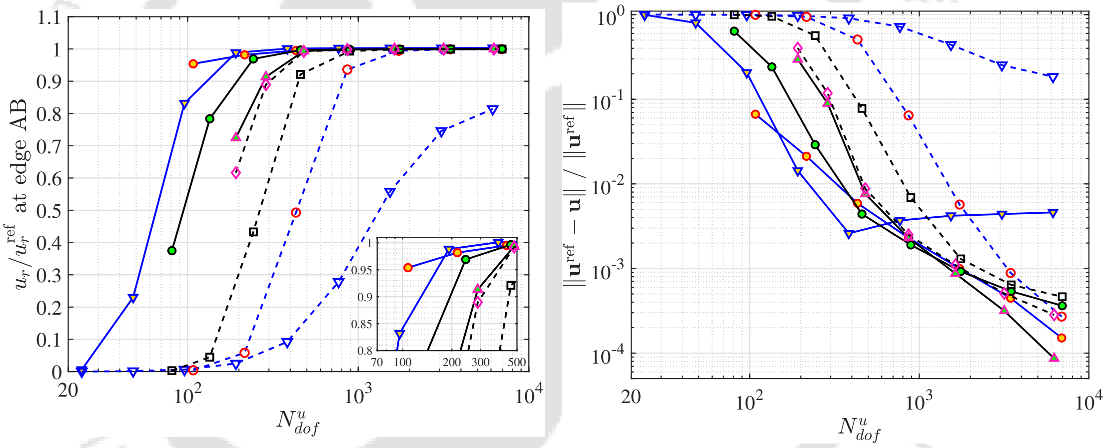

(c) u_r/u_r^{ref} for $R/t = 100$ **(d)** $L_2^{\boldsymbol{u}}$ for $R/t = 100$

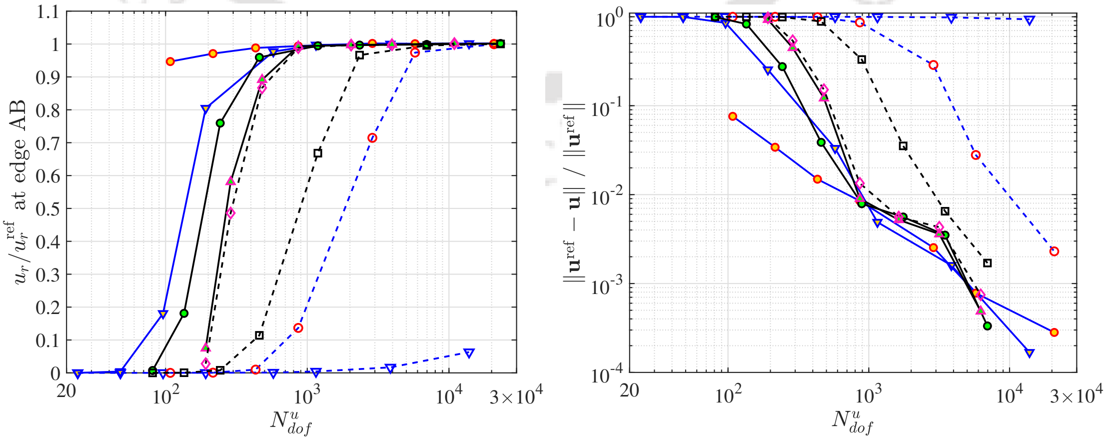

(e) u_r/u_r^{ref} for $R/t = 1000$ **(f)** $L_2^{\boldsymbol{u}}$ for $R/t = 1000$

Figure 6.21: Normalized radial displacement at point 'A' and L_2 error norm of displacement for a curved cantilever beam problem for three R/t ratios.

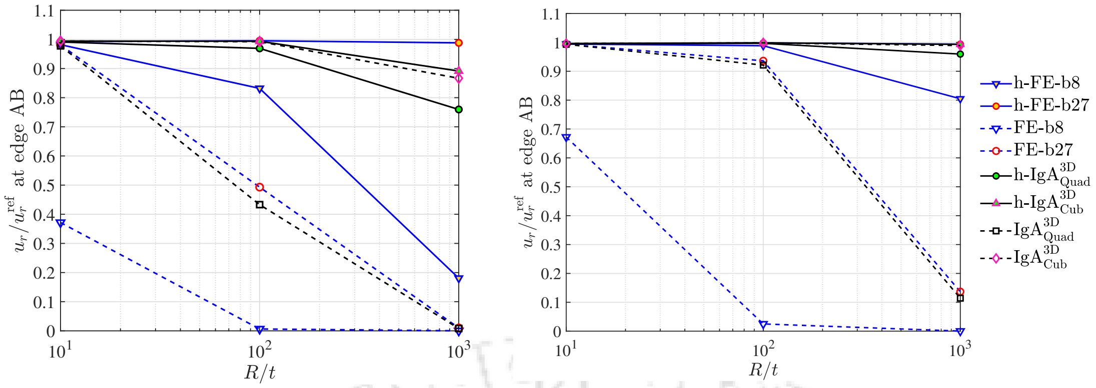

(a) Mesh: $1 \times 8 \times 1$ **(b)** Mesh: $1 \times 16 \times 1$

Figure 6.22: Normalized radial displacement at edge AB versus R/t ratio for a curved cantilever beam problem.

curved beam of mean radius R, thickness t, and width $w = 1$, fixed on one end and subjected to the horizontal load f_x along the edge of the opposite end, see Fig. 6.20 [101]. Here, R_{in} and R_{out} are the inner and outer radii, E is the Young's modulus, and ν is the Poisson's ratio.

Similar to the previous example, the problem is evaluated for different slenderness ratios (R/t) to gradually introduce locking and determine the response of the hybrid NURBS-elements. The problem parameters consist of three R/t ratios, i.e., 10, 100, and 1000, obtained by gradually reducing the thickness as 1.2, 0.12, and 0.012 for the constant mean radius $R = 12$. The load per unit length along the edge is given by $f_x = 0.1t^3$. The reference solution (u_r^{ref}) at the tip is determined using the converged results of highly refined mesh. It is found to be 1.6338, 1.6236, and 1.5852 for $R/t =$ 10, 100, and 1000, respectively. The control point coordinates and the corresponding weights to design the initial coarse mesh illustrating the exact geometry of the problem domain are presented in the Appendix (Table B.6). Due to the involvement of the curved circular surface of the problem domain, the geometric description demands a minimum of second-degree NURBS interpolations along the curvature. After defining the coarse mesh, further refinement is carried out using h- or k-refinement techniques. The meshes used to solve the problem are defined as $n^R_{\text{ele}} \times n^\theta_{\text{ele}} \times n^z_{\text{ele}}$, where n^R_{ele}, n^θ_{ele}, and n^z_{ele} are the number of elements in R, θ, and z direction, respectively. The refinement is done along the θ direction in such a way that $n^\theta_{\text{ele}} = 2, 4, 8, 16, \ldots, 256$ while keeping $n^R_{\text{ele}} = n^z_{\text{ele}} = 1$ for $R/t = 10$ and 100. However, the stress convergence for $R/t = 1000$ is obtained after performing refinement in z (width) direction. Hence the meshes used for $R/t = 1000$ is obtained by considering $n^\theta_{\text{ele}} = 2,\ 4,\ 8,\ 16,\ \ldots,\ 256$, $n^z_{\text{ele}} = 1,\ 1,\ 1,\ 1,\ 2,\ 2,\ 4,\ 8$, and $n^R_{\text{ele}} = 1$.

The problem is solved for the radial displacement at the tip. The normalized displacement and the relative L_2 error norm of displacement against N^u_{dof} are shown in Fig. 6.21. The normalized tip displacement corresponding to the varying R/t ratio for

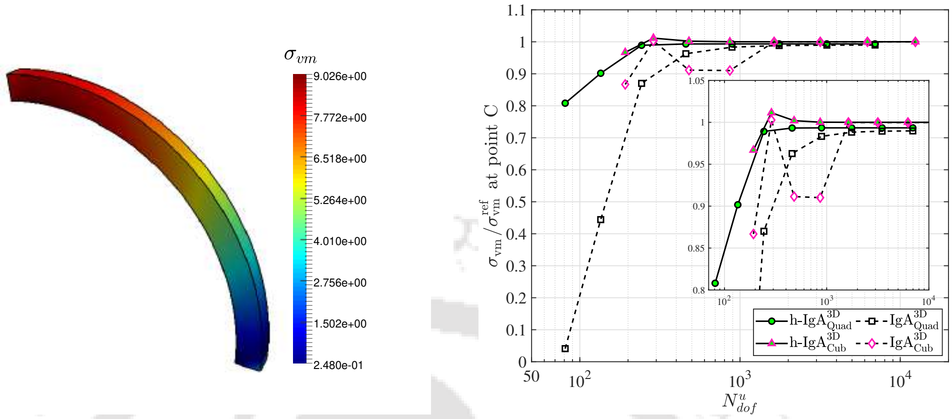

(a) σ_{vm} ($R/t = 10$; mesh: $1 \times 32 \times 1$) **(b)** Normalized von Mises stress ($R/t = 10$)

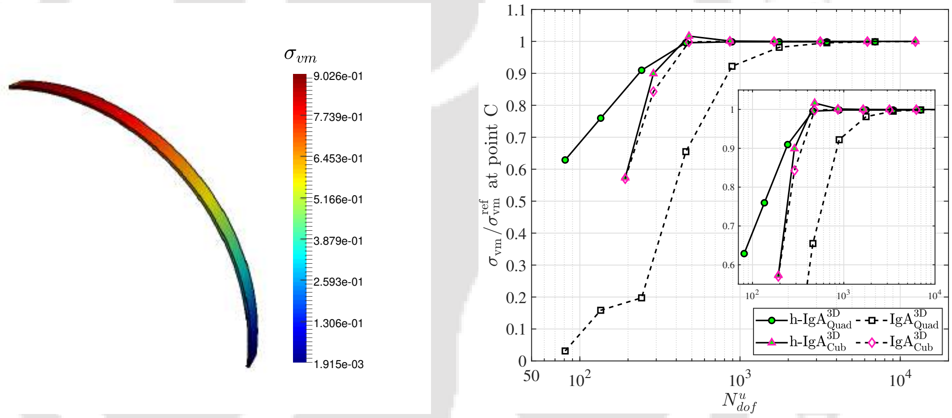

(c) σ_{vm} ($R/t = 100$; mesh: $1 \times 128 \times 1$) **(d)** Normalized von Mises stress ($R/t = 100$)

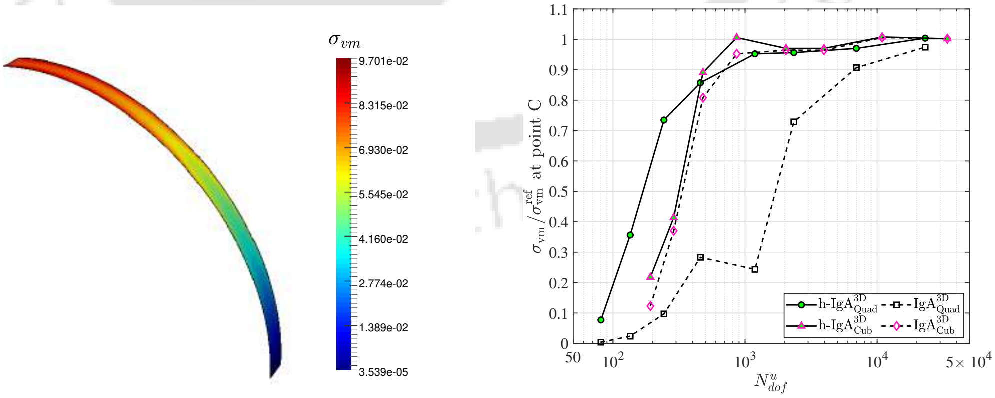

(e) σ_{vm} ($R/t = 1000$; mesh: $1 \times 256 \times 8$) **(f)** Normalized von Mises stress ($R/t = 1000$)

Figure 6.23: Curved cantilever beam problem: ((a), (c), and (e)) Contour plot of σ_{vm} distribution for different R/t ratios using h-IgA$_2^3$ elements; ((b), (d), and (f)) Normalized von Mises stress at point 'C'.

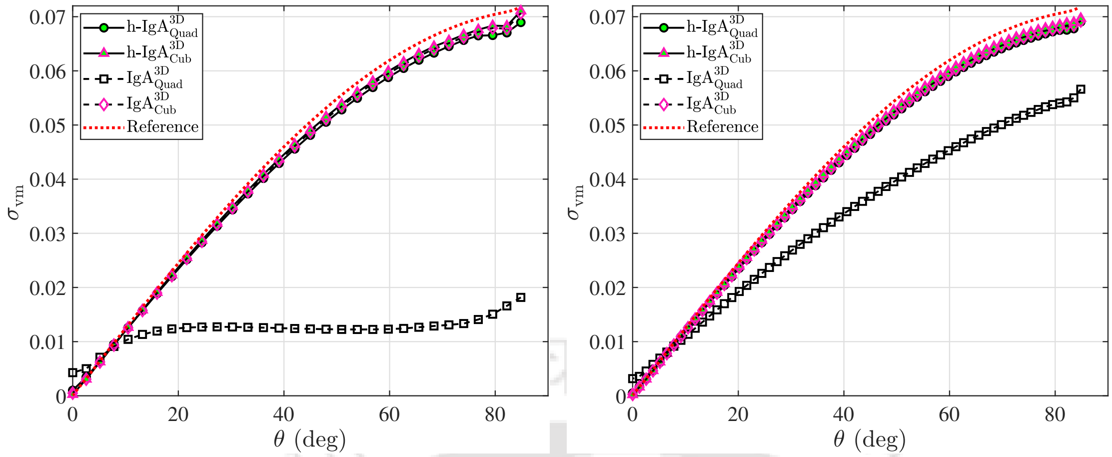

(a) σ_{vm} (mesh: $1 \times 32 \times 2$) **(b)** σ_{vm} (mesh: $1 \times 64 \times 2$)

Figure 6.24: The σ_{vm} evaluated at the boundary with $R = R_{\text{in}}$, $z = 0$ along θ for two different mesh descriptions for a curved cantilever beam problem with $R/t = 1000$.

two different mesh descriptions is shown in Fig. 6.22 to better visualize the performance of the proposed elements against the conventional formulation. As the R/t increases, significant locking can be seen in IgA$^{\text{3D}}_{\text{Quad}}$ elements; however, h-IgA$^{\text{3D}}_{\text{Quad}}$ performs consistently throughout. IgA$^{\text{3D}}_{\text{Cub}}$ and h-IgA$^{\text{3D}}_{\text{Cub}}$ are less susceptible to locking in all three cases.

For the low value of R/t (Figs. 6.21a and 6.21b), the locking is insignificant. In this case, conventional formulations are effective enough to converge to the analytical solution with a reasonably low number of elements. However, the proposed stress-based elements provide improved coarse mesh accuracy, where a mesh of eight quadratic elements (h-IgA$^{\text{3D}}_{\text{Quad}}$, $N^u_{dof} = 243$, mesh: $1 \times 8 \times 1$) converges to the desired analytical solution with L_2 error of 0.73%. The results for IgA$^{\text{3D}}_{\text{Quad}}$ ($N^u_{dof} = 243$, mesh: $1 \times 8 \times 1$) and IgA$^{\text{3D}}_{\text{Cub}}$ ($N^u_{dof} = 288$, mesh: $1 \times 4 \times 1$) are inferior for nearly the same N^u_{dof} with L_2 error of 2.03% and 1.17%, respectively. To achieve a comparable accuracy with conventional IgA$^{\text{3D}}_{\text{Quad}}$, it requires double the number of elements as that of h-IgA$^{\text{3D}}_{\text{Quad}}$ formulation.

For higher R/t ratios, the effect of locking deteriorates the solution quality for lower-degree NURBS elements in the case of conventional formulation. For instance, IgA$^{\text{3D}}_{\text{Quad}}$ locks at higher R/t ratios, see Figs. 6.21c, 6.21e, 6.21d, and 6.21f, and considerable refinement is required for the convergence. On the other hand, the performance of h-IgA$^{\text{3D}}_{\text{Quad}}$ formulation is consistently superior irrespective of the R/t ratios. For instance, a mesh of sixteen h-IgA$^{\text{3D}}_{\text{Quad}}$ elements ($N^u_{dof} = 459$, mesh: $1 \times 16 \times 1$) for $L/t = 100$ and $L/t = 1000$ provides a close approximation with the reference value with L_2 error of 0.44% and 3.87%, respectively. However, to achieve a comparable accuracy with the conventional IgA$^{\text{3D}}_{\text{Quad}}$ elements, it requires four times the number of elements for $L/t = 100$ (IgA$^{\text{3D}}_{\text{Quad}}$, $N^u_{dof} = 1755$, mesh: $1 \times 64 \times 1$, $L_2 = 0.13\%$) and eight times the number of elements for $L/t = 1000$ (IgA$^{\text{3D}}_{\text{Quad}}$, $N^u_{dof} = 2340$, mesh: $1 \times 64 \times 2$, $L_2 =$ 3.53%). Furthermore, the application of higher-degree interpolations for conventional

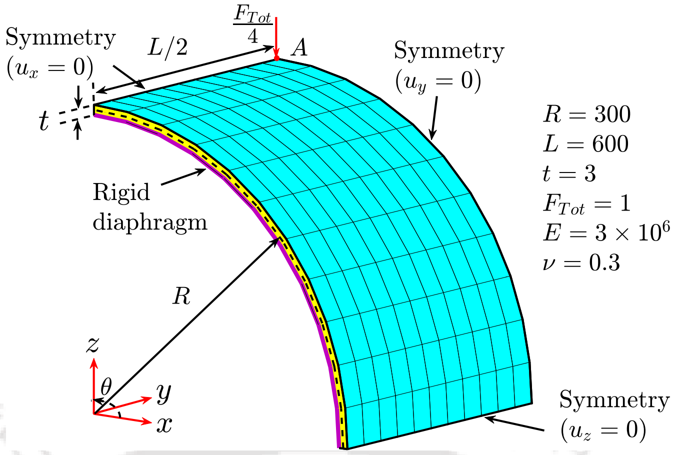

Figure 6.25: One-eighth domain of a pinched cylinder problem, material data, and boundary conditions.

formulation, i.e., IgA$^{\text{3D}}_{\text{Cub}}$, reduces the locking effect, but h-IgA$^{\text{3D}}_{\text{Cub}}$ results are marginally better than its conventional IGA counterpart.

The von Mises stress (σ_{vm}) is evaluated at $r = R_{in}$, $\theta = 45°$, $z = 0$ (point 'C') for all three R/t ratios. The results are normalized with the reference value ($\sigma^{\text{ref}}_{\text{vm}}$) of 6.4025, 0.5963, and 0.0505 for R/t ratios 10, 100, and 1000, respectively. The reference value is the converged solution of the highly refined mesh using h-IgA$^3_2$ elements. Figs. 6.23a, 6.23c, and 6.23e show the contour plot of σ_{vm} distribution for different R/t ratios, whereas Figs. 6.23b, 6.23d, and 6.23f focus on a point in the domain to show the convergence of the von Mises stress for different elements. In all three cases, the h-IgA$^{\text{3D}}_{\text{Quad}}$ shows better coarse mesh accuracy as compared to the conventional IgA$^{\text{3D}}_{\text{Quad}}$ elements. In addition, the σ_{vm} is evaluated at the boundary with $R = R_{\text{in}}$, $z = 0$ along θ for two fixed mesh descriptions, see Fig. 6.24. It can be seen that the h-IgA$^{\text{3D}}_{\text{Quad}}$ elements perform consistently better than the IgA$^{\text{3D}}_{\text{Quad}}$ elements.

6.4.7 Pinched cylinder

The pinched cylinder with an end diaphragm is one of the shell obstacle course problems where both shear and membrane locking are dominant [101]. The problem consists of a circular cylinder of length L, mean radius R, and thickness t, restrained at both the ends with rigid diaphragms and subjected to two equal and opposite concentrated load F_{Tot} at the mid-section, see Fig. 6.25. Due to the symmetry of the problem, only one-eighth of the cylinder is investigated. The geometric description to design the coarse mesh while maintaining the exact problem domain using the NURBS interpolations is given in the Appendix (Table B.8). The minimum requirement on the degree of interpolation functions is to use quadratic NURBS along the curvature to accurately model the circular surface of the domain. After defining the coarse mesh, further refinement is carried out using h- or k-refinement techniques. The meshes used to solve the problem are defined as $n^R_{\text{ele}} \times n^\theta_{\text{ele}} \times n^L_{\text{ele}}$, where n^R_{ele}, n^θ_{ele}, and n^L_{ele} are the number of elements in R, θ, and

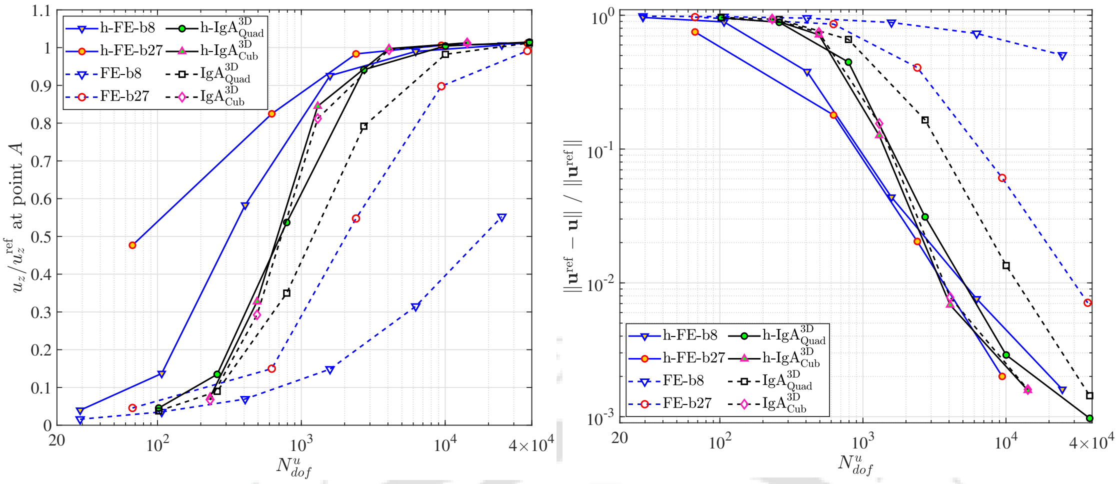

(a) u_z/u_z^{ref} **(b)** $L_2^{\boldsymbol{u}}$

Figure 6.26: (a) Normalized vertical displacement at point ‘A’; (b) L_2 error norm of displacement for a pinched cylinder problem.

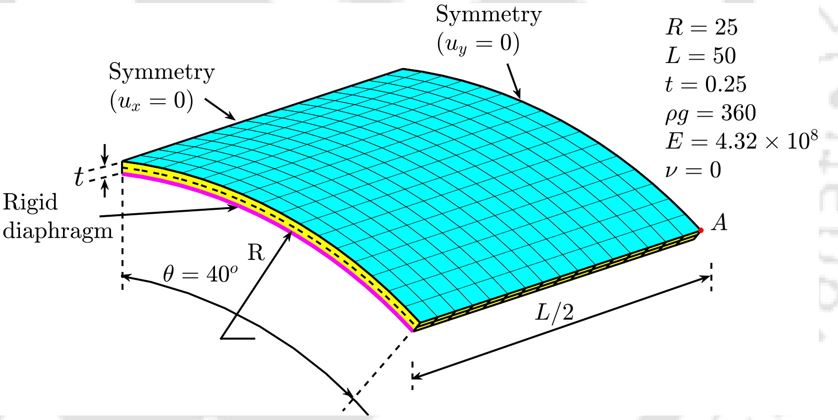

Figure 6.27: Quarter domain of a Scordelis–Lo roof problem, material data, and boundary conditions.

L direction, respectively. The refinement is done along the θ and L direction in such a way that $n^{\theta}_{\text{ele}} = n^{L}_{\text{ele}} = 2,\ 4,\ 8,\ 16,\ 32$ while keeping $n^{R}_{\text{ele}} = 1$.

The problem is solved for the radial displacement at the point of application of load. The vertical displacement is normalized by the analytical solution ($u_z^{\text{ref}} = 1.8248 \times 10^{-5}$ [101]) and the results are shown in Fig. 6.26a. Moreover, the relative L_2 error norm of displacement against the total number of active degrees of freedom is shown in Fig. 6.26b. A solution of highly refined mesh consisting of $1 \times 64 \times 64$ cubic elements is taken as a reference to evaluate the L_2 norm. It can be seen that a much better coarse mesh accuracy of h-IgA$^{\text{3D}}_{\text{Quad}}$ elements over the conventional IgA$^{\text{3D}}_{\text{Quad}}$ elements is obtained. Higher-order elements are less affected by locking, whether it is h-IgA$^{\text{3D}}_{\text{Cub}}$ or IgA$^{\text{3D}}_{\text{Cub}}$ elements.

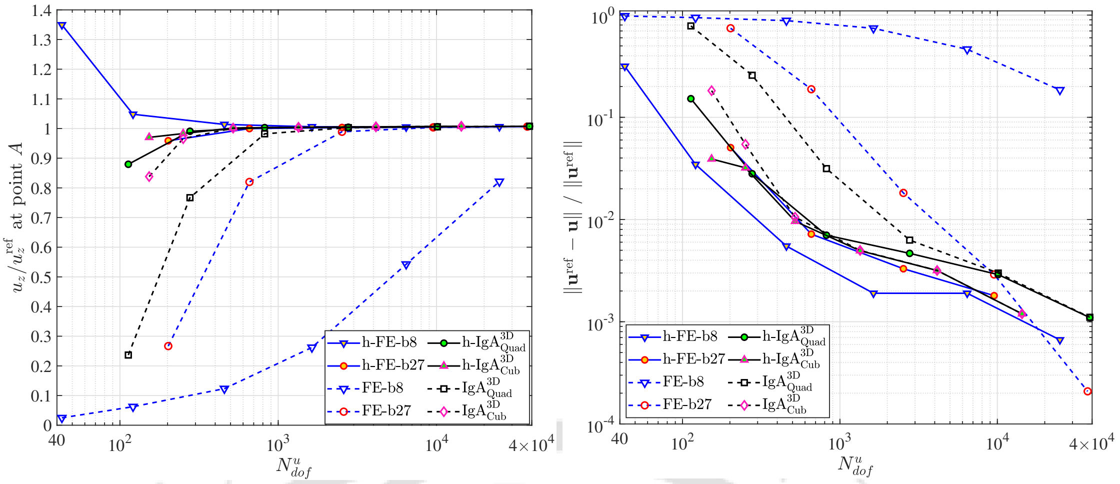

(a) u_z/u_z^{ref} **(b)** $L_2^{\boldsymbol{u}}$

Figure 6.28: (a) Normalized vertical displacement at point ‘A’; (b) L_2 error norm of displacement for a Scordelis–Lo roof problem.

6.4.8 Scordelis–Lo roof problem

The next problem we considered is the Scordelis–Lo roof problem [175]. The problem consists of an 80° circular section of a cylinder of length L, mean radius R, and thickness t, restrained at the opposite ends with rigid diaphragms and the other two sides remain free, see Fig. 6.27. The described problem set-up is studied under the influence of body force per unit volume ρg. Here ρ is the specific mass of the body and g is the acceleration due to gravity. Owing to the symmetry of the problem, only one-fourth of the cylindrical section is investigated. The geometric description to design the coarse mesh while maintaining the exact problem domain using the NURBS interpolations is defined in the Appendix (Table B.7). After defining the coarse mesh, further refinement is carried out using h- or k-refinement techniques. The meshes used to solve the problem are defined as $n^R_{\text{ele}} \times n^\theta_{\text{ele}} \times n^L_{\text{ele}}$, where n^R_{ele}, n^θ_{ele}, and n^L_{ele} are the number of elements in R, θ, and L direction, respectively. The refinement is done along the θ and L direction in such a way that $n^\theta_{\text{ele}} = n^L_{\text{ele}} = 2,\ 4,\ 8,\ 16,\ 32$ while keeping $n^R_{\text{ele}} = 1$.

The problem is solved for the vertical displacement at the mid-point of the free side (denoted as point ‘A’ in Fig. 6.27). The normalized results against the analytical solution ($u_z^{\text{ref}} = 0.3024$ [175]) are presented in Fig. 6.28a. Further, the relative L_2 error norm of the displacement against N^u_{dof} is evaluated, see Fig. 6.28b. A converged solution of highly refined mesh consisting of $1 \times 64 \times 64$ cubic elements is taken as a reference to evaluate the L_2 norm. It can be seen that the performance of the proposed h-IgA$^{\text{3D}}_{\text{Quad}}$ formulation results in a faster convergence to the analytical value. Even with the mesh of $1 \times 4 \times 4$ ($N^u_{dof} = 277$), the h-IgA$^{\text{3D}}_{\text{Quad}}$ provides a very good approximation to the analytical solution with a small L_2 error of 2.8056%. In contrast, the IgA$^{\text{3D}}_{\text{Quad}}$ formulation needs four times the total number of elements ($1 \times 8 \times 8$, $N^u_{dof} = 821$) to

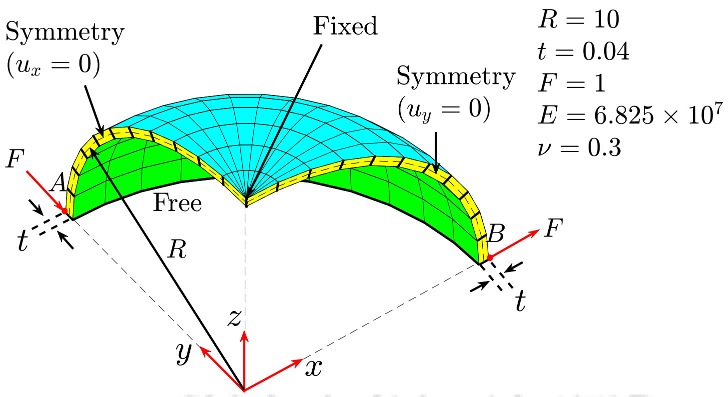

Figure 6.29: Quarter domain of a pinched hemisphere problem, material data, and boundary conditions.

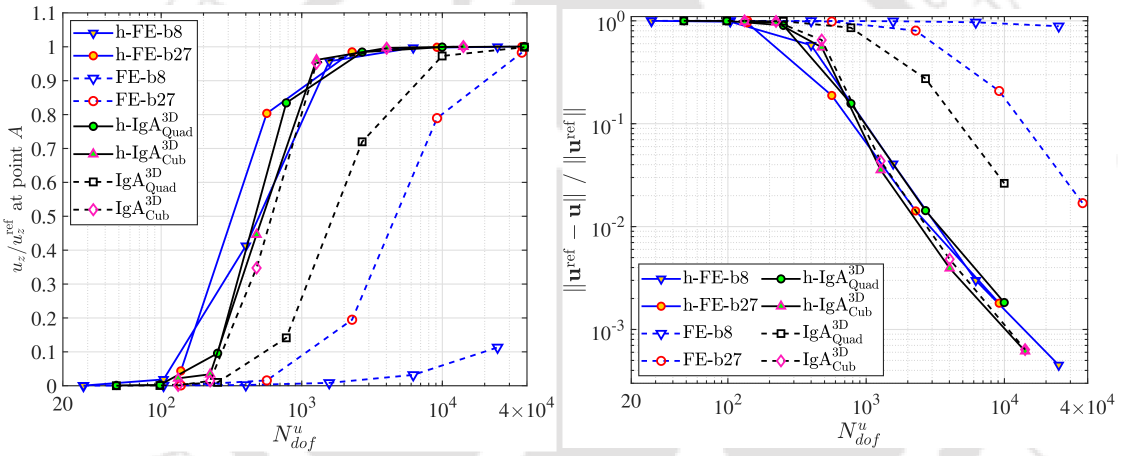

(a) u_z/u_z^{ref} **(b)** $L_2^{\boldsymbol{u}}$

Figure 6.30: (a) Normalized vertical displacement at point 'A'; (b) L_2 error norm of displacement for pinched hemisphere problem.

reach a comparable accuracy with L_2 error of 3.1487%. In fact, even in comparison to IgA$^{\text{3D}}_{\text{Cub}}$, the h-IgA$^{\text{3D}}_{\text{Quad}}$ results are superior for approximately the same number of N^u_{dof}.

Next, we investigated the additional computational burden required for the proposed hybrid elements. The extra time taken by the proposed formulation is small as compared to the conventional IGA formulation. The additional cost is around 2–4% for quadratic elements and 2–6% for cubic elements against the respective conventional IGA elements. Similar observations in the case of large deformation contact formulation in FEA using the hybrid elements have been reported by Agrawal et al. [148]. It has been shown that the time taken by the hybrid elements is roughly 1.01 times that of conventional elements for the same mesh description [148]. It provides strong numerical evidence that the hybrid elements require only marginal extra computational efforts as compared to the conventional elements.

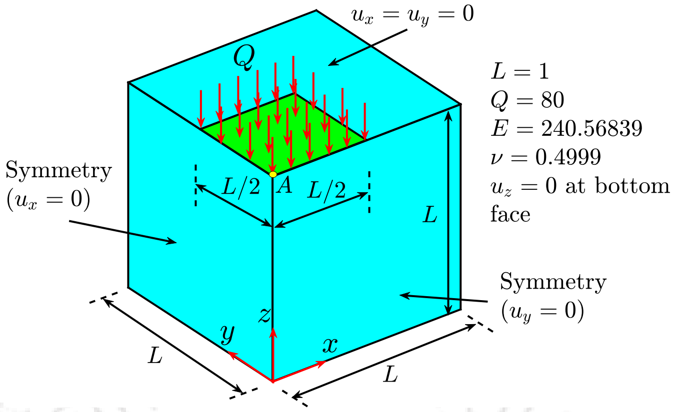

Figure 6.31: Quarter domain of an incompressible square block problem, material data, and boundary conditions.

6.4.9 Pinched hemisphere problem

The last shell obstacle course problem considered is the pinched hemisphere problem [60]. The problem comprises of a hemispherical domain of mean radius R, thickness t, and it is subjected to the equal and diametrically opposite pair of concentrated load F on the plane of equator, see Fig. 6.29. The peripheral boundary of the problem domain at $z = 0$ is free, and the top center point is fixed to avoid any rigid body motions. Similar to the preceding problems, only one-fourth of the geometry is investigated due to the symmetry of the problem domain. The geometric description to design the coarse mesh while maintaining the exact problem domain using the NURBS interpolations is defined in the Appendix (Table B.9). The meshes used to solve the problem are defined as $n^R_{\text{ele}} \times n^\theta_{\text{ele}} \times n^\phi_{\text{ele}}$, where n^R_{ele}, n^θ_{ele}, and n^ϕ_{ele} are the number of elements in R, θ, and ϕ direction, respectively. The angles θ and ϕ are the azimuthal angle in the xy-plane and the polar angle, respectively. The refinement is done along the θ and ϕ direction in such a way that $n^\theta_{\text{ele}} = n^\phi_{\text{ele}} = 2,\ 4,\ 8,\ 16,\ 32$ while keeping $n^R_{\text{ele}} = 1$.

The problem is simulated to evaluate the displacement along the direction of applied load at point 'A'. The normalized results against the analytical solution ($u_y^{\text{ref}} = 0.0924$ [60]) are presented in Fig. 6.30a. Furthermore, the relative L_2 error norm of displacement against N^u_{dof}, with reference as a converged solution of highly refined mesh consisting of $1\times64\times64$ cubic elements, is shown in Fig. 6.30b. Consistent with the previous examples, similar improvement in the quality of results for h-IgA formulation is observed. A mesh of $1 \times 16 \times 16$ ($N^u_{dof} = 2688$) of the proposed h-IgA$^{\text{3D}}_{\text{Quad}}$ elements is sufficient enough to provide a very good approximation with the analytical value with L_2 error of 1.4300%. However, the conventional IgA$^{\text{3D}}_{\text{Quad}}$, even with the four times the elements ($1 \times 32 \times 32$, $N^u_{dof} = 9968$), provides a lower accuracy (L_2 error $= 2.6339\%$) as compared to the h-IgA$^{\text{3D}}_{\text{Quad}}$ elements.

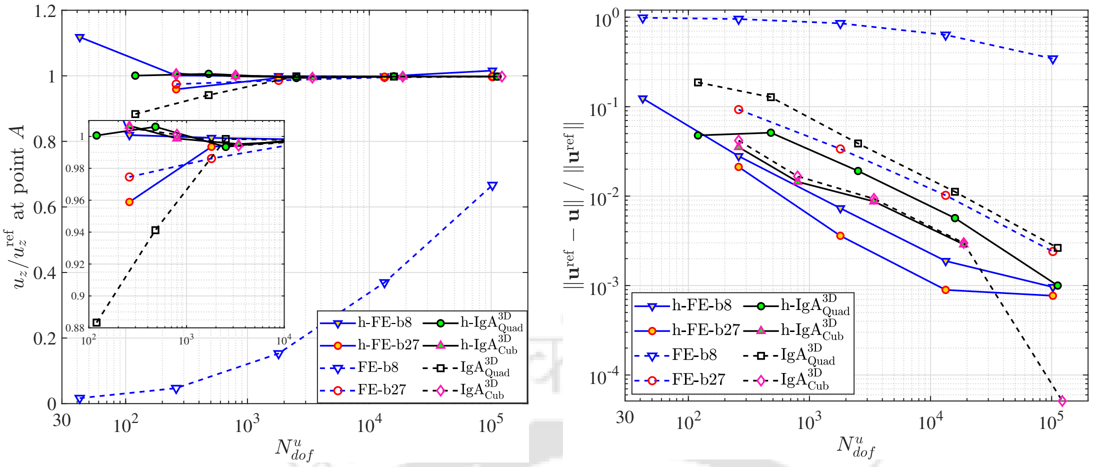

(a) u_z/u_z^{ref} **(b)** $L_2^{\boldsymbol{u}}$

Figure 6.32: (a) Normalized vertical displacement at point 'A'; (b) L_2 error norm of displacement for a nearly incompressible square block problem.

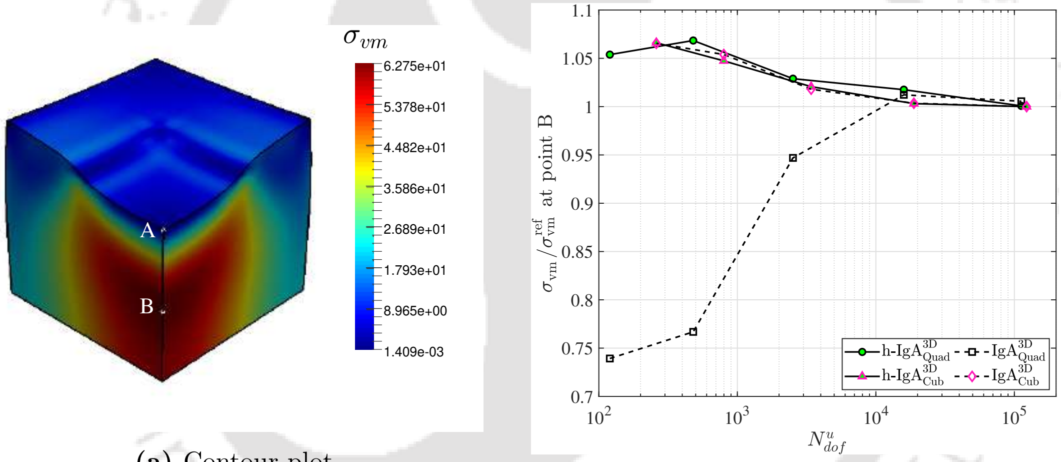

(a) Contour plot

(b) Normalized von Mises stress

Figure 6.33: (a) Contour plot of von Mises stress (σ_{vm}) using a mesh of 32 × 32 × 32 h-IgA$_2^3$ elements; (b) Normalized von Mises stress at point 'B' for a nearly incompressible square block problem.

6.4.10 Incompressible block

The next example is a well-established test to assess the formulation in near-incompressibility limit where the volumetric locking is dominant [54, 176]. The problem consists of a rectangular block of dimension $2L\times 2L\times L$. A pressure load Q is applied on a cross-sectional area of $L \times L$ at the center of the top surface of the block. Due to the symmetry of the problem, only one-fourth of the problem domain is considered for the analysis. The problem setup and the associated boundary conditions are shown in Fig. 6.31. The geometric description to design the coarse mesh with the lowest possible degree of NURBS interpolations is similar to the rectangular beam problem in the Appendix (Table B.5) after substituting $L = w = t = 1$. Further refinement is carried out using

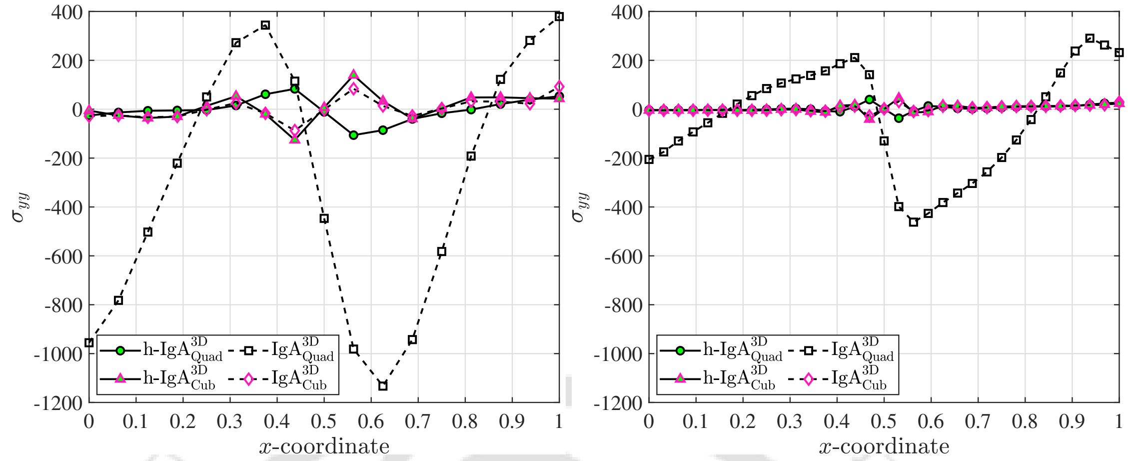

(a) σ_{yy} (mesh: $16 \times 16 \times 16$) **(b)** σ_{yy} (mesh: $32 \times 32 \times 32$)

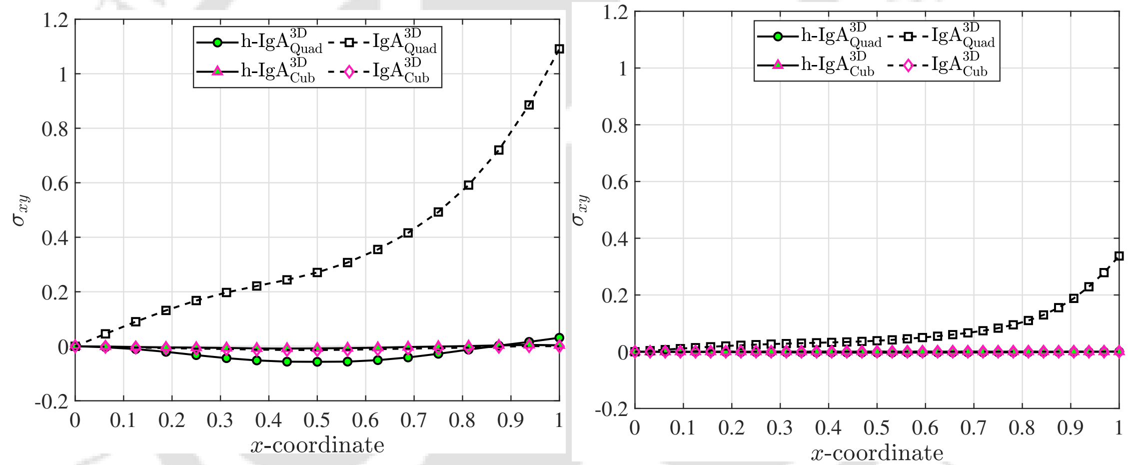

(c) σ_{xy} (mesh: $16 \times 16 \times 16$) **(d)** σ_{xy} (mesh: $32 \times 32 \times 32$)

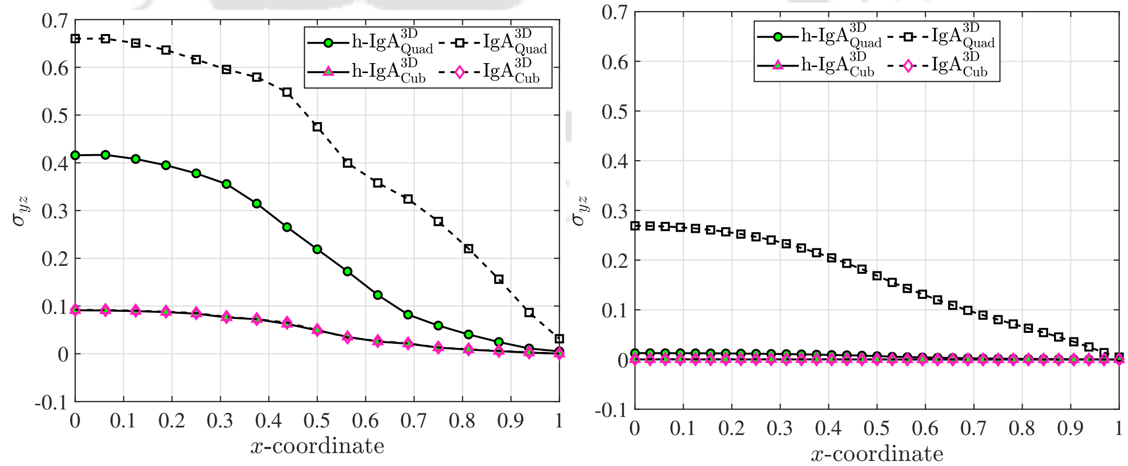

(e) σ_{yz} (mesh: $16 \times 16 \times 16$) **(f)** σ_{yz} (mesh: $32 \times 32 \times 32$)

Figure 6.34: Stresses on 'y' plane ($x = 0$ to 1, $y = 0$, $z = 0.5$) for a mesh description involving $16 \times 16 \times 16$ and $32 \times 32 \times 32$ elements for a nearly incompressible square block problem.

h- or k-refinement techniques. The meshes used to solve the problem are defined as $n^x_{\text{ele}} \times n^y_{\text{ele}} \times n^z_{\text{ele}}$, where n^x_{ele}, n^y_{ele}, and n^z_{ele} are the number of elements in x, y, and z direction, respectively. Uniform meshing is employed throughout the problem in such a way that $n^x_{\text{ele}} = n^y_{\text{ele}} = n^z_{\text{ele}} = 2,\ 4,\ 8,\ 16$, and 32.

The problem is solved for the $\nu = 0.4999$ to simulate the near-incompressible behavior of the block under the influence of volumetric locking. The normalized displacement along the z direction at point 'A' is evaluated against the reference solution ($u^{\text{ref}}_z = 0.2165$), see Fig. 6.32a. Further, the relative L_2 error norm of displacement against N^u_{dof} is evaluated in Fig. 6.32b. A converged solution of highly refined mesh consisting of $32 \times 32 \times 32$ cubic elements is taken as a reference to determine the L_2 error. The effects of locking can be seen with $\text{IgA}^{\text{3D}}_{\text{Quad}}$, whereas IGA with higher degree interpolations is capable of alleviating the locking with refinement. However, the hybrid IGA formulation consistently provides a better coarse mesh accuracy. For instance, the $\text{h-IgA}^{\text{3D}}_{\text{Quad}}$ converges to the solution with a mesh of $4 \times 4 \times 4$ ($N^u_{dof} = 2520$) elements with the relative L_2 error as 1.9093%, whereas $\text{IgA}^{\text{3D}}_{\text{Quad}}$ needs twice ($8 \times 8 \times 8$, $N^u_{dof} = 15912$) the elements in each direction to achieve a comparable accuracy with L_2 error of 1.1179%.

Further, the von Mises stress (σ_{vm}) is evaluated at $x = 0$, $y = 0$, $z = 0.5$ (point 'B'). The results are normalized against the reference value ($\sigma^{\text{ref}}_{\text{vm}}$) of 62.7484, which is the converged solution obtained while solving the problem using $32 \times 32 \times 32$ h-IgA^3_2 elements. Fig. 6.33 shows the contour plot of σ_{vm} distribution and the convergence of normalized von Mises stress at point 'B' against the active N^u_{dof}. The results show better coarse mesh accuracy of $\text{h-IgA}^{\text{3D}}_{\text{Quad}}$ elements over the conventional $\text{IgA}^{\text{3D}}_{\text{Quad}}$ elements, whereas marginal improvement is seen in $\text{h-IgA}^{\text{3D}}_{\text{Cub}}$ elements. To understand the effect of hybrid elements on the stress distribution, a thorough investigation of the stresses on the 'y' plane for different mesh descriptions is shown in Fig. 6.34. The stresses are calculated along x from 0 to 1 and keeping $y = 0$ and $z = 0.5$. Note that due to the symmetric boundary conditions, various stress components σ_{yy}, σ_{xy}, and σ_{zy} should be identically equal to zero at this location. The results, however, show that these traction boundary conditions are not accurately satisfied by the conventional $\text{IgA}^{\text{3D}}_{\text{Quad}}$ elements and significant oscillations are present in the predicted normal stress (σ_{yy}). Even with the high refinement, the conventional $\text{IgA}^{\text{3D}}_{\text{Quad}}$ fails to accurately predict the desired solution, see Figs. 6.34a and 6.34b. On the contrary, the stress field predicted from $\text{h-IgA}^{\text{3D}}_{\text{Quad}}$ elements shows no such oscillations, and their magnitude is also quite close to zero. The condition on shear stresses σ_{xy} and σ_{yz} equal to zero is better satisfied for the case of $\text{h-IgA}^{\text{3D}}_{\text{Quad}}$ elements in contrast to the $\text{IgA}^{\text{3D}}_{\text{Quad}}$ elements, see Figs. 6.34c, 6.34d, 6.34e, and 6.34f. The $\text{h-IgA}^{\text{3D}}_{\text{Cub}}$ elements also show marginal improvement over the conventional $\text{IgA}^{\text{3D}}_{\text{Cub}}$ elements.

6.5 Summary

In the present chapter, stress-displacement based hybrid elements are proposed to alleviate the adverse locking effects in NURBS-based IGA. The proposed NURBS-based hybrid elements are derived on the basis of the two-field HR variation principle, where the separate interpolation techniques are adopted for approximating the two field variables independently. Standard NURBS interpolation functions are utilized for approximating the displacement field, whereas the proposed stress interpolation functions are used to approximate the stress field. We further describe a systematic evaluation of the feasible stress interpolation functions for different order NURBS-based elements. It is mathematically shown that the proposed elements are free of any spurious zero-energy modes.

The results of numerous linear elasticity problems show that the proposed elements provide a locking-free response in problems having high aspect ratio or near-incompressibility of the domain. In most of the problems, it can be observed that the proposed elements require considerably low N_{dof}^{u} to attain a comparable accuracy with the conventional NURBS-based elements. The higher-order elements, either h-IgA$^{\mathrm{3D}}_{\mathrm{Cub}}$, h-IgA$^{\mathrm{2D}}_{\mathrm{Cub}}$, IgA$^{\mathrm{3D}}_{\mathrm{Cub}}$ or IgA$^{\mathrm{2D}}_{\mathrm{Cub}}$ are less affected by locking; however, h-IgA$^{\mathrm{3D}}_{\mathrm{Cub}}$ and h-IgA$^{\mathrm{2D}}_{\mathrm{Cub}}$ provides comparatively better coarse mesh accuracy than its conventional IGA counterpart. Moreover, the formulation is generic and does not involve any kinematic assumptions. This allows the effective implementation of proposed elements in 'thin' as well as 'chunky' geometries without any special treatment, which further complements the robustness of the method.

Chapter 7

Development of EAS Elements for Alleviating Locking in IGA

In the present chapter, we propose strain-based EAS elements to alleviate locking in IGA. The key highlight of the present work is the evaluation of enhanced strain interpolation functions for VHW principle-based EAS elements in NURBS-based IGA. These enhanced strain interpolation functions have been derived systemically for various orders of NURBS displacement interpolation through the investigation of the interrelation between the two-field HR and three-field VHW variational formulations. Additionally, the chapter demonstrates the efficacy and robustness of the proposed elements with the treatment of several 2D and 3D linear-elastic benchmark problems against the existing EAS, conventional, and hybrid IGA elements. Finally, the distinctive performance advantage of the proposed elements is demonstrated through several time-dependent problems.

7.1 Introduction

As discussed in preceding chapter, IGA has emerged as a powerful numerical method with widespread applications across diverse engineering fields. However, it is not without limitations. Notably, IGA is susceptible to locking [183], which manifests over-stiff behavior along with the high oscillations of the resulting stresses on a range of applications. Further, locking adversely affects convergence rates, leading to impractical solutions within a realistic range of discretization. These issues pose challenges to the accuracy of solutions achieved through IGA.

In the literature, numerous attempts have been made to alleviate the locking in the context of IGA, refer to Section 1.5. Despite these efforts, the strain-based formulation, particularly the EAS method, has received limited attention. EAS method has shown promising capabilities in FEA [54, 121–134, 165–167]. However, its extension to IGA is currently limited to 2D quadratic EAS elements that are specifically designed to mitigate volumetric locking in IGA [135]. Furthermore, these elements necessitate an additional stabilization strategy to address non-locking scenarios and are ineffective in mitigating shear and membrane locking. Motivated by this research gap, the present work introduces a robust class of strain-based solid EAS elements tailored for NURBS-based IGA.

A key consideration in formulating the proposed EAS elements involves the careful selection of a feasible set of interpolation functions to approximate the enhanced strain field. Similar to Chapter 4, this is achieved by utilizing the equivalence between the stress-based HR and the VHW-based EAS formulation. Attaining equivalence requires ensuring orthogonality between the independent stress field in the HR-based hybrid elements and the enhanced strain field in EAS formulations, while also satisfying specific conditions on their respective spaces [125, 126, 177, 178]. The present work utilizes the independent stress field proposed in [143, 152], which provides efficient and robust NURBS-based hybrid IGA elements, and explores the orthogonality condition to derive an efficient choice for the enhanced strain field in several 2D and 3D NURBS-based EAS elements. The methodology outlined in this work is generic and can be employed to generate a variety of EAS elements from their corresponding stress-based elements in a systematic framework.

The efficacy of the proposed EAS elements is extensively tested through numerous benchmark numerical examples, which showcase their ability to alleviate locking and provide higher coarse mesh accuracy compared to conventional elements. The efficiency, reliability, and robustness of the proposed elements make them a viable option for solving a diverse range of problem domains, especially in cases where volumetric, transverse shear and membrane locking are dominant factors. Moreover, the proposed 2D EAS elements exhibit superior performance compared to their existing counterparts. Contrary to existing EAS elements, they do not require additional stabilization techniques to handle non-locking scenarios, and are devoid of the hourglass modes, especially in locking affected problem descriptions. As a result, it presents an attractive alternative to the available EAS elements. Further, the current work also presents a set of novel 3D EAS elements. These elements have been shown to perform well in diverse situations, whether the problem involves thin or thick structures or requires handling near-incompressibility of materials, without compromising their performance. The inherent versatility of this methodological framework promotes its applicability across a broad spectrum of problems in IGA, thereby contributing to the advancement of EAS elements in the field of computational mechanics.

The rest of the chapter is organized as follows: In **Section 7.2**, the key expressions in the two-field stress-based HR formulation and VHW variational principle for the EAS method are recollected from the preceding chapters. It further discusses the conditions that lead to their equivalence. **Section 7.3** provides a systematic procedure for evaluating the strain interpolation functions utilized in the proposed EAS elements.

Subsequently, a comprehensive derivation of the strain interpolation matrix for 3D cubic EAS elements is presented in **Section 7.4**. Following this, the strain interpolation matrices for 3D quadratic and various 2D EAS elements are presented in **Section 7.5** and **Section 7.6**. In **Section 7.7**, the proposed EAS elements are assessed by analyzing their performance in multiple benchmark numerical examples. Finally, **Section 7.8** summarizes the work and additional supporting information is provided in the **Appendix**.

7.2 VHW-based EAS and stress-based HR formulation

The section initially introduces the primary field variables and their respective function spaces involved in the VHW-based EAS method and stress-based HR formulation. Following this, it revisits the key expressions that define the variational principle for the EAS method and the two-field stress-based HR formulation. Additionally, the section explores the conditions that establish equivalence between these two approaches.

7.2.1 Primary field variables and respective function spaces

The HR and VHW-based EAS variational principles necessitate the use of independent interpolation techniques for approximating the independent displacement ($\boldsymbol{u}$), stress ($\bar{\boldsymbol{\sigma}}$), and enhanced strain ($\bar{\varepsilon}^{\alpha}$) fields. These primary field variables and their involved function spaces are defined as follows:

$$\mathcal{V}_{\boldsymbol{u}} = \left\{ \boldsymbol{u} \in \mathcal{H}^1(\mathcal{R}) \,:\, \boldsymbol{u} = \boldsymbol{R}\hat{\boldsymbol{u}},\ \hat{\boldsymbol{u}} \in \mathbb{R}^{n_d \times n_e} \right\}, \tag{7.1}$$

$$\mathcal{V}_{\boldsymbol{\sigma}} = \left\{ \bar{\boldsymbol{\sigma}} \in \mathcal{L}^2(\mathcal{R}) \,:\, \bar{\boldsymbol{\sigma}} = \boldsymbol{P}\hat{\boldsymbol{\beta}} = \boldsymbol{T}_0\tilde{\boldsymbol{P}}\hat{\boldsymbol{\beta}},\ \hat{\boldsymbol{\beta}} \in \mathbb{R}^{n_{\hat{\beta}}} \right\}, \tag{7.2}$$

$$\mathcal{V}_{\boldsymbol{\varepsilon}^{\alpha}} = \left\{ \bar{\varepsilon}^{\alpha} \in \mathcal{L}^2(\mathcal{R}) \,:\, \bar{\varepsilon}^{\alpha} = \boldsymbol{G}\hat{\boldsymbol{\alpha}} = \frac{|\,\boldsymbol{J}_0\,|}{|\,\boldsymbol{J}\,|}\boldsymbol{T}_0^{-T}\tilde{\boldsymbol{G}}\hat{\boldsymbol{\alpha}},\ \hat{\boldsymbol{\alpha}} \in \mathbb{R}^{n_{\hat{\alpha}}} \right\}, \tag{7.3}$$

where $\mathcal{V}_{\boldsymbol{u}}$, $\mathcal{V}_{\boldsymbol{\sigma}}$, and $\mathcal{V}_{\boldsymbol{\varepsilon}^{\alpha}}$ denotes the function spaces for $\boldsymbol{u}$, $\bar{\boldsymbol{\sigma}}$, and $\bar{\varepsilon}^{\alpha}$, respectively, n_e represents the number of control points per element, while n_d denotes the degrees of freedom for each control point. The number of stress and strain parameters per element is given by $n_{\hat{\beta}}$ and $n_{\hat{\alpha}}$, respectively. The matrices $\boldsymbol{R}$, $\boldsymbol{P}$, and $\boldsymbol{G}$ represent displacement, stress, and strain interpolation matrices, respectively. Matrices $\tilde{\boldsymbol{P}}$ and $\tilde{\boldsymbol{G}}$ are the stress and strain interpolation matrices defined in the master space. Jacobian that relates the physical and master space is denoted by $\boldsymbol{J}$, whereas $\boldsymbol{J}_0$ is the Jacobian evaluated at the element center. As IGA involves two mapping spaces, $\boldsymbol{J}$ is evaluated as $\boldsymbol{J} = \boldsymbol{J}_2\boldsymbol{J}_1$, where $\boldsymbol{J}_1$ and $\boldsymbol{J}_2$ are the Jacobians for mapping parametric space to physical space and master space to parametric space, respectively. The transformation matrix, $\boldsymbol{T}_0$, connects the matrices $\tilde{\boldsymbol{P}}$ and $\tilde{\boldsymbol{G}}$ in the master space to their corresponding counterparts in the physical space. The expression for $\boldsymbol{T}_0$ can be found in Eq. 2.24. In addition to the above spaces, the spaces for dependent variables are defined as follows:

$$\mathcal{V}_{\boldsymbol{\sigma}^u} = \{\bar{\boldsymbol{\sigma}}^u : \bar{\boldsymbol{\sigma}}^u = \boldsymbol{C}\bar{\boldsymbol{\varepsilon}}^u = \boldsymbol{C}\boldsymbol{B}\hat{\boldsymbol{u}} \ \forall \ \boldsymbol{u} \in \mathcal{V}_{\boldsymbol{u}}\}\,, \tag{7.4}$$

$$\mathcal{V}_{\boldsymbol{\sigma}^\alpha} = \{\bar{\boldsymbol{\sigma}}^\alpha : \bar{\boldsymbol{\sigma}}^\alpha = \boldsymbol{C}\bar{\varepsilon}^\alpha \ \forall \ \bar{\varepsilon}^\alpha \in \mathcal{V}_{\varepsilon^\alpha}\}\,, \tag{7.5}$$

where $\mathcal{V}_{\boldsymbol{\sigma}^u}$ and $\mathcal{V}_{\boldsymbol{\sigma}^\alpha}$ is the function space of $\bar{\boldsymbol{\sigma}}^u$ and $\bar{\boldsymbol{\sigma}}^\alpha$, respectively, $\boldsymbol{C}$ is the material constitutive tensor, and $\boldsymbol{B}$ is the strain-displacement matrix.

7.2.2 Variational principles for EAS and hybrid formulation

The variational formulation is obtained by employing the method of weighted residuals. If $\delta\boldsymbol{u}$, $\delta\bar{\boldsymbol{\sigma}}$, and $\delta\bar{\varepsilon}^\alpha$ represent variations of $\boldsymbol{u}$, $\bar{\boldsymbol{\sigma}}$, and $\bar{\varepsilon}^\alpha$, respectively, then the variational principle associated with the VHW-based EAS method can be written as follows (Refer Chapter 2, Section 2.3):

$$\int_{\mathcal{R}} (\delta\bar{\boldsymbol{\varepsilon}}^u)^T \bar{\boldsymbol{\sigma}}^\varepsilon \, \mathrm{d}\mathcal{R} = \int_{\mathcal{R}} \delta\boldsymbol{u}^T \boldsymbol{b} \, \mathrm{d}\mathcal{R} + \int_{\partial\mathcal{R}_t} \delta\boldsymbol{u}^T \bar{\boldsymbol{t}} \, \mathrm{d}A \qquad \forall \ \delta\boldsymbol{u} \in \mathcal{V}_{\boldsymbol{u}}, \tag{7.6}$$

$$\int_{\mathcal{R}} (\delta\bar{\varepsilon}^\alpha)^T (\bar{\boldsymbol{\sigma}}^\varepsilon - \bar{\boldsymbol{\sigma}}) \, \mathrm{d}\mathcal{R} = 0, \tag{7.7}$$

whereas the stress-based hybrid elements adhere to the following HR variational principle (Refer Chapter 2, Section 2.4):

$$\int_{\mathcal{R}} (\delta\bar{\boldsymbol{\varepsilon}}^u)^T \bar{\boldsymbol{\sigma}} d\mathcal{R} = \int_{\mathcal{R}} \delta\boldsymbol{u}^T \boldsymbol{b} \, \mathrm{d}\mathcal{R} + \int_{\partial\mathcal{R}_t} \delta\boldsymbol{u}^T \bar{\boldsymbol{t}} \, \mathrm{d}A \qquad \forall \ \delta\boldsymbol{u} \in \mathcal{V}_{\boldsymbol{u}}, \tag{7.8}$$

$$\int_{\mathcal{R}} \delta\bar{\boldsymbol{\sigma}}^T \left[\bar{\varepsilon}^u(\boldsymbol{u}) - \boldsymbol{C}^{-1}\bar{\boldsymbol{\sigma}}\right] \mathrm{d}\mathcal{R} = 0 \qquad \forall \ \delta\bar{\boldsymbol{\sigma}}. \tag{7.9}$$

7.2.3 Conditions for equivalence

The VHW-based EAS and HR-based formulation lead to identical elements and exhibit exact equivalence if the following two conditions are satisfied (refer Chapter 4, Section 4.2.4):

(a) *Orthogonality condition:* An orthogonality condition is introduced between $\boldsymbol{\sigma}$ and ε^α that implies

$$\int_{\mathcal{R}} \delta\boldsymbol{\sigma} : \varepsilon^\alpha \ \mathrm{d}\mathcal{R} = 0 \quad \text{or} \quad \int_{\mathcal{R}} \delta\bar{\boldsymbol{\sigma}}^T \bar{\varepsilon}^\alpha \ \mathrm{d}\mathcal{R} = 0. \tag{7.10}$$

The above criterion also entails that the $\mathcal{V}_{\boldsymbol{\sigma}}$ and $\mathcal{V}_{\varepsilon^\alpha}$ do not share the function space, i.e., $\mathcal{V}_{\boldsymbol{\sigma}} \cap \mathcal{V}_{\varepsilon^\alpha} = \varnothing$. Finally, by substituting Eq. 7.2 and 7.3 in Eq. 7.10, a following relation for the interpolation matrices can be derived:

$$\int_{\tilde{\mathcal{R}}} \tilde{\boldsymbol{P}}^T \tilde{\boldsymbol{G}} \ \mathrm{d}\tilde{\mathcal{R}} = 0, \tag{7.11}$$

where $\tilde{R}$ represent the domain in master space.

(b) *Direct sum of functional spaces:* The condition on the functional spaces of stresses requires that the direct sum of $\mathcal{V}_{\boldsymbol{\sigma}}$ and $\mathcal{V}_{\boldsymbol{\sigma}^{\alpha}}$ should include $\mathcal{V}_{\boldsymbol{\sigma}^{u}}$, i.e.,

$$\mathcal{V}_{\boldsymbol{\sigma}^{u}} \subseteq \mathcal{V}_{\boldsymbol{\sigma}} \oplus \mathcal{V}_{\boldsymbol{\sigma}^{\alpha}} \tag{7.12}$$

Since $\boldsymbol{C}$ is a positive definite matrix, the Eq. 7.12 can be further expressed as

$$\mathcal{V}_{\boldsymbol{\sigma}^{u}} \subseteq \mathcal{V}_{\boldsymbol{\sigma}} \oplus \mathcal{V}_{\boldsymbol{\varepsilon}^{\alpha}} \tag{7.13}$$

The above equation, along with the orthogonality condition, implies that for every $\boldsymbol{\sigma}^{u} \in \mathcal{V}_{\boldsymbol{\sigma}^{u}}$ there exists a unique $\boldsymbol{\sigma} \in \mathcal{V}_{\boldsymbol{\sigma}}$ and $\boldsymbol{\varepsilon}^{\alpha} \in \mathcal{V}_{\boldsymbol{\varepsilon}^{\alpha}}$ such that $\boldsymbol{\sigma}^{u} = \boldsymbol{\sigma} - \boldsymbol{C}\boldsymbol{\varepsilon}^{\alpha}$.

Additionally, there exists the concept of weak equivalence. It implies that both the HR and VHW-based elements result in identical displacements. Furthermore, it indicates that the stresses computed using strains for EAS elements ($\boldsymbol{\sigma}^{\text{eas}} = \boldsymbol{C}\left[\boldsymbol{\varepsilon}^{\boldsymbol{u}} + \boldsymbol{\varepsilon}^{\alpha}\right] = \boldsymbol{C}\left[\boldsymbol{B}\hat{\boldsymbol{u}} + \boldsymbol{G}\hat{\boldsymbol{\alpha}}\right]$) are the same as those obtained from the hybrid elements ($\bar{\boldsymbol{\sigma}} = \boldsymbol{P}\hat{\boldsymbol{\beta}}$) at the Gauss integration points [178]. The conditions under which the weak equivalence exists are given as follows:

(a) *Orthogonality condition:* The assumed stress and the enhanced strain fields satisfy Eq. 7.11 while evaluating the expression using Gaussian quadrature integration rules. This means that the equation is true for the Gauss integration points in the element domain and that the assumptions about the stress and enhanced strain fields are accurate within this context.

(b) *Relation between number of parameters:* The involved parameters must follow

$$n_{\hat{\beta}} + n_{\hat{\alpha}} = n_{gp} \times n_{\sigma}, \tag{7.14}$$

where $n_{\hat{\beta}}$ and $n_{\hat{\alpha}}$ are the number of stress and strain parameters per element. n_{gp} is the number of Gauss integration points and n_{σ} is the total number of stress components.

(c) *Linear independence:* The matrix $\left[\tilde{\boldsymbol{P}}^{gp}; \tilde{\boldsymbol{G}}^{gp}\right]$ composed of linearly independent column vectors. Here, $\tilde{\boldsymbol{P}}^{gp} = \left[\tilde{\boldsymbol{P}}^{1}\ \tilde{\boldsymbol{P}}^{2}\ \ldots\ \tilde{\boldsymbol{P}}^{n_{gp}}\right]^{T}$ and $\tilde{\boldsymbol{G}}^{gp} = \left[\tilde{\boldsymbol{G}}^{1}\ \tilde{\boldsymbol{G}}^{2}\ \ldots\ \tilde{\boldsymbol{G}}^{n_{gp}}\right]^{T}$. The terms $\tilde{\boldsymbol{P}}^{i}$ and $\tilde{\boldsymbol{G}}^{i}$ denote the stress and enhanced strain interpolation matrix evaluated at the i^{th} Gauss integration point.

7.3 Exploring feasible function space in NURBS-based EAS elements through orthogonality

The process of evaluating the interpolation functions for approximating $\bar{\boldsymbol{\varepsilon}}^{\alpha}$ in NURBS-based EAS elements follow a similar approach as explained in Chapter 4, Section 4.3.

The main distinction is the use of NURBS interpolations instead of Lagrange interpolations and deriving the functional space corresponding to this modification. For the completeness of the chapter, we provide a brief overview of the steps involved in the derivation, emphasizing its distinction for IGA.

The methodology is based on the orthogonality of $\bar{\boldsymbol{\sigma}}$ and $\bar{\boldsymbol{\varepsilon}}^{\alpha}$ as stated in Eq. 7.10 which must hold for any pair of $(\bar{\boldsymbol{\sigma}}, \bar{\boldsymbol{\varepsilon}}^{\alpha}) \in (\mathcal{V}_{\boldsymbol{\sigma}} \times \mathcal{V}_{\boldsymbol{\varepsilon}^{\alpha}})$. To ensure this, let's express Eq. 7.10 in the following manner:

$$\int_{\mathcal{R}} \bar{\boldsymbol{\sigma}}^T \bar{\boldsymbol{\varepsilon}}^{\alpha} \; \mathrm{d}\mathcal{R} = 0 \rightarrow \int_{\mathcal{R}} \boldsymbol{P}^T \bar{\boldsymbol{\varepsilon}}^{\alpha} \; \mathrm{d}\mathcal{R} = 0. \tag{7.15}$$

The choice of $\boldsymbol{P}$ is taken from the stress-based hybrid IGA elements proposed in Chapter 6 or [143, 152]. Note that the present work has utilized matrix $\boldsymbol{T}_0$ while in [143, 152] the transformation matrix has been calculated at each Gauss point. In these elements, the interpolation of each component of the stress is independent of each other, thus giving rise to the following block structure of $\boldsymbol{P}$:

$$\boldsymbol{P} = \boldsymbol{T}_0 \tilde{\boldsymbol{P}} = \boldsymbol{T}_0 \begin{bmatrix} \tilde{\boldsymbol{P}}_L & \tilde{\boldsymbol{P}}_H \end{bmatrix} = \boldsymbol{T}_0 \begin{bmatrix} \tilde{\boldsymbol{P}}_1 & \mathbf{0}_b & \mathbf{0}_c & \mathbf{0}_d & \mathbf{0}_e & \mathbf{0}_f \\ \mathbf{0}_a & \tilde{\boldsymbol{P}}_2 & \mathbf{0}_c & \mathbf{0}_d & \mathbf{0}_e & \mathbf{0}_f \\ \mathbf{0}_a & \mathbf{0}_b & \tilde{\boldsymbol{P}}_3 & \mathbf{0}_d & \mathbf{0}_e & \mathbf{0}_f \\ \mathbf{0}_a & \mathbf{0}_b & \mathbf{0}_c & \tilde{\boldsymbol{P}}_4 & \mathbf{0}_e & \mathbf{0}_f \\ \mathbf{0}_a & \mathbf{0}_b & \mathbf{0}_c & \mathbf{0}_d & \tilde{\boldsymbol{P}}_5 & \mathbf{0}_f \\ \mathbf{0}_a & \mathbf{0}_b & \mathbf{0}_c & \mathbf{0}_d & \mathbf{0}_e & \tilde{\boldsymbol{P}}_6 \end{bmatrix}, \tag{7.16}$$

where $\tilde{\boldsymbol{P}}_i$ represents the set of stress interpolation functions and $\mathbf{0}_a$, $\mathbf{0}_b$, …, $\mathbf{0}_f$ are zero vectors.

The block nature of the $\tilde{\boldsymbol{P}}$ matrix implies that the orthogonality condition can be restated as follows:

$$\int_{\mathcal{R}} \tilde{\boldsymbol{P}}_i^T \bar{\varepsilon}_i^{\alpha} \; \mathrm{d}\mathcal{R} = \mathbf{0} \qquad \Big(i = 1 \;, \, 2, \, \ldots, \, 6. \text{ no summation over `}i\text{'} \Big), \tag{7.17}$$

where $\tilde{\boldsymbol{P}}_i$ refers to the vectors $\tilde{\boldsymbol{P}}_1$, $\tilde{\boldsymbol{P}}_2$, …, $\tilde{\boldsymbol{P}}_6$ and the corresponding $\bar{\varepsilon}_i^{\alpha}$ is the i^{th} component of a vector $\bar{\boldsymbol{\varepsilon}}^{\alpha}$.

For interpolation of $\bar{\boldsymbol{\varepsilon}}^{\alpha}$, we similarly assume that all the enhanced strain components are independently interpolated from each other. Thus, the strain interpolation matrix also has the block form and is given by the following expression:

$$\bar{\boldsymbol{\varepsilon}}^{\alpha} = \frac{\mid \boldsymbol{J}_0 \mid}{\mid \boldsymbol{J} \mid} \boldsymbol{T}_0^{-T} \tilde{\boldsymbol{G}} \hat{\boldsymbol{\alpha}}, \tag{7.18}$$

such that

$$\tilde{\boldsymbol{G}} = \begin{bmatrix} \tilde{\boldsymbol{G}}_1 & \mathbf{0}_{b^*} & \mathbf{0}_{c^*} & \mathbf{0}_{d^*} & \mathbf{0}_{e^*} & \mathbf{0}_{f^*} \\ \mathbf{0}_{a^*} & \tilde{\boldsymbol{G}}_2 & \mathbf{0}_{c^*} & \mathbf{0}_{d^*} & \mathbf{0}_{e^*} & \mathbf{0}_{f^*} \\ \mathbf{0}_{a^*} & \mathbf{0}_{b^*} & \tilde{\boldsymbol{G}}_3 & \mathbf{0}_{d^*} & \mathbf{0}_{e^*} & \mathbf{0}_{f^*} \\ \mathbf{0}_{a^*} & \mathbf{0}_{b^*} & \mathbf{0}_{c^*} & \tilde{\boldsymbol{G}}_4 & \mathbf{0}_{e^*} & \mathbf{0}_{f^*} \\ \mathbf{0}_{a^*} & \mathbf{0}_{b^*} & \mathbf{0}_{c^*} & \mathbf{0}_{d^*} & \tilde{\boldsymbol{G}}_5 & \mathbf{0}_{f^*} \\ \mathbf{0}_{a^*} & \mathbf{0}_{b^*} & \mathbf{0}_{c^*} & \mathbf{0}_{d^*} & \mathbf{0}_{e^*} & \tilde{\boldsymbol{G}}_6 \end{bmatrix} \text{ and } \hat{\boldsymbol{\alpha}} = \begin{Bmatrix} \hat{\boldsymbol{\alpha}}^1 \\ \hat{\boldsymbol{\alpha}}^2 \\ \hat{\boldsymbol{\alpha}}^3 \\ \hat{\boldsymbol{\alpha}}^4 \\ \hat{\boldsymbol{\alpha}}^5 \\ \hat{\boldsymbol{\alpha}}^6 \end{Bmatrix},$$

where $\tilde{\boldsymbol{G}}_i$ is the set of strain interpolation functions in master space and $\mathbf{0}_{a^*}$, $\mathbf{0}_{b^*}$, …, $\mathbf{0}_{f^*}$ are zero vectors.

Furthermore, it is assumed that the function space of components of the $\tilde{\boldsymbol{G}}$, i.e., $\mathcal{V}_{\tilde{\boldsymbol{G}}_i}$, is defined in the following manner:

$$\mathcal{V}_{\tilde{\boldsymbol{G}}_i} = \left\{ \tilde{\boldsymbol{\phi}} \cdot \boldsymbol{a} \ : \ \int_{\tilde{\mathcal{R}}} \tilde{\boldsymbol{P}}_i^T \tilde{\boldsymbol{\phi}} \cdot \boldsymbol{a} \ \mathrm{d}\tilde{\mathcal{R}} = \mathbf{0} \right\}, \tag{7.19}$$

where $\tilde{\boldsymbol{\phi}}$ represents a set of functions in master space and $\boldsymbol{a}$ corresponds to a vector of constants. The functions in $\tilde{\boldsymbol{\phi}}$ are chosen to satisfy Eq. 7.13, particularly in the case of constant Jacobian. The most direct approach is to consider all deformation modes within the displacement field, which is interpolated using NURBS basis functions. Given that these are rational entities, we assume constant weights, simplifying NURBS interpolations to B-spline interpolation functions.

After determining the suitable $\tilde{\boldsymbol{\phi}}$, the Eq. 7.19 leads to the following system of linear equations:

$$\int_{\tilde{\mathcal{R}}} \tilde{\boldsymbol{P}}_i^T \left[\sum_{k=1}^{r} a_k \phi_k(\xi, \eta, \zeta) \right] \mathrm{d}\tilde{\mathcal{R}} = \mathbf{0}. \tag{7.20}$$

The above equation indicates that the assumed $\tilde{\boldsymbol{\phi}} \cdot \boldsymbol{a}$ should be orthogonal to every component of $\tilde{\boldsymbol{P}}_i$, and can be written in a concise form as follows:

$$\bar{\boldsymbol{A}} \boldsymbol{a} = \mathbf{0}, \tag{7.21}$$

where $\bar{\boldsymbol{A}}$ is the matrix of the coefficients of a_k after performing the integration over the domain $\tilde{\mathcal{R}}$. Every feasible vector in the null space of $\bar{\boldsymbol{A}}$ is an acceptable solution for $\boldsymbol{a}$. If $\boldsymbol{a}^j$ be the basis of the null space of $\bar{\boldsymbol{A}}$ of dimension n_A. Then, the expression for $\tilde{\boldsymbol{G}}_i$ is evaluated as follows:

$$\tilde{\boldsymbol{G}}_i = \begin{bmatrix} \boldsymbol{a}^1 \cdot \tilde{\boldsymbol{\phi}} & \boldsymbol{a}^2 \cdot \tilde{\boldsymbol{\phi}} & \ldots & \boldsymbol{a}^{n_A} \cdot \tilde{\boldsymbol{\phi}} \end{bmatrix} \tag{7.22}$$

By following the above-mentioned methodology, enhanced strain interpolation functions can be obtained for any arbitrary element. To better understand the involved procedure, a detailed proof is provided for a 3D cubic NURBS-based EAS element in the next section.

7.4 Evaluation of strain interpolation matrix for 3D cubic element

In the present section, a systematic derivation of $\tilde{\boldsymbol{G}}$ matrix for the proposed 3D cubic EAS element is presented. The term "cubic element" refers to NURBS-based elements with 3rd degree NUBRS basis function along all three parametric directions with C^2 continuous displacements across the element boundary. The process initiates by recalling the $\tilde{\boldsymbol{P}}(\tilde{\xi}, \tilde{\eta}, \tilde{\zeta})$ matrix, proposed in Chapter 6 or [143], for a cubic hybrid element. The expression of $\tilde{\boldsymbol{P}}(\tilde{\xi}, \tilde{\eta}, \tilde{\zeta})$ is given as follows:

$$\begin{Bmatrix} \sigma_{\tilde{\xi}\tilde{\xi}} \\ \sigma_{\tilde{\eta}\tilde{\eta}} \\ \sigma_{\tilde{\zeta}\tilde{\zeta}} \\ \sigma_{\tilde{\xi}\tilde{\eta}} \\ \sigma_{\tilde{\eta}\tilde{\zeta}} \\ \sigma_{\tilde{\xi}\tilde{\zeta}} \end{Bmatrix} = \begin{bmatrix} \tilde{\boldsymbol{P}}^e_L & \tilde{\boldsymbol{P}}^e_H \end{bmatrix} \begin{bmatrix} \hat{\boldsymbol{\beta}}^e_L \\ \hat{\boldsymbol{\beta}}^e_H \end{bmatrix} = \underbrace{\begin{bmatrix} \tilde{\boldsymbol{P}}_1 & \mathbf{0}_c & \mathbf{0}_c & \mathbf{0}_d & \mathbf{0}_d & \mathbf{0}_d \\ \mathbf{0}_c & \tilde{\boldsymbol{P}}_2 & \mathbf{0}_c & \mathbf{0}_d & \mathbf{0}_d & \mathbf{0}_d \\ \mathbf{0}_c & \mathbf{0}_c & \tilde{\boldsymbol{P}}_3 & \mathbf{0}_d & \mathbf{0}_d & \mathbf{0}_d \\ \mathbf{0}_c & \mathbf{0}_c & \mathbf{0}_c & \tilde{\boldsymbol{P}}_4 & \mathbf{0}_d & \mathbf{0}_d \\ \mathbf{0}_c & \mathbf{0}_c & \mathbf{0}_c & \mathbf{0}_d & \tilde{\boldsymbol{P}}_5 & \mathbf{0}_d \\ \mathbf{0}_c & \mathbf{0}_c & \mathbf{0}_c & \mathbf{0}_d & \mathbf{0}_d & \tilde{\boldsymbol{P}}_6 \end{bmatrix}}_{\tilde{\boldsymbol{P}}(\tilde{\xi},\tilde{\eta},\tilde{\zeta})} \underbrace{\begin{Bmatrix} \tilde{\beta}_1 \\ \tilde{\beta}_2 \\ \tilde{\beta}_3 \\ \tilde{\beta}_4 \\ \vdots \\ \tilde{\beta}_{252} \end{Bmatrix}}_{\hat{\boldsymbol{\beta}}}, \tag{7.23}$$

where $\mathbf{0}_c$ and $\mathbf{0}_d$ are the null or zero vectors of the size 1×48 and 1×36, respectively. The vectors $\tilde{\boldsymbol{P}}_1, \tilde{\boldsymbol{P}}_2, \ldots, \tilde{\boldsymbol{P}}_6$ can be given as $\tilde{\boldsymbol{P}}_i = \begin{bmatrix} \tilde{\boldsymbol{P}}^L & \tilde{\boldsymbol{P}}^H_i \end{bmatrix}$, where

$$\begin{aligned}
\tilde{\boldsymbol{P}}^L =& \Big[\, 1 \;\; \tilde{\zeta} \;\; \tilde{\zeta}^2 \;\; \tilde{\eta} \;\; \tilde{\zeta}\tilde{\eta} \;\; \tilde{\zeta}^2\tilde{\eta} \;\; \tilde{\eta}^2 \;\; \tilde{\zeta}\tilde{\eta}^2 \;\; \tilde{\zeta}^2\tilde{\eta}^2 \;\; \tilde{\xi} \;\; \tilde{\zeta}\tilde{\xi} \;\; \tilde{\zeta}^2\tilde{\xi} \;\; \tilde{\eta}\tilde{\xi} \;\; \tilde{\zeta}\tilde{\eta}\tilde{\xi} \;\; \tilde{\zeta}^2\tilde{\eta}\tilde{\xi} \;\; \tilde{\eta}^2\tilde{\xi} \;\; \tilde{\zeta}\tilde{\eta}^2\tilde{\xi} \;\; \tilde{\zeta}^2\tilde{\eta}^2\tilde{\xi} \\
& \tilde{\xi}^2 \;\; \tilde{\zeta}\tilde{\xi}^2 \;\; \tilde{\zeta}^2\tilde{\xi}^2 \;\; \tilde{\eta}\tilde{\xi}^2 \;\; \tilde{\zeta}\tilde{\eta}\tilde{\xi}^2 \;\; \tilde{\zeta}^2\tilde{\eta}\tilde{\xi}^2 \;\; \tilde{\eta}^2\tilde{\xi}^2 \;\; \tilde{\zeta}\tilde{\eta}^2\tilde{\xi}^2 \;\; \tilde{\zeta}^2\tilde{\eta}^2\tilde{\xi}^2 \,\Big], \\
\tilde{\boldsymbol{P}}^H_1 =& \Big[\, \tilde{\zeta}^3 \;\; \tilde{\zeta}^3\tilde{\eta} \;\; \tilde{\zeta}^3\tilde{\eta}^2 \;\; \tilde{\eta}^3 \;\; \tilde{\zeta}\tilde{\eta}^3 \;\; \tilde{\zeta}^2\tilde{\eta}^3 \;\; \tilde{\zeta}^3\tilde{\eta}^3 \;\; \tilde{\zeta}^3\tilde{\xi} \;\; \tilde{\zeta}^3\tilde{\eta}\tilde{\xi} \;\; \tilde{\zeta}^3\tilde{\eta}^2\tilde{\xi} \;\; \tilde{\eta}^3\tilde{\xi} \;\; \tilde{\zeta}\tilde{\eta}^3\tilde{\xi} \;\; \tilde{\zeta}^2\tilde{\eta}^3\tilde{\xi} \;\; \tilde{\zeta}^3\tilde{\eta}^3\tilde{\xi} \\
& \tilde{\zeta}^3\tilde{\xi}^2 \;\; \tilde{\zeta}^3\tilde{\eta}\tilde{\xi}^2 \;\; \tilde{\zeta}^3\tilde{\eta}^2\tilde{\xi}^2 \;\; \tilde{\eta}^3\tilde{\xi}^2 \;\; \tilde{\zeta}\tilde{\eta}^3\tilde{\xi}^2 \;\; \tilde{\zeta}^2\tilde{\eta}^3\tilde{\xi}^2 \;\; \tilde{\zeta}^3\tilde{\eta}^3\tilde{\xi}^2 \,\Big], \\
\tilde{\boldsymbol{P}}^H_2 =& \Big[\, \tilde{\zeta}^3 \;\; \tilde{\zeta}^3\tilde{\eta} \;\; \tilde{\zeta}^3\tilde{\eta}^2 \;\; \tilde{\zeta}^3\tilde{\xi} \;\; \tilde{\zeta}^3\tilde{\eta}\tilde{\xi} \;\; \tilde{\zeta}^3\tilde{\eta}^2\tilde{\xi} \;\; \tilde{\zeta}^3\tilde{\xi}^2 \;\; \tilde{\zeta}^3\tilde{\eta}\tilde{\xi}^2 \;\; \tilde{\zeta}^3\tilde{\eta}^2\tilde{\xi}^2 \;\; \tilde{\xi}^3 \;\; \tilde{\zeta}\tilde{\xi}^3 \;\; \tilde{\zeta}^2\tilde{\xi}^3 \;\; \tilde{\zeta}^3\tilde{\xi}^3 \;\; \tilde{\eta}\tilde{\xi}^3 \\
& \tilde{\zeta}\tilde{\eta}\tilde{\xi}^3 \;\; \tilde{\zeta}^2\tilde{\eta}\tilde{\xi}^3 \;\; \tilde{\zeta}^3\tilde{\eta}\tilde{\xi}^3 \;\; \tilde{\eta}^2\tilde{\xi}^3 \;\; \tilde{\zeta}\tilde{\eta}^2\tilde{\xi}^3 \;\; \tilde{\zeta}^2\tilde{\eta}^2\tilde{\xi}^3 \;\; \tilde{\zeta}^3\tilde{\eta}^2\tilde{\xi}^3 \,\Big], \\
\tilde{\boldsymbol{P}}^H_3 =& \Big[\, \tilde{\eta}^3 \;\; \tilde{\zeta}\tilde{\eta}^3 \;\; \tilde{\zeta}^2\tilde{\eta}^3 \;\; \tilde{\eta}^3\tilde{\xi} \;\; \tilde{\zeta}\tilde{\eta}^3\tilde{\xi} \;\; \tilde{\zeta}^2\tilde{\eta}^3\tilde{\xi} \;\; \tilde{\eta}^3\tilde{\xi}^2 \;\; \tilde{\zeta}\tilde{\eta}^3\tilde{\xi}^2 \;\; \tilde{\zeta}^2\tilde{\eta}^3\tilde{\xi}^2 \;\; \tilde{\xi}^3 \;\; \tilde{\zeta}\tilde{\xi}^3 \;\; \tilde{\zeta}^2\tilde{\xi}^3 \;\; \tilde{\eta}\tilde{\xi}^3 \;\; \tilde{\zeta}\tilde{\eta}\tilde{\xi}^3 \\
& \tilde{\zeta}^2\tilde{\eta}\tilde{\xi}^3 \;\; \tilde{\eta}^2\tilde{\xi}^3 \;\; \tilde{\zeta}\tilde{\eta}^2\tilde{\xi}^3 \;\; \tilde{\zeta}^2\tilde{\eta}^2\tilde{\xi}^3 \;\; \tilde{\eta}^3\tilde{\xi}^3 \;\; \tilde{\zeta}\tilde{\eta}^3\tilde{\xi}^3 \;\; \tilde{\zeta}^2\tilde{\eta}^3\tilde{\xi}^3 \,\Big], \\
\tilde{\boldsymbol{P}}^H_4 =& \Big[\, \tilde{\zeta}^3 \;\; \tilde{\zeta}^3\tilde{\eta} \;\; \tilde{\zeta}^3\tilde{\eta}^2 \;\; \tilde{\zeta}^3\tilde{\xi} \;\; \tilde{\zeta}^3\tilde{\eta}\tilde{\xi} \;\; \tilde{\zeta}^3\tilde{\eta}^2\tilde{\xi} \;\; \tilde{\zeta}^3\tilde{\xi}^2 \;\; \tilde{\zeta}^3\tilde{\eta}\tilde{\xi}^2 \;\; \tilde{\zeta}^3\tilde{\eta}^2\tilde{\xi}^2 \,\Big], \\
\tilde{\boldsymbol{P}}^H_5 =& \Big[\, \tilde{\xi}^3 \;\; \tilde{\zeta}\tilde{\xi}^3 \;\; \tilde{\zeta}^2\tilde{\xi}^3 \;\; \tilde{\eta}\tilde{\xi}^3 \;\; \tilde{\zeta}\tilde{\eta}\tilde{\xi}^3 \;\; \tilde{\zeta}^2\tilde{\eta}\tilde{\xi}^3 \;\; \tilde{\eta}^2\tilde{\xi}^3 \;\; \tilde{\zeta}\tilde{\eta}^2\tilde{\xi}^3 \;\; \tilde{\zeta}^2\tilde{\eta}^2\tilde{\xi}^3 \,\Big], \\
\tilde{\boldsymbol{P}}^H_6 =& \Big[\, \tilde{\eta}^3 \;\; \tilde{\zeta}\tilde{\eta}^3 \;\; \tilde{\zeta}^2\tilde{\eta}^3 \;\; \tilde{\eta}^3\tilde{\xi} \;\; \tilde{\zeta}\tilde{\eta}^3\tilde{\xi} \;\; \tilde{\zeta}^2\tilde{\eta}^3\tilde{\xi} \;\; \tilde{\eta}^3\tilde{\xi}^2 \;\; \tilde{\zeta}\tilde{\eta}^3\tilde{\xi}^2 \;\; \tilde{\zeta}^2\tilde{\eta}^3\tilde{\xi}^2 \,\Big].
\end{aligned}$$

Assuming that the required $\tilde{\boldsymbol{G}}$ is in the form of Eq. 7.18, the next step is to select the appropriate $\tilde{\boldsymbol{\phi}}$ that defines the components of the enhanced strain field in the master space. The optimal choice of $\tilde{\boldsymbol{\phi}}$ is a set of functions that contains all the modes in $\boldsymbol{u}$ in order to satisfy the second condition for equivalence stated in Eq. 7.13. This results in the collection of functions that define a full cubic polynomial in $\tilde{\xi}$, $\tilde{\eta}$ and $\tilde{\zeta}$ such that

$$\begin{aligned}\tilde{\boldsymbol{\phi}} = \Big[\, & 1 \;\; \tilde{\zeta} \;\; \tilde{\zeta}^2 \;\; \tilde{\zeta}^3 \;\; \tilde{\eta} \;\; \tilde{\eta}\tilde{\zeta} \;\; \tilde{\eta}\tilde{\zeta}^2 \;\; \tilde{\eta}\tilde{\zeta}^3 \;\; \tilde{\eta}^2 \;\; \tilde{\eta}^2\tilde{\zeta} \;\; \tilde{\eta}^2\tilde{\zeta}^2 \;\; \tilde{\eta}^2\tilde{\zeta}^3 \;\; \tilde{\eta}^3 \;\; \tilde{\eta}^3\tilde{\zeta} \;\; \tilde{\eta}^3\tilde{\zeta}^2 \;\; \tilde{\eta}^3\tilde{\zeta}^3 \;\; \tilde{\xi} \;\; \tilde{\xi}\tilde{\zeta} \\ & \tilde{\xi}\tilde{\zeta}^2 \;\; \tilde{\xi}\tilde{\zeta}^3 \;\; \tilde{\xi}\tilde{\eta} \;\; \tilde{\xi}\tilde{\eta}\tilde{\zeta} \;\; \tilde{\xi}\tilde{\eta}\tilde{\zeta}^2 \;\; \tilde{\xi}\tilde{\eta}\tilde{\zeta}^3 \;\; \tilde{\xi}\tilde{\eta}^2 \;\; \tilde{\xi}\tilde{\eta}^2\tilde{\zeta} \;\; \tilde{\xi}\tilde{\eta}^2\tilde{\zeta}^2 \;\; \tilde{\xi}\tilde{\eta}^2\tilde{\zeta}^3 \;\; \tilde{\xi}\tilde{\eta}^3 \;\; \tilde{\xi}\tilde{\eta}^3\tilde{\zeta} \;\; \tilde{\xi}\tilde{\eta}^3\tilde{\zeta}^2 \\ & \tilde{\xi}\tilde{\eta}^3\tilde{\zeta}^3 \;\; \tilde{\xi}^2 \;\; \tilde{\xi}^2\tilde{\zeta} \;\; \tilde{\xi}^2\tilde{\zeta}^2 \;\; \tilde{\xi}^2\tilde{\zeta}^3 \;\; \tilde{\xi}^2\tilde{\eta} \;\; \tilde{\xi}^2\tilde{\eta}\tilde{\zeta} \;\; \tilde{\xi}^2\tilde{\eta}\tilde{\zeta}^2 \;\; \tilde{\xi}^2\tilde{\eta}\tilde{\zeta}^3 \;\; \tilde{\xi}^2\tilde{\eta}^2 \;\; \tilde{\xi}^2\tilde{\eta}^2\tilde{\zeta} \;\; \tilde{\xi}^2\tilde{\eta}^2\tilde{\zeta}^2 \\ & \tilde{\xi}^2\tilde{\eta}^2\tilde{\zeta}^3 \;\; \tilde{\xi}^2\tilde{\eta}^3 \;\; \tilde{\xi}^2\tilde{\eta}^3\tilde{\zeta} \;\; \tilde{\xi}^2\tilde{\eta}^3\tilde{\zeta}^2 \;\; \tilde{\xi}^2\tilde{\eta}^3\tilde{\zeta}^3 \;\; \tilde{\xi}^3 \;\; \tilde{\xi}^3\tilde{\zeta} \;\; \tilde{\xi}^3\tilde{\zeta}^2 \;\; \tilde{\xi}^3\tilde{\zeta}^3 \;\; \tilde{\xi}^3\tilde{\eta} \;\; \tilde{\xi}^3\tilde{\eta}\tilde{\zeta} \;\; \tilde{\xi}^3\tilde{\eta}\tilde{\zeta}^2 \\ & \tilde{\xi}^3\tilde{\eta}\tilde{\zeta}^3 \;\; \tilde{\xi}^3\tilde{\eta}^2 \;\; \tilde{\xi}^3\tilde{\eta}^2\tilde{\zeta} \;\; \tilde{\xi}^3\tilde{\eta}^2\tilde{\zeta}^2 \;\; \tilde{\xi}^3\tilde{\eta}^2\tilde{\zeta}^3 \;\; \tilde{\xi}^3\tilde{\eta}^3 \;\; \tilde{\xi}^3\tilde{\eta}^3\tilde{\zeta} \;\; \tilde{\xi}^3\tilde{\eta}^3\tilde{\zeta}^2 \;\; \tilde{\xi}^3\tilde{\eta}^3\tilde{\zeta}^3 \,\Big].\end{aligned} \tag{7.24}$$

After selecting the suitable $\tilde{\boldsymbol{\phi}}$ and substituting it into Eq. 7.20, a system of linear equations can be formed for each individual enhanced strain component. To illustrate the procedure, the evaluation of the strain interpolation function for $\bar{\varepsilon}^{\alpha}_{\tilde{\xi}\tilde{\xi}}$ is explained in detail. Following the relation expressed in Eq. 7.20, let us assume that the $\mathcal{V}_{\tilde{\boldsymbol{G}}_1}$ is the function space of $\tilde{\boldsymbol{G}}_1$ such that $\int_{\tilde{\mathcal{R}}} \tilde{\boldsymbol{P}}_1^T \tilde{\boldsymbol{\phi}} \cdot \boldsymbol{a} \; \mathrm{d}\tilde{\mathcal{R}} = \boldsymbol{0}$. This orthogonality condition leads to the following linear system:

$$\bar{\boldsymbol{A}}\boldsymbol{a} = \boldsymbol{0}. \tag{7.25}$$

The above set of linear equations is solved for $\boldsymbol{a}$, where the feasible solutions for $\boldsymbol{a}$ are vectors that lie in the null space of $\bar{\boldsymbol{A}}$. The null space dimension n_A for Eq. 7.25 is sixteen, and the basis vectors $\boldsymbol{a}^j$ for the null space are evaluated as follows:

$$\begin{aligned}
\boldsymbol{a}^1 &= \left[\boldsymbol{0}_{1\times 31} \;\; -\frac{3}{5} \;\; \boldsymbol{0}_{1\times 31} \;\; 1\right]^T, & \boldsymbol{a}^9 &= \left[\boldsymbol{0}_{1\times 23} \;\; -\frac{3}{5} \;\; \boldsymbol{0}_{1\times 31} \;\; 1 \;\; \boldsymbol{0}_{1\times 8}\right]^T, \\
\boldsymbol{a}^2 &= \left[\boldsymbol{0}_{1\times 30} \;\; -\frac{3}{5} \;\; \boldsymbol{0}_{1\times 31} \;\; 1 \;\; 0\right]^T, & \boldsymbol{a}^{10} &= \left[\boldsymbol{0}_{1\times 22} \;\; -\frac{3}{5} \;\; \boldsymbol{0}_{1\times 31} \;\; 1 \;\; \boldsymbol{0}_{1\times 9}\right]^T, \\
\boldsymbol{a}^3 &= \left[\boldsymbol{0}_{1\times 29} \;\; -\frac{3}{5} \;\; \boldsymbol{0}_{1\times 31} \;\; 1 \;\; \boldsymbol{0}_{1\times 2}\right]^T, & \boldsymbol{a}^{11} &= \left[\boldsymbol{0}_{1\times 21} \;\; -\frac{3}{5} \;\; \boldsymbol{0}_{1\times 31} \;\; 1 \;\; \boldsymbol{0}_{1\times 10}\right]^T, \\
\boldsymbol{a}^4 &= \left[\boldsymbol{0}_{1\times 28} \;\; -\frac{3}{5} \;\; \boldsymbol{0}_{1\times 31} \;\; 1 \;\; \boldsymbol{0}_{1\times 3}\right]^T, & \boldsymbol{a}^{12} &= \left[\boldsymbol{0}_{1\times 20} \;\; -\frac{3}{5} \;\; \boldsymbol{0}_{1\times 31} \;\; 1 \;\; \boldsymbol{0}_{1\times 11}\right]^T, \\
\boldsymbol{a}^5 &= \left[\boldsymbol{0}_{1\times 27} \;\; -\frac{3}{5} \;\; \boldsymbol{0}_{1\times 31} \;\; 1 \;\; \boldsymbol{0}_{1\times 4}\right]^T, & \boldsymbol{a}^{13} &= \left[\boldsymbol{0}_{1\times 19} \;\; -\frac{3}{5} \;\; \boldsymbol{0}_{1\times 31} \;\; 1 \;\; \boldsymbol{0}_{1\times 12}\right]^T, \\
\boldsymbol{a}^6 &= \left[\boldsymbol{0}_{1\times 26} \;\; -\frac{3}{5} \;\; \boldsymbol{0}_{1\times 31} \;\; 1 \;\; \boldsymbol{0}_{1\times 5}\right]^T, & \boldsymbol{a}^{14} &= \left[\boldsymbol{0}_{1\times 18} \;\; -\frac{3}{5} \;\; \boldsymbol{0}_{1\times 31} \;\; 1 \;\; \boldsymbol{0}_{1\times 13}\right]^T, \\
\boldsymbol{a}^7 &= \left[\boldsymbol{0}_{1\times 25} \;\; -\frac{3}{5} \;\; \boldsymbol{0}_{1\times 31} \;\; 1 \;\; \boldsymbol{0}_{1\times 6}\right]^T, & \boldsymbol{a}^{15} &= \left[\boldsymbol{0}_{1\times 17} \;\; -\frac{3}{5} \;\; \boldsymbol{0}_{1\times 31} \;\; 1 \;\; \boldsymbol{0}_{1\times 14}\right]^T, \\
\boldsymbol{a}^8 &= \left[\boldsymbol{0}_{1\times 24} \;\; -\frac{3}{5} \;\; \boldsymbol{0}_{1\times 31} \;\; 1 \;\; \boldsymbol{0}_{1\times 7}\right]^T, & \boldsymbol{a}^{16} &= \left[\boldsymbol{0}_{1\times 16} \;\; -\frac{3}{5} \;\; \boldsymbol{0}_{1\times 31} \;\; 1 \;\; \boldsymbol{0}_{1\times 15}\right]^T,
\end{aligned}$$

where $\mathbf{0}_{1\times n}$ is the zero vector of size $1 \times n$. Substituting the above null space vectors in the Eq. 7.22 the strain component $\bar{\varepsilon}^{\alpha}_{\tilde{\xi}\tilde{\xi}}$ is given by the following expression:

$$\bar{\varepsilon}^{\alpha}_{\tilde{\xi}\tilde{\xi}} = \tilde{\boldsymbol{G}}_1 \hat{\boldsymbol{\alpha}}_1,$$

where

$$\begin{aligned}\tilde{\boldsymbol{G}}_1 = \Big[\, & \tilde{\xi}\tilde{\eta}^3\tilde{\zeta}^3\Phi(\tilde{\xi}) \;\; \tilde{\xi}\tilde{\eta}\tilde{\zeta}^2\Phi(\tilde{\xi}) \;\; \tilde{\xi}\tilde{\eta}\tilde{\zeta}\Phi(\tilde{\xi}) \;\; \tilde{\xi}\tilde{\eta}\Phi(\tilde{\xi}) \;\; \tilde{\xi}\tilde{\zeta}^3\Phi(\tilde{\xi}) \;\; \tilde{\xi}\tilde{\zeta}^2\Phi(\tilde{\xi}) \;\; \tilde{\xi}\tilde{\zeta}\Phi(\tilde{\xi}) \;\; \tilde{\xi}\Phi(\tilde{\xi}) \\ & \tilde{\xi}\tilde{\eta}^3\tilde{\zeta}^2\Phi(\tilde{\xi}) \;\; \tilde{\xi}\tilde{\eta}^3\tilde{\zeta}\Phi(\tilde{\xi}) \;\; \tilde{\xi}\tilde{\eta}^3\Phi(\tilde{\xi}) \;\; \tilde{\xi}\tilde{\eta}^2\tilde{\zeta}^3\Phi(\tilde{\xi}) \;\; \tilde{\xi}\tilde{\eta}^2\tilde{\zeta}^2\Phi(\tilde{\xi}) \;\; \tilde{\xi}\tilde{\eta}^2\tilde{\zeta}\Phi(\tilde{\xi}) \;\; \tilde{\xi}\tilde{\eta}^2\Phi(\tilde{\xi}) \\ & \tilde{\xi}\tilde{\eta}\tilde{\zeta}^3\Phi(\tilde{\xi}) \,\Big] \\ \hat{\boldsymbol{\alpha}}_1 = & \begin{bmatrix}\hat{\alpha}_1 & \hat{\alpha}_2 & \dots & \hat{\alpha}_{16}\end{bmatrix}^T, \text{ and } \Phi(\xi) = (5\tilde{\xi}^2 - 3).\end{aligned}$$

A similar approach is adopted to evaluate the participating function space of the rest of $\tilde{\boldsymbol{G}}_i$ vectors. This results in the following $\tilde{\boldsymbol{G}}$ matrix for a 3D cubic EAS element:

$$\begin{Bmatrix} \bar{\varepsilon}^{\alpha}_{\tilde{\xi}\tilde{\xi}} \\ \bar{\varepsilon}^{\alpha}_{\tilde{\eta}\tilde{\eta}} \\ \bar{\varepsilon}^{\alpha}_{\tilde{\zeta}\tilde{\zeta}} \\ \bar{\varepsilon}^{\alpha}_{\tilde{\xi}\tilde{\eta}} \\ \bar{\varepsilon}^{\alpha}_{\tilde{\eta}\tilde{\zeta}} \\ \bar{\varepsilon}^{\alpha}_{\tilde{\xi}\tilde{\zeta}} \end{Bmatrix} = \tilde{\boldsymbol{G}}\hat{\boldsymbol{\alpha}} = \tilde{\boldsymbol{G}} \begin{Bmatrix} \hat{\boldsymbol{\alpha}}_1 \\ \hat{\boldsymbol{\alpha}}_2 \\ \hat{\boldsymbol{\alpha}}_3 \\ \hat{\boldsymbol{\alpha}}_4 \\ \hat{\boldsymbol{\alpha}}_5 \\ \hat{\boldsymbol{\alpha}}_6 \end{Bmatrix} = \begin{bmatrix} \tilde{\boldsymbol{G}}_1 & \mathbf{0}_{a^*} & \mathbf{0}_{a^*} & \mathbf{0}_{b^*} & \mathbf{0}_{b^*} & \mathbf{0}_{b^*} \\ \mathbf{0}_{a^*} & \tilde{\boldsymbol{G}}_2 & \mathbf{0}_{a^*} & \mathbf{0}_{b^*} & \mathbf{0}_{b^*} & \mathbf{0}_{b^*} \\ \mathbf{0}_{a^*} & \mathbf{0}_{a^*} & \tilde{\boldsymbol{G}}_3 & \mathbf{0}_{b^*} & \mathbf{0}_{b^*} & \mathbf{0}_{b^*} \\ \mathbf{0}_{a^*} & \mathbf{0}_{a^*} & \mathbf{0}_{a^*} & \tilde{\boldsymbol{G}}_4 & \mathbf{0}_{b^*} & \mathbf{0}_{b^*} \\ \mathbf{0}_{a^*} & \mathbf{0}_{a^*} & \mathbf{0}_{a^*} & \mathbf{0}_{b^*} & \tilde{\boldsymbol{G}}_5 & \mathbf{0}_{b^*} \\ \mathbf{0}_{a^*} & \mathbf{0}_{a^*} & \mathbf{0}_{a^*} & \mathbf{0}_{b^*} & \mathbf{0}_{b^*} & \tilde{\boldsymbol{G}}_6 \end{bmatrix} \begin{Bmatrix} \hat{\alpha}_1 \\ \hat{\alpha}_2 \\ \hat{\alpha}_3 \\ \hat{\alpha}_4 \\ \vdots \\ \hat{\alpha}_{132} \end{Bmatrix}, \tag{7.27}$$

where $\mathbf{0}_{a^*}$ and $\mathbf{0}_{b^*}$ denotes the zero vectors with dimensions 1×16 and 1×28, respectively. The vectors $\hat{\boldsymbol{\alpha}}_i$ are of size 16×1 for $i = 1$ to 3 and 28×1 for $i = 4$ to 6. The vectors $\tilde{\boldsymbol{G}}_1, \tilde{\boldsymbol{G}}_2, \dots, \tilde{\boldsymbol{G}}_6$ are derived as:

$$\begin{aligned}\tilde{\boldsymbol{G}}_1 = \Big[\, & \tilde{\xi}\tilde{\eta}^3\tilde{\zeta}^3\Phi(\tilde{\xi}) \;\; \tilde{\xi}\tilde{\eta}\tilde{\zeta}^2\Phi(\tilde{\xi}) \;\; \tilde{\xi}\tilde{\eta}\tilde{\zeta}\Phi(\tilde{\xi}) \;\; \tilde{\xi}\tilde{\eta}\Phi(\tilde{\xi}) \;\; \tilde{\xi}\tilde{\zeta}^3\Phi(\tilde{\xi}) \;\; \tilde{\xi}\tilde{\zeta}^2\Phi(\tilde{\xi}) \;\; \tilde{\xi}\tilde{\zeta}\Phi(\tilde{\xi}) \;\; \tilde{\xi}\Phi(\tilde{\xi}) \\ & \tilde{\xi}\tilde{\eta}^3\tilde{\zeta}^2\Phi(\tilde{\xi}) \;\; \tilde{\xi}\tilde{\eta}^3\tilde{\zeta}\Phi(\tilde{\xi}) \;\; \tilde{\xi}\tilde{\eta}^3\Phi(\tilde{\xi}) \;\; \tilde{\xi}\tilde{\eta}^2\tilde{\zeta}^3\Phi(\tilde{\xi}) \;\; \tilde{\xi}\tilde{\eta}^2\tilde{\zeta}^2\Phi(\tilde{\xi}) \;\; \tilde{\xi}\tilde{\eta}^2\tilde{\zeta}\Phi(\tilde{\xi}) \;\; \tilde{\xi}\tilde{\eta}^2\Phi(\tilde{\xi}) \\ & \tilde{\xi}\tilde{\eta}\tilde{\zeta}^3\Phi(\tilde{\xi}) \,\Big] \\ \tilde{\boldsymbol{G}}_2 = \Big[\, & \tilde{\xi}^3\tilde{\eta}\tilde{\zeta}^3\Phi(\tilde{\eta}) \;\; \tilde{\xi}\tilde{\eta}\tilde{\zeta}^2\Phi(\tilde{\eta}) \;\; \tilde{\xi}\tilde{\eta}\tilde{\zeta}\Phi(\tilde{\eta}) \;\; \tilde{\xi}\tilde{\eta}\Phi(\tilde{\eta}) \;\; \tilde{\eta}\tilde{\zeta}^3\Phi(\tilde{\eta}) \;\; \tilde{\eta}\tilde{\zeta}^2\Phi(\tilde{\eta}) \;\; \tilde{\eta}\tilde{\zeta}\Phi(\tilde{\eta}) \;\; \tilde{\eta}\Phi(\tilde{\eta}) \\ & \tilde{\xi}^3\tilde{\eta}\tilde{\zeta}^2\Phi(\tilde{\eta}) \;\; \tilde{\xi}^3\tilde{\eta}\tilde{\zeta}\Phi(\tilde{\eta}) \;\; \tilde{\xi}^3\tilde{\eta}\Phi(\tilde{\eta}) \;\; \tilde{\xi}^2\tilde{\eta}\tilde{\zeta}^3\Phi(\tilde{\eta}) \;\; \tilde{\xi}^2\tilde{\eta}\tilde{\zeta}^2\Phi(\tilde{\eta}) \;\; \tilde{\xi}^2\tilde{\eta}\tilde{\zeta}\Phi(\tilde{\eta}) \;\; \tilde{\xi}^2\tilde{\eta}\Phi(\tilde{\eta}) \\ & \tilde{\xi}\tilde{\eta}\tilde{\zeta}^3\Phi(\tilde{\eta}) \,\Big] \\ \tilde{\boldsymbol{G}}_3 = \Big[\, & \tilde{\xi}^3\tilde{\eta}^3\tilde{\zeta}\Phi(\tilde{\zeta}) \;\; \tilde{\xi}\tilde{\eta}^2\tilde{\zeta}\Phi(\tilde{\zeta}) \;\; \tilde{\xi}\tilde{\eta}\tilde{\zeta}\Phi(\tilde{\zeta}) \;\; \tilde{\xi}\tilde{\zeta}\Phi(\tilde{\zeta}) \;\; \tilde{\eta}^3\tilde{\zeta}\Phi(\tilde{\zeta}) \;\; \tilde{\eta}^2\tilde{\zeta}\Phi(\tilde{\zeta}) \;\; \tilde{\eta}\tilde{\zeta}\Phi(\tilde{\zeta}) \;\; \tilde{\zeta}\Phi(\tilde{\zeta}) \\ & \tilde{\xi}^3\tilde{\eta}^2\tilde{\zeta}\Phi(\tilde{\zeta}) \;\; \tilde{\xi}^3\tilde{\eta}\tilde{\zeta}\Phi(\tilde{\zeta}) \;\; \tilde{\xi}^3\tilde{\zeta}\Phi(\tilde{\zeta}) \;\; \tilde{\xi}^2\tilde{\eta}^3\tilde{\zeta}\Phi(\tilde{\zeta}) \;\; \tilde{\xi}^2\tilde{\eta}^2\tilde{\zeta}\Phi(\tilde{\zeta}) \;\; \tilde{\xi}^2\tilde{\eta}\tilde{\zeta}\Phi(\tilde{\zeta}) \;\; \tilde{\xi}^2\tilde{\zeta}\Phi(\tilde{\zeta}) \\ & \tilde{\xi}\tilde{\eta}^3\tilde{\zeta}\Phi(\tilde{\zeta}) \,\Big]\end{aligned}$$

$$
\begin{aligned}
\tilde{\boldsymbol{G}}_4 = \Big[\; & \tilde\xi\tilde\eta\tilde\zeta^3\Psi(\tilde\xi,\tilde\eta)\;\; \tilde\xi\tilde\eta\tilde\zeta^2\Phi(\tilde\xi)\;\; \tilde\xi\tilde\eta\tilde\zeta\Phi(\tilde\xi)\;\; \tilde\xi\tilde\eta\Phi(\tilde\xi)\;\; \tilde\xi\tilde\zeta^3\Phi(\tilde\xi)\;\; \tilde\xi\tilde\zeta^2\Phi(\tilde\xi)\;\; \tilde\xi\tilde\zeta\Phi(\tilde\xi)\;\; \tilde\xi\Phi(\tilde\xi) \\
& \tilde\xi^2\tilde\eta\tilde\zeta^3\Phi(\tilde\eta)\;\; \tilde\xi^2\tilde\eta\tilde\zeta^2\Phi(\tilde\eta)\;\; \tilde\xi^2\tilde\eta\tilde\zeta\Phi(\tilde\eta)\;\; \tilde\xi\tilde\eta\tilde\zeta^2\Psi(\tilde\xi,\tilde\eta)\;\; \tilde\xi^2\tilde\eta\Phi(\tilde\eta)\;\; \tilde\xi\tilde\eta\tilde\zeta^3\Phi(\tilde\eta)\;\; \tilde\xi\tilde\eta\tilde\zeta^2\Phi(\tilde\eta) \\
& \tilde\xi\tilde\eta\tilde\zeta\Phi(\tilde\eta)\;\; \tilde\xi\tilde\eta\Phi(\tilde\eta)\;\; \tilde\eta\tilde\zeta^3\Phi(\tilde\eta)\;\; \tilde\eta\tilde\zeta^2\Phi(\tilde\eta)\;\; \tilde\eta\tilde\zeta\Phi(\tilde\eta)\;\; \tilde\eta\Phi(\tilde\eta)\;\; \tilde\xi\tilde\eta\tilde\zeta\Psi(\tilde\xi,\tilde\eta)\;\; \tilde\xi\tilde\eta\Psi(\tilde\xi,\tilde\eta) \\
& \tilde\xi\tilde\eta^2\tilde\zeta^3\Phi(\tilde\xi)\;\; \tilde\xi\tilde\eta^2\tilde\zeta^2\Phi(\tilde\xi)\;\; \tilde\xi\tilde\eta^2\tilde\zeta\Phi(\tilde\xi)\;\; \tilde\xi\tilde\eta^2\Phi(\tilde\xi)\;\; \tilde\xi\tilde\eta\tilde\zeta^3\Phi(\tilde\xi)\;\Big] \\
\tilde{\boldsymbol{G}}_5 = \Big[\; & \tilde\xi^3\tilde\eta\tilde\zeta\Psi(\tilde\eta,\tilde\zeta)\;\; \tilde\xi^2\tilde\eta\tilde\zeta\Phi(\tilde\eta)\;\; \tilde\xi^2\tilde\eta\Phi(\tilde\eta)\;\; \tilde\xi^2\tilde\eta^2\tilde\zeta\Phi(\tilde\zeta)\;\; \tilde\xi^2\tilde\eta\tilde\zeta\Phi(\tilde\zeta)\;\; \tilde\xi^2\tilde\zeta\Phi(\tilde\zeta)\;\; \tilde\xi\tilde\eta\tilde\zeta\Psi(\tilde\eta,\tilde\zeta) \\
& \tilde\xi\tilde\eta\tilde\zeta^2\Phi(\tilde\eta)\;\; \tilde\xi\tilde\eta\tilde\zeta\Phi(\tilde\eta)\;\; \tilde\xi\tilde\eta\Phi(\tilde\eta)\;\; \tilde\xi\tilde\eta^2\tilde\zeta\Phi(\tilde\zeta)\;\; \tilde\xi^3\tilde\eta\tilde\zeta^2\Phi(\tilde\eta)\;\; \tilde\xi\tilde\eta\tilde\zeta\Phi(\tilde\zeta)\;\; \tilde\xi\tilde\zeta\Phi(\tilde\zeta)\;\; \tilde\eta\tilde\zeta\Psi(\tilde\eta,\tilde\zeta) \\
& \tilde\eta\tilde\zeta^2\Phi(\tilde\eta)\;\; \tilde\eta\tilde\zeta\Phi(\tilde\eta)\;\; \tilde\eta\Phi(\tilde\eta)\;\; \tilde\eta^2\tilde\zeta\Phi(\tilde\zeta)\;\; \tilde\eta\tilde\zeta\Phi(\tilde\zeta)\;\; \tilde\zeta\Phi(\tilde\zeta)\;\; \tilde\xi^3\tilde\eta\tilde\zeta\Phi(\tilde\eta)\;\; \tilde\xi^3\tilde\eta\Phi(\tilde\eta) \\
& \tilde\xi^3\tilde\eta^2\tilde\zeta\Phi(\tilde\zeta)\;\; \tilde\xi^3\tilde\eta\tilde\zeta\Phi(\tilde\zeta)\;\; \tilde\xi^3\tilde\zeta\Phi(\tilde\zeta)\;\; \tilde\xi^2\tilde\eta\tilde\zeta\Psi(\tilde\eta,\tilde\zeta)\;\; \tilde\xi^2\tilde\eta\tilde\zeta^2\Phi(\tilde\eta)\;\Big] \\
\tilde{\boldsymbol{G}}_6 = \Big[\; & \tilde\xi\tilde\eta^3\tilde\zeta\Psi(\tilde\xi,\tilde\zeta)\;\; \tilde\xi\tilde\eta\tilde\zeta^2\Phi(\tilde\xi)\;\; \tilde\xi\tilde\eta\tilde\zeta\Phi(\tilde\xi)\;\; \tilde\xi\tilde\eta\Phi(\tilde\xi)\;\; \tilde\xi\tilde\zeta\Psi(\tilde\xi,\tilde\zeta)\;\; \tilde\xi\tilde\zeta^2\Phi(\tilde\xi)\;\; \tilde\xi\tilde\zeta\Phi(\tilde\xi)\;\; \tilde\xi\Phi(\tilde\xi) \\
& \tilde\xi^2\tilde\eta^3\tilde\zeta\Phi(\tilde\zeta)\;\; \tilde\xi^2\tilde\eta^2\tilde\zeta\Phi(\tilde\zeta)\;\; \tilde\xi^2\tilde\eta\tilde\zeta\Phi(\tilde\zeta)\;\; \tilde\xi\tilde\eta^3\tilde\zeta^2\Phi(\tilde\xi)\;\; \tilde\xi^2\tilde\zeta\Phi(\tilde\zeta)\;\; \tilde\xi\tilde\eta^3\tilde\zeta\Phi(\tilde\zeta)\;\; \tilde\xi\tilde\eta^2\tilde\zeta\Phi(\tilde\zeta) \\
& \tilde\xi\tilde\eta\tilde\zeta\Phi(\tilde\zeta)\;\; \tilde\xi\tilde\zeta\Phi(\tilde\zeta)\;\; \tilde\eta^3\tilde\zeta\Phi(\tilde\zeta)\;\; \tilde\eta^2\tilde\zeta\Phi(\tilde\zeta)\;\; \tilde\eta\tilde\zeta\Phi(\tilde\zeta)\;\; \tilde\zeta\Phi(\tilde\zeta)\;\; \tilde\xi\tilde\eta^3\tilde\zeta\Phi(\tilde\xi)\;\; \tilde\xi\tilde\eta^3\Phi(\tilde\xi) \\
& \tilde\xi\tilde\eta^2\tilde\zeta\Psi(\tilde\xi,\tilde\zeta)\;\; \tilde\xi\tilde\eta^2\tilde\zeta^2\Phi(\tilde\xi)\;\; \tilde\xi\tilde\eta^2\tilde\zeta\Phi(\tilde\xi)\;\; \tilde\xi\tilde\eta^2\Phi(\tilde\xi)\;\; \tilde\xi\tilde\eta\tilde\zeta\Psi(\tilde\xi,\tilde\zeta)\;\Big]
\end{aligned}
$$

where $\Phi(x)$ and $\Psi(x,y)$ are given as $\Phi(x) = (5x^2 - 3)$ and $\Psi(x,y) = (25x^2y^2 - 9)$, respectively.

In addition, the proposed cubic EAS element satisfies the second condition required to achieve exact equivalence with HR-based elements in the case of a constant Jacobian. It can be validated by considering a space $\mathcal{V}_{\tilde{\phi}}$, which corresponds to a complete tri-cubic space in the master space for the given element. Under constant Jacobian, the following condition can be formulated:

$$\mathcal{V}_{\boldsymbol{\sigma}} \oplus \mathcal{V}_{\boldsymbol{\varepsilon}^{\alpha}} = \mathcal{V}_{\tilde{\phi}}. \tag{7.28}$$

Furthermore, since $\mathcal{V}_{\tilde{\phi}}$ is chosen as specified in Eq. 7.24 along with $\mathcal{V}_{\tilde{\phi}} \supseteq \mathcal{V}_{\boldsymbol{u}}$, it can be inferred that

$$\mathcal{V}_{\tilde{\phi}} \supseteq \mathcal{V}_{\boldsymbol{\sigma}^{u}}, \tag{7.29}$$

which implies the following relation:

$$\mathcal{V}_{\boldsymbol{\sigma}} \oplus \mathcal{V}_{\boldsymbol{\varepsilon}^{\alpha}} \supseteq \mathcal{V}_{\boldsymbol{\sigma}^{u}}. \tag{7.30}$$

Hence, satisfying the condition on the spaces mentioned in Eq. 7.13.

7.5 Strain interpolation matrix for 3D quadratic EAS element

The $\tilde{\boldsymbol{G}}$ matrix for a 3D quadratic EAS element, having 2nd degree NUBRS basis function along three parametric directions with C^1 continuous displacements across the element boundary, is given as follows:

$$\begin{Bmatrix} \bar{\varepsilon}^{\alpha}_{\tilde{\xi}\tilde{\xi}} \\ \bar{\varepsilon}^{\alpha}_{\tilde{\eta}\tilde{\eta}} \\ \bar{\varepsilon}^{\alpha}_{\tilde{\zeta}\tilde{\zeta}} \\ \bar{\varepsilon}^{\alpha}_{\tilde{\xi}\tilde{\eta}} \\ \bar{\varepsilon}^{\alpha}_{\tilde{\eta}\tilde{\zeta}} \\ \bar{\varepsilon}^{\alpha}_{\tilde{\xi}\tilde{\zeta}} \end{Bmatrix} = \tilde{\boldsymbol{G}}\hat{\boldsymbol{\alpha}} = \tilde{\boldsymbol{G}} \begin{Bmatrix} \hat{\boldsymbol{\alpha}}_1 \\ \hat{\boldsymbol{\alpha}}_2 \\ \hat{\boldsymbol{\alpha}}_3 \\ \hat{\boldsymbol{\alpha}}_4 \\ \hat{\boldsymbol{\alpha}}_5 \\ \hat{\boldsymbol{\alpha}}_6 \end{Bmatrix} = \begin{bmatrix} \tilde{\boldsymbol{G}}_1 & \mathbf{0}_{a^*} & \mathbf{0}_{a^*} & \mathbf{0}_{b^*} & \mathbf{0}_{b^*} & \mathbf{0}_{b^*} \\ \mathbf{0}_{a^*} & \tilde{\boldsymbol{G}}_2 & \mathbf{0}_{a^*} & \mathbf{0}_{b^*} & \mathbf{0}_{b^*} & \mathbf{0}_{b^*} \\ \mathbf{0}_{a^*} & \mathbf{0}_{a^*} & \tilde{\boldsymbol{G}}_3 & \mathbf{0}_{b^*} & \mathbf{0}_{b^*} & \mathbf{0}_{b^*} \\ \mathbf{0}_{a^*} & \mathbf{0}_{a^*} & \mathbf{0}_{a^*} & \tilde{\boldsymbol{G}}_4 & \mathbf{0}_{b^*} & \mathbf{0}_{b^*} \\ \mathbf{0}_{a^*} & \mathbf{0}_{a^*} & \mathbf{0}_{a^*} & \mathbf{0}_{b^*} & \tilde{\boldsymbol{G}}_5 & \mathbf{0}_{b^*} \\ \mathbf{0}_{a^*} & \mathbf{0}_{a^*} & \mathbf{0}_{a^*} & \mathbf{0}_{b^*} & \mathbf{0}_{b^*} & \tilde{\boldsymbol{G}}_6 \end{bmatrix} \begin{Bmatrix} \hat{\alpha}_1 \\ \hat{\alpha}_2 \\ \hat{\alpha}_3 \\ \hat{\alpha}_4 \\ \vdots \\ \hat{\alpha}_{72} \end{Bmatrix}, \tag{7.31}$$

where $\mathbf{0}_{a^*}$ and $\mathbf{0}_{b^*}$ denotes the zero vectors with dimensions 1×9 and 1×15, respectively. The vectors $\hat{\boldsymbol{\alpha}}_i$ are of size 9×1 for $i = 1$ to 3 and 15×1 for $i = 4$ to 6. The vectors $\tilde{\boldsymbol{G}}_1, \tilde{\boldsymbol{G}}_2, \ldots, \tilde{\boldsymbol{G}}_6$ are derived as:

$$\begin{aligned}
\tilde{\boldsymbol{G}}_1 &= \Big[\; \Phi(\tilde{\xi}) \;\; \tilde{\zeta}\Phi(\tilde{\xi}) \;\; \tilde{\zeta}^2\Phi(\tilde{\xi}) \;\; \tilde{\eta}\Phi(\tilde{\xi}) \;\; \tilde{\zeta}\tilde{\eta}\Phi(\tilde{\xi}) \;\; \tilde{\zeta}^2\tilde{\eta}\Phi(\tilde{\xi}) \;\; \tilde{\eta}^2\Phi(\tilde{\xi}) \;\; \tilde{\zeta}\tilde{\eta}^2\Phi(\tilde{\xi}) \;\; \tilde{\zeta}^2\tilde{\eta}^2\Phi(\tilde{\xi}) \;\Big], \\
\tilde{\boldsymbol{G}}_2 &= \Big[\; \Phi(\tilde{\eta}) \;\; \tilde{\zeta}\Phi(\tilde{\eta}) \;\; \tilde{\zeta}^2\Phi(\tilde{\eta}) \;\; \Phi(\tilde{\eta})\tilde{\xi} \;\; \tilde{\zeta}\Phi(\tilde{\eta})\tilde{\xi} \;\; \tilde{\zeta}^2\Phi(\tilde{\eta})\tilde{\xi} \;\; \Phi(\tilde{\eta})\tilde{\xi}^2 \;\; \tilde{\zeta}\Phi(\tilde{\eta})\tilde{\xi}^2 \;\; \tilde{\zeta}^2\Phi(\tilde{\eta})\tilde{\xi}^2 \;\Big], \\
\tilde{\boldsymbol{G}}_3 &= \Big[\; \Phi(\tilde{\zeta}) \;\; \Phi(\tilde{\zeta})\tilde{\eta} \;\; \Phi(\tilde{\zeta})\tilde{\eta}^2 \;\; \Phi(\tilde{\zeta})\tilde{\xi} \;\; \Phi(\tilde{\zeta})\tilde{\eta}\tilde{\xi} \;\; \Phi(\tilde{\zeta})\tilde{\eta}^2\tilde{\xi} \;\; \Phi(\tilde{\zeta})\tilde{\xi}^2 \;\; \Phi(\tilde{\zeta})\tilde{\eta}\tilde{\xi}^2 \;\; \Phi(\tilde{\zeta})\tilde{\eta}^2\tilde{\xi}^2 \;\Big], \\
\tilde{\boldsymbol{G}}_4 &= \Big[\; \Phi(\tilde{\eta}) \;\; \tilde{\zeta}\Phi(\tilde{\eta}) \;\; \tilde{\zeta}^2\Phi(\tilde{\eta}) \;\; \Phi(\tilde{\eta})\tilde{\xi} \;\; \tilde{\zeta}\Phi(\tilde{\eta})\tilde{\xi} \;\; \tilde{\zeta}^2\Phi(\tilde{\eta})\tilde{\xi} \;\; \Phi(\tilde{\xi}) \;\; \tilde{\zeta}\Phi(\tilde{\xi}) \;\; \tilde{\zeta}^2\Phi(\tilde{\xi}) \;\; \tilde{\eta}\Phi(\tilde{\xi}) \\
&\qquad \tilde{\zeta}\tilde{\eta}\Phi(\tilde{\xi}) \;\; \tilde{\zeta}^2\tilde{\eta}\Phi(\tilde{\xi}) \;\; \Psi(\tilde{\xi},\tilde{\eta}) \;\; \tilde{\zeta}\Psi(\tilde{\xi},\tilde{\eta}) \;\; \tilde{\zeta}^2\Psi(\tilde{\xi},\tilde{\eta}) \;\Big], \\
\tilde{\boldsymbol{G}}_5 &= \Big[\; \Phi(\tilde{\zeta}) \;\; \Phi(\tilde{\zeta})\tilde{\eta} \;\; \Phi(\tilde{\eta}) \;\; \tilde{\zeta}\Phi(\tilde{\eta}) \;\; \Psi(\tilde{\eta},\tilde{\zeta}) \;\; \Phi(\tilde{\zeta})\tilde{\xi} \;\; \Phi(\tilde{\zeta})\tilde{\eta}\tilde{\xi} \;\; \Phi(\tilde{\eta})\tilde{\xi} \;\; \tilde{\zeta}\Phi(\tilde{\eta})\tilde{\xi} \;\; \Psi(\tilde{\eta},\tilde{\zeta})\tilde{\xi} \\
&\qquad \Phi(\tilde{\zeta})\tilde{\xi}^2 \;\; \Phi(\tilde{\zeta})\tilde{\eta}\tilde{\xi}^2 \;\; \Phi(\tilde{\eta})\tilde{\xi}^2 \;\; \tilde{\zeta}\Phi(\tilde{\eta})\tilde{\xi}^2 \;\; \Psi(\tilde{\eta},\tilde{\zeta})\tilde{\xi}^2 \;\Big], \\
\tilde{\boldsymbol{G}}_6 &= \Big[\; \Phi(\tilde{\zeta}) \;\; \Phi(\tilde{\zeta})\tilde{\eta} \;\; \Phi(\tilde{\zeta})\tilde{\eta}^2 \;\; \Phi(\tilde{\zeta})\tilde{\xi} \;\; \Phi(\tilde{\zeta})\tilde{\eta}\tilde{\xi} \;\; \Phi(\tilde{\zeta})\tilde{\eta}^2\tilde{\xi} \;\; \Phi(\tilde{\xi}) \;\; \tilde{\zeta}\Phi(\tilde{\xi}) \;\; \Psi(\tilde{\xi},\tilde{\zeta}) \;\; \tilde{\eta}\Phi(\tilde{\xi}) \\
&\qquad \tilde{\zeta}\tilde{\eta}\Phi(\tilde{\xi}) \;\; \tilde{\eta}\Psi(\tilde{\xi},\tilde{\zeta}) \;\; \tilde{\eta}^2\Phi(\tilde{\xi}) \;\; \tilde{\zeta}\tilde{\eta}^2\Phi(\tilde{\xi}) \;\; \tilde{\eta}^2\Psi(\tilde{\xi},\tilde{\zeta}) \;\Big],
\end{aligned}$$

where $\Phi(x)$ and $\Psi(x,y)$ are given as $\Phi(x) = (1 - 3x^2)$ and $\Psi(x,y) = (9x^2y^2 - 1)$, respectively.

7.6 Strain interpolation matrix for proposed 2D NURBS-based EAS element

A similar approach is employed to assess the strain interpolation functions for the proposed 2D EAS elements. Analogous to the 3D elements, the term “cubic or quadratic element” in this context denotes the utilization of cubic or quadratic interpolation functions in both parametric directions with the highest possible continuity. The resultant feasible interpolations in $\tilde{\boldsymbol{G}}$ matrix for the these elements are presented in subsequent section.

7.6.1 2D cubic EAS element

The $\tilde{\boldsymbol{G}}$ matrix for 2D cubic EAS element, featuring third-degree NURBS interpolation in both ξ and η directions with C^2 inter-element continuity for approximating displacements, is given as follows:

$$\begin{Bmatrix} \bar{\varepsilon}^{\alpha}_{\tilde{\xi}\tilde{\xi}} \\ \bar{\varepsilon}^{\alpha}_{\tilde{\eta}\tilde{\eta}} \\ \bar{\varepsilon}^{\alpha}_{\tilde{\xi}\tilde{\eta}} \end{Bmatrix} = \tilde{\boldsymbol{G}}\hat{\boldsymbol{\alpha}} = \tilde{\boldsymbol{G}} \begin{Bmatrix} \hat{\boldsymbol{\alpha}}_1 \\ \hat{\boldsymbol{\alpha}}_2 \\ \hat{\boldsymbol{\alpha}}_3 \end{Bmatrix} = \begin{bmatrix} \tilde{\boldsymbol{G}}_1 & \mathbf{0}_{a^*} & \mathbf{0}_{b^*} \\ \mathbf{0}_{a^*} & \tilde{\boldsymbol{G}}_2 & \mathbf{0}_{b^*} \\ \mathbf{0}_{a^*} & \mathbf{0}_{a^*} & \tilde{\boldsymbol{G}}_3 \end{bmatrix} \begin{Bmatrix} \hat{\alpha}_1 \\ \hat{\alpha}_2 \\ \vdots \\ \hat{\alpha}_{15} \end{Bmatrix}, \tag{7.32}$$

where $\mathbf{0}_{a^*}$ and $\mathbf{0}_{b^*}$ denotes the zero vectors with dimensions 1×4 and 1×7, respectively. The vectors $\hat{\boldsymbol{\alpha}}_i$ are of size 4×1 for $i = 1$ to 2 and 7×1 for $i = 3$. The vectors $\tilde{\boldsymbol{G}}_1$, $\tilde{\boldsymbol{G}}_2$, and $\tilde{\boldsymbol{G}}_6$ are derived as:

$$\begin{aligned} \tilde{\boldsymbol{G}}_1 &= \begin{bmatrix} \tilde{\xi}\tilde{\eta}^2\Phi(\tilde{\xi}) & \tilde{\xi}\tilde{\eta}\Phi(\tilde{\xi}) & \tilde{\xi}\tilde{\eta}^3\Psi(\tilde{\xi}) & \tilde{\xi}\Phi(\tilde{\xi}) \end{bmatrix}, \\ \tilde{\boldsymbol{G}}_2 &= \begin{bmatrix} \tilde{\xi}^3\tilde{\eta}\Psi(\tilde{\eta}) & \tilde{\xi}^2\tilde{\eta}\Phi(\tilde{\eta}) & \tilde{\xi}\tilde{\eta}\Phi(\tilde{\eta}) & \tilde{\eta}\Phi(\tilde{\eta}) \end{bmatrix}, \\ \tilde{\boldsymbol{G}}_3 &= \begin{bmatrix} \tilde{\xi}\tilde{\eta}^2\Phi(\tilde{\xi}) & \tilde{\xi}\tilde{\eta}\Phi(\tilde{\xi}) & \tilde{\xi}^2\tilde{\eta}\Phi(\tilde{\eta}) & \tilde{\xi}\tilde{\eta}\Phi(\tilde{\eta}) & \tilde{\xi}\tilde{\eta}F(\tilde{\xi},\tilde{\eta}) & \tilde{\eta}\Phi(\tilde{\eta}) & \tilde{\xi}\Phi(\tilde{\xi}) \end{bmatrix}, \end{aligned}$$

where $\Phi(x)$, $\Psi(x)$, and $F(x,y)$ are given as $\Phi(x) = (3 - 5x^2)$, $\Psi(x) = (-3 + 5x^2)$, and $F(x,y) = (9 - 25x^2y^2)$, respectively.

7.6.2 2D quadratic EAS element

The $\tilde{\boldsymbol{G}}$ matrix for 2D quadratic EAS element, having second-degree NURBS interpolation in both ξ and η directions with C^1 inter-element continuity for approximating displacements, is given as follows:

$$\tilde{\boldsymbol{G}} = \begin{bmatrix} f(\tilde{\xi}) & \tilde{\eta}f(\tilde{\xi}) & f(\tilde{\xi})f(\tilde{\eta}) & 0 & 0 & 0 & 0 & 0 & 0 & 0 & 0 \\ 0 & 0 & 0 & f(\tilde{\eta}) & \tilde{\xi}f(\tilde{\eta}) & f(\tilde{\xi})f(\tilde{\eta}) & 0 & 0 & 0 & 0 & 0 \\ 0 & 0 & 0 & 0 & 0 & 0 & f(\tilde{\xi}) & \tilde{\eta}f(\tilde{\xi}) & f(\tilde{\eta}) & \tilde{\xi}f(\tilde{\eta}) & f(\tilde{\xi})f(\tilde{\eta}) \end{bmatrix},$$

where $f(x) = 3x^2 - 1$. The above expression is identical to the existing nine-node EAS element in the context of Lagrangian-based FEA [168]. However, the mathematical foundation and its successful implementation in the context of IGA are still unique to the present study.

7.7 Numerical examples

The present section demonstrates the performance of the proposed EAS elements for NURBS-based IGA. The coarse mesh accuracy, efficacy, and robustness of the method are shown using several benchmark numerical examples. The process commences by

Table 7.1: List of elements abbreviation used in the present study.

Element abbreviation	Description
$\text{IgA}^{2D}_{\text{Quad}}$	Conventional 2D NURBS-based quadratic element
$\text{IgA}^{2D}_{\text{Cub}}$	Conventional 2D NURBS-based cubic element
$\text{h-IgA}^{2D}_{\text{Quad}}$	Proposed stress-based hybrid 2D quadratic element for NURBS-based IGA (Refer Chapter 6 or [152])
$\text{h-IgA}^{2D}_{\text{Cub}}$	Proposed stress-based hybrid 2D cubic element for NURBS-based IGA (Refer Chapter 6 or [152])
$\alpha\text{-IgA}^{2D}_{\text{Quad}}$	Proposed strain-based EAS 2D quadratic element for NURBS-based IGA
$\alpha\text{-IgA}^{2D}_{\text{Cub}}$	Proposed strain-based EAS 2D cubic element for NURBS-based IGA
$\alpha\text{4S-IgA}^{2D}_{\text{Quad}}$	EAS 2D quadratic element for NURBS-based IGA with four enhanced strain parameters paired with stabilization technique [135]
$\alpha\text{6S-IgA}^{2D}_{\text{Quad}}$	EAS 2D quadratic element for NURBS-based IGA with six enhanced strain parameters paired with stabilization technique [135]
$\alpha\text{4-IgA}^{2D}_{\text{Quad}}$	EAS 2D quadratic element for NURBS-based IGA with four enhanced strain parameters [135]
$\alpha\text{6-IgA}^{2D}_{\text{Quad}}$	EAS 2D quadratic element for NURBS-based IGA with six enhanced strain parameters [135]
$\text{IgA}^{3D}_{\text{Quad}}$	Conventional 3D NURBS-based quadratic element
$\text{IgA}^{3D}_{\text{Cub}}$	Conventional 3D NURBS-based cubic element
$\text{h-IgA}^{3D}_{\text{Quad}}$	Proposed stress-based hybrid 3D quadratic element for NURBS-based IGA (Refer Chapter 6 or [143])
$\text{h-IgA}^{3D}_{\text{Cub}}$	Proposed stress-based hybrid 3D cubic element for NURBS-based IGA (Refer Chapter 6 or [143])
$\alpha\text{-IgA}^{3D}_{\text{Quad}}$	Proposed strain-based EAS 3D quadratic element for NURBS-based IGA
$\alpha\text{-IgA}^{3D}_{\text{Cub}}$	Proposed strain-based EAS 3D cubic element for NURBS-based IGA

assessing the proposed 2D quadratic and cubic EAS elements, with initial two scenarios, where the problem is under the effect of volumetric locking. These problems include a curved cantilever beam subjected to end shear load and the standard Cook's membrane problem with varying values of Poisson's ratio. The proposed elements are also tested against the existing 2D quadratic EAS elements that are known for alleviating volumetric locking in IGA. Subsequently, we analyze the clamped-clamped curved beam problem, evaluating the element's performance under the shear locking.

Later, we redirect our attention towards the proposed 3D quadratic and cubic EAS elements. These elements are assessed by analyzing the behavior of different types of beams under the influence of coupled shear-membrane locking. These problems involve the 3D twisted beam and curved cantilever beam problem. Next, we present the well-established shell obstacle course problems to validate the efficacy of the proposed

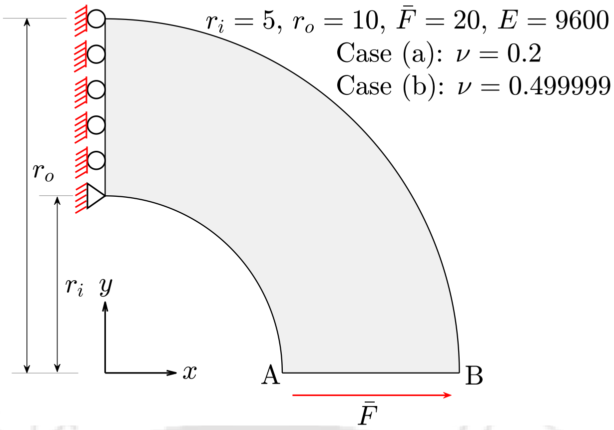

Figure 7.1: The problem setup, boundary conditions, and material parameters for the curved cantilever beam problem

formulations against the conventional formulation. The problems include the pinched cylinder, pinched hemisphere, and Scordelis–Lo roof problem. Finally, a problem dominated by volumetric locking is solved to establish the robustness of the method.

Subsequently, we shift the focus to time-dependent problems, where the advantages offered by the proposed elements become more apparent. The impact of locking is more pronounced with conventional elements, whereas the proposed elements exhibit distinctive advantages in performance. The problems include a clamped circular plate under ring pressure load and a clamped skew plate subjected to uniform pressure load. The consistent system of units (SI/FPS) is assumed for all parameters used in numerical simulations. Abbreviations that frequently appear in the subsequent problems are defined in Table 7.1.

7.7.1 Curved cantilever beam subjected to end shear

In the present example, the linear elastic behavior of a 2D curved cantilever beam under plane strain condition is investigated. The problem is composed of a curved beam subjected to horizontal load on one end and fixed on the other end. The problem configuration, boundary conditions, and material parameters are shown in Fig. 7.1, where r_i and r_o are the inner and outer radii measured from the origin, $\bar{F}$ is the load per unit length, E is the Young's modulus, and ν is the Poisson's ratio. The problem is solved for two values of ν to assess the performance of the proposed EAS elements alongside conventional, existing EAS [135], hybrid IGA elements for volumetric locking.

Refinement is achieved through h- or k- refinement techniques, with meshes defined as $n^r_{\text{ele}} \times n^\theta_{\text{ele}}$, where n^r_{ele} and n^θ_{ele} represent the number of elements in the radial and circumferential directions, respectively. Refinement is conducted with $n^r_{\text{ele}} = n^\theta_{\text{ele}} = 2, 4, 8, 16, \ldots, 128$ for both the cases. The reference solution (u_x^{ref}) at the tip (point 'B') is determined using the results of a refined mesh consisting of 256×256 h-IgA$^{\text{2D}}_{\text{Cub}}$ elements, yielding values of 0.3558 and 0.2720 for $\nu = 0.2$ and $\nu = 0.499999$, respectively.

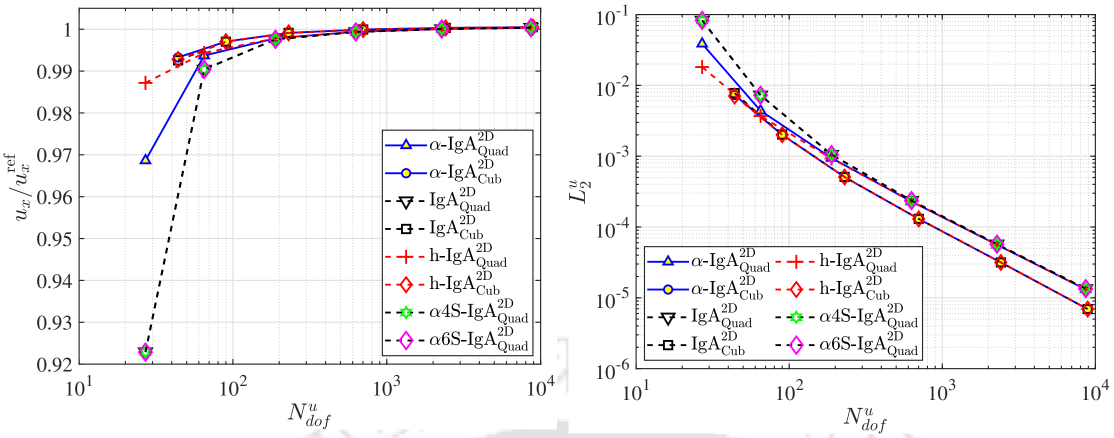

(a) u_x/u_x^{ref} for $\nu = 0.2$

(b) L_2^u for $\nu = 0.2$

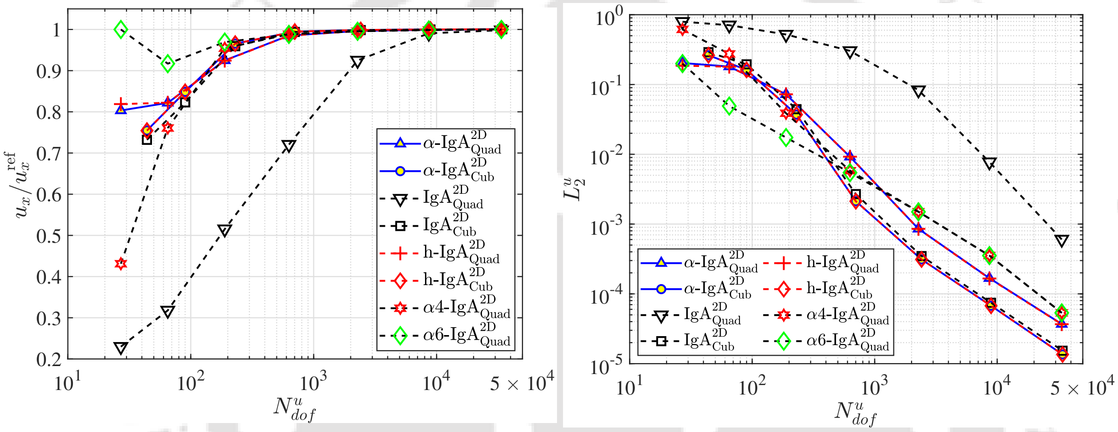

(c) u_x/u_x^{ref} for $\nu = 0.499999$

(d) L_2^u for $\nu = 0.499999$

Figure 7.2: Investigation of normalized displacement and L_2 error norm of displacement for two different values of Poisson's ratio in curved cantilever beam subjected to end shear.

The plots for normalized displacement along x-direction at point 'B' and the relative L_2 error norm of displacement against number of free degrees of freedom (N^u_{dof}) are shown in Fig. 7.2. In the first case, when $\nu = 0.2$, the domain is not affected by volumetric locking. Here, all elements converge to the solution with a fairly low number of elements. However, upon comparing the proposed EAS elements with existing ones, it becomes apparent that the α4S-IgA$^{2D}_{\mathrm{Quad}}$ or α6S-IgA$^{2D}_{\mathrm{Quad}}$ EAS elements require stabilization techniques to handle non-locking situations. In contrast, the proposed α-IgA$^{2D}_{\mathrm{Quad}}$ or α-IgA$^{2D}_{\mathrm{Cub}}$ converges to the solution regardless of the problem description.

For the second case, when ν is 0.499999, conventional IgA$^{2D}_{\mathrm{Quad}}$ elements exhibit locking and require significant refinement to converge to the solution. In contrast, the proposed α-IgA$^{2D}_{\mathrm{Quad}}$ elements successfully alleviate locking and show high coarse mesh accuracy. For instance, a mesh of 16 × 16 α-IgA$^{2D}_{\mathrm{Quad}}$ elements ($N^u_{dof} = 629$) provides a close approximation with the reference value with L_2^u error of 0.9208%. However, to achieve a comparable accuracy of 0.7321% with the conventional IgA$^{2D}_{\mathrm{Quad}}$ elements, it

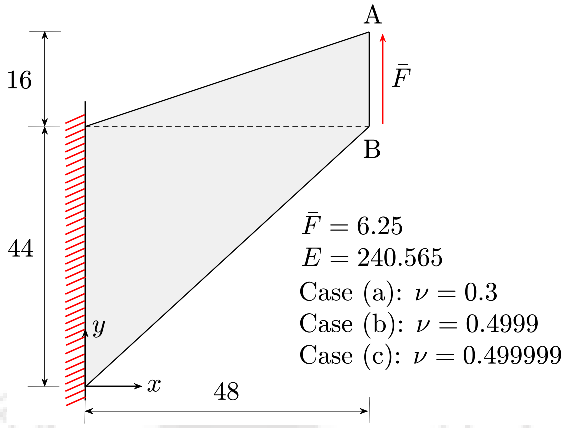

Figure 7.3: The problem setup, boundary conditions, and material parameters for the Cook's membrane problem

requires a mesh of 128 × 128 elements ($N^u_{dof} = 33669$). Higher-order IgA$^{2D}_{\text{Cub}}$ elements, in this case, are less affected by locking, and the proposed α-IgA$^{2D}_{\text{Cub}}$ shows marginal improvement over IgA$^{2D}_{\text{Cub}}$.

Furthermore, for both cases, the results show close similarity between the displacement fields obtained from h-IgA and α-IgA elements. It is important to note that the h-IgA elements are derived from the formulation outlined in Chapter 6, see reference [143, 152], where the transformation matrix is computed at each Gauss point. The small disparity between h-IgA and α-IgA elements can be entirely eliminated by adopting the similar strategy for computing the transformation matrix in α-IgA elements.

7.7.2 Cook's membrane problem

In the next example, the linear elastic behavior of a Cook's membrane problem is investigated. The problem is composed of a tapered plate subjected to vertical load on one end and fixed on the other end. The problem configuration, boundary conditions, and material parameters are shown in Fig. 7.3, where $\bar{F}$ is the load per unit length, E is Young's modulus, and ν is the Poisson's ratio. The problem is solved for three different values of ν to assess the proposed elements. Assuming a plane strain condition and taking ν close to 0.5, the problem becomes a typical case of volumetric locking while analyzing the near-incompressible behavior of the domain under combined bending and shear deformation.

The reference solution (u_y^{ref}) at the tip (point 'A') is 9.5776, 8.0405, and 8.0091 for $\nu = 0.3$, 0.4999, and 0.499999, respectively [188]. Refinement is achieved through h- or k- refinement techniques, with meshes defined as $n^x_{\text{ele}} \times n^y_{\text{ele}}$, where n^x_{ele} and n^y_{ele} represent the number of elements in the x- and y- directions, respectively. Refinement is conducted with $n^x_{\text{ele}} = n^y_{\text{ele}} = 2, 4, 8, 16, 32, 64, 128$ for all three cases. A solution of highly refined mesh, comprising of 256 × 256 well-established h-IgA$^{2D}_{\text{Cub}}$ elements, is taken as a reference to evaluate the L_2 norm.

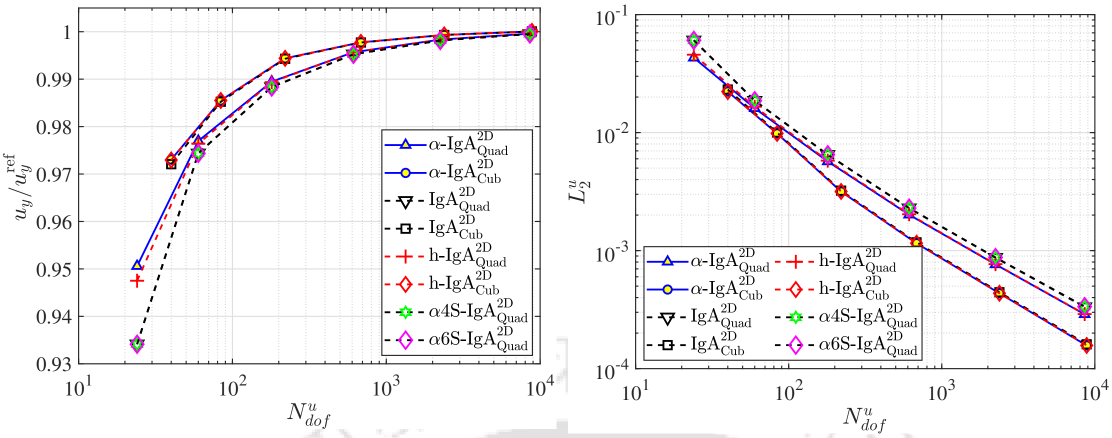

(a) u_y/u_y^{ref} for $\nu = 0.3$ **(b)** L^u_2 for $\nu = 0.3$

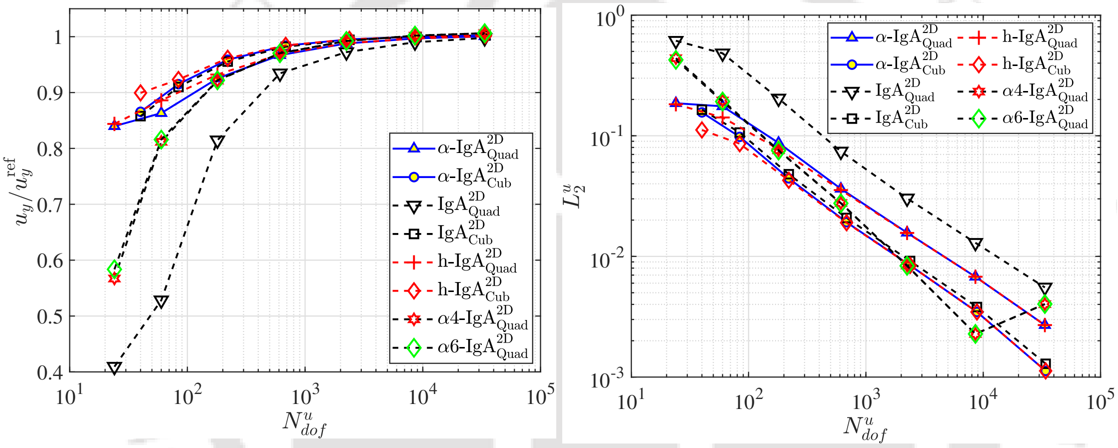

(c) u_y/u_y^{ref} for $\nu = 0.4999$ **(d)** L^u_2 for $\nu = 0.4999$

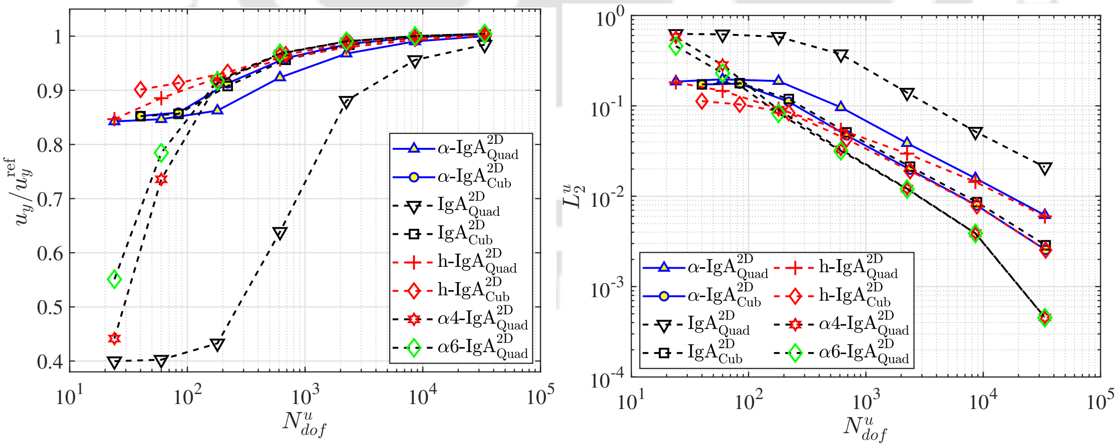

(e) u_y/u_y^{ref} for $\nu = 0.499999$ **(f)** L^u_2 for $\nu = 0.499999$

Figure 7.4: Investigation of normalized displacement and L_2 error norm of displacement for three different values of Poisson's ratio in Cook's membrane problem.

The plots for normalized displacement along y-direction at point 'A' and the relative L_2 error norm of displacement against N^u_{dof} are shown in Fig. 7.4. In the case of $\nu = 0.3$, where the domain is not affected by volumetric locking, all elements converge to the

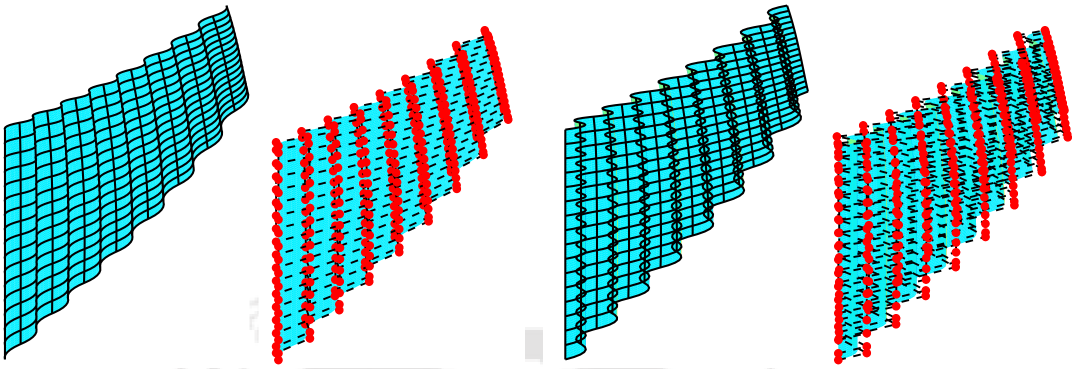

(a) Mesh: 16 × 16 elements ($\nu = 0.4999$) **(b)** Mesh: 16 × 16 elements ($\nu = 0.499999$)

Figure 7.5: Analysis of the deformed configuration of the Cook's membrane problem obtained using existing α6-IgA$^{2D}_{\text{Quad}}$ EAS elements in nearly-incompressible range. Each sub-figure shows the discretized deformed domain along with a control point mesh, where the red points represent control points.

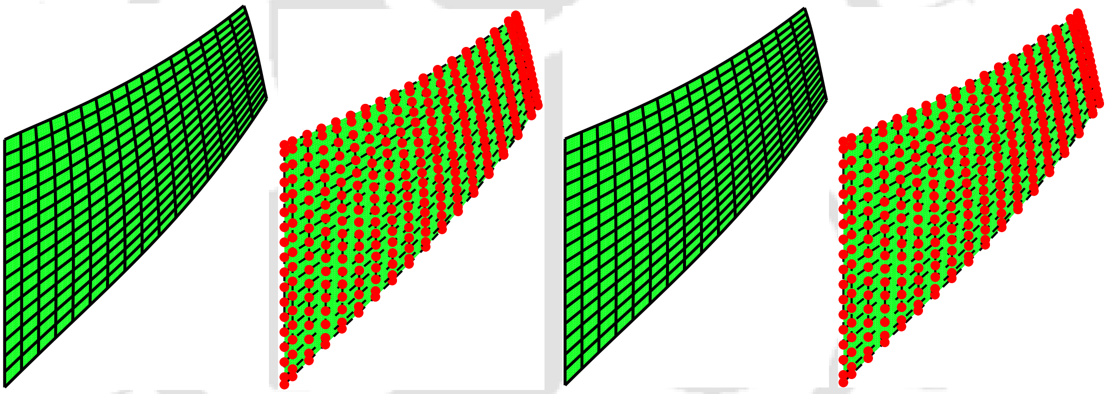

(a) α-IgA$^{2D}_{\text{Quad}}$ elements ($\nu = 0.4999$) **(b)** α-IgA$^{2D}_{\text{Quad}}$ elements ($\nu = 0.499999$)

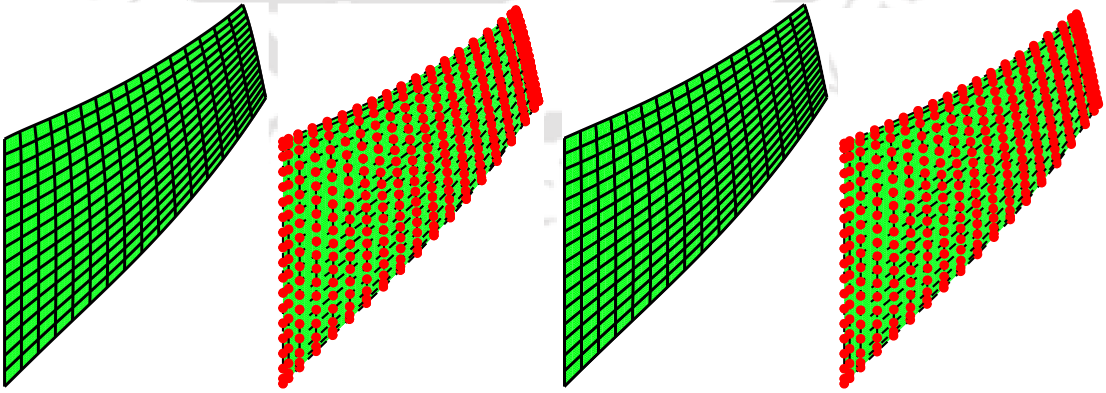

(c) α-IgA$^{2D}_{\text{Cub}}$ elements ($\nu = 0.4999$) **(d)** α-IgA$^{2D}_{\text{Cub}}$ elements ($\nu = 0.499999$)

Figure 7.6: Analysis of the deformed configuration of the Cook's membrane problem obtained using a mesh of 16 × 16 proposed α-IgA$^{2D}_{\text{Quad}}$ and α-IgA$^{2D}_{\text{Cub}}$ EAS elements in nearly-incompressible range. Each sub-figure shows the discretized deformed domain along with a control point mesh, where the red points represent control points.

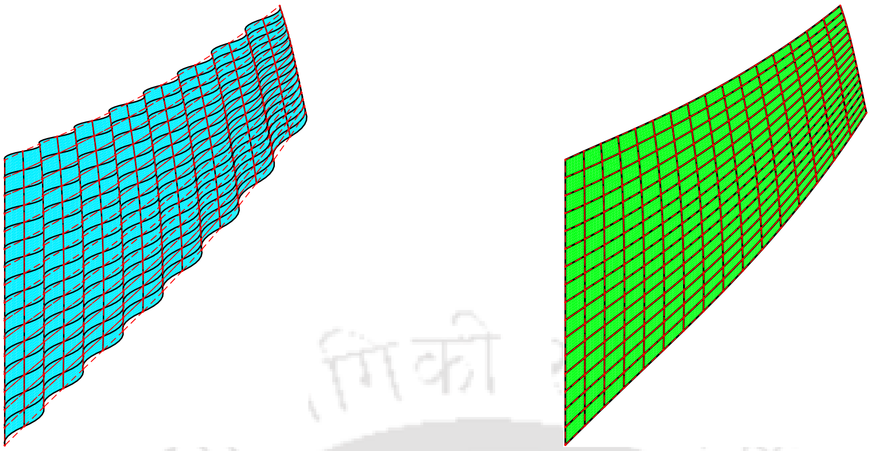

(a) Existing α6-IgA$^{2D}_{\text{Quad}}$ elements **(b)** Proposed α-IgA$^{2D}_{\text{Quad}}$ elements

Figure 7.7: Discretized deformed problem domain along with the equivalent four-node mesh created for post-processing in IGA for a Cook's membrane problem with 16 × 16 quadratic EAS elements and $\nu = 0.4999$.

solution with a relatively low number of elements. However, similar to previous example, existing α4S-IgA$^{2D}_{\text{Quad}}$ or α6S-IgA$^{2D}_{\text{Quad}}$ EAS elements require stabilization techniques to handle non-locking situations, whereas the proposed α-IgA$^{2D}_{\text{Quad}}$ or α-IgA$^{2D}_{\text{Cub}}$ converges to the solution regardless of the problem description.

For the next two cases, as ν approaches 0.5, the impact of volumetric locking becomes more pronounced. In particular, the conventional IgA$^{2D}_{\text{Quad}}$ elements exhibit significant locking with increasing ν and demand substantial refinement to converge to the solution. In contrast, the proposed α-IgA$^{2D}_{\text{Quad}}$ elements successfully alleviate locking and show consistently better coarse mesh accuracy irrespective of the ν values. Higher-order IgA$^{2D}_{\text{Cub}}$ elements are less affected by locking and perform similar to α-IgA$^{2D}_{\text{Cub}}$ elements. Moreover, the proposed α-IgA$^{2D}_{\text{Quad}}$ and α-IgA$^{2D}_{\text{Cub}}$ consistently outperform the existing α4-IgA$^{2D}_{\text{Quad}}$ and α6-IgA$^{2D}_{\text{Quad}}$ elements.

Further, while examining the normalized displacements (Figs. 7.4c and 7.4e) or L_2 error norm of displacement (Figs. 7.4d and 7.4f), the existing α6-IgA$^{2D}_{\text{Quad}}$ EAS elements appear to be a viable option for simulation. However, upon closer examination of the deformed configuration of the problem (Fig. 7.5), it becomes evident that these elements still exhibit hourglass modes, whereas the proposed EAS elements exhibit no such anomaly, see Fig. 7.6. Identifying this issue during the evaluation of the L_2 error norm of displacement might be easily overlooked in post-processing in IGA. This is because, in typical IGA post-processing practices, the mesh is converted to four-node element structures corresponding to unique knot entries. However, in this situation, this approach is non-reliant as the most significant errors occur between two unique knot entries rather than at the extremities, see Fig. 7.7.

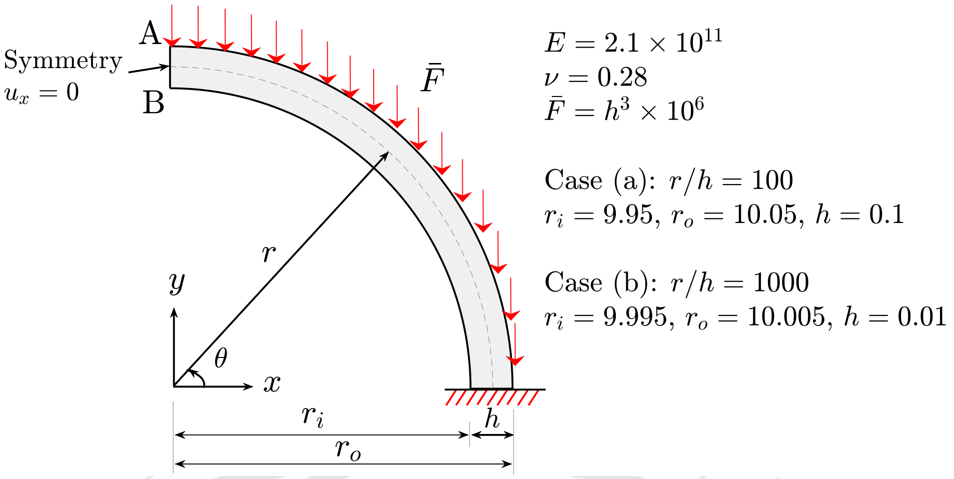

Figure 7.8: The problem setup, boundary conditions, and material parameters for the clamped-clamped semi-circular beam clamped under a uniform distributed load.

7.7.3 Clamped-clamped semi-circular beam

The problem consists of a clamped-clamped semi-circular beam fixed at both ends and subjected to a uniform distributed load on the top edge. Since the problem exhibits symmetry, only half of the beam is analyzed. The detailed problem configuration, boundary conditions, and material parameters are shown in Fig. 7.8, where r_i and r_o are the inner and outer radii measured from the origin, r is the mean radius, h is the thickness, $\bar{F}$ is the load per unit length, E is Young's modulus and ν is the Poisson's ratio. The problem is solved for two different values of slenderness ratio (r/h) to assess the elements in gradually increasing shear locking effect.

The problem is solved using the plane stress condition with width considered as 0.1. The reference solution (u_y^{ref}) at the tip (point 'A') is 3.6×10^{-2} for both the r/h ratios [189]. Refinement is achieved through h- or k- refinement techniques, with meshes defined as $n_{\text{ele}}^{r} \times n_{\text{ele}}^{\theta}$, where n_{ele}^{r} and n_{ele}^{θ} represent the number of elements in the radial and circumferential directions, respectively. Refinement is carried out using $n_{\text{ele}}^{\theta} = 2, 4, 8, 16, 32, 64, 128$ while keeping $n_{\text{ele}}^{r} = 1$ for both the cases. A solution of highly refined mesh, comprising of 1×256 well-established h-IgA$^{\text{2D}}_{\text{Cub}}$ elements, is taken as a reference to evaluate the L_2 error norm.

The problem is solved for normalized displacement at point 'A' and L_2 error in displacement and stress. The corresponding results are shown in Fig. 7.9. The effect of shear locking becomes more pronounced with increasing slenderness ratios, particularly for the IgA$^{\text{2D}}_{\text{Quad}}$ elements. For instance, the proposed α-IgA$^{\text{2D}}_{\text{Quad}}$ elements converge to the solution with L_2^u of 1.707% ($r/h = 100$, Mesh: 16×1, $N_{dof}^u = 99$) and 2.167% ($r/h = 1000$, Mesh: 32×1, $N_{dof}^u = 195$), whereas conventional IgA$^{\text{2D}}_{\text{Quad}}$ elements requires double the number of elements to achieve a comparable accuracy of 1.444% ($r/h = 100$, Mesh: 32×1, $N_{dof}^u = 195$) and 7.052% ($r/h = 1000$, Mesh: 64×1, $N_{dof}^u = 387$). The difference in L_2^σ is more pronounced when comparing conventional and EAS elements,

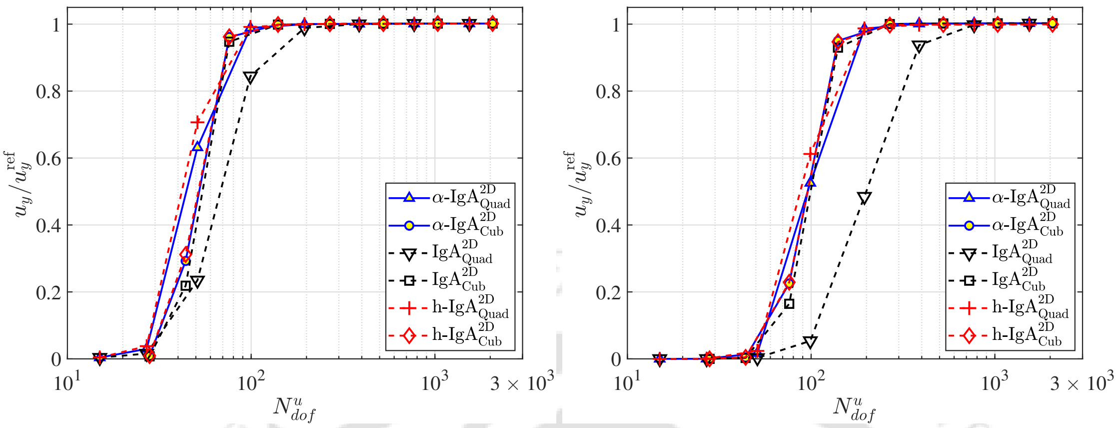

(a) u_y/u_y^{ref} for $r/h = 100$ **(b)** u_y/u_y^{ref} for $r/h = 1000$

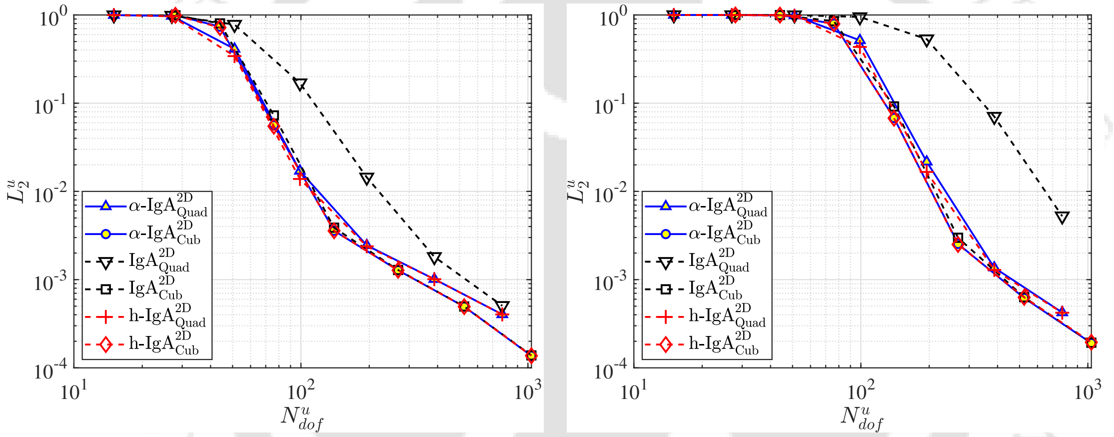

(c) L_2^u for $r/h = 100$ **(d)** L_2^u for $r/h = 1000$

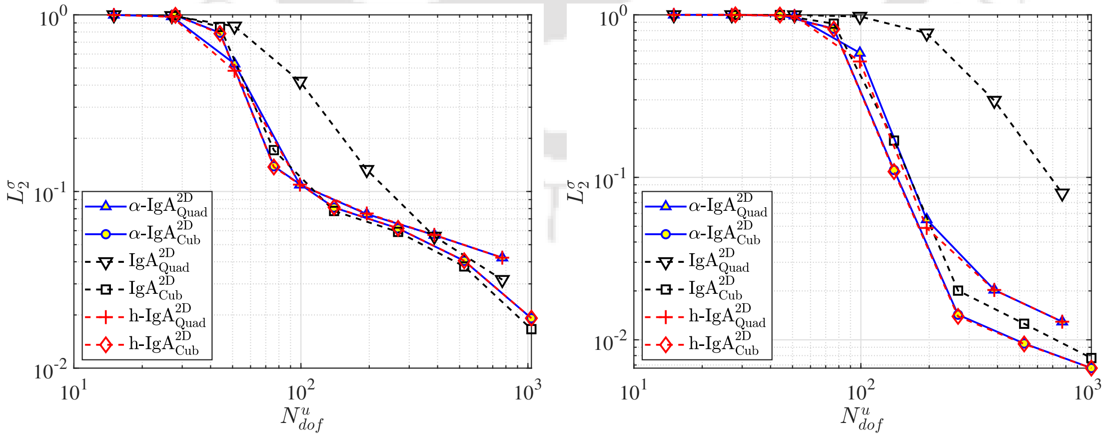

(e) L_2^σ for $r/h = 100$ **(f)** L_2^σ for $r/h = 1000$

Figure 7.9: Investigation of normalized displacement and L_2 error norm of displacement and stress for two different slenderness ratios for a clamped-clamped semi-circular beam.

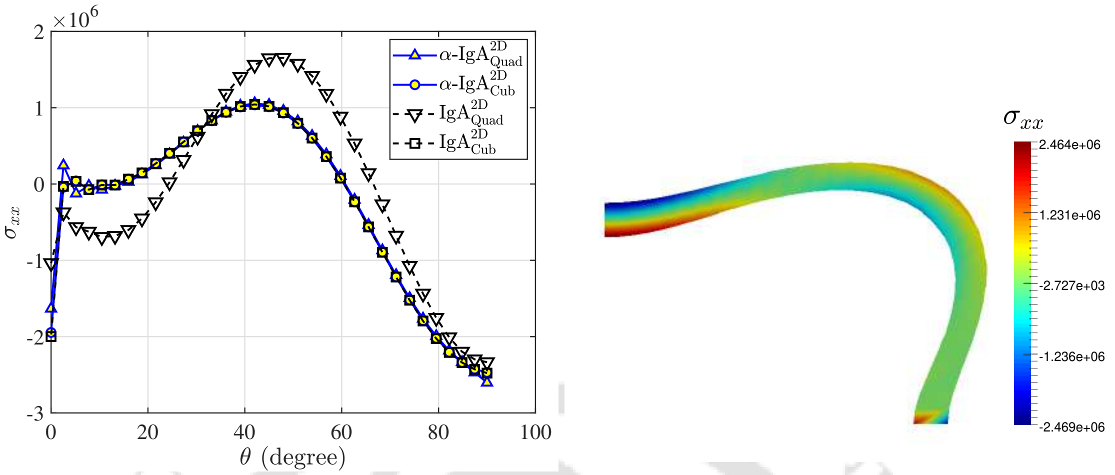

(a) σ_{xx} along θ **(b)** σ_{xx} over domain

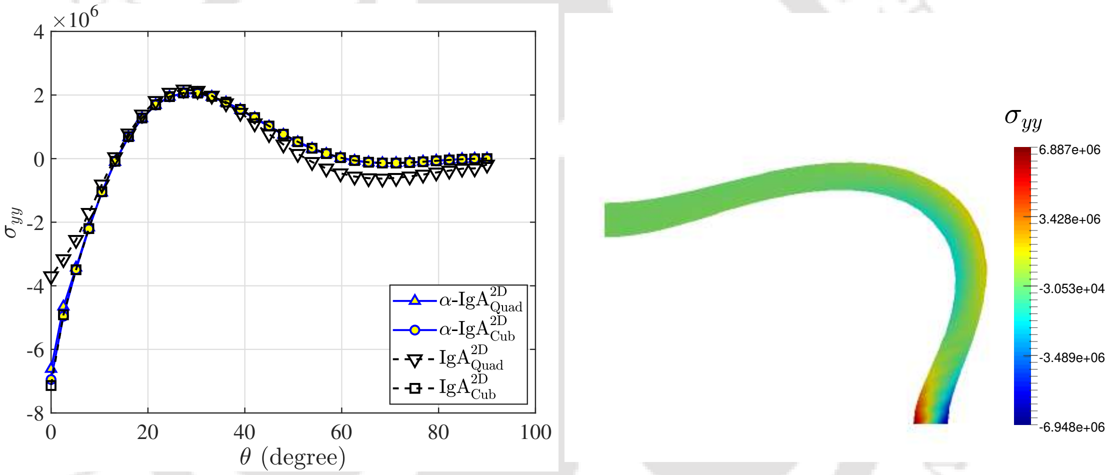

(c) σ_{yy} **(d)** σ_{yy} over domain

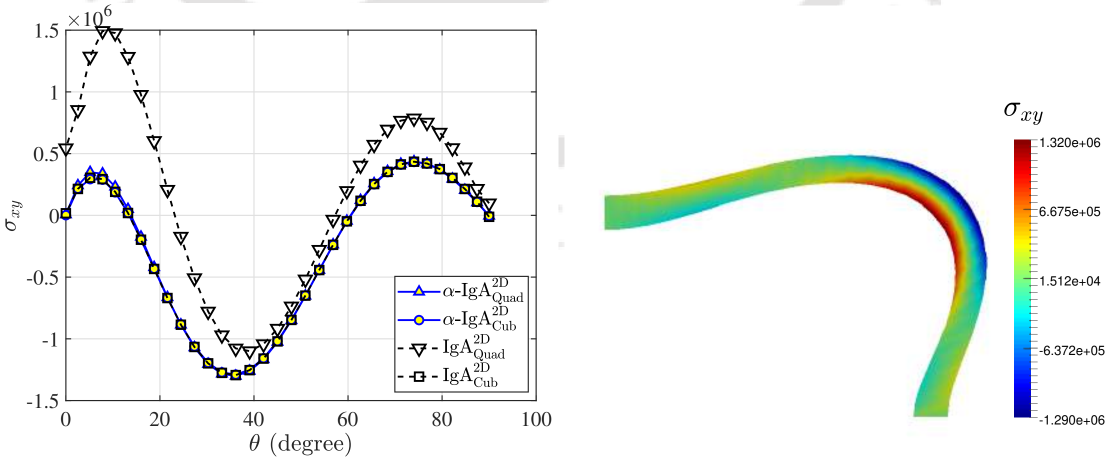

(e) σ_{xy} **(f)** σ_{xy} over domain

Figure 7.10: Investigation of stresses for $r/h = 1000$ at $r = r_o$ along θ for various elements using a mesh of 32×1 elements. A contour plot of stresses over the entire domain using the proposed α-IgA$^{2D}_{\text{Cub}}$ elements with a mesh of 32×1 elements. (Deformation and thickness are scaled with a factor of 100 for better visualization.)

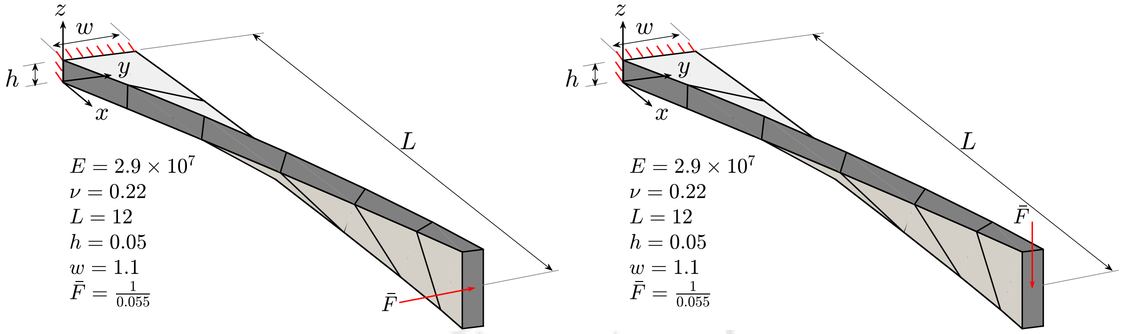

(a) Subjected to load along y direction **(b)** Subjected to load along z direction

Figure 7.11: The problem setup, boundary conditions, and material parameters for a twisted beam problem.

and the gap widens with higher r/h ratios for quadratic elements. This is elaborately shown in Fig. 7.10, which shows stresses along θ at $r = r_o$ for $r/h = 1000$ using a mesh of 32×1 elements. Finally, we present a contour plot for various stresses using the proposed α-IgA$^{\text{2D}}_{\text{Cub}}$ elements to show the absence of spurious stress values in the domain.

7.7.4 Twisted beam problem

In the first 3D example, the linear elastic response of a twisted cantilever beam is studied to assess the performance of the proposed EAS elements under shear and membrane locking. The problem consists of a helicoidal solid shell, fixed at one end and subjected to two different loading conditions at the other end. The detailed problem configuration, boundary conditions, and material parameters are shown in Fig. 7.11, where L, h, and w are the length, thickness, and width of the beam, respectively, $\bar{F}$ is the load per unit area, E is Young's modulus and ν is the Poisson's ratio.

The initial coarse mesh is designed based on the geometric descriptions characterized by Bouclier et al. [190], which utilizes a NURBS curve along the length to capture the helical characteristics of the beam. The refinement is carried out using h- or k-refinement techniques, with meshes defined as $n^L_{\text{ele}} \times n^w_{\text{ele}} \times n^h_{\text{ele}}$, where n^L_{ele}, n^w_{ele}, and n^h_{ele} represent the number of elements along the length, width, and thickness directions, respectively. Successive refinement considers $n^L_{\text{ele}} = n^w_{\text{ele}} = 2, 4, 8, 16, \ldots, 64$ while keeps $n^h_{\text{ele}} = 1$ for both the cases.

The present geometric description yields a smooth contour along the edge; however, this leads to minor variation in geometry against the well-established benchmark twisted beam model in conventional FEA practices. As a result, a solution of highly refined mesh, comprising of $128 \times 128 \times 1$ h-IgA$^{\text{2D}}_{\text{Cub}}$ elements, is taken as a reference. The revised benchmark values for displacement at the center of the loaded face in the direction of loading are $u^{\text{ref}}_y = 0.3635$ and $u^{\text{ref}}_z = 1.3623$ for loading cases (a) and (b), respectively [154].

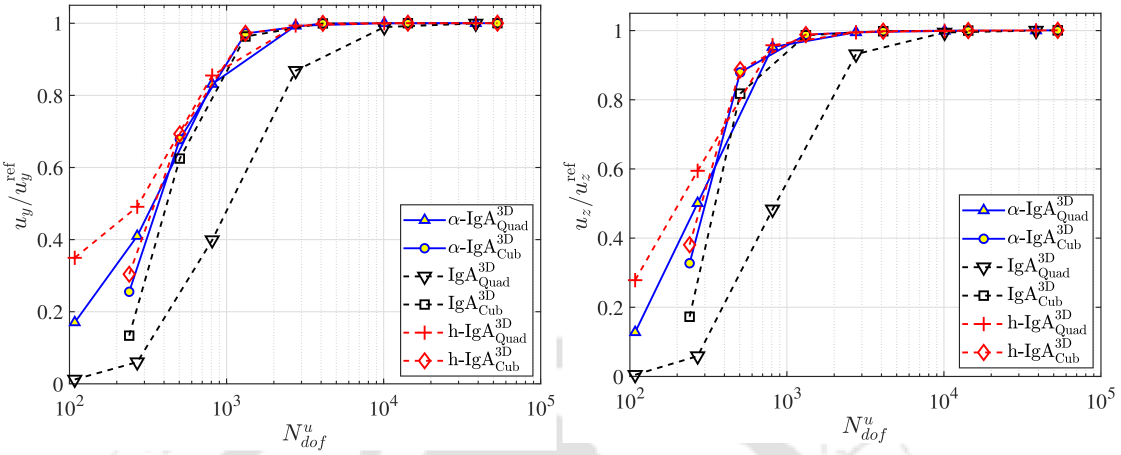

(a) u_y/u_y^{ref} (case (a)) **(b)** u_z/u_z^{ref} (case (b))

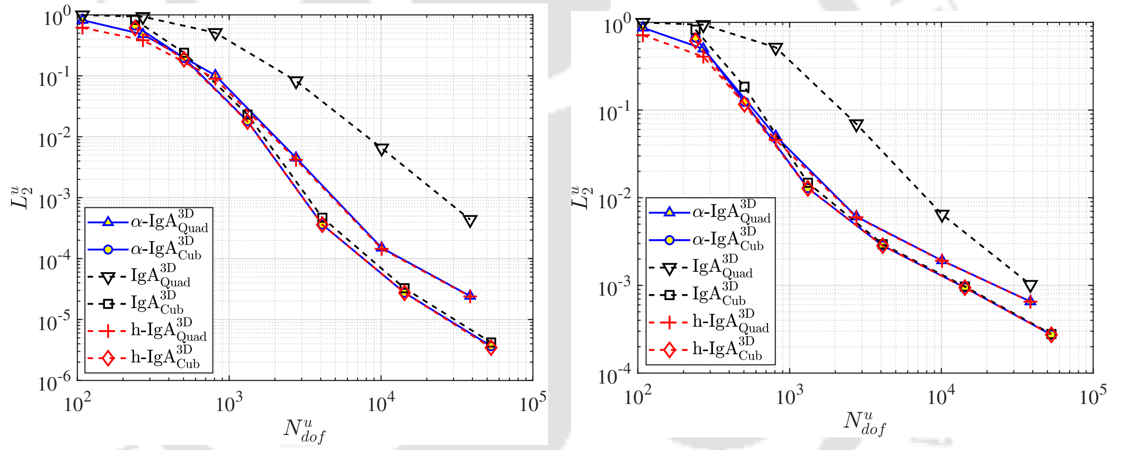

(c) L_2^u (case (a)) **(d)** L_2^u (case (b))

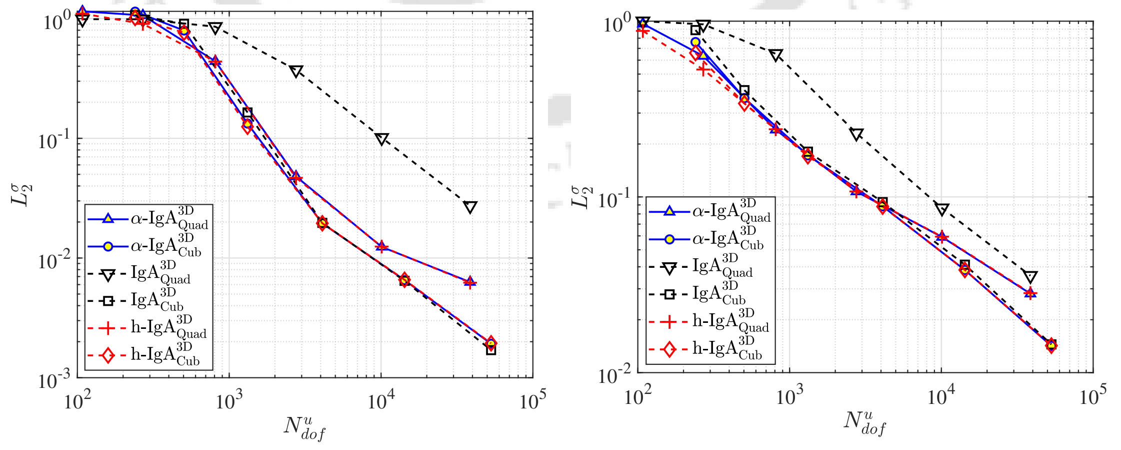

(e) L_2^σ (case (a)) **(f)** L_2^σ (case (b))

Figure 7.12: Investigation of normalized displacement and L_2 error norm of displacement and stress for two different loading conditions for twisted beam problem.

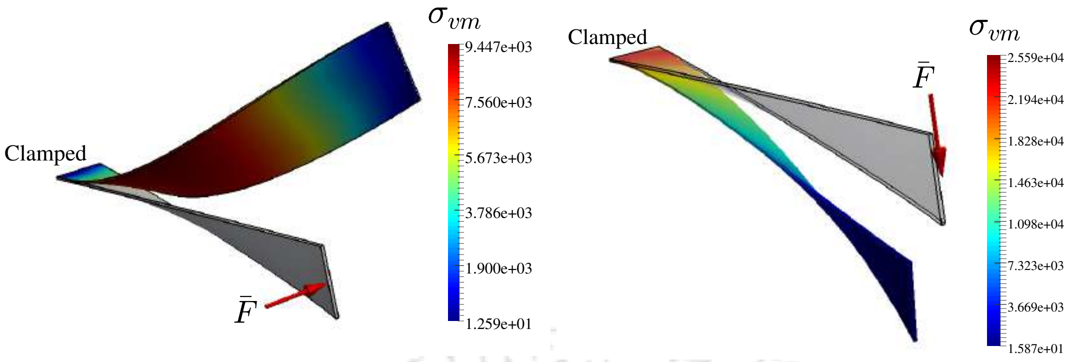

(a) σ_{vm} for case (a) **(b)** σ_{vm} for case (b)

Figure 7.13: A contour plot of von Mises stress over the entire domain using the proposed α-IgA$^{\text{3D}}_{\text{Cub}}$ elements with a mesh of $32 \times 32 \times 1$ elements. (Deformation is scaled for better visualization.)

The tip displacement along the direction of loading has been evaluated and normalized against the reference solution, see Figs. 7.12a and 7.12b. Further, the relative L_2 norm of displacement and stress against the total number of active degrees of freedom (N^u_{dof}) has been shown in Figs. 7.12c, 7.12d, 7.12e, and 7.12f. In both cases, the performance of IgA$^{\text{3D}}_{\text{Quad}}$ is adversely affected by locking, requiring significant refinement for convergence. In contrast, the proposed α-IgA$^{\text{3D}}_{\text{Quad}}$ elements converge to the solution with fewer elements, regardless of loading conditions. This distinction becomes more pronounced when considering the L^{σ}_2 norm. For instance, in the first case, the proposed α-IgA$^{\text{3D}}_{\text{Quad}}$ elements converge to the solution with L^{σ}_2 of 4.8% (Mesh: $16\times16\times1$, $N^u_{dof} = 10098$), whereas conventional IgA$^{\text{3D}}_{\text{Quad}}$ elements requires sixteen times the number of elements to achieve a comparable accuracy of 2.73% (Mesh: $64 \times 64 \times 1$, $N^u_{dof} = 38610$), see Fig. 7.12e. Higher-order elements, regardless of their type, are less affected by locking and show only marginal differences in performance. Furthermore, for both cases, the results show close similarity between the results obtained from h-IgA and α-IgA elements, which is expected as a result of the strategy that has been used to derive the proposed elements. The small disparity between the results of h-IgA and α-IgA elements can be entirely eliminated by adopting the same strategy for computing the transformation matrix in both formulations. Finally, the distribution of σ_{vm} across the domain for both loading cases is presented in Fig. 7.13, showing the absence of any spurious stress values in the domain.

7.7.5 Curved cantilever beam

The present example investigates the response of a 3D curved cantilever beam under the effects of combined shear and membrane locking. The problem consists of a curved beam of thickness h, mean radius r, and width w. The beam is fixed at one end while the edge at the opposite extremity is subjected to a horizontal load $\bar{F}$, see Fig. 7.14

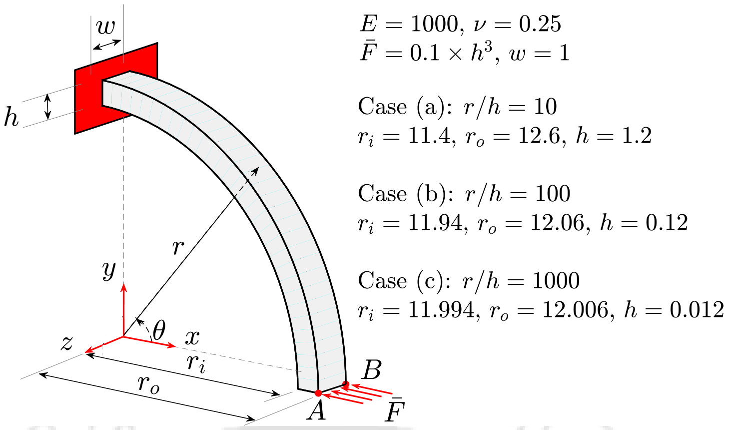

Figure 7.14: The problem setup, boundary conditions, and material parameters for a curved cantilever beam problem.

[101]. Here, r_i and r_o are the inner and outer radii measured from the origin, E is the Young's modulus and ν is the Poisson's ratio.

In order to assess the performance of the proposed EAS elements, the problem is solved for various slenderness ratios (r/h), encompassing situations where locking is a dominant issue. The problem consists of three r/h ratios, i.e., 10, 100, and 1000, which are attained by gradually decreasing h to 1.2, 0.12, and 0.012, respectively, while keeping $r = 12$ and $w = 1$. The benchmark radial displacements (u_x^{ref}) at the tip are 1.6338, 1.6236, and 1.5852 for $r/h = 10$, 100, and 1000, respectively [143].

The mesh used for solving the problem is denoted as $n_{\text{ele}}^{r} \times n_{\text{ele}}^{\theta} \times n_{\text{ele}}^{z}$, where n_{ele}^{r}, n_{ele}^{θ}, and n_{ele}^{z} are the number of elements in the radial, circumferential, and transverse directions, respectively. The control point coordinates and the corresponding weights to design the initial coarse mesh illustrating the exact geometry of the problem domain are presented in the Appendix (Table B.6). After defining the coarse mesh, further refinement is carried out using h- or k- refinement techniques. The refinement of the mesh is performed along the circumferential direction, with n_{ele}^{θ} ranging from 2 to 128 ($n_{\text{ele}}^{\theta} = 2, 4, 8, 16, 32, 64, 128$), while keeping respective $n_{\text{ele}}^{r} = n_{\text{ele}}^{z} = 1, 1, 1, 1, 2, 4, 8$ for $r/h = 10$. However, for $r/h = 100$ and 1000, the stress convergence is achieved after refining the mesh in the transverse direction while keeping a single element along the thickness. As a result, the mesh for $r/h = 100$ and 1000 is obtained by setting $n_{\text{ele}}^{\theta} = 2, 4, 8, 16, 32, 64, 256$, $n_{\text{ele}}^{z} = 1, 1, 1, 1, 2, 2, 4, 8$, and $n_{\text{ele}}^{r} = 1$.

The radial displacement at the loaded edge has been evaluated and normalized against the reference solution, see Figs. 7.15a, 7.15c, and 7.15e. Further, Figs. 7.15b, 7.15d, and 7.15f show the relative L_2 error norm of displacement against the total number of active degrees of freedom (N_{dof}^{u}). The results show that as the r/h ratio increases, $\text{IgA}_{\text{Quad}}^{\text{3D}}$ elements experience significant locking, whereas α-$\text{IgA}_{\text{Quad}}^{\text{3D}}$ perform consistently well throughout. The $\text{IgA}_{\text{Cub}}^{\text{3D}}$ are less affected by the locking, however α-$\text{IgA}_{\text{Cub}}^{\text{3D}}$ shows comparatively better coarse mesh accuracy.

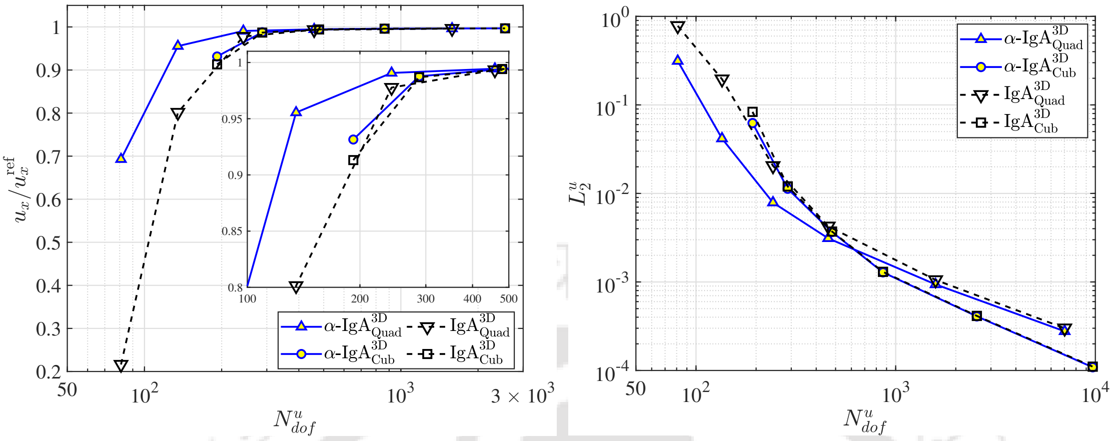

(a) u_x/u_x^{ref} $(r/h = 10)$

(b) L_2^u $(r/h = 10)$

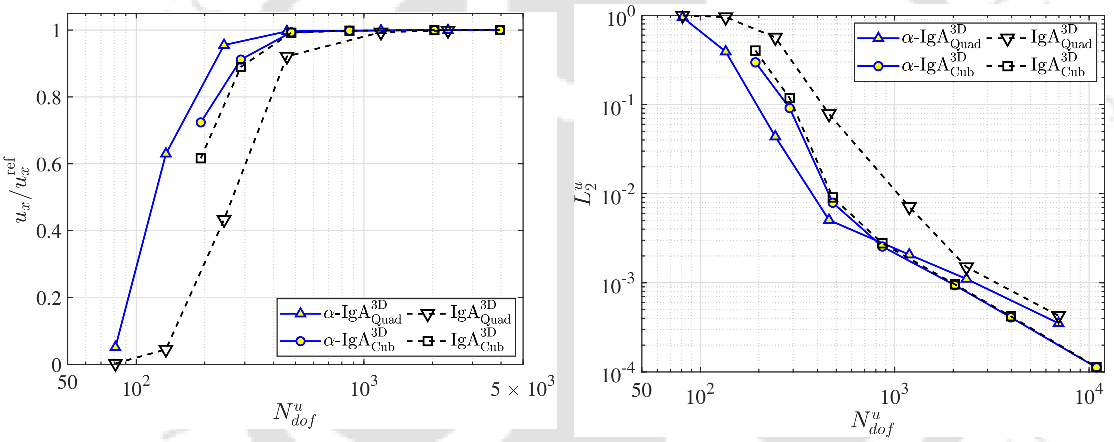

(c) u_x/u_x^{ref} $(r/h = 100)$

(d) L_2^u $(r/h = 100)$

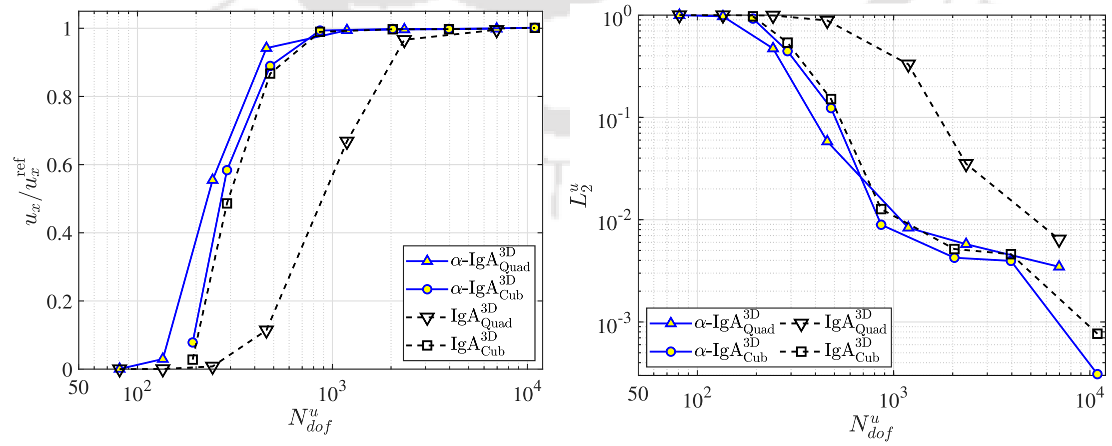

(e) u_x/u_x^{ref} $(r/h = 1000)$

(f) L_2^u $(r/h = 1000)$

Figure 7.15: Investigation of normalized displacement at the loaded edge and L_2 error norm of displacement for a curved cantilever beam problem with varying r/h ratios.

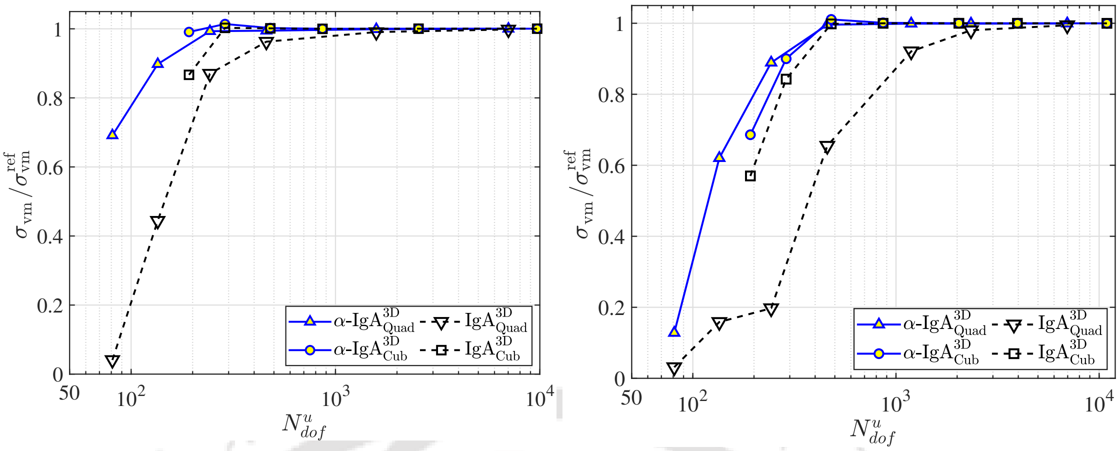

(a) $\sigma_{\mathrm{vm}}/\sigma_{\mathrm{vm}}^{\mathrm{ref}}$ for $r/h = 10$

(b) $\sigma_{\mathrm{vm}}/\sigma_{\mathrm{vm}}^{\mathrm{ref}}$ for $r/h = 100$

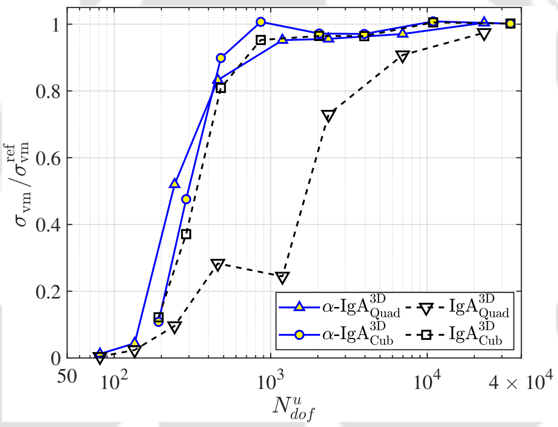

(c) $\sigma_{\mathrm{vm}}/\sigma_{\mathrm{vm}}^{\mathrm{ref}}$ for $r/h = 1000$

Figure 7.16: Normalized von Mises stress at $r = r_i$, $\theta = 45°$, $z = 0$ for three different r/h ratios of a curved cantilever beam problem.

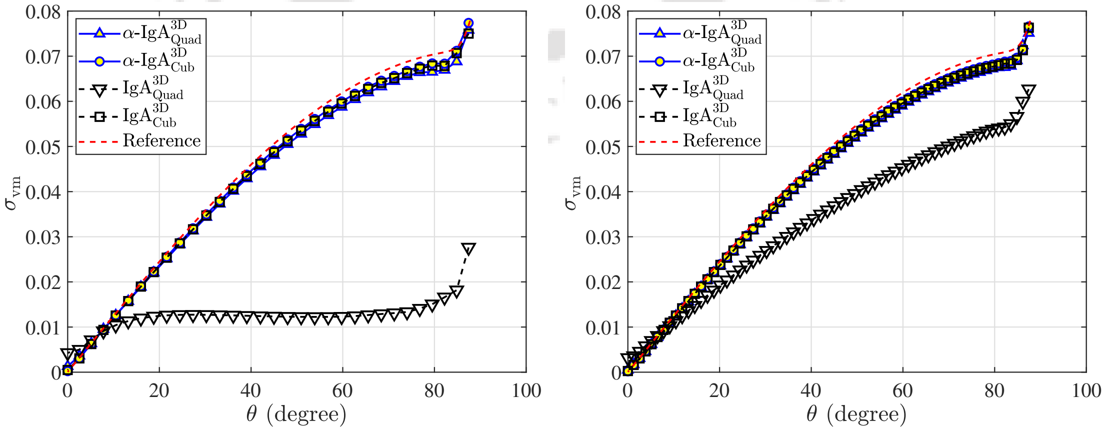

(a) σ_{vm} (mesh: $1 \times 32 \times 2$)

(b) σ_{vm} (mesh: $1 \times 64 \times 2$)

Figure 7.17: The σ_{vm} evaluated at the boundary with $r = r_{\mathrm{i}}$, $z = 0$ along θ for two different mesh descriptions for a curved cantilever beam problem with $r/h = 1000$.

The locking is relatively less for the lower values of r/h, see Figs. 7.15a and 7.15b. In such cases, conventional elements can adequately converge to the analytical solution with relatively few N^u_{dof}. At higher values of the r/h ratio, i.e., 100 and 1000, the quality of the solution for conventional elements is considerably degraded by locking. For instance, in the case of $r/h = 100$, a mesh of $1 \times 16 \times 1$ ($N^u_{dof} = 459$) α-IgA$^{\text{3D}}_{\text{Quad}}$ elements is able to provide a solution that closely matches the reference value with L_2 error of 0.5055%. However, to attain comparable accuracy with IgA$^{\text{3D}}_{\text{Quad}}$ elements, it is necessary to use four times the number of elements (mesh: $1 \times 32 \times 2$, $N^u_{dof} = 1188$, $L_2 = 0.7117\%$). This disparity in performance widens with a higher r/h ratio. For example, a mesh of $1 \times 32 \times 2$ ($N^u_{dof} = 1188$) α-IgA$^{\text{3D}}_{\text{Quad}}$ elements converges to the reference value with L_2 errors of 0.8346% when r/h ratios is 1000. However, to attain similar accuracy with IgA$^{\text{3D}}_{\text{Quad}}$ elements, it requires thirty-two times the number of elements (mesh: $1 \times 256 \times 8$, $N^u_{dof} = 23130$, $L_2 = 0.6421\%$).

Finally, for each of the three r/h ratios, the von Mises stress (σ_{vm}) is calculated at $r = r_i$, $\theta = 45°$, and $z = 0$. The benchmark values ($\sigma^{\text{ref}}_{\text{vm}}$) of 6.4025, 0.5963, and 0.0505 [143] corresponding to r/h ratios of 10, 100, and 1000, respectively, have been utilized to normalize the obtained results. The convergence behavior is shown in Fig. 7.16. The results consistently show better coarse mesh accuracy of the α-IgA elements, regardless of the r/h ratio. Additionally, the distribution of σ_{vm} is evaluated along θ with $r = r_i$ and $z = 0$ for two mesh configurations, as illustrated in Fig. 7.17. The results show the absence of anomalous stress values along the periphery of the beam, eliminating the large oscillations often observed in conventional FE practices, see Fig. 4.12.

7.7.6 Pinched cylinder

One of the shell obstacle course problems [101] concerns a pinched cylinder with a rigid diaphragm at both of its ends and is prone to shear and membrane locking. The ends of the cylinder are fixed with rigid diaphragms and the mid-section is subjected to a pair of equal and opposite concentrated loads $\bar{F}$. Since the problem exhibits symmetry, only one-eighth of the cylinder is analyzed. The detailed problem configuration, boundary conditions, and material parameters are shown in Fig. 7.18, where r, l, and h are the mean radius, axial length, and thickness, respectively, E is the Young's modulus, and ν is the Poisson's ratio.

The geometric description to design the coarse mesh while maintaining the exact problem domain using the NURBS interpolations is given in the Appendix (Table B.8). After defining the coarse mesh, further refinement is carried out using h- or k- refinement. The meshes used to solve the problem are defined as $n^r_{\text{ele}} \times n^\theta_{\text{ele}} \times n^l_{\text{ele}}$, where n^r_{ele}, n^θ_{ele}, and n^l_{ele} denote the number of elements in the radial, circumferential, and axial directions, respectively. The meshes are refined along the θ and l directions, with values of n^θ_{ele} and n^l_{ele} set to 2, 4, 8, 16, 32, and 64, while n^r_{ele} is kept constant at 1.

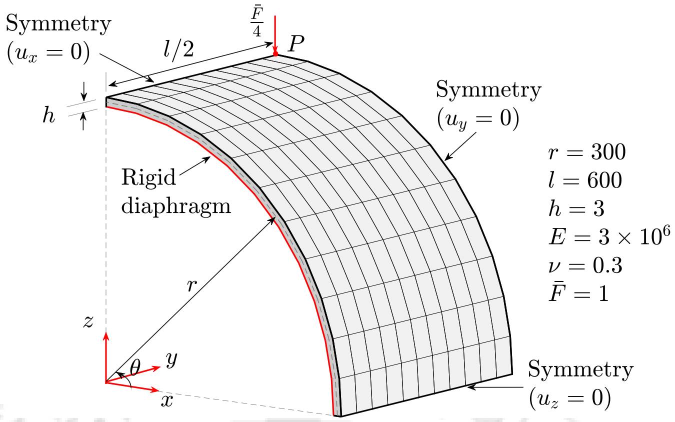

Figure 7.18: The one-eighth problem domain, boundary conditions, and material parameters for pinched cylinder problem.

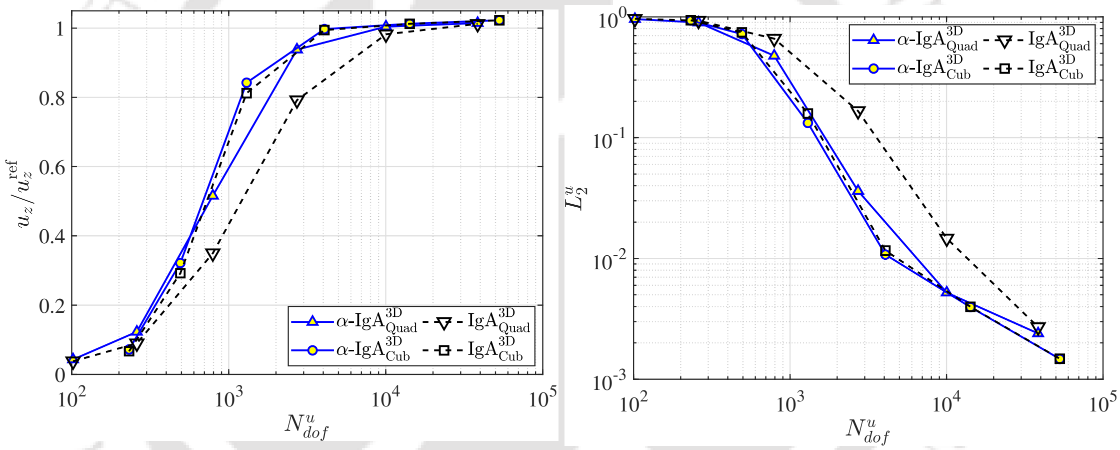

(a) u_z/u_z^{ref} **(b)** L^u_2

Figure 7.19: Investigation of normalized displacement at the point of application of load and L^u_2 error norm of displacement for a pinched cylinder problem.

The displacement in the radial direction at the point where the load is applied has been evaluated. Fig. 7.19a shows the obtained vertical displacement at the point of interest normalized by the benchmark solution ($u_z^{\text{ref}} = 1.8248 \times 10^{-5}$ [101]). Fig. 7.19b shows the relative L^u_2 error norm of displacement with respect to corresponding N^u_{dof}. To evaluate the L^u_2 norm, a reference solution is established using a significantly fine mesh of $1 \times 128 \times 128$ h-IgA$^{\text{3D}}_{\text{Cub}}$ elements. A better coarse mesh accuracy of the proposed α-IgA$^{\text{3D}}_{\text{Quad}}$ elements over the conventional IgA$^{\text{3D}}_{\text{Quad}}$ elements is observed. Higher-order elements are less affected by locking, whether it is α-IgA$^{\text{3D}}_{\text{Cub}}$ or IgA$^{\text{3D}}_{\text{Cub}}$ elements. Further, the convergence rates of the proposed elements in comparison to conventional elements are investigated in Fig. 7.20. It shows higher convergence rate for α-IgA$^{\text{3D}}_{\text{Quad}}$ compared to IgA$^{\text{3D}}_{\text{Quad}}$ elements. However, there is close similarity for the convergence order for α-IgA$^{\text{3D}}_{\text{Cub}}$ and IgA$^{\text{3D}}_{\text{Cub}}$ elements.

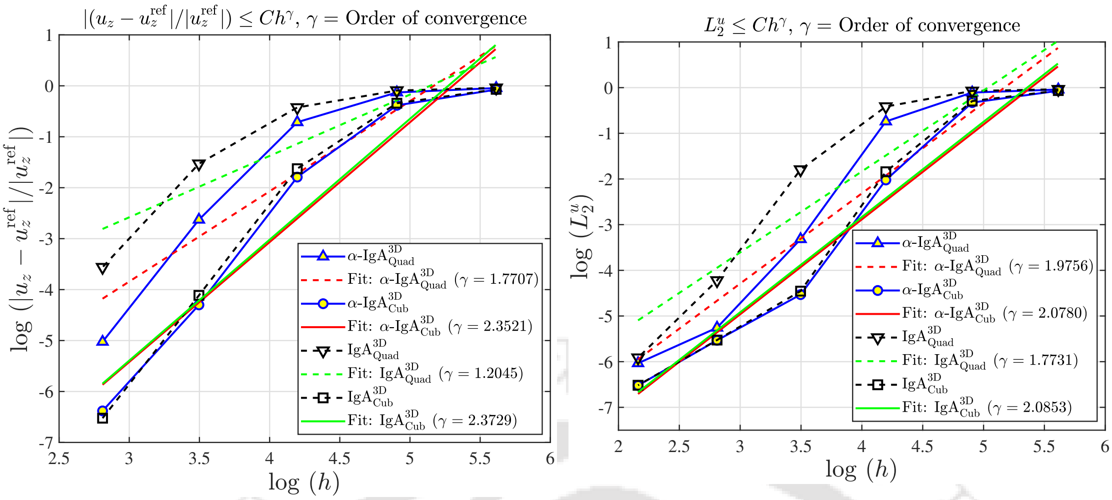

(a) Evaluation of γ using relative error

(b) Evaluation of γ using L_2^u error

Figure 7.20: Investigation of convergence rates with respect to the relative error at the point of application of load and L_2^u error norm of displacement for a pinched cylinder problem. ('Fit: element type' represents a linear fit for the respective element type, and h is the smallest diagonal length of an element in the selected mesh.)

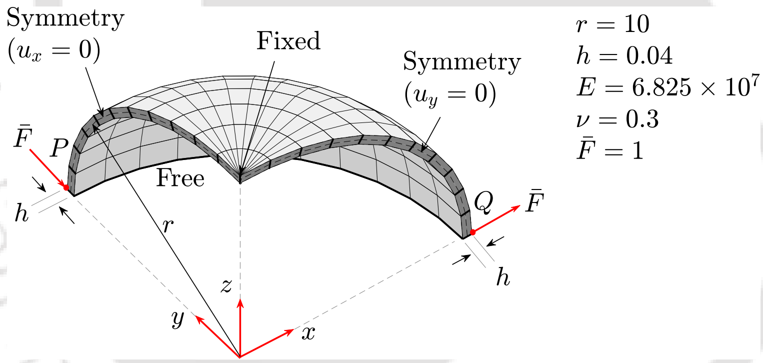

Figure 7.21: The quarter domain of pinched hemisphere problem, boundary conditions, and material parameters.

7.7.7 Pinched hemisphere problem

The present numerical example involves a hemispherical shell subjected to a pair of concentrated loads of equal magnitude and opposite direction, applied at the equator plane and in a diametrically opposite direction. Similar to the previous problem, only one-quarter of the domain is considered due to the problem's symmetry. The detailed problem configuration, boundary conditions, and material parameters are presented in Fig. 7.21, where r is the mean radius, h is thickness, $\bar{F}$ is the point load, E and ν are Young's modulus and Poisson's ratio, respectively. The boundary at $z = 0$ in the peripheral region of the shell is unconstrained, while a point at the top is fixed to avoid rigid body motions.

The geometric description to design the coarse mesh is defined in the Appendix (Table B.9). The problem is discretized using a mesh composed of elements in three

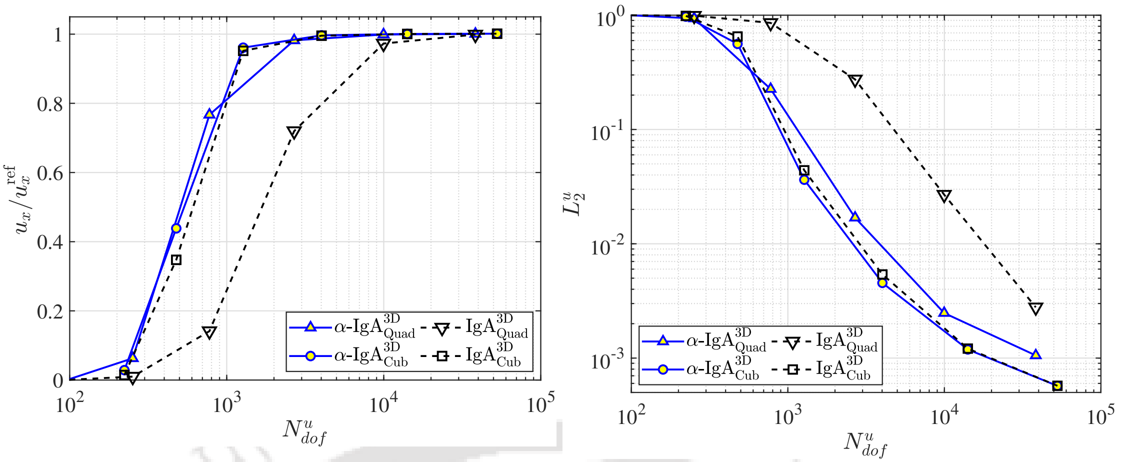

(a) u_x/u_x^{ref} **(b)** L_2^u

Figure 7.22: Investigation of normalized displacement at the point of application of load (point 'Q') and L_2^u error norm of displacement for the pinched hemisphere problem.

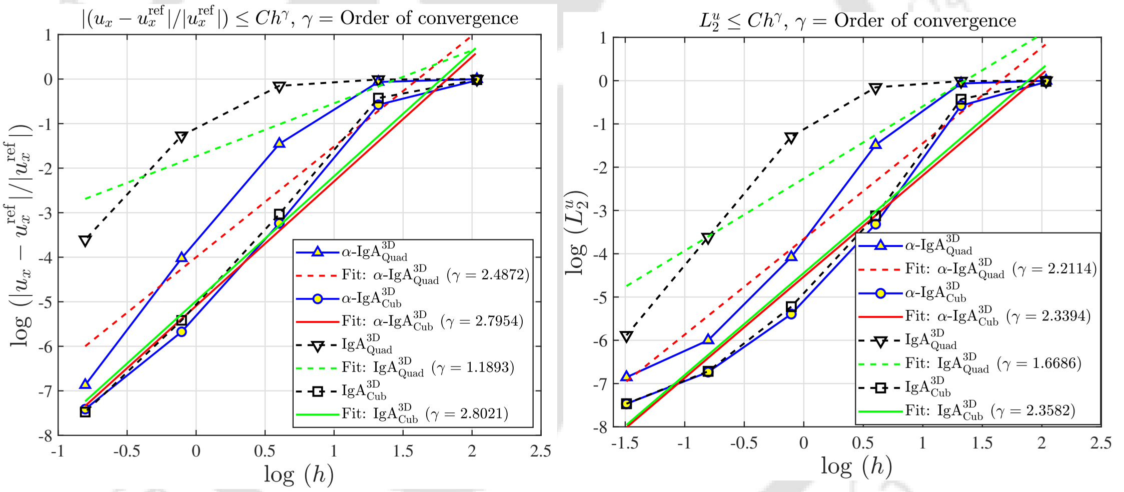

(a) Evaluation of γ using relative error **(b)** Evaluation of γ using L_2^u error

Figure 7.23: Investigation of convergence rates with respect to the relative error at the point of application of load and L_2^u error norm of displacement for a pinched hemisphere problem. ('Fit: element type' represents a linear fit for the respective element type, and h is the smallest diagonal length of an element in the selected mesh.)

directions: r, θ, and ϕ. The mesh is defined as $n_{\text{ele}}^r \times n_{\text{ele}}^\theta \times n_{\text{ele}}^\phi$, where n_{ele}^r, n_{ele}^θ, and n_{ele}^ϕ represent the number of elements in each direction. The angles θ and ϕ correspond to the azimuthal and polar angles, respectively, with θ being the angle in the xy-plane. The mesh is refined in the θ and ϕ directions using $n_{\text{ele}}^\theta = n_{\text{ele}}^\phi = 2$, 4, 8, 16, 32, and 64, while the number of elements in the r direction is kept constant at $n_{\text{ele}}^r = 1$.

The problem is solved to determine the displacement at point 'Q' in the direction of the applied load. The x-displacement at point 'Q' is computed and normalized to the benchmark solution $u_x^{\text{ref}} = 0.0924$ [141], see Fig. 7.22a. In addition, the relative L_2^u error norm of displacement against N_{dof}^u is presented in Fig. 7.22b. The L_2^u norm is computed

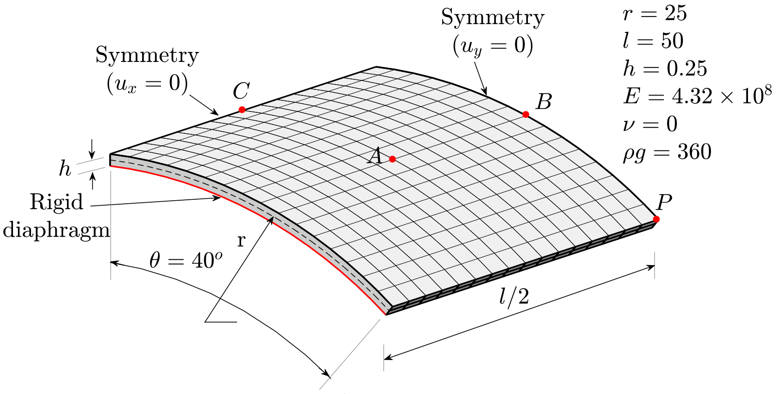

Figure 7.24: The quarter domain of Scordelis-Lo roof problem, boundary conditions, and material parameters.

using a reference solution obtained from a finely refined mesh composed of $1 \times 128 \times 128$ h-IgA$^{\text{3D}}_{\text{Cub}}$ elements. The results show that the conventional IgA$^{\text{3D}}_{\text{Quad}}$ elements are prone to locking and demand a considerable degree of refinement to converge to the solution, whereas α-IgA$^{\text{3D}}_{\text{Quad}}$ elements converge with fewer N^u_{dof}. For instance, a mesh of $1\times16\times16$ ($N^u_{dof} = 2688$) of α-IgA$^{\text{3D}}_{\text{Quad}}$ elements is capable of providing an accurate approximation to the reference solution with an L^u_2 error of 1.6916%. In contrast, the conventional IgA$^{\text{3D}}_{\text{Quad}}$, despite four times as many elements ($1 \times 32 \times 32$, $N^u_{dof} = 9968$), offers lower accuracy with an L^u_2 error of 2.6898% compared to the α-IgA$^{\text{3D}}_{\text{Quad}}$ elements. Further, the higher order α-IgA$^{\text{3D}}_{\text{Cub}}$ elements shows better coarse mesh accuracy compared to the IgA$^{\text{3D}}_{\text{Cub}}$ elements.

Additionally, the convergence rates of the proposed elements in comparison to conventional elements are shown in Fig. 7.23. There is a substantial difference in the order of convergence between α-IgA$^{\text{3D}}_{\text{Quad}}$ and IgA$^{\text{3D}}_{\text{Quad}}$ elements, with the former exhibiting an order that is more than twice as compared to IgA$^{\text{3D}}_{\text{Quad}}$ elements, particularly when evaluated using the relative error at the point of load application. The order of convergence, evaluated with respect to the overall L^u_2 error, consistently favors α-IgA$^{\text{3D}}_{\text{Quad}}$. However, there is a close similarity in the convergence order between α-IgA$^{\text{3D}}_{\text{Cub}}$ and IgA$^{\text{3D}}_{\text{Cub}}$ elements.

7.7.8 Scordelis–Lo roof problem

The Scordelis–Lo roof problem [175] is the next shell obstacle course problem that is being examined using the proposed elements. It involves an 80° portion of a cylinder with rigid diaphragms at opposite ends, while the remaining two sides are unconstrained. As the problem exhibits symmetry, only one-quarter of the cylindrical section is analyzed. The detailed problem configuration, boundary conditions, and material parameters are presented in Fig. 7.24, where r, h, and l are the mean radius, thickness, and axial length, respectively. The material parameters E and ν represent Young's modulus and Poisson's

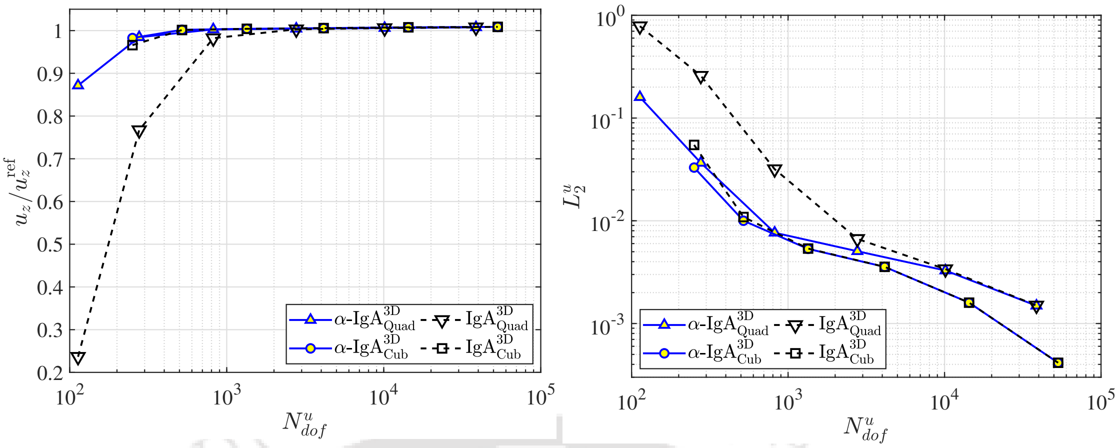

(a) u_z/u_z^{ref} **(b)** L^u_2

Figure 7.25: Investigation of normalized displacement at the point 'P' and L^u_2 error norm of displacement for a Scordelis–Lo roof problem.

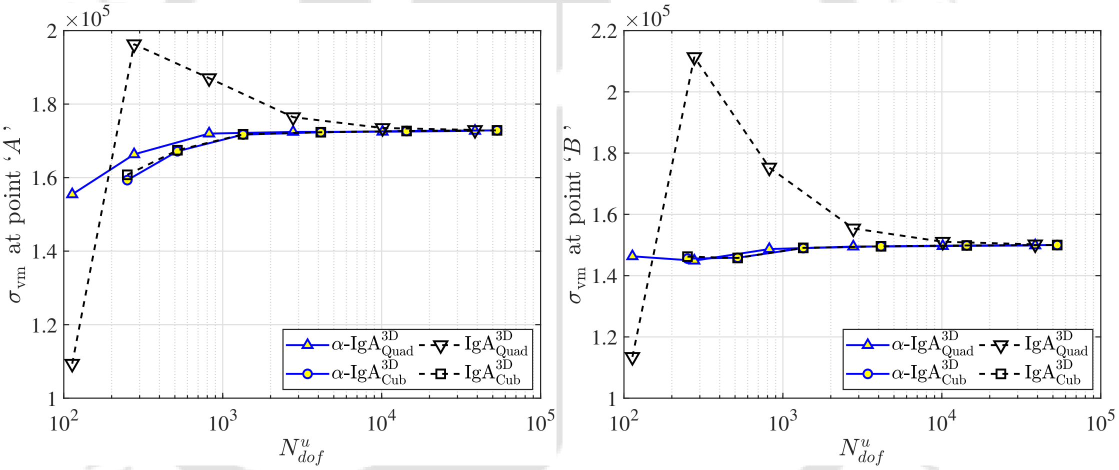

(a) σ_{vm} at point A **(b)** σ_{vm} at point B

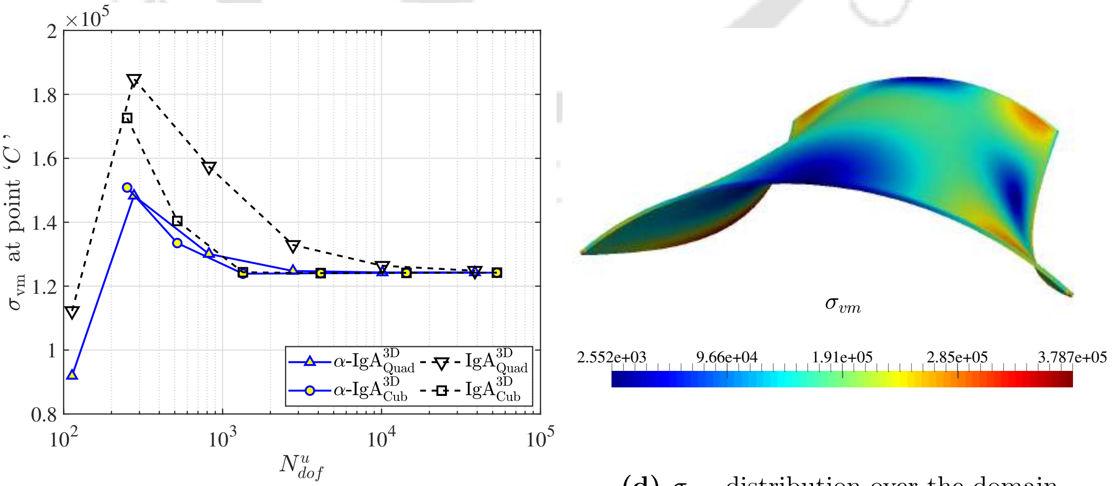

(c) σ_{vm} at point C **(d)** σ_{vm} distribution over the domain

Figure 7.26: Investigation of von Mises stress at different points in the domain and contour plot of σ_{vm} distribution for a Scordelis–Lo roof problem. (Deformed geometry is scaled for visualization.)

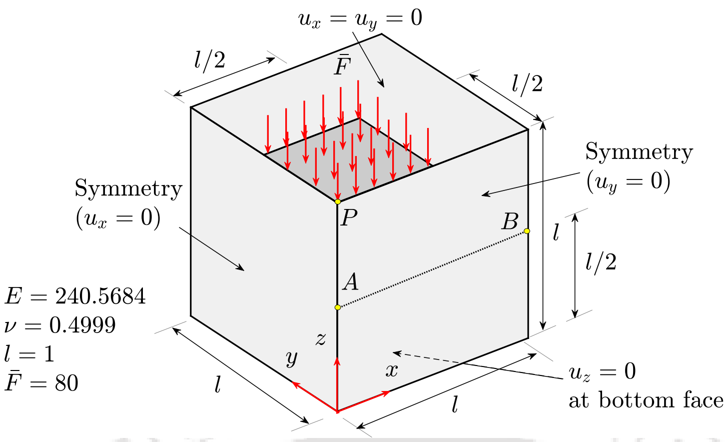

Figure 7.27: A quarter problem domain, material data, and boundary conditions for an incompressible block problem.

ratio, respectively. The problem is subjected to a body force per unit volume ρg, where ρ is the specific mass of the body and g is the acceleration due to gravity.

The geometric description to design the coarsest possible mesh is defined in the Appendix (Table B.7). After defining the coarse mesh, further refinement is carried out using h- or k- refinement. The meshes used to solve the problem are defined as $n^r_{\text{ele}} \times n^\theta_{\text{ele}} \times n^l_{\text{ele}}$, where n^r_{ele}, n^θ_{ele}, and n^l_{ele} are the number of elements in the radial, circumferential, and axial direction, respectively. The mesh is refined in the θ and l directions with values of $n^\theta_{\text{ele}} = n^l_{\text{ele}} = 2$, 4, 8, 16, 32, and 64, while n^r_{ele} is kept constant at 1.

The displacement at the center of the free side of a cylindrical shell (point 'P') has been evaluated. The results shown in Fig. 7.25a have been normalized by the benchmark solution $u^{\text{ref}}_z = 0.3024$ [175]. Additionally, Fig. 7.25b shows the relative L^u_2 error norm of displacement with respect to the total number of active degrees of freedom. The L^u_2 norm is calculated using a reference solution obtained from a refined mesh comprising of $1 \times 128 \times 128$ h-IgA$^{\text{3D}}_{\text{Cub}}$ elements. Results show that α-IgA$^{\text{3D}}_{\text{Quad}}$ elements converge to the solution with relatively high coarse mesh accuracy. The problem is further examined by analyzing the stresses at three different points within the domain. The convergence of von Mises stresses at points A, B, and C is shown in Fig. 7.26, along with the distribution of σ_{vm} over the entire domain. The α-IgA$^{\text{3D}}_{\text{Quad}}$ elements provide favorable stress values at all three points with superior accuracy compared to IgA$^{\text{3D}}_{\text{Quad}}$ elements. Higher-order elements IgA$^{\text{3D}}_{\text{Cub}}$ elements are less affected by locking and exhibit similar performance as α-IgA$^{\text{3D}}_{\text{Cub}}$ elements.

7.7.9 Incompressible block

The next example serves as a standard test to assess the performance of the proposed elements under volumetric locking due to the material's incompressibility [54, 143]. The problem comprises a rectangular block whose central region of the upper face is subjected

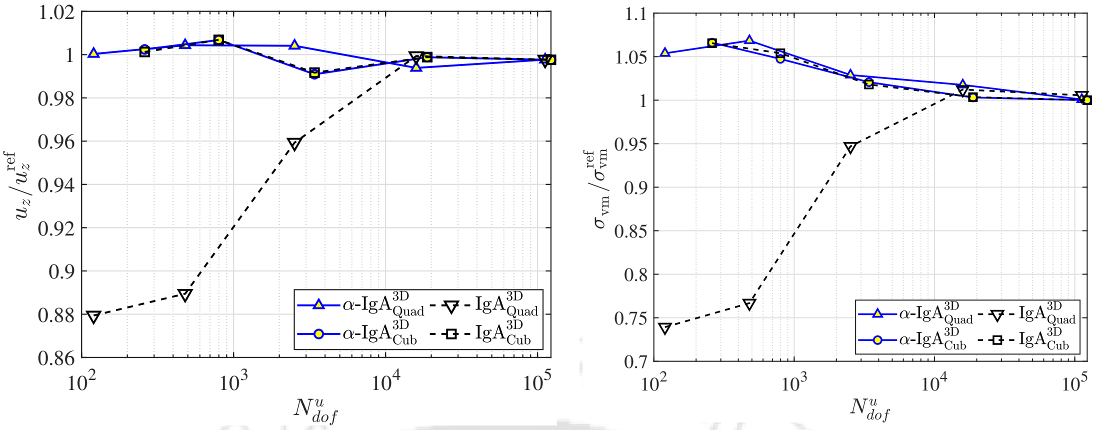

(a) u_z/u_z^{ref} **(b)** $\sigma_{\text{vm}}/\sigma_{\text{vm}}^{\text{ref}}$

Figure 7.28: Investigation of normalized displacement at a point 'P' and von Mises stress at point 'A' corresponding to $x = 0$, $y = 0$, $z = 0.5$ for incompressible block problem.

to a pressure load of $\bar{F}$. Due to the symmetry of the problem, only one-fourth of the problem domain is considered for the analysis. The detailed problem set-up, boundary conditions, and material parameters are presented in Fig. 7.27. The geometric description to design the coarse mesh with the lowest possible degree of NURBS interpolations is defined in the Appendix (Table B.5). Further refinement is carried out using h- or k- refinement. The problem is uniformly meshed, with $n^x_{\text{ele}} = n^y_{\text{ele}} = n^z_{\text{ele}} = 2$, 4, 8, 16, and 32, where n^x_{ele}, n^y_{ele}, and n^z_{ele} are the number of elements in x, y, and z direction, respectively.

The vertical displacement at point 'P' has been evaluated and results are normalized using $u_z^{\text{ref}} = 0.2165$ [143], see Fig. 7.28a. In addition, the von Mises stress (σ_{vm}) is computed at the location which corresponds to point 'A' with coordinates [0, 0, 0.5]. The results are normalized using $\sigma_{\text{vm}}^{\text{ref}} = 62.7484$ [143] and presented in Fig. 7.28b. The results shows that the proposed α-IgA$^{3D}_{\text{Quad}}$ elements converge to the solution with fewer N^u_{dof} compared to IgA$^{3D}_{\text{Quad}}$. The results obtained using higher-order, either α-IgA$^{3D}_{\text{Cub}}$ or α-IgA$^{3D}_{\text{Cub}}$, are closely comparable. Further, the performance of conventional IgA$^{3D}_{\text{Quad}}$ is not far behind from α-IgA$^{3D}_{\text{Quad}}$ elements and with refinement they too converge to the solution. However, the apparent improvement in solution quality for IgA$^{3D}_{\text{Quad}}$ elements through refinement does not provide a comprehensive representation of the situation. Upon further examination of the stress distribution on the 'y' plane, it shows that the IgA$^{3D}_{\text{Quad}}$ elements are not immune to locking. In fact, the results obtained from these elements are significantly plagued with volumetric locking.

To examine these effects, the stresses along a line AB (x varies from 0 to 1, $y = 0$, and $z = 0.5$) have been analyzed. Notably, when assessing stresses along the line AB, substantial oscillation can be observed in normal stresses obtained using IgA$^{3D}_{\text{Quad}}$ elements. Despite considerable refinement, these oscillations persist, see Fig. 7.29. Moreover, given the symmetric boundary conditions at this location, the shear stresses σ_{xy} and σ_{zy} should be ideally zero. However, conventional IgA$^{3D}_{\text{Quad}}$ elements fail to predict

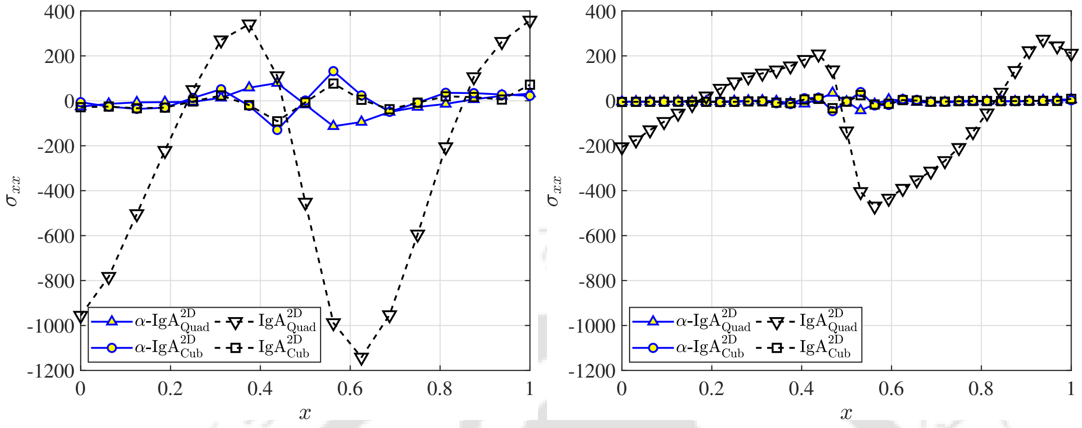

(a) σ_{xx}, Mesh: 16 × 16 × 16 elements **(b)** σ_{xx}, Mesh: 32 × 32 × 32 elements

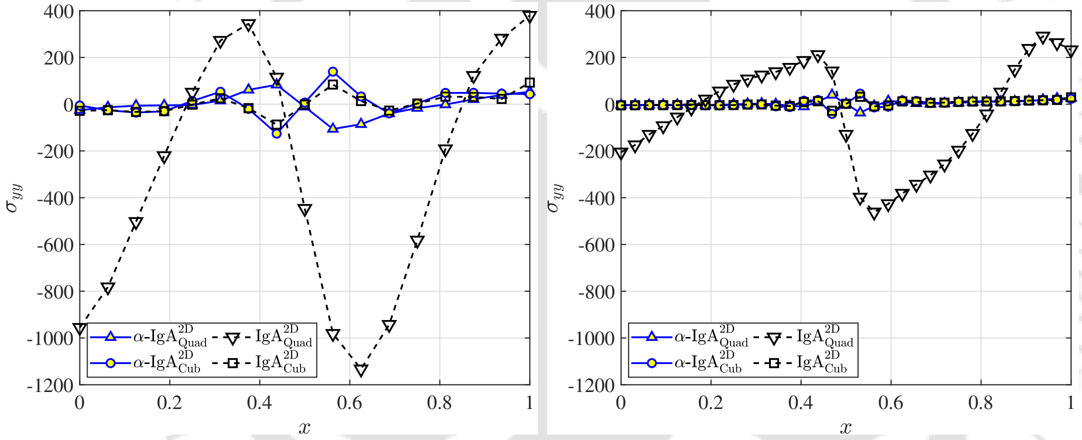

(c) σ_{yy}, Mesh: 16 × 16 × 16 elements **(d)** σ_{yy}, Mesh: 32 × 32 × 32 elements

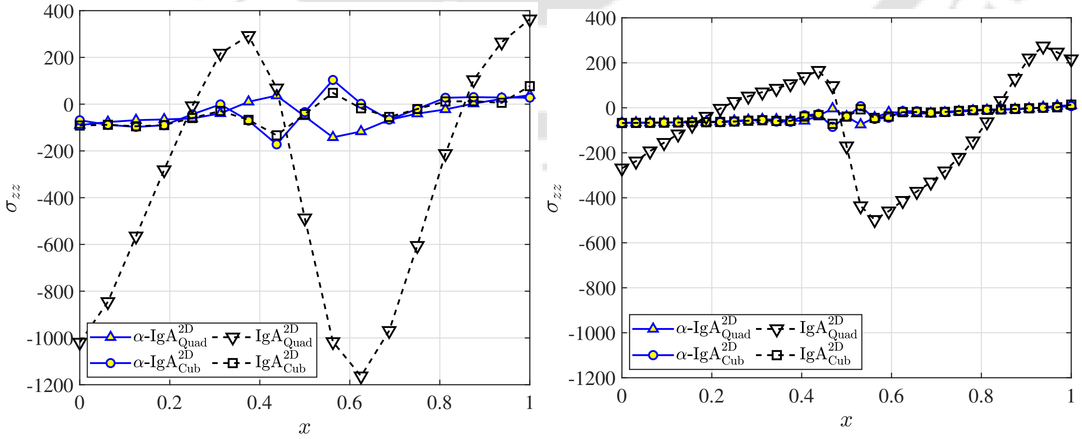

(e) σ_{zz}, Mesh: 16 × 16 × 16 elements **(f)** σ_{zz}, Mesh: 32 × 32 × 32 elements

Figure 7.29: Assessment of normal stresses along line AB in an incompressible block problem with two different mesh descriptions.

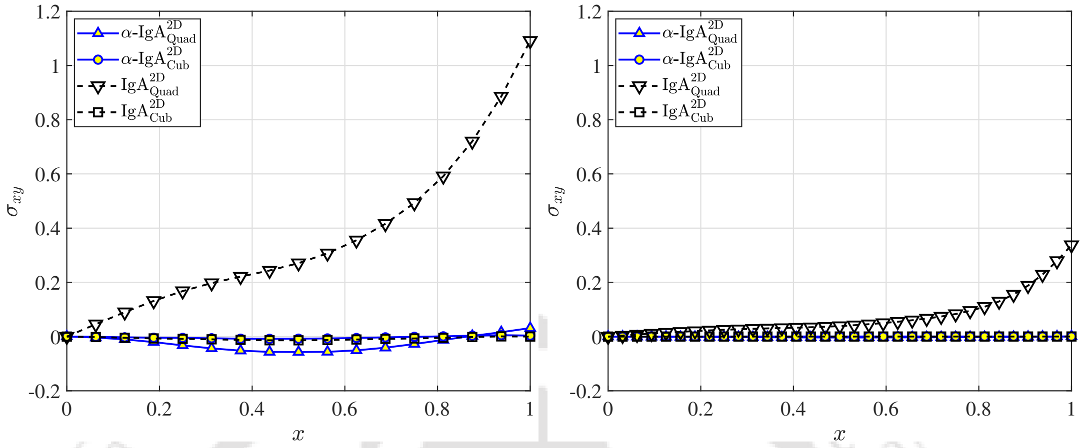

(a) σ_{xy}, Mesh: 16 × 16 × 16 elements **(b)** σ_{xy}, Mesh: 32 × 32 × 32 elements

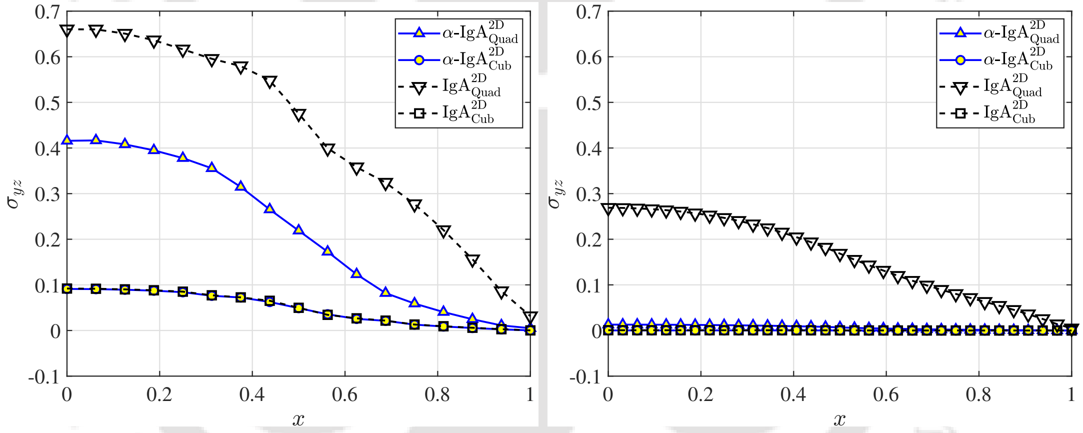

(c) σ_{yz}, Mesh: 16 × 16 × 16 elements **(d)** σ_{yz}, Mesh: 32 × 32 × 32 elements

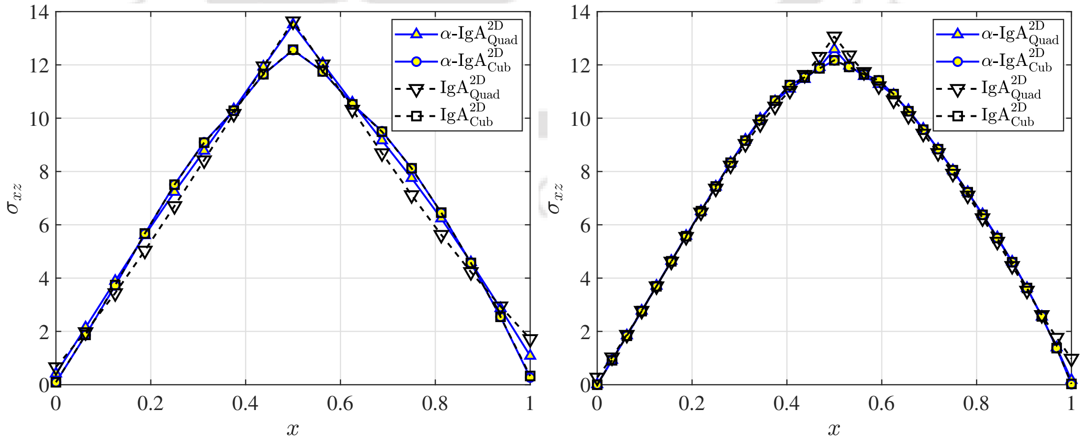

(e) σ_{xz}, Mesh: 16 × 16 × 16 elements **(f)** σ_{xz}, Mesh: 32 × 32 × 32 elements

Figure 7.30: Assessment of shear stresses along line AB in an incompressible block problem with two different mesh descriptions.

accurate solutions for this condition, see Fig. 7.30. In contrast, the proposed α-IgA$^{\text{3D}}_{\text{Quad}}$ elements do not exhibit any oscillations in normal stresses. Further, the shear stress condition is better satisfied with α-IgA$^{\text{3D}}_{\text{Quad}}$ elements compared to the conventional IgA$^{\text{3D}}_{\text{Quad}}$ elements, with the magnitude of σ_{xy} and σ_{zy} being very close to zero.

7.7.10 Time-dependent problems

In the present section, the performance of the proposed EAS elements is assessed using several time-dependent problems. For completeness, the section begins with a concise introduction to time-dependent problems and outlines the methodology that is utilized to address them. Subsequently, several numerical examples are solved and the discussion based on the obtained results is presented.

Time-dependent structural problems typically fall into a category where the response of a structure varies over time due to several dynamic or time-varying factors such as loads, boundary conditions, material properties, or environmental conditions. The present work primarily focuses on the response of the structure under the influence of dynamic loading. To understand the underlying concepts, let us revisit the differential equation that governs a linear elasticity problem (refer Chapter 2, Section 2.1), which is given as follows:

$$\boldsymbol{\nabla} \cdot \boldsymbol{\sigma} + \boldsymbol{b} = \rho \frac{\partial^2 \boldsymbol{u}}{\partial t^2}. \tag{7.33}$$

The variational formulation is obtained by employing the method of weighted residuals. Utilizing the semi-discretization process, where only the space variables are discretized, the Eq. 7.33 leads to the following hyperbolic expression:

$$\bar{\boldsymbol{M}} \ddot{\hat{\boldsymbol{u}}} + \boldsymbol{K} \hat{\boldsymbol{u}} = \hat{\boldsymbol{f}}, \tag{7.34}$$

where $\bar{\boldsymbol{M}}$ and $\boldsymbol{K}$ are the mass and stiffness matrix, respectively, $\hat{\boldsymbol{f}}$ is the load vector, and $\ddot{\hat{\boldsymbol{u}}}$ is the acceleration. Furthermore, for a realistic structural response, damping is introduced. Hence, Eq. 7.34 can be written as follows:

$$\bar{\boldsymbol{M}} \ddot{\hat{\boldsymbol{u}}} + \bar{\boldsymbol{C}} \dot{\hat{\boldsymbol{u}}} + \boldsymbol{K} \hat{\boldsymbol{u}} = \hat{\boldsymbol{f}}, \tag{7.35}$$

where $\bar{\boldsymbol{C}}$ is the damping matrix and $\dot{\hat{\boldsymbol{u}}}$ represents the velocity. The system is provided with initial displacement and velocity. Irrespective of formulation type, all three methods (conventional, EAS, or hybrid) will result in the above expression, with the distinction lying in the definition of the $\boldsymbol{K}$ matrix. The expression of $\boldsymbol{K}$ for different formulations is given as follows:

1. Conventional single-field displacement-based formulation (refer Chapter 2, Section 2.2):

$$\boldsymbol{K} = \int_{\mathcal{R}} \boldsymbol{B}^T \boldsymbol{C} \boldsymbol{B} \, \mathrm{d}\mathcal{R} \tag{7.36}$$

2. VHW-principle based EAS formulation (refer Chapter 2, Section 2.3):

$$\boldsymbol{K} = \int_{\mathcal{R}} \boldsymbol{B}^T \boldsymbol{C} \boldsymbol{B} \, \mathrm{d}\mathcal{R} - \boldsymbol{M}^T \boldsymbol{H}^{-1} \boldsymbol{M} \tag{7.37}$$

3. Two-field stress-displacement based hybrid formulation (refer Chapter 2, Section 2.4):

$$\boldsymbol{K} = \boldsymbol{G}^T \boldsymbol{H}^{-1} \boldsymbol{G} \tag{7.38}$$

If the Rayleigh damping model is assumed, then the matrix $\bar{\boldsymbol{C}}$ is evaluated using the following relation:

$$\bar{\boldsymbol{C}} = \alpha \bar{\boldsymbol{M}} + \beta \boldsymbol{K}, \tag{7.39}$$

where α and β are damping coefficients. Finally, the matrix $\bar{\boldsymbol{M}}$ and load vector $\hat{\boldsymbol{f}}$ is evaluated using the following expression:

$$\bar{\boldsymbol{M}} = \int_{\mathcal{R}} \rho \boldsymbol{R}^T \boldsymbol{R} \, \mathrm{d}\mathcal{R}, \tag{7.40}$$

$$\hat{\boldsymbol{f}} = \int_{\mathcal{R}} \boldsymbol{R}^T \boldsymbol{b} \, \mathrm{d}\mathcal{R} + \int_{\partial \mathcal{R}_t} \boldsymbol{R}^T \bar{\boldsymbol{t}} \, \mathrm{d}A, \tag{7.41}$$

where $\boldsymbol{R}$ is the matrix of NURBS interpolation functions and ρ denotes density.

After defining each entity, the hyperbolic expression given in Eq. 7.35 is solved using the Newmark method. To formulate the stated time-stepping strategy, let us introduce the variables $\hat{\boldsymbol{u}}_n$, $\dot{\hat{\boldsymbol{u}}}_n$, and $\ddot{\hat{\boldsymbol{u}}}_n$, representing the displacement, velocity, and acceleration at time t_n. Subsequently, the Newmark scheme can be expressed as follows:

$$\bar{\boldsymbol{M}} \ddot{\hat{\boldsymbol{u}}}_{n+1} + \bar{\boldsymbol{C}} \dot{\hat{\boldsymbol{u}}}_{n+1} + \boldsymbol{K} \hat{\boldsymbol{u}}_{n+1} = \hat{\boldsymbol{f}}_{n+1}, \tag{7.42}$$

$$\hat{\boldsymbol{u}}_{n+1} = \hat{\boldsymbol{u}}_n + \delta t \dot{\hat{\boldsymbol{u}}}_n + \frac{\delta t^2}{2} [(1 - 2\gamma_1) \ddot{\hat{\boldsymbol{u}}}_n + 2\gamma_1 \ddot{\hat{\boldsymbol{u}}}_{n+1}], \tag{7.43}$$

$$\dot{\hat{\boldsymbol{u}}}_{n+1} = \dot{\hat{\boldsymbol{u}}}_n + \delta t [(1 - \gamma_2) \ddot{\hat{\boldsymbol{u}}}_n + \gamma_2 \ddot{\hat{\boldsymbol{u}}}_{n+1}]. \tag{7.44}$$

After substituting Eqs. 7.43 and 7.44 into Eq. 7.42, it simplifies to the following expression:

$$\begin{aligned} \left[\bar{\boldsymbol{M}} + \gamma_2 \delta t \bar{\boldsymbol{C}} + \gamma_1 \delta t^2 \boldsymbol{K}\right] \ddot{\hat{\boldsymbol{u}}}_{n+1} = & \hat{\boldsymbol{f}}_{n+1} - \bar{\boldsymbol{C}} \left[\dot{\hat{\boldsymbol{u}}}_n + \delta t (1 - \gamma_2) \ddot{\hat{\boldsymbol{u}}}_n\right] \\ & - \boldsymbol{K} \left[\hat{\boldsymbol{u}}_n + \delta t \dot{\hat{\boldsymbol{u}}}_n + \frac{\delta t^2}{2} (1 - 2\gamma_1) \ddot{\hat{\boldsymbol{u}}}_n\right], \end{aligned} \tag{7.45}$$

where γ_1 and γ_2 define the stability and accuracy of the algorithm. The problems solved herein use $\gamma_1 = \frac{1}{4}$ and $\gamma_2 = \frac{1}{2}$, corresponding to the average acceleration (also known as the trapezoidal rule) Newmark method, which is unconditionally stable.

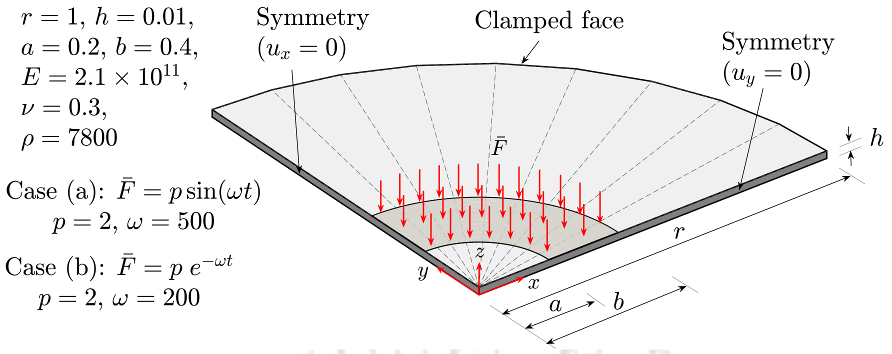

Figure 7.31: A quarter problem domain, material data, and boundary conditions for a clamped circular plate under ring pressure load.

7.7.10.1 Clamped circular plate under ring pressure load

The present example investigates the transient response of a 3D solid curved plate, constrained at its boundary and subjected to a uniformly distributed ring pressure load on its top surface. As the problem exhibits symmetry, only one-quarter of the curved plate is examined. Detailed specifications regarding the problem set-up, boundary conditions, and material parameters are presented in Fig. 7.31, where r and h denote the radius and thickness of the plate, respectively. The material parameters E, ν, and ρ represent Young's modulus, Poisson's ratio and density, respectively. The ring pressure load, denoted as $\bar{F}$, is uniformly applied at a radial distance of a to b from the origin. The structural damping is assumed to be Rayleigh damping, characterized by the relation $\boldsymbol{C} = \alpha \boldsymbol{M} + \beta \boldsymbol{K}$, where α and β are damping coefficients. The ratio r/h is chosen to be sufficiently large to introduce the effects of locking. The problem is solved for the following two cases of $\bar{F}$:

1. Sinusoidal loading: $\bar{F} = p \sin(\omega t)$ with $p = 2$ and $\omega = 500$. $\alpha = 5.517$, $\beta = 8.62 \times 10^{-6}$, $\delta t = 2 \times 10^{-4}$, $t = 0$ to 2,
2. Exponentially decaying loading: $\bar{F} = p e^{-\omega t}$ with $p = 2$ and $\omega = 200$. $\alpha = \beta = 0$, $\delta t = 10^{-4}$, $t = 0$ to 0.3,

where t is the time and δt is the time step.

The analytical solution for the vertical displacement at radial distance $\bar{r}$ and time t is given as follows [147]:

$$u_z^{\text{ref}}(\bar{r}, t) = \sum_{m=0}^{\infty} [\eta(t)]_m [U_z(\bar{r})]_m$$

The term $[U_z(\bar{r})]_m$ represents deformation modes and is evaluated using the following expression:

$$[U_z(\bar{r})]_m = J_0\left(\frac{\lambda_m \bar{r}}{r}\right) - \frac{J_0(\lambda_m)}{I_0(\lambda_m)} I_0\left(\frac{\lambda_m \bar{r}}{r}\right),$$

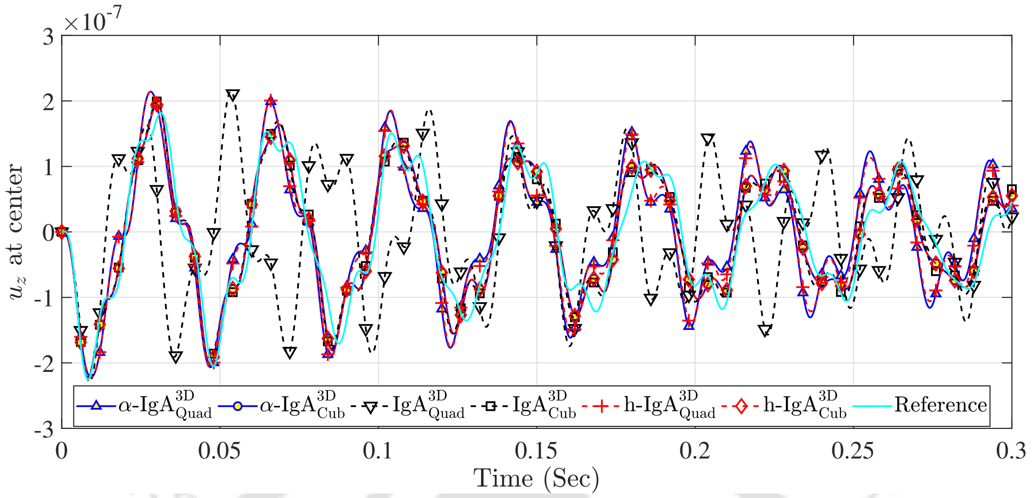

(a) u_z, Mesh: $5 \times 5 \times 1$ elements

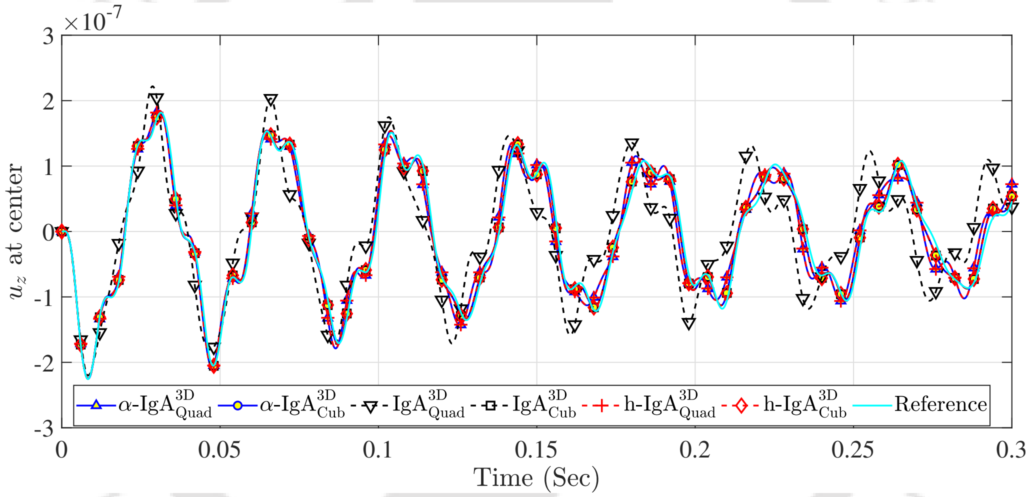

(b) u_z, Mesh: $10 \times 10 \times 1$ elements

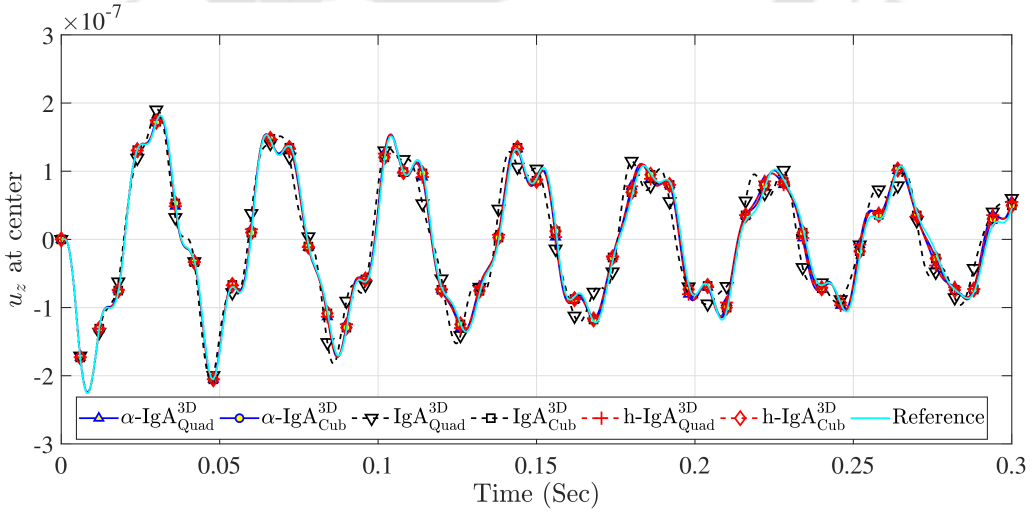

(c) u_z, Mesh: $15 \times 15 \times 1$ elements

Figure 7.32: Initial transient response of a clamped circular plate under a ring pressure load of $p\sin(\omega t)$ with $p = 2$ and $\omega = 500$ for different mesh descriptions.

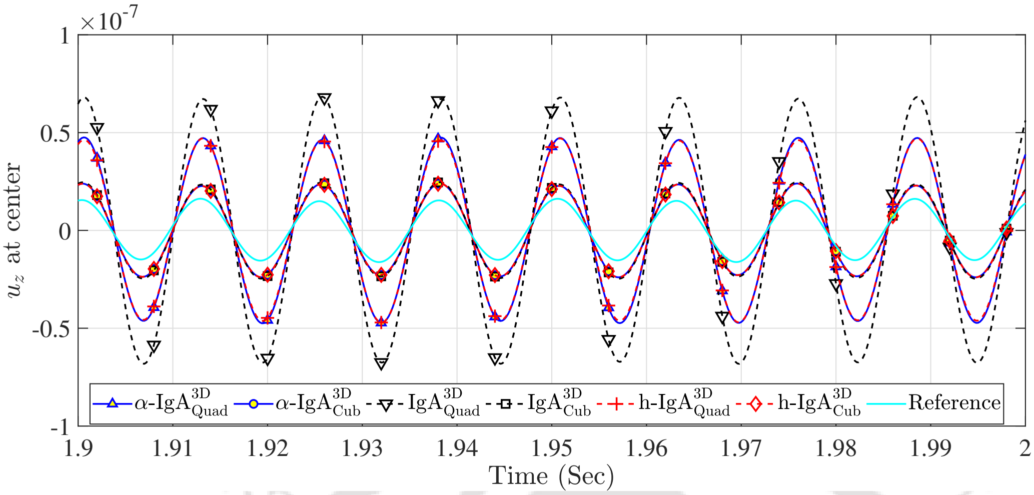

(a) u_z, Mesh: 5 × 5 × 1 elements

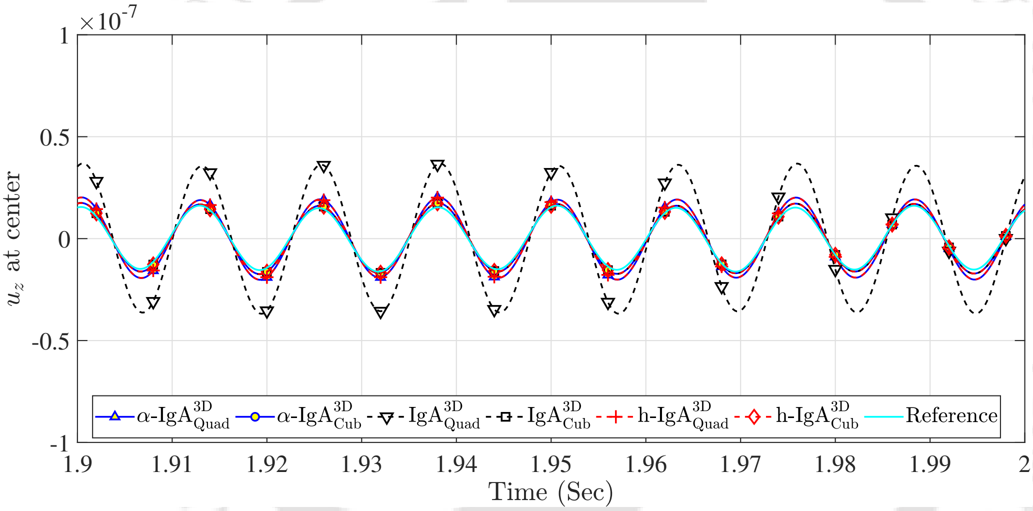

(b) u_z, Mesh: 10 × 10 × 1 elements

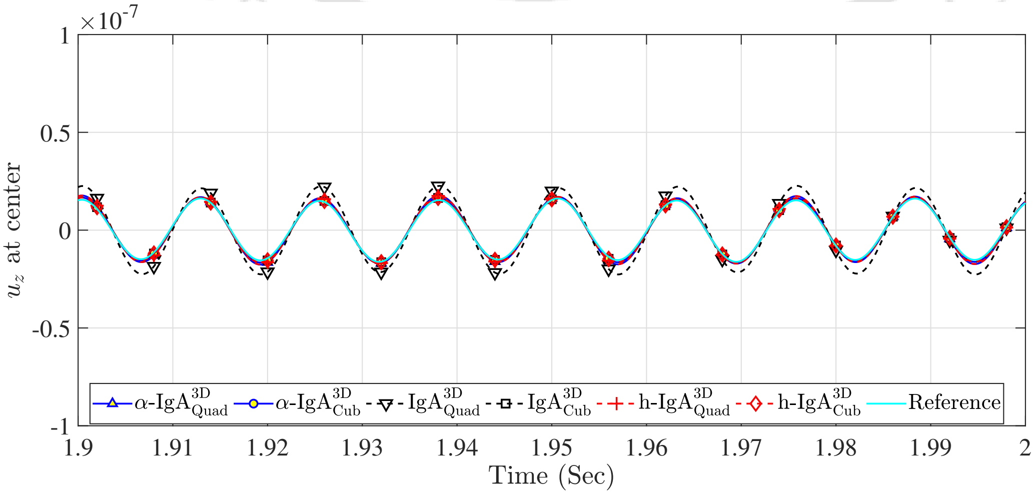

(c) u_z, Mesh: 15 × 15 × 1 elements

Figure 7.33: Periodic steady-state transient response of a clamped circular plate under a ring pressure load of $p\sin(\omega t)$ with $p = 2$ and $\omega = 500$ for different mesh descriptions.

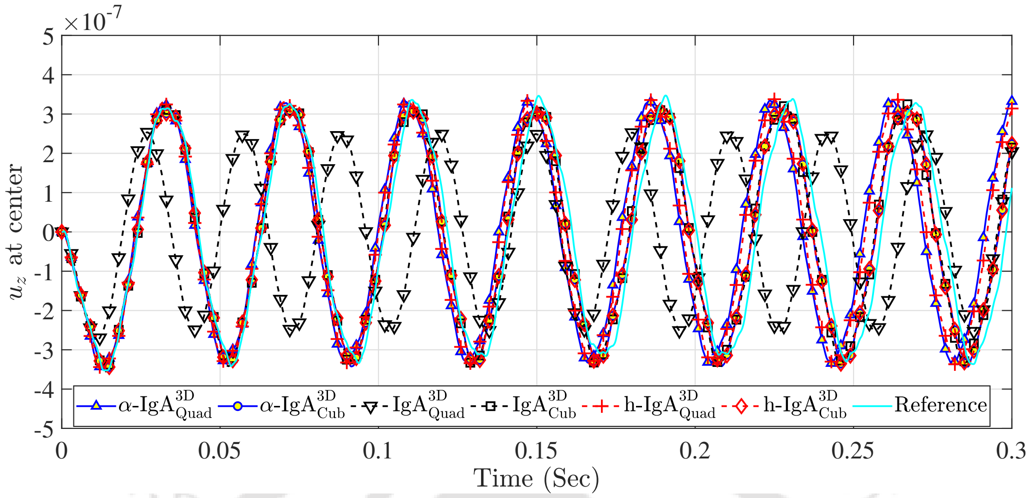

(a) u_z, Mesh: 5 × 5 × 1 elements

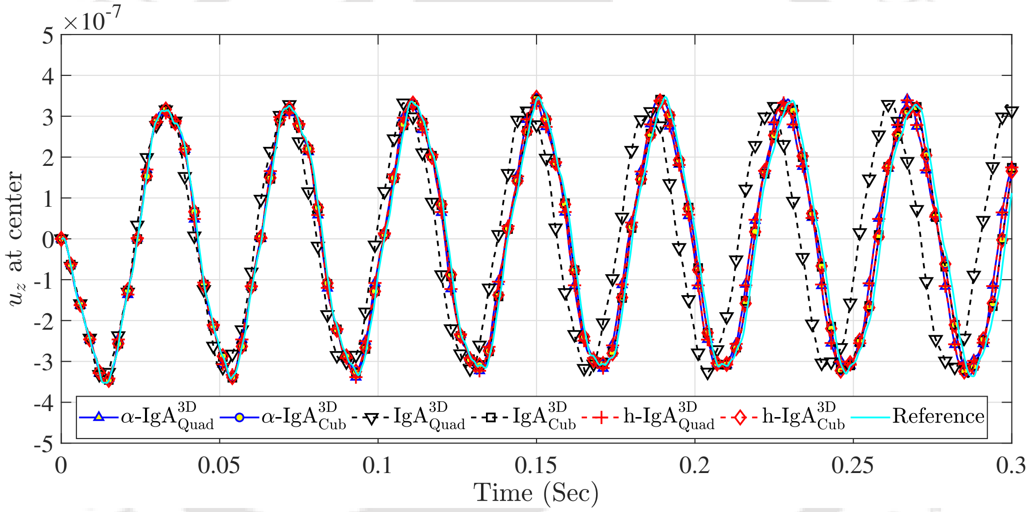

(b) u_z, Mesh: 10 × 10 × 1 elements

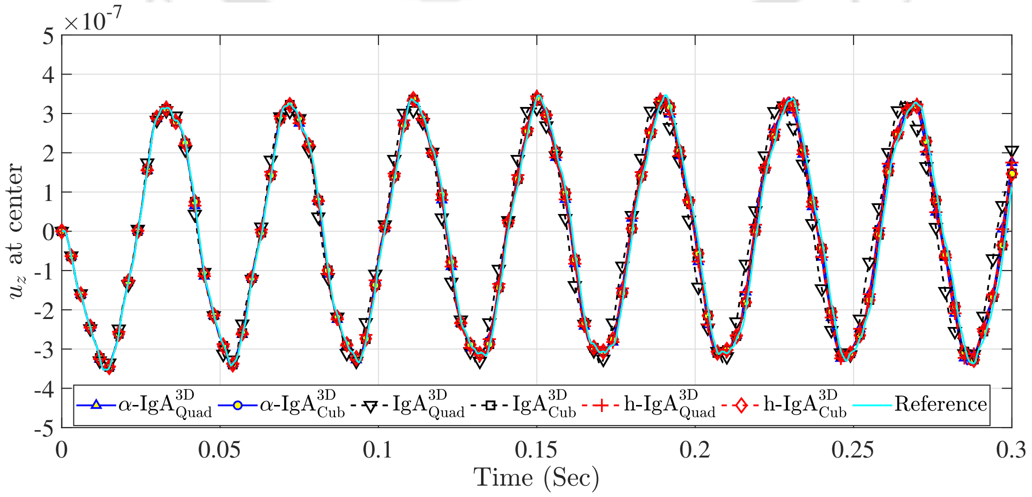

(c) u_z, Mesh: 15 × 15 × 1 elements

Figure 7.34: Periodic steady-state transient response of a clamped circular plate under a ring pressure load of $pe^{-\omega t}$ with $p = 2$ and $\omega = 200$ for different mesh descriptions.

where λ_m with $m = 1, 2, \ldots, \infty$ are the infinite roots of

$$J_0(\lambda) I_1(\lambda) + I_0(\lambda) J_1(\lambda) = 0,$$

where J_0 and I_0 represent the Bessel and modified Bessel functions of the first kind. Lastly, the term $[\eta(t)]_m$ is evaluated using the following equation:

$$[\eta(t)]_m = \frac{p D_m T_m}{r \rho h S_m},$$

where

$$D_m = \frac{\left[b J_1 \left(\frac{\lambda_m b}{r} \right) - a J_1 \left(\frac{\lambda_m a}{r} \right) \right] - C_m \left[b I_1 \left(\frac{\lambda_m b}{r} \right) - a I_1 \left(\frac{\lambda_m a}{r} \right) \right]}{\gamma_m \lambda_m J_0^2(\lambda_m)},$$

$$C_m = \frac{J_0(\lambda_m)}{I_0(\lambda_m)},\ \gamma_m = \omega_m \sqrt{1 - \zeta_m^2},\ \zeta_m = \frac{\alpha + \beta \omega_m^2}{2\omega_m},\ \omega_m = \frac{\lambda_m^2}{r^2} \sqrt{\frac{D}{\rho h}},\ D = \frac{E h^3}{12(1 - \mu^2)}.$$

For the first case, when $\bar{F} = p \sin(\omega t)$, the expressions for T_m and S_m are given as follows:

$$\begin{aligned}
T_m = {} & \gamma_m \left[(\omega_m^2 - \omega^2) \sin(\omega t) - 2 \zeta_m \omega_m \omega \cos(\omega t) \right] + \\
& e^{-\zeta_m \omega_m t} \left[\omega (\zeta_m^2 \omega_m^2 + \omega^2 - \gamma_m^2) \sin(\gamma_m t) + 2 \zeta_m \omega_m \omega \gamma_m \cos(\gamma_m t) \right], \\
S_m = {} & \zeta_m^4 \omega_m^4 + (\omega^2 - \gamma_m^2)^2 + 2 \zeta_m^2 \omega_m^2 (\omega^2 + \gamma_m^2),
\end{aligned}$$

whereas, for the second case, when $\bar{F} = p e^{-\omega t}$, T_m and S_m are given as follows:

$$\begin{aligned}
T_m &= e^{-\zeta_m \omega_m t} \left[(\omega - \zeta_m \omega_m) \sin(\gamma_m t) - \gamma_m \cos(\gamma_m t) \right] + \gamma_m e^{-\omega t}, \\
S_m &= (\omega - \zeta_m \omega_m)^2 + \gamma_m^2.
\end{aligned}$$

The geometric description to design the coarse mesh is defined in the Appendix (Table B.10). After defining the coarse mesh, further refinement is carried out using h- or k- refinement. The meshes used to solve the problem are defined as $n_{\text{ele}}^r \times n_{\text{ele}}^\theta \times n_{\text{ele}}^h$, where n_{ele}^r, n_{ele}^θ, and n_{ele}^h are the number of elements in the radial, circumferential, and thickness direction, respectively. The mesh is refined in the r and θ directions with values of $n_{\text{ele}}^r = n_{\text{ele}}^\theta = 5, 10, 15, 20, 25$, while n_{ele}^h is kept constant at 1.

The proposed elements are evaluated by assessing the vertical displacement at the center of the plate for both loading cases. Average acceleration Newmark method is utilized as a time-stepping strategy to solve the problem. In the case of sinusoidal loading, the transient responses during the initial period ($t = 0$ to 0.3) and the periodic steady-state phase ($t = 1.9$ to 2) are compared against the analytical solution, see Figs. 7.32 and 7.33. The results show that the proposed α-IgA$_{\text{Quad}}^{\text{3D}}$ exhibits higher accuracy on coarse meshes compared to IgA$_{\text{Quad}}^{\text{3D}}$ elements. To quantify the error, the

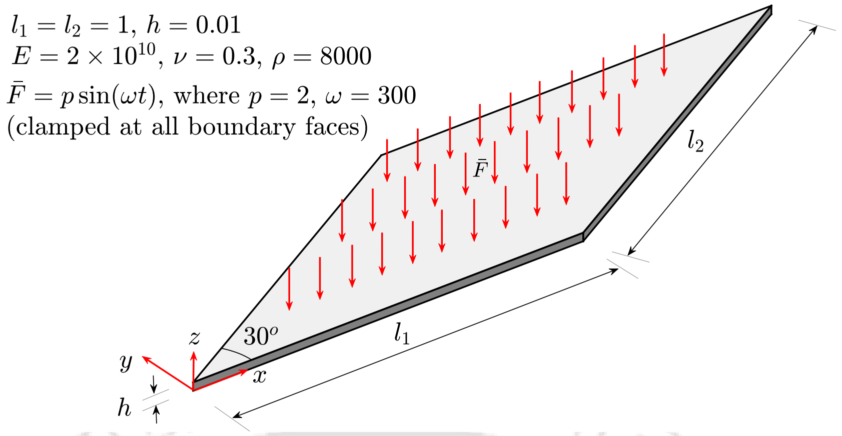

Figure 7.35: A problem set-up, material data, and boundary conditions for a clamped skew plate subjected to uniform pressure load.

L_2 error norm for vertical displacement at the center of the plate over time is evaluated using the following expression:

$$\bar{L}_2^{u_z} = \frac{\|u_z - u_z^{\text{ref}}\|}{\|u_z^{\text{ref}}\|} = \left[\frac{\sum_{i=1}^{n}[(u_z)_i - (u_z^{\text{ref}})_i]^2}{\sum_{i=1}^{n}[(u_z^{\text{ref}})_i]^2}\right]^{\frac{1}{2}}, \tag{7.46}$$

where n represents the number of time intervals corresponding to the chosen start time, time step, and end time.

The results show that in the case of the initial transient response (Fig.7.32c), a mesh of $15 \times 15 \times 1$ α-IgA$^{\text{3D}}_{\text{Quad}}$ elements converge with a $\bar{L}_2^{u_z}$ error of 9.3430 %, whereas IgA$^{\text{3D}}_{\text{Quad}}$ elements performs less favorably with $\bar{L}_2^{u_z}$ error of 28.5722 %. The $\bar{L}_2^{u_z}$ errors for higher-order α-IgA$^{\text{3D}}_{\text{Cub}}$ and IgA$^{\text{3D}}_{\text{Cub}}$ elements are comparable, with values of 5.0911 % and 5.1480 %, respectively. Similarly, in the case of steady-state response and for the same mesh (Fig. 7.33c), α-IgA$^{\text{3D}}_{\text{Quad}}$ elements shows $\bar{L}_2^{u_z}$ error of 10.9759 %, whereas IgA$^{\text{3D}}_{\text{Quad}}$ converges with 44.5369 % error. The α-IgA$^{\text{3D}}_{\text{Cub}}$ and IgA$^{\text{3D}}_{\text{Cub}}$ elements shows $\bar{L}_2^{u_z}$ error of 5.3132 % and 5.4004 %, respectively.

Similar improvements are observed in the case of exponentially decaying loading, see Fig. 7.34. In this situation as well, a mesh of $15 \times 15 \times 1$ elements α-IgA$^{\text{3D}}_{\text{Quad}}$ elements converges to the analytical solution with $\bar{L}_2^{u_z}$ error of 11.4826 %, whereas IgA$^{\text{3D}}_{\text{Quad}}$ elements exhibits 24.8673 % error. Higher-order elements are less susceptible to locking and show comparable performance.

7.7.10.2 Clamped skew plate subjected to uniform pressure load

In the present example, the dynamic response of a skewed plate is investigated. The problem is composed of a rhomboid plate constrained at its boundary and subjected

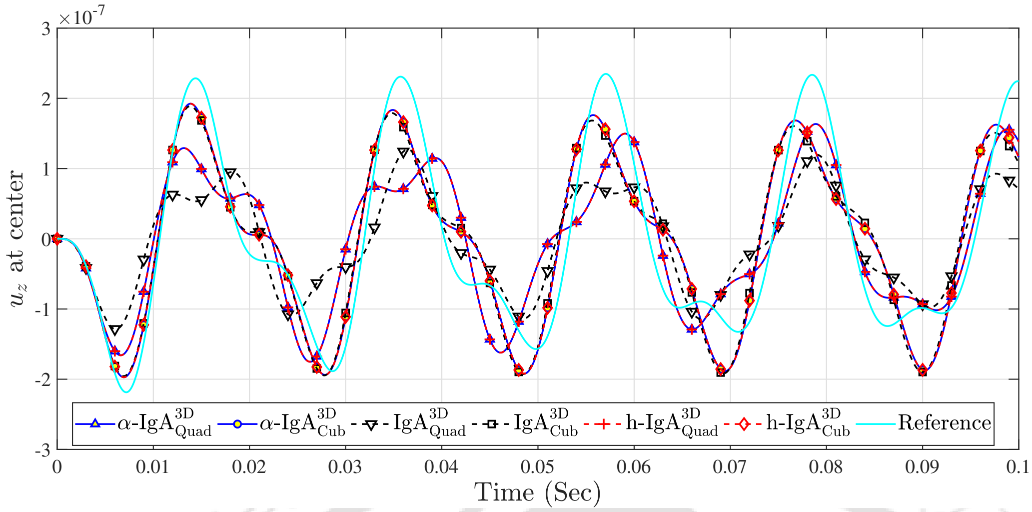

(a) u_z, Mesh: $8 \times 8 \times 1$ elements

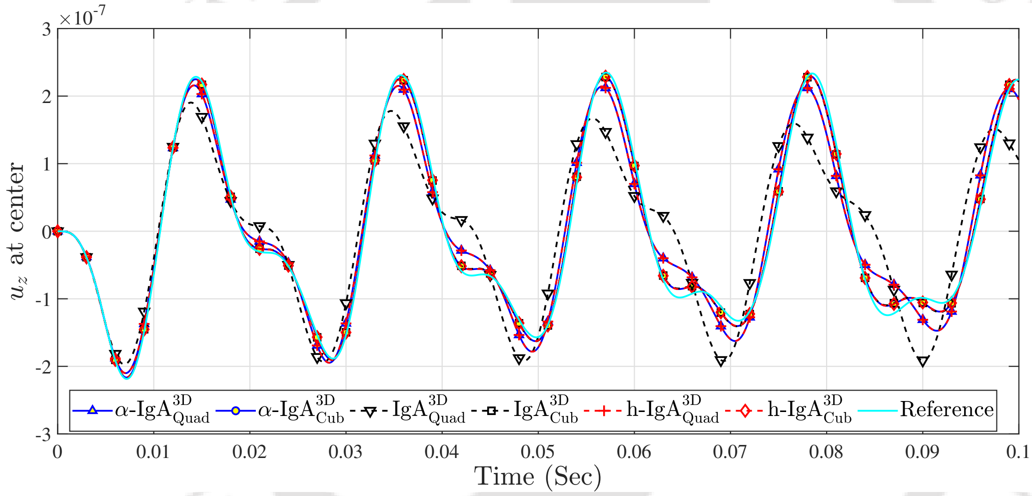

(b) u_z, Mesh: $16 \times 16 \times 1$ elements

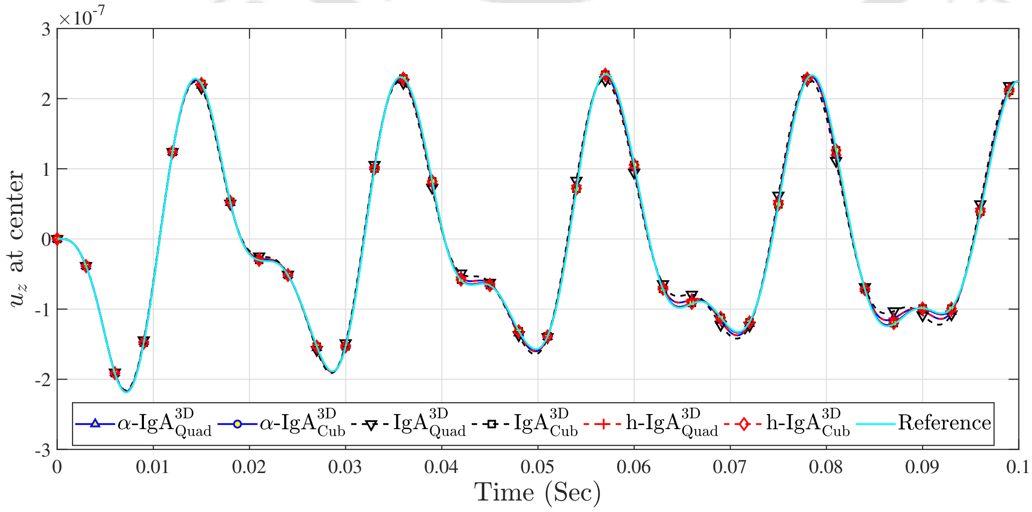

(c) u_z, Mesh: $32 \times 32 \times 1$ elements

Figure 7.36: Dynamic response of a clamped skew plate subjected to uniform pressure load of $p\sin(\omega t)$ with $p = 2$ and $\omega = 300$ for different mesh descriptions.

Table 7.2: Percentage $\bar{L}_2^{u_z}$ error for different mesh configurations for a clamped skew plate subjected to uniform pressure load.

Mesh	Quadratic basis			Cubic basis		
	$\text{IgA}^{3\text{D}}_{\text{Quad}}$	$\alpha\text{-IgA}^{3\text{D}}_{\text{Quad}}$	$\text{h-IgA}^{3\text{D}}_{\text{Quad}}$	$\text{IgA}^{3\text{D}}_{\text{Cub}}$	$\alpha\text{-IgA}^{3\text{D}}_{\text{Cub}}$	$\text{h-IgA}^{3\text{D}}_{\text{Cub}}$
$4 \times 4 \times 1$	88.9389	75.4218	75.4218	57.6508	57.0123	57.0123
$8 \times 8 \times 1$	59.2256	51.9277	51.9277	44.2076	41.3329	41.3329
$16 \times 16 \times 1$	44.5630	18.8739	18.8739	5.5675	5.2278	5.2278
$32 \times 32 \times 1$	6.7256	3.1181	3.1181	0.6167	0.5873	0.5873

to a uniformly distributed load on its top surface. The detailed problem configuration, boundary conditions, and material parameters are presented in Fig. 7.35, where l and h denote the length and thickness of the plate, respectively. The material parameters E, ν, and ρ represent Young's modulus, Poisson's ratio and density, respectively. Rayleigh structural damping is assumed, with α and β as damping coefficients. The problem is solved for a time interval of 0 to 0.1 with the time steps (δt) as 10^{-4} utilizing the average acceleration Newmark strategy.

The geometric description to design the coarse mesh is defined in the Appendix (Table B.11). Successive refinement is carried out using h- or k- refinement. The meshes used to solve the problem are defined as $n_{\text{ele}}^{l_1} \times n_{\text{ele}}^{l_2} \times n_{\text{ele}}^{h}$, where $n_{\text{ele}}^{l_1}$ and $n_{\text{ele}}^{l_2}$ are the number of elements along the side of length l_1 ans l_2, respectively. n_{ele}^{h} represents the number of elements in thickness direction. The problem is refined uniformly by considering $n_{\text{ele}}^{l_1} = n_{\text{ele}}^{l_2} = 2,\ 4,\ 8,\ 16,\ 32$, while n_{ele}^{h} is kept constant at 1.

The vertical displacement at the center of the plate is computed within a specified time interval using defined time steps. The results corresponding to various mesh descriptions are shown in Fig. 7.36. Given the unavailability of an analytical solution for this problem, the reference solution is established using the solution obtained from a fine mesh of $1 \times 40 \times 40$ $\text{h-IgA}^{3\text{D}}_{\text{Cub}}$ elements. Similar to previous example, $\bar{L}_2^{u_z}$ error norm is evaluated using the Eq. 7.46 and results are tabulated in the Table 7.2. Results show exact equivalence between the results obtained by α-IgA and h-IgA elements. Furthermore, it consistently highlight the improved performance of $\alpha\text{-IgA}^{3\text{D}}_{\text{Quad}}$ elements over $\text{IgA}^{3\text{D}}_{\text{Quad}}$ elements. The higher-order elements yield comparable results, with $\alpha\text{-IgA}^{3\text{D}}_{\text{Cub}}$ elements exhibiting marginally better performance than $\text{IgA}^{3\text{D}}_{\text{Cub}}$ elements.

7.8 Summary

In the present work, strain-based EAS elements are proposed to alleviate locking in IGA. The key highlight is the evaluation of enhanced strain interpolation functions through the investigation of the interrelation between the two-field HR and three-field VHW variational formulations. The present work largely focuses on the assessment of proposed quadratic and cubic EAS elements in 2D and 3D regime. However, the methodology outlined in this work is generalized and can be employed to generate a variety of EAS elements from their corresponding stress-based elements in a systematic framework.

The efficacy of the proposed elements is demonstrated through a comprehensive analysis of numerous benchmark examples. Results obtained from diverse linear elasticity problems show that the proposed elements provides a locking-free response in situations that are characterized by high aspect ratios or near-incompressibility of the domain. Observations across various problems shows that the proposed elements show substantially high coarse mesh accuracy for the α-IgA$^{\text{3D}}_{\text{Quad}}$ and α-IgA$^{\text{2D}}_{\text{Quad}}$ elements. The higher-order elements, either α-IgA$^{\text{3D}}_{\text{Cub}}$, α-IgA$^{\text{2D}}_{\text{Cub}}$, IgA$^{\text{3D}}_{\text{Cub}}$ or IgA$^{\text{2D}}_{\text{Cub}}$ are less affected by locking; however, α-IgA$^{\text{3D}}_{\text{Cub}}$ and α-IgA$^{\text{2D}}_{\text{Cub}}$ provides comparatively better coarse mesh accuracy than its conventional IGA counterpart in certain situations. Moreover, while comparing the performance with existing EAS elements, it is observed that these elements require supplementary stabilization techniques to converge to the solution in non-locking scenarios. Further, in specific instances of locking, these elements shows hourglass modes, indicating that they are not entirely immune to locking. On the other hand, the proposed elements shows no such anomaly and consistently exhibit stable behavior regardless of whether the problem is susceptible to locking or not. This complements the overall robustness of the elements and highlights its applicability across a broad spectrum of problems in NURBS-based IGA.

Chapter 8

Conclusions and Scope for Future Work

This chapter summarizes the key findings and conclusions derived from the work conducted to address each objective outlined in Section 1.8, subsequently presenting conclusions based on the contributions and outcomes derived from it. Finally, the chapter provides an outlook on various potential directions for future research, followed by a list of publications derived from the current work.

8.1 Performance evaluation of various numerical strategies to alleviate shear, membrane, and volumetric locking

In the present work, a comprehensive performance evaluation of various FE strategies, that are developed to alleviate locking, is conducted. The strategies under evaluation are VHW principle-based EAS, a specific class of HR principle-based hybrid formulation, SRI, ANS, and the conventional FE formulation. It begins by discussing the fundamental concepts, such as additional constraints, modified weak forms, and stress/enhanced strain interpolation functions, along with the step-wise implementation procedures, highlighting their distinctions from conventional FE formulation. Subsequently, the performance of these FE strategies is assessed by the evaluation of normalized displacement against the reference solution and the relative L_2 error norms of displacement and stress on numerous benchmark examples. The study provides a comprehensive understanding of the optimal method for locking-dominated problems by scrutinizing each method for its applicability, robustness, and efficiency.

The results obtained for each numerical example and the comparative performance of individual methods lead to the following conclusions:

1. The SRI approach provides high convergence rates in the problems affected by volumetric locking. However, the method is restricted to alleviate volumetric locking in conventional solid elements. The method's effectiveness lies in how

efficiently we can isolate the part that is responsible for locking. This separation is not possible for other types of locking in solid elements. Hence, the method is less robust and applicability is restricted to compatible problem domains.

2. The classical ANS method is restricted to problems affected by shear locking. The extension of the method to the 3D problems is not a viable option as the elements developed show no considerable improvement over conventional elements.
3. The EAS method based on VHW and hybrid formulation based on the HR principle performs effectively and consistently irrespective of the type of locking.
4. The EAS method provides equivalent accuracy in many cases but is marginally inferior to hybrid elements in certain situations. However, EAS elements exhibit greater stability in severely distorted meshes compared to the presented class of hybrid elements.

8.2 Development of a novel family of EAS elements to alleviate locking in FEA

Next, the work explores the EAS elements that are commonly utilized in the literature to address locking. Notably, the existing literature in the context of 3D elasticity problems is predominantly restricted to the eight-node linear EAS elements. Thus, existing 3D EAS elements do not exploit the superior performance offered by quadratic elements over linear elements. Motivated by this research gap, three novel strain-based EAS elements are introduced: twenty-seven-node hexahedral, six-node wedge, and eighteen-node wedge EAS elements. A systematic procedure for deriving enhanced strain interpolation is presented in the study which utilizes the the interrelation between the two-field HR and three-field VHW variational formulations. Lastly, the robustness and performance of the proposed EAS elements are demonstrated through numerous examples, with the following conclusions:

1. The proposed twenty-seven node hexahedral, six-node wedge, and eighteen-node wedge EAS elements successfully alleviate the locking in FEA.
2. The proposed twenty-seven node hexahedral EAS elements offer the combined benefits of the EAS formulation and quadratic elements while demonstrating higher accuracy on coarse meshes, yielding results without any stress oscillations, and devoid of any unstable behavior.
3. Compared to existing eight-node brick EAS elements, the twenty-seven node hexahedral EAS elements deliver improved or similar performance, making it a compelling alternative to existing options.
4. The proposed six-node and eighteen-node wedge EAS elements effectively mitigate the stress oscillations in locking-dominated domains.

5. The methodology outlined is generic and can be employed to generate a variety of EAS elements from their corresponding stress-based elements in a systematic manner.

8.3 Development of HR principle-based stress-displacement formulation to alleviate locking in NURBS-based IGA

The study further explores the issue of locking in IGA. Notably, most of the explored contributions in the development of locking-free mixed formulations in IGA are restricted to strain-based approaches. The potential advantages of stress-based approaches, that have successfully distinguished themselves in FEA, are not explored in IGA. Motivated by this, the work introduces a family of stress-based hybrid solid elements, with a specific emphasis on quadratic and cubic NURBS-based elements, to alleviate locking in IGA. The key highlight of the present work is the evaluation of stress interpolation functions for HR principle-based hybrid elements in NURBS-based IGA. Furthermore, the study showcases the efficacy and robustness of the proposed elements through the treatment of several 2D and 3D linear-elastic benchmark problems, alongside conventional single-field IGA, Lagrangian-based FEA, and hybrid FEA formulations.

Based on the results presented in Chapter 6, the following conclusions are drawn:

1. The study presents a systematic procedure to evaluate the feasible stress interpolation functions for different order NURBS-based elements.
2. Proposed stress-displacement based hybrid elements provide a locking-free response in problems having a high aspect ratio or near-incompressibility of the domain.
3. It is mathematically shown that the proposed elements are free of any spurious zero-energy modes.
4. The proposed elements effectively eliminate the stress oscillations and provide better coarse mesh accuracy than its conventional IGA counterpart.
5. The formulation is generic and does not involve any kinematic assumptions. This allows the effective implementation of proposed elements in 'thin' as well as 'chunky' geometries without any special treatment, which further complements the robustness of the method.

8.4 Development of a robust family of strain-based EAS elements to alleviate locking in NURBS-based IGA

Extending the work on locking alleviation techniques in IGA, the study shifts towards strain-based approaches, specifically exploring the EAS method. The existing literature primarily includes 2D EAS elements that are developed to address volumetric locking in IGA. However, these elements necessitate an additional stabilization strategy to address non-locking scenarios and are ineffective in mitigating shear and membrane locking. Motivated by this research gap, the subsequent part of our work introduces a robust class of strain-based solid EAS elements tailored for NURBS-based IGA. This is achieved by extending the concepts developed during the derivation of the proposed EAS element in the context of FEA to IGA. The performance of these elements is evaluated through several benchmark numerical examples covering static and transient problems. Based on the findings presented in Chapter 7, the following conclusions are drawn:

1. A systematic procedure to evaluate the enhanced strain interpolation functions, through the investigation of the interrelation between the two-field HR and three-field VHW variational formulations, is presented.
2. The proposed elements provide a locking-free response during the analysis of thin structural geometries or problems involving near-incompressible materials.
3. The proposed elements effectively eliminate stress oscillations, provide higher accuracy on coarse meshes and consistently exhibit stable behavior across a broad spectrum of problems in NURBS-based IGA.
4. In comparison to the existing EAS elements, the proposed elements do not necessitate a supplementary stabilization technique to perform effectively in non-locking scenarios. Moreover, in certain locking situations where existing EAS elements have shown hourglass modes, such issues are non-existent in the proposed elements.

8.5 Summary of the contributions of the thesis

A comprehensive evaluation of various locking alleviation strategies is carried out by investigating them for several parameters to establish an elaborate understanding of the optimal choice of the method in locking-dominated problems. Further, three novel strain-based EAS elements, namely twenty-seven node hexahedral, six-node wedge, and eighteen-node wedge EAS elements are proposed to alleviate the locking effects in conventional FEA. These elements offer combined benefits of the EAS formulation and quadratic elements, showcasing superior accuracy on coarse meshes, producing results without stress oscillations, and ensuring stability throughout the analysis. As a result, they substantially enhance the applicability of EAS elements in the FEA community.

Additionally, the current work proposes novel quadratic and cubic stress-based solid hybrid elements and strain-based EAS elements for NURBS-based IGA to effectively address locking. Through extensive assessment of several standard examples, it is demonstrated that both the families of proposed elements consistently deliver locking-free responses, particularly in problems characterized by high aspect ratios or near-incompressibility of the domain. The proposed elements can be effectively used in ‘thin’ as well as ‘chunky’ geometries without any special treatment, which further complements the robustness of the elements. These elements marks a progressive advancement in enhancing the versatility of IGA, broadening their potential within the computational mechanics community.

8.6 Scope for future work

In the present section, various potential extensions and opportunities for the development of the current research are discussed. The prospective scope, aligning with the research outlined in this thesis, is broadly classified into two categories. In the first category, the efforts will be directed toward the development of elements specifically designed to alleviate locking. The emphasis lies on advancing the current understanding and exploring other methodologies to effectively address and mitigate locking issues. In the second category, our focus shifts towards the application of the proposed elements across a diverse spectrum of domains. This involves a systematic exploration of their performance in diverse applications to gain deeper insights into the capabilities of the proposed elements, thereby contributing to their broader utilization in the computational mechanics community.

8.6.1 Development of axisymmetric elements to address locking

Axisymmetric elements are particularly useful for problems involving cylindrical or rotationally symmetric geometries. While there exists literature wherein the framework of IGA is employed to develop IGA axisymmetric elements for various applications [191–197], the efforts to alleviate locking in such elements has received limited attention. Drawing from our experience in stress-based hybrid elements for NURBS-based IGA (refer to Chapter 6), we believe that extending the study to develop axisymmetric hybrid NURBS-based elements is a viable option. Furthermore, building on the methodology discussed in Chapter 4 and 7, where the equivalence between the two-field stress-based HR and VHW-based EAS formulations is investigated, there is potential for the development of axisymmetric EAS elements in IGA and FEA.

8.6.2 Locking in shell elements

While shell elements are specifically designed for relatively thin geometries, they are not entirely immune to locking. They do exhibit signs of shear and membrane locking in thin structures and experiences volumetric locking in the incompressible range [32, 125, 139, 144, 145, 198, 199]. However, the issue of locking in such situations can also be effectively addressed through the implementation of mixed formulations [32, 139, 199]. Therefore, looking ahead, it is possible to extend the concepts investigated in the current study to shell elements by formulating a viable space of interpolation functions within the selected mixed formulation. This notion is further supported by the observation that the interpolations derived in Chapter 6, in specific cases, align with interpolations derived for certain shell elements in the work of Echter et al. [32, 146] to address the membrane locking. This presents an opportunity to extend research not only in the development of locking-free shell elements in FEA but also in IGA.

8.6.3 Time complexity

Based on our experience in the current study, we recognize that achieving a fair comparison of computational time is a formidable challenge. The complexities lie in various aspects, such as the efficiency of coding, selection of solvers, data management, and other factors. Even a slight alteration in the formulation often requires a large reconstruction of the code to optimize the computational resources.

Though a comprehensive FE code involves numerous steps, solver time plays an important role. As we progress toward higher levels of refinement, the dominant factor influencing computational time shifts towards the evaluation of the system of linear equations hence diminishing the difference in total time required for both conventional and mixed-formulation based elements. This is attributed to the fact that the time required to compute the local stiffness scales linearly with the degrees of freedom (N^u_{dof}), whereas the time to solve $\boldsymbol{K}\hat{\boldsymbol{u}} = \hat{\boldsymbol{f}}$ scales nonlinearly with N^u_{dof}. Acknowledging this, in future work, we could concentrate on understanding how the mixed-formulation influences the stiffness matrix properties and explore alternative solvers tailored for these elements.

8.6.4 Application oriented future work

The present section briefly discusses another avenue for the development or extension of the present work, where the emphasis is on the application of the proposed elements to diverse engineering fields. This aims to enhance our understanding of the capabilities and limitations of the proposed elements, which could provide insights for further improvements.

8.6.4.1 Performance assessment of locking alleviation strategies in IGA

A promising initial step in this direction involves initiating a comparative assessment of various methods designed to address locking in IGA, including the elements proposed in this work. There are currently no studies that focus on the relative accuracies of individual methods, the shortcomings of the available strategies, and the parameters deciding the selection of a particular method in the context of IGA. Therefore, such efforts would provide a valuable resource by offering a comparative perspective on various locking alleviation strategies. The primary focus could be testing various locking alleviation strategies for suitability in different locking situations, robustness, and efficiency. The findings will potentially facilitate the optimal choice of technique in the chosen problem domain in the context of IGA.

8.6.4.2 Non-linear locking dominated problems

Another potential progression in the expansion of the current work involves the assessment of the proposed elements for non-linear analysis of elastic structures in locking-dominated situations. This could consists both geometric and material non-linearity. In literature, it has been shown that stress-based hybrid elements exhibit promising advantages compared to conventional elements in the context of non-linear FEA [142, 200]. Given that the proposed NURBS-based hybrid elements are developed on a similar structure, we anticipate similar advantages. Moreover, there is a possibility that these advantages could be more pronounced, owing to the strengths of IGA in conjunction with existing advantages. Similarly, it also presents an opportunity to evaluate the proposed EAS elements in both FE and IGA frameworks for non-linear analysis of structures.

8.6.4.3 Contact mechanics

The contact problems involving thin structures and nearly incompressible materials are prone to locking and require a significant computational effort to solve the problem. To address this issue, stress-based hybrid elements have shown great potentials in context of FE [148]. Furthermore, the application of IGA in contact mechanics has yielded favorable results compared to conventional FE formulations [22]. However, implementing IGA framework does not guarantee a locking-free response while analyzing thin structures or nearly incompressible materials. Therefore, we believe that the application of the proposed stress-based hybrid NURBS-based elements or strain-based EAS IGA elements could be a promising choice in such situations. These elements can offer a combined advantage of IGA and mixed formulation, potentially providing better solution quality.

8.6.4.4 Electromagnetic analysis

Utilizing conventional FE formulation for solving Maxwell's equations in electromagnetics has certain limitations. These include issues like the presence of spurious modes and the inability to predict singular eigenvalues in non-convex domains [151]. In addressing these limitations, mixed formulations have shown promising results by accurately predicting eigenfrequencies, including their multiplicities, even in non-convex domains [151]. Further, the extension of IGA to electromagnetic problems has demonstrated various advantages. These include the ability to handle complex geometries, spectrally correct discretization of the Maxwell PDEs, and higher accuracy per degree of freedom [201–203]. However, the potential advantages of combining mixed formulation with IGA remain unexplored in the context of electromagnetics. This presents an opportunity to extend the insights gained from the current work to the field of electromagnetics and potentially utilize the strengths of both approaches to offer an attractive alternative for solving the problems.

8.6.4.5 Biomechanics

Biomechanics stands as another promising frontier where the potential of IGA has been prominently highlighted. The characteristics of IGA, including its capability to model precise geometry, high continuity of interpolation functions, efficient handling of complex geometries, and accurate representation of sliding contact between smooth surfaces, have proven to be invaluable tools in modeling physiologically realistic intricate biostructures [204–209]. One category of these biostructures comprises thin biological membranes such as skin, alveoli, blood vessels, and heart valves. The application of conventional FE or IGA formulations in such cases leads to locking and requires substantial computational efforts to address these challenges. To overcome this, efforts have been made to incorporate isogeometric shell elements, which combine the advantages of IGA and shell theories, to study the response of thin biological membranes [210, 211]. Moreover, the mechanical behavior of such biological structures is often modeled as incompressible hence making the simulation susceptible to volumetric locking [210, 212]. Hence, the combination of complex geometry, thin structure, and nearly incompressible material behavior makes it an ideal situation to extend the current work and assess the performance of the proposed isogeometric stress-based hybrid and strain-based EAS elements.

The potential future avenues listed above do not encompass all possible applications where we envision the extension of the current work. However, they provide a glimpse into the diverse possibilities for extending the current work. Essentially, in any domain where mixed FE formulations have demonstrated advantages, there exists an opportunity to explore the synergy between IGA and mixed formulations. This integration has the potential to enhance performance and offer innovative solutions in diverse engineering applications.

8.7 List of publications

Journals

1. **D. S. Bombarde**, S. S. Gautam, A. Nandy, “A novel hybrid isogeometric element based on two-field Hellinger–Reissner principle to alleviate different types of locking”, *Sadhana* (2022), 47:148.
   `https://doi.org/10.1007/s12046-022-01867-6`
2. **D. S. Bombarde**, M. Agrawal, S. S. Gautam, A. Nandy, “Hellinger–Reissner principle based stress–displacement formulation for three-dimensional isogeometric analysis in linear elasticity”, *Computer Methods in Applied Mechanics and Engineering* 394 (2022) 114920.
   `https://doi.org/10.1016/j.cma.2022.114920`

3. **D. S. Bombarde**, M. Agrawal, S. S. Gautam, A. Nandy, “Development of quadratic enhanced assumed strain elements for three-dimensional linear elasticity”, *Computers and Structures* 291 (2024) 107217.
   https://doi.org/10.1016/j.compstruc.2023.107217.
4. **D. S. Bombarde**, S. L. Narayan, S. S. Gautam, A. Nandy, “A comprehensive comparative review of various advanced finite elements to alleviate shear, membrane and volumetric locking”, *Archives of Computational Methods in Engineering.* **(In Press)**
5. **D. S. Bombarde**, M. Agrawal, S. S. Gautam, A. Nandy, “Development of enhanced assumed strain elements for alleviating locking in NURBS-based isogeometric analysis”. **(Under preparation)**

Book chapters

1. **D. S. Bombarde**, A. Nandy, and S. S. Gautam, “A two-field formulation in isogeometric analysis to alleviate locking,” *in Advances in Engineering Design, Lecture Notes in Mechanical Engineering*, pp.191-199, Springer, Singapore, 2021.
   https://doi.org/10.1007/978-981-33-4684-0_20.
2. S. L. Narayan, **D. S. Bombarde**, S. S. Gautam, A. Nandy, “Comparison of Selective Reduced Integration, Enhanced Assumed Strain and Assumed Natural Strain Formulation in Alleviating Locking,” in *Recent Advances in Mechanical Engineering, Lecture Notes in Mechanical Engineering*, pp.643-654, Springer, Singapore, 2022.
   https://doi.org/10.1007/978-981-19-2188-9_58

Conferences

1. **D. S. Bombarde**, S. S. Gautam, and A. Nandy, “A Two-Field Variation Technique in Isogeometric Analysis to Alleviate Locking,” 14th World Congress on Computational Mechanics (WCCM) ECCOMAS Congress 2020, Paris, France, January 11-15, 2021.
2. **D. S. Bombarde**, S. S. Gautam, and A. Nandy, “Stress and strain-based mixed formulations in NURBS-based isogeometric analysis,” 16th International Conference on Computational Plasticity. Fundamentals and Applications (COMPLAS 2021), Barcelona-Spain, September 7-10, 2021.
3. **D. S. Bombarde**, M. Agrawal, S. S. Gautam, A. Nandy, “A locking-free formulation for three-dimensional isogeometric analysis,” *Materials Today: Proceedings*, 66 (4), pp.1710-1715, 2022.
   https://doi.org/10.1016/j.matpr.2022.05.266

Appendices

Appendix A

Essential algorithms

The chapter introduces essential supporting algorithms that enhance the overall completeness of the thesis. These algorithms cover step-wise implementation procedures for the methods discussed in Chapter 2, in particularly the VHW principle-based EAS method, the HR principle-based hybrid formulation, and the Generalized ANS method. Additionally, the chapter presents Mathematica pseudocodes, offering step-by-step guidance for generating a compatible enhanced strain interpolation matrix and deriving symbolic expressions for NURBS basis functions.

Algorithm 1: An algorithm for implementing the EAS formulation based on the Veubeke-Hu-Washizu principle.

```
Input: nodal coordinates and connectivity of the elements.
Initialize: $\boldsymbol{K}^{\mathrm{eas}}$ and $\hat{\boldsymbol{f}}$.
for element cycle do
    for Gauss point cycle do
        Calculate $\boldsymbol{J}$    /* relates the natural and physical coordinate systems. */
        Calculate $\boldsymbol{B}$    /* stain-displacement matrix. */
        Calculate $\boldsymbol{K}_e^c = \boldsymbol{B}^T \boldsymbol{C} \boldsymbol{B}$    /* the conventional element stiffness matrix. */
        Select $\tilde{\boldsymbol{G}}_e$    /* specific to the element type. */
        Calculate $\boldsymbol{T}_0$    /* transformation matrix at element center. */
        Calculate $\boldsymbol{G}_e = \frac{\boldsymbol{J}_0}{|\boldsymbol{J}|} \boldsymbol{T}_0^{-T} \tilde{\boldsymbol{G}}_e$
        Calculate $\boldsymbol{M}_e = \boldsymbol{G}_e^T \boldsymbol{C} \boldsymbol{B}_e$ and $\boldsymbol{H}_e = \boldsymbol{G}_e^T \boldsymbol{C} \boldsymbol{G}_e$
    end
    Compute $\boldsymbol{K}_e^{\mathrm{eas}} = \left[\boldsymbol{K}_e^c - \boldsymbol{M}_e^T \boldsymbol{H}_e^{-1} \boldsymbol{M}_e\right]$    /* EAS specific element stiffness matrix. */
    Assemble    /* to generate the global $\boldsymbol{K}^{\mathrm{eas}}$. */
end
Result: $\hat{\boldsymbol{u}}$    /* evaluated using $\hat{\boldsymbol{u}} = [\boldsymbol{K}^{\mathrm{eas}}]^{-1} \hat{\boldsymbol{f}}$. */
Post-processing: compute $\boldsymbol{\varepsilon}$ and $\boldsymbol{\sigma}$    /* choose an appropriate stress-recovery option, we used Gauss point extrapolation method. */
```

Algorithm 2: An algorithm for implementing the stress-based hybrid formulation based on the Hellinger-Reissner principle.

```
Input: nodal coordinates and connectivity of the elements.
Initialize: $\boldsymbol{K}$ and $\hat{\boldsymbol{f}}$.
for element cycle do
    for Gauss point cycle do
        Calculate $\boldsymbol{J}$    /* relates the natural and physical coordinate systems.    */
        Calculate $\boldsymbol{B}$    /* stain-displacement matrix.    */
        Select $\tilde{\boldsymbol{P}}_e$    /* specific to the element type.    */
        Calculate $\boldsymbol{T}$    /* transformation matrix.    */
        Calculate $\boldsymbol{P}_e = \boldsymbol{T}\tilde{\boldsymbol{P}}_e$
        Calculate $\boldsymbol{G}_e = \boldsymbol{P}_e^T \boldsymbol{B}_e$ and $\boldsymbol{H}_e = \boldsymbol{P}_e^T \boldsymbol{S} \boldsymbol{P}_e$
    end
    Compute $\boldsymbol{K}_e = \boldsymbol{G}_e^T \boldsymbol{H}_e^{-1} \boldsymbol{G}_e$    /* stress-based HR specific element stiffness matrix.    */
    Assemble    /* to generate the global $\boldsymbol{K}$.    */
end
Evaluate $\hat{\boldsymbol{f}}$    /* force vector    */
Incorporate the boundary conditions.
Result: $\hat{\boldsymbol{u}}$    /* evaluated using $\hat{\boldsymbol{u}} = \boldsymbol{K}^{-1}\hat{\boldsymbol{f}}$.    */
Post-processing: compute $\boldsymbol{\sigma}$    /* choose an appropriate stress-recovery option, we used Gauss point extrapolation method.    */
```

Algorithm 3: Algorithm for implementation of generalized ANS method.

```
Input: nodal coordinates and connectivity of the elements.
Initialize: $\boldsymbol{K}$ and $\hat{\boldsymbol{f}}$.
for element cycle do
    for Gauss point cycle do
        Calculate $\boldsymbol{J}$    /* relates the natural and physical coordinate systems.    */
        Calculate $\bar{\boldsymbol{B}}$    /* stain-displacement matrix in covariant frame.    */
        for tying point cylce do
            Evaluate $\bar{\boldsymbol{N}}$    /* Lagrange polynomials interpolating at the tying points.    */
            Evaluate modified $(\boldsymbol{B}^*)^{\mathrm{ANS}}$ for respective components.
            Replace the appropriate rows of conventional $\bar{\boldsymbol{B}}$ with $(\boldsymbol{B}^*)^{\mathrm{ANS}}$.
            Define the modified $\bar{\boldsymbol{B}}^{\mathrm{ANS}}$.
        end
        Perform mapping: $\boldsymbol{B} = \boldsymbol{T}^{-T}\bar{\boldsymbol{B}}^{\mathrm{ANS}}$.
        Evaluate $\boldsymbol{K}_e = \boldsymbol{B}^T \boldsymbol{C} \boldsymbol{B}$.
    end
    Assemble    /* to generate the global $\boldsymbol{K}$.    */
end
Evaluate $\hat{\boldsymbol{f}}$    /* force vector    */
Incorporate the boundary conditions.
Result: $\hat{\boldsymbol{u}}$    /* evaluated using $\hat{\boldsymbol{u}} = \boldsymbol{K}^{-1}\hat{\boldsymbol{f}}$.    */
```

Algorithm 4: A pseudocode for generating a compatible strain interpolation matrix using Mathematica commands.

```
Input: element information
  /* element type, stress interpolation matrix used in HR-based
     hybrid elements in particular the vectors $\tilde{\boldsymbol{P}}_1, \tilde{\boldsymbol{P}}_2, \dots, \tilde{\boldsymbol{P}}_6$      */
Initialize: Choose $g(\xi, \eta, \zeta)$   /* based on element type and involved
     modes.  For instance, $g(\xi, \eta, \zeta)$ is a full trilinear and
     triquadratic polynomial for eight-node and twenty-seven node
     brick elements, respectively.  For six-node wedge $g(\xi, \eta, \zeta)$ is
     given as $g(\xi, \eta, \zeta) = a_1 + a_2\xi + a_3\eta + a_4\zeta + a_5\eta\zeta + a_6\xi\zeta$ and for
     eighteen-node wedge it is
     $g(\xi, \eta, \zeta) = a_1 + a_2\xi^2\zeta^2 + a_3\xi^2\zeta + a_4\xi^2 + a_5\xi\eta\zeta^2 + a_6\xi\eta\zeta + a_7\xi\eta + a_8\xi\zeta^2 + a_9\xi\zeta + a_{10}\xi + a_{11}\eta^2\zeta^2 + a_{12}\eta^2\zeta + a_{13}\eta^2 + a_{14}\eta\zeta^2 + a_{15}\eta\zeta + a_{16}\eta + a_{17}\zeta^2 + a_{18}\zeta$
     */
for each $\tilde{\boldsymbol{P}}_i$ do
    /* let $n$ = number of entries in $\tilde{\boldsymbol{P}}_i$      */
    Initialize: f = ConstantArray [ 0, $n$ ]
    for $j \leftarrow 1$ to $n$ do
        f [[ $j$ ]] = Integrate [$\tilde{\boldsymbol{P}}_i$ * $g$, {$\xi$, $L_\xi$, $U_\xi$}, {$\eta$, $L_\eta$, $U_\eta$}, {$\zeta$, $L_\zeta$, $U_\zeta$}]
            /* $L_\xi$, $L_\eta$ and $L_\zeta$ = lower limit of integration, $U_\xi$, $U_\eta$, and
               $U_\zeta$ = upper limit of integration      */
    end
    tempMat = Normal [ CoefficientArrays [ {f [[ 1 ]] == 0, f [[ 2 ]] == 0, ..., f [[ n
        ]] == 0}, {$a_1$, $a_2$, ..., $a_m$ } ]]   /* $m$ = number of constants in $g$ */
    mat = tempMat [[ 2 ]]
    NullA = Transpose [ NullSpace [ mat ]]
    SumA = $c_1$ * $\gamma_1$ * NullA [[ 1 ; ;, 1 ]] + $c_2$ * $\gamma_2$ * NullA [[ 1 ; ;, 2 ]] + ... + $c_{n^\phi}$
        * $\gamma_{n^\phi}$ * NullA [[ 1 ; ;, $n^\phi$ ]]   /* $c_1$, $c_2$, ..., $c_{n^\phi}$ are the constants
        introduce for mathematical manipulation, $n^\phi$ is the number of
        null space vectors.      */
    functions = { $h_1(\xi, \eta, \zeta)$, $h_2(\xi, \eta, \zeta)$, ..., $h_3(\xi, \eta, \zeta)$ }   /* $h_1$, $h_2$, ..., $h_3$
        are functions associated with each constant in $g(\xi, \eta, \zeta)$      */
    Simplify [ SumA.functions ]
    Total@MonomialList [ SumA.functions, { $\gamma_1$, $\gamma_2$, ..., $\gamma_{n^\phi}$ } ]
    Result: $g(\xi, \eta, \zeta)$ orthogonal to each function in $\tilde{\boldsymbol{P}}_i$
end
Result: $\tilde{\boldsymbol{G}}^e$   /* strain interpolation matrix for the specific
     element.      */
```

Algorithm 5: Pseudocode for deriving the symbolic expressions for NURBS basis function: A Mathematica implementation.

```
Initialize: Polynomial degree: $p$, $q$, and $r$. Knot vectors: $\boldsymbol{U}$, $\boldsymbol{V}$, and $\boldsymbol{W}$ in $\xi$, $\eta$, and $\zeta$
  direction. Weight vector: $w = \{w_1 \;\; w_2 \;\; w_3 \;\; \dots w_{n^e_{cp}}\}$.
Evaluate $size\_u$, $size\_v$, and $size\_w$      /* size of knot vectors                                  */
Evaluate $uniq\_u$, $uniq\_v$, and $uniq\_w$      /* unique knot vector entries                            */
Evaluate $n_\phi$ ,$n_\psi$, and $n_\theta$      /* number of basis functions in $\xi$, $\eta$, and $\zeta$
    direction. For instance, $size\_u$ = Length [ $\boldsymbol{U}$ ], $uniq\_u$ = Sort [
    DeleteDuplicates [ $\boldsymbol{U}$ ]], $n_\phi = size\_u - p - 1$. Similarly evaluate $size\_v$,
    $size\_w$, $uniq\_v$, $uniq\_w$ ,$n_\psi$, and $n_\theta$.                                   */
Initialize and evaluate $basis\_u$, $basis\_v$, and $basis\_w$      /* the B-Spline basis
    function matrix in $\xi$, $\eta$, and $\zeta$ direction.                                    */
for $\alpha = 0,\ \alpha < n_\phi,\ \alpha{+}{+}$ do
    $basis$ = PiecewiseExpand [ BSplineBasis [ { $p$, $\boldsymbol{U}$ }, $\alpha$, $\xi$ ] ]; $count = 1$; for $j = 1$,
      $j <$ Length [ $uniq\_u$ ], $j{+}{+}$ do
        $basis\_u$ [[ $j, \alpha + 1$ ]] = Refine [ $basis\_u$, $uniq\_u$ [[ $count$ ]] $< \xi <$ $uniq\_u$ [[
          $count + 1$ ]]; $count{+}{+}$;
    end
end
Similarly, evaluate for $basis\_v$ and $basis\_w$.
Evaluate the participating tensor product terms for individual element.      /* For e.g.
    Eq. 5.15 i.e. $N_{\alpha,p}(\xi) M_{\beta,q}(\eta) L_{\gamma,r}(\zeta)$.                   */
Initialize: $element = 1$
Do [ $count = 1$;
for $\gamma = 1,\ \gamma \leq n_\theta,\ \gamma{+}{+}$ do
    for $\beta = 1,\ \beta \leq n_\psi,\ \beta{+}{+}$ do
        for $\alpha = 1,\ \alpha \leq n_\phi,\ \alpha{+}{+}$ do
            $tensor\_prod$ [[ $element, count$ ]] = $basis\_u$ [[ $x, \alpha$ ]] $\times$ $basis\_v$ [[ $y, \beta$ ]] $\times$
              $basis\_w$ [[ $z, \gamma$ ]]; $count{+}{+}$;
        end
    end
end
$element{+}{+}$, { $z$,1, Length [ $uniq\_w$ ] - 1},{ $y$,1, Length [ $uniq\_v$ ] - 1},{ $x$,1, Length [
  $uniq\_u$ ] - 1}];
Summation and rationalize B-Spline functions to derive NURBS functions.
for $j = 1,\ j \leq tot\_element,\ j{+}{+}$ do
    $Temp = 0$
    for $i = 1,\ i \leq n_\phi \times n_\psi \times n_\theta,\ i{+}{+}$ do
        $sum$ [[ $j$ ]] = $Temp + tensor\_prod$ [[ $j, i$ ]] $\times$ $w$ [[ $i$ ]]; $Temp = sum$ [[ $j$ ]]
    end
end
$NURBS\_basis$ = ArrayReshape[ ConstantArray [ 0, $tot\_element \times n_\phi \times n_\psi \times n_\theta$, {
  $tot\_element$, $n_\phi \times n_\psi \times n_\theta$ } ]
for $k = 1,\ k \leq tot\_element,\ k{+}{+}$ do
    for $i = 1,\ i \leq n_\phi \times n_\psi \times n_\theta,\ i{+}{+}$ do
        $NURBS\_basis = Tensor\_prod$ [[ $k, i$ ]] $\times w$ [[ $i$ ]] $/sum$ [[ $k$ ]]
    end
end
Evaluate derivatives with respect to natural coordinates: D[$NURBS\_basis, \xi$].
```

Appendix B

Geometric data for construction of initial meshes

This section provides the required geometric data to construct the initial coarse mesh for the numerical examples presented in the current work. The data includes control point coordinates and corresponding weights. Further refinement is carried out by performing the knot insertion or the degree elevation of participating NURBS interpolation in one or more directions. For the reader's interest, the NURBS toolbox [213], an open-source MATLAB code library, contains the code for the refinement strategies. The functions utilized for the refinement are ***nrbdegelev*** and ***nrbkntins***.

Table B.1: Control point coordinates ($P_{i,j} = [x,\ y,\ z]$) for modeling the initial coarse mesh for a rectangular beam of length L and thickness t with linear basis along ξ and η direction (weights associated with each control point is 1, knot vector along ξ and η direction is [0, 0, 1, 1]).

j	$P_{1,j}$	$P_{2,j}$
1	$[\ 0,\ 0,\ 0\ ]$	$[\ L,\ 0,\ 0\ ]$
2	$[\ 0,\ t,\ 0\ ]$	$[\ L,\ t,\ 0\ ]$

Table B.2: Control point coordinates and respective weights ($P_{i,j} = [x,\ y,\ z,\ w]$) for modeling a single element representing a exact domain of a curved beam with quadratic basis along ξ and linear basis along η direction, the respective knot vectors are $\boldsymbol{\Xi} = [0,\ 0,\ 0,\ 1,\ 1,\ 1]$ and $\boldsymbol{\mathcal{H}} = [0,\ 0,\ 1,\ 1]$.

j	$P_{1,j}$	$P_{2,j}$	$P_{3,j}$
1	$[0,\ R_{in},\ 0,\ 1]$	$[R_{in},\ R_{in},\ 0,\ \frac{1}{\sqrt{2}}]$	$[R_{in},\ 0,\ 0,\ 1]$
2	$[0,\ R_{out},\ 0,\ 1]$	$[R_{out},\ R_{out},\ 0,\ \frac{1}{\sqrt{2}}]$	$[R_{out},\ 0,\ 0,\ 1]$

Table B.3: Control point coordinates ($P_{i,j} = [x,\ y,\ z]$) for modeling a single element representing the domain of a Cook's membrane problem with linear basis along ξ and η direction (weights associated with all the control points = 1 and knot vector along ξ and η direction is $[0,\ 0,\ 1,\ 1]$).

j	$P_{1,j}$	$P_{2,j}$
1	$[\ 0,\ 0,\ 0\ ]$	$[\ 48,\ 44,\ 0\ ]$
2	$[\ 0,\ 44,\ 0\ ]$	$[\ 48,\ 60,\ 0\ ]$

Table B.4: Control point coordinates ($P_{i,j} = [x,\ y,\ z]$) and respective weights ($w_{i,j}$) for modeling a quarter portion of a plate with a hole problem using two quadratic elements (two elements along ξ direction and one element along η direction), knot vectors along ξ and η are given as; $\boldsymbol{\Xi} = [0,\ 0,\ 0,\ 0.5,\ 1,\ 1,\ 1]$, $\boldsymbol{\mathcal{H}} = [0,\ 0,\ 0,\ 1,\ 1,\ 1]$, radius $= r = 1$, length $= L = 4$, weight $= w^{cp} = 0.5(1 + 1/\sqrt{2})$.

j	$P_{1,j}$	$P_{2,j}$	$P_{3,j}$	$P_{4,j}$	$w_{1,j}$	$w_{2,j}$	$w_{3,j}$	$w_{4,j}$
1	$[\,-r,\ 0,\ 0\,]$	$[-r,\ 0.414,\ 0]$	$[-0.414,\ r,\ 0]$	$[\,0,\ 1,\ 0\,]$	1	w^{cp}	w^{cp}	1
2	$[\,-\frac{5}{2},\ 0,\ 0\,]$	$[\,-\frac{5}{2},\ \frac{3}{4},\ 0\,]$	$[\,-\frac{3}{4},\ \frac{5}{2},\ 0\,]$	$[\,0,\ \frac{5}{2},\ 0\,]$	1	1	1	1
3	$[\,-L,\ 0,\ 0\,]$	$[\,-L,\ L,\ 0\,]$	$[\,-L,\ L,\ 0\,]$	$[\,0,\ L,\ 0\,]$	1	1	1	1

Table B.5: Control point coordinates and corresponding weights $P_{i,j,k} = [x,\ y,\ z,\ wt]$ to construct a single NURBS element representing the exact domain of a straight cantilever beam problem ($L = 60$, $w = 1$, and $t = 6$, 0.6, or 0.06 for the desired L/t ratio) and incompressible block problem ($L = w = t = 1$). Linear interpolation functions are used in all three directions and knot vector along ξ, η, and ζ direction is $[0,\ 0,\ 1,\ 1]$.

j	k	$P_{i,j,k} = [x,\ y,\ z,\ wt]$	
		$P_{1,j,k}$	$P_{2,j,k}$
1	1	$[0,\ 0,\ 0,\ 1]$	$[L,\ 0,\ 0,\ 1]$
2	1	$[0,\ t,\ 0,\ 1]$	$[L,\ t,\ 0,\ 1]$
1	2	$[0,\ 0,\ w,\ 1]$	$[L,\ 0,\ w,\ 1]$
2	2	$[0,\ t,\ w,\ 1]$	$[L,\ t,\ w,\ 1]$

Table B.6: Control point coordinates and corresponding weights $P_{i,j,k} = [x,\ y,\ z,\ wt]$ to construct a single NURBS element representing the exact domain of a curved cantilever beam problem (Quadratic interpolation functions are incorporated along the curvature and linear basis functions are used in other two directions. The knot vector along ξ is $[0,\ 0,\ 0,\ 1,\ 1,\ 1]$ whereas the knot vector along η and ζ direction is $[0,\ 0,\ 1,\ 1]$. $R = 12$, $w = 1$, and $t = 1.2$, 0.12, or 0.012 for the desired R/t ratio).

j	k	$P_{i,j,k} = [x,\ y,\ z,\ wt]$		
		$P_{1,j,k}$	$P_{2,j,k}$	$P_{3,j,k}$
1	1	$\left[0,\ R-\frac{t}{2},\ 0,\ 1\right]$	$\left[R-\frac{t}{2},\ R-\frac{t}{2},\ 0,\ \frac{1}{\sqrt{2}}\right]$	$\left[R-\frac{t}{2},\ 0,\ 0,\ 1\right]$
2	1	$\left[0,\ R+\frac{t}{2},\ 0,\ 1\right]$	$\left[R+\frac{t}{2},\ R+\frac{t}{2},\ 0,\ \frac{1}{\sqrt{2}}\right]$	$\left[R+\frac{t}{2},\ 0,\ 0,\ 1\right]$
1	2	$\left[0,\ R-\frac{t}{2},\ w,\ 1\right]$	$\left[R-\frac{t}{2},\ R-\frac{t}{2},\ w,\ \frac{1}{\sqrt{2}}\right]$	$\left[R-\frac{t}{2},\ 0,\ w,\ 1\right]$
2	2	$\left[0,\ R+\frac{t}{2},\ w,\ 1\right]$	$\left[R+\frac{t}{2},\ R+\frac{t}{2},\ w,\ \frac{1}{\sqrt{2}}\right]$	$\left[R+\frac{t}{2},\ 0,\ w,\ 1\right]$

Table B.7: Control point coordinates and corresponding weights $P_{i,j,k} = [x,\ y,\ z,\ wt]$ to construct a single NURBS element representing the exact domain of a quarter portion of Scordelis–Lo roof problem (Quadratic interpolation functions are incorporated along the curvature, and linear basis functions are used in other two directions. The knot vector along ξ is $[0,\ 0,\ 0,\ 1,\ 1,\ 1]$ whereas the knot vector along η and ζ direction is $[0,\ 0,\ 1,\ 1]$. $R = 25$, $L = 50$, and $h = 0.25$).

j	k	$P_{i,j,k} = [x,\ y,\ z,\ wt]$		
		$P_{1,j,k}$	$P_{2,j,k}$	$P_{3,j,k}$
1	1	$[0,\ 24.875,\ 0,\ 1]$	$[9.0538,\ 24.875,\ 0,\ 0.9397]$	$[15.9893,\ 19.0554,\ 0,\ 1]$
2	1	$[0,\ 25.125,\ 0, 1]$	$[9.1448,\ 25.125,\ 0,\ 0.9397]$	$[16.15,\ 19.2469,\ 0,\ 1]$
1	2	$[0,\ 24.875,\ 25,\ 1]$	$[9.0538,\ 24.875,\ 25,\ 0.9397]$	$[15.9893,\ 19.0554,\ 25,\ 1]$
2	2	$[0,\ 25.125,\ 25, 1]$	$[9.1448,\ 25.125,\ 25,\ 0.9397]$	$[16.15,\ 19.2469,\ 25,\ 1]$

Table B.8: Control point coordinates and corresponding weights $P_{i,j,k} = [x,\ y,\ z,\ wt]$ to construct a single NURBS element representing the exact domain of a one-eighth portion of pinched cylinder problem (Quadratic interpolation functions are incorporated along the curvature, and linear basis functions are used in other two directions. The knot vector along ξ is $[0,\ 0,\ 0,\ 1,\ 1,\ 1]$ whereas the knot vector along η and ζ direction is $[0,\ 0,\ 1,\ 1]$. $R = 300$, $L = 600$, and $h = 3$).

j	k	$P_{i,j,k} = [x,\ y,\ z,\ wt]$		
		$P_{1,j,k}$	$P_{2,j,k}$	$P_{3,j,k}$
1	1	$\left[0,\ R-\frac{h}{2},\ 0,\ 1\right]$	$\left[R-\frac{h}{2},\ R-\frac{h}{2},\ 0,\ \frac{1}{\sqrt{2}}\right]$	$\left[R-\frac{h}{2},\ 0,\ 0,\ 1\right]$
2	1	$\left[0,\ R+\frac{h}{2},\ 0,\ 1\right]$	$\left[R+\frac{h}{2},\ R+\frac{h}{2},\ 0,\ \frac{1}{\sqrt{2}}\right]$	$\left[R+\frac{h}{2},\ 0,\ 0,\ 1\right]$
1	2	$\left[0,\ R-\frac{h}{2},\ \frac{L}{2},\ 1\right]$	$\left[R-\frac{h}{2},\ R-\frac{h}{2},\ \frac{L}{2},\ \frac{1}{\sqrt{2}}\right]$	$\left[R-\frac{h}{2},\ 0,\ \frac{L}{2},\ 1\right]$
2	2	$\left[0,\ R+\frac{h}{2},\ \frac{L}{2},\ 1\right]$	$\left[R+\frac{h}{2},\ R+\frac{h}{2},\ \frac{L}{2},\ \frac{1}{\sqrt{2}}\right]$	$\left[R+\frac{h}{2},\ 0,\ \frac{L}{2},\ 1\right]$

Table B.9: Control point coordinates and corresponding weights $P_{i,j,k} = [x,\ y,\ z,\ wt]$ to construct a single NURBS element representing the exact domain of a quarter portion of pinched hemisphere problem (Quadratic interpolation functions are incorporated along the curvature in two directions, and linear basis functions are used in the third direction. The knot vector along ξ and ζ is $[0,\ 0,\ 0,\ 1,\ 1,\ 1]$ whereas the knot vector along η direction is $[0,\ 0,\ 1,\ 1]$. $R = 10$, and $h = 0.04$).

j	k	$P_{i,j,k} = [x,\ y,\ z,\ wt]$		
		$P_{1,j,k}$	$P_{2,j,k}$	$P_{3,j,k}$
1	1	$[0,\ 9.98,\ 0,\ 1]$	$\left[9.98,\ 9.98,\ 0,\ \frac{1}{\sqrt{2}}\right]$	$[9.98,\ 0,\ 0,\ 1]$
2	1	$[0,\ 10.02,\ 0,\ 1]$	$\left[10.02,\ 10.02,\ 0,\ \frac{1}{\sqrt{2}}\right]$	$[10.02,\ 0,\ 0,\ 1]$
1	2	$\left[0,\ 9.98,\ 9.98,\ \frac{1}{\sqrt{2}}\right]$	$\left[9.98,\ 9.98,\ 9.98,\ \frac{1}{2}\right]$	$\left[9.98,\ 0,\ 9.98,\ \frac{1}{\sqrt{2}}\right]$
2	2	$\left[0,\ 10.02,\ 10.02,\ \frac{1}{\sqrt{2}}\right]$	$\left[10.02,\ 10.02,\ 10.02,\ \frac{1}{2}\right]$	$\left[10.02,\ 0,\ 10.02,\ \frac{1}{\sqrt{2}}\right]$
1	3	$[0,\ 0,\ 9.98,\ 1]$	$\left[0,\ 0,\ 9.98,\ \frac{1}{\sqrt{2}}\right]$	$[0,\ 0,\ 9.98,\ 1]$
2	3	$[0,\ 0,\ 10.02,\ 1]$	$\left[0,\ 0,\ 10.02,\ \frac{1}{\sqrt{2}}\right]$	$[0,\ 0,\ 10.02,\ 1]$

Table B.10: Control point coordinates and corresponding weights $P_{i,j,k} = [x,\ y,\ z,\ wt]$ to construct a single NURBS element representing the exact domain of a quarter portion of the curved plate problem (Quadratic interpolation functions are incorporated along the curvature, and linear basis functions are used in other two directions. The knot vector along ξ is $[0,\ 0,\ 0,\ 1,\ 1,\ 1]$ whereas the knot vector along η and ζ direction is $[0,\ 0,\ 1,\ 1]$. $R_{\text{in}} = 0$, $R_{\text{out}} = 1$, $h = 0.01$).

j	k	$P_{i,j,k} = [x,\ y,\ z,\ wt]$		
		$P_{1,j,k}$	$P_{2,j,k}$	$P_{3,j,k}$
1	1	$[0,\ R_{\text{in}},\ 0,\ 1]$	$\left[R_{\text{in}},\ R_{\text{in}},\ 0,\ \frac{1}{\sqrt{2}}\right]$	$[R_{\text{in}},\ 0,\ 0,\ 1]$
2	1	$[0,\ R_{\text{out}},\ 0,\ 1]$	$\left[R_{\text{out}},\ R_{\text{out}},\ 0,\ \frac{1}{\sqrt{2}}\right]$	$[R_{\text{out}},\ 0,\ 0,\ 1]$
1	2	$[0,\ R_{\text{in}},\ h,\ 1]$	$\left[R_{\text{in}},\ R_{\text{in}},\ h,\ \frac{1}{\sqrt{2}}\right]$	$[R_{\text{in}},\ 0,\ h,\ 1]$
2	2	$[0,\ R_{\text{out}},\ h,\ 1]$	$\left[R_{\text{out}},\ R_{\text{out}},\ h,\ \frac{1}{\sqrt{2}}\right]$	$[R_{\text{out}},\ 0,\ h,\ 1]$

Table B.11: Control point coordinates and corresponding weights $P_{i,j,k} = [x,\ y,\ z,\ wt]$ to construct a single NURBS element representing the exact domain of a skew plate problem (Linear interpolation functions are used in all three directions and the knot vector along ξ, η, and ζ direction is [0, 0, 1, 1]).

j	k	$P_{i,j,k} = [x,\ y,\ z,\ wt]$	
		$P_{1,j,k}$	$P_{2,j,k}$
1	1	[0, 0, 0, 1]	[1, 0, 0, 1]
2	1	[0.8660, 0.5000, 0, 1]	[1.8660, 0.5000, 0, 1]
1	2	[0, 0, 0.0100, 1]	[1, 0, 0.0100, 1]
2	2	[0.8660, 0.5000, 0.0100, 1]	[1.8660, 0.5000, 0.0100, 1]

References

[1] W. K. Liu, S. Li, H. S. Park, Eighty Years of the Finite Element Method: Birth, Evolution, and Future, Archives of Computational Methods in Engineering 29 (6) (2022) 4431–4453. arXiv:2107.04960, doi:10.1007/s11831-022-09740-9.

[2] A. Hrennikoff, Solution of Problems of Elasticity by the Framework Method, Journal of Applied Mechanics 8 (4) (1941) A169–A175. doi:10.1115/1.4009129.

[3] R. Courant, Variational methods for the solution of problems of equilibrium and vibrations, Bulletin of the American Mathematical Society 49 (1) (1943) 1–23. doi:10.1090/S0002-9904-1943-07818-4.

[4] D. McHenry, A Lattice Analogy for the Solution of Stress Problem, Journal of the Institution of Civil Engineers 21 (2) (1943) 59–82. doi:10.1680/ijoti.1943.13967.

[5] W. Prager, J. L. Synge, Approximations in Elasticity Based on the Concept of Function Space, Quarterly of Applied Mathematics 5 (3) (1947) 241–269.

[6] R. W. Clough, The finite element method in plane stress analysis, In: Proceedings of 2nd ASCE conference on electronic computation. Pittsburgh PA, 8–9 Sept, 1960.

[7] R. W. Clough, The stress distribution of norfork dam, California Univ Berkeley Inst of Engineering Research, California, 1962.

[8] K. J. Bathe, Finite Element Procedures, Englewood Cliffs New Jersey, 1996.

[9] J. N. Reddy, An Introduction to The Finite Element Method (third Edition), McGraw-Hill, 2005.

[10] T. J. R. Hughes, J. A. Cottrell, Y. Bazilevs, Isogeometric analysis: CAD, finite elements, NURBS, exact geometry and mesh refinement, Computer Methods in Applied Mechanics and Engineering 194 (39-41) (2005) 4135–4195. doi:10.1016/j.cma.2004.10.008.

[11] J. A. Cottrell, T. J. R. Hughes, Y. Bazilevs, Isogeomatric analysis: Towards integration of CAD and FEA, John Wiley & Sons Ltd, Chichester, UK, 2009.

[12] L. Piegl, W. Tiller, The NURBS book, 2nd Edition, Springer, New York, 1997.

[13] V. Agrawal, S. S. Gautam, IGA: A simplified introduction and implementation details for finite element users, Journal of The Institution of Engineers (India): Series C 100 (3) (2019) 561–585. doi:10.1007/s40032-018-0462-6.

[14] C. Provatidis, A Review on Attempts towards CAD/CAE Integration Using Macroelements, Computational Research 1 (3) (2013) 61–84. doi:10.13189/cr.2013.010302.

[15] W. J. Gordon, C. A. Hall, Construction of curvilinear coordinate systems and applications to mesh generation, International Journal for Numerical Methods in Engineering 7 (4) (1973) 461–477. doi:10.1002/nme.1620070405.

[16] J. C. Cavendish, W. J. Gordon, C. A. Hall, Ritz-Galerkin approximations in blending function spaces, Numerische Mathematik 26 (2) (1976) 155–178. doi:10.1007/BF01395970.

[17] C. G. Provatidis, Bézier versus Lagrange polynomials-based finite element analysis of 2-D potential problems, Advances in Engineering Software 73 (2014) 22–34. doi:10.1016/j.advengsoft.2014.02.006.

[18] K. Hollig, D. Benson, Finite Element Methods with B-Splines, Applied Mechanics Reviews 57 (2) (2004) B9. doi:10.1115/1.1704619.

[19] C. G. Provatidis, Precursors of Isogeometric Analysis, 2018.

[20] U. Schramm, W. D. Pilkey, The coupling of geometric descriptions and finite elements using NURBs - A study in shape optimization, Finite Elements in Analysis and Design 15 (1) (1993) 11–34. doi:10.1016/0168-874X(93)90067-Z.

[21] U. Schramm, W. D. Pilkey, Higher order boundary elements for shape optimization using rational B-splines, Engineering Analysis with Boundary Elements 14 (3) (1994) 255–266. doi:10.1016/0955-7997(94)90041-8.

[22] L. De Lorenzis, P. Wriggers, T. J. R. Hughes, Isogeometric contact: a review, GAMM-Mitteilungen 37 (2014) 85–123. doi:10.1002/gamm.201410005.

[23] V. Agrawal, S. S. Gautam, Varying-order NURBS discretization: An accurate and efficient method for isogeometric analysis of large deformation contact problems, Computer Methods in Applied Mechanics and Engineering 367 (2020) 113125. arXiv:1903.05859, doi:10.1016/j.cma.2020.113125.

[24] V. Agrawal, S. S. Gautam, NURBS-based isogeometric analysis for stable and accurate peeling computations, Sadhana - Academy Proceedings in Engineering Sciences 46 (1) (2021). doi:10.1007/s12046-020-01513-z.

[25] W. A. Wall, M. A. Frenzel, C. Cyron, Isogeometric structural shape optimization, Computer Methods in Applied Mechanics and Engineering 197 (2008) 2976–2988. doi:10.1016/j.cma.2008.01.025.

[26] X. Qian, Full analytical sensitivities in NURBS based isogeometric shape optimization, Computer Methods in Applied Mechanics and Engineering 199 (2010) 2059–2071. doi:10.1016/j.cma.2010.03.005.

[27] H. Gomez, T. J. R. Hughes, X. Nogueira, V. M. Calo, Isogeometric analysis of the isothermal Navier-Stokes-Korteweg equations, Computer Methods in Applied Mechanics and Engineering 199 (25-28) (2010) 1828–1840. doi:10.1016/j.cma.2010.02.010.

[28] Y. Bazilevs, I. Akkerman, Large eddy simulation of turbulent Taylor-Couette flow using isogeometric analysis and the residual-based variational multiscale method, Journal of Computational Physics 229 (9) (2010) 3402–3414. doi:10.1016/j.jcp.2010.01.008.

[29] J. A. Cottrell, A. Reali, Y. Bazilevs, T. J. R. Hughes, Isogeometric analysis of structural vibrations, Computer Methods in Applied Mechanics and Engineering 195 (41-43) (2006) 5257–5296. doi:10.1016/j.cma.2005.09.027.

[30] T. J. R. Hughes, A. Reali, G. Sangalli, Duality and unified analysis of discrete approximations in structural dynamics and wave propagation: Comparison of p-method finite elements with k-method NURBS, Computer Methods in Applied Mechanics and Engineering 197 (49-50) (2008) 4104–4124. doi:10.1016/j.cma.2008.04.006.

[31] D. J. Benson, S. Hartmann, Y. Bazilevs, M.-C. Hsu, T. J. R. Hughes, Blended isogeometric shells, Computer Methods in Applied Mechanics and Engineering 255 (2013) 133–146. doi:10.1016/j.cma.2012.11.020.

[32] R. Echter, B. Oesterle, M. Bischoff, A hierarchic family of isogeometric shell finite elements, Computer Methods in Applied Mechanics and Engineering 254 (2013) 170–180. doi:10.1016/j.cma.2012.10.018.

[33] S. Hartmann, D. J. Benson, D. Lorenz, About Isogeometric Analysis and the new NURBS-based Finite Elements in LS-DYNA, 8th European LS-DYNA Users Conference (Strasbourg, France, May 23 - 24, 2011).

[34] A. Duval, F. Maurin, T. Elguedj, Abaqus user element implementation of NURBS based isogeometric analysis, 6th European Congress on Computational Methods in Applied Sciences and Engineering (Vienna, Austria, Sep 10 - 14, 2012).

[35] S. Khakalo, J. Niiranen, Isogeometric analysis of higher-order gradient elasticity by user elements of a commercial finite element software, Computer-Aided Design 82 (2017) 154–169. doi:10.1016/j.cad.2016.08.005.

[36] C. de Falco, A. Reali, R. Vázquez, GeoPDEs: A research tool for Isogeometric Analysis of PDEs, Advances in Engineering Software 42 (12) (2011) 1020–1034. doi:10.1016/j.advengsoft.2011.06.010.

[37] L. Dalcin, N. Collier, P. Vignal, A. M. A. Côrtes, V. M. Calo, PetIGA: A framework for high-performance isogeometric analysis, Computer Methods in Applied Mechanics and Engineering 308 (2016) 151–181. doi:10.1016/j.cma.2016.05.011.

[38] A. Ratnani, Pigasus : Python for isogeometric analysis and unified simulations., Technical report (Dec. 2012).

[39] G. Prathap, The Finite Element Method in Structural Mechanics, Vol. 24 of Solid Mechanics and Its Applications, Springer Netherlands, Dordrecht, 1993. doi:10.1007/978-94-017-3319-9.

[40] O. C. Zienkiewicz, R. L. Taylor, J. M. Too, Reduced integration technique in general analysis of plates and shells, International Journal for Numerical Methods in Engineering 3 (2) (1971) 275–290. doi:10.1002/nme.1620030211.

[41] T. J. R. Hughes, R. L. Taylor, W. Kanoknukulchai, A simple and efficient finite element for plate bending, International Journal for Numerical Methods in Engineering 11 (10) (1977) 1529–1543. doi:10.1002/nme.1620111005.

[42] H. Stolarski, T. Belytschko, Membrane locking and reduced integration for curved elements, Journal of Applied Mechanics 49 (1) (1982) 172–176. doi:10.1115/1.3161961.

[43] M. Bischoff, E. Ramm, J. Irslinger, Models and finite elements for thin-walled structures, no. 1859, John Wiley & Sons, Ltd, 2017. doi:10.1002/9781119176817.ecm2026.

[44] I. Babuška, M. Suri, Locking effects in the finite element approximation of elasticity problems, Numerische Mathematik 62 (1) (1992) 439–463. doi:10.1007/BF01396238.

[45] I. Babuska, M. Suri, On locking and robustness in the finite element method, SIAM Journal on Numerical Analysis 29 (5) (1992) 1261–1293. doi:10.1137/0729075.

[46] M. Ainsworth, C. Parker, Unlocking the secrets of locking: Finite element analysis in planar linear elasticity, Computer Methods in Applied Mechanics and Engineering 395 (2022) 115034. doi:10.1016/j.cma.2022.115034.

[47] D. N. Arnold, Discretization by finite elements of a model parameter dependent problem, Numerische Mathematik 37 (3) (1981) 405–421. doi:10.1007/BF01400318.

[48] N. H. Nguyen, Development of solid-shell elements for large deformation simulation and springback prediction, Ph.D. thesis, University of Liège, Belgium (2009).

[49] P. Betsch, F. Gruttmann, E. Stein, A 4-node finite shell element for the implementation of general hyperelastic 3D-elasticity at finite strains, Computer Methods in Applied Mechanics and Engineering 130 (1-2) (1996) 57–79. doi:10.1016/0045-7825(95)00920-5.

[50] K. Y. Sze, On immunizing five-beta hybrid-stress element models from 'trapezoidal locking' in practical analyses, International Journal for Numerical Methods in Engineering 47 (4) (2000) 907–920. doi:10.1002/(SICI)1097-0207(20000210)47:4<907::AID-NME808>3.0.CO;2-A.

[51] R. H. MacNeal, Finite Elements Their Design and Performance, Marcel Dekke, New York, 1993.

[52] T. J. R. Hughes, The finite element method: linear static and dynamic finite element analysis, Prentice-Hall, Englewood Cliffs, New Jersey, 1987.

[53] F. Brezzi, K.-J. Bathe, Studies of finite element procedures: The Inf-Sup condition equivalent, forms and applications, in: Reliability of Methods for Engineering Analysis, Swansea, U.K., 1986.

[54] R. J. Alves De Sousa, R. M. Natal Jorge, R. A. Fontes Valente, J. M. César De Sá, A new volumetric and shear locking-free 3D enhanced strain element, Engineering Computations (Swansea, Wales) 20 (7-8) (2003) 896–925. doi:10.1108/02644400310502036.

[55] E. Reissner, On the theory of bending of elastic plates, Journal of Mathematics and Physics 23 (1-4) (1944) 184–191. arXiv:https://onlinelibrary.wiley.com/doi/pdf/10.1002/sapm1944231184, doi:https://doi.org/10.1002/sapm1944231184.

[56] E. Reissner, The Effect of Transverse Shear Deformation on the Bending of Elastic Plates, Journal of Applied Mechanics 12 (2) (1945) A69–A77. doi:10.1115/1.4009435.

[57] R. D. Mindlin, Influence of Rotatory Inertia and Shear on Flexural Motions of Isotropic, Elastic Plates, Journal of Applied Mechanics 18 (1) (1951) 31–38. doi:10.1115/1.4010217.

[58] T. J. R. Hughes, T. E. Tezduyar, Finite Elements Based Upon Mindlin Plate Theory With Particular Reference to the Four-Node Bilinear Isoparametric Element, Journal of Applied Mechanics 48 (3) (1981) 587–596. doi:10.1115/1.3157679.

[59] W. Dornisch, S. Klinkel, B. Simeon, Isogeometric Reissner-Mindlin shell analysis with exactly calculated director vectors, Computer Methods in Applied Mechanics and Engineering 253 (2013) 491–504. doi:10.1016/j.cma.2012.09.010.

[60] C. Adam, T. J. R. Hughes, S. Bouabdallah, M. Zarroug, H. Maitournam, Selective and reduced numerical integrations for NURBS-based isogeometric analysis, Computer Methods in Applied Mechanics and Engineering 284 (2015) 732–761. doi:10.1016/j.cma.2014.11.001.

[61] D. J. Benson, Y. Bazilevs, M. C. Hsu, T. J. R. Hughes, Isogeometric shell analysis: The Reissner-Mindlin shell, Computer Methods in Applied Mechanics and Engineering 199 (2010) 276–289. doi:10.1016/j.cma.2009.05.011.

[62] L. Beirão Da Veiga, T. J. R. Hughes, J. Kiendl, C. Lovadina, J. Niiranen, A. Reali, H. Speleers, A locking-free model for Reissner-Mindlin plates: Analysis and isogeometric implementation via NURBS and triangular NURPS, Mathematical Models and Methods in Applied Sciences 25 (8) (2015) 1519–1551. doi:10.1142/S0218202515500402.

[63] A. E. H. Love, The small free vibrations and deformation of a thin elastic shell, Philosophical Transactions of the Royal Society of London. (A.) 179 (1888) 491–546. doi:10.1098/rsta.1888.0016.

[64] S. Timoshenko, S. Woinowsky-Krieger, Theory of plates and shells, 2nd Edition, McGraw-Hill, New York, 1959.

[65] J. Kiendl, K.-U. Bletzinger, J. Linhard, R. Wüchner, Isogeometric shell analysis with Kirchhoff-Love elements, Computer Methods in Applied Mechanics and Engineering 198 (49-52) (2009) 3902–3914. doi:10.1016/j.cma.2009.08.013.

[66] L. Leonetti, D. Magisano, A. Madeo, G. Garcea, J. Kiendl, A. Reali, A simplified Kirchhoff–Love large deformation model for elastic shells and its effective isogeometric formulation, Computer Methods in Applied Mechanics and Engineering 354 (2019) 369–396. doi:10.1016/j.cma.2019.05.025.

[67] J. Kiendl, M. C. Hsu, M. C. Wu, A. Reali, Isogeometric Kirchhoff-Love shell formulations for general hyperelastic materials, Computer Methods in Applied Mechanics and Engineering 291 (2015) 280–303. doi:10.1016/j.cma.2015.03.010.

[68] M. Ambati, J. Kiendl, L. De Lorenzis, Isogeometric KirchhoffLove shell formulation for elasto-plasticity, Computer Methods in Applied Mechanics and Engineering 340 (2018) 320–339. doi:10.1016/j.cma.2018.05.023.

[69] T. X. Duong, F. Roohbakhshan, R. A. Sauer, A new rotation-free isogeometric thin shell formulation and a corresponding continuity constraint for patch boundaries, Computer Methods in Applied Mechanics and Engineering 316 (2017) 43–83. doi:10.1016/j.cma.2016.04.008.

[70] H. T. Yang, S. Saigal, A. Masud, R. K. Kapania, A survey of recent shell finite elements, International Journal for Numerical Methods in Engineering 47 (1-3) (2000) 101–127. doi:10.1002/(SICI)1097-0207(20000110/30)47:1/3<101::AID-NME763>3.0.CO;2-C.

[71] H. T. Yang, S. Saigal, D. G. Liaw, Advances of thin shell finite elements and some applications-version I, Computers and Structures 35 (4) (1990) 481–504. doi:10.1016/0045-7949(90)90071-9.

[72] E. N. Dvorkin, K. J. Bathe, A continuum mechanics based four-node shell element for general nonlinear analysis, Engineering Computations 1 (1) (1984) 77–88. doi:10.1108/eb023562.

[73] P.-S. Lee, K.-J. Bathe, Development of MITC isotropic triangular shell finite elements, Computers & Structures 82 (11-12) (2004) 945–962. doi:10.1016/j.compstruc.2004.02.004.

[74] Y. Ko, P.-S. Lee, K.-J. Bathe, A new MITC4+ shell element, Computers & Structures 182 (2017) 404–418. doi:10.1016/j.compstruc.2016.11.004.

[75] Y. Ko, P.-S. Lee, K.-J. Bathe, A new 4-node MITC element for analysis of two-dimensional solids and its formulation in a shell element, Computers & Structures 192 (2017) 34–49. doi:10.1016/j.compstruc.2017.07.003.

[76] Y. Lee, P.-S. Lee, K.-J. Bathe, The MITC3+ shell element and its performance, Computers & Structures 138 (2014) 12–23. doi:10.1016/j.compstruc.2014.02.005.

[77] Y. Ko, Y. Lee, P.-S. Lee, K.-J. Bathe, Performance of the MITC3+ and MITC4+ shell elements in widely-used benchmark problems, Computers & Structures 193 (2017) 187–206. doi:10.1016/j.compstruc.2017.08.003.

[78] M. L. Bucalem, K.-J. Bathe, Higher-order MITC general shell elements, International Journal for Numerical Methods in Engineering 36 (21) (1993) 3729–3754. doi:10.1002/nme.1620362109.

[79] T. J. R. Hughes, W. K. Liu, Nonlinear finite element analysis of shells: Part I. three-dimensional shells, Computer Methods in Applied Mechanics and Engineering 26 (3) (1981) 331–362. doi:10.1016/0045-7825(81)90121-3.

[80] S. Ahmad, B. M. Irons, O. C. Zienkiewicz, Analysis of thick and thin shell structures by curved finite elements, International Journal for Numerical Methods in Engineering 2 (3) (1970) 419–451. doi:10.1002/nme.1620020310.

[81] N. Buechter, E. Ramm, Shell theory versus degenerationa comparison in large rotation finite element analysis, International Journal for Numerical Methods in Engineering 34 (1) (1992) 39–59. doi:10.1002/nme.1620340105.

[82] D. Marinković, H. Köppe, U. Gabbert, Degenerated shell element for geometrically nonlinear analysis of thin-walled piezoelectric active structures, Smart Materials and Structures 17 (1) (2008). doi:10.1088/0964-1726/17/01/015030.

[83] D. J. Naylor, Stresses in nearly incompressible materials by finite elements with application to the calculation of excess pore pressures, International Journal for Numerical Methods in Engineering 8 (3) (1974) 443–460. doi:10.1002/nme.1620080302.

[84] D. S. Malkus, T. J. R. Hughes, Mixed finite element methods - Reduced and selective integration techniques: A unification of concepts, Computer Methods in Applied Mechanics and Engineering 15 (1978) 63–81.

[85] T. J. R. Hughes, M. Cohen, M. Haroun, Reduced and selective integration techniques in the finite element analysis of plates, Nuclear Engineering and Design 46 (1) (1978) 203–222. doi:10.1016/0029-5493(78)90184-X.

[86] D. V. Griffiths, G. G. W. Mustoe, Selective reduced integration of four-node plane element in closed form, Journal of Engineering Mechanics 121 (6) (1995) 725–729. doi:10.1061/(ASCE)0733-9399(1995)121:6(725).

[87] S. Reese, On the Equivalent of Mixed Element Formulations and the Concept of Reduced Integration in Large Deformation Problems, International Journal of Nonlinear Sciences and Numerical Simulation 3 (1) (2002) 1–34. doi:10.1515/IJNSNS.2002.3.1.1.

[88] S. Reese, A large deformation solid-shell concept based on reduced integration with hourglass stabilization, International Journal for Numerical Methods in Engineering 69 (July) (2006) 1671–1716. arXiv:1010.1724, doi:10.1002/nme.

[89] E. D. L. Pugh, E. Hinton, O. C. Zienkiewicz, A study of quadrilateral plate bending elements with reduced' integration, International Journal for Numerical Methods in Engineering 12 (7) (1978) 1059–1079. doi:10.1002/nme.1620120702.

[90] T. Belytschko, C.-S. Tsay, A stabilization procedure for the quadrilateral plate element with one-point quadrature, International Journal for Numerical Methods in Engineering 19 (3) (1983) 405–419. doi:10.1002/nme.1620190308.

[91] G. Prathap, G. R. Bhashyam, Reduced integration and the shear-flexible beam element, International Journal for Numerical Methods in Engineering 18 (2) (1982) 195–210. doi:10.1002/nme.1620180205.

[92] Ted Belytschko, Bak Leong Wong, Huai-Yang Chiang, Advances in one-point quadrature shell elements, Computer Methods in Applied Mechanics and Engineering 96 (1) (1992) 93–107. doi:10.1016/0045-7825(92)90100-X.

[93] T. Belytschko, I. Leviathan, Physical stabilization of the 4-node shell element with one point quadrature, Computer Methods in Applied Mechanics and Engineering 113 (3-4) (1994) 321–350. doi:10.1016/0045-7825(94)90052-3.

[94] W. K. Liu, Y.-K. Hu, T. Belytschko, Multiple quadrature underintegrated finite elements, International Journal for Numerical Methods in Engineering 37 (19) (1994) 3263–3289. doi:10.1002/nme.1620371905.

[95] R. Hauptmann, K. Schweizerhof, A systematic development of 'solid-shell' element formulations for linear and non-linear analyses employing only displacement degrees of freedom, International Journal for Numerical Methods in Engineering 42 (1) (1998) 49–69. doi:10.1002/(SICI)1097-0207(19980515)42:1<49::AID-NME349>3.0.CO;2-2.

[96] K. Y. Sze, L. Q. Yao, A hybrid stress ANS solid-shell element and its generalization for smart structure modelling. Part I - Solid-shell element formulation, International Journal for Numerical Methods in Engineering 48 (4) (2000) 545–564. doi:10.1002/(SICI)1097-0207(20000610)48:4<545::AID-NME889>3.0.CO;2-6.

[97] J. C. Simo, T. J. R. Hughes, On the Variational Foundations of Assumed Strain Methods, Journal of Applied Mechanics 53 (1) (1986) 51–54. doi:10.1115/1.3171737.

[98] M. Schwarze, S. Reese, A reduced integration solid-shell finite element based on the EAS and the ANS concept-Geometrically linear problems, International Journal for Numerical Methods in Engineering 80 (10) (2009) 1322–1355. doi:10.1002/nme.2653.

[99] M. Schwarze, S. Reese, A reduced integration solid-shell finite element based on the EAS and the ANS concept-Large deformation problems, International Journal for Numerical Methods in Engineering 85 (3) (2011) 289–329. doi:10.1002/nme.2966.

[100] R. P. R. Cardoso, J. W. Yoon, M. Mahardika, S. Choudhry, R. J. Alves de Sousa, R. A. Fontes Valente, Enhanced assumed strain (EAS) and assumed natural strain (ANS) methods for one-point quadrature solid-shell elements, International Journal for Numerical Methods in Engineering 75 (2) (2008) 156–187. doi:10.1002/nme.2250.

[101] J. F. Caseiro, R. A. F. Valente, A. Reali, J. Kiendl, F. Auricchio, R. J. Alves de Sousa, On the Assumed Natural Strain method to alleviate locking in solid-shell NURBS-based finite elements, Computational Mechanics 53 (6) (2014) 1341–1353. doi:10.1007/s00466-014-0978-4.

[102] J. F. Caseiro, R. A. Valente, A. Reali, J. Kiendl, F. Auricchio, R. J. Alves de Sousa, Assumed natural strain NURBS-based solid-shell element for the analysis of large deformation elasto-plastic thin-shell structures, Computer Methods in Applied Mechanics and Engineering 284 (2015) 861–880. doi:10.1016/j.cma.2014.10.037.

[103] K. D. Kim, G. Z. Liu, S. C. Han, A resultant 8-node solid-shell element for geometrically nonlinear analysis, Computational Mechanics 35 (5) (2005) 315–331. doi:10.1007/s00466-004-0606-9.

[104] X. G. Tan, L. Vu-Quoc, Efficient and accurate multilayer solid-shell element: Non-linear materials at finite strain, International Journal for Numerical Methods in Engineering 63 (15) (2005) 2124–2170. doi:10.1002/nme.1360.

[105] C. Militello, C. A. Felippa, A variational justification of the assumed natural strain formulation of finite elements-II. The C0 four-node plate element, Computers and Structures 34 (3) (1990) 439–444. doi:10.1016/0045-7949(90)90268-7.

[106] C. Militello, C. A. Felippa, A variational justification of the assumed natural strain formulation of finite elements-I. Variational principles, Computers and Structures 34 (3) (1990) 431–438. doi:10.1016/0045-7949(90)90267-6.

[107] T. J. R. Hughes, Generalization of selective integration procedures to anisotropic and nonlinear media, International Journal for Numerical Methods in Engineering 15 (9) (1980) 1413–1418. doi:https://doi.org/10.1002/nme.1620150914.

[108] T. J. R. Hughes, Equivalence of finite elements for nearly incompressible elasticity, Journal of Applied Mechanics 44 (1) (1977) 181–183. doi:10.1115/1.3423994.

[109] D. P. Recio, R. M. Natal Jorge, L. M. Dinis, Locking and hourglass phenomena in an element-free Galerkin context: The B-bar method with stabilization and an enhanced strain method, International Journal for Numerical Methods in Engineering 68 (13) (2006) 1329–1357. doi:10.1002/nme.1741.

[110] T. Elguedj, Y. Bazilevs, V. M. Calo, T. J. R. Hughes, $\bar{\mathrm{B}}$ and $\bar{\mathrm{F}}$ bar projection methods for nearly incompressible linear and non-linear elasticity and plasticity using higher-order NURBS elements, Computer Methods in Applied Mechanics and Engineering 197 (33-40) (2008) 2732–2762. doi:10.1016/j.cma.2008.01.012.

[111] E. A. De Souza Neto, D. Perić, M. Dutko, D. R. Owen, Design of simple low order finite elements for large strain analysis of nearly incompressible solids, International Journal of Solids and Structures 33 (20-22) (1996) 3277–3296. doi:10.1016/0020-7683(95)00259-6.

[112] E. A. De Souza Neto, F. M. Andrade Pires, D. R. Owen, F-bar-based linear triangles and tetrahedra for finite strain analysis of nearly incompressible solids. Part I: Formulation and benchmarking, International Journal for Numerical Methods in Engineering 62 (3) (2005) 353–383. doi:10.1002/nme.1187.

[113] T. H. T. Elguedj, Y. Bazilevs, V.M. Calo, F-bar Projection Method for Finite Deformation Elasticity and Plasticity using NURBS based Isogeometric Analysis T., International Journal of Material Forming 1 (2008) 1091–1094. doi:10.1007/s12289-008-0.

[114] O. C. Zienkiewicz, Displacement and equilibrium models in the finite element method by B. Fraeijs de Veubeke, Chapter 9, Pages 145197 of Stress Analysis, Edited by O. C. Zienkiewicz and G. S. Holister, Published by John Wiley & Sons, 1965, International Journal for Numerical Methods in Engineering 52 (3) (2001) 287–342. doi:10.1002/nme.339.

[115] L. R. Herrmann, Elasticity equations for incompressible and nearly incompressible materials by a variational theorem., AIAA Journal 3 (10) (1965) 1896–1900. doi:10.2514/3.3277.

[116] D. N. Arnold, F. Brezzi, M. Fortin, A stable finite element for the stokes equations, Calcolo 21 (4) (1984) 337–344. doi:10.1007/BF02576171.

[117] T. Sussman, K. J. Bathe, A finite element formulation for nonlinear incompressible elastic and inelastic analysis, Computers and Structures 26 (1-2) (1987) 357–409. doi:10.1016/0045-7949(87)90265-3.

[118] M. Chiumenti, Q. Valverde, C. Agelet De Saracibar, M. Cervera, A stabilized formulation for incompressible elasticity using linear displacement and pressure interpolations, Computer Methods in Applied Mechanics and Engineering 191 (46) (2002) 5253–5264. doi:10.1016/S0045-7825(02)00443-7.

[119] M. Pastor, M. Quecedo, O. C. Zienkiewicz, A mixed displacement-pressure formulation for numerical analysis of plastic failure, Computers and Structures 62 (1) (1997) 13–23. doi:10.1016/S0045-7949(96)00208-8.

[120] O. C. Zienkiewicz, R. L. Taylor, Finite Element Method: Volume 1 - The Basis, 5th Edition, Butterworth-Heinemann, Oxford, United Kingdom, 2000.

[121] D. Roehl, E. Ramm, Large elasto-plastic finite element analysis of solids and shells with the enhanced assumed strain concept, International Journal of Solids and Structures 33 (20-22) (1996) 3215–3237. doi:10.1016/0020-7683(95)00246-4.

[122] J. Korelc, P. Wriggers, An efficient 3D enhanced strain element with Taylor expansion of the shape functions, Computational Mechanics 19 (1) (1996) 30–40.

[123] J. C. Simo, M. S. Rifai, A class of mixed assumed strain methods and the method of incompatible modes, International Journal for Numerical Methods in Engineering 29 (8) (1990) 1595–1638. doi:10.1002/nme.1620290802.

[124] J. C. Simo, F. Armero, Geometrically non-linear enhanced strain mixed methods and the method of incompatible modes, International Journal for Numerical Methods in Engineering 33 (7) (1992) 1413–1449. doi:10.1002/nme.1620330705.

[125] U. Andelfinger, E. Ramm, EAS-elements for two-dimensional, three-dimensional, plate and shell structures and their equivalence to HR-elements, International Journal for Numerical Methods in Engineering 36 (8) (1993) 1311–1337. doi:10.1002/nme.1620360805.

[126] M. Bischoff, E. Ramm, D. Braess, A class of equivalent enhanced assumed strain and hybrid stress finite elements, Computational Mechanics 22 (6) (1999) 443–449. doi:10.1007/s004660050378.

[127] J. Korelc, U. Šolinc, P. Wriggers, An improved EAS brick element for finite deformation, Computational Mechanics 46 (4) (2010) 641–659. doi:10.1007/s00466-010-0506-0.

[128] R. J. Alves de Sousa, R. P. Cardoso, R. A. Fontes Valente, J. W. Yoon, J. J. Grácio, R. M. Natal Jorge, A new one-point quadrature enhanced assumed strain (EAS) solid-shell element with multiple integration points along thickness: Part I - Geometrically linear applications, International Journal for Numerical Methods in Engineering 62 (7) (2005) 952–977. doi:10.1002/nme.1226.

[129] R. J. Alves de Sousa, R. P. Cardoso, R. A. Fontes Valente, J. W. Yoon, J. J. Grácio, R. M. Natal Jorge, A new one-point quadrature enhanced assumed strain (EAS) solid-shell element with multiple integration points along thickness - Part II: Nonlinear applications, International Journal for Numerical Methods in Engineering 67 (2) (2006) 160–188. doi:10.1002/nme.1609.

[130] R. A. Valente, R. J. De Sousa, R. M. Jorge, An enhanced strain 3D element for large deformation elastoplastic thin-shell applications, Computational Mechanics 34 (1) (2004) 38–52. doi:10.1007/s00466-004-0551-7.

[131] R. A. Fontes Valente, R. M. Natal Jorge, R. P. Cardoso, J. M. César de Sá, J. J. Grácio, On the use of an enhanced transverse shear strain shell element for problems involving large rotations, Computational Mechanics 30 (4) (2003) 286–296. doi:10.1007/s00466-002-0388-x.

[132] E. P. Kasper, R. L. Taylor, Mixed-enhanced strain method. Part I: Geometrically linear problems, Computers and Structures 75 (3) (2000) 237–250. doi:10.1016/S0045-7949(99)00134-0.

[133] R. Piltner, An implementation of mixed enhanced finite elements with strains assumed in Cartesian and natural element coordinates using sparse B-matrices, Engineering Computations (Swansea, Wales) 17 (8) (2000) 933–949. doi:10.1108/02644400010379776.

[134] J. M. De César Sá, R. M. Natal Jorge, R. A. Fontes Valente, P. M. Almeida Areias, Development of shear locking-free shell elements using an enhanced assumed strain formulation, International Journal for Numerical Methods in Engineering 53 (7) (2002) 1721–1750. doi:10.1002/nme.360.

[135] R. P. R. Cardoso, J. M. A. Cesar de Sa, The enhanced assumed strain method for the isogeometric analysis of nearly incompressible deformation of solids, International Journal for Numerical Methods in Engineering 92 (1) (2012) 56–78. doi:10.1002/nme.4328.

[136] T. H. H. Pian, K. Sumihara, Rational approach for assumed stress finite elements, International Journal for Numerical Methods in Engineering 20 (9) (1984) 1685–1695. doi:10.1002/nme.1620200911.

[137] H. Stolarski, T. Belytschko, On the equivalence of mode decomposition and mixed finite elements based on the hellinger-reissner principle. part I: Theory, Computer Methods in Applied Mechanics and Engineering 58 (3) (1986) 249–263. doi:10.1016/0045-7825(86)90149-0.

[138] J. G. Kim, Y. Y. Kim, A new higher-order hybrid-mixed curved beam element, International Journal for Numerical Methods in Engineering 43 (5) (1998) 925–940. doi:10.1002/(SICI)1097-0207(19981115)43:5<925::AID-NME457>3.0.CO;2-M.

[139] Y. Lee, K. Yoon, P. S. Lee, Improving the MITC3 shell finite element by using the Hellinger-Reissner principle, Computers and Structures 110-111 (2012) 93–106. doi:10.1016/j.compstruc.2012.07.004.

[140] Z. Zou, M. A. Scott, D. Miao, M. Bischoff, B. Oesterle, W. Dornisch, An isogeometric Reissner-Mindlin shell element based on Bézier dual basis functions: Overcoming locking and improved coarse mesh accuracy, Computer Methods in Applied Mechanics and Engineering 370 (2020) 113283. doi:10.1016/j.cma.2020.113283.

[141] C. S. Jog, A 27-node hybrid brick and a 21-node hybrid wedge element for structural analysis, Finite Elements in Analysis and Design 41 (11-12) (2005) 1209–1232. doi:10.1016/j.finel.2004.11.007.

[142] C. S. Jog, Improved hybrid elements for structural analysis, Journal of Mechanics of Materials and Structures 5 (2010) 507–528.

[143] D. S. Bombarde, M. Agrawal, S. S. Gautam, A. Nandy, Hellinger–Reissner principle based stress-displacement formulation for three-dimensional isogeometric analysis in linear elasticity, Computer Methods in Applied Mechanics and Engineering 394:114920 (2022). doi:10.1016/j.cma.2022.114920.

[144] D. Magisano, L. Leonetti, G. Garcea, Isogeometric analysis of 3D beams for arbitrarily large rotations: Locking-free and path-independent solution without displacement DOFs inside the patch, Computer Methods in Applied Mechanics and Engineering 373 (2021) 113437. doi:10.1016/j.cma.2020.113437.

[145] L. Greco, M. Cuomo, An isogeometric implicit G1 mixed finite element for Kirchhoff space rods, Computer Methods in Applied Mechanics and Engineering 298 (2016) 325–349. doi:10.1016/j.cma.2015.06.014.

[146] R. Echter, Isogeometric Analysis of Shells, Ph.D. thesis, University of Stuttgart (2013).

[147] C. S. Jog, A. Nandy, Conservation properties of the trapezoidal rule in linear time domain analysis of acoustics and structures, Journal of Vibration and Acoustics, Transactions of the ASME 137 (2) (2015) 021010. doi:10.1115/1.4029075.

[148] M. Agrawal, A. Nandy, C. S. Jog, A hybrid finite element formulation for large-deformation contact mechanics, Computer Methods in Applied Mechanics and Engineering 356 (2019) 407–434. doi:10.1016/j.cma.2019.07.017.

[149] A. Roychowdhury, A. Nandy, C. S. Jog, R. Pratap, Hybrid elements for modelling squeeze film effects coupled with structural interactions in vibratory mems devices, Computer Modeling in Engineering & Sciences 103 (2) (2014) 91–110. doi:10.3970/cmes.2014.103.091.

[150] M. Agrawal, C. S. Jog, Monolithic formulation of electromechanical systems within the context of hybrid finite elements, Computational Mechanics 59 (3) (2017) 443–457. doi:10.1007/s00466-016-1356-1.

[151] C. S. Jog, A. Nandy, Mixed finite elements for electromagnetic analysis, Computers and Mathematics with Applications 68 (8) (2014) 887–902. doi:10.1016/j.camwa.2014.08.006.

[152] D. S. Bombarde, S. S. Gautam, A. Nandy, A novel hybrid isogeometric element based on two-field Hellinger–Reissner principle to alleviate different types of lockingy, Sadhana 47:148 (2022). doi:10.1007/s12046-022-01867-6.

[153] D. S. Bombarde, A. Nandy, S. S. Gautam, A two-field formulation in isogeometric analysis to alleviate locking, in: P. Joshi, S. S. Gupta, A. K. Shukla, S. S. Gautam (Eds.), Advances in Engineering Design, Springer Singapore, Singapore, 2021, pp. 191–199.

[154] D. S. Bombarde, M. Agrawal, S. S. Gautam, A. Nandy, A locking-free formulation for three-dimensional isogeometric analysis, Materials Today: Proceedings 66 (2022) 1710–1715, 2022 In-

ternational Conference on Recent Advances in Engineering Materials. doi:https://doi.org/10.1016/j.matpr.2022.05.266.

[155] L. Beirão da Veiga, A. Buffa, C. Lovadina, M. Martinelli, G. Sangalli, An isogeometric method for the Reissner-Mindlin plate bending problem, Computer Methods in Applied Mechanics and Engineering 209-212 (2012) 45–53. doi:10.1016/j.cma.2011.10.009.

[156] D. J. Benson, Y. Bazilevs, M.-C. Hsu, T. J. R. Hughes, A large deformation, rotation-free, isogeometric shell, Computer Methods in Applied Mechanics and Engineering 200 (13-16) (2011) 1367–1378. doi:10.1016/j.cma.2010.12.003.

[157] S. Hosseini, J. J. C. Remmers, C. V. Verhoosel, R. de Borst, An isogeometric solid-like shell element for nonlinear analysis, International Journal for Numerical Methods in Engineering 95 (3) (2013) 238–256. doi:10.1002/nme.4505.

[158] A. Combescure, R. Bouclier, T. Elguedj, On the development of NURBS-based isogeometric solid shell elements : 2D problems and preliminary extension to 3D, Computational Mechanics 52 (2013) 1085–1112. doi:10.1007/s00466-013-0865-4.

[159] T. J. R. Hughes, A. Reali, G. Sangalli, Efficient quadrature for NURBS-based isogeometric analysis, Computer Methods in Applied Mechanics and Engineering 199 (5-8) (2010) 301–313. doi:10.1016/j.cma.2008.12.004.

[160] G. Zhang, R. Alberdi, K. Khandelwal, On the locking free isogeometric formulations for 3-D curved Timoshenko beams, Finite Elements in Analysis and Design 143 (2018) 46–65. doi:10.1016/j.finel.2018.01.007.

[161] C. Kadapa, W. G. Dettmer, D. Perić, Subdivision based mixed methods for isogeometric analysis of linear and nonlinear nearly incompressible materials, Computer Methods in Applied Mechanics and Engineering 305 (2016) 241–270. doi:10.1016/j.cma.2016.03.013.

[162] R. L. Taylor, Isogeometric analysis of nearly incompressible solids, International Journal for Numerical Methods in Engineering 87 (2011) 273–288. doi:10.1002/nme.3048.

[163] T. C. Gmür, A. M. Schorderet, A set of three-dimensional solid to shell transition elements for structural dynamics, Computers and Structures 46 (4) (1993) 583–591. doi:10.1016/0045-7949(93)90387-S.

[164] G. M. Kulikov, S. V. Plotnikova, Assumed Stress-Strain Quadrilateral Plate Elements based on Analytical and Numerical Integration, Transactions TSTU 12 (2006) 107–121.

[165] J. C. Simo, F. Armero, R. L. Taylor, Improved versions of assumed enhanced strain tri-linear elements for 3D finite deformation problems, Computer Methods in Applied Mechanics and Engineering 110 (3-4) (1993) 359–386. doi:10.1016/0045-7825(93)90215-J.

[166] C. Freischläger, K. Schweizerhof, On a systematic development of trilinear three-dimensional solid elements based on Simo's enhanced strain formulation, International Journal of Solids and Structures 33 (20-22) (1996) 2993–3017. doi:10.1016/0020-7683(95)00251-0.

[167] S. Klinkel, W. Wagner, A geometrical non-linear brick element based on the EAS-method, International Journal for Numerical Methods in Engineering 40 (24) (1997) 4529–4545. doi:10.1002/(SICI)1097-0207(19971230)40:24<4529::AID-NME271>3.0.CO;2-I.

[168] M. Bischoff, E. Ramm, Shear deformable shell elements for large strains and rotations, International Journal for Numerical Methods in Engineering 40 (23) (1997) 4427–4449. doi:10.1002/(SICI)1097-0207(19971215)40:23<4427::AID-NME268>3.0.CO;2-9.

[169] S. P. Timoshenko, J. N. Goodier, Theory of elasticity, Engineering societies monographs, McGraw-Hill Education (India) Pvt Limited, 2010.

[170] R. D. Cook, Improved two-dimensional finite element, Journal of the Structural Division 100 (9) (1974) 1851–1863. doi:10.1061/JSDEAG.0003877.

[171] K. B. Nakshatrala, A. Masud, K. D. Hjelmstad, On finite element formulations for nearly incompressible linear elasticity, Computational Mechanics 41 (4) (2008) 547–561. doi:10.1007/s00466-007-0212-8.

[172] R. L. Taylor, P. J. Beresford, E. L. Wilson, A non-conforming element for stress analysis, International Journal for Numerical Methods in Engineering 10 (6) (1976) 1211–1219. doi:https://doi.org/10.1002/nme.1620100602.

[173] J. Dolbow, T. Belytschko, Volumetric locking in the element free Galerkin method, International Journal for Numerical Methods in Engineering 46 (6) (1999) 925–942. doi:10.1002/(SICI)1097-0207(19991030)46:6<925::AID-NME729>3.0.CO;2-Y.

[174] A. Huerta, S. Fernández-Méndez, Locking in the incompressible limit for the elementfree Galerkin method, International Journal for Numerical Methods in Engineering 51 (11) (2001) 1361–1383. doi:10.1002/nme.213.

[175] C. Scordelis, K. S. Lo, Computer Analysis of Cylindrical Shells, ACI Journal Proceedings 61 (5) (1964) 539–562. doi:10.14359/7796.

[176] C. Kadapa, Mixed Galerkin and Least-Squares formulations for Isogeometric analysis, Ph.D. thesis, Swansea University (2014). doi:10.13140/2.1.1546.1442.

[177] H. Stolarski, T. Belytschko, Limitation principles for mixed finite elements based on the Hu-Washizu variational formulation, Computer Methods in Applied Mechanics and Engineering 60 (2) (1987) 195–216. doi:10.1016/0045-7825(87)90109-5.

[178] S. T. Yeo, B. C. Lee, Equivalence between enhanced assumed strain method and assumed stress hybrid method based on the hellinger-reissner principle, International Journal for Numerical Methods in Engineering 39 (18) (1996) 3083–3099. doi:10.1002/(SICI)1097-0207(19960930)39:18<3083::AID-NME996>3.0.CO;2-F.

[179] M. Dabrowski, M. Krotkiewski, D. W. Schmid, MILAMIN: MATLAB-based finite element method solver for large problems, Geochemistry, Geophysics, Geosystems 9 (4) (2008) 1–24. doi:10.1029/2007GC001719.

[180] T. H. Pian, P. Tong, Relations between incompatible displacement model and hybrid stress model, International Journal for Numerical Methods in Engineering 22 (1) (1986) 173–181. doi:10.1002/nme.1620220112.

[181] Y. Ko, K.-J. Bathe, A new 8-node element for analysis of three-dimensional solids, Computers & Structures 202 (2018) 85–104. doi:10.1016/j.compstruc.2018.02.015.

[182] D. F. Rogers, An Introduction to NURBS: With Historical Perspective, Morgan Kaufmann Publishers Inc., San Francisco, CA, USA, 2001.

[183] R. Echter, M. Bischoff, Numerical efficiency, locking and unlocking of NURBS finite elements, Computer Methods in Applied Mechanics and Engineering 199 (5-8) (2010) 374–382. doi:10.1016/j.cma.2009.02.035.

[184] S. Reese, P. Wriggers, A stabilization technique to avoid hourglassing in finite elasticity, International Journal for Numerical Methods in Engineering 48 (1) (2000) 79–109. doi:10.1002/(SICI)1097-0207(20000510)48:1<79::AID-NME869>3.0.CO;2-D.

[185] S. W. Lee, J. J. Rhiu, A new efficient approach to the formulation of mixed finite element models for structural analysis, International Journal for Numerical Methods in Engineering 23 (9) (1986) 1629–1641. doi:10.1002/nme.1620230905.

[186] J. J. Rhiu, S. W. Lee, A new efficient mixed formulation for thin shell finite element models, International Journal for Numerical Methods in Engineering 24 (3) (1987) 581–604. doi:10.1002/nme.1620240309.

[187] K. Y. Sze, A novel approach for devising higher-order hybrid elements, International Journal for Numerical Methods in Engineering 36 (19) (1993) 3303–3316. doi:10.1002/nme.1620361907.

[188] J. M. César De Sá, R. M. Natal Jorge, New enhanced strain elements for incompressible problems, International Journal for Numerical Methods in Engineering 44 (2) (1999) 229–248. doi:10.1002/(SICI)1097-0207(19990120)44:2<229::AID-NME503>3.0.CO;2-I.

[189] M. Golestanian, H. Casquero, Extending CAS elements to remove shear and membrane locking from quadratic NURBS-based discretizations oflinear plane Timoshenko rods, International Journal for Numerical Methods in Engineering (September 2022) (2023) 1–25. doi:10.1002/nme.7257.

[190] R. Bouclier, T. Elguedj, A. Combescure, An isogeometric locking-free NURBS-based solid-shell element for geometrically nonlinear analysis, International Journal for Numerical Methods in Engineering 101 (10) (2015) 774–808. doi:10.1002/nme.4834.

[191] A. Back, A. Crestetto, A. Ratnani, E. Sonnendrücker, An axisymmetric PIC code based on isogeometric analysis, ESAIM: Proceedings 32 (October) (2011) 118–133. doi:10.1051/proc/2011016.

[192] A. Simona, L. Bonaventura, C. de Falco, S. Schöps, IsoGeometric approximations for electromagnetic problems in axisymmetric domains, Computer Methods in Applied Mechanics and Engineering 369 (2020) 113211. doi:10.1016/j.cma.2020.113211.

[193] Q. Zang, J. Liu, L. Lu, G. Lin, A NURBS-based isogeometric boundary element method for analysis of liquid sloshing in axisymmetric tanks with various porous baffles, European Journal of Mechanics - B/Fluids 81 (2020) 129–150. doi:10.1016/j.euromechflu.2020.01.010.

[194] Q. Zang, J. Liu, W. Ye, G. Lin, Isogeometric boundary element method for axisymmetric steady-state heat transfer, Engineering Analysis with Boundary Elements 160 (August 2023) (2024) 89–105. doi:10.1016/j.enganabound.2023.12.030.

[195] A. M. Shaaban, C. Anitescu, E. Atroshchenko, T. Rabczuk, Isogeometric boundary element analysis and shape optimization by PSO for 3D axi-symmetric high frequency Helmholtz acoustic problems, Journal of Sound and Vibration 486 (2020) 115598. doi:10.1016/j.jsv.2020.115598.

[196] T. Rückwald, A. Held, R. Seifried, Flexible multibody impact simulations based on the isogeometric analysis approach, Multibody System Dynamics 54 (1) (2022) 75–95. doi:10.1007/s11044-021-09804-x.

[197] Y. Bazilevs, C. Long, I. Akkerman, D. Benson, M. Shashkov, Isogeometric analysis of Lagrangian hydrodynamics: Axisymmetric formulation in the rz-cylindrical coordinates, Journal of Computational Physics 262 (2014) 244–261. doi:10.1016/j.jcp.2014.01.001.

[198] A. F. Saleeb, T. Y. Chang, W. Graf, A quadrilateral shell element using a mixed formulation, Computers and Structures 26 (5) (1987) 787–803. doi:10.1016/0045-7949(87)90028-9.

[199] A. Madeo, F. S. Liguori, G. Zucco, S. Fiore, An efficient isostatic mixed shell element for coarse mesh solution, International Journal for Numerical Methods in Engineering 122 (1) (2021) 82–121. doi:10.1002/nme.6526.

[200] C. S. Jog, P. P. Kelkar, Non-linear analysis of structures using high performance hybrid elements, International Journal for Numerical Methods in Engineering 68 (4) (2006) 473–501. doi:10.1002/nme.1725.

[201] A. Buffa, R. Vázquez, Isogeometric analysis for electromagnetic scattering problems, 2014 International Conference on Numerical Electromagnetic Modeling and Optimization for RF, Microwave, and Terahertz Applications, NEMO 2014 46 (8) (2014) 3305–3308. doi:10.1109/NEMO.2014.6995712.

[202] Z. Bontinck, J. Corno, H. De Gersem, S. Kurz, A. Pels, S. Schöps, F. Wolf, C. de Falco, J. Dölz, R. Vázquez, U. Römer, Recent Advances of Isogeometric Analysis in Computational Electromagnetics (sep 2017). arXiv:1709.06004.

[203] A. Buffa, G. Sangalli, R. Vázquez, Isogeometric analysis in electromagnetics: B-splines approximation, Computer Methods in Applied Mechanics and Engineering 199 (17-20) (2010) 1143–1152. doi:10.1016/j.cma.2009.12.002.

[204] D. Kamensky, M. C. Hsu, D. Schillinger, J. A. Evans, A. Aggarwal, Y. Bazilevs, M. S. Sacks, T. J. Hughes, An immersogeometric variational framework for fluid-structure interaction: Application to bioprosthetic heart valves, Computer Methods in Applied Mechanics and Engineering 284 (2015) (2015) 1005–1053. doi:10.1016/j.cma.2014.10.040.

[205] A. Krishnamurthy, M. J. Gonzales, G. Sturgeon, W. P. Segars, A. D. McCulloch, Biomechanics simulations using cubic Hermite meshes with extraordinary nodes for isogeometric cardiac modeling, Computer Aided Geometric Design 43 (2016) 27–38. doi:10.1016/j.cagd.2016.02.016.

[206] S. Morganti, F. Auricchio, D. J. Benson, F. I. Gambarin, S. Hartmann, T. J. Hughes, A. Reali, Patient-specific isogeometric structural analysis of aortic valve closure, Computer Methods in Applied Mechanics and Engineering 284 (2015) 508–520. doi:10.1016/j.cma.2014.10.010.

[207] Y. Bazilevs, V. M. Calo, Y. Zhang, T. J. Hughes, Isogeometric fluid-structure interaction analysis with applications to arterial blood flow, Computational Mechanics 38 (4-5) (2006) 310–322. doi:10.1007/s00466-006-0084-3.

[208] R. Willems, K. L. Janssens, P. H. Bovendeerd, C. V. Verhoosel, O. van der Sluis, An isogeometric analysis framework for ventricular cardiac mechanics, Computational Mechanics (2023). doi:10.1007/s00466-023-02376-x.

[209] D. Kamensky, M. C. Hsu, Y. Yu, J. A. Evans, M. S. Sacks, T. J. Hughes, Immersogeometric cardiovascular fluidstructure interaction analysis with divergence-conforming B-splines, Computer Methods in Applied Mechanics and Engineering 314 (2017) (2017) 408–472. doi:10.1016/j.cma.2016.07.028.

[210] A. B. Tepole, H. Kabaria, K. U. Bletzinger, E. Kuhl, Isogeometric Kirchhoff-Love shell formulations for biological membranes, Computer Methods in Applied Mechanics and Engineering 293 (2015) 328–347. doi:10.1016/j.cma.2015.05.006.

[211] L. Leonetti, D. Magisano, A. Madeo, G. Garcea, J. Kiendl, A. Reali, A simplified KirchhoffLove large deformation model for elastic shells and its effective isogeometric formulation, Computer Methods in Applied Mechanics and Engineering 354 (2019) 369–396. doi:10.1016/j.cma.2019.05.025.

[212] A. Bijalwan, B. P. Patel, M. Marieswaran, D. Kalyanasundaram, Volumetric locking free 3D finite element for modelling of anisotropic visco-hyperelastic behaviour of anterior cruciate ligament, Journal of Biomechanics 73 (2018) 1–8. doi:10.1016/j.jbiomech.2018.03.016.

[213] D. Spink, NURBS toolbox by D.M. Spink (2020).
URL https://www.mathworks.com/matlabcentral/fileexchange/26390-nurbs-toolbox-by-d-m-spink